Photophysical and Catalytic Properties of Multicomponent Metal-Organic Frameworks

A thesis presented in partial fulfilment of the requirements for the degree of

Doctor of Philosophy

in

Chemistry

at Massey University, Manawatū, New Zealand

JOEL CORNELIO

2021

To everyone who’s been mocked for their dreams,

This one’s for you...! Dream on...!

Abstract

Multicomponent metal-organic frameworks (MC-MOFs) are crystalline, porous materials built from multiple geometrically distinct organic ligands. The ligands are located in specific lattice sites in the MOF. The properties of these materials can be tuned by incorporating ligands with functional groups for a desired application. This thesis deals with studying the applications of MC-MOFs named Massey University Frameworks (MUFs) for luminescence, energy transfer, photochromism, and catalysis.

Firstly, we obtain white-light emission in MC-MOFs from the combination of blue and yellow luminescence of the ligands. The trends observed in the emission spectra originate from inter-ligand energy transfer interactions. These interactions have been explored further using a variety of crystallographic and spectroscopic techniques including time-resolved luminescence at the nanosecond and picosecond timescales. In another chapter, we have studied photochromism in some MC-MOFs which is caused by light-generated organic radicals. The differences between their radical and non-radical forms has been elucidated using X-ray crystallography. We also research the impact of pore environment on the outcome of an enantioselective intramolecular aldol reaction catalysed by MC-MOFs. Finally, a number of ideas are proposed as part of future work, that take advantage of the multicomponent nature of these materials.

.

Contributions

All the work in this thesis was completed by Joel Cornelio

Except:

- Synthesis of H_2gua in Chapter 2 was first done by Dr. Tian-You Zhou.
- For Chapter 3, Time-correlated single photon counting (TCSPC) was performed by Joel Cornelio in collaboration with Dr. Nathaniel Davis and Dr. Michael Price at Victoria University, Wellington.
- Transient Grating Photoluminescence Spectroscopy (TGPLS) was done in collaboration with Isabella Wagner, Dr. Kai Chen and Prof. Justin Hodgkiss at Victoria University, Wellington.
- Synthesis of H_2bdc-dpq in Chapter 4 and H_2bpdc-guanidine in Chapter 5 was first done by Dr. Tian-You Zhou.
- Electron Paramagnetic Resonance Spectroscopy presented in Chapter 4 was performed by Kavipriya T. and Prof. Andreas Pöppl at Leipzig University, Germany.
- UV-Visible spectra of MUF-77 suspensions presented in Chapter 4 were recorded by Joel Cornelio in collaboration with Johann Grand, Dr. Geoffry Laufersky and Prof. Eric Le Ru at Victoria University, Wellington.
- Seok-June Lee and Dr. Adil Alkaş aided with the SCXRD analyses presented in Chapter 4.
- All HRMS-ESI was measured by David Lun.
- All SEM images were collected by staff at the Mananwatū Microscopy and Imaging Centre (MMIC).

Acknowledgements

It’s been a crazy journey of nearly four years during this Ph.D. Firstly, I would like to thank my supervisor, Prof. Shane Telfer for choosing me to work in his lab and for his guidance. Thank you for your support and motivation throughout this journey. Thank you also for encouraging me to research on the many aspects of these wonderful materials called MOFs, especially on their spectroscopic and catalytic side.

I would also like to thank my co-supervisor, Assoc. Prof. Gareth Rowlands for his support, especially on matters related to organic chemistry. Special thanks go to Dr. Tian-You Zhou who helped me in the first two years of my Ph.D. He cultivated a lot of ideas, helped me in the lab and was patient enough to deal with my weirdness. I also thank my other colleagues for their help, Dr. Adil Alkaş (for help with chemistry and for company), Seok-June Lee (for crystallography), Dr. David Perl, Dr. Omid Taheri, Dr. Heather Jameson, Dr. Maulik Mungalpara, Bernhard Auer, Nisansala Bandara, Yiming Zhang, and Victoria-Jayne Reid. David Lun has been constantly helpful for a variety of analytical techniques.

My gratitude goes to the students and staff who have collaborated with me in this research. This includes Isabella Wagner, Dr. Kai Chen and Prof. Justin Hodgkiss of VUW, who helped me with ultrafast spectroscopy, Dr. Nate Davis and Dr. Michael Price helped with TCSPC. Thank you, Johann Grand, Dr. Geoff Laufersky, and Prof. Eric Le Ru for the UV-Vis spectra of MUF-77 suspensions. Both these collaborations are a result of the wider network of the MacDiarmid Institute, to which I am thankful. Prof. Andreas Pöppl deserves a special mention for being so enthusiastic about collecting EPR data for me and also for giving me an opportunity to present my work at Leipzig University.

I wish to thank the administration of SFS, for paying my student fees, and for the Marsden grant which paid my stipend. Other funding opportunities include the SFS travel grant, Massey University Conference Presentation Grants to participate in the EuroMOF-2019 conference, for which I am ever grateful.

I had a lot of support and guidance in things other than chemistry from my flatmates, Dr. Chanjief Chandrakumar, Dr. Nikhil Srivastava (thanks for your car), and Dr. Maulik Mungalpara. It was wonderful time cooking and baking together and going on many trips in beautiful Aotearoa.

On a more personal note, my parents and brother have been of constant support to me. Their prayers and blessings have kept me going. Finally, I would like to thank my wife, Aviva for sticking with me all these years. This Ph.D. journey is finally over and I will be with you… soon!

Publications and thesis structure

Publications relevant to this thesis:

1) **Cornelio, J.**; Zhou, T.-Y.; Alkaş, A.; Telfer, S. G. Systematic Tuning of the Luminescence Output of Multicomponent Metal–Organic Frameworks, *J. Am. Chem. Soc.* **2018,** *140*, 15470.
2) **Cornelio, J.** Luminescence in Metal-Organic Frameworks: Origin and Applications, *Chem. N.Z.* **2019,** *83*, 30.

Additional publications

1) Alkaş, A.; **Cornelio, J**.; Telfer, S.G.; Tritopic Triazatruxene Ligands for Multicomponent Metal-Organic Frameworks, *Chem. Asian J.* **2019**, *14*, 1167.
2) Guan, H,; Li, J.; Zhou, T-Y.; Pang, Z.; Fu, Y.; **Cornelio, J**.; Wang, Q.; Telfer, S. G.; Kong, X.; Probing Nonuniform Adsorption in Multicomponent Metal–Organic Frameworks via Segmental Dynamics by Solid-State Nuclear Magnetic Resonance. *J. Phys. Chem. Lett.* **2020**, *11*, 7176.

List of Abbreviations:

ACN	Acetonitrile
BET	Brunauer-Emmet-Teller
CT	Charge Transfer
COF	Covalent Organic Framework
D-A	Donor-Acceptor
DBF	*N*,*N*-dibutylformamide
DCM	Dichloromethane
DEF	*N*,*N*-diethylformamide
DET	Dexter Electron Transfer
DMF	*N*,*N*-dimethylformamide
DMSO	dimethyl sulfoxide
d.r.	diastereomeric ratio
esd	experimental standard deviation
ee	enantiomeric excess
ENDOR	Electron Nuclear Double Resonance
EPR	Electron Paramagnetic Resonance
ESEEM	Electron Spin Echo Envelope Modulation
ESPT	Excited State Proton Transfer
FDM	Fudan Material
FRET	Förster Resonance Energy Transfer
FSRS	Femtosecond Stimulated Raman Spectroscopy
HKUST	Hong Kong University of Science and Technology
HYSCORE	Hyperfine Structure Correlation
ILCT	Inter-Ligand Charge Transfer
irf	Instrument Response Function
IRMOF	Isoreticular Metal-Organic Framework
IUPAC	International Union of Pure and Applied Chemistry
JBNN	Jumping Beyond Nearest Neighbour
LMCT	Ligand-to-Metal Charge Transfer
MC-MOF	Multicomponent Metal-Organic Framework
MIL	Matérial Institut Lavoisier
MLCT	Metal-To-Ligand Charge Transfer
MOF	Metal-Organic Framework
MTV	Multivariate
MUF	Massey University Framework

NMR	Nuclear Magnetic Resonance
PCN	Porous Coordination Network
PSM	Post-Synthetic Modification
PXRD	Powder X-ray Diffraction
s-b-s	step-by-step
SEM	Scanning Electron Microscopy
SCXRD	Single Crystal X-ray Diffraction
TCSPC	Time-Correlated Single Photon Counting
TGA	Thermogravimetric Analysis
TGPLS	Transient Grating Photoluminescence Spectroscopy
UiO	Universitetet i Oslo
UFS	Ultrafast Spectroscopy
UMCM	University of Michigan Crystalline Material
ZIF	Zeolitic Imidazolate Framework

Table of Contents

Crystallographic Information Files (CIFs) of MOFs presented in Chapter 4 can be found at the link below:

https://drive.google.com/drive/folders/1c4unyFa4vUeXKQnRLt7rKzXBN9QWmfJ9?usp=sharing

Chapter 1 – Introduction

1.1 What are MOFs?

'It is proposed that a new and potentially extensive class of scaffolding-like materials may be afforded by linking together centres with either a tetrahedral or an octahedral array of valences by rod like connecting units.'

These were the first words of a seminal paper published by Hoskins and Robson in 1990.[1] They described the synthesis and crystallography of a new class of materials and predicted that these materials would exhibit useful properties like high porosity, unimpeded diffusion of species, catalytic ability and molecular sieving. This is, arguably, the genesis of metal-organic frameworks (MOFs). The ideas put forward in this publication are presently very ubiquitous concepts in MOF research and are being further improved upon by scientists around the world.

By way of definition, the IUPAC terms metal-organic frameworks as '*coordination networks with organic ligands containing potential voids*'.[2] To elaborate, MOFs are crystalline, porous materials made by joining metal ions or clusters to organic ligands by strong bonds. The unique properties of MOFs along with the added features of stability and modularity have made them highly useful materials in a variety of areas. The applications of MOFs are an unending list that includes areas like gas sorption and separation, catalysis, luminescence and sensing, metal ion removal, and studies of reaction intermediates.[3]

MOFs have also been known by other names like porous coordination polymers,[4] porous coordination networks,[5,6] and microporous coordination polymers.[7] All these materials are collectively referred to as MOFs in this thesis.

1.2 A brief history of MOFs

The story of MOFs begins with Hoskins and Robson and continues with pioneering work led independently by Kitagawa and Yaghi. Studies on the adsorption of CH_4 performed by the Kitagawa group on a MOF made of 4,4′-bipyridine linked to Co^{2+} ions (Fig. 1.1) showed that about 2.3 mmol of CH_4 could be absorbed per gram at a pressure of 30 atmospheres.[8] Additionally, the stability of these materials under such high pressures was demonstrated by unchanging powder X-ray diffraction (PXRD) patterns.

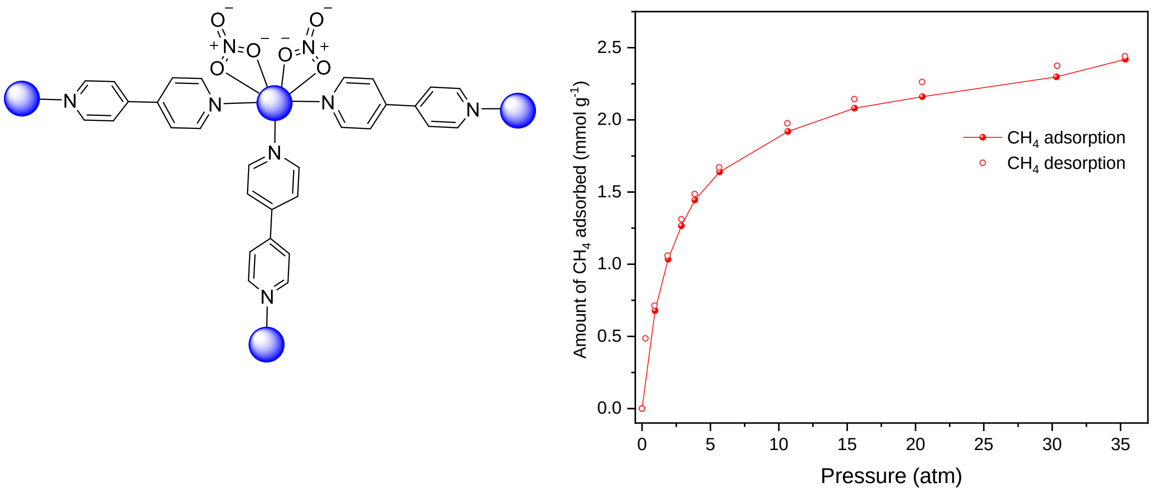

Figure 1.1: (Left) The cobalt centre of the MOF reported by Kitagawa, with the Co^{2+} ions shown as blue spheres.[8] Each cobalt is bonded to two nitrate ions as shown. (Right) The methane gas sorption isotherm of the MOF showing sorption at high pressures.

Yaghi led the study in which the unmet challenge of adsorption at low pressures was achieved.[9] Using a MOF named MOF-5 built from Zn_4O clusters and 1,4-benzenedicarboxylate (bdc) linkers (Figure 1.2) more than 800 mg of N_2 per gram could be adsorbed at pressures less than 1 atm. From these data, the Langmuir surface area of MOF-5 was calculated to be 2900 m^2 g^{-1}, an area equal to fifteen tennis courts! The structural parameters of MOF-5 were unchanged even after heating at 300 °C, meaning that it had exceptional thermal stability.

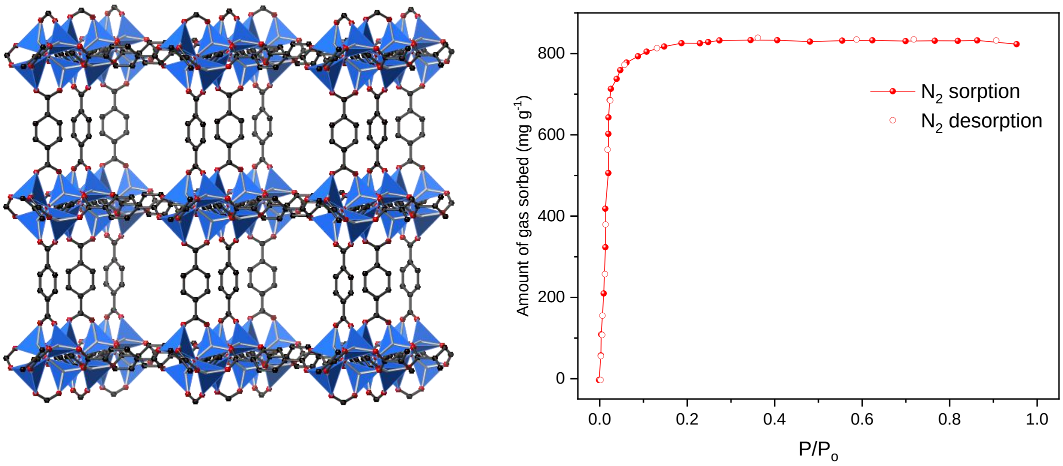

Figure 1.2: (Left) The crystal structure of MOF-5 showing Zn_4O clusters linked to 1,4-benzenedicarboxylate linkers. Colour code: Deep blue: Zn, black: carbon, red: oxygen. (Right) The nitrogen gas sorption isotherm for MOF-5.[9]

The modularity of MOFs *i.e.* the replacement of bare linkers with functionalised ones of a similar geometry was shown to be possible by Eddaoudi *et al.*[10] This idea named the isoreticular approach made MOFs endlessly tunable provided the appropriate linkers were synthesised. The increased surface areas and changing pore environments of these isoreticular frameworks called isoreticular MOFs (IRMOFs) showed that a plethora of applications could be explored with MOFs. Isoreticularity had perhaps, the greatest impact on MOF research, uniting scientists and engineers of different disciplines contributing their skills to solve both fundamental and applied scientific problems.

To date, more than 70,000 MOF structures have been reported showing a true explosion of research in a mere 30 years from the proposal of the concept.[11] The metals forming the clusters span the entire periodic table (excluding some transuranic elements) and the linkers range from simple organic molecules to more exotic and complex molecules such as proteins.[12,13] All in all, the field seems to be booming and the subsequent sections of this Chapter are dedicated to exploring some well-known structures and applications of MOFs.

1.3 Some Classical MOFs

Out of the more than 70,000 MOF structures that exist, some are termed ‘classical’ in the way that these MOFs were the first few to be published and that each of them explored some special features. For example, MOF-5 had exceptional thermal stability, HKUST-1 was the first MOF to have vacant metal sites, MIL-101 and UiO-66 showed high chemical stabilities, and ZIF-8 had bare metal ions instead of clusters connecting its linkers.

MOF-5: First reported in 1999 by Yaghi, MOF-5 was made by diffusing triethylamine into a mixture of $Zn(NO_3)_2$ and 1,4-benzenedicarboxylic acid (bdc) in a solution of *N*,*N*-dimethylformamide (DMF) and chlorobenzene. A small amount of H_2O_2 was added to form the μ_4-oxygen of the Zn_4O cluster. The triethylamine aided in the deprotonation of terephthalic acid to promote bonding to Zn^{+2}.

On analysing the crystal structure, MOF-5 was found to have Zn_4O clusters. Such clusters are also present in basic zinc acetate, $Zn_4O(CH_3COO)_6$.[14] Each cluster links to six terephthalate units in an octahedral geometry, giving the overall network a cubic topology (Figure 1.2) with the formula $Zn_4O(bdc)_3$. About 80% of the crystal volume was calculated to be free space, making MOF-5 highly porous. A benefit of its thermal stability was that heating at high temperatures could be used to expel the occluded solvent making MOF-5 permanently porous. Though the Langmuir surface area was calculated to be 2900 m^2g^{-1}, an even higher Brunauer-Emmet-Teller (BET) surface area of 3800 m^2g^{-1} could be obtained under optimal conditions of synthesis and handling.

Another classical MOF reported in 1999 was **HKUST-1.**[15] This structure reported by Ian Williams of the Hong Kong University of Science and Technology (HKUST) was of a copper based MOF. In addition to thermal stability, and high porosity, HKUST-1 had potential open metal sites.

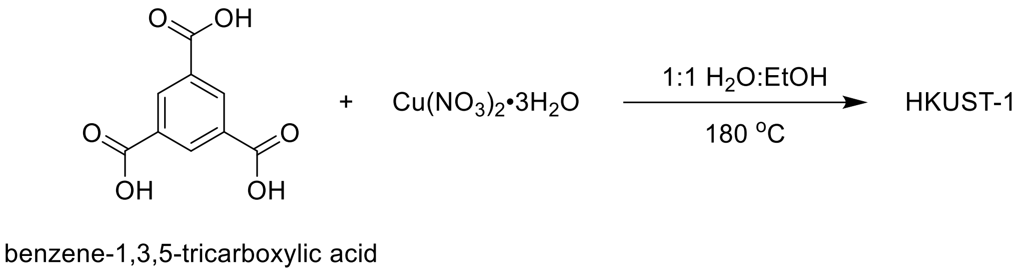

Scheme 1.1: The method for preparing HKUST-1 as reported by Williams and co-workers.[15]

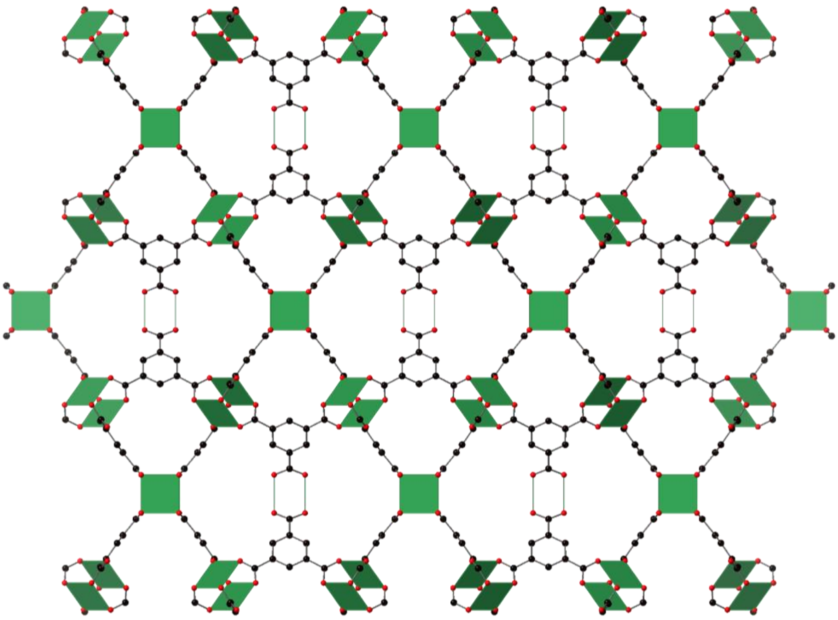

Figure 1.3: The single crystal structure of HKUST-1. Copper atoms are represented by green squares. Colour code: Copper: green, carbon: black, oxygen: red. Hydrogen atoms have been omitted for clarity.

A reaction between benzene-1,3,5-tricarboxylate (H_3btc) and copper nitrate was used to synthesise HKUST-1 (Scheme 1.1). The btc linkers bond to copper paddlewheel clusters giving a structure with the formula $[Cu_3(btc)_2(H_2O)_3]_n$ (Figure 1.3). Water molecules coordinate to the axial sites of the copper paddlewheels, which can be removed by heating revealing open metal sites. HKUST-1 was the first MOF used for post-synthetic modification, (using the MOF as a reactant without destroying its structure). Treatment of anhydrous

HKUST-1 *i.e.* $[Cu_3(btc)_2]_n$ with pyridine (py) gave a green derivative $[Cu_3(btc)_2(py)_3]_n$ in quantitative yield. HKUST-1 has a high volumetric methane storage capacity.[16] The use of 7,7,8,8-tetracyanoquinododimethane (TCNQ) instead of btc results in electrically conductive HKUST-1. Furthermore, publications on using it as a heterogeneous catalyst are numerous.[17-19]

The race for increasing surface areas had begun. In 2004, the material with the highest surface area was activated carbon (2,030 $m^2\ g^{-1}$) and zeolite Y held this record for crystalline materials at 904 $m^2\ g^{-1}$. A strong contender for this race was MOF-177, which was published by Yaghi.[20] MOF-177 was made in a manner similar to MOF-5, by heating zinc nitrate and 1,3,5-benzenetribenzoate (H_3btb) in *N*,*N*-diethylformamide (DEF) (Scheme 1.2). It consists of Zn_4O clusters linked to six btb units, which are each linked to three Zn_4O clusters, making the formula $Zn_4O(btb)_2$ (Figure 1.4). MOF-177 has two pores with diameters 11.8 and 10.8 Å, respectively. The smaller pores form continuous channels giving the framework lots of available free space.

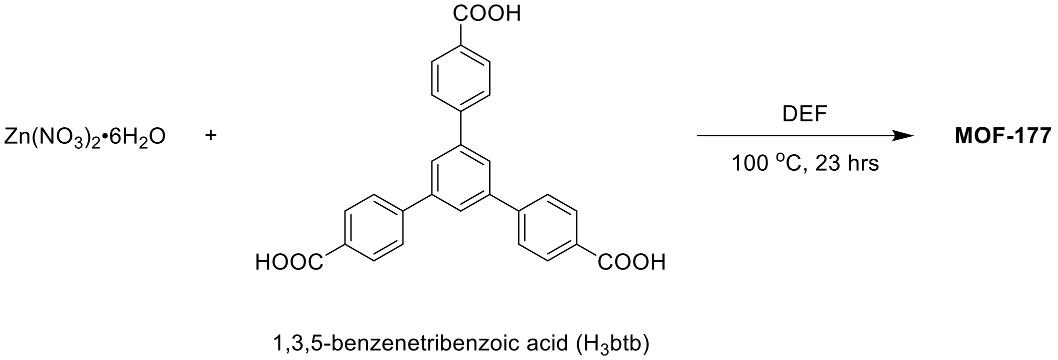

Scheme 1.2: Synthesis of MOF-177.

Like MOF-5 and HKUST-1, MOF-177 was also stable on removal of occluded solvent and remained intact up to 350 °C. Indeed, calculations from the N_2 sorption isotherm show a Langmuir surface area of 4500 $m^2\ g^{-1}$! MOF-177 was used for size selective encapsulation of guest molecules. The authors trapped C_{60} fullerene and dye molecules like Astrazon orange R, Nile Red and Reichardt's dye within the pores. Only one molecule of Reichardt's dye could fit inside the pores as opposed to the smaller Astrazon R for which 16 molecules could fit inside the pore, indicating size-selective inclusion.[20]

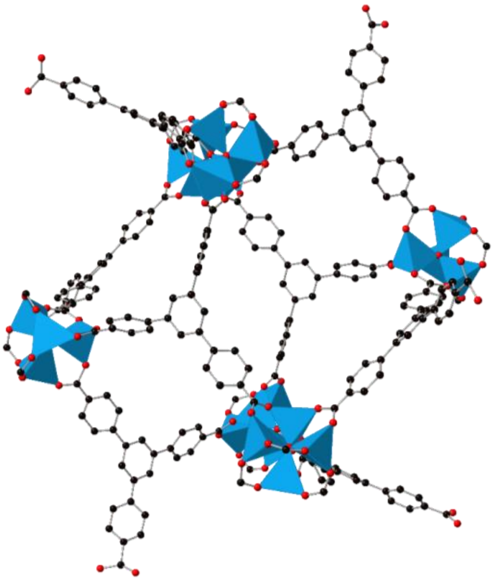

Figure 1.4: The crystal structure of MOF-177 showing Zn_4O clusters linked to btb linkers. Colour code: zinc: blue, oxygen: red, carbon: black. Hydrogen atoms have been omitted for clarity.

In 2005, researchers of the Institut Lavoisier, France reported the synthesis of a chromium-bdc MOF named MIL-101 (Matérial Institut Lavoisier-101).[21] The synthesis (Scheme 1.3) involved the use of chromium (III) nitrate and H_2bdc and with water as a solvent and hydrofluoric acid as a modulator to give MIL-101 as a crystalline green powder with the formula $Cr_3F(H_2O)_2O(bdc)_3.nH_2O$ (n ≈ 25). Other methods of synthesis have also been reported.[22]

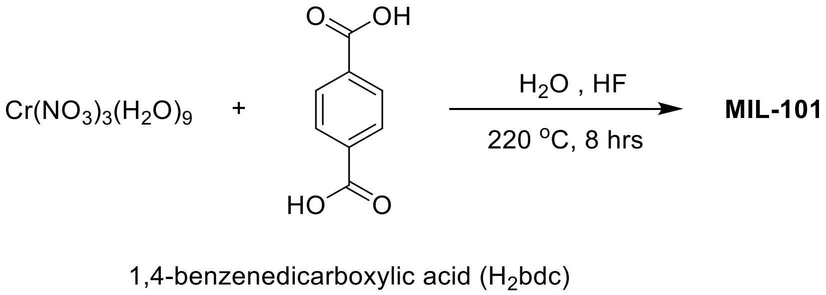

Scheme 1.3: Preparation of MIL-101 as reported by Férey et al.[21]

The crystal structure of MIL-101 shows a large cubic unit cell with a length of 89 Å. The arrangement of the constituents gives rise to two types of cages, present in a 2:1 ratio, with internal pore diameters of 29 Å and 34 Å, respectively. The smaller cages have pentagonal pores with size 12 Å and the larger cages have both the pentagonal and hexagonal pores (dimensions 14.7 Å x 16 Å) (Figure 1.5). These large pores result in a BET surface area of 4100 $m^2 g^{-1}$ and the N_2 sorption isotherms shows two steps indicating two types of pores.

MIL-101 is highly stable even after heating in organic solvents and maintains its structure for months when kept in air. This stability makes MIL-101 amenable for post-synthetic modification. As an example of this concept, the original publication reports the encapsulation of a Keggin polyanion $PW_{11}O_{40}^{-7}$ within the MIL-101 pores. This was shown by infrared and ^{31}P NMR spectroscopy, which proved that the Keggin anion retains its structure. Reduced surface areas also give corroboratory proof of the anion encapsulation. The two types of pores can discriminate guests based on their size; a property also seen in MOF-177. The $PW_{11}O_{40}^{-7}$ has a van der Waals radius of 13.1 Å, meaning it would fit only in the larger hexagonal pore and not in the smaller pentagonal pore.

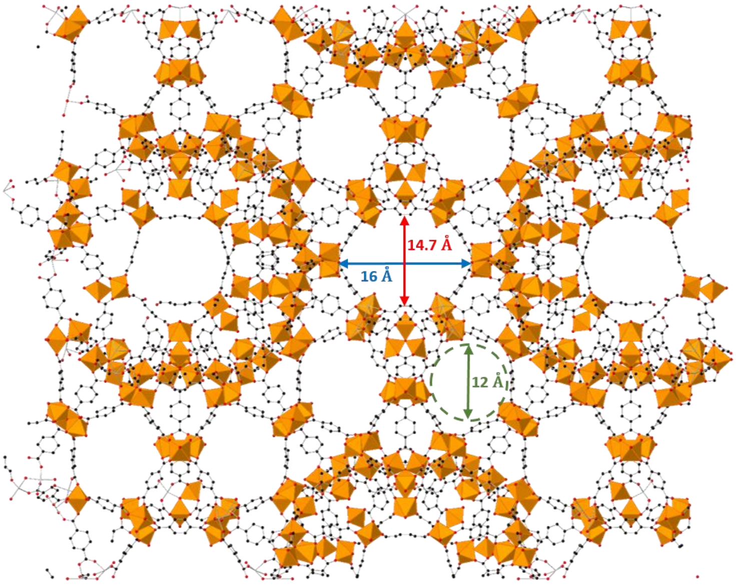

Figure 1.5: The crystal structure of MIL-101. The pentagonal and hexagonal pores are shown, along with their dimensions. Colour code: chromium: orange, carbon: black, oxygen: red. Hydrogen atoms have been omitted for clarity.

Other MIL systems are also known. Examples include MIL-100, where the bdc has been replaced with btc, MIL-47 (Cr^{+3} replaced with V^{+4}) and MIL-53 (Al^{+3} instead of Cr^{+3}). These systems have been used for gas sorption,[23] separation and chromatography,[22] studying properties of encapsulated guests,[24] surface chemistry,[25] catalysis[22] and refridgeration.[26]

Research regarding Zeolitic Imidazolate Frameworks (ZIFs) was first published in 2005 by Chen[27] and later independently by Yaghi in the same year.[28] A typical ZIF such as ZIF-8 has zinc(II) ions coordinated to 2-methylimidazole linkers (mim), arranged in a tetrahedral geometry having a formula $Zn(mim)_2$ (Scheme 1.4 and Figure 1.6). The bond angle between Zn-mim-Zn is about 145°, which is close to the Si-O-Si bond angle in many zeolites. Hence, these frameworks have topologies similar to many zeolites and hence the word 'Zeolitic' appears in their name.

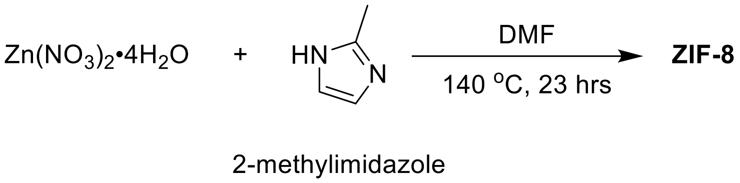

Scheme 1.4: Preparation of ZIF-8. Changing the ligand to imidazole or benzimidazole gives other ZIFs. This can also be achieved the changing the metal salt.

Other ZIFs can be made by changing the ligand (from 2-methylimidazole, to imidazole, or benzimidazole) or by changing the metal ion. Many other phases of ZIFs are also known. Each ZIF has a unique structural topology and similarity to a known zeolite.[29] ZIFs are thermally stable, and highly porous. For example, ZIF-8 has a BET surface area of 1,630 m^2/g.

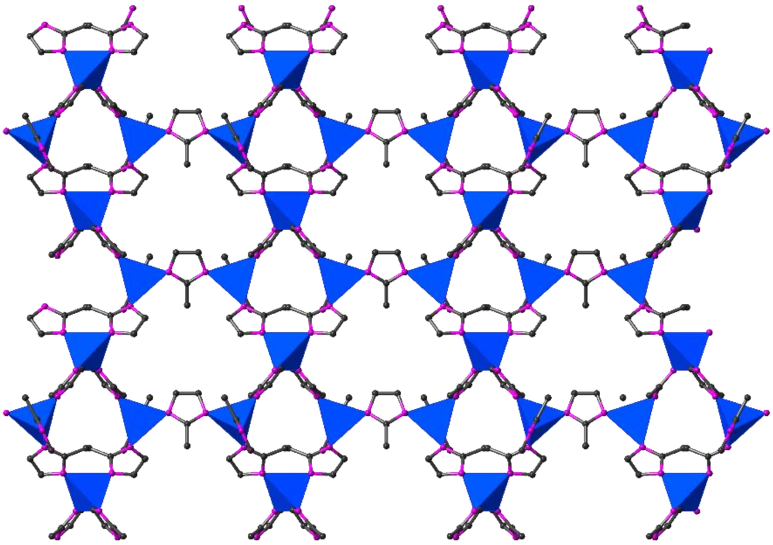

Figure 1.6: The SCXRD structure of ZIF-8. Colour code: zinc: deep blue, nitrogen: pink, carbon: black. Hydrogen atoms have been omitted for clarity.

One amazing feature of ZIFs are their exceptional stabilities against water and aqueous bases brought about by the strong bonding between imidazole and zinc. Consequently, synthesis in water can be performed with many such syntheses being reported.[28,30,31] This makes it possible for trapping biomolecules like peptides, enzymes and drugs, which may breakdown in some organic solvents.[32-34]

A favourite among MOF chemists are MOFs of the UiO series namely UiO-66, UiO-67 and UiO-68. These were first reported in 2008 by Lillerud's group of the University of Oslo (Universitetet i Oslo in Norwegian and hence the name UiO).[35] UiO-66 is made of linear bdc units linked to $Zr_6O_4(OH)_4(CO_2)_{12}$ clusters, in a cubic **fcu** topology (Figure 1.7). This cluster being 12-coordinated is the highest coordination for a MOF. During synthesis, replacing the bdc ligand with biphenyl-4,4′-dicarboxylic acid or *p*-terphenyl-4,4″-dicarboxylic acid gives UiO-67 and UiO-68 respectively. (Scheme 1.5)

UiO-66 is among the most stable MOFs known. Heating to 300 °C, causes two of four μ_3–OH groups of the cluster to leave along with two hydrogens from the two other –OH groups. This reaction is completely reversible, and the structure is fully retained. However, the MOF decomposes above 540 °C, losing benzene as fragments. Amazingly, UiO-66 can withstand pressures up to 10,000 kg/cm^2, without any change in structure, as evidenced by unaffected PXRD patterns. Treatment with water, acids or bases does not destroy the MOF.[36]

The strong bonding between the carboxylate oxygens and the Zr^{+4} atoms is the key to the exceptional stability of these MOFs. This makes MOFs of the UiO series probably the most widely studied among MOFs. A Scifinder^n search (as of November 2020) returns nearly 4000 references for the term ‘UiO-66’. Applications range from gas storage,[37,38] gas separation with membranes,[39,40] ion transport, luminescence and sensing,[41-43] catalysis,[44,45] enzyme encapsulation[33] and the list continues. One aspect of UiO MOFs that is recently attracting a lot of attention is the study of its defects, the engineering of which can be used to tune the performance of these materials.[46,47]

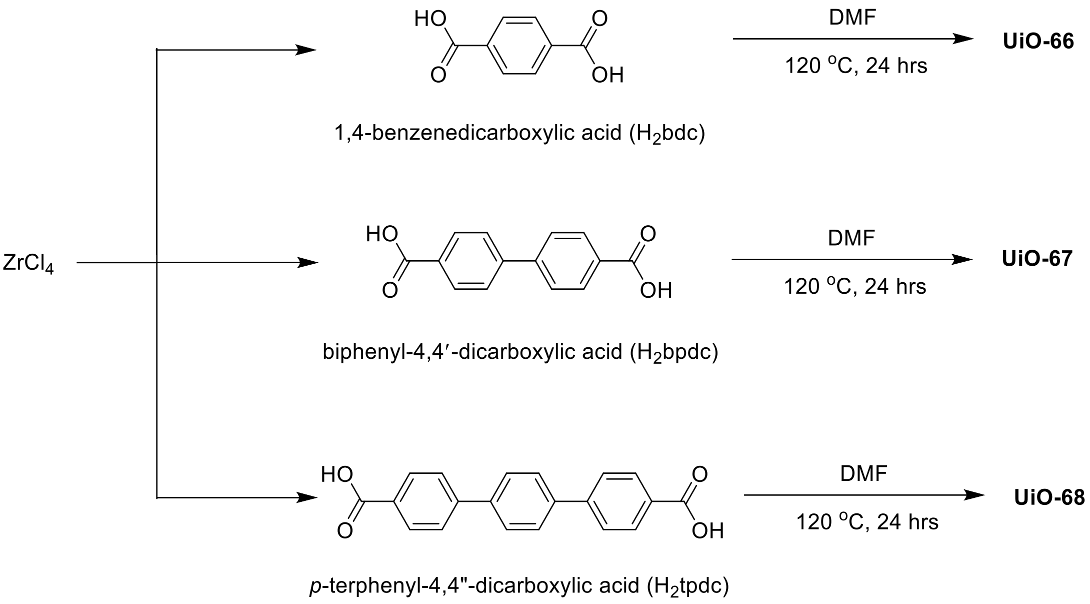

Scheme 1.5: The synthetic method to prepare UiO-66, UiO-67, and UiO-68.[35]

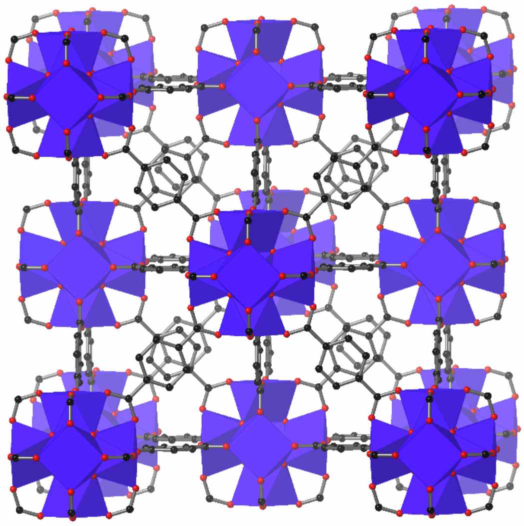

Figure 1.7: The crystal structure of UiO-66. This MOF typically forms microcrystals, and hence this structure was obtained by refining PXRD data and not from single crystal XRD.[35] Colour code: zirconium: deep blue, carbon: black, oxygen: red.

1.4 Isoreticular MOFs (IRMOFs)

The isoreticular principle is the phenomenon where the use of functionalised organic linkers for making MOFs results in frameworks with the same topology. For example, in Figure 1.7, the bdc ligands in UiO-66, can be changed to bpdc and tpdc ligands to give UiO-67 and UiO-68. The changed ligands occupy the same position as the original bdc ligand. This means that all three MOFs share the same **fcu** topology making them examples for isoreticular MOFs. The ligands are all linear but have different lengths, and hence these isoreticular MOFs feature increased pore sizes and increased surface areas. Functional groups can be appended to the ligands and many more applications can be explored.[48]

The prototypical example for isoreticular MOFs was MOF-5. The functional groups of bdc-based linkers were changed from a non-functionalised aryl C-H to C-Br, C–NH_2, C–OC_3H_7, C–OC_5H_{11}, C–C_2H_4, and C–C_4H_4 (Figure 1.8). The seven MOFs called IRMOF-1 through IRMOF-7, had cubic unit cells and showed similar PXRD patterns (Figure 1.8).[10] This implied that the same MOF was obtained, with the same cubic framework topology. However, their pore environments were different, due to the different functional groups surrounding them.

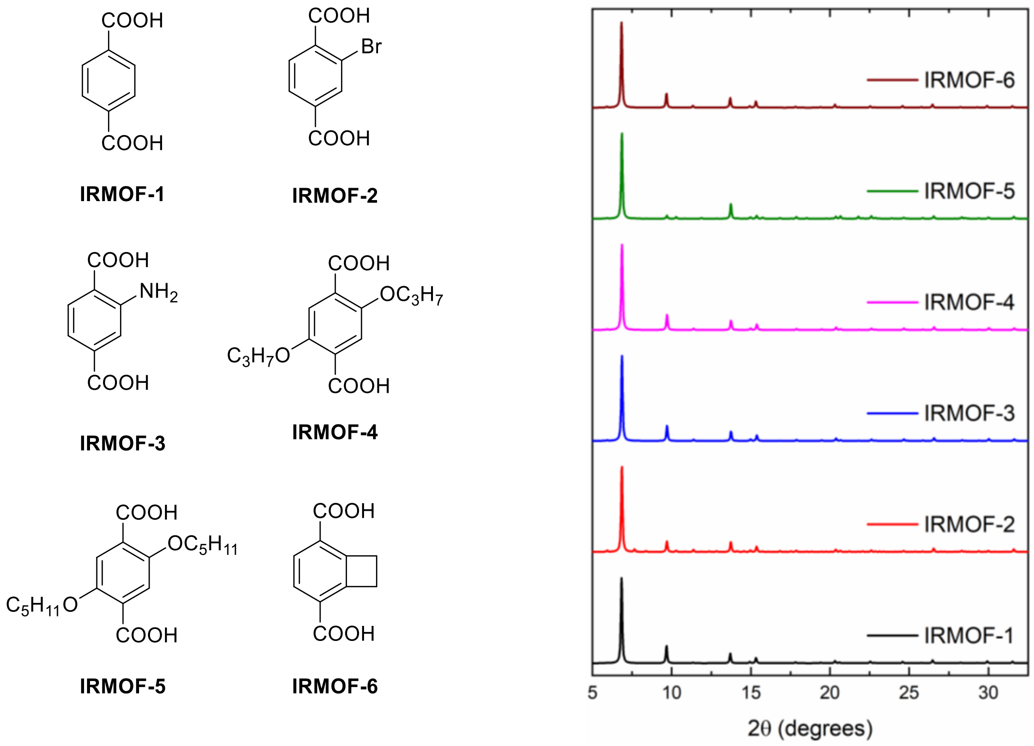

Figure 1.8: (Left) The functionalised ligands used to make IRMOFs 1-6. (Right) The PXRD patterns of the IRMOFs simulated from their corresponding crystal structures.

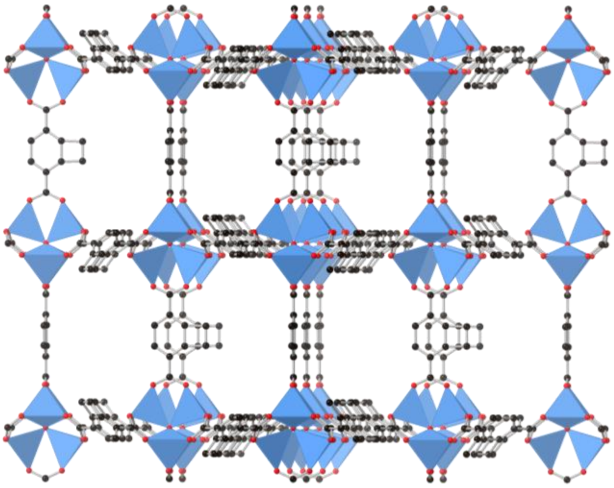

Figure 1.9: The SCXRD structure of IRMOF-6. This MOF has bdc-C_4H_4 ligands which are seen in the structure. Hydrogen atoms are omitted for clarity. Colour code: Blue: zinc, black: carbon, red: oxygen.

This principle had major implications in the field of MOF chemistry. Obtaining the same framework meant that the properties of same type of MOF could be tuned only by functionalising the ligands. A wide range of applications like enhanced sorption, catalysis, luminescence, chemical sensing among many others could be explored by incorporating ligands with appropriate functional groups.[3,49] For example: IRMOF-6 with bdc-C_2H_4 (Figure 1.9) ligands has a methane uptake of 155 $cm^3\ g^{-1}$ at standard temperature and pressure. This is higher than IRMOF-1 with unfunctionalised bdc (135 $cm^3\ g^{-1}$) and IRMOF-3 with bdc-NH_2 (120 $cm^3\ g^{-1}$).

Isoreticularity is not only restricted to ligand functionalisation. In the same paper, Yaghi describes IRMOFs 8, 10, 12, 14, and 16 which were made by using dicarboxylate linkers which are lengthier than H_2bdc. During synthesis, the H_2bdc was replaced with lengthier $H_2$2,6-ndc, H_2bpdc, H_2thpdc, H_2pdc and H_2tpdc (Figure 1.10). Increases in percentage free volume were seen, consequently the IRMOFs had reduced densities.

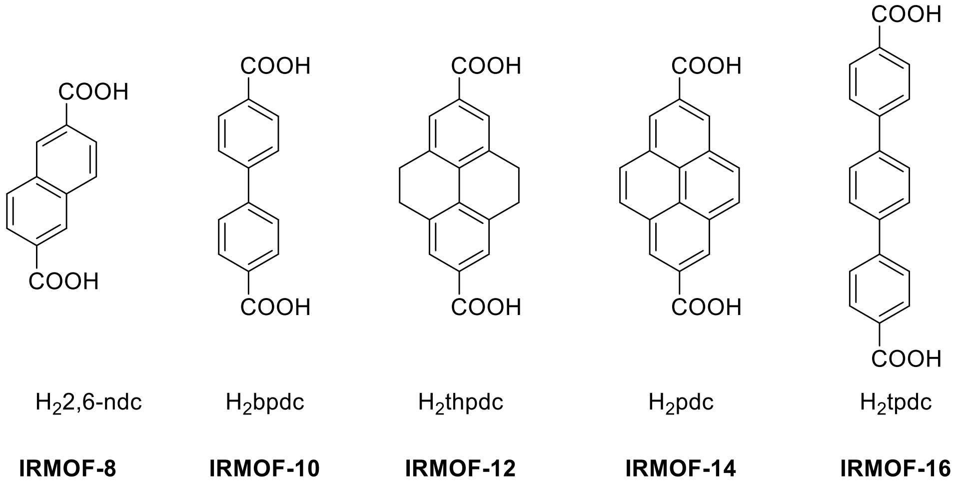

Figure 1.10: The structures of the ligands used to make IRMOFs 8, 10, 12, 14, and 16.

1.5 Multivariate vs Multicomponent Metal-Organic Frameworks (MC-MOFs)

The MOFs mentioned above have some common features in their design. These MOFs categorised as binary MOFs are made of two components i.e. one metal ion or cluster linked to one ligand. In fact, most MOFs are of this category. If a binary MOF is compared to a biological material such as DNA or an enzyme, the differences in complexity are startling.[50,51] Biological materials are made of multiple building blocks, placed in specific order so that a particular function is enhanced. The high degree of complexity in a such materials is complemented by sophisticated features like controlled reaction microenvironments, substrate recognition, substrate selectivity, and enhanced catalytic efficiency.[52,53] Evidently, limiting to only two components for constructing a MOF impedes diversity in its structure and composition ultimately reducing its applicability.

The use of multiple ligands or metal ions can be one of the strategies to overcome these limitations. By careful choice of the number and the relative ratios of these components, more diverse and complex frameworks could be explored. With this strategy, mixtures of multiple ligands or metals salts could be used as precursors during MOF synthesis. The MOFs obtained can be applied to study more challenging chemistry, especially in those areas which replicate the features seen in biological materials.

This strategy gives rise to two types of multivariate and multicomponent MOFs. There are several key differences between these types:

a) In multivariate MOFs, the ligands have a similar geometry and length but differ in their functional groups, whereas in multicomponent MOFs, ligands with different geometry and lengths can be used.

b) Multivariate MOFs have ligands randomly dispersed within the lattice *i.e.* the exact position of a ligand with a specific functional group cannot be pinpointed with XRD methods.

c) In MC-MOFs, the ligands , due to their different shapes, discriminate during self-assembly. Hence, multicomponent MOFs have ligands at crystallographically distinct positions. The ligands can be located by XRD techniques.

d) As a corollary of b) and c) knowing the position of one ligand, is adequate to predict the ligand at the next position in multicomponent MOFs but not in multivariate MOFs.

e) The distinct arrangement of ligands means that pore environments can be designed precisely in multicomponent MOFs. The moieties surrounding a guest molecule in the pore of the MOF can be studied well. This makes the pores in such MOFs homogenous, as opposed to multivariate MOFs which have heterogeneous pores.

1.5.1 Multivariate MOFs

Multivariate MOFs (MTV-MOFs) are synthesised by using organic ligands that have the same backbone but different functional groups. The ligands do not position themselves at distinct positions with respect to each other. They are more so dispersed within the lattice, with no specific distribution patterns to them. A well-known example is the work led by Yaghi in developing the MTV-MOF-5 series.[54] Nine different bdc-based ligands with eight different functionalities were used to build the MOF (Figure 1.11). NMR spectroscopy showed that all ligands were incorporated into the MOF. For MTV-MOF-5, acid-digested sliced sections of single crystals were studied by NMR spectroscopy. Nearly identical NMR spectra were observed, meaning that there was random distribution of ligands without clustering.

There are multivariate versions of other MOFs including the classical MOFs UiO-66,[55] MIL-101,[56] and MIL-53,[57] and many more. The combined aspects of structural periodicity but compositional aperiodicity in multivariate MOFs is quite difficult to study. Understanding multivariate MOFs has implications in the engineering of materials like block copolymers, and also for measuring defects in crystals.[58] Further research has been done to map the positions of specific ligands in multivariate MOFs by advanced solid state NMR methods, isotope labelling, and NMR spin diffusion all in tandem with computational modelling.[55,58-60] Organic solvents have been let to diffuse into the MOF and changes in diffusion coefficients have been analysed to study the same problem.[61]

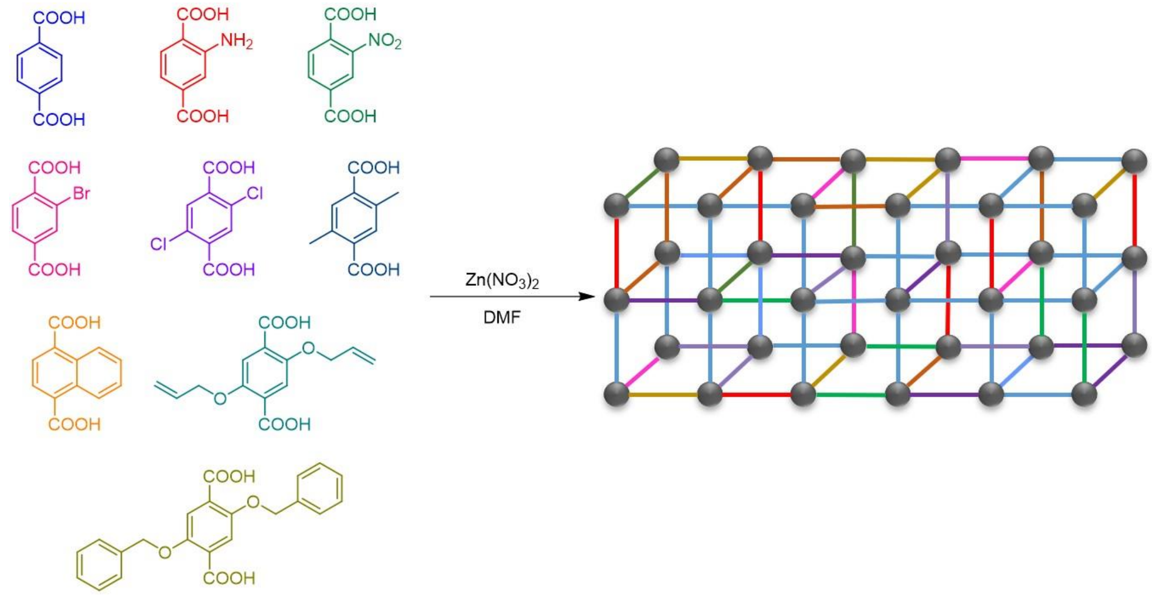

Figure 1.11: The ligands used to make MTV-MOF-5. Zinc clusters are shown as black circles and the ligands are shown as coloured rods. Note that there is no specific relative arrangement between ligands of different functionalities.

1.5.2 Multicomponent MOFs (MC-MOFs)

Multicomponent MOFs have geometrically distinct ligands, or metal clusters arranged at unique positions. These constituents are discriminated during self-assembly and position themselves at specific positions within the lattice. Unlike multivariate MOFs, MC-MOFs are both structurally and compositionally periodic. Multicomponent MOFs have many benefits over their multivariate counterparts, which are detailed in further sections.

The first MC-MOF was made of bdc and btc linked Zn_3 clusters with the formula $Zn_3(BDC)(BTC)_2(2NH(CH_3)_2)2NH_2(CH_3)_2$. The bdc ligand coordinates linearly and the btc ligand with threefold symmetry coordinates in a triangular fashion. These differences result in the ligands positioning themselves at specific sites, giving an MC-MOF.[62]

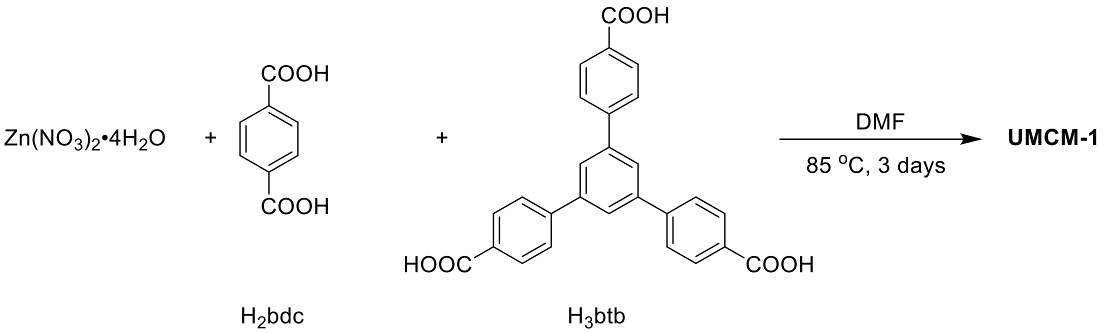

Scheme 1.6: Synthesis of UMCM-1.

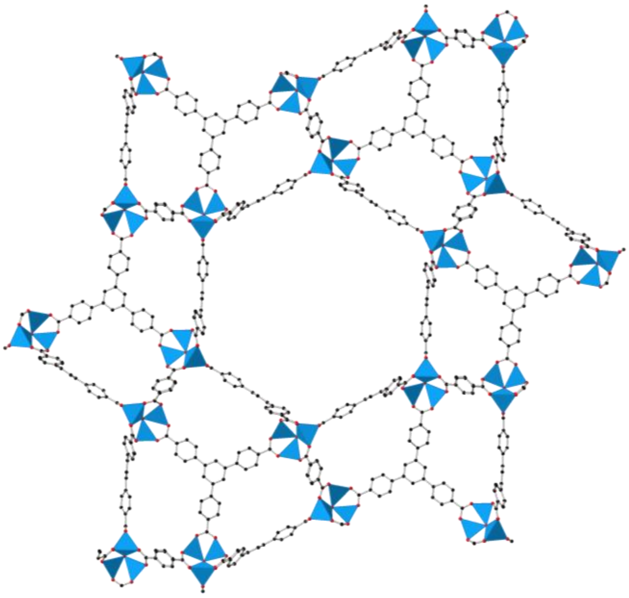

Figure 1.12: The SCXRD structure of UMCM-1 showing btb and bdc ligands connected to Zn_4O clusters. Colour code: Blue: zinc, black: carbon, red: oxygen.

Perhaps the most famous example of MC-MOFs is UMCM-1 (University of Michigan Crystalline Material-1), developed by Matzger's group at the University of Michigan.[63,64] The synthesis of UMCM-1 was achieved by mixing H_2bdc and H_3btb with zinc nitrate (Scheme 1.6). The optimal mole ratio of H_2bdc to H_3btb should be between 3:2 and 1:1. Maintaining this ratio is critical, as higher amounts of H_2bdc results in MOF-5 formation and increasing H_3btb levels gives MOF-177, both of which are unwanted, competing binary MOF phases.

UMCM-1 consists of a triclinic unit cell with Zn_4O clusters connected to four btb linkers at the equatorial positions and two bdc linkers at the axial sites (Figure 1.12). SCXRD and elemental analysis was used to show that the formula was $Zn_4O(bdc)(btb)_{4/3}$. This arrangement results in the first known structure with both micro and mesopores. UMCM-1 exhibited an exceptionally high surface area of 6500 m^2 g^{-1}, as proven by N_2 sorption isotherms. The unique structure of UMCM-1 makes way for some interesting applications like theoretical and experimental studies on gas storage and separation,[65,66] catalysis,[67,68] post-synthetic modification,[69] luminescence,[70] studying dynamics of encapsulated guests,[71] and chiral separation.[72]

MC-MOFs represent the next stage of complexity in ordered materials, as they are made of an increasing number of components in their repeating units. More MC-MOFs started appearing in the literature. One notable example is SUMOF-4, synthesised by Yao et al. of Stockholm University.[73] SUMOF-4 was made by heating bdc, bpdc and zinc nitrate in DMF at 130 °C. The structure consists of Zn_4O clusters connected to four bdc linkers to form a square and further to two bpdc linkers to form an orthorhombic framework. SUMOF-4 features interpenetration, a phenomenon where a second framework grows inside the pores of one framework. MC-MOFs with geometrically distinct metals clusters instead of ligands are also known.[74,75]

1.6 Massey University Frameworks (MUFs)

The first MOF consisting of three distinct ligands i.e. the first quaternary MOF was reported by the Telfer group and was aptly named Massey University Framework-7 or MUF-7.[76] The ligands used were btb, bpdc and bdc which are linked to Zn_4O clusters (Scheme 1.7 and Figure 1.13). Like other multicomponent MOFs, all the ligands position themselves at distinct crystallographic positions to give MUF-7. SCXRD proved that the formula was $Zn_4O[(btb)_{4/3}(bpdc)_{1/2}(bdc)_{1/2}]$. This was further confirmed by ^1H NMR spectroscopy on acid digested MOF samples, showing that there were no other phases formed.

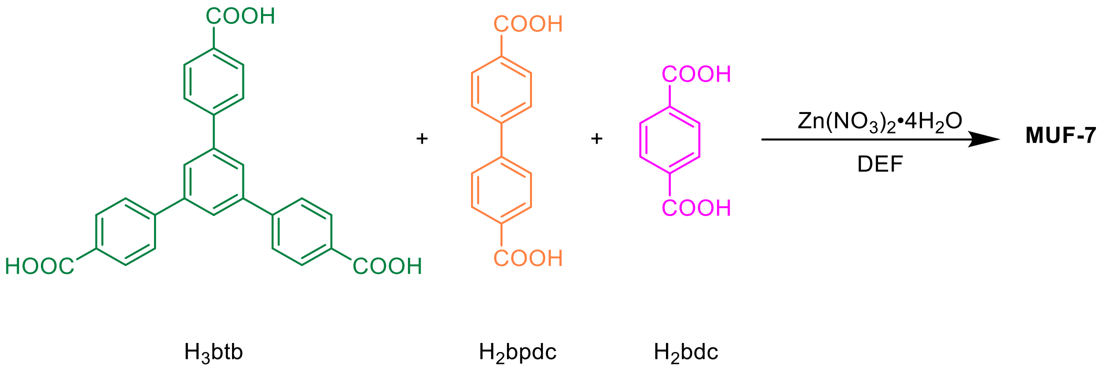

Scheme 1.7: The ligands used in the synthesis of MUF-7.

Like UMCM-1, the maintainance of a proper feed ratio was important to prevent the formation of competing phases like MOF-5 ($[Zn_4O(bdc)_3]$), MOF-177 ($[Zn_4O(bdc)_3]$), UMCM-1 ($[Zn_4O(btb)_{4/3}(bdc)]$), and SUMOF-4 ($[Zn_4O(bpdc)(bdc)_2]$). Using a feed ratio similar to the MUF-7 formula gives MOF-177. The greater number of carboxylate groups causes the tritopic linkers to have a reactivity 1.5 times higher than the ditopics.[77] To counteract this, higher amounts of ditopics were used which was successful in avoiding the formation of competing phases.

MUF-7 has four types of pores, a larger dodecahedral pore and three smaller tetrahedral pores. The environments of these pores can be changed by using functionalised linkers, thanks to the isoreticular nature of MUF-7. Eight different MUF-7 frameworks were reported in the same study, each with a unique combination of linkers, a varying surface area and a different CO_2 sorption capacity. Although, MUF-7 was stable up to 400 °C, it decomposed easily in moist environments due to the hydrolysis of the zinc-carboxylate bonds.

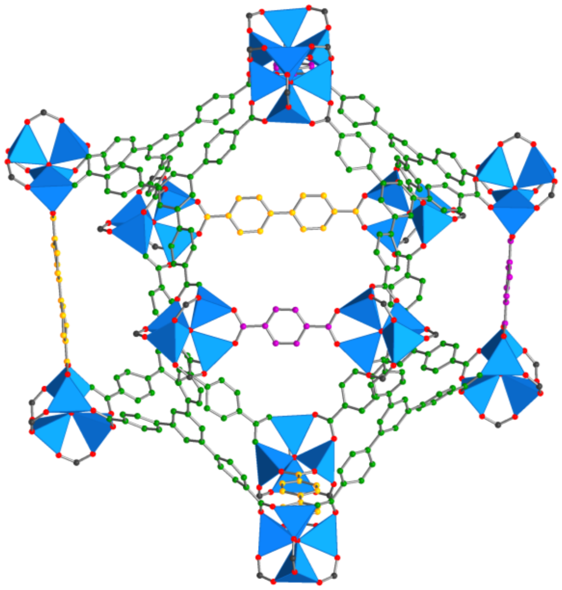

Figure 1.13: The SCXRD structure of MUF-7. The ligands are coloured as shown in Scheme 6. Oxygen atoms are shown in red and zinc atoms are represented by blue tetrahedra. Hydrogen atoms are omitted for clarity.

Finally, I come to star of the show, **MUF-77**, first reported in 2015, once again by the Telfer group.[78] This new class of moisture stable frameworks MOFs called MUF-77 were also quaternary zinc MOFs with the ligands in a ratio similar to MUF-7, with one key difference. The btb linker was replaced with a rigid, truxene-based linker, drastically changing its properties (Scheme 1.8).

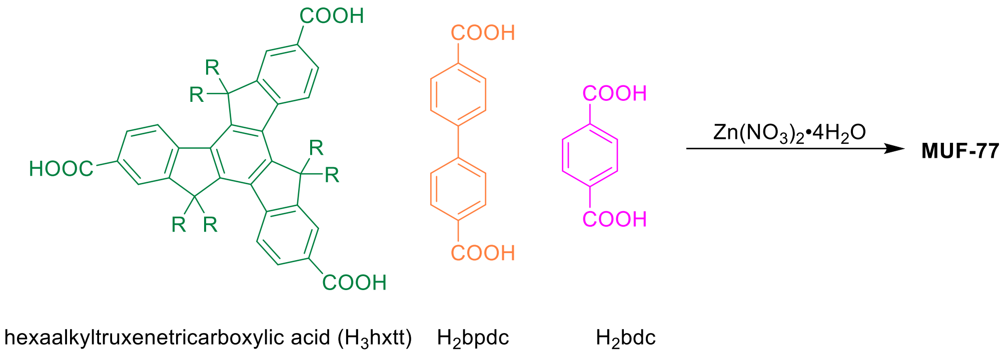

Scheme 1.8: Synthesis of MUF-77. The R group on the hxtt ligand is typically a linear alkyl chain with number of C atoms varying between 1 and 10.

MUF-77 was much more stable in water vapour than its precursor MUF-7. Many other MOFs made of Zn_4O clusters such as MOF-5, UMCM-1 and MOF-177 degrade easily in moist environments. The increased stability of MUF-77 is due to rigid truxene-based linkers, which are more hydrophobic than btb. Tuning the stability is possible by changing the pendant alkyl groups on the truxene linkers. When these alkyl groups are methyl, ethyl or butyl, the generated MUF-77 frameworks are stable up to 70% relative humidity. However, using longer chains like hexyl, octyl or decyl lowers this stability.

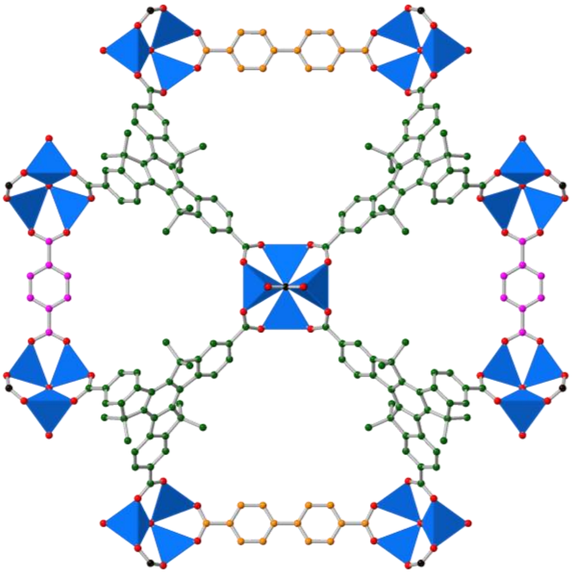

Figure 1.14: The SCXRD structure of MUF-77. The ligands are coloured as shown in Scheme 1.7. For this structure, the R group on the hxtt ligand is methyl. Oxygen atoms are shown in red and Zn are represented by the blue tetrahedra. Hydrogen atoms are omitted for clarity.

Structurally, the unit cell of MUF-77 is cubic with a length of around 29.95 Å. The nodes are Zn_4O clusters connected to four tritopic truxene ligands at the axial positions with one bdc and one bpdc ligand at the equatorial positions (Figure 1.14). The bdc and bpdc ligands alternate each other along the x and y axes (Figure 1.15). The relative ratio of ligands in MUF-77 is similar to that in MUF-7 i.e. $Zn_4O[(hxtt)_{4/3}(bpdc)_{1/2}(bdc)_{1/2}]$. MUF-77 is formed phase pure in most cases and is not very sensitive to the feed ratio of the ligands.

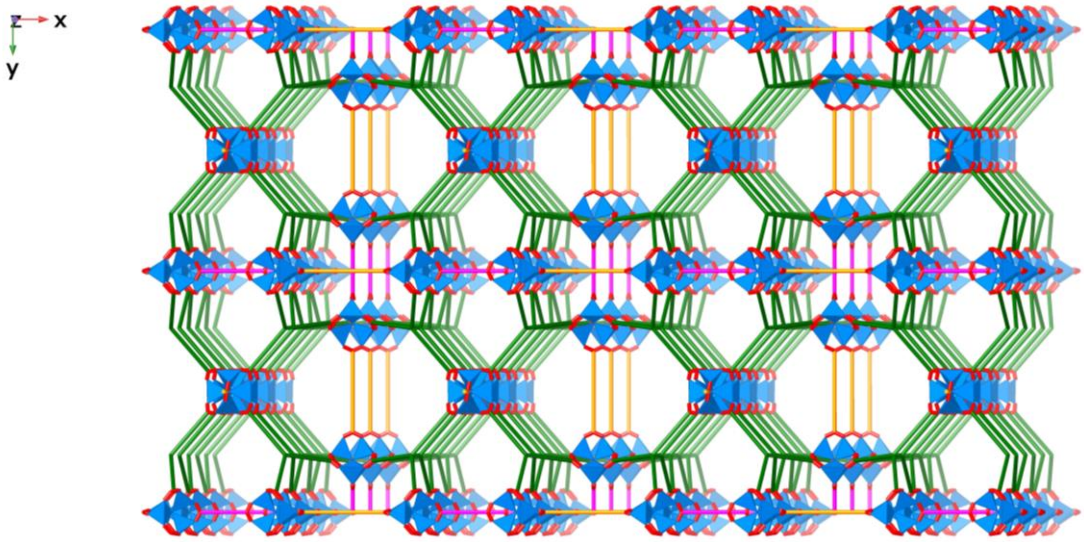

Figure 1.15: The extended crystal structure of MUF-77. The ligands are represented by rods, coloured as per scheme 1.7. Oxygen atoms are shown in red and Zn atoms by blue tetrahedra**.**

There are three pores in MUF-77; two large dodecahedral pores and one tetrahedral pore (Figure 1.16). The larger among the dodecahedral pores is 34.5 Å wide, which is surrounded by hxtt and bpdc ligands. The second dodecahedral pore is 32.6 Å wide and is surrounded by hxtt and bdc. The smaller, tetrahedral pore spans 10 Å and is surrounded by all three ligands. The isoreticular principle can be applied to a quaternary MOF like MUF-77. All three ligands (hxtt, bpdc and bdc) can be functionalised to programme the pore environments. This means that phenomena like gas sorption and catalysis which more so ‘occur’ in the pores can be tuned to obtain a desired result. Such control over pores and properties is not possible with MTV-MOFs.

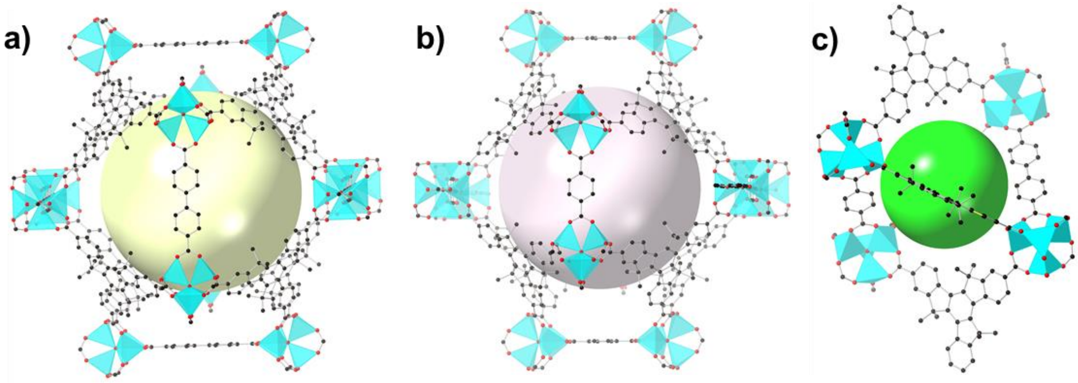

Figure 1.16: The three types of pores in MUF-77 represented by spheres **a)** the larger dodecahedral pore surrounded by hxtt and bpdc **b)** the smaller dodecahedral pore surrounded by hxtt and bdc and **c)** the tetrahedral pore surrounded by all three ligands.

Additionally, MUF-77 is an interesting candidate for spectroscopic applications like luminescence and photochromism, provided the right ligands are used. Exploring synergistic interactions like energy transfer is also possible. This whole thesis is dedicated to exploring photophysics and catalytic ability of some MUF-77 systems by introducing various functional groups to the ligands while maintaining the network structure.

1.7 Luminescence in MOFs

Luminescence occurs when a substance emits light on the application of energy. This energy can be delivered in the form of photons (fluorescence and phosphorescence), chemical reactions,[79] electricity, ionising radiation, sound, or in some cases even by mechanical stress.[80] When the energy is supplied by incident photons, luminescence occurs due to transitions between a molecule's electronic energy states, as shown by the Jablonski diagram in Figure 1.17. The molecule undergoes excitation from a singlet ground state (S_0) to a singlet excited state (S_1). In this S_1 state, the molecule loses energy as heat and relaxes to the lowest vibrational level of S_1 (internal conversion) and finally returns to the ground state (S_0) with the emission of a photon. Due to the loss of energy by internal conversion, the emitted photon has a lower energy than the incident photon. This process, where the photon release is by transitions between *singlet* states, is called fluorescence.

On the other hand, some molecules can change their spin in the excited singlet state (S_1) and undergo intersystem crossing to an excited triplet state (T_1). Further decay from the T_1 back to the singlet ground state (S_0) is termed phosphorescence. However, the $T_1 \rightarrow S_0$ transition is 'forbidden' and hence the rate constants for phosphorescence are much lower than those for fluorescence.[81,82]

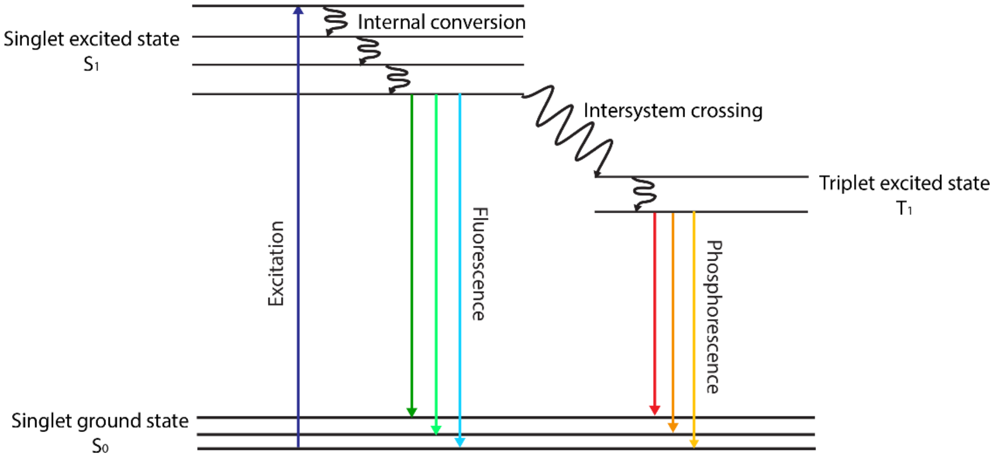

Figure 1.17: Jablonski diagram for fluorescence and phosphorescence. The wavy lines represent non-radiative transitions and the straight lines show radiative transitions.

Various molecules are known to show fluorescence. Examples include aromatic molecules like perylene, fluorescein, rhodamine dyes, and complexes of lanthanides.[81] Examples of phosphorescent substances include iodine,[81] complexes of noble metals,[83] and brominated BODIPY dyes.[84] All these luminescent molecules have been used in applications ranging from probes for detection of chemicals, phosphors in display screens, components of optical instruments, lasers, and cellular imaging.[82,85]

Luminescent moieties can be used as building blocks for MOFs to make the resulting MOF luminescent. This offers distinct advantages: Firstly, the synthesis of MOFs is straightforward requiring metal salts and appropriate linkers. Secondly, the crystalline nature of MOFs arranges luminophores in precise positions making it easier to explain luminescent behaviour. The third advantage is that the porosity of MOFs can be used to encapsulate photoactive guests to perform photophysical studies. The constituents of the MOF interact with the guests and consequently modify the luminescence making them ideal candidates for chemical sensors.[86,87] Fourth, stable MOFs can be reused and also be processed into coatings or membranes.

1.8 Mechanisms of MOF Luminescence

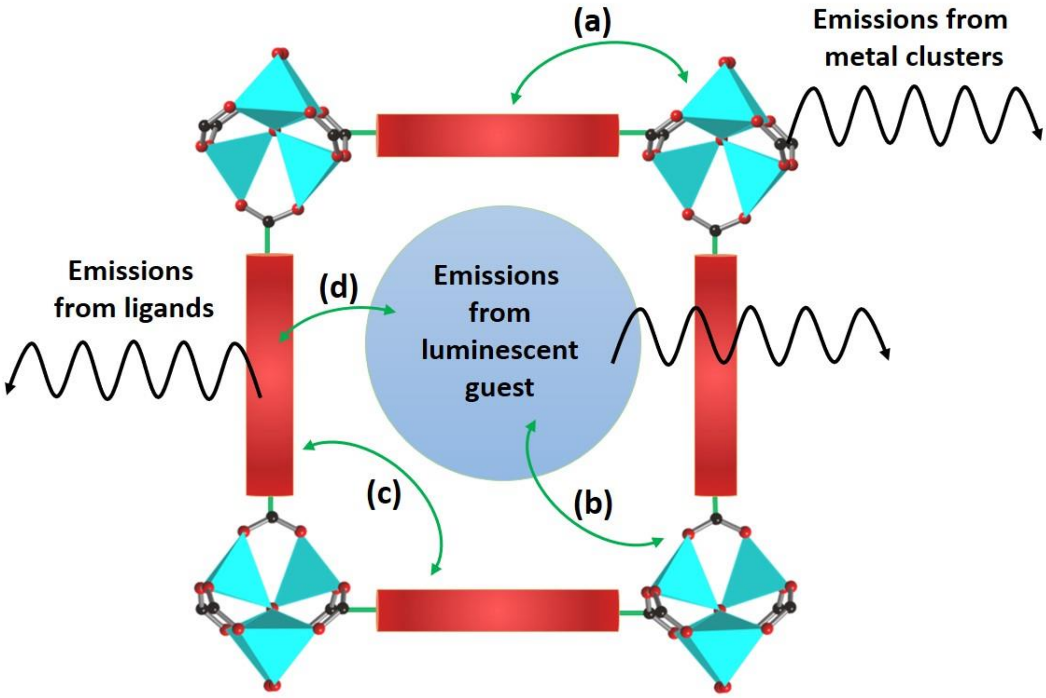

Figure 1.18: Diagram showing the possible mechanisms for luminescence in metal-organic frameworks. Ligands are shown as red rectangles. The black wavy arrows represent photon emission and the green arrows represent interactions leading to emissions: (**a**) metal-ligand interactions (**b**) guest-metal interactions (**c**) ligand-ligand interactions (**d**) ligand-guest interactions.

Figure 1.19 shows the approaches that have been explored to make MOFs luminescent which can be broadly categorised as: (i) Using luminescent organic linkers (ii) emission from the metal clusters (iii) encapsulated guest molecules (iv) energy and charge transfer processes. An overview of these approaches is given below:[88]

***Using Luminescent Organic Linkers*:** Organic compounds with strongly conjugated backbones have strong emissions which are possible because of electronic transitions involving their π orbitals. The increased degree of conjugation causes a decrease in the π-π* energy gap, and thus competing luminescence pathways involving the metal clusters become less efficient. It also helps when the MOF consists of metals with closed shell configurations e.g. Mg^{2+}, Zn^{2+}, and Cd^{2+}. This reduces the probability of charge transfer interactions, making the luminescence completely ligand-centered.[89] Functionalised fluorophores containing anthracene, stilbene, pyrene, ruthenium and osmium complexes, have been used to make MOFs and their fluorescence properties have been studied.[90,91]

Using Photoactive Guests: The porous nature of MOFs can be used to encapsulate photoactive guests which may lead to interesting photophysical behaviour. Fluorescent dyes trapped in MOFs have been used for applications like temperature sensing and white-light emission.[92,93] Another interesting idea is the trapping of lanthanide ions in non-lanthanide MOFs, which is seen to increase the luminescence efficiency of the lanthanides.[94]

***Luminescence from Metal Clusters*:** Lanthanide and actinide ions are known for their sharp emission bands. These arise from f-f transitions from the inner 4f or 5f orbitals, which are less sensitive to the chemical environment than those arising from π-π* transitions of organic ligands.[95] MOFs made using these ions have been well explored for their luminescence properties.[96] Unfortunately, their luminescence is weak since these f-f transitions are forbidden by the Laporte selection rule. The rule states that electronic transitions without a change in azimuthal quantum number ($\Delta\ell$) of ±1 are not allowed. For f-f transitions, the $\Delta\ell = 0$ making them Laporte forbidden. Thus, direct excitation is very inefficient, leading to weak emission. By complexing the lanthanide ion to an appropriate linker, more intense luminescence can be obtained by exploiting the antenna effect.[86,96] This effect involves the use of appropriate linkers, which absorb incident photons and directly transfer energy to the lanthanide energy levels.[97] Oxalic acid, 3-nitrophthalic acid, 4-pyridinecarboxylic acid, and thiophene-derivatised carboxylates are some of the linkers used to explore the antenna effect in MOFs.[91,98,99]

***Charge Transfer Interactions*:** A MOF relies on metal-ligand interactions for its stability. These interactions may enable new electronic transitions to occur. Such transitions have low bandgaps and hence result in the MOF having new absorption bands at longer wavelengths when compared to its components. When the MOF is excited at these wavelengths, a red-shifted emission is observed.[100] This is possible only when the metal and ligand are bonded and not when they are studied independently. Charge transfer between metal to ligand or vice-versa is a prime example for such transitions and is a well-researched area in MOF chemistry.[91,101]

For example: MOF-5 has a broader, more red-shifted absorption band beginning at 350 nm when compared to disodium bdc, whose absorption begins at 322 nm.[102] The shift is a result of a ligand to metal charge transfer (LMCT) between bdc to Zn^{2+}.[103] This LMCT transition causes MOF-5 to have a green emission at 525 nm. However, the emission of disodium bdc is 100 nm lower than MOF-5 and centered at 418 nm. Such LMCT based emissions are also seen in many other MOFs.[91]

Instances of metal-to-ligand charge transfer (MLCT) are also common.[104] In a MOF consisting of Zn^{2+} based clusters with formate and tetratopic polypyridyl ligands, an MLCT event from Zn^{+2} to polypyridyl caused a shift in the MOF absorption band from 315 nm to 330 nm. The MOF showed intense blue luminescence (456 nm) which was about 45 nm red shifted compared to the polypyridyl ligand, whose luminescence was much weaker.[105]

1.9 Quenching of Luminescence and Energy Transfer

Upon absorption of energy a fluorophore is excited from the singlet ground state (S_0) to the singlet excited state (S_1). The fluorophore stays in the excited state for some time and relaxes back to ground state with the emission of a fluorescent photon. The duration of time for which the fluorophore stays in the S_1 state is called the excited state lifetime (symbolised by the Greek letter, **τ**) which is typically in the range of tens of picoseconds to tens of nanoseconds. The value of **τ** for a molecule changes based on its environment; the polarity and viscosity of the solvent also plays a role. **τ** can be significantly affected by the presence of neighbouring molecules which can change the fluorescence intensity and hence reduce its lifetime.

Some species (called quenchers) can complex with a fluorescent molecule in its ground state and change its photophysical behaviour, reducing its emission intensity and making it non-fluorescent. This type of quenching is called static quenching. The quencher gives an alternate non-radiative pathway for the molecule to decay to its ground state involving vibrational and rotational motion. Energy is thus given off as heat and hence no fluorescence is seen.

The other type of quenching is dynamic or collisional quenching. Here, a molecule in its excited state transfers energy to a neighbouring molecule. Based on the mechanism of quenching, it is further classified into three categories: Excimer formation, Förster Resonance Energy Transfer (FRET) and Dexter Electron Transfer (DET).[106-108]

1.9.1 Excimer Formation

An excimer or an excited dimer is an association of two similar fluorophores one in the excited state and the other in the ground state. If the fluorophores are dissimilar such an association is called an exciplex or excited complex. Excimer formation causes the emission spectrum to broaden and be more red-shifted when compared to the monomer.[91] An increase in the **τ** is also seen. In MOFs, the self-assembly of ligands places them close to each other and excimer formation can occur. Cofacial arrangements and low inter-ligand distances of less than 10 Å are known to promote excimer formation in MOFs.

Pyrene is well known to form exciplexes, both in concentrated solutions and in crystal form.[109,110] To mimic this behaviour in MOFs, one In^{3+} and two Zr^{4+} based MOFs with tetratopic pyrene linkers were studied using Density Functional Theory and ultrafast spectroscopy.[111] The studies showed that among these MOFs, the In^{3+} based MOF had the maximum capability of forming excimers due to its lower pyrene-pyrene distance (8.76 Å) and nearly cofacial ligand arrangement. The Zr^{4+} MOFs, had larger distances (9.52 Å and 10.94 Å) and non-cofacial ligands. The average lifetime was also the highest for the In^{3+} MOF (5.44 ns) and much lower for other MOFs (1.48 ns and 1.38 ns).

1.9.2 Förster Resonance Energy Transfer

Consider two molecules, a donor (D) and an acceptor (A) which have distinct absorption and emission spectra. For example, the D-A pair can be two different ligands in an MC-MOF. If an emission peak from the acceptor is seen when the donor is excited, FRET or DET could be a possible reason for this phenomenon. In both cases, a decrease in the **τ** of the donor is seen, with an increase in the τ of the acceptor.

Förster Resonance Energy Transfer (FRET) is a dynamic quenching pathway in which the **τ** can be affected. FRET is a dipole-dipole interaction (Figure 1.19) and requires the D-A pair to be separated within a distance of 10 - 100 Å.[106] The angle or orientation between their transition moments and the degree of spectral overlap between donor emission and acceptor absorption also play a role. FRET is a sixth power dependent phenomenon and hence is very sensitive to changes in the distance.[81,112] In other words, a doubling of the distance can reduce the FRET efficiency by a factor of $2^6 = 64$.

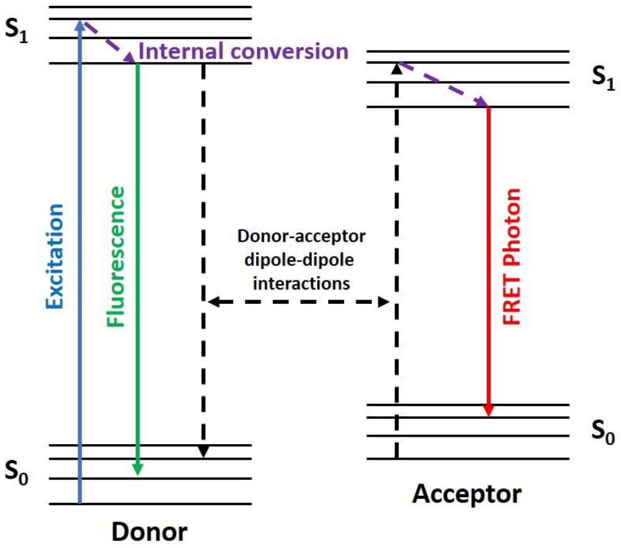

Figure 1.19: A representative Jablonski diagram for FRET. The distance between the donor and acceptor is in the range of 1-10 nm.

The efficiency (E) and rate (k_{FRET}) of the energy transfer process can be calculated using equations 1.1 and 1.2:

$$k_{FRET} = \frac{1}{\tau_d}\left(\frac{R_0}{R}\right)^6 \qquad \text{(Eq. 1.1)}$$

$$E_{FRET} = \left(\frac{R_o^6}{R_o^6 + R^6}\right) * 100 \qquad \text{(Eq. 1.2)}$$

Here, τ_d is lifetime of the donor in the absence of the acceptor. R is the D-A distance. R_0 which is also called the Förster distance, is the distance at which the FRET efficiency is 50%. The value of R_0 is dependent on the integral of the D-A spectral overlap and their mutual orientation. R_0 in Ångström can be calculated by the following equation:

$$R_0 = [8.79 * 10^{-5} (\eta^{-4} Q_D \kappa^2 J)]^{\frac{1}{6}} \qquad \text{(Eq. 1.3)}$$

Where η is the refractive index of the medium, Q_d is the quantum yield of the donor in the absence of the acceptor, κ^2 is the orientation factor calculated from the donor and acceptor transition moments and J is the spectral overlap.

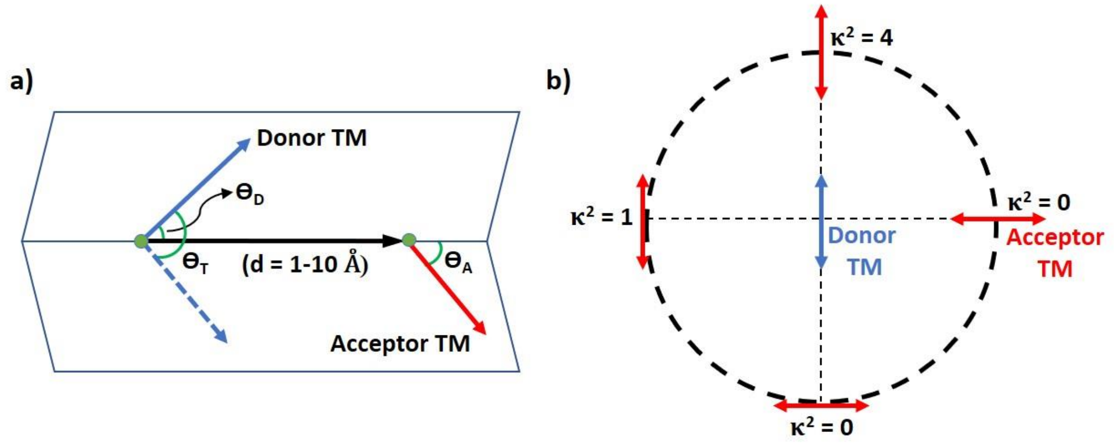

Figure 1.20: a) The angles relevant for calculating the orientation factor in FRET. TM denotes transition dipole moment represented by blue and red arrows. The green circles are the donor and acceptor molecules. **b)** Variation of κ^2 with angle. Note that κ^2 is zero when the donor-acceptor TM are orthogonal. κ^2 is 1 and 4 when the angle is 0° and 180°, respectively.

The orientation factor (κ^2) is a parameter that determines the effect of the angle between the D-A transition dipole moments. For a given donor-acceptor pair, the κ^2 value is given by:

$$\kappa^2 = [\cos\Theta_T - 3\cos(\Theta_D)\cos(\Theta_A)]^2 \qquad \text{(Eq. 1.4)}$$

Where Θ_T is the angle between the donor-acceptor transition moments (Figure 1.20a), Θ_D and Θ_A are angles between the donor and acceptor transition moments and the distance vector separating them. κ^2 varies between 0 and 4 (Figure 1.20b). For proteins and molecules in solution, the rotational motion of the donor and acceptor are fast compared to the fluorescence lifetime. Hence, κ^2 for such systems is approximated to (2/3).[113] However, in MOFs the ligands are rigid and rotational motion is restricted and hence this approximation cannot be used in many cases. Certain DFT methods maybe necessary to determine the κ^2 value.[114-116] Polarisation angle dependent absorption-emission has been used to determine κ^2.[117,118]

The last parameter determining R_0 is the overlap between the normalised emission spectrum of the donor and absorption spectrum of the acceptor (Figure 1.21). This is calculated using the equation,

$$J = \int_0^\infty \varepsilon_A(\lambda)\lambda^4 F_D(\lambda)\, d\lambda \qquad \text{(Eq. 1.5)}$$

Where, ε_A is the absorptivity (in $M^{-1}cm^{-1}$) of the acceptor at wavelength, λ. F_D is the donor emission spectrum normalised to an area of 1.

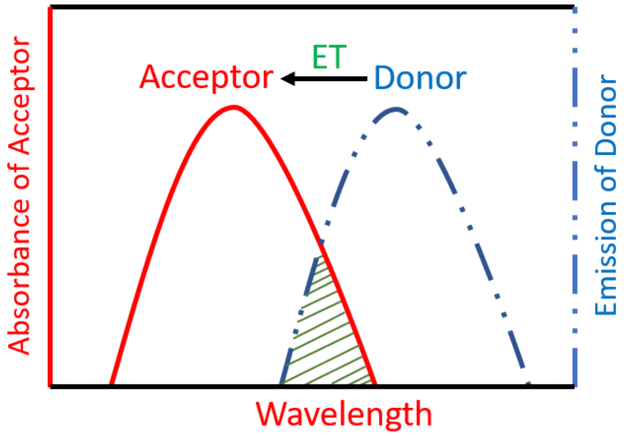

Figure 1.21: Spectral overlap (shown by the green shaded area) between absorption of the acceptor and the emission of the donor. ET stands for energy transfer.

To summarise, FRET is a quenching process occurring through dipole-dipole interactions. From the equations 1.1 – 1.5, it is evident that FRET varies inversely as the sixth power of the D-A distance. The κ^2 value is high when the D-A transition dipoles are parallel or collinear. Furthermore, a high quantum yield of donor and higher absorptivity of the acceptor leads to higher spectral overlap leading to more efficient energy transfer.

1.9.3 Dexter Electron Transfer (DET)

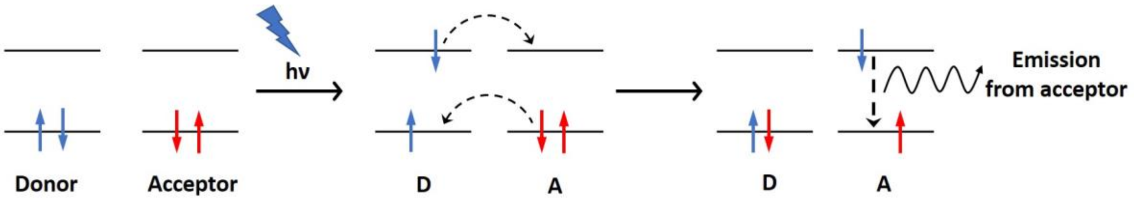

Figure 1.22: Schematic representation of DET, the red and blue arrows represent electrons.

$$k_{DET} \propto J\exp\left(\frac{-2r}{L}\right) \qquad \text{Eq. 1.6}$$

In DET, an electron in the excited state is transferred from the donor to the excited state of the acceptor (Figure 1.22). To compensate charge, an electron from the ground state of the acceptor moves to the ground state of the donor. The excited state electron returns to its ground state with the emission of a photon. Equation 1.6 shows that the rate of DET (k_{DET}) is proportional to the D-A distance (r), the spectral overlap (J) and also the sum of the Van der Waals radii of the donor and acceptor (L). Due to the exponential relationship, k_{DET}

decays rapidly with increase in the D-A distance. DET is a short range energy transfer interaction and occurs only at short distances within 1 - 10 Å, as it requires a D-A wavefunction overlap.[107]

1.9.4 Studying Energy Transfer in MC-MOFs

There are many reports of inter-ligand FRET in MOFs but reports of DET are less common.[119-121] In all cases, the crystallinity of MOFs has been the biggest advantage for studying energy transfer. This means that SCXRD studies have been used in conjunction with spectroscopic measurements to study parameters such as those required for equations 1.1 - 1.6. With MC-MOFs which feature dissimilar but well-ordered ligands, more complex FRET based applications such as light-harvesting, sensing and exciton migration can be achieved. [86] These applications are discussed below.

For example: A Zn^{+2}-based paddlewheel MC-MOF with dipyridyl boron dipyrromethene (BODIPY) as pillars and tetrakis(4-carboxyphenyl)porphyrin as layers showed inter-ligand FRET. Treating this MOF with pyridine results in the removal of the BODIPY protons and the emission spectrum spans the full visible light range, making it useful for solar energy conversion.[122] Even though the ligands were arranged orthogonally, slight deviations from this angle enabled FRET to take place. Another Zn MOF with thiazolothiate pillars and naphthalene-based layers also showed inter-ligand FRET. A red shift was seen when Hg^{+2} was introduced into the pores, an aspect which was used for sensing.[123] In both these MOFs, LMCT transitions were prevented due to the d^{10} configuration of the metal clusters.

FRET studies have been carried out by the Shustova group on two different MC-MOFs made with Zn paddlewheels with H_4TCPP and DPB-BI as pillars (Figure 1.23).[124] Here, the porphyrins act as acceptors and DPB-BI ligands as donors. This system was designed to replicate a FRET process seen in green fluorescent protein (GFP). Using crystallography and time-resolved fluorescence, parameters like Förster distance, spectral overlap, and FRET efficiency were calculated. An efficiency of about 72 % was found for both MOFs. This was lower than GFP (FRET efficiency ≈ 100%), however the stability and crystallinity of the MOF makes this approach more applicable for light-harvesting assemblies.

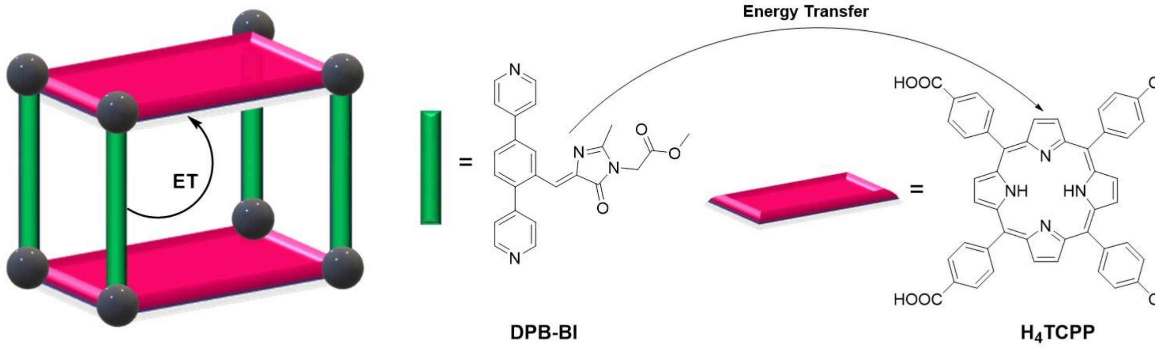

Figure 1.23: Inter-ligand energy transfer (ET) in a MOF developed by the Shustova group. The Cu-paddlewheels are shown as black spheres, DPB-BI as green rods and H_4TCPP as maroon rectangles.

In crystalline solids such as MOFs, excitation forms a quasiparticle called an exciton. This exciton consists of a bound electron-electron hole pair which are attracted to each other electrostatically. An exciton is neutral and can diffuse across the MOF thus transporting energy in a phenomenon called exciton hopping or exciton migration. A neighbouring electron replaces the pre-existing hole, creating a new hole. The process repeats many times, thus transporting energy across the MOF crystal before recombining with the electron and being quenched. Exciton migration can occur by dipole-dipole interactions, a phenomenon which is governed by the FRET theory.

For each material, the exciton migrates a specific distance which is dependent on the materials diffusion coefficient and fluorescence lifetime. This distance, which is also called the exciton diffusion length (L_D), can be measured with various techniques.[125] By finely tuning the ligand and MOF structure, the L_D can be increased. The longer the fluorescence lifetime, the longer this distance, which aids in developing MOFs for photovoltaic applications.

Detailed time-resolved spectroscopy of FRET in MC-MOFs was performed by Son et. al. An MC-MOF (called DA-MOF) was made of porphyrin struts and tetracarboxylate linkers connected to Zn paddlewheel clusters.[126] A combination of ferrocene-based quenchers, ultrafast spectroscopy, and computational studies were done to determine fluorescence lifetimes and exciton hopping distances. Changing the original porphyrin linker to a more conjugated acetylene bridged porphyrin linker proved useful in increasing the number of exciton hops from 8 to 2025. This corresponds to an increase in the L_D from 3 nm in the original MOF to about 60 nm in the acetylene functionalised MOF. This study, however only investigated step-by-step hopping of excitons i.e. the migration of excitons between adjacent ligands.

Research by the Lin group studied another class of exciton migration which was called jumping beyond nearest neighbour (JBNN) hopping.[127] In this case, the exciton diffuses by skipping over adjacent ligands over long distances to distances about 40 – 50 nm (Figure 1.24). This is much higher when compared to step-by-step hopping distances which are typically 20-25 nm. Lin and co-workers studied two Zn MOFs with truxene-based ligands and used coumarin 143 as a quencher. JBNN hopping was proven to contribute about 67% of the energy transfer in these frameworks.

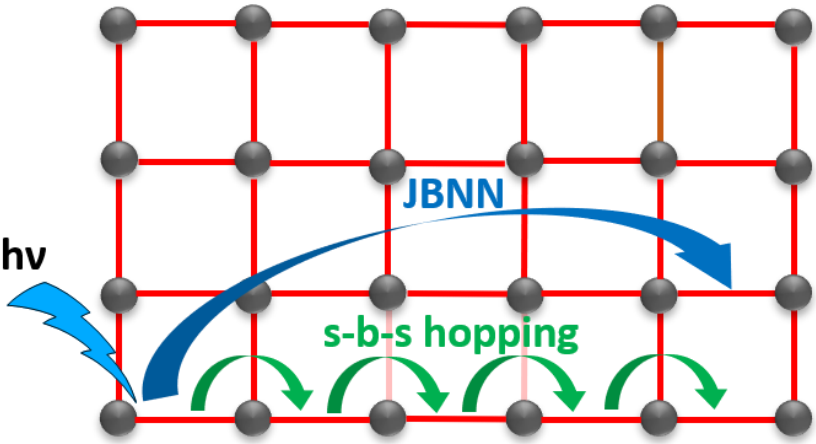

Figure 1.24: A schematic showing the modes of exciton migration in MOFs. Ligands are shown as red lines and clusters as black circles. The green arrows indicate s-b-s (step-by-step) hopping and JBNN (jumping beyond nearest neighbour) is shown with a blue arrow.

1.10 Photochromism in MOFs

Photochromism is the phenomenon where the colour of a substance changes in response to exposed light. On absorption of incident light, the substance changes its structure, affecting its light absorption properties and hence its colour. To make the substance revert to its original colour light or heat can be used. Based on the mode used for reversal, photochromic materials are classified into two types i.e. T type (thermally reversed) and P type (light reversed).[128]

Molecules like azobenzene, diarylethene and spiropyrans are some of the commonly used structural motifs used to make photochromic MOFs (Figure 1.25a – 1.25c). For the above examples, the structure of the molecule changes on light absorption, sometimes changing the degree of conjugation. However, photochromic materials can also be made from molecules with redox active cores like naphthalene diimide (Figure 1.25d).[129] On photoexcitation, the colour change is a result of a radical being formed, which is stabilised by delocalisation due to the high degree of conjugation in NDI.[130] Irradiation may also cause an electron to be released to form a radical cation with a different colour. The released electron can be picked by a neighbouring ligand forming a radical anion.[131]

Photochromic MOFs are a subset of the broader class of stimuli responsive MOFs.[132] The properties of these MOFs can be turned on or off based on stimuli like light, heat, pressure, magnetic field. For example, Figure 1.25a shows a *cis-trans* isomerisable azobenzene linker MOF reported by Zhou.[133] This MOF shows reversible changes in CO_2 sorption before and after UV light irradiation. A similar light reversed effect for argon adsorption was seen for a spiropyran linker containing MOF shown in Figure 1.25c.[134]

Figure 1.25d depicts the formation of a radical in a redox active naphthalene diimide (NDI) linker, which was used for inkless printing.[130] Redox active linkers have also been used to make conductive MOFs. Typically, MOFs are insulating materials due to their porous nature. However, employing linkers comprising of tetrathiafulvalene, tetracyanoquinodimethane, and porphyrins can make MOFs conductive.[135,136] On applied potential, radicals are formed changing the colour of the MOF. Light-induced conductivity i.e. photoconductivity has recently been studied and further probed using time-resolved terahertz spectroscopy.[137,138]

Many techniques are employed to characterise photochromic MOFs. Diffuse reflectance spectroscopy (DRS) can monitor changes in the UV-Vis spectrum for MOFs suspended in solvents. Radical generating MOFs are characterised using electron paramagnetic resonance (EPR) spectroscopy and cyclic voltammetry. In azobenzene linkers, the photoisomerization proceeds without bond breaking or formation, but its electronic structure does change. FT-IR spectroscopy may not be sensitive to such changes; Raman spectroscopy, however is a much better tool to probe them.[139]

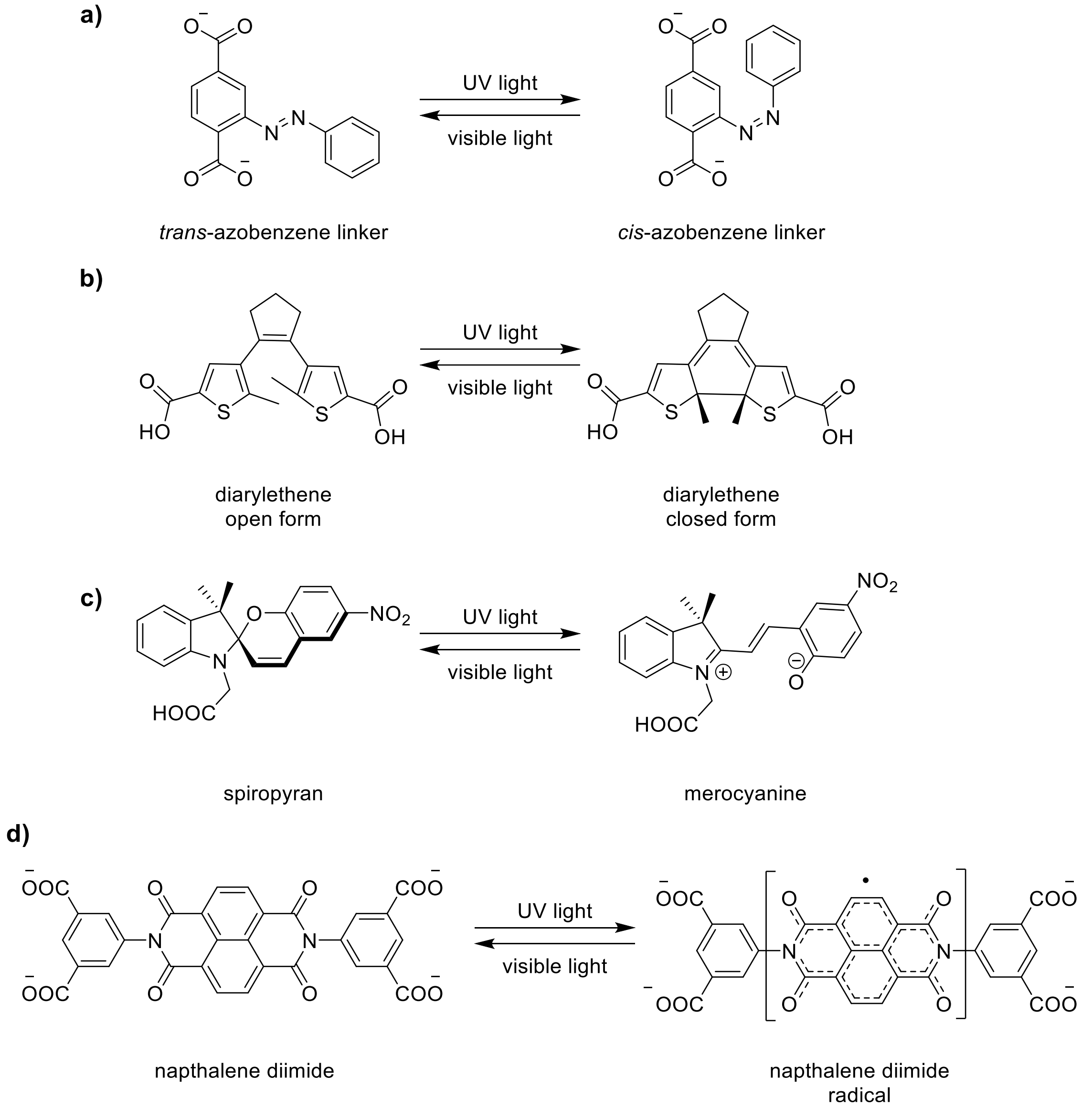

Figure 1.25: Examples of photochromic moieties incorporated into MOFs found in the literature **a)** azobenzene linkers reported by Zhou's group.[133] **b)** diarylethenes reported by Benedict's group.[140] **c)** spiropyrans reported by D'Alessandro's group.[134] **d)** redox-active naphthalene diimide (NDI) linkers reported by Banerjee's group.[130]

1.12 Catalysis in MOFs

The high surface area of MOFs makes these materials an ideal platform for catalysis. Many reviews have compilations of a pretty exhaustive list of MOF based catalysts.[141-146] MOF's combine two highly desirable properties that make them ideal candidates for heterogeneous catalysis. First, the enhanced porosity of MOFs facilitates easy diffusion of reactants to interact with the active site. Second, due to their highly crystalline nature, the position of each atom can be precisely determined by crystallographic techniques. This makes it less challenging to establish structure-activity relationships.

To design MOFs for heterogenous catalysis, one or more of the following strategies have been used:

i. **Catalysis by encapsulated species:** The pores of MOFs can serve as a physical space in which a catalytic species can be confined. The MOF serves as a support to stabilise the catalyst. Metal oxide nanoparticles,[147] inorganic clusters,[148] transition metal complexes,[149] and dyes[150] have been successfully confined into the pores. This strategy has been used to explore photocatalysis and electrocatalysis[151] for the production of valuable materials such as hydrogen and methanol.

ii. **Catalysis at the metal clusters:** Some MOFs (such as **MIL-101** or **HKUST-1**) consist of metal clusters which are coordinatively unsaturated. Such clusters are Lewis acid sites which can strongly bind to substrates.[152,153] More energy demanding reactions like C-H activation can be catalysed using this method.[154,155] The self-assembly of some MOFs can generate defects. The level of these defects depends on the synthesis conditions, which can generate missing clusters or missing ligands. Defect sites can provide a rich platform for catalysis. However, controlling defects is quite a challenge and a lot of recent studies have tried to precisely ‘engineer’ these defects to exhibit desirable properties.[156-159] UiO-66, MOF-808, and NU-1000 are some commonly used MOFs for defect-based catalysis. Applications of defect catalysed reactions found in the literature are epoxide ring-opening, water oxidation,[160] Paal-Knorr reactions, dimerisation of ethylene and the decomposition of chemical warfare agents.[161,162]

iii. **Incorporating a catalytic unit on the organic linker:** This approach involves functionalising the organic linker with catalytic units. Organocatalytic moieties like proline,[163] urea,[164] thiourea,[165] or squaramides,[166] can be appended to bdc or bpdc backbones to make a useable ligand. Organic transformations such as aldol reactions,[167] Michael addition,[168] Henry reactions,[169] Friedel-Crafts alkylations,[170] Morita-Baylis-Hilman Reactions,[171] epoxide methanolysis[165,172] have all been well catalysed by this approach to give excellent yields and enantioselectivities. Some examples of catalysis with post-synthetically generated Ir, Pd, and Pt complexes also exist.[146]

Even though catalysis in MOFs is extensively researched, only few reports in literature speak about catalysis in MC-MOFs. A notable example was the FDM series of MOFs from Li’s group synthesised by combining trinuclear copper pyrazolate as a tritopic metalloligand with ditopic ligands such as 4-pyrazolecarboxylic acid, bdc, and 2,6-

naphthalenedicarboxylic acid. Oxidation of benzyl alcohol to benzaldehyde was successfully catalysed by this MC-MOF with high yields.[173] In another example for MC-MOF catalysis, Zr^{+4} based PCN-700 frameworks with bipyridine dicarboxylate and terphenyl dicarboxylate based ligands could perform size selective oxidation of alcohols.[174]

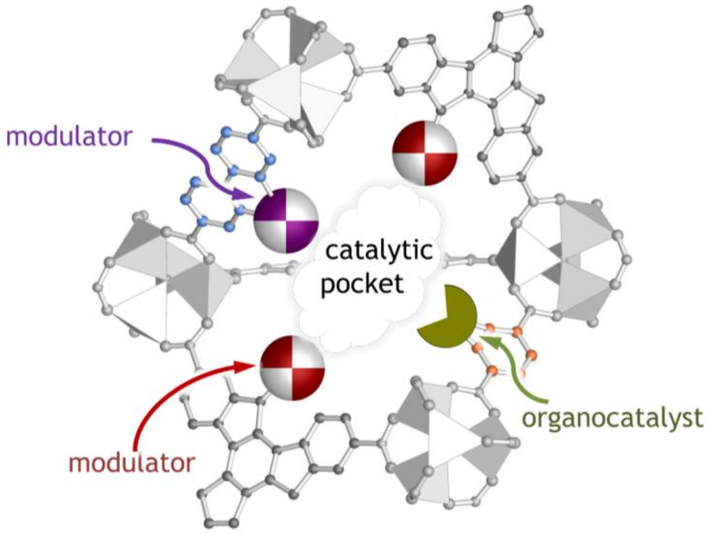

Figure 1.26: A cartoon representation of the modulator approach for catalysis in MUF-77. The catalytic pockets are the pores within the MOF which have well-defined environments. Programming these pores using modulators can influence the outcome of the reaction.[175]

Changing the the catalytic unit within a MOF would surely change the outcome of a reaction. But could the pores be programmed in such a way that the outcome be controlled within the same MOF system containing the same catalytic unit? The Telfer group has achieved this attaching the other ligand(s) with *modulators*, groups that do not bear a catalytic site. The substrate enters the pore, noncovalent interactions between the substrate and the modulator can influence the reaction (Figure 1.26). MC-MOFs like MUF-77 are ideal candidates as multiple ligands arrange in a pre-determined manner around the pore. If one ligand bears a catalytic group, the other two ligands can be incorporated with non-catalytic groups serving as modulators. For the proline-catalysed aldol reaction of *p*-nitrobenzaldehyde and acetone, modulators such as alkyl groups on the tritopic ligand can change the rate and enantiomeric excess of the reaction.[175]

More questions pop up: Could a substrate be made to favour one out of two reactants for a specific reaction pathway? In other words, could selectivity, a feature seen in enzymes, be explored in MC-MOFs? MUF-77 provides a platform to obtain such a result as published in a 2019 publication by the Telfer group.[176] *m*-Nitrobenzaldehyde can react with acetone via an aldol reaction or add to nitromethane via a Henry reaction. Both these reactions are proline catalysed. By using dppdc or bpdc as a selectivity modulator and alkyl functionalised truxenes as a reactivity modulator, selectivity can be achieved (Figure 1.27). A ratio of 6.43:1 was observed between aldol and Henry products for the MUF-77 catalyst [Zn_4O(bdc-proline)$_{1/2}$(dppdc)$_{1/2}$(hdtt)$_{4/3}$].

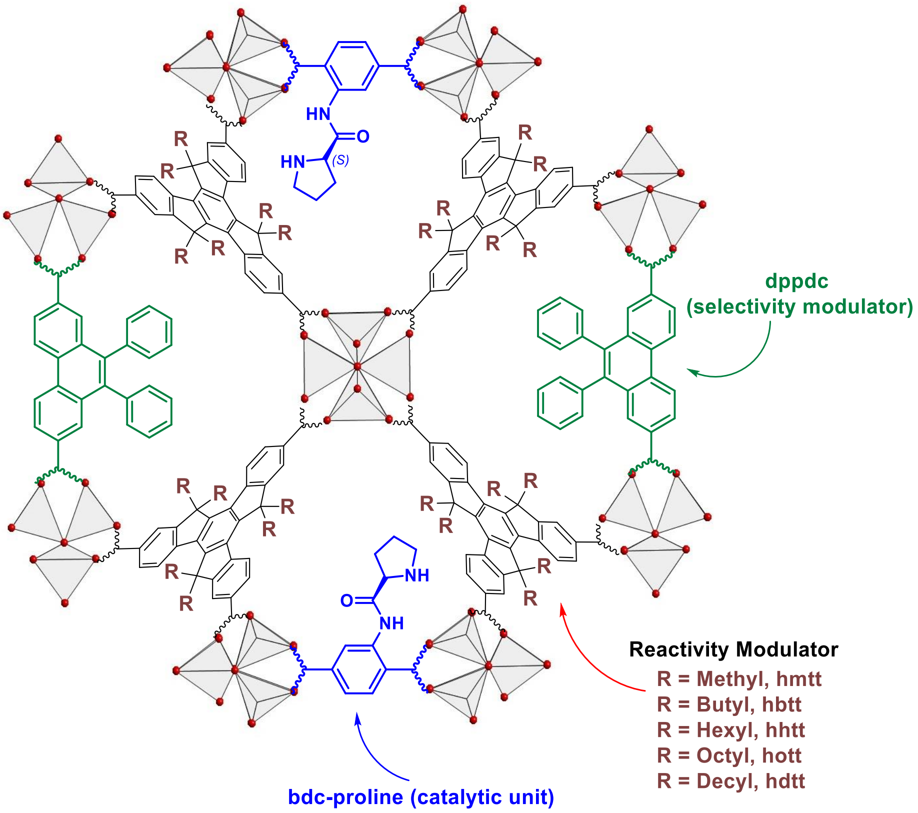

Figure 1.27: A representation of the reactivity and selectivity modulator for the catalysis of aldol and Henry reactions in MUF-77.[176]

So, what are the first few steps in developing MOF catalysts? Firstly, catalyst screening is performed as follows: An ester version of the ligand is synthesised bearing the appropriate catalytic unit. If this ester is able to catalyse the reaction, it is hydrolysed to get the carboxylic acid. The carboxylic acid is then incorporated into a MUF-77 system and used to catalyse the same reaction. Comparison of yields and ee between homogenous and heterogeneous catalysis are done using techniques such as NMR, chiral HPLC and chiral GC. Chapter 5 of this thesis outlines our attempts to catalyse the intramolecular exo-cyclisation of 1,6-hexanedial with MUF-77.

1.13 Aims of the thesis

This thesis is written with the goal of answering the following questions:

a) Could we make MUF-77 systems amenable for fluorescence measurements?

b) Could multiple fluorescent ligands having different emission maxima be combined into MC-MOFs to tune the spectral output? As a consequence, could white-light emission be obtained?

c) If tunable emission is achievable, then the fluorescent ligands will be arranged at defined positions and orientations in the framework. Based on this feature, inter-ligand FRET processes between the ligands may be possible. What are the rates, lifetimes, and efficiencies of these processes? What techniques could be used to study them?

d) If redox-active ligands are incorporated into MC-MOFs, would inter-ligand charge transfer be possible? How does it affect the structure of the MOF?

e) Catalytically active ligands have already been reported to be incorporated into MUF-77, could this framework be used to catalyse *intramolecular* reactions as opposed to the more common *intermolecular* reactions?

Chapter 2 – Systematic Tuning of the Luminescence Output of Multicomponent Metal–Organic Frameworks

2.1 Introduction

MOFs exhibit interesting and useful properties. One of the foremost principles in the chemistry of MOFs is the isoreticular principle.[3,10] This principle posits that making small changes in the functional groups of a ligand while retaining their length will preserve the topology and lattice structure of a MOF. The isoreticular nature of many metal-organic frameworks (MOFs) has made it possible to induce tunability in their properties, making them usable for a variety of applications including luminescence. This has been true of luminescent MOFs which have been made by using luminescent moieties as building blocks. As discussed in the introduction, MOFs use one or more of the following strategies to exhibit luminescence: emission from luminescent linkers, emission from the metal clusters, encapsulation of emissive guest molecules, and energy transfer interactions.[91] This has resulted in the application of MOF luminescence in chemical, and biological sensing, thermometry, second and third harmonic generation and white-light emission.[87,93,101,177-179]

Even though the mechanisms of MOF luminescence have been explored to a certain extent, there are only a few methods used to induce tunability in the emission profile. For example, Gai *et. al.* were able to tune emissions by using MOFs with varying ratios of emissive lanthanide metals.[180] Many other groups have used trivalent lanthanide ions as guests or as part of the metal clusters for tunability.[181-184] Lanthanide emissions, though predictable, are sharp and consequently lanthanide MOFs have low colour rendering indices (CRIs).[185]

On the other hand, using luminescence from organic linkers coordinated to d^{10} ions like Zn(II) has distinct advantages. The diamagnetic nature of zinc makes the linker retain its emission behaviour.[89,186] These emissions being broad result in higher CRI values. Zinc MOFs have been used for tunable luminescence. Guest molecules such as lanthanide ions, metal complexes, fluorescent dyes, and volatile organic compounds have been used for further improvement of this tunability.[92,179,187,188]

Achieving white-light (WL) emission is another active area in luminescence research, due to the wide applicability of these emitters in display devices. A variety of materials have been used to generate white light.[189-194] Reports of WL emission from MOFs has shown some common strategies *i.e.* multivariate MOFs with a controlled combination of red-green-blue or blue-yellow emitters,[180,195-198] and also by multiple, simultaneous photophysical process occurring within or between the constituents of the MOF.[86,199] This chapter demonstrates a new strategy for WL emission taking advantage of the multicomponent nature of MUF-77.[200]

2.2 Results and Discussion

2.2.1 Synthesis of luminescent MUF-77 nanocrystals

We present a series of intrinsically luminescent, multicomponent, quaternary MUF-77 MOFs. [78,175] These MOFs contain three chemically and geometrically distinct ligands bonded to a Zn_4O cluster in an **ith-d** topology with the formula $[Zn_4O(hxtt)_{4/3}(bpdc)_{1/2}(bdc)_{1/2}]$ (Figure 2.1). MUF-77 is completely isoreticular in that any of the three ligands can be replaced by analogues that bear functional groups without changing the lattice structure.

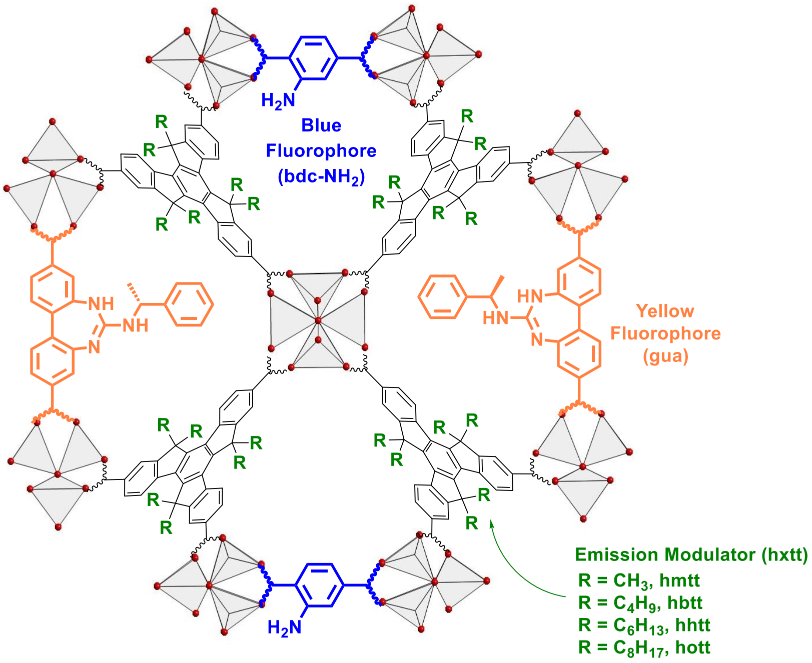

Figure 2.1: Schematic of the structure of MUF-77 showing the relative arrangement of the ligands**.**

The tritopic ligands were synthesised based on an existing procedure.[78] bdc-NH_2 was obtained from commercial sources. The gua ligand was synthesised by Dr. Tian-You Zhou, originally for the using it as catalyst due to its guanidine moiety. Yellow emission was seen for its ester during column chromatography and hence the idea of combining blue and yellow emitters in MUF-77 to obtain white light was born.

In contrast to the traditional solvothermal synthesis of MUF-77,[175] which gives single crystals about 500 μm in size, we developed a method for preparing MUF-77 nanocrystals. By replacing zinc nitrate with zinc acetate and mixing it with a solution of ligands at room temperature, MUF-77 nanocrystals were obtained. (Figure 2.2, Table 2.1 and experimental section 2.4.3, Table 2.2).[201] This technique offered multiple advantages, namely: (a) formation of MUF-77 nanocrystals which are nearly uniform in size, (b) the method can be potentially used to incorporate ligands which are sensitive to the solvothermal method,[202] (c) the nanocrystals can be easily suspended in solvents and their emission properties can be measured, and (d) use in further applications such as coatings on surfaces like LEDs or membranes.

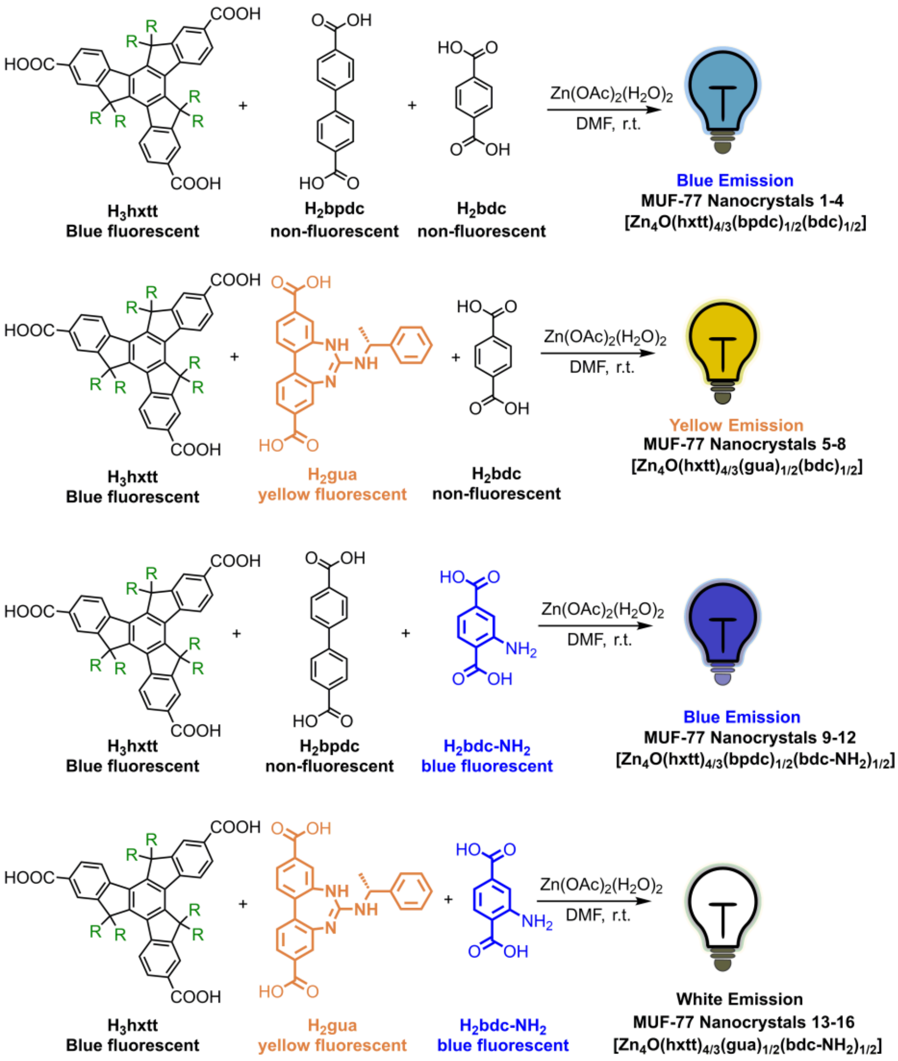

Figure 2.2: Preparation of luminescent MUF-77 Nanocrystals (**1**–**16**).

We used the following strategies for MUF-77 to exhibit tunable luminescence: (a) We made the simplest set of MUF-77 frameworks (**1**, **2**, **3**, and **4**) with the formula $[Zn_4O(hxtt)_{4/3}(bpdc)_{1/2}(bdc)_{1/2}]$ by using different tritopic truxene ligands, each having different alkyl chains on the 5, 10, and 15 positions. (b) A second set of frameworks (**5**, **6**, **7**, and **8**) were made by changing the bpdc linker with a unique, guanidine functionalised bpdc (**gua**), having a fluorophore emitting in the yellow region (λ_{em} = 570 nm). We slightly tune this yellow emission by truxene linkers with different alkyl substituents, obtaining MUF-77 systems [$Zn_4O(hxtt)_{4/3}$(**gua**)$_{1/2}$(bdc)$_{1/2}$] (c) By using a strong blue emitter bdc-NH_2 (λ_{em} = 427 nm) instead of bare bdc, we make a MUF-77 library of [$Zn_4O(hxtt)_{4/3}(bpdc)_{1/2}$(bdc-$NH_2$)$_{1/2}$] which are coded **9**, **10**, **11** and **12** (d) Finally, we combine both **gua** and bdc-NH_2 in the same MUF-77 system [$Zn_4O(hxtt)_{4/3}$(**gua**)$_{1/2}$(bdc-NH_2)$_{1/2}$] and get MOFs (**13**, **14**, **15** and **16**) giving highly tunable luminescence in both the blue and yellow regions. These combinations give shades of white light with different correlated colour temperature (CCT) values.

Table 2.1: Synthesised MUF-77 MOFs with their corresponding ligand combinations.

MOF Code	Ligand combination	MOF Code	Ligand Combination
1	hmtt/ bpdc/ bdc	**9**	hmtt/ bpdc/ bdc-NH_2
2	hbtt/ bpdc/ bdc	**10**	hbtt/ bpdc/ bdc-NH_2
3	hhtt/ bpdc/ bdc	**11**	hhtt/ bpdc/ bdc-NH_2
4	hott/ bpdc/ bdc	**12**	hott/ bpdc/ bdc-NH_2
5	hmtt/ gua/ bdc	**13**	hmtt/ gua/ bdc-NH_2
6	hbtt/gua/ bdc	**14**	hbtt/ gua/ bdc-NH_2
7	hhtt/ gua/ bdc	**15**	hhtt/ gua/ bdc-NH_2
8	hott/ gua/ bdc	**16**	hott/ gua/ bdc-NH_2

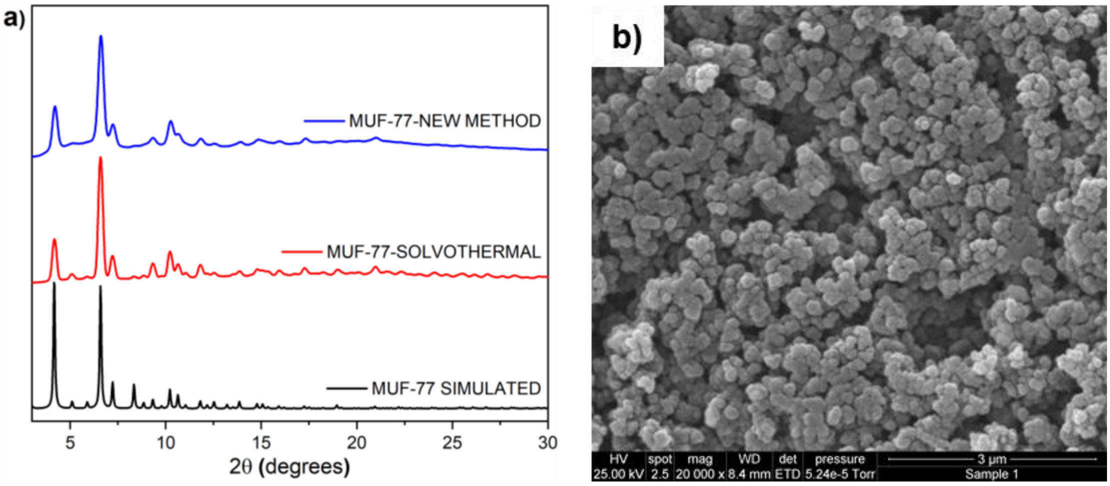

Figure 2.3: a) Representative PXRD pattern (Cu_{α} radiation) of the MUF-77 nanocrystals. The PXRD patterns of large MUF-77 crystals synthesized under solvothermal conditions and simulated from the SCXRD structure are shown for comparison. **b)** SEM image showing of the MUF-77 nanocrystals.

Nanocrystals of sixteen isoreticular MUF-77 frameworks (**1** - **16**) were synthesised by using the new method (Experimental section 2.4.3). Powder X-ray diffraction (PXRD) of each of the synthesised frameworks showed that their structure was of MUF-77 (Figure 2.3 and experimental section, Figure 2.13). Scanning electron microscopy (SEM) showed that the particles were monodisperse with sizes ranging from 100-200 nm. (Figure 2.3). The PXRD patterns could also indexed to the lattice planes as predicted from the SCXRD structure (Figure 2.4). All these experiments provided corroboratory proof that the MUF-77 structure was retained. ^{1}H-NMR spectroscopy of the acid digested MOFs was used to determine the ratio of the ligand integrals, which matched to that expected of MUF-77 *i.e.* [$Zn_4O(hxtt)_{4/3}(bpdc)_{1/2}(bdc)_{1/2}$] (ESI; Figure S1-S16).

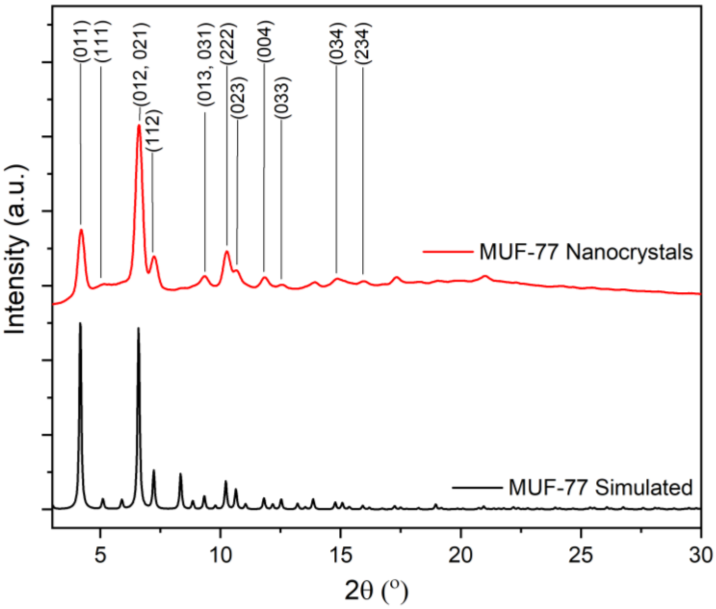

Figure 2.4: A comparison of the PXRD patterns of the synthesised MUF-77-nanocrystals to that simulated from the SCXRD structure. hkl indices for the peaks are also shown.

2.2.2 Luminescence MUF-77 nanocrystals and white-light emission

The fluorescence of DMF suspensions of the synthesised MUF-77 nanocrystals was measured with an excitation wavelength of 390 nm. I also took photographs of the MOFs under UV irradiation for easier colour visualisation (Figure 2.6). All sixteen MUF-77 frameworks showed unique emission spectra.

For the MOFs **1**, **2**, **3** and **4**, the emission spectra are similar to their truxene-based tritopic linkers (Figure 2.5a and Experimental section, Figure 2.15). This can be attributed to the fact that ligand coordination to Zn results in low spin-orbit coupling, leading to the retention of emission.[186] The emissions were blue and centred between 430 to 445 nm. The bdc and bpdc are non-emissive at 390 nm and hence no contribution from these linkers is seen in the emission spectrum.

MOFs **5**, **6**, **7**, and **8** possess a yellow fluorescent guanidine (gua) (λ_{em} = 570 nm, experimental section, Figure 2.16) ligand which as expected gives rise to yellow emission in the MOF. The emission maximum for **5** was slightly red-shifted centred at 575 nm. **6** and **7** also showed blue-shifted yellow emissions centred at 565 nm, with a minor peak at 468 nm (Figure 2.5b). A further blue-shift moving to 560 nm was observed for **8**. Here, it is evident that increasing the length of the alkyl chains on the tritopic linker results in a shift to lower wavelengths for the yellow emission. Very little contribution from the characteristic blue peaks of truxene component was noted for these frameworks. These patterns may be caused by an excited-state energy transfer from the tritopic ligand to the gua ligand, which subsequently enhances yellow emission of the gua. Further studies on these systems are described in Chapter 3.

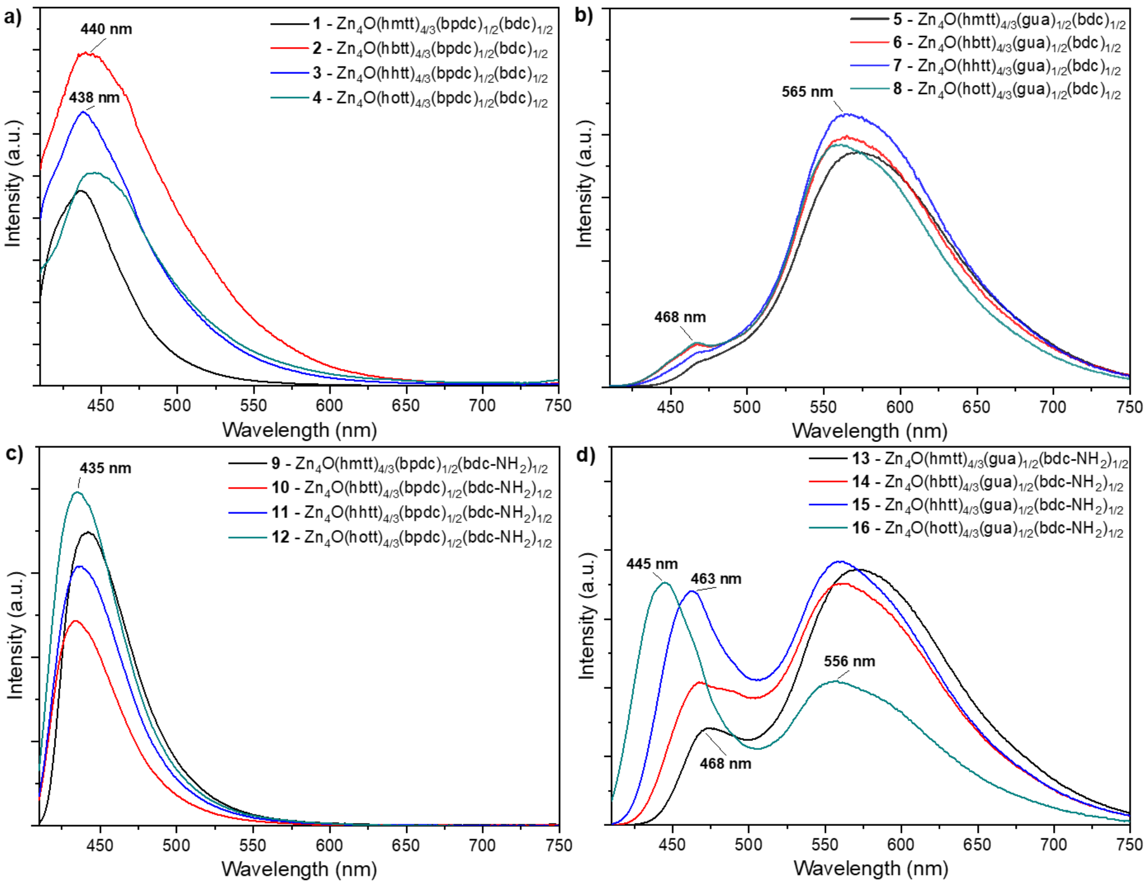

Figure 2.5: Luminescence of DMF suspensions of MUF-77 nanocrystals suspended with an excitation wavelength of 390 nm. **a) 1** – **4 b) 5** – **8 c) 9** – **12** and **d) 13** – **16**.

The highly emissive nature of bdc-NH$_2$ makes **9**, **10**, **11** and **12** to all have strong blue emissions (Figure 2.5c and Experimental section, Figure 2.15). These change slightly on changing the tritopic ligand with all of them having emission maxima between 425-440 nm.

The best results for tunability were achieved when we used both blue and yellow emissive ligands for making frameworks **13**, **14**, **15**, and **16** (Figure 2.5d). By increasing the length of the alkyl chain on the tritopic linkers we obtained distinct spectra for each framework. The blue band shows a steady blue shift from 468 nm for **13** to 445 nm for **16** accompanied by increases in intensity relative to the yellow emission band. These trends result in the increased contribution of the blue emissive band, with **16** showing a much stronger blue band. Additionally, the peak at 570 nm seen for **13**, moves to lower wavelengths, with **16** having a broad peak centred in the green region (556 nm). It is important to note that this range of tunability with these systems is achievable only when all three fluorophores work in tandem, which draws on the multicomponent nature of MUF-77.

1

2

3

4

5

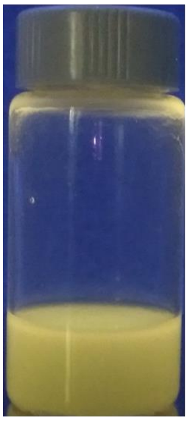

6

7

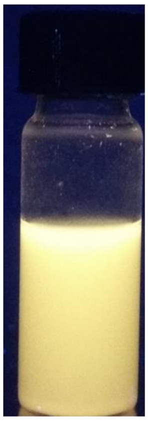

8

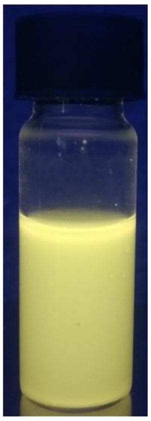

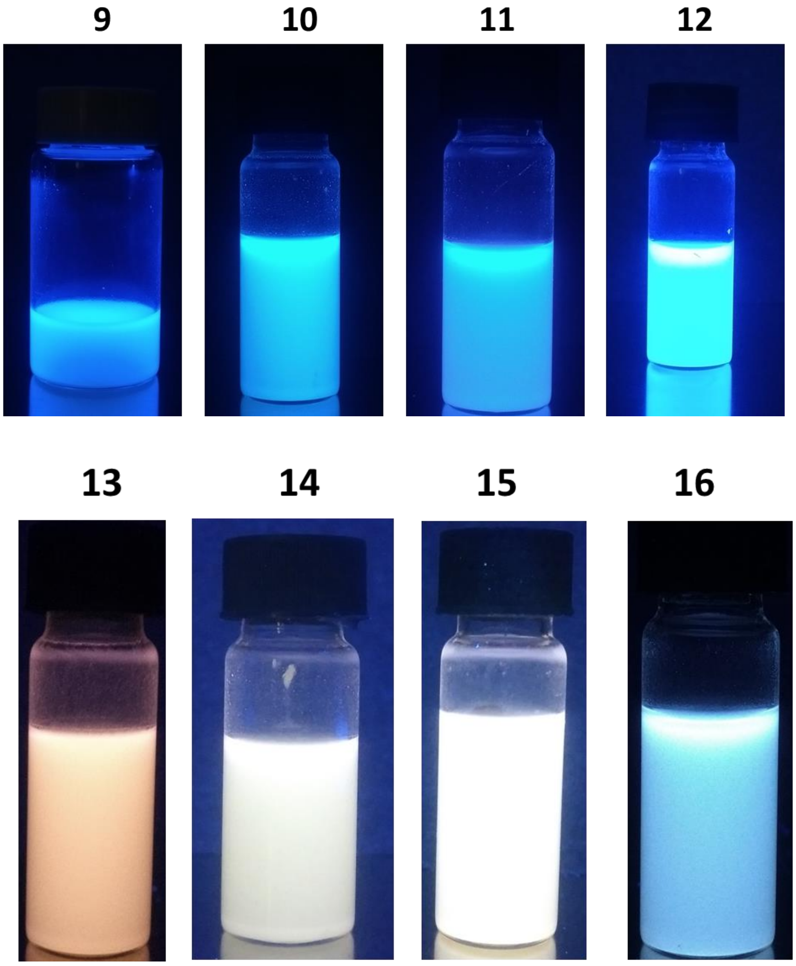

Figure 2.6: Photos of Luminescent MUF-77 nanocrystals were suspended in DMF and illuminated under a UV lamp (λ = 365 nm). MOF codes are shown above each image.

2.2.3 Calculation of CIE Coordinates

We translated the emission spectra of all the MOFs into CIE coordinates and plotted them onto a 1931 CIE chromaticity diagram to know the colour of the emission. Calculation of correlated colour temperate (CCT) was also done. CIE diagrams are useful to visualise the colour of the emissions. CCT values relate this colour to an ideal black-body at a certain temperature that radiates light of the same colour. Colours with CCT values over 5000 K are called ‘cool’ colours and can be used for indoor lighting. On the other hand, lower CCTs also called ‘warm’ colours are applied for outdoor lighting.[203] However, not all colours can be translated to a CCT for example bright blue, green, and deep red emissions do not have a CCT associated with them.

1, **2**, **3**, **4**, **9**, **10**, **11**, and **12** showed CIE coordinates which were all in the blue region of the CIE diagram (Figure 2.7a and 2.7c, Experimental section, Table 2.3), a region where CCT cannot be calculated. Among these MUF-77 systems, saturated blue emission[204] with CIE coordinate of $y < 0.10$ was observed for **1**, **9**, **11**, and **12**. On the other hand, Figure 2.7b shows that **5**, **6**, **7**, and **8** have CIE coordinates (*x*, *y*) in the yellow region ranging between (0.45–0.42 to 0.49–0.48). Their CCT values are range from 3300 K for **5** to 3828 K for **8**, which translate to warm colours.

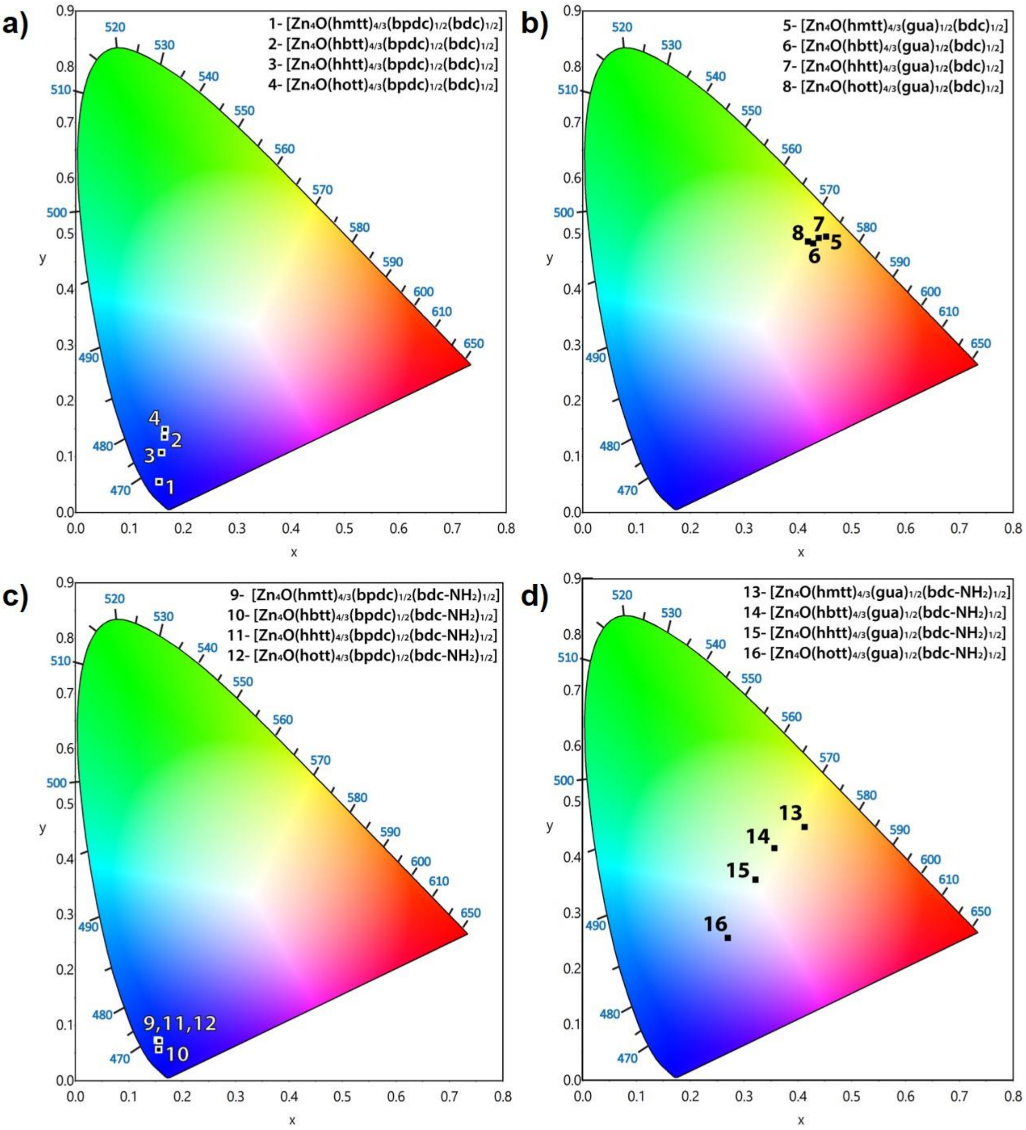

Figure 2.7: The CIE diagrams showing the tunability of the spectral output of the MUF-77 nanocrystals **1-16** upon excitation at 390 nm.

The trend in relative contributions of blue and yellow peaks from **13**, **14**, **15**, and **16** resulted in white-light emission of different CCT values (Figure 2.7d). **15** shows white-light emission with CIE coordinates (0.3218, 0.3590), close to that of pure white-light (0.33, 0.33) with a CCT of 5935 K. The higher contribution of blue band in **16** translates to a cool, (CCT = 16033 K) bluish-white emission, while **13** (CIE 0.4129, 0.4535) and **14** (CIE 0.3569, 0.4156) have warm, yellow-white emissions (CCT 3780 K and 4837 K respectively).

2.2.4 Tunability by the addition of guests.

Guanidine groups are well known for their ability for hydrogen bonding with various groups.[205-207] Since the gua ligand contains a luminescent guanidine moiety, MUF-77 systems containing gua must be able to H bond to substrates, affecting the fluorescence behaviour. The chiral centre of gua may also be able to change emission based on the stereochemistry of the substrate molecule. As a proof of principle experiment for H-bonding based tunability, we took crystals of **5** ($[Zn_4O(hmtt)_{4/3}(gua)_{1/2}(bdc)_{1/2}]$) which were originally dispersed in DMF and exchanged them with dichloromethane by repeated centrifugation.

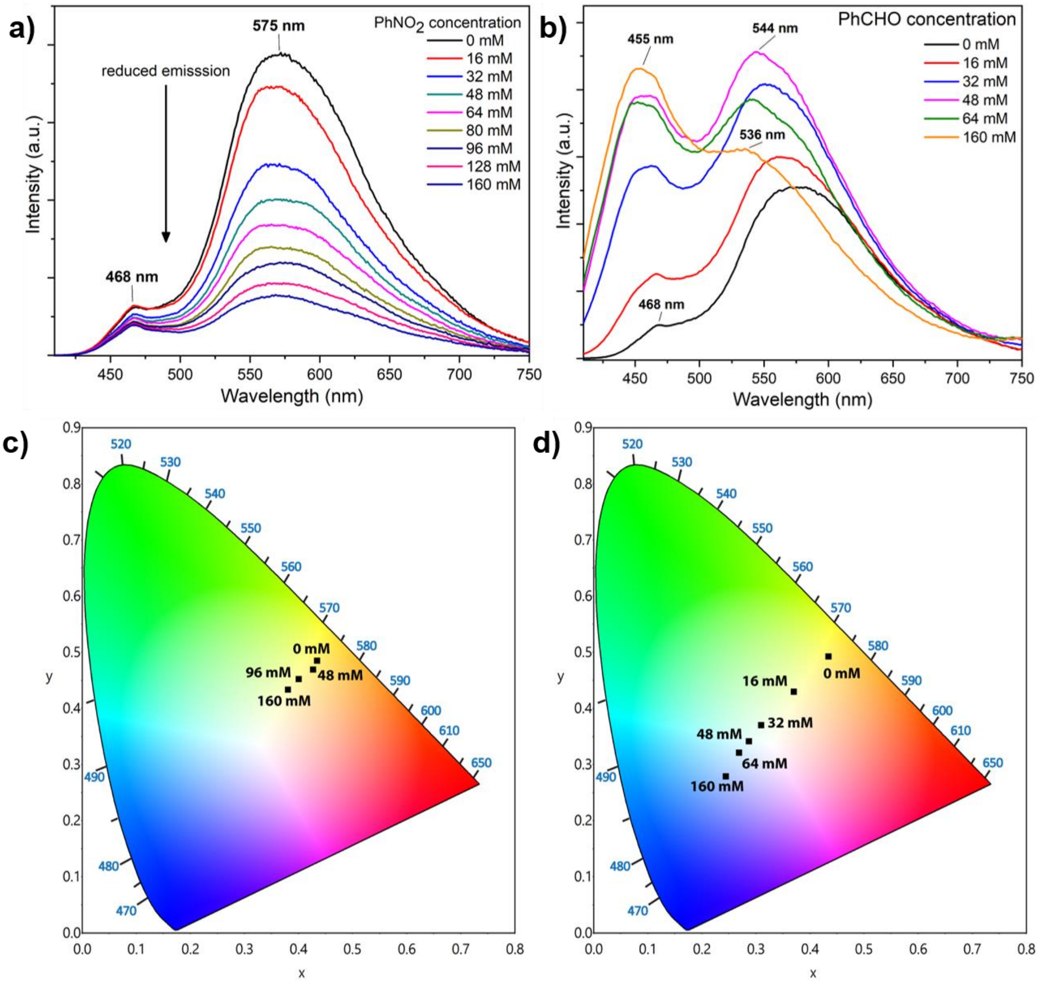

Figure 2.8: Emission spectra of **5** on adding **a)** nitrobenzene and **b)** benzaldehyde. The corresponding CIE diagrams with concentration are shown in **c)** and **d)** respectively. λ_{exc} = 390 nm.

On adding small quantities of H-bonding guests like nitrobenzene and measuring the fluorescence, **5** showed quenching. The quenching was higher for the yellow peak (570 nm) compared to the smaller blue peak (468 nm), which caused the CIE coordinates to shift from (0.4354, 0.4848) at 0 mM nitrobenzene to (0.3855, 0.4330) at 160 mM nitrobenzene (Figure

2.8a and 2.8c). Other H-bonding guests such as benzaldehyde must also be able to affect the emission. Apart from showing reduced yellow band, the addition of benzaldehyde showed another feature i.e. a steady increase in the blue component of the emission, originating from the tritopic hmtt ligand (Figure 2.8b). Consequently, higher tunability is achievable in this case. The CIE coordinates move from the yellow region to the blue region as the concentration of benzaldehyde increases. (Figure 2.8d)

The CIE coordinates move from (0.3714, 0.4292) in 16 mM benzaldehyde to near white light (0.3109, 0.3692) in 32 mM benzaldehyde. The coordinates move further to the blue region of the CIE diagram at higher concentrations of benzaldehyde (Figure 2.5d). However, the emission was unaffected on adding a non-H-bonding guest like benzonitrile (Experimental section, Figure 2.17). These features make MUF-77 systems unique in that their emissions can be finely tuned by addition of H-bonding guests.

2.2.5 Tunability by diluting with non-fluorescent linkers

A complex interplay of photophysical processes results in the trends in the white-light emissive spectra of **13**, **14**, **15**, and **16**. One prerequisite for energy transfer is that emission of the donors and the absorption of the acceptor must overlap.[81,86] We measured the absorption spectrum of the gua ligand (the acceptor) and compared it with the emission spectra of the donors *i.e.* hmtt and bdc-NH_2 (Figure 2.9). Indeed, a clear spectral overlap was observed indicating that energy transfer is possible.

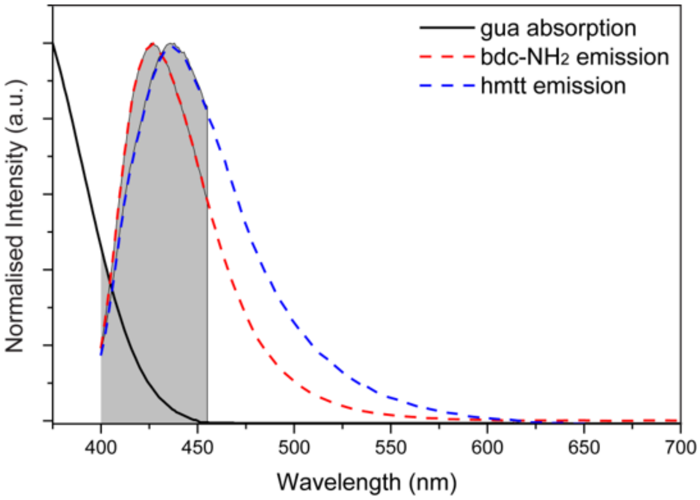

Figure 2.9: Emission spectra of bdc-NH_2 and hmtt show a spectral overlap (shown in grey) with absorption spectrum of the gua ligand.

The energy transfer behaviour proved to be advantageous in that it gave us another method to tune the emission. By variably diluting the yellow-emissive gua ligand with non-luminescent bpdc ligand, we prepared nanocrystals MUF-77 frameworks **17**, **18**, **19**, **20**, **21**, and **22** (Scheme 2.1, Experimental section, Table 2.3). PXRD patterns showed that MUF-77 was formed (Figure 2.10) and ^{1}H-NMR spectroscopy on the acid digested MOFs showed that the levels of ratios of gua to bpdc were 1:0.25, 1:1, 1:3, 1:5.6, 1:9, 1:19 respectively (ESI; Figure S17-S22).

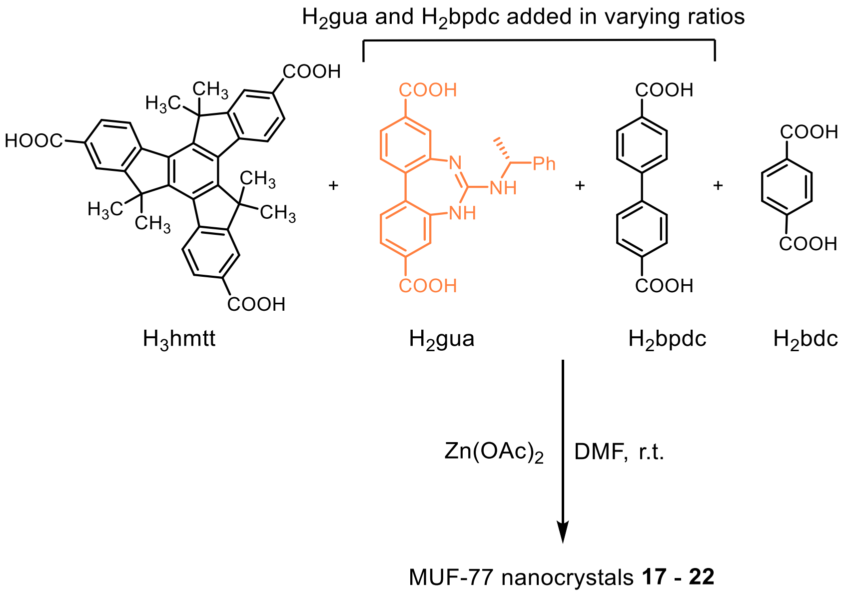

Scheme 2.1: Preparation of MUF-77 nanocrystals 17–22 by systematically diluting the yellow fluorescent gua with nonfluorescent bpdc in different ratios.

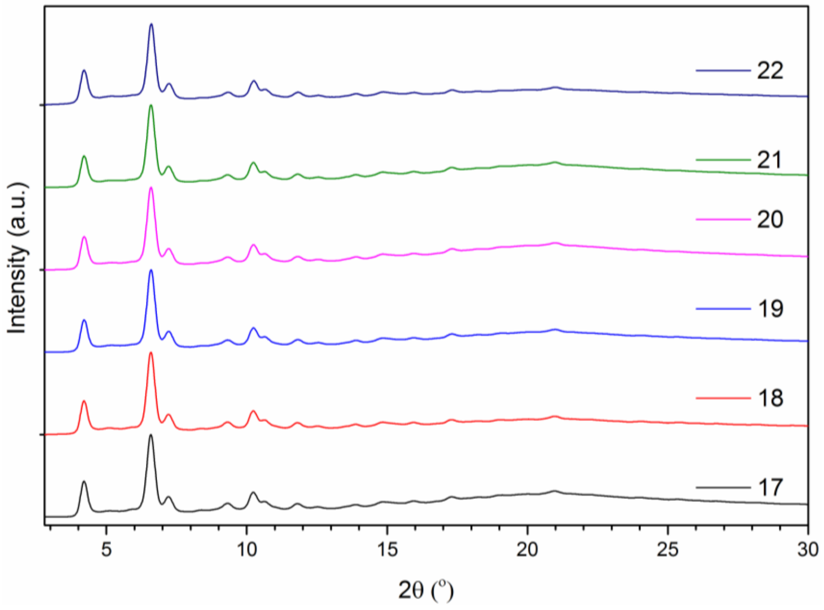

Figure 2.10: PXRD patterns of MUF-77 nanocrystals **17 - 22** with diluted bpdc linkers having the general formula $[Zn_4O(hmtt)_{4/3}(gua)_x(bpdc)_y(bdc\text{-}NH_2)_{1/2}]$.

Based on our hypothesis, the emission spectra of **17 - 22** should a show steady increase in truxene-based blue emission. We think that this happens due to reduced energy transfer between truxene and gua. Decreasing the levels of gua (the acceptor) in the MOFs leads to some of the truxene based blue emission to remain unabsorbed by the gua during energy transfer.

The emission spectra of the **17** – **22** showed a reduction in intensity of the yellow peak (575 nm) and a corresponding increase in the blue peak originating from the hmtt (Figure 2.11) Consequently, the CIE coordinates derived from these emission spectra (Experimental section, Figure 2.14, and Table 2.3), traverse across the CIE diagram along the Planckian locus from the yellow region for **5** (0.4541, 0.4945) to blue region for **1** (0.1547, 0.0578). The CIE coordinates for **20** were (0.3519, 0.3780) which are indicative of white-light emission, showing that ligand dilution is another method for achieving white-light. The coordinates move to the blue region (0.2900, 0.2998) for **21**, and further to (0.2120, 0.1750) for **22**. These results show that both the multicomponent and isoreticular nature of MUF-77 can be used in combination to tune emission.

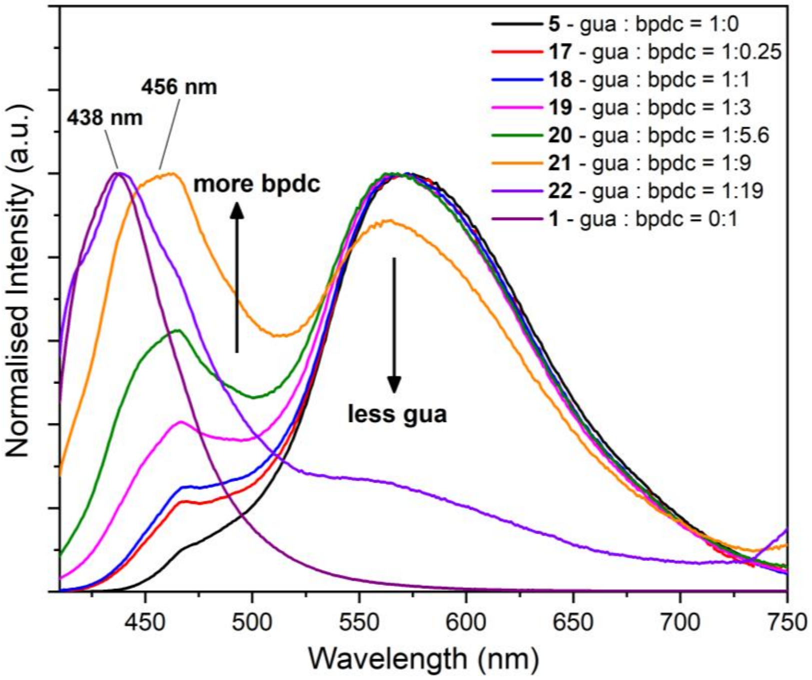

Figure 2.11: Emission spectra of MUF-77 nanocrystals with various ratios of gua and bpdc linkers (λ_{ex} = 390 nm). The formula for these frameworks is $[Zn_4O(hmtt)_{4/3}(gua)_x(bpdc)_y(bdc)_{1/2}]$, and the *x*:*y* ratio is shown in the figure legend.

2.2.6 Coating MUF-77 on UV LED:

One of the advantages of nanocrystalline MUF-77 is its suitability for use as LED coatings. To achieve this, we exchanged nanocrystals of **15** (which were originally in DMF) with acetone by repeated centrifugation and suspended them in acetone. On coating a UV LED with cyanoacrylate glue and then by repeatedly dipping it into the acetone suspension, we obtained a coating of **15** on the LED. On illumination, the LED glowed white, indicating that MUF-77 nanocrystals can be used as solid-state phosphors (Figure 2.12).

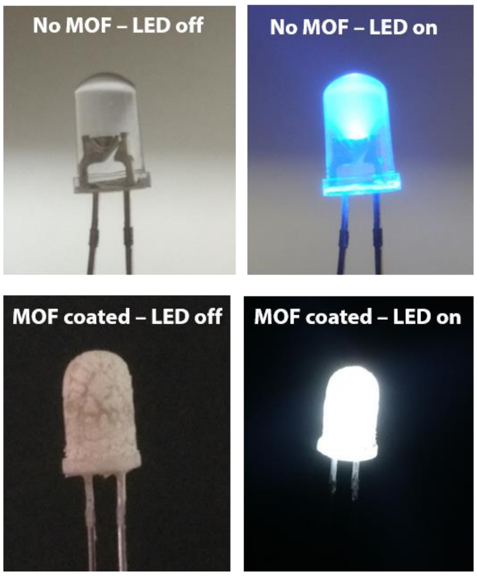

Figure 2.12: Photographs of an UV LED (λ_{em}=393 nm) before and after coating with **15**, which acts as a phosphor to generate white light.

2.3 Conclusions

In conclusion, we have shown that the emissions of MUF-77 systems, can be tuned using different approaches. By keeping the ditopic fluorophores unchanged, the overall emission of MUF-77 can be modified by changing the substituents on the tritopic linkers. The combination of blue and yellow emissions in **13**, **14**, **15**, and **16** gives various shades of white-light emission with **15** having an emission with CIE coordinates (0.3218, 0.3590) close to that pure white-light. The newly synthesised **gua** ligand can H-bond to encapsulated guest molecules and this gives another handle for fine-tuning of emissions. The changes in emission in frameworks **13** – **16** is indicative of a combination of inter-ligand photophysical processes. This is possible due to the multicomponent nature of MUF-77, which places donor-acceptor ligands at precise positions due to its crystallinity. A combined approach using time-resolved emission spectroscopy and X-ray crystallography have been used to further understand these interactions which are described in Chapter 3.

2.4 Experimental Section

2.4.1 General procedures

All starting materials and solvents were used as received from commercial sources without further purification unless otherwise noted. NMR spectra were collected at room temperature using a Bruker Avance 400 MHz or 500 MHz spectrometer, with the use of the solvent proton as an internal standard. All chemical shift (δ) values are in parts per million (ppm). X-ray diffraction data were collected using a Rigaku Spider diffractometer equipped with a Micromax MM007 rotating anode generator with Cu_{α} radiation (wavelength = 1.54180 Å), high flux Osmic multilayer mirror optics, and a curved image plate detector, and finally processed using 2DP.

Fluorescence spectra were recorded with a Horiba Scientific Fluoromax-4 Spectrofluorimeter. Spectra were corrected for detector and grating efficiencies using FluorEssence, the inhouse software of the fluorimeter. CIE coordinates and correlated colour temperature values were calculated using Osram ColorCalculator 7.23.

2.4.2 Ligand synthesis and characterization

H_3hmtt, H_3hbtt, H_3hhtt and H_3hott were synthesised according to a literature procedure.[78]

Synthesis of H_2gua:

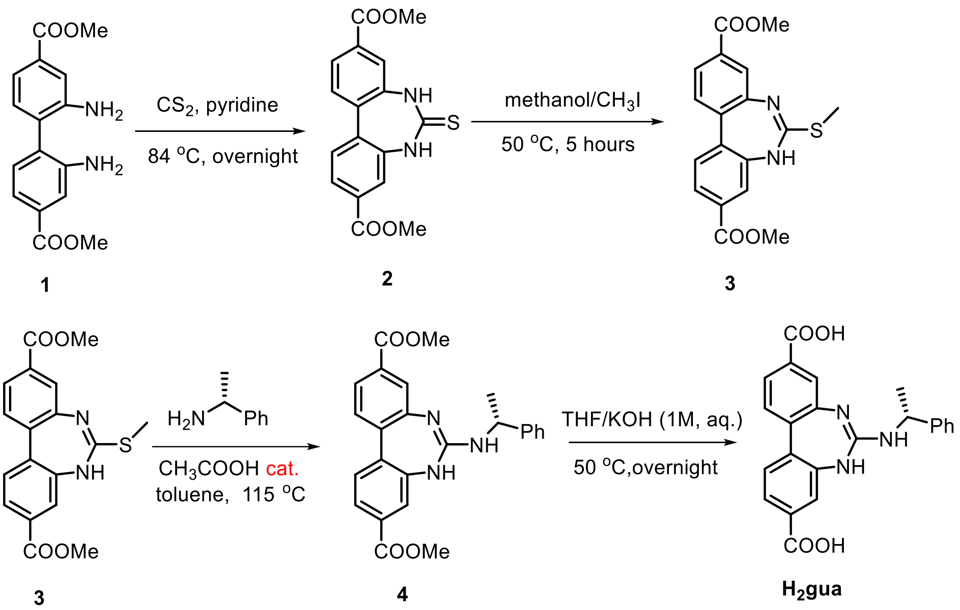

Compound 2:

1 (2.0 g, 6.6 mmol) was dissolved in pyridine (50 ml) and CS_2 (10 mL) was added. The solution was heated at 85 °C, overnight. The product precipitates from the reaction mixture which was filtered, washed with acetone and dried. (**Yield**: 1.8 g, 79%). ^1H NMR (500 MHz, DMSO-*d*$_6$, ppm) δ 10.40 (s, 1H), 7.79 (d, *J* = 8.1 Hz, 1H), 7.76 (s, 1H), 7.64 (d, *J* = 8.1 Hz, 1H), 3.89 (s, 3H).

Compound 3:

To a solution of compound **2** (1.0 g, 2.9 mmol) in methanol (20 mL), K_2CO_3 (2.4 g) and CH_3 I (20 mL) were added. This was heated at 50 °C in an oil bath for 5 hours. The solvent was evaporated, and water was added to dissolve K_2CO_3. The product precipitates as a yellow solid and was separated by filtration (**Yield**: 940 mg, 2.64 mmol, 90%). ^{1}H NMR (500 MHz, DMSO-*d*$_6$, ppm) δ 7.93 (dd, *J* = 8.2, 1.6 Hz, 2H), 7.83 (d, *J* = 1.5 Hz, 2H), 7.73 (d, *J* = 8.2 Hz, 2H), 3.89 (s, 6H), 2.96 (s, 2H). HRMS (ESI) m/z: $[M+H]^+$ Calcd for $C_{18}H_{17}N_2O_4S$: 357.0904; Found: 357.0898.

Compound 4:

Compound **3** (1.5 g, 4.21 mmol) was mixed with (*R*)-1-phenylethan-1-amine (1.5 g, 12.42 mmol) in 10 ml of toluene. 0.6 ml of acetic acid was added. The mixture was heated at 115 °C for 48 hrs. The hot reaction mixture was directly loaded onto a silica column and chromatographed with dichloromethane: MeOH, with the product eluting at 30:1 CH_2Cl_2:MeOH (**Yield**: 1.42 g, 3.31 mmol, 78%). ^{1}H NMR (500 MHz, DMSO-*d*$_6$/DCl, ppm) δ 7.90 (d, *J* = 8.1 Hz, 1H), 7.85 (s, 2H), 7.75 (d, *J* = 8.1 Hz, 1H), 7.69 (d, *J* = 8.0 Hz, 1H), 7.52 (d, *J* = 7.5 Hz, 2H), 7.42 (t, *J* = 7.6 Hz, 3H), 7.32 (t, *J* = 7.3 Hz, 1H), 5.53 (q, *J* = 6.5 Hz, 1H), 3.89 (d, *J* = 7.2 Hz, 6H), 1.57 (d, *J* = 6.6 Hz, 3H). ^{13}C NMR (126 MHz, DMSO-*d*$_6$/DCl) δ 165.14, 165.02, 161.65, 142.05, 139.71, 137.63, 134.86, 133.63, 131.03, 130.58, 128.86, 127.90, 127.60, 127.22, 125.99, 124.70, 122.71, 67.06, 52.58, 52.18, 39.52, 25.06, 22.94. HRMS (ESI) m/z: $[M+H]^+$ Calcd for $C_{25}H_{24}N_3O_4$: 430.1761; Found: 430.1755.

H$_2$gua:

4 (1.3 g, 3.03 mmol) was added to 1:1 solution of 1 M KOH/THF and stirred at room temperature for 40 hours. The THF was evaporated and the aqueous phase was acidified, first with 3 M HCl and then with 1 M HCl to a pH of 4. The solid obtained was filtered, washed with water, and dried overnight under high vacuum. (**Yield**: 1.1 g, 2.74 mmol, 90%) ^{1}H NMR (500 MHz, DMSO-*d*$_6$/DCl) δ ^{1}H NMR (500 MHz, DMSO-*d*$_6$/DCl, ppm) δ 7.92 – 7.81 (m, 3H), 7.75 (d, *J* = 8.1 Hz, 1H), 7.70 (d, *J* = 8.2 Hz, 1H), 7.50 (t, *J* = 8.9 Hz, 3H), 7.41 (t, *J* = 7.6 Hz, 2H), 7.31 (t, *J* = 7.3 Hz, 1H), 5.48 (q, *J* = 12.2, 6.2 Hz, 1H), 1.57 (d, *J* = 6.7 Hz, 3H).^{13}C NMR (126 MHz, DMSO-*d*$_6$/DCl) δ 166.45, 161.96, 142.41, 140.06, 137.91, 135.21, 133.75, 132.62, 132.29, 130.79, 129.16, 128.38, 127.71, 126.40, 125.27, 123.51, 52.29, 23.34. HRMS (ESI) m/z: $[M+H]^+$ Calcd for $C_{25}H_{20}N_3O_4$: 402.1454; Found: 402.1442.

2.4.3 Synthetic method for MUF-77 nanocrystals

MUF-77 nanocrystals were prepared by stirring and dissolving the required tritopic and two ditopic ligands in a 50:1 (v/v) DMF: water solution. Solid $Zn(OAc)_2·2H_2O$ was added to this solution and the stirring was continued for 30 minutes. The resulting suspension was centrifuged thrice with fresh DMF and placed in an isothermal oven at 85 °C overnight. The crystals were centrifuged again with fresh dry DMF and stored at room temperature. Details about the exact quantities of ligands and salt used are mentioned in the table below:

Table 2.2: Quantities used for synthesising MUF-77 nanocrystals.

MOF Code	Linker set	tritopic (mg, µmol, eq.)	bpdc ligand (mg, µmol, eq.)	bdc ligand (mg, µmol, eq.)	$Zn(OAc)_2·2H_2O$ (mg, µmol, eq.)	Vol of DMF: H_2O soln. (mL)
1	hmtt/ bpdc/ bdc	35, 63, 2.5	6, 25, 1	4.1, 25, 1	55, 250, 10	2.5
2	hbtt/ bpdc/ bdc	25, 30.8, 2.5	3, 12.3, 1	2, 12.3, 1	27, 122, 10	1.25
3	hhtt/ bpdc/ bdc	25, 23.5, 2.5	2.3, 9.4, 1	1.6, 9.4, 1	27, 122, 13	1.25
4	hott/ bpdc/ bdc	25, 20.3, 2.5	2, 8.1, 1	1.4, 8.1, 1	23, 105, 13	1.25
5	hmtt/ gua/ bdc	35, 63, 2.5	10.2, 25.4, 1	4.1, 25, 1	55, 250, 10	2.5
6	hbtt/gua/ bdc	25, 30.8, 2.5	4.9, 12.3, 1	2, 12.3, 1	27, 123, 10	1.25
7	hhtt/ gua/ bdc	25, 23.5, 2.5	4.1, 10.3, 1.1	1.6, 9.4, 0.9	27, 122, 13	1.25
8	hott/ gua/ bdc	25, 20.3, 2.5	3.3, 8.1, 1	1.4, 8.1, 1	23, 105, 13	1.25
9	hmtt/ bpdc/ bdc-NH_2	35, 63, 2.5	5.6, 23.2, 0.9	4.6, 25.3, 1	55, 250, 10	2.5
10	hbtt/ bpdc/ bdc-NH_2	25, 30.8, 2.5	2.8, 11.7, 0.95	1.8, 9.8, 0.8	27, 123, 10	1.25
11	hhtt/ bpdc/ bdc-NH_2	25, 23.5, 2.5	2.3, 9.4, 1	1.7, 9.4, 1	27, 122, 13	1.25
12	hott/ bpdc/ bdc-NH_2	25, 20.3, 2.5	3.1, 8.1, 1.1	1.5, 8.1, 1	23, 105, 13	1.25
13	hmtt/ gua/ bdc-NH_2	35, 63, 2.5	10.2, 25.4, 1	4.6, 25.3, 1	55, 250, 10	2.5

14	hbtt/ gua/ bdc-NH_2	25, 30.8, 2.5	3.9, 12.3, 1	1.8, 9.8, 1	27, 123, 10	1.25
15	hhtt/ gua/ bdc-NH_2	25, 23.5, 2.5	3.8, 9.4, 1	1.7, 9.4, 1	27, 123, 13	1.25
16	hott/ gua/ bdc-NH_2	25, 20.3, 2.5	4.7, 11.7, 1	1.5, 8.1, 1	23, 105, 13	1.25

2.4.4 PXRD of MUF-77 nanocrystals

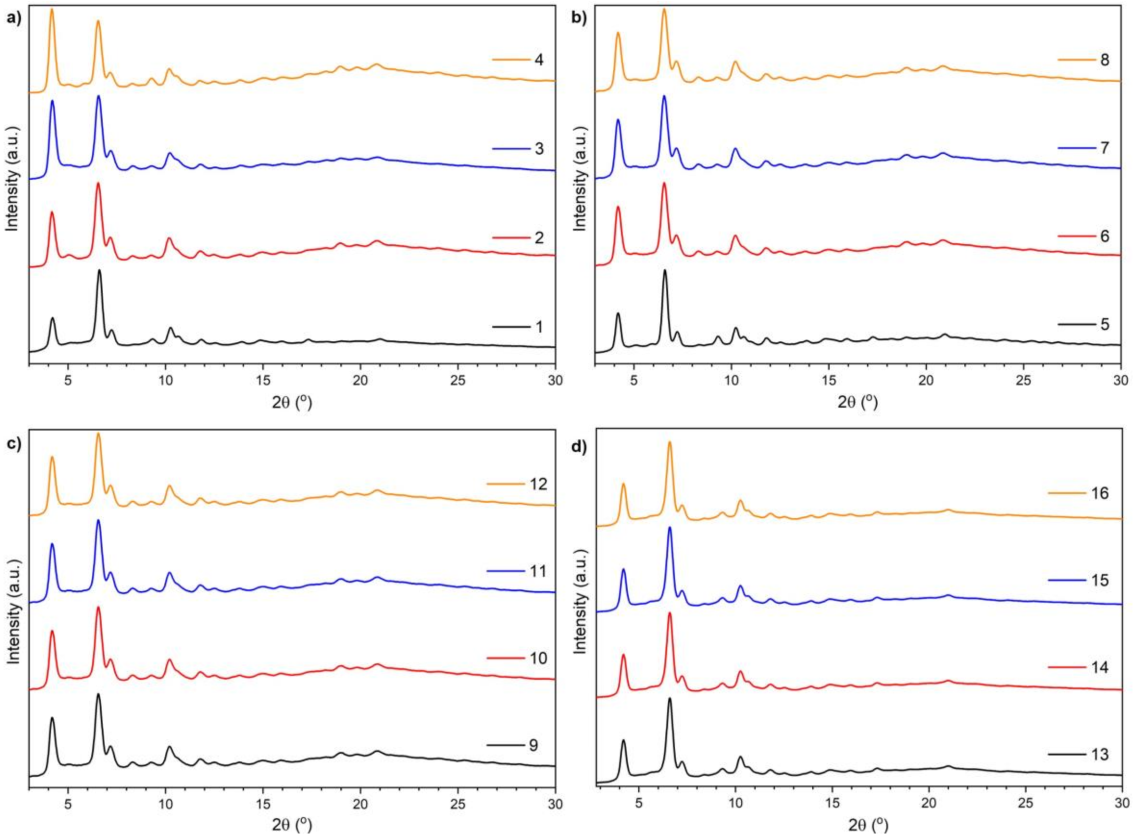

Figure 2.13: PXRD of MUF-77 nanocrystals **1** – **16** (Cu_α radiation).

2.4.5 CIE coordinates for emission spectra

Table 2.3: CIE coordinates for all MUF-77 frameworks along with their constituent ligand combinations.

		CIE Coordinates	
MOF Code	**Ligand combination**	**x**	**y**
1	hmtt/ bpdc/ bdc	0.1547	0.0578
2	hbtt/ bpdc / bdc	0.1667	0.1495
3	hhtt/ bpdc/ bdc	0.1602	0.1081
4	hott/ bpdc/ bdc	0.1658	0.1363
5	hmtt/ gua/ bdc	0.4574	0.4940
6	hbtt/gua/ bdc	0.4299	0.4822
7	hhtt/ gua/ bdc	0.4401	0.4920
8	hott/ gua/ bdc	0.4201	0.4856
9	hmtt/ bpdc/ bdc-NH_2	0.1503	0.0947
10	hbtt/ bpdc/ bdc-NH_2	0.1512	0.1110
11	hhtt/ bpdc/ bdc-NH_2	0.1539	0.0668
12	hott/ bpdc/ bdc-NH_2	0.1555	0.0699
13	hmtt/ gua/ bdc-NH_2	0.4130	0.4535
14	hbtt/ gua/ bdc-NH_2	0.3569	0.4156
15	hhtt/ gua/ bdc-NH_2	0.3218	0.3590
16	hott/ gua/ bdc-NH_2	0.2704	0.2547

2.4.6 Synthesis and CIE coordinates for MUF-77 nanocrystals 17-22

MUF-77 nanocrystals were prepared by stirring and dissolving H_3hmtt (35 mg, 63 µmol, 2.5 eq.), H_2gua, H_2bpdc (details in Table 2.3) and bdc (4.1 mg, 25 µmol, 1 eq.) in 2.5 ml of 50:1 (v/v) DMF: water solution. Solid $Zn(OAc)_2{\cdot}2H_2O$ (55 mg, 250 µmol, 10 eq.) was added to this solution and the stirring was continued for 30 minutes. The resulting suspension was centrifuged thrice with fresh DMF and placed in an isothermal oven at 85 °C overnight. The crystals were centrifuged again with fresh dry DMF and stored at room temperature.

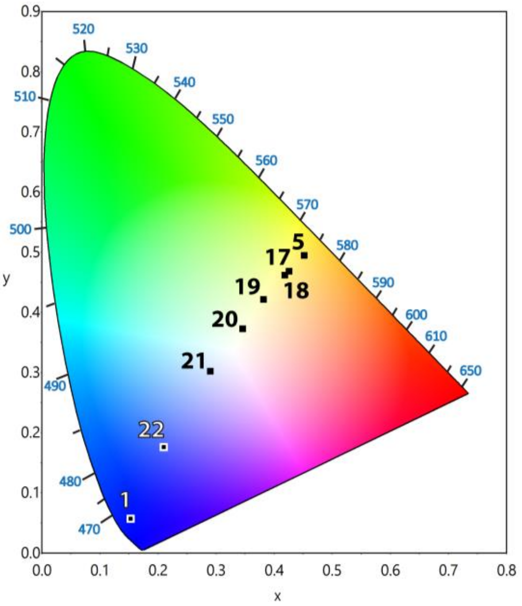

Figure 2.14: CIE diagram for **17** – **22** showing emission tunability (λ_{ex} = 390 nm) by diluting gua with non-luminescent bpdc. CIE coordinates of **1** and **5** are also shown.

Table 2.4: Quantities of H_2gua and H_2bpdc used for the synthesis of MUF-77 nanocrystals 17-22. The CIE coordinates for their emission spectra are also shown.

				CIE Coordinates	
MOF Code	gua : bpdc ratio	H_2gua (mg, µmol, eq.)	H_2bpdc (mg, µmol, eq.)	**x**	**y**
17	gua : bpdc = 1 : 0.25	8, 20, 0.8	1.2, 5, 0.2	0.4279	0.4681
18	gua : bpdc = 1 : 1	5.0, 12.5, 0.5	3.0, 12.5, 0.5	0.4206	0.4616
19	gua : bpdc = 1 : 3	2.5, 6.2, 0.25	4.5, 18.8, 0.75	0.3836	0.4211
20	gua : bpdc = 1 : 5.6	1.5, 3.7, 0.15	5.1, 21.3, 0.85	0.3480	0.3722
21	gua : bpdc = 1 : 9	1, 2.5, 0.1	5.4, 22.5, 0.90	0.2922	0.3015
22	gua : bpdc = 1 : 19	0.5, 1.25, 0.05	5.7, 23.8, 0.95	0.2120	0.1750

2.4.7 Emission spectra of ligands in solution

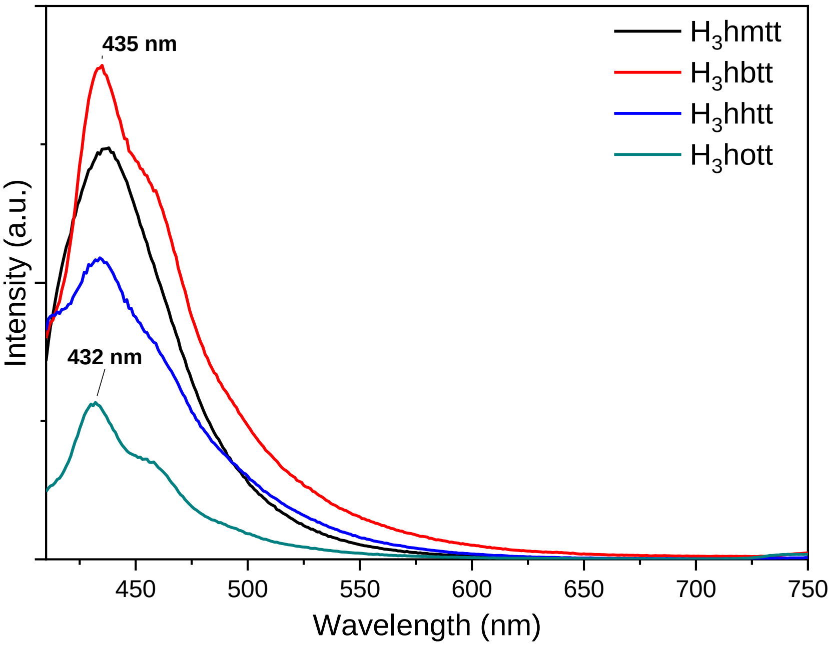

Figure 2.15: Emission spectra of the tritopic truxene linkers dissolved in DMF when excited at 390 nm. The solutions were diluted so that their absorbance at 390 nm was 0.05 units.

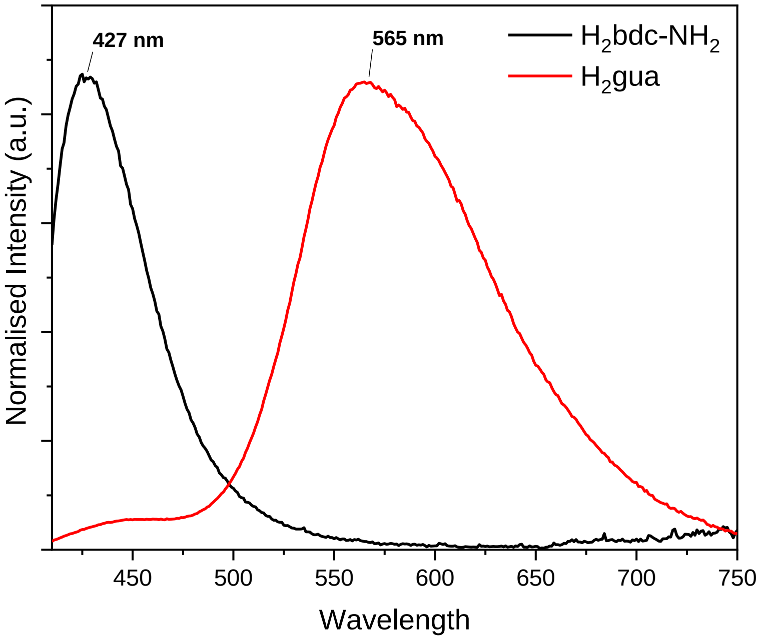

Figure 2.16: Emission spectra from the ditopic linkers in DMF when excited at 390 nm. Absorbance of the H_2gua solution at 390 nm was 0.05 units. A 2.5% neutral-density filter was used for H_2bdc-NH_2.

2.4.8 Emission spectra of 5 on adding benzonitrile

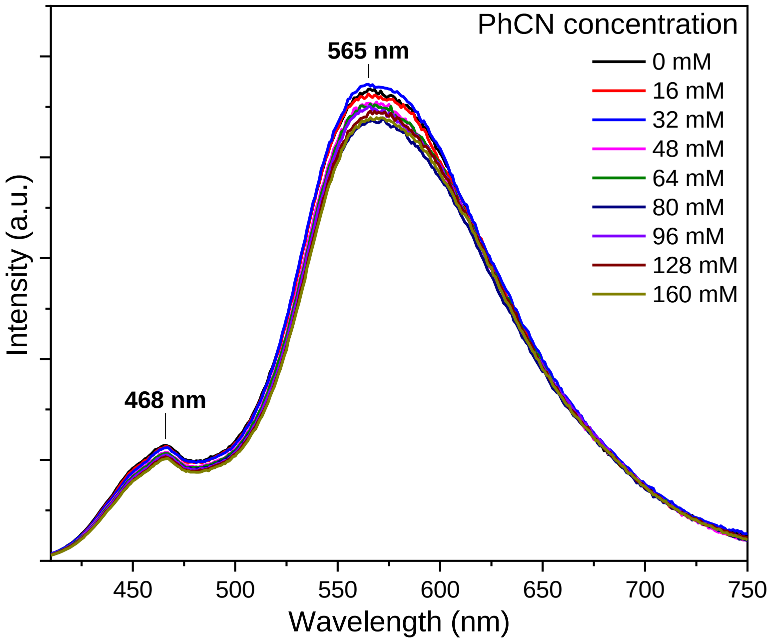

Figure 2.17: Emission spectra of **5** on titrating in benzonitrile.

Chapter 3 – Probing Energy Transfer in MUF-77

3.1 Introduction

The previous chapter detailed our efforts to obtain white-light emission in MUF-77 by combining the luminescence of yellow and blue emissive ligands in the same framework. Changing the alkyl groups on the tritopic truxene ligands changed the emission spectrum of the resulting MOF.[200] This was intriguing as alkyl groups are not typically known to strongly effect absorption or emission properties.[208,209] Our hypothesis was that the changes in the alkyl groups affects the extent of photophysical interactions amongst the ligands, thus impacting the emission spectrum.

I have described the factors and equations that ultimately determine energy transfer efficiency in section 1.9 of this thesis. Key to determining this efficiency is the distance between the donor and acceptor pair, the spectral overlap between acceptor absorption and donor emission, and their mutual orientation. This chapter deals with calculating all these factors and aims to pinpoint the role of each of the luminescent ligands in MUF-77. A variety of complementary crystallographic and spectroscopic techniques have been employed to develop a better understanding of energy transfer in these fascinating, multicomponent frameworks. This includes some time-resolved fluorescence techniques which operate in the nanosecond and picosecond regimes whose descriptions are given below:

3.1.1 Time-Correlated Single Photon Counting

Forster Resonance Energy Transfer (FRET) causes the lifetime of the donor to reduce, and would enable the acceptor to reach its excited state.[81] Hence, the measurement of the excited-state lifetimes is crucial to the understanding of energy transfer. Many techniques can be used to determine this parameter. Three common methods are fluorescence upconversion, optical Kerr gating spectroscopy, and time-correlated single photon counting (TCSPC). The first two methods can be used to probe ultrafast fluorescence decays occurring within 250 femtoseconds to hundreds of picoseconds. TCSPC, on the other hand is useful to measure relatively slower decays ranging from 200 picoseconds to tens of nanoseconds. This chapter heavily relies on TCSPC to study excited state lifetimes of luminescent MUF-77 systems and their constituent ligands. Figure 3.1 gives a visual representation of a TCSPC setup.

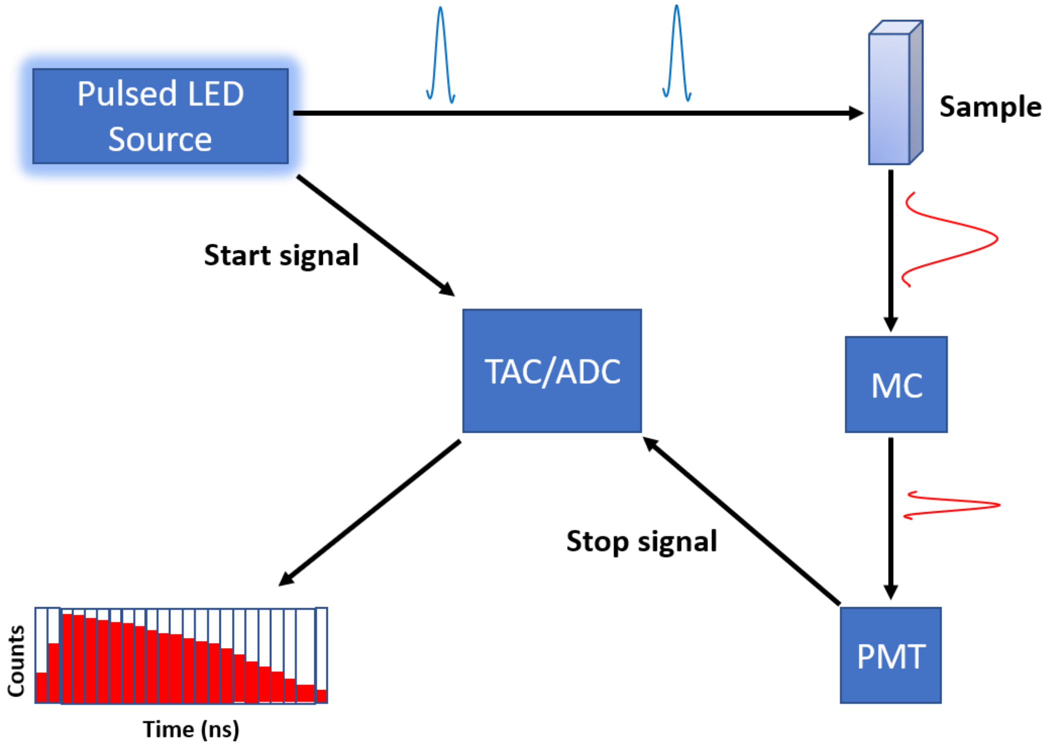

Figure 3.1: A schematic representation of a typical TCSPC setup. MC: monochromator, PMT: photomultiplier tube, TAC: Time-to-Amplitude Converter and ADC: Analog-to-Digital Converter.

Lifetime measurement with TCSPC begins with an excitation from a pulsed LED source, with a width of 0.5 -1 ns, incident on the sample (in this case, nanocrystalline MUF-77). At the same time, a start signal is sent to the time-to-amplitude converter (TAC) which performs analog-to-digital conversion (ADC). The MUF-77 sample absorbs the excitation pulse and after a short duration of time, a fraction of the excited MUF-77 re-emits fluorescent photons. The monochromator (MC) selects photons of the user-specified wavelength which are detected by the photomultiplier tube (PMT). PMTs designed for TCSPC measurements have a high gain and hence are able to detect single photons. The detected photon knocks out an electron in the PMT, generating a current, which is amplified and received by the TAC/ADC, which is the stop signal. The TAC/ADC starts building a voltage on receiving the start signal and this voltage grows at a constant rate with time. When the stop signal (generated from the fluorescent photon) hits the TAC/ADC, the voltage build-up is stopped, measured, correlated to a time and taken as one count. In other words, the TAC/ADC functions as a highly accurate stopwatch. Additionally, the pulse rate of the LED source can be controlled and can range up to 1 MHz. This repeats the counting millions of times per second resulting in many start-stop signals to be detected per second. From the TCSPC experiments, a plot of photon counts (or intensity) versus time is obtained.

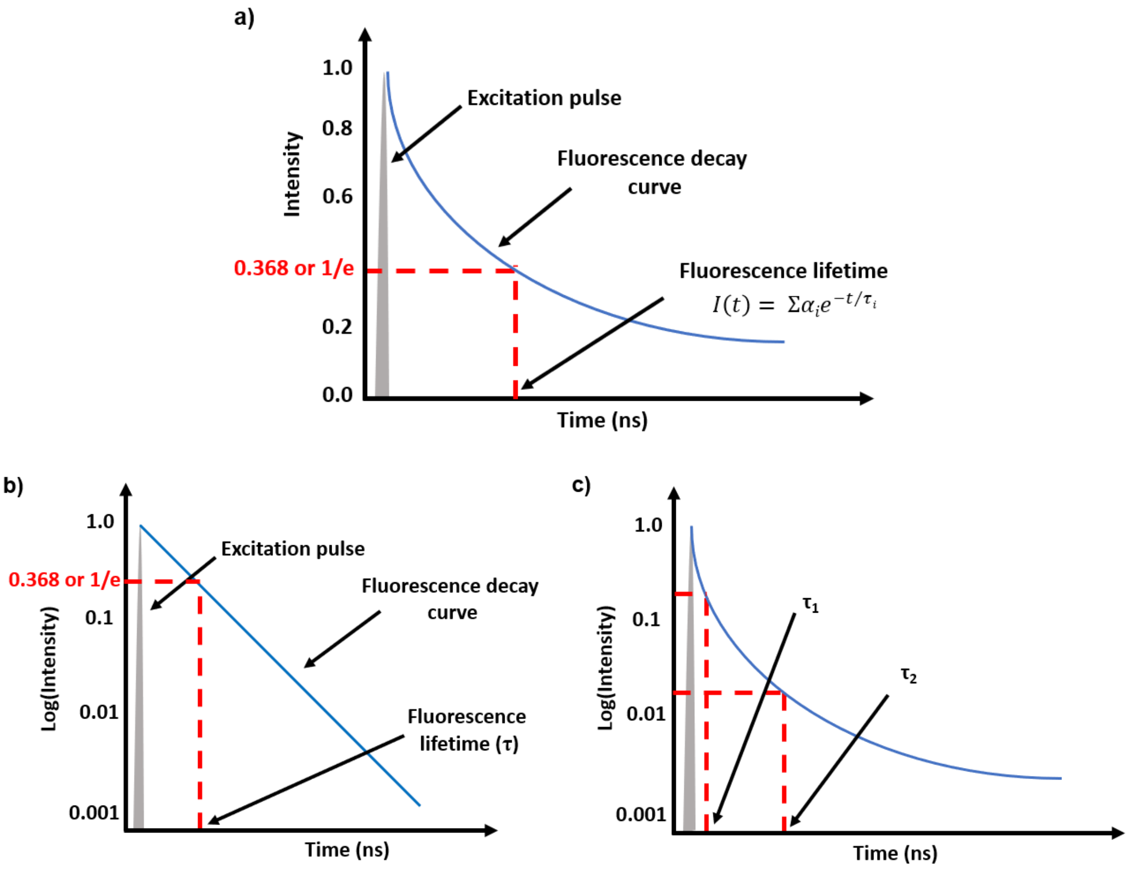

Figure 3.2: a) Plot of fluorescence intensity versus time obtained from TCSPC experiments. **b)** log(Intensity) versus time for a species showing monoexponential decay. **c)** log(Intensity) versus time for a species showing multiexponential decay, where τ_1 and τ_2 are fluorescence lifetimes.

$$\mathrm{I(t)} = \Sigma\alpha_i \mathrm{e}^{-t/\tau_i} \qquad \text{(Eq. 3.1)}$$

This plot of fluorescence intensity vs time (Figure 3.2a) decays over time, which can be fit using equation 3.1. Here, I(t) is the intensity at time, t, and α_i is the amplitude of the ith decay curve with lifetime, τ_i. The time at which the intensity of the curve has decayed to 36.8% or (1/e) % of its initial value is the lifetime, τ. If the species under measurement decays in a single step, then the decay will be monoexponential. For such decays, a plot of log(intensity) versus time gives a straight line (Figure 3.2b). On the other hand, luminescence can also arise from multiple processes, with each process causing the excited state population to decay with its own characteristic lifetime. In such a case, the decays will be multiexponential, and a plot of log(intensity) versus time will be non-linear (Figure 3.2c).

3.1.2 Transient Grating Photoluminescence Spectroscopy (TGPLS)

Fluorescence upconversion (FU) and optical Kerr gating spectroscopy (OKG) are some other ultrafast spectroscopic techniques for probing fluorescence decays.[210-213] While, FU has low background signals, it is a single-wavelength detection technique. On the other hand, OKG spectroscopy is capable of broadband detection, it however suffers from intense background signals that mask the desired Kerr gated signals.

Transient Grating Photoluminescence Spectroscopy (TGPLS) is an alternative to both these methods. TGPLS can be used to study lifetimes as fast at 100 fs . In contrast to TCSPC and fluorescence upconversion, both of which are single wavelength detection methods, TGPLS is a broadband detection method. In other words, excited-state luminescence dynamics from the entire UV or visible region can be measured at the same time.[214,215] For this chapter, we have employed TGPLS to probe some FRET processes in MUF-77 using specialised equipment available at VUW.

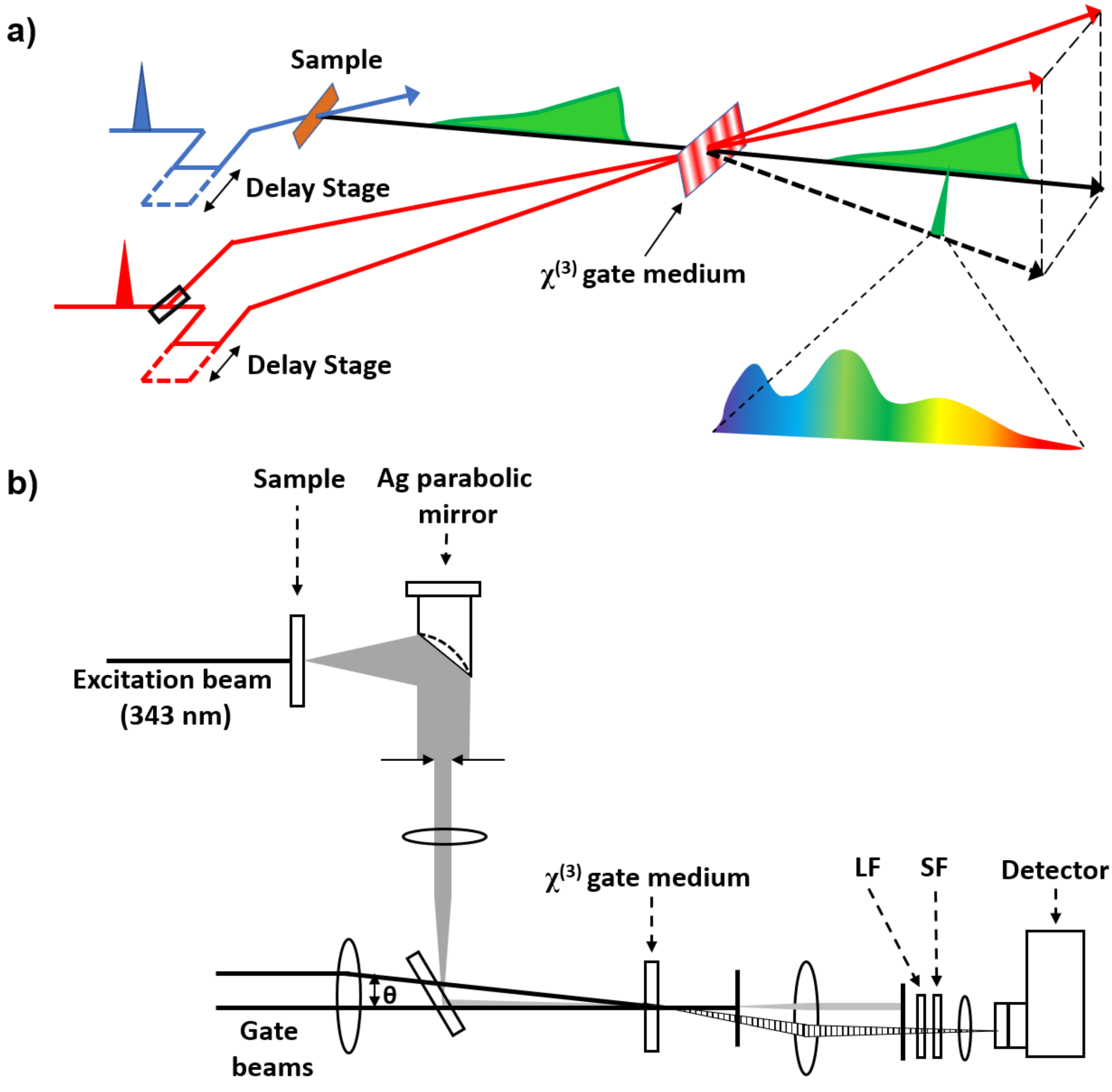

Figure 3.3: a) A schematic representation of a TGPLS setup, showing the delay stage used to achieve temporal overlap. The $\chi^{(3)}$ gate medium is a highly polished fused silica surface. **b)** Top view of the optical setup of the TGPLS setup used for this chapter. Here LF and SF stand for long- and short-pass filters, respectively. Lenses are shown as ellipses. The grey areas represent the fluorescence from the sample.

Figure 3.3a shows the setup of a TGPLS system. An ultrafast pulse beam is focused on the sample, and the sample's photoluminescence is focused on the third-order nonlinear ($\chi^{(3)}$) gate medium. Another beam arrives a certain time after the first beam. This time difference, called the delay time, is on the order of femtoseconds to picoseconds and is precisely monitored by the use of a computer-controlled motorised delay stage. The two beams undergo interference at the highly polished fused silica surface which serves as the $\chi^{(3)}$ gate medium. The low luminescence, fast response, and transparency to UV, visible, and IR radiation makes silica an ideal material for gating.[216] A series of lenses and filters are used to focus the gated interference signals onto a CCD (charge-coupled device) camera, which serves as the detector (Figure 3.3b). To summarise, TGPLS combines the best features of two methods i.e. the low background of FU and the broadband detection of OKG spectroscopy to give an ideal technique to probe ultrafast excited-state dynamics of a broad range of materials. For the TGPLS experiments described in this chapter, an excitation wavelength of 343 nm was used.

3.1.3 Aims of the TCSPC and TGPLS experiments on MUF-77

We began studying energy transfer in MUF-77 with the TCSPC of their constituent ligands and then performing the same for the MOFs. All the ligands were taken in their carboxylic acid form dissolved in DMF. In MOFs, bonding to the metal clusters results in the rigidification of the ligands, and consequently their lifetimes are expected to increase in the MOF.[91,217] The relative arrangement of ligands also enables energy transfer and exciton migration to occur across the MOF crystal. This combination of direct relaxation and long-distance exciton migration may give rise to multiple lifetime components. While monoexponential decay will arise from direct relaxation, multiexponential decay profiles will be observed if exciton migration occurs on a competitive timescale.

Due to the quaternary nature of MUF-77, there are multiple possible FRET pathways i.e. hxtt to hxtt, bdc-NH_2 to hxtt or vice-versa, hxtt to gua, and bdc-NH_2 to gua (Figure 3.4). Furthermore, the isoreticular principle can be utilised. Luminescent ligands can be substituted with their non-luminescent analogues. bdc-NH_2 and gua can be replaced by bdc and bpdc which are both non-luminescent, thus influencing the photophysics. Calculating the lifetimes in these substituted MUF-77 frameworks could pinpoint the direction and efficiency of FRET between the ligands.

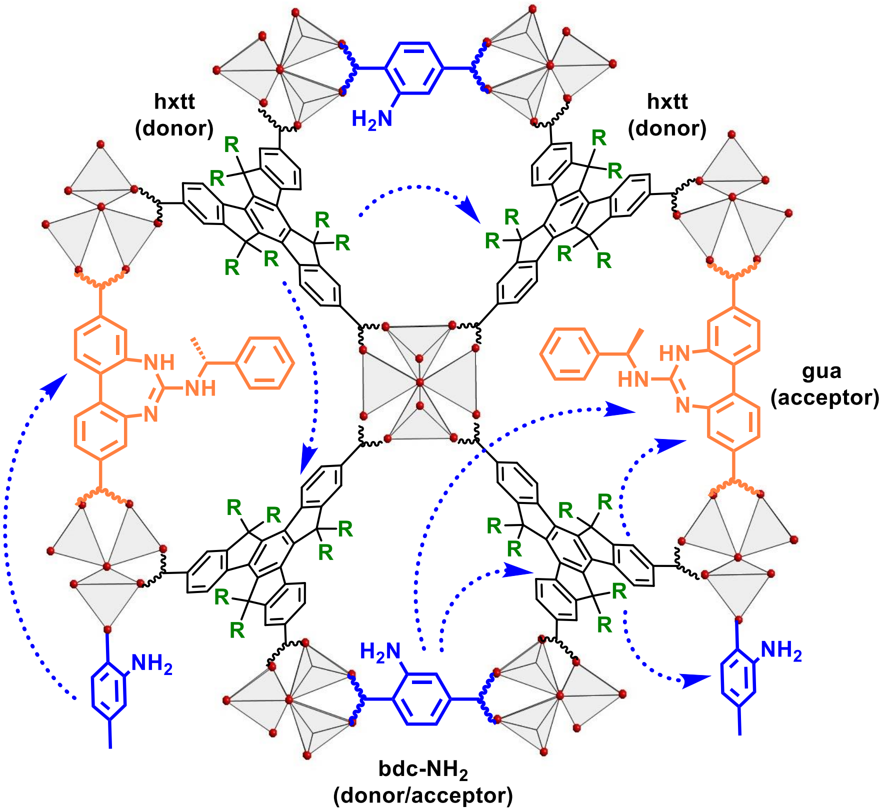

Figure 3.4: A cartoon image showing the relative arrangement of ligands in MUF-77 with the energy transfer (ET) pathways represented with dashed blue arrows. Zn4O clusters are represented by grey tetrahedra and oxygen atoms are shown as red spheres.

We asked the following questions to further investigate the photophysics of MUF-77 systems:

a) Do the lifetimes of the ligands change when incorporated into MUF-77?
b) How far does the exciton migrate in MUF-77 crystals? In other words, what is the exciton diffusion length?
c) Is there energy transfer between the tritopic hxtt and ditopic gua ligands in MUF-77 constituting of hxtt/gua/bdc i.e. **5**, **6**, **7**, and **8**? Or does the yellow fluorescence originate exclusively from the gua?
d) Which energy transfer processes occur in the white-light emitting systems, **13**, **14**, **15**, and **16**? What are their FRET efficiencies?

3.2 Results and Discussion

3.2.1 Calculation of spectral overlaps and quantum yields of ligands

For studying any energy transfer process, there are some prerequisites that need to be determined. These include the spectral overlap (*J*) of the acceptor (A) absorption with the emission profile of the donor (D), the distances between the D-A ligands (R), and their orientation factors (κ^2). Furthermore, to calculate the spectral overlap the quantum yield of the donor and absorptivity of the acceptor must be known. Finally, the fluorescence lifetime needs to be experimentally determined using TCSPC or TGPLS. So, our goal was to measure all these parameters and ultimately calculate FRET efficiencies for each potential D-A pair.

Firstly, absorption and emission spectra (λ_{ex} = 343 nm) of the free ligands were measured using their solutions in DMF. Quantum yields were determined using the integrating sphere method.[218] We identified twenty-two donor-acceptor ligand pairs, and we were able to calculate J values for all these combinations (Figure 3.5a - 3.5i and Table 3.1), which meant that first prerequisite for energy transfer was satisfied and a multitude of energy transfer pathways are possible in MUF-77 in principle.

The calculated J values ranged from a minimum of 10^{10} nm^4/mol/cm to a maximum of about 10^{13} nm^4/mol/cm. When considering the gua ligand as the donor with the tritopic ligands or bdc-NH_2 as acceptors, the lowest J values of 10^{10} to 10^{11} nm^4/mol/cm were obtained (Table 3.1, entries r -v). In another case, when bdc-NH_2 was the donor and the tritopic ligands were acceptors, the J values were also 10^{11} nm^4/mol/cm (Entries f - g). However, the key difference between these two donors are their quantum yields. The low quantum yield of 0.01 for gua coupled with low J values makes it unlikely to be a donor. On the other hand, the low J of bdc-NH_2 is compensated by its high quantum yield of 0.62, making bdc-NH_2 a possible donor ligand.

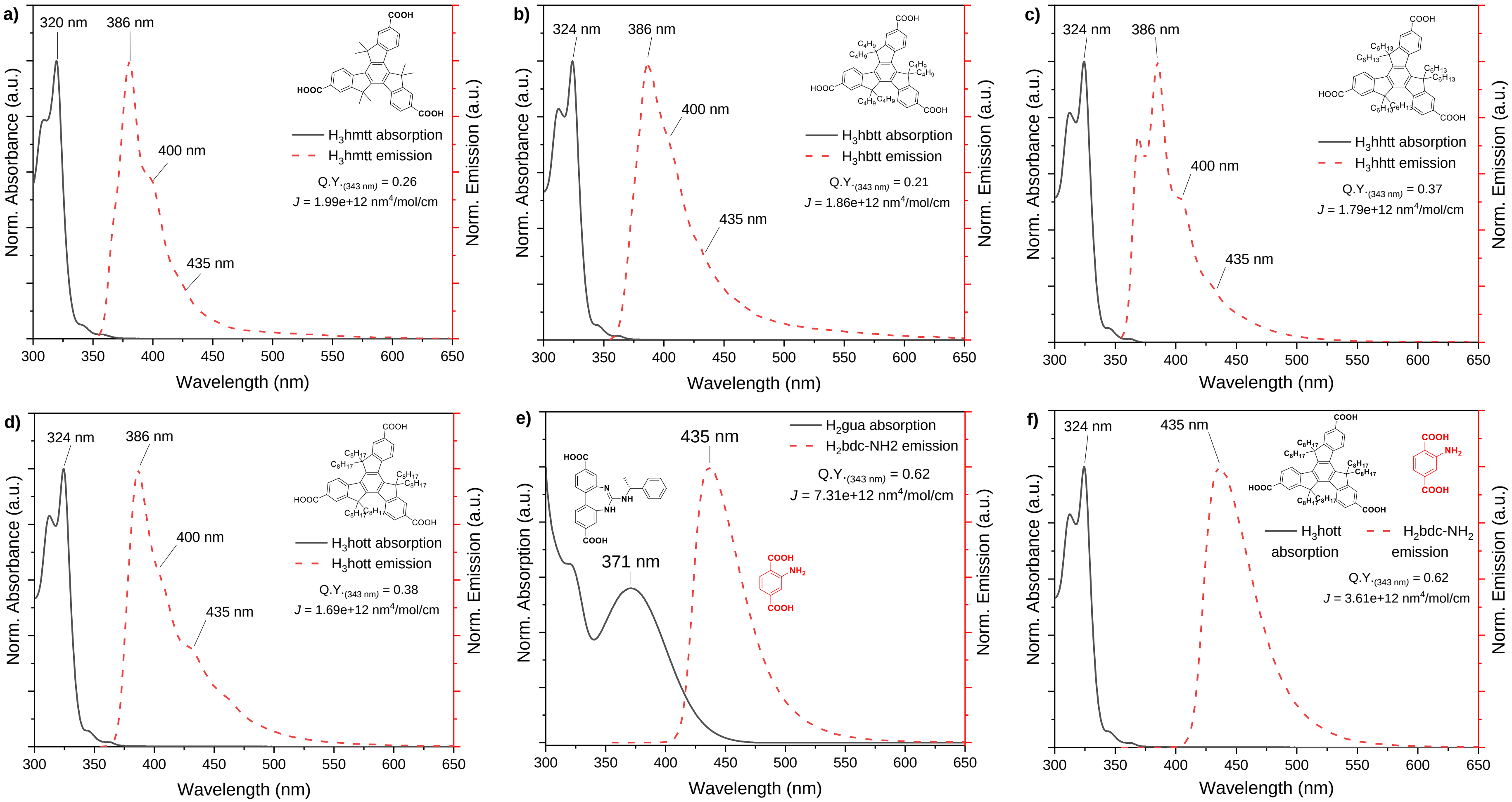
a)
320 nm
386 nm
400 nm
435 nm
H_3hmtt absorption
H_3hmtt emission
Q.Y.$_{(343\ nm)}$ = 0.26
J = 1.99e+12 nm^4/mol/cm
Norm. Absorbance (a.u.)
Norm. Emission (a.u.)
Wavelength (nm)
b)
324 nm
386 nm
400 nm
435 nm
H_3hbtt absorption
H_3hbtt emission
Q.Y.$_{(343\ nm)}$ = 0.21
J = 1.86e+12 nm^4/mol/cm
c)
324 nm
386 nm
400 nm
435 nm
H_3hhtt absorption
H_3hhtt emission
Q.Y.$_{(343\ nm)}$ = 0.37
J = 1.79e+12 nm^4/mol/cm
d)
324 nm
386 nm
400 nm
435 nm
H_3hott absorption
H_3hott emission
Q.Y.$_{(343\ nm)}$ = 0.38
J = 1.69e+12 nm^4/mol/cm
e)
435 nm
371 nm
H_2gua absorption
H_2bdc-NH2 emission
Q.Y.$_{(343\ nm)}$ = 0.62
J = 7.31e+12 nm^4/mol/cm
Norm. Absorption (a.u.)
f)
324 nm
435 nm
H_3hott absorption
H_2bdc-NH_2 emission
Q.Y.$_{(343\ nm)}$ = 0.62
J = 3.61e+12 nm^4/mol/cm
COOH
HOOC
NH_2
NH
N
C_4H_9
C_6H_{13}
C_8H_{17}
300
350
400
450
500
550
600
650

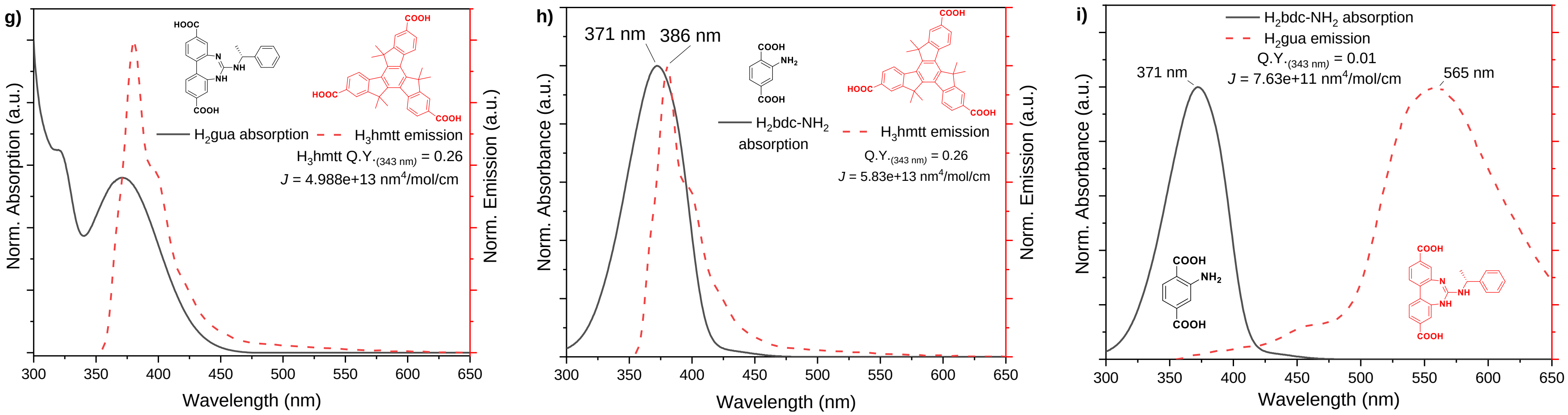

Figure 3.5: Normalised absorption and emission spectra of the free ligands dissolved in DMF showing spectral overlap. **a)** H_3hmtt absorption with H_3hmtt emission **b)** H_3hbtt absorption with H_3hbtt emission **c)** H_3hhtt absorption with H_3hhtt emission **d)** H_3hott absorption with H_3hott emission **e)** H_2gua absorption with H_3hmtt emission **f)** H_3hott absorption with H_2bdc-NH_2 emission **g)** H_2bdc-NH_2 absorption with H_3hmtt emission **h)** H_2bdc-NH_2 absorption with H_3hmtt emission and **i)** H_2bdc-NH_2 absorption with H_2gua emission. In all figures, the black solid lines are absorption spectra and red dashed lines are emission spectra (λ_{ex} = 343 nm). Quantum yields of the donor at 343 nm are also displayed.

Table 3.1: Quantum yields (Q.Y.), absorptivity (**ε**) and spectral overlaps of possible donor-acceptor ligand pairs in MUF-77.

Entry	**Donor ligand**	**Acceptor ligand**	**Donor Q.Y. at 343 nm (ϕ_D)**	**ε of acceptor (343 nm, 375 nm)[(a)]**	**Spectral Overlap, *J* (nm^4/mol/cm)**
a	hmtt	hmtt	0.26	4245, 73	$1.99*10^{12}$
b	hbtt	hbtt	0.21	4390, 206	$1.86*10^{12}$
c	hhtt	hhtt	0.37	4505, 344	$1.79*10^{12}$
d	hott	hott	0.38	4935, 50	$1.69*10^{12}$
e	bdc-NH_2	gua	0.62	2292, 3345	$7.31*10^{12}$
f	bdc-NH_2	hmtt	0.62	4245, 73	$1.21*10^{11}$
g	bdc-NH_2	hbtt	0.62	4390, 206	$8.23*10^{11}$
h	bdc-NH_2	hhtt	0.62	4505, 344	$5.56*10^{11}$
i	bdc-NH_2	hott	0.62	4935, 50	$3.61*10^{12}$
j	hmtt	gua	0.26	2292, 3345	$4.99*10^{13}$
k	hbtt	gua	0.21	2292, 3345	$4.01*10^{13}$
l	hhtt	gua	0.37	2292, 3345	$4.85*10^{13}$
m	hott	gua	0.38	2292, 3345	$3.87*10^{13}$
n	hmtt	bdc-NH_2	0.26	2010, 4027	$5.83*10^{13}$
o	hbtt	bdc-NH_2	0.21	2010, 4027	$4.26*10^{13}$
p	hhtt	bdc-NH_2	0.37	2010, 4027	$5.62*10^{13}$
q	hott	bdc-NH_2	0.38	2010, 4027	$4.06*10^{13}$
r	gua	bdc-NH_2	0.01	2010, 4027	$7.63*10^{11}$
s	gua	hmtt	0.01	4245, 73	$2.04*10^{10}$
t	gua	hbtt	0.01	4390, 206	$2.86*10^{10}$
u	gua	hhtt	0.01	4505, 344	$1.18*10^{10}$
v	gua	hott	0.01	4935, 50	$4.69*10^{10}$

(a)Absorptivity in $L \cdot mol^{-1} \cdot cm^{-1}$.

3.2.2 Studying inter-ligand distances in MUF-77

The studies mentioned above were all conducted on DMF solutions of the ligands. The next step would be to determine other parameters such as inter-ligand distances and orientation factors in the MUF-77. One of the advantages of using crystalline materials like MUF-77 is that the precise distance and orientations of the D-A ligands can be determined by single-crystal X-ray diffraction (SCXRD). Such measurements are challenging for molecules in solution and hence computational methods need to be employed for determining D-A distances and in many cases an approximated orientation factor (κ^2) value of 2/3 is used.[219]

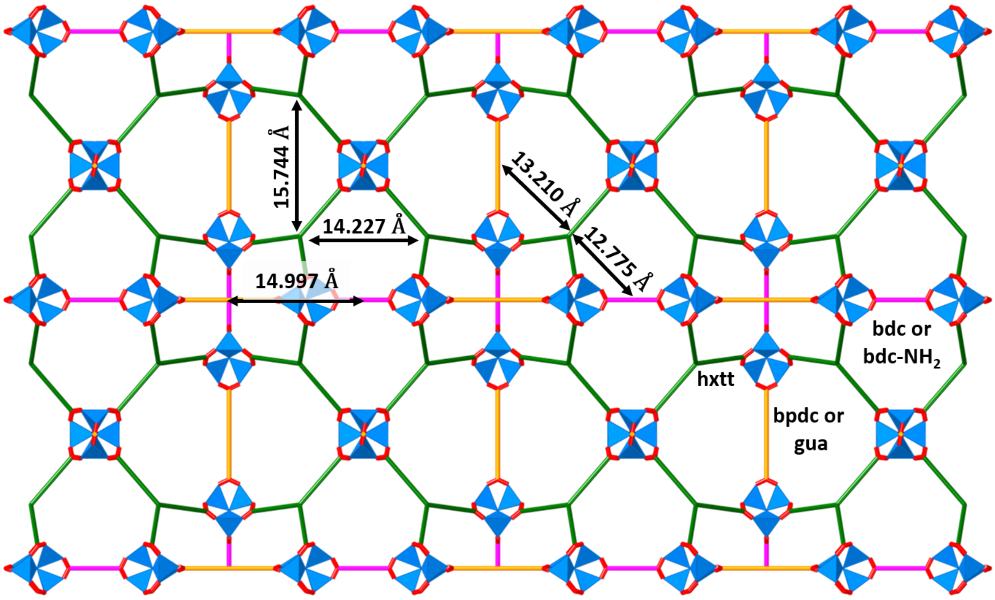

Figure 3.6: SCXRD structure of MUF-77 showing the view along the z-axis. The distances are also marked. Tritopic ligands (hxtt) are shown in green, the bpdc and bdc ligands are shown as yellow and pink rods, respectively. Zn atoms are shown as blue tetrahedra and oxygen atoms as red spheres.

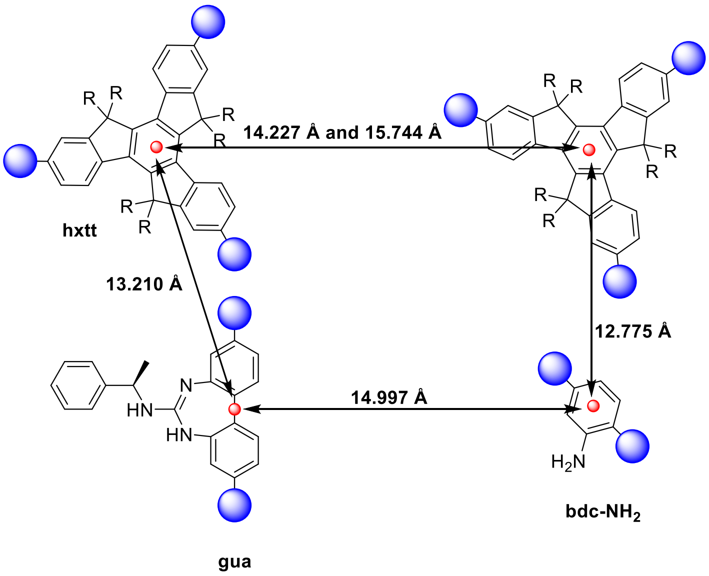

Figure 3.7: Schematic showing the distances between ligands. The red spheres are the points for each ligand from which the distances were measured. Blue spheres represent the $[Zn_4O(COO)_6]$ clusters.

So, what are the actual distances between the ligands? How are they arranged with respect to each other? The answer to all these questions lies in studying the crystal structure (Figure 3.6). We measured the distances between the central phenyl rings of the tritopic ligands (Figure 3.7) i.e. hmtt, hbtt, hhtt, and hott (collectively called hxtt) and found out that they are separated by two distinct distances. This is caused by the unequal lengths of the two ditopic ligands, causing the hxtt ligands to be separated by 14.227 Å and 15.744 Å. The bdc-NH_2 and gua ligands are placed 14.997 Å apart (Figure 3.7). This places the hxtt ligand 12.775 Å away from bdc-NH_2 and 13.210 Å from the gua ligands.

One question does arise: Are the variations in emission spectra (observed in Chapter 2, Figure 2.5d) a consequence of changes in donor-acceptor distances? In other words, are the inter-ligand distances perturbed when the tritopic ligands are changed? To confirm or eliminate this possibility, we grew single crystals of white-light emitting MUF-77 frameworks (**13**, **14**, **15**, and **16**) and measured their unit cell lengths using SCXRD. The lengths were virtually identical meaning that the D-A distances did not vary among the different frameworks (Table 3.2), thus eliminating their role in modulating the spectral output.

Table 3.2: Unit cell lengths of various MOFs determined by SCXRD with esd in brackets.

MOF Code	Ligand Combination	Unit cell length (Å)
1	hmtt/bpdc/bdc	29.953(8)
5	hmtt/gua/bdc	29.939(3)
13	hmtt/gua/bdc-NH_2	29.981(3)
14	hbtt/gua/bdc-NH_2	29.917(3)
15	hhtt/gua/bdc-NH_2	29.890(3)
16	hott/gua/bdc-NH_2	29.839(3)

3.2.3 Studying orientation factors for D-A pairs in MUF-77

Using the SCXRD structure of MUF-77, the μ_4-oxo atoms of the Zn_4O clusters were used as anchor points and the orientation factors between the tritopic ligands were calculated. Along the shorter distance of 14.227 Å, the hxtt ligands are placed at an angle of 84°, from which a κ^2 value of 1.91 is obtained (Figure 3.8). Along the longer distance of 15.744 Å, the hxtt-hxtt angle is 95.5°, giving a κ^2 value of 2.05. Even though the orientation factor is higher in the second case, distances have a stronger impact on the FRET efficiency. This efficiency varies inversely as the sixth power of the distance, but not on the orientation factor. Hence, the hxtt ligands separated by the shorter distance of 14.227 Å have a higher FRET efficiency.

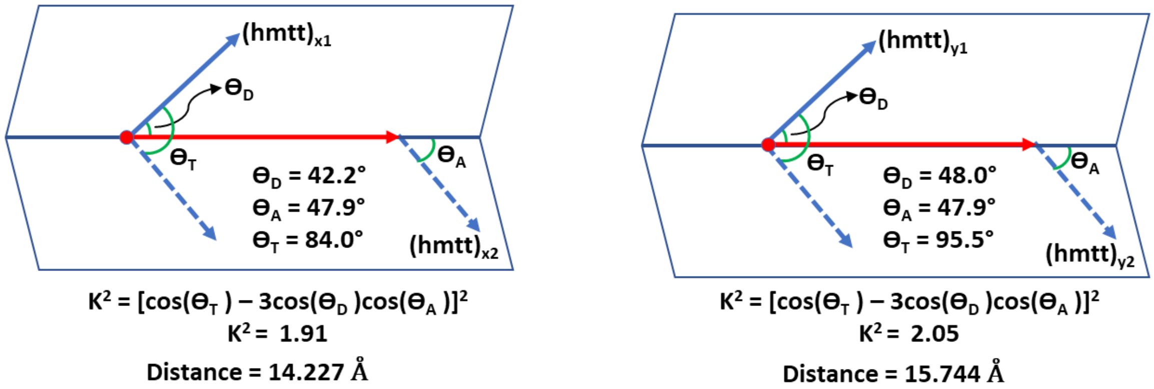

Figure 3.8: Cartoon representation of κ^2 calculation. The hmtt ligands are represented by blue arrows, with the distance vector shown with a red arrow. The μ_4-oxo atom is shown with a red circle which serves as an anchor point.

The bdc and bpdc ligands are 14.997 Å apart, but they are arranged in two different orientations. Along the z-axis, they are arranged perpendicularly and along the x-axis they are collinear (Figure 3.9). The perpendicular arrangement of ligands may result in perpendicularly arranged transition dipole moments for which κ^2 is zero, meaning zero FRET efficiency.[220] However, when considering the energy transfer from bdc-NH_2 to gua, these dipoles are not perpendicular. It is likely that the transition dipole of bdc-NH_2 lies along the direction of the amino functional groups (Figure 3.10a), thus avoiding orthogonal positioning and consequently enabling FRET.[122]

Additionally, the amino groups are disordered over four positions and the gua ligands are disordered over two positions, further preventing their orthogonal arrangement (Figure 3.10). On the other hand, the collinearly arranged ditopic ligands along the x-axis have the maximum possibility of energy transfer as their κ^2 value could be 4. Once again, transition dipole angles have to be considered which are challenging to be modelled accurately and hence the κ^2 is assumed to be equal to 4 for this chapter. In both these cases, FRET is possible albeit with different efficiencies as the linearly arranged ditopic ligands have a higher FRET efficiency compared to those arranged orthogonally.

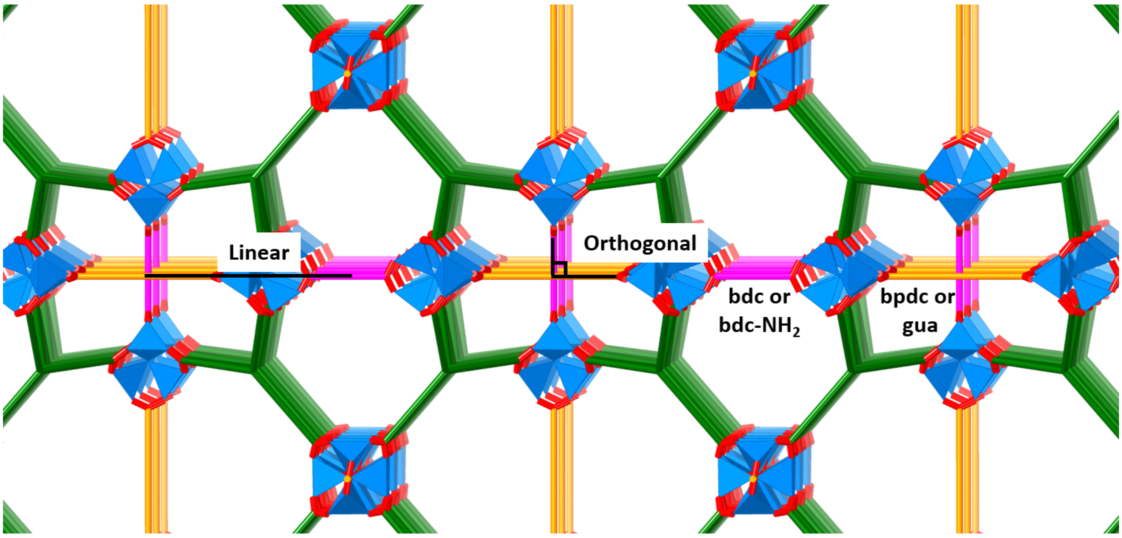

Figure 3.9: View along the z-axis of the SCXRD structure of MUF-77 showing the linear and orthogonal arrangements of gua and bdc-NH$_2$ ligands. Zn(II) ions are shown as blue tetrahedra and O atoms as red spheres. Tritopic linkers are shown as green rods.

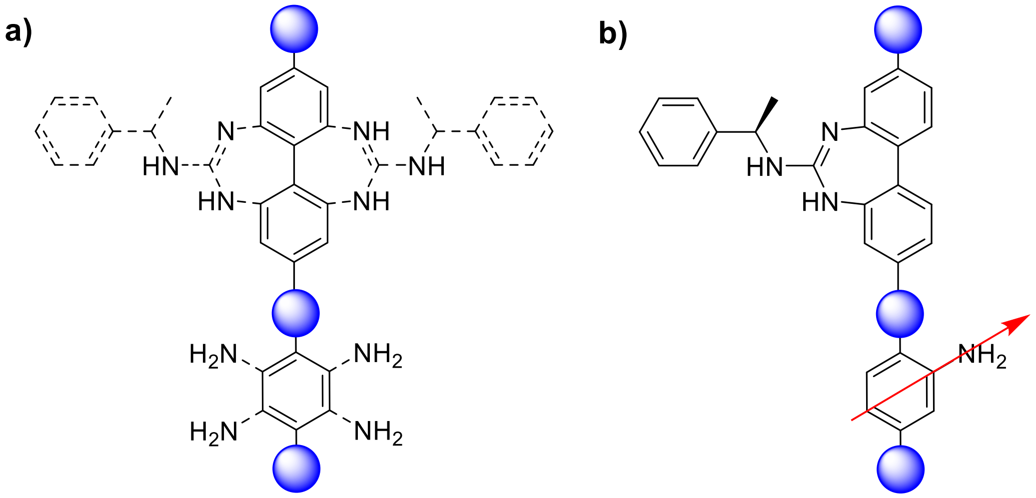

Figure 3.10: Figure showing the crystallographic disorder for the ditopic ligands in MUF-77 with the symmetry disordered groups shown with dashed bonds. **b)** The possible orientation of the transition dipole moment in bdc-NH$_2$ indicated by the red arrow. Blue spheres represent the [$Zn_4O(COO)_6$] clusters.

What about the other D-A pairs shown in entries f – v in Table 3.1? What are their orientation factors? Those entries involve all ligands, including bdc-NH$_2$ and gua both of which are disordered. Could these pairs be approximated as randomly arranged and the κ^2 value of 2/3 be used? This random value is more applicable to materials whose fluorophores reorient themselves within the fluorescence lifetime. However, in MOFs, the coordination of ligands to the metal clusters restricts their motion and hence the random approximation of 2/3 cannot be used.

Recent solid-state NMR studies have shown that the bdc and bpdc ligands in MUF-77 undergo rotation and libration.[221] The rotation rates correspond to a timescale of about 14 ns for the unfunctionalised bpdc ligand. The functionalised ligand, gua should rotate much slower than 14 ns. The same NMR study showed that the bdc ligand undergoes rotation at much longer timescale than 14 ns. This means that in summary, all the ligands involved in the energy transfer process in MUF-77 can be modelled as static, rather than dynamic.

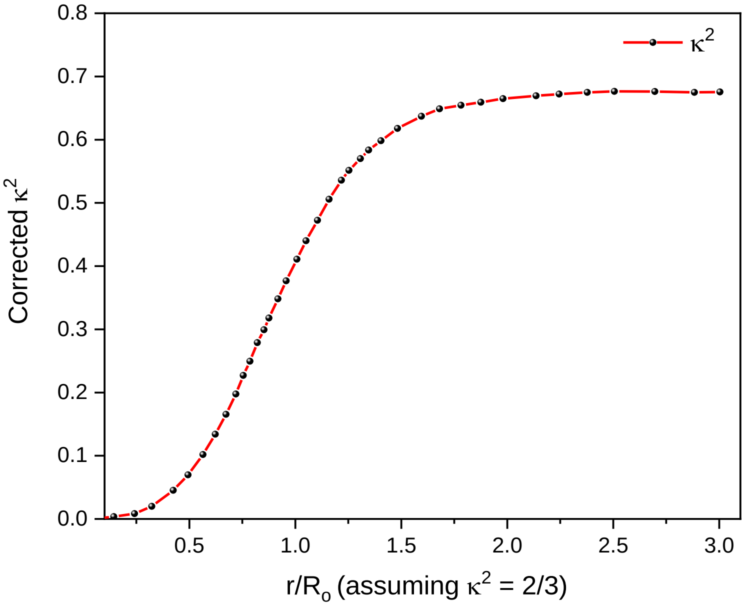

Figure 3.11: Plot showing the variation of κ^2 for static quenching. Values were digitised from a graph by Steinberg et. al.,[222] using a Web Digitiser tool.[223]

For static quenching, κ^2 can be obtained from a method developed by Steinberg et al.[222] In this method, a corrected κ^2 value is calculated by first assuming the random value of 2/3 and calculating the Förster distance, R_o using equation 3.2. Here, η is the refractive index (1.43 for DMF), Q_D is the quantum yield of the donor, κ^2 is the orientation factor which is assumed to be 2/3 in this case, and J is the spectral overlap. The ratio between the actual distance (r) and the Förster distance i.e. r/R_o is then used to estimate corrected κ^2. This corrected κ^2 is shown in Figure 3.11. As the r/R_o ratio increases, the corrected κ^2 approaches the random approximation value of 0.66 or 2/3. In other words, at longer D-A separation distances, there is little to no difference between static and dynamic quenching.

$$R_0 = [8.79 * 10^{-5} (\eta^{-4} Q_D \kappa^2 J)]^{\frac{1}{6}} \qquad \text{Eq. 3.2}$$

The corrected κ^2 values for D-A pairs in MUF-77 are displayed in Table 3.4. These values were between 0.05 – 0.55 (Entries i – m, o - w). The exception was when the gua ligand was considered as the donor with hmtt and bdc-NH_2 as the acceptors (entries x and y), very high r/R_o ratios of 3.5 and 2.1, respectively were obtained. This meant that these pairs were placed 3.5 times and 2.1 times longer than the Förster distance causing their corrected κ^2 to be 0.66. Additionally, these distance ratios meant that these pairs were placed far away for efficient FRET to occur.

3.2.4 Measuring fluorescence lifetimes of ligands

The final parameter to measure was the lifetime of the ligands without the acceptors. We first measured the lifetimes of ligands in solution. On excitation at 375 nm, the strongly emissive H_2bdc-NH_2 had a long lifetime of 12.56 ns detected at 435 nm (Figure 3.12a). However, all the tritopic ligands showed fast decays which could not be resolved by the TCSPC instrument (Figure 3.8b and Experimental section, Figure 3.28d). Similar observations were made when we studied the decay of yellow emissive H_2gua ligand, which decayed within 250 ps (Experimental section, Figure 3.28). To compensate for the lack of information about the lifetimes of the tritopic ligands and H_2gua, the ultrafast spectroscopic technique, TGPLS was used. Time-resolved emission spectra were collected with an excitation wavelength of 343 nm to obtain a three-dimensional contour plot. This plot has wavelength along the horizontal axis, time along the vertical axis and the intensity of emission is represented by colour (Figure 3.12c and d). By averaging the intensities between 400-450 nm for the tritopic ligands, and between 550-700 nm for H_2gua, kinetics plots were obtained. Fitting the kinetics to monoexponential decay profiles gave the fluorescence lifetimes of the ligands (Table 3.3 and Figure 3.13a and b). H_2gua gave a lifetime of 231 ps, which is close to the detection limit of TCSPC (250 ps). The tritopic ligands had lifetimes between 214 – 169 ps. The lifetimes decreased with increase in alkyl chain length.

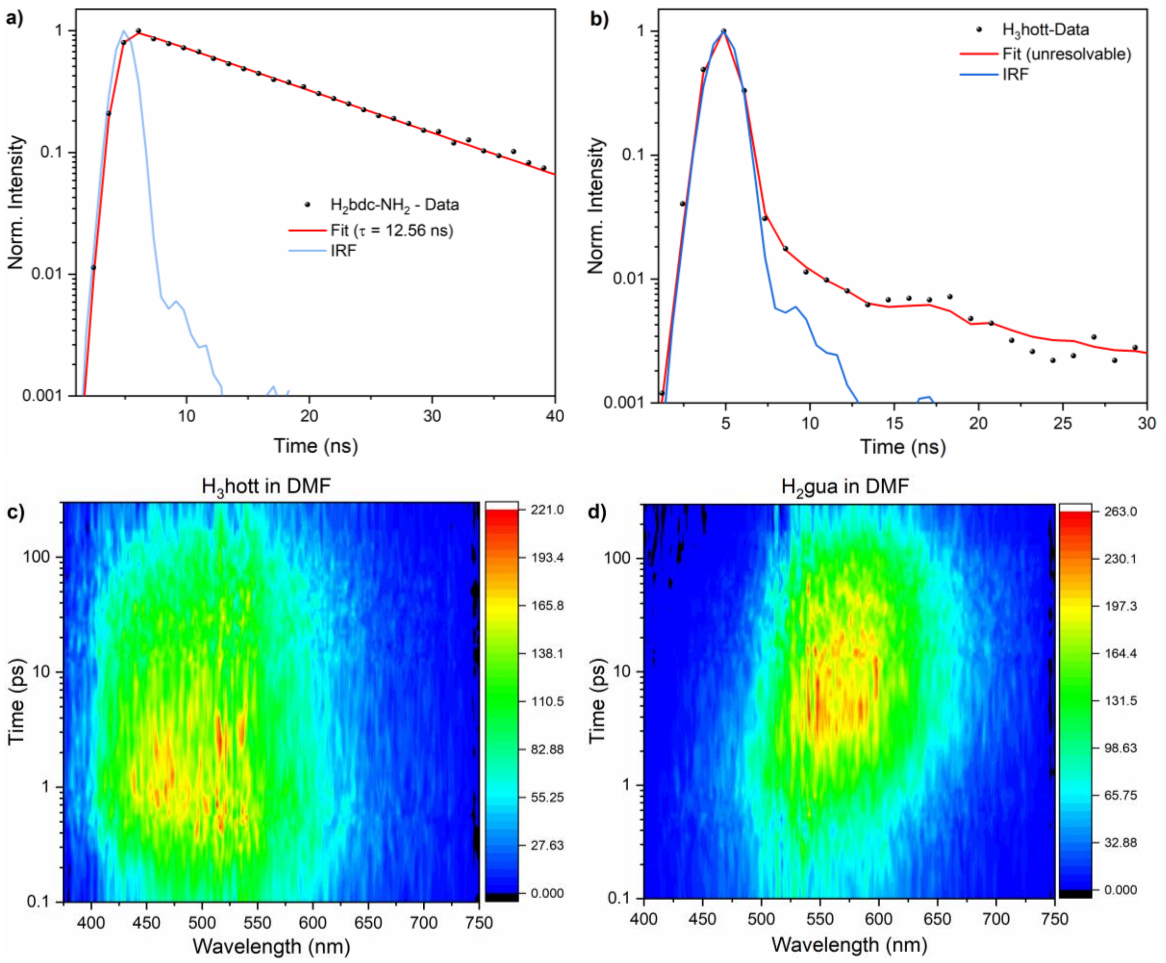

Figure 3.12: Representative TGPLS plots of ligands in solution **a)** TCSPC of $H_2bdc\text{-}NH_2$ (λ_{det} = 435 nm) with kinetics fit to a lifetime of 12.56 ns. **b)** Representative TCSPC (λ_{det} = 430 nm) of fast decaying tritopic ligands with H_3hott as an example. The other decays are shown in the experimental section, Figure 3.28 **c)** TGPLS of H_3hott in DMF and **d)** TGPLS of H_2gua in DMF.

Table 3.3: Lifetimes of ligands in DMF calculated by fitting their decay kinetics.

Ligand	Detection wavelength (nm)	Fluorescence Lifetime (ns)	Technique used
H_3hmtt	400-450 nm	214 ± 9 ps	TGPLS
H_3hbtt	400-450 nm	186 ± 7 ps	TGPLS
H_3hhtt	400-450 nm	179 ± 5ps	TGPLS
H_3hott	400-450 nm	169 ± 9 ps	TGPLS
H_2gua	550-700 nm	231 ± 4 ps	TGPLS
$H_2bdc\text{-}NH_2$	430 nm	12.5 ± 0.3 ns	TCSPC

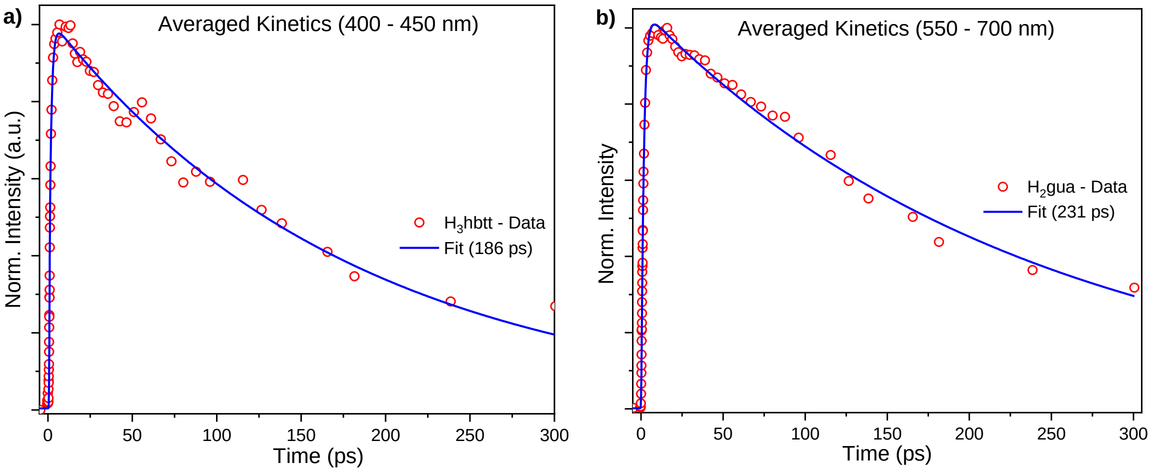

Figure 3.13: Representative averaged TGPLS kinetics **a)** H_3hbtt in DMF between 400 - 450 nm and **b)** H_2gua in DMF averaged between 550-700 nm. Red circles are data points and the blue curves represent fitted data.

Now that quantum yields, spectral overlaps, orientation factors, fluorescence lifetimes were all experimentally determined using appropriate techniques, the FRET rate (k_{FRET}) and FRET efficiencies (E_{FRET}) could be calculated using equations 3.3 and 3.4

$$k_{FRET} = \frac{1}{\tau_D}\left(\frac{R_o}{R}\right)^6 \qquad \text{(Eq. 3.3)}$$

$$E_{FRET} = \left(\frac{R_o^6}{R_o^6 + R^6}\right) * 100 \qquad \text{(Eq. 3.4)}$$

Here, τ_D is the lifetime of the donor without the acceptor, R is the D-A separation distance and R_o is the Förster distance. The FRET time (t_{FRET}) is the reciprocal of the FRET rate obtained in equation 3.3 The FRET efficiencies (E_{FRET}) for all donor pairs are tabulated in Table 3.4.

Some key observations can be made from Table 3.4. Firstly, there are many possibilities for energy transfer in MUF-77. Secondly, transfer efficiencies vary from very high (> 80 %) to moderate (50 – 80 %) to extremely low (< 10 %). These low efficiencies are characteristic of FRET processes in which the gua is the donor (entries x, y). This means that in MUF-77, the gua ligand is behaves exclusively as an acceptor and the possibility of gua being a donor is remote.

Thirdly, timescales for energy transfer also vary from tens of picoseconds (entries h - l) to tens of nanoseconds (entries o - r). So, do these predicted FRET lifetimes square with experimentally observed times for MUF-77?

Table 3.4: Calculation of FRET rates, times and efficiencies for various D-A pairs possible in MUF-77.

Entry	**Donor**	**Acceptor**	**Q_D(*)**	**J (nm^4/mol/cm)**	**κ^2**	**R (Å)**	**τ_D(†)**	**Ro (Å)**	**k_{FRET} (s^{-1})**	**t_{FRET}**	**E_{FRET} (%)(‡)**
a	hmtt	hmtt	0.26	$1.99*10^{12}$	1.91	14.227	214 ps	16.58	$1.17*10^{10}$	85 ps	71
b	hmtt	hmtt	0.26	$1.99*10^{12}$	2.05	15.744	214 ps	16.78	$6.84*10^{9}$	146 ps	59
c	hbtt	hbtt	0.21	$1.22*10^{12}$	1.91	14.227	186 ps	14.75	$6.67*10^{9}$	150 ps	55
d	hbtt	hbtt	0.21	$1.22*10^{12}$	2.05	15.744	186 ps	14.92	$3.90*10^{9}$	256 ps	42
e	hhtt	hhtt	0.37	$1.31*10^{12}$	1.91	14.227	179 ps	16.39	$1.31*10^{10}$	76 ps	70
f	hhtt	hhtt	0.37	$1.31*10^{12}$	2.05	15.744	179 ps	16.59	$7.64*10^{9}$	131 ps	57
g	hott	hott	0.38	$4.04*10^{12}$	1.91	14.227	169 ps	19.87	$4.39*10^{10}$	22 ps	88
h	hott	hott	0.38	$4.04*10^{12}$	2.05	15.744	169 ps	20.11	$2.57*10^{10}$	38 ps	81
i	hmtt	gua	0.26	$4.99*10^{13}$	0.09	13.212	214 ps	17.05	$2.16*10^{10}$	46 ps	82
j	hbtt	gua	0.21	$4.01*10^{13}$	0.11	13.212	186 ps	16.40	$1.97*10^{10}$	50 ps	78
k	hhtt	gua	0.37	$4.85*10^{13}$	0.07	13.212	179 ps	17.26	$2.78*10^{10}$	36 ps	83
l	hott	gua	0.38	$3.87*10^{13}$	0.09	13.212	169 ps	17.41	$3.10*10^{10}$	32 ps	83
m	bdc-NH_2	gua	0.62	$7.31*10^{12}$	0.21	14.997	12.5 ns	16.48	$1.41*10^{8}$	7.1 ns	63
n	bdc-NH_2	gua	0.62	$7.31*10^{12}$	4	14.997	12.5 ns	26.93	$2.68*10^{9}$	370 ps	97

o	bdc-NH$_2$	hmtt	0.62	$1.21*10^{11}$	0.55	12.775	12.5 ns	9.77	$1.59*10^{7}$	62 ns	16
p	bdc-NH$_2$	hbtt	0.62	$8.26*10^{11}$	0.34	12.775	12.5 ns	12.41	$6.70*10^{7}$	15 ns	45
q	bdc-NH$_2$	hhtt	0.62	$5.56*10^{11}$	0.39	12.775	12.5 ns	11.89	$5.18*10^{7}$	19 ns	39
r	bdc-NH$_2$	hott	0.62	$3.61*10^{12}$	0.19	12.775	12.5 ns	14.41	$1.64*10^{8}$	6 ns	47
s	hmtt	bdc-NH$_2$	0.26	$5.83*10^{13}$	0.07	12.775	214 ps	16.78	$2.40*10^{10}$	40 ps	83
t	hbtt	bdc-NH$_2$	0.21	$4.26*10^{13}$	0.10	12.775	186 ps	16.31	$2.33*10^{10}$	43 ps	81
u	hhtt	bdc-NH$_2$	0.37	$5.62*10^{13}$	0.07	12.775	179 ps	17.69	$3.39*10^{10}$	25 ps	87
v	hott	bdc-NH$_2$	0.38	$4.06*10^{13}$	0.07	12.775	169 ps	16.82	$3.09*10^{10}$	32 ps	83
w	hmtt	gua	0.26	$4.99*10^{13}$	0.44	25.422	214 ps	22.21	$2.08*10^{9}$	480 ps	30
x	gua	hmtt	0.01	$2.04*10^{10}$	0.66	13.21	231 ps	3.76	$2.31*10^{6}$	433 ns	3
y	gua	bdc-NH$_2$	0.01	$7.63*10^{11}$	0.66	14.98	231 ps	6.88	$4.06*10^{7}$	24 ns	2

(*) Error in Q_D is about ± 0.02 units. (†) Errors for the lifetime (τ_D) are mentioned in Table 3.3. (‡) Considering errors in both Q_D and τ_D, error in percentage efficiency is about ± 3 %.

3.2.5 Measuring fluorescence lifetimes of parent MUF-77

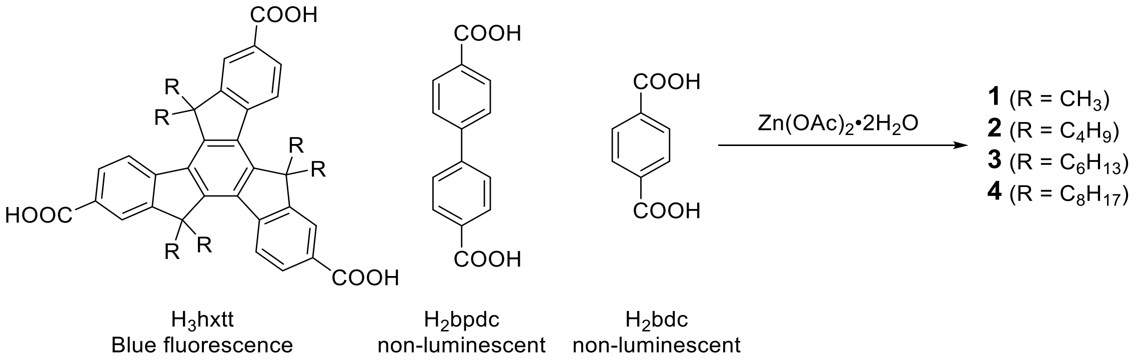

Scheme 3.1: Synthesis of MUF-77 frameworks **1**, **2**, **3**, and **4**.

We first measured the TCSPC of **1**, **2**, **3,** and **4** (Scheme 3.1) which contain only tritopic ligands as emitters (the bdc and bpdc being considered as non-emissive). We monitored at the emission maximum of 435 nm. All MOFs gave biexponential decay profiles with one lifetime less than 3.5 ns and another more than 10 ns (Table 3.5 and Figure 3.14). This meant that there were two decay processes occurring in these frameworks. For both these lifetime components, there was no obvious trend with increase of the alkyl chain length. However, the average lifetime (τ_{avg}) did show an increasing trend, from 2.42 ns for **1** (methyl groups on truxene) to 7.06 ns for **4** (octyl groups on truxene).

Table 3.5: Fluorescence lifetimes of **1**, **2**, **3**, and **4** detected at 435 nm.

MOF Code	Ligand combination	Fluorescence Lifetime (ns)		
		τ_1 (A_1)	τ_2 (A_2)	τ_{avg} $^{(a)}$
1	hmtt/bpdc/bdc	1.1 (87.6 %)	11.9 (12.4 %)	2.42
2	hbtt/bpdc/bdc	0.9 (79.0 %)	20.9 (21.0 %)	5.03
3	hhtt/bpdc/bdc	1.5 (72.1 %)	17.0 (27.9 %)	5.86
4	hott/bpdc/bdc	3.1 (65.2 %)	14.5 (34.8%)	7.06

(a) $\tau_{avg} = \tau_1(A_1) + \tau_2(A_2)$.

From TGPLS, we had found that the truxene ligands have a lifetime of 169 – 214 ps in solution (Table 3.3). In **1**, **2**, **3**, and **4**, the truxene ligands (hmtt, hbtt, hhtt, hott) are coordinated to the metal clusters, which can increase their lifetime in MUF-77. Hence, the shorter of the two components (0.9 – 3.1 ns) may originate from direct relaxation of the truxene chromophores.

Another reason for the shorter component may be exciton-exciton annhilation (EEA).[125] Excitation of truxene ligands, may give rise to multiple excitons within the crystals. As these excitons diffuse across the crystals, two excitons meet and recombine (or annhilate) and emit a photon. This process has been observed in MOFs and other crystalline materials and may give rise to a short component in TCSPC.[126,224,225]

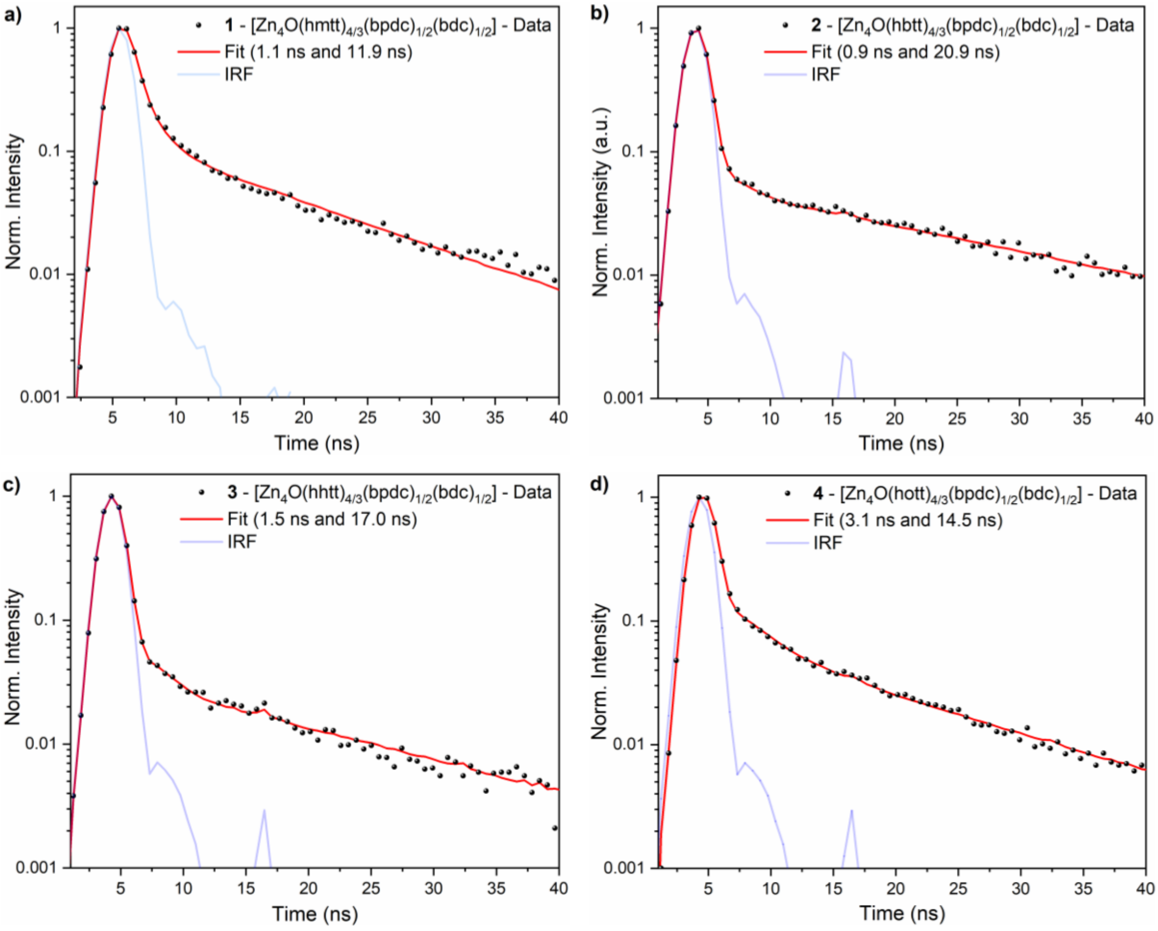

Figure 3.14: TCSPC of MUF-77 frameworks detected at 430 nm (λ_{ex} = 375 nm) **a) 1 b) 2 c) 3** and **d) 4**.

3.2.6 Calculating exciton diffusion lengths

From the TCSPC lifetimes observed for **1**, **2**, **3**, and **4**, we assigned the longer component to long-range exciton migration between adjacent tritopic ligands. MUF-77 being a crystalline, ordered material would enable such long-range transport via the FRET mechanism (Figure 3.15). So, how far does this exciton migrate across the crystal? In other words, what is the exciton diffusion length (L_D)? Does this exciton diffuse using a step-by-step (s-b-s) hopping or by the jumping beyond nearest neighbour (JBNN) mechanism?

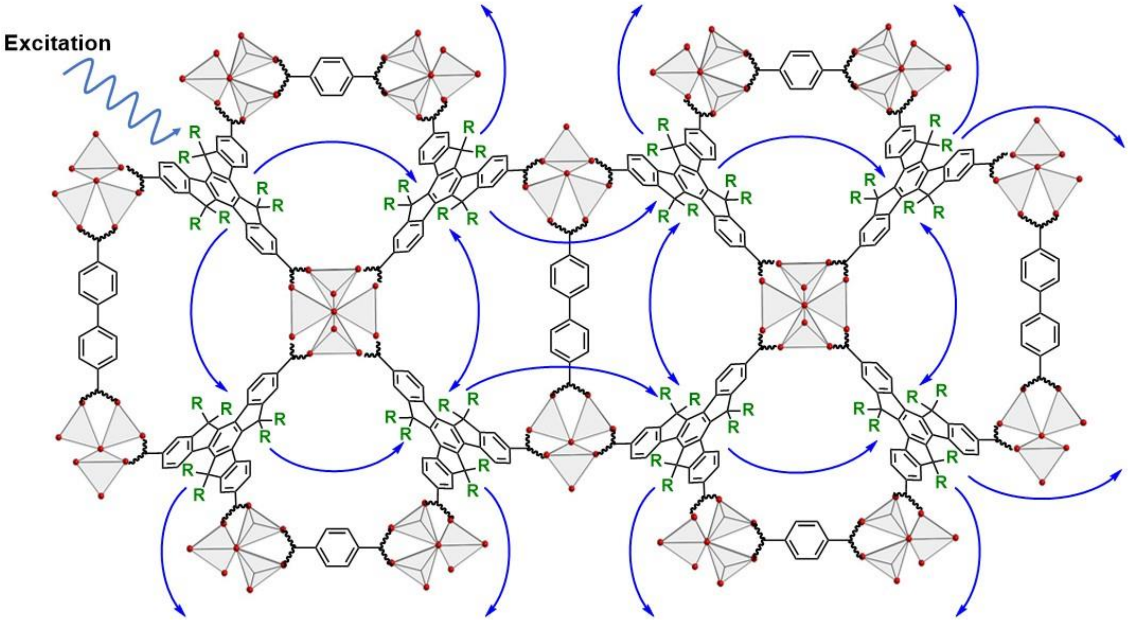

Figure 3.15: Cartoon representation of MUF-77, showing the different exciton migration pathways (blue arrows) following excitation (wavy arrow). For simplicity, only step-by-step hopping is shown.

From a survey of relevant literature, there are many methods of determining the L_D.[125,226] One of the methods, which is a standard for many materials including MOFs, calculates L_D using equation 3.5. It utilises the diffusion coefficient, D of the exciton and the fluorescence lifetime, τ.[227,228] However, D has to be experimentally determined using advanced computational tools.[229] Ultrafast spectroscopic techniques in which spectra are collected with different power densities can also aid in calculating this parameter.[230,231] However, in many cases, D is not experimentally determined. Instead, known D values of related materials are used.[232,233]

$$L_D = \sqrt{D\tau} \qquad \text{(Eq. 3.5)}$$

For this chapter, especially for MOFs **1**, **2**, **3**, and **4**, diffusivity values from Zhang et al. have been applied.[127] This study used a combination of computational and experimental data to calculate D for two different cubic, zinc containing, truxene-based MOFs (named TruMOF-1 and TruMOF-2). For each MOF, two distinct diffusion coefficients were obtained. One of them factored in both JBNN and s-b-s mechanisms and the other considered only s-b-s hopping. Among these two MOFs, TruMOF-2 has a D value of $2.30*10^{12}$ nm^2/s when JBNN is considered. It's s-b-s diffusivity is significantly lower at $6.25*10^{11}$ nm^2/s.

Furthermore, TruMOF-2 has truxene ligands separated by about 13 Å, a distance which is comparable to hxtt-hxtt separation in **1**, **2**, **3**, and **4**. Hence, the D value of TruMOF-2 has been applied to calculate L_D.

Table 3.6 shows L_D for MUF-77 frameworks **1**, **2**, **3**, and **4**. For each MOF, two different L_D values have been calculated (using equation 3.5) which correspond to exciton diffusion by two different mechanisms. L_D values by JBNN are about two times higher than those obtained by s-b-s. More importantly, we have observed that the lifetime increases with an increase in alkyl chain length. Consequently, the L_D also increases from 74.6 nm for **1** to 127.4 nm for **4**.

As a comparison, Zhang et al. found an L_D of 48 nm for TruMOF-2. In another study, distances of up to 58 nm were obtained for a zinc MOF composed of ethynyl porphyrin linkers.[126] This means that diffusion lengths in MUF-77 are comparable to these literature values but are much higher, possibly due to well-ordered ligand arrangements, high spectral overlaps and lack of defects.[175] Additionally, L_D in MUF-77 can be tuned by just changing the alkyl groups on the truxene ligands, a feature which was unexplored in TruMOF-2. These diffusion lengths correspond to exciton migration across many unit cells in MUF-77. The unit cell lengths do not change between **1**, **2**, **3**, and **4** and are about 29.9 Å long. This means that an increase in the L_D also increases the number of unit cells the exciton migrates through (Table 3.6). When JBNN is considered, the lifetimes of MUF-77 systems correspond to exciton migration of 25, 36, 39, and 43 unit cells for **1**, **2**, **3**, and **4**, respectively. These values drop significantly (13 – 22 unit cells) when only s-b-s migration is taken into account.

Table 3.6: Calculating exciton diffusion length (L_D) using diffusivity values of truxene MOFs reported in the literature.[127]

MOF Code	Ligand combination	Avg. Lifetime (ns)	Diffusivity with JBNN and s-b-s (nm^2/s)	L_D with JBNN and s-b-s (nm)[(a)]	No. of unit cells [(b)]	Diffusivity s-b-s only (nm^2/s)	L_D with s-b-s only (nm)[(a)]	No. of unit cells [(b)]
1	hmtt/bpdc/bdc	2.42	$2.30*10^{12}$	74	≈ 25	$6.25*10^{11}$	39	≈ 13
2	hbtt/bpdc/bdc	5.03	$2.30*10^{12}$	107	≈ 36	$6.25*10^{11}$	56	≈ 19
3	hhtt/bpdc/bdc	5.86	$2.30*10^{12}$	116	≈ 39	$6.25*10^{11}$	60	≈ 20
4	hott/bpdc/bdc	7.06	$2.30*10^{12}$	127	≈ 43	$6.25*10^{11}$	66	≈ 22

(a) Calculated using eq. 3.5. **(b)** Calculated by dividing L_D by the unit cell length.[78]

3.2.7 TGPLS of 1 to probe hmtt-hmtt energy transfer

We have shown that FRET between adjacent hxtt ligands is predicted to take place within 22 – 256 ps (Table 3.4, Entries a - h). These times are too short to be probed by TCSPC and hence TGPLS has to be utilised. We measured TGPLS on single crystals of **1** with an excitation wavelength of 343 nm.

The TGPLS plot of **1** showed that emission begins after 0.1 ps of excitation and continues up to about 80 ps (Figure 3.16a). After this point weaker emission is observed. The emission band spans the region between 400 – 650 nm. For analysis, we spilt this emission into two regions. The first one between 400 – 450 nm corresponding to the emission from hmtt, and the second one between 550 – 650 nm. This second region likely arises from an energy transfer from the organic ligands to the Zn_4O_{13} cluster.[102,234] Here, the organic ligands absorbs light and the Zn_4O_{13} clusters acts as a ZnO quantum dot.

The kinetic profile averaged between 400 – 450 nm, corresponding to the emission from hmtt, showed a three-component decay (Figure 3.16b). 46.2 % of the emission decayed within 0.75 ps, another 44.6 % decayed within 34.9 ps. About 9.2 % of the emission did not decay within 300 ps. This long component is the emission detected by TCSPC and is possibly due to direct relaxation of the hmtt ligand and long-range exciton diffusion across the MOF crystal. For the fast decaying components, we formulated two theories regarding their origin.

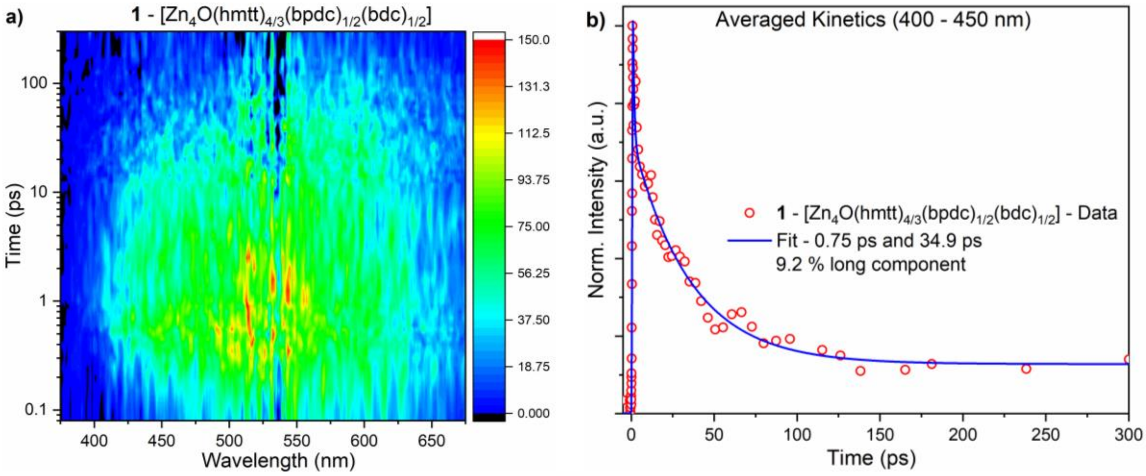

Figure 3.16: a) TGPLS plot of **1**. **b)** Averaged TGPLS decay kinetics of **1** between 400 – 450 nm. Decay times are mentioned in the figure legend.

3.2.7.1 Theory 1: s-b-s versus JBNN exciton migration

In the first theory, we assign the 0.75 ps component to s-b-s migration of excitons between adjacent hmtt ligands. The 34.9 ps component may arise from JBNN migration i.e.

the migration of exciton by skipping adjacent hmtt linkers. If the hopping time for an exciton is known, then the diffusivity (D) of the exciton in the material can be approximated using equation 3.5.[125]

$$\mathrm{D} = \frac{r^2}{6\mathrm{t}_{\mathrm{hop}}} \qquad \text{(Eq. 3.5)}$$

Here, t_{hop} is the hopping time and r is the distance between the chromophores. In the case of **1**, the t_{hop} is 0.75 ps and r is 14.227 Å. Plugging these values into equation 3.5 gives a diffusivity of 4.5×10^{11} nm^2/sec for **1**. Applying this diffusivity to equation 3.4 gives an exciton diffusion length (L_D) of 32.9 nm. This value is very close to the L_D of **1** (38.9 nm), calculated using the diffusivity of TruMOF-2 (Table 3.6). This means that the 0.75 ps may likely arise from s-b-s migration.

Table 3.7: Comparing diffusion length using values from the literature with that obtained from our TGPLS data.

MOF Code	Ligand combination	Hopping Time	Diffusivity (nm^2/sec)	L_D (nm)$^{(a)}$
1	hmtt/bpdc/bdc	-	6.25×10^{11} **(b)**	38.9
1	hmtt/bpdc/bdc	0.75 ps	4.50×10^{11} **(c)**	32.9

(a) Calculated using eq. 3.4. **(b)** D value from Ref. 33. **(c)** Calculated using eq. 3.5.

The second fast component i.e. 34.9 ps can be assigned to JBNN hopping. We know that FRET times vary inversely with the sixth power of distance. If 0.75 ps is the time required for an exciton migration to move by 14.227 Å, what would be the distance covered in 34.9 ps? To answer this question, we first obtain the ratio of the decay times, 34.9 ps/0.75 ps = 46.5. Multiplying the sixth root of this value with the inter-ligand distance of 14.227 Å, we get a value of 26.908 Å. This distance is roughly equal to the unit cell length of **1** (29.953 Å), which is also the distance between two non-adjacent hmtt ligands (Figure 3.17).

Correlating these calculations with the TGPLS decays, exciton migration in **1** occurs using both, s-b-s and JBNN pathways. Since, the percentage contribution for both the short components is roughly equal (46.2 % and 44.6 %), we can assume that s-b-s and JBNN pathways contribute to exciton diffusion in roughly equal amounts.

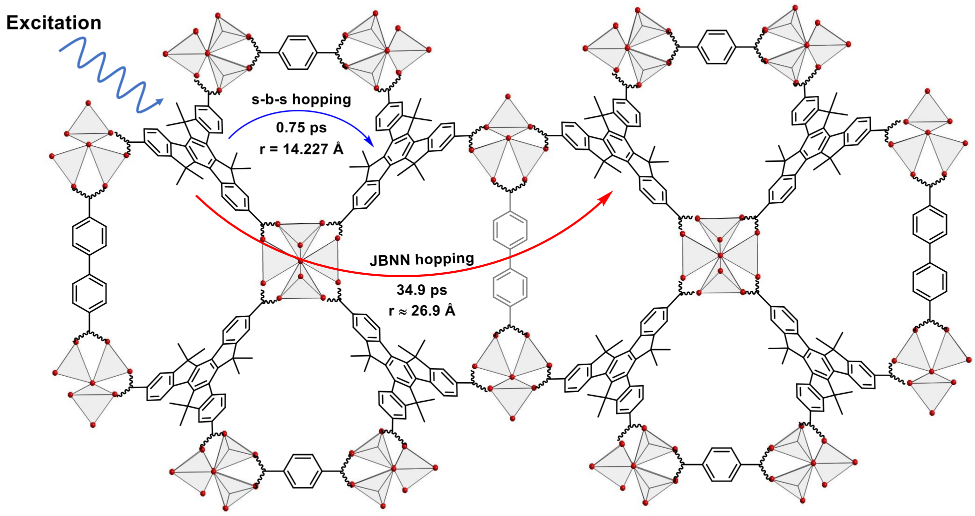

Figure 3.17: Schematic diagram showing exciton migration by the step-by-step (s-b-s) and jumping beyond nearest neighbour (JBNN) mechanisms in 1. Distances (r) and hopping times are also shown.

So how does one prove such a mechanism? Zhang et al. had demonstrated the JBNN mechanism by loading the pores of TruMOF-2 with Coumarin 343 which functioned as an acceptor.[127] They used computational methods to evaluate the energy transfer efficiency as a function of the dye loading level. When considering JBNN migration, the efficiency showed a much stronger dependency on the coumarin loading level.

A similar approach can be used for MUF-77, where dyes like coumarin 343 or coumarin 153 can be loaded into the pores at different concentrations. A combined experimental and computational approach will be used to determine the contribution of both JBNN and s-b-s pathways in MUF-77. These studies are part of proposed research for the future.

3.2.7.1 Theory 2: Exciton-exciton annihilation and exciton migration

In the second theory, we assign the 1.9 ps component to exciton-exciton annhilation (EEA). This process is known to take place in this timescale.[230] However, this assignment is speculative at this stage. The ultimate proof for EEA is dependence of this lifetime component on the excitation density. For the TGPLS described here, an excitation density of 34 μJ/cm^2 was used. Further studies with higher and lower excitation densities are to be performed as part of future work. These experiments would enable us to confirm or eliminate the possibility of EEA in these frameworks.

The second component i.e. the longer, 40 ps component is from FRET between hmtt ligands at distances of 14.227 Å and 15.774 Å. The predicted lifetimes for these FRET events (85 ps and 146 ps, Table 3.4, entries a and b) are close to what we observed experimentally and hence this component can be matched to this FRET process. In **1** where the hmtt ligands are separated by two different distances, which should give rise to two distinct lifetimes. However, since the distances are not very different, only a single component of 40 ps is seen which represents an approximate time for FRET between these ligands at both distances.

However, there are slight differences between the predicted (85 ps and 146 ps) and the observed FRET lifetime (40 ps). The Förster theory of energy transfer which we have used to predict lifetimes seemed to overestimate them. However, this theory approximates D-A pairs as point dipoles, an approximation which can breakdown when D-A pairs are at short distances.[117,235,236] A more accurate method to estimate FRET times would be to compute atomic transition densities and exciton coupling between excited states of the D-A pair. Such computations have been used for MOFs but primarily for those containing only binary MOFs (MOFs containing only one ligand and metal).[111,127,237] In many binary MOFs, the ligands are separated by equal distances on all directions and hence exciton migration is uniform or isotropic and many parameters can be calculated which relate to exciton migration.[226,237-239]

Applying this idea to multicomponent MOFs as complex and anisotropic as MUF-77 could be significantly more challenging.[126,232] However, we aim to perform these computations as part of future work to obtain a more accurate picture of excited-state processes in MUF-77.

3.2.8 Is there energy transfer from hxtt to gua?

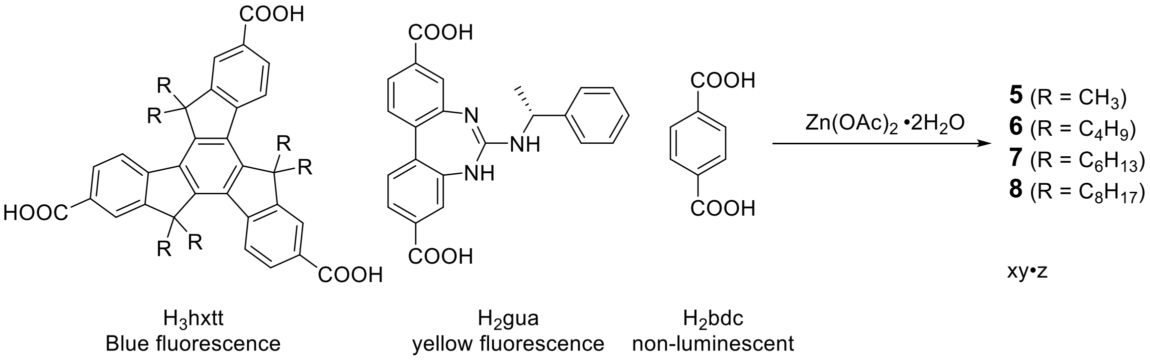

Scheme 3.2: Synthesis of MUF-77 frameworks **5**, **6**, **7** and **8.**

MOFs **5**, **6**, **7**, and **8** comprise the linker sets hxtt/gua/bdc (Scheme 3.2). Their yellow fluorescence must arise from the gua component (Figure 3.18a). We have seen in Chapter 2 that the emission of these MOFs matches the emission from gua ligand and truxene emission is no longer visible. This yellow emission may stem from direct excitation of the gua ligand or from energy transfer from the hxtt ligand to the gua ligand. How does one differentiate these possibilities?

We measured the excitation spectra of nanocrystalline **5**, **6**, **7**, and **8** with a detection wavelength of 565 nm, which corresponds to the emission peak maximum of the gua ligand. We compared these spectra to the excitation spectra of the dissolved H_3hbtt and H_2gua in solution (Figure 3.18b). The spectrum of H_3hbtt had peak at 363 nm with a shoulder at 355 nm. On the other hand, H_2gua gave two peaks with one of them centred at 400 nm.

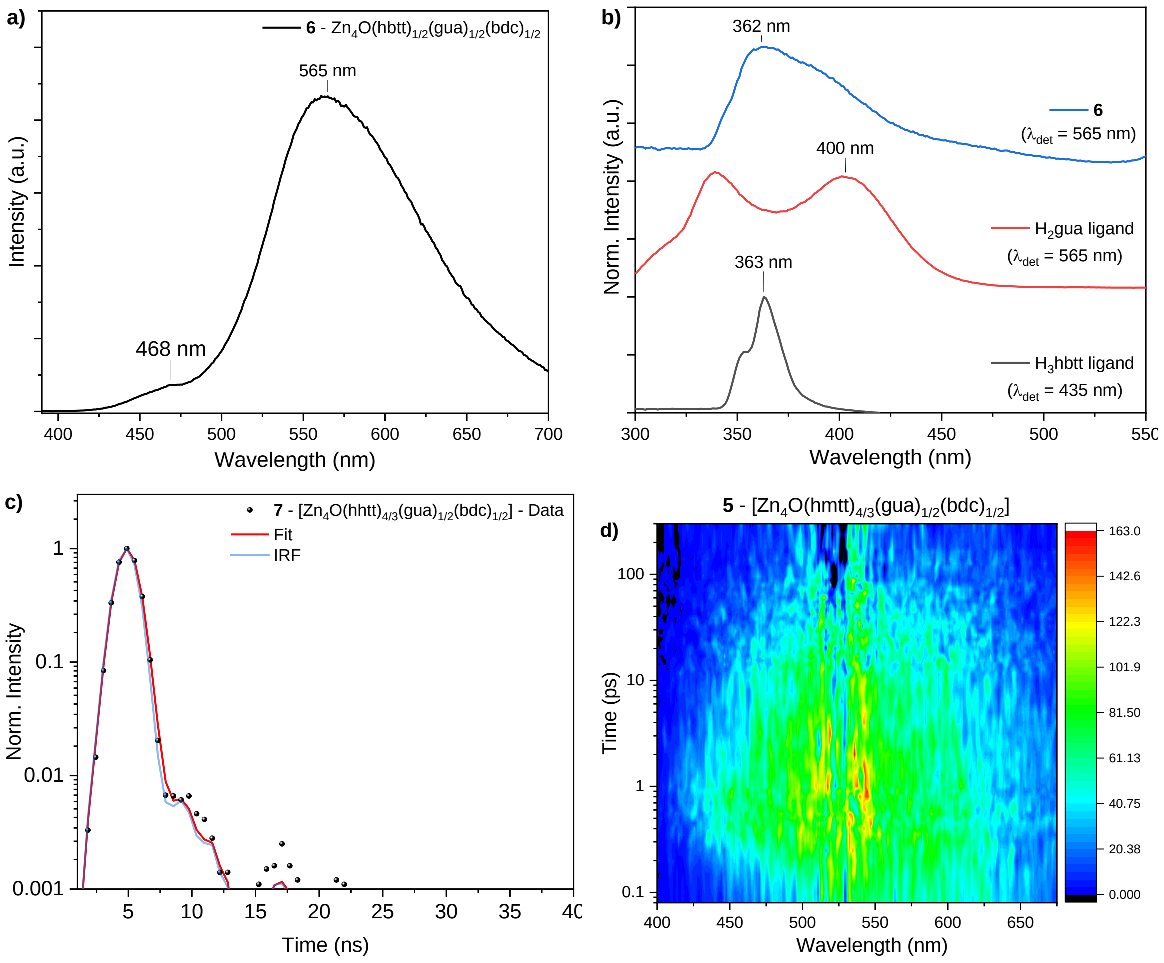

Figure 3.18: a) Representative emission spectra of MUF-77 with the ligand combination hxtt/gua/bdc (λ_{ex} = 375 nm). **b)** Comparison of excitation spectra of DMF solutions of H_3hbtt, H_2gua, with **6**. **c)** Representative TCSPC decay of MUF-77 (λ_{det} = 565 nm) with the ligand combination hxtt/gua/bdc, showing fast decay. **d)** TGPLS of **5**.

The excitation spectrum of **6** gave a broad peak with a peak centred at 362 nm, which corresponds to the excitation peak of H_3hbtt in solution. Since this peak is broad, some excitation may also arise from gua. From this comparison, it is evident that excitation spectra of **5, 6**, **7**, and **8** match the excitation of both hxtt and gua ligands. Since no H_3hbtt emission is seen, we conclude that the yellow luminescence arises due to a FRET process from the H_3hbtt to the gua ligand, giving off yellow emission centred at 565 nm (Figure 3.18a). Spectral overlap and FRET timescale calculations shown in Table 3.4 (entries i - l) have proven that energy transfer is possible between these ligands. The excitation spectra are in accord with these calculations. The next thing to do would be to match the calculated FRET times with experimental values obtained from time-resolved fluorescence.

We measured TCSPC of MOFs **5**, **6**, **7**, and **8** at a detection wavelength of 565 nm, corresponding to their emission maxima. We observed fast decays comparable to the 250 ps IRF of the instrument (Figure 3.18c). This meant that there were processes faster than this time occurring in these frameworks, which necessitated the use of TGPLS for these MOFs.

TGPLS on single crystals of **5**, showed that emission begins within 100 femtoseconds of excitation and spans the region between 420 – 650 nm (Figure 3.18d). Two decay profiles were collected from two different regions of the TGPLS plot. One between 400 - 450 nm and another between 550 – 700 nm, which corresponded to emission from hmtt and gua, respectively (Figure 3.19a and b).

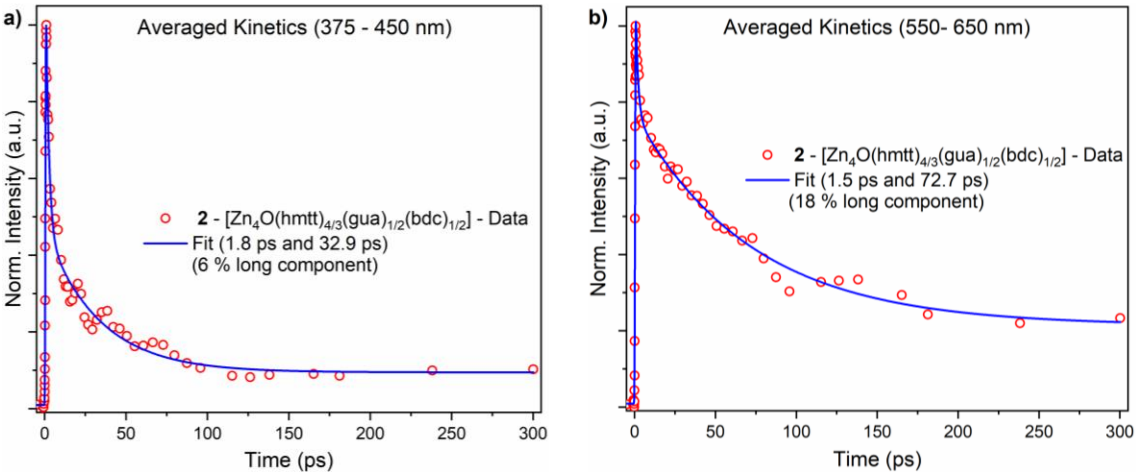

Figure 3.19: Picosecond kinetics of **6** at two different wavelength regions **a)** 400 nm – 450 nm and **b)** 550 – 650 nm.

From the decay profiles, most of the emission in the short wavelength region (375 – 450 nm) decays within 300 ps and hence only a weak feature is observed at this wavelength range in the steady-state emission spectrum. This decay could be resolved into three components, 1.8 ps, 32.9 ps, and a long component with contributions of 62.8 % and 31.2 % and 6 %, respectively. We compared this TGPLS kinetic profile to that of **1** at the same wavelength region (Compare Figures 3.16b and 3.19a). The short, 1.8 ps component is once again probably from the suspected EEA process or hmtt-hmtt s-b-s hopping.

Table 3.8: A comparison of lifetimes obtained from TGPLS of **1** and **5.**

MOF Code	Ligand combination	Wavelength	τ_1 (%) ps	τ_2 (%) ps	% long component
1	hmtt/bpdc/bdc	400 – 450 nm	0.75 (46.2)	34.9 ± 4.1 (44.6)	9.2
5	hmtt/gua/bdc	400 – 450 nm	1.8 ± 0.1 (62.8)	32.9 ± 4.7 (31.2)	6
5	hmtt/gua/bdc	550 – 650 nm	1.5 (32.4)	72.7 ± 13.1 (49.6)	18

The 32.9 ps component could likely arise from hmtt-gua energy transfer. The predicted lifetime for this process is 46 ps, which matches closely with the experimental observations. The question does arise: The decay times of **6** match closely with those of **1** (Table 3.8), so is there energy transfer from hmtt to gua? Checking the percentage contributions could answer this question. In **1**, both these lifetimes have roughly equal contributions, but not in **6**. FRET from hmtt to gua is predicted to be more efficient than hmtt-hmtt. This causes the lifetime and its percentage contribution to be reduced. This trend is also observed for the contribution of the non-decaying component, which decreases from 11 % in **1** to 6 % in **6**.

The decay of the yellow region (550 - 650 nm) could also be decomposed into three components (Figure 3.19b). The lifetimes 72.7 ps and 18% non-decaying component are higher than those at the low wavelength region. The emission here must stem exclusively from the gua ligand. From the TGPLS of the H_2gua ligand (Figure 3.10b), we know that it shows a monoexponential decay of 231 ps. However, when incorporated into MUF-77, this is not what is observed and instead a three-component decay is seen.

The 72.7 ps component and the non-decaying profile are possibly from hmtt-gua energy transfer. The percentage contribution of this component is higher than that observed in the low wavelength region. This means that the hmtt transfers energy to gua within 32.9 ps and the causing gua to have a much longer lifetime than what is observed in solution. Even though a non-decaying component is observed, **6** decays very quickly in its TCSPC profile. This may arise from the weaker emission intensity of **6**, making it challenging to obtain its lifetime with TCPSC.

The origin of the shorter component, and 1.5 ps in the long wavelength regions, is probably from another photophysical process. Guanidine derivatives are known to show interesting excited-state properties including excited-state proton transfer (ESPT).[240] The

TGPLS data was collected with the MOFs suspended in DMF, which is a hydrogen bond accepting solvent. Excitation may cause ESPT between gua and DMF.[241] ESPT is an ultrafast process and can occur anywhere between femtoseconds to picoseconds[242] and hence, it is likely that the fast component arises from an ESPT process.

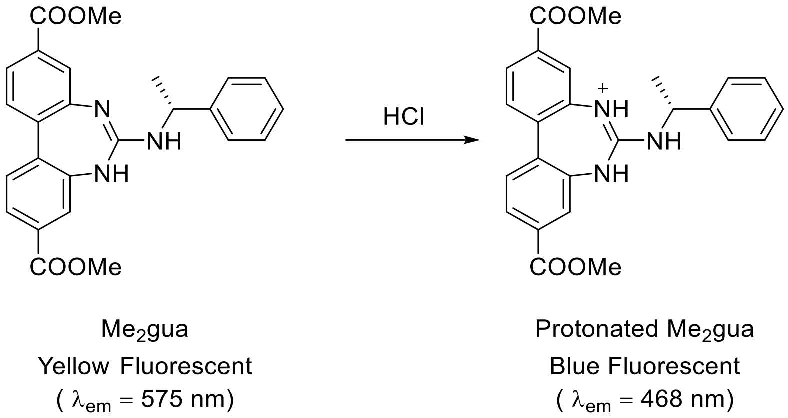

Scheme 3.3: Protonation of Me$_2$gua by HCl causing a shift in the emission maximum.

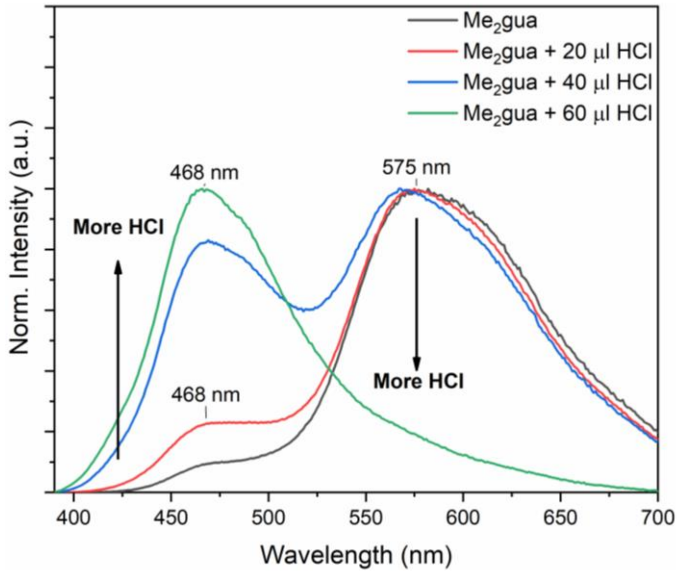

Figure 3.20: Emission spectra (λ_{ex} = 375 nm) of Me$_2$gua on titrating 0.2 % HCl.

As a preliminary experiment, we measured steady state emission spectra of the ester form of the gua, (Me$_2$gua) dissolved in DMF. Two peaks were visible, a less intense peak at 468 nm and a more intense peak at 575 nm (Figure 3.20). To this DMF solution, we added small amounts of 0.2 % HCl and measured emission spectra. Changes in the spectra were immediately observable. Addition of acid caused protonation of the guanidine moiety (Scheme 3.3) that affected the relative intensities of 468 nm and 575 nm peaks, causing the emission to shift to the blue region. This means that the 468 nm peak is indicative of protonation of the guanidine. These spectra are evidence that protonation affects the emission properties of the gua ligand, and the fast component could arise from an ESPT process between DMF and the gua ligand.

3.2.9 TCSPC of 9, 10, 11, and 12

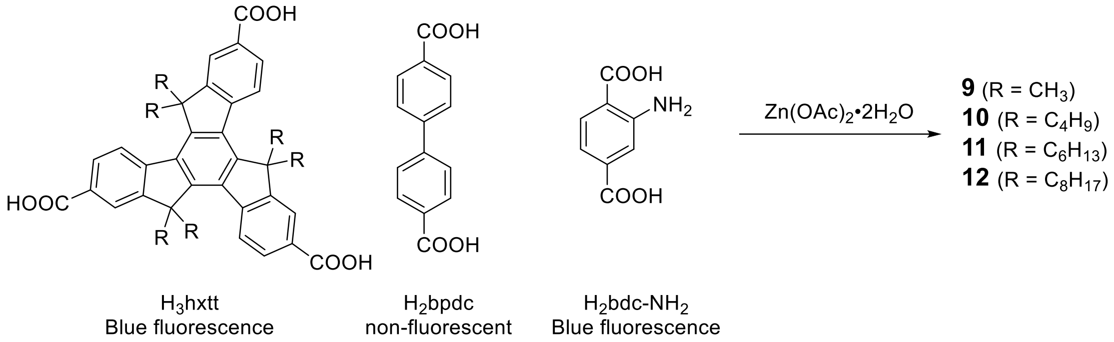

Scheme 3.4: Synthesis of MUF-77 frameworks **9**, **10**, **11**, and **12**.

9, **10**, **11**, and **12** with the linker set hxtt/bpdc/bdc-NH_2 (Scheme 3.4) have bright blue fluorescence (λ_{em} = 430 nm) due to the highly emissive nature of the bdc-NH_2 ligand. The truxene ligands also emit at the same region and hence they may also contribute to the fluorescence. However, their quantum yields are not the same so the H_3hxtt contribution would be weak. We note that H_3hxtt ligands have quantum yields ranging between 0.2 – 0.4, however, bdc-NH_2 has a higher yield of 0.62.

TCSPC of these MOFs showed a monoexponential decays of ~ 10 – 11 ns (Table 3.9 and Figure 3.21). This is very close to the lifetime of H_2bdc-NH_2 in solution (12.5 ns), but slightly lower. Incorporation of a ligand into a MOF should increase its lifetime since the ligand's motion is restricted due to coordination with the metal ion.[91,217] However, we have to note that the tritopic ligands also emit at this wavelength and hence decay profile may be a mix of both tritopic and bdc-NH_2 ligand emissions.

Table 3.9: Fluorescence lifetimes of **9**, **10**, **11**, and **12** detected at 435 nm.

MOF Code	Ligand combination	Fluorescence Lifetime (ns)
9	hmtt/bpdc/bdc-NH_2	10.0 ± 0.2
10	hbtt/bpdc/bdc-NH_2	10.1 ± 0.3
11	hhtt/bpdc/bdc-NH_2	10.9 ± 0.3
12	hott/bpdc/bdc-NH_2	10.2 ± 0.2

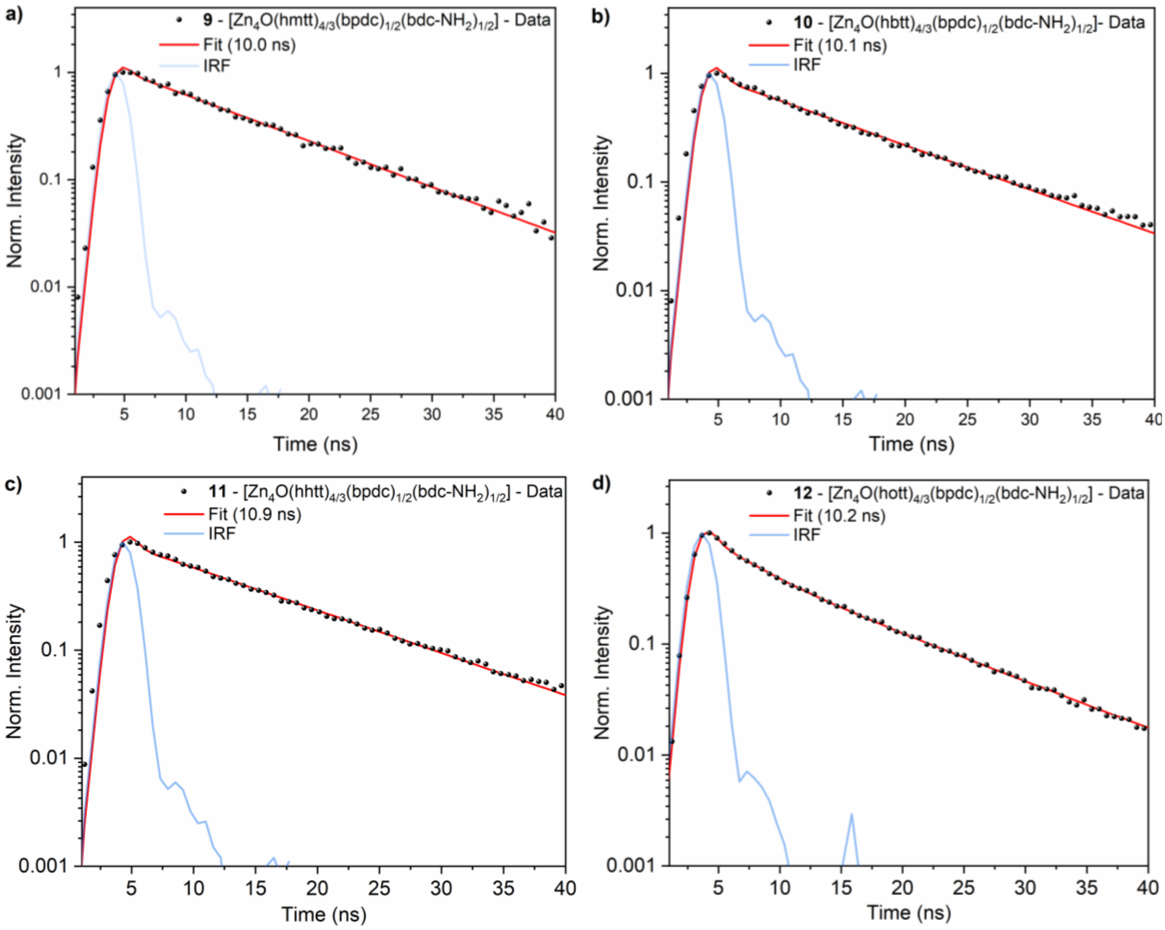

Figure 3.21: TCSPC of MUF-77 frameworks detected at 435 nm (λ_{ex} = 375 nm) **a) 9 b) 10 c) 11** and **d) 12.**

Calculations of FRET rates and efficiencies shown in Table 3.4 have shown that hxtt-bdc-NH$_2$ energy transfer is more efficient than the energy transfer in the opposite direction. The former is predicted to be occur with an efficiency of 75 – 85 % (Table 3.4, entries s - v) and and within tens of picoseconds. The latter has a lower efficiency between 15-50 % and occurs in tens of nanoseconds, which is much slower. Based on these calculations, the patterns in the TCSPC decays are combination of direct emission from bdc-NH$_2$ along with picosecond energy transfer from hmtt to bdc-NH$_2$. TGPLS of these frameworks are yet to be collected and with this technique, the FRET between hxtt to bdc-NH$_2$ must be easily visible in the averaged kinetic profile between the wavelength range of 400 – 450 nm.

3.2.10 TCSPC of MUF-77 13, 14, 15, and 16

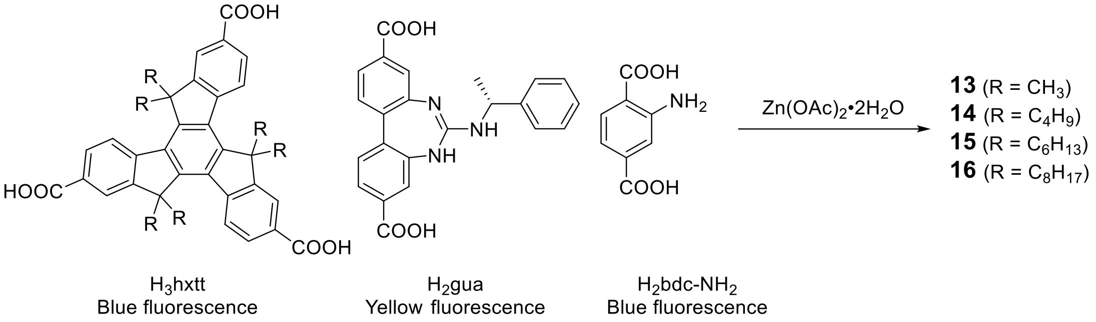

Scheme 3.5: Synthesis of MUF-77 frameworks **13**, **14**, **15**, and **16**.

The final set of MOFs and arguably the most interesting were the white-light emitters **13**, **14**, **15**, and **16**. These MUF-77 frameworks have two blue-emissive organic ligands, hxtt and bdc-NH_2 and one yellow emissive ligand, gua (Scheme 3.2). We had used their combined luminescence to produce white light, which was detailed in Chapter 2. Variations in their emission spectra are observed when the alkyl groups on the tritopic linker were changed (Figure 3.17). Each of these MOFs gave two distinct emission peaks, one in the blue region and another in the yellow region (Figure 2.4).

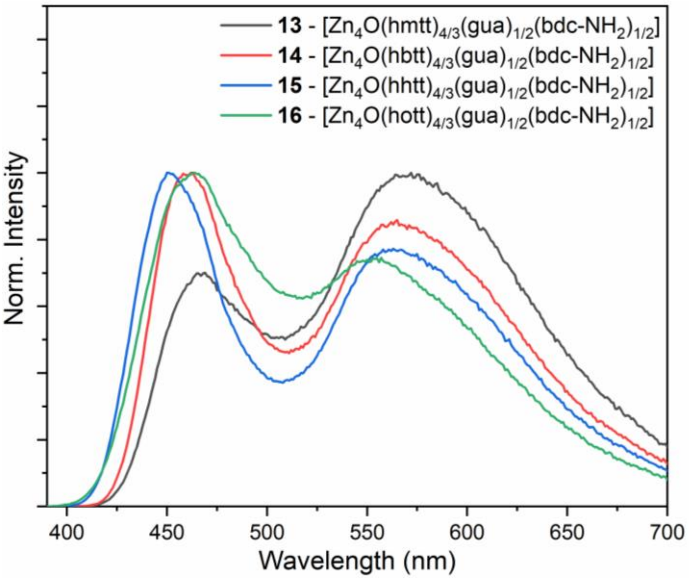

Figure 3.22: Emission spectra of DMF suspensions of white-light emissive MUF-77 (λ_{ex} = 375 nm) containing both blue emissive and yellow emissive ligands.

We collected TCSPC of these MOFs (λ_{ex} = 375 nm) for both these emission peaks. In the blue region, **13** and **14** have weak emission and hence TCSPC at 468 nm for both these MOFs were not measurable. However, for **15** and **16** we obtained biexponential decays, from which lifetimes were obtained. In **15** and **16**, the blue peak intensities are greater than the yellow peak intensity (Table 3.10). This caused the lifetimes to be higher at 463 nm (4.85 ns for **15**) and 450 nm (1.54 ns for **16**) than at 565 nm.

TCSPC decays detected at the yellow peak maximum (~560 nm) could be resolved into two components. One ranging between 0.5 – 1.3 ps and another longer emission ranging between 2.2 – 12 ns (Table 3.10). The only ligand which emits at this wavelength is gua, and all emission must arise from this ligand. If we compare the decays of **13**, **14**, **15**, and **16** to that of another set of MUF-77 frameworks containing only gua and without bdc-NH$_2$ i.e. **5**, **6**, **7**, and **8**, differences are immediately noticeable. The former set (with bdc-NH$_2$) shows biexponential decays with longer lifetimes and while the latter set (with bdc) show only fast unresolvable decays.

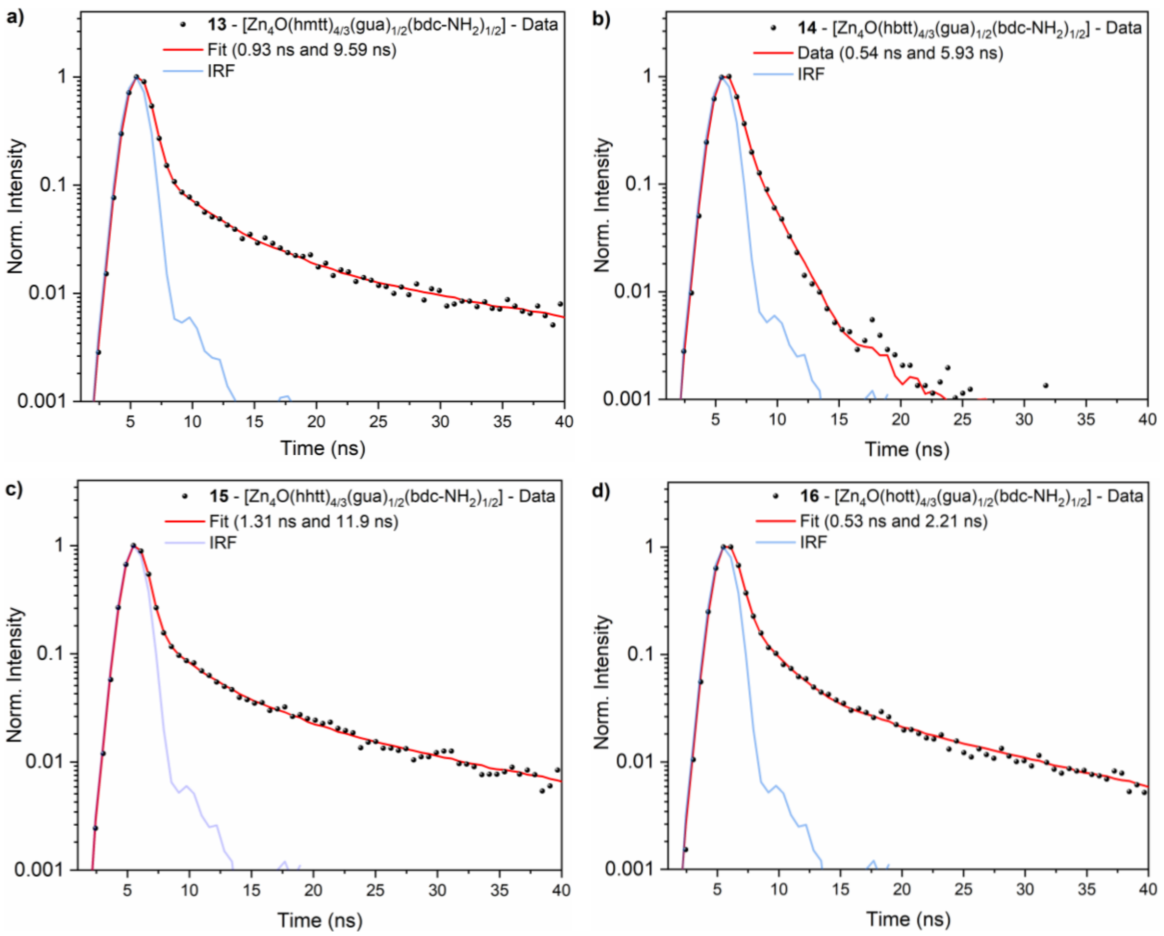

Figure 3.23: TCSPC decay profiles for the white-light emissive MOFs **a) 13** detected at 565 nm **b)** 14 detected at 565 nm **c) 15** and detected at 560 nm **d) 16** detected at detected at 556 nm.

Table 3.10: Fluorescence lifetimes of **13**, **14**, **15**, and **16** calculated from TCSPC decays detected at the blue and yellow emission peaks.

MOF Code (λ_{det})	**Ligand combination**	**Fluorescence Lifetime (ns)**		
		τ_1	τ_2	τ_{avg}
13 (565 nm)	hmtt/gua/bdc-NH_2	0.93 (91.2%)	9.59 (8.8%)	1.69
14 (565 nm)	hbtt/gua/bdc-NH_2	0.54 (96.9%)	5.93 (3.1%)	0.70
15 (460 nm)	hhtt/gua/bdc-NH_2	2.11 (78.1%)	14.6 (21.9%)	4.85
15 (560 nm)	hhtt/gua/bdc-NH_2	1.31 (83.0%)	11.9 (17%)	3.11
16 (460 nm)	hott/gua/bdc-NH_2	0.90 (92.6%)	9.59 (7.4%)	1.54
16 (556 nm)	hott/gua/bdc-NH_2	0.53 (82.9%)	2.21 (7.3%)	0.82

These differences can be attributed to energy transfer from bdc-NH_2 to the gua ligand. From Table 3.4, we have seen that such a FRET process is possible. The architecture of MUF-77 places these ligands in two different mutual orientations (Figure 3.9). Along the x-axis, these ligands are placed collinear. For this arrangement, the FRET time is calculated to be 370 ps, with an extremely high efficiency of > 97% (Table 3.4, entry n). The second orientation places these ligands perpendicular. The κ^2 for perpendicular transition dipoles is zero, resulting in zero FRET efficiency. However, the actual ligand orientation and transition dipole orientation are unlikely to be exactly alike.[122] This means, that the positioning of the functional groups on these ligands cause deviations from the perpendicular arrangement enabling some FRET ($\kappa^2 \neq 0$). Additionally, the ligands are disordered adding to these deviations. This perpendicular ligand arrangement is predicted to have a FRET lifetime of 7.1 ns, with a lower efficiency of 64% (Table 3.4, entry m). These predictions agree with the data from TCSPC of these MOFs, and hence these two components can be assigned to the energy transfer between bdc-NH_2 to gua.

From the previous sections of this chapter, we know that the other ligands also transfer energy to each other. These transfers occur in tens of picoseconds, which cannot be detected by TCSPC technique. So, are these processes visible in the TGPLS spectra of these MOFs? Do the decays between 375-450 nm and 550-650 nm shown any differences?

We collected TGPLS spectra of **13**, **14**, **15**, and **16** with an excitation wavelength of 343 nm. These spectra gave broad emission between 400 – 650 nm (Figure 3.24). The emission begins within 1 picosecond and lasts upto a delay time of 100 ps, after which weaker emission is observed. Between 400 – 450 nm, this intense emission lasts even shorter, up to tens of picoseconds. The tritopic ligands and bdc-NH_2 are emissive in this region. H_2bdc-NH_2 has a long lifetime of 12.56 ns and so do MUF-77 frameworks **9**, **10**, **11**, and **12** which have lifetimes greater than 10 ns. However, the TGPLS shows that the tritopic ligands and bdc-NH_2 transfer energy to the gua making the emission last for a shorter duration.

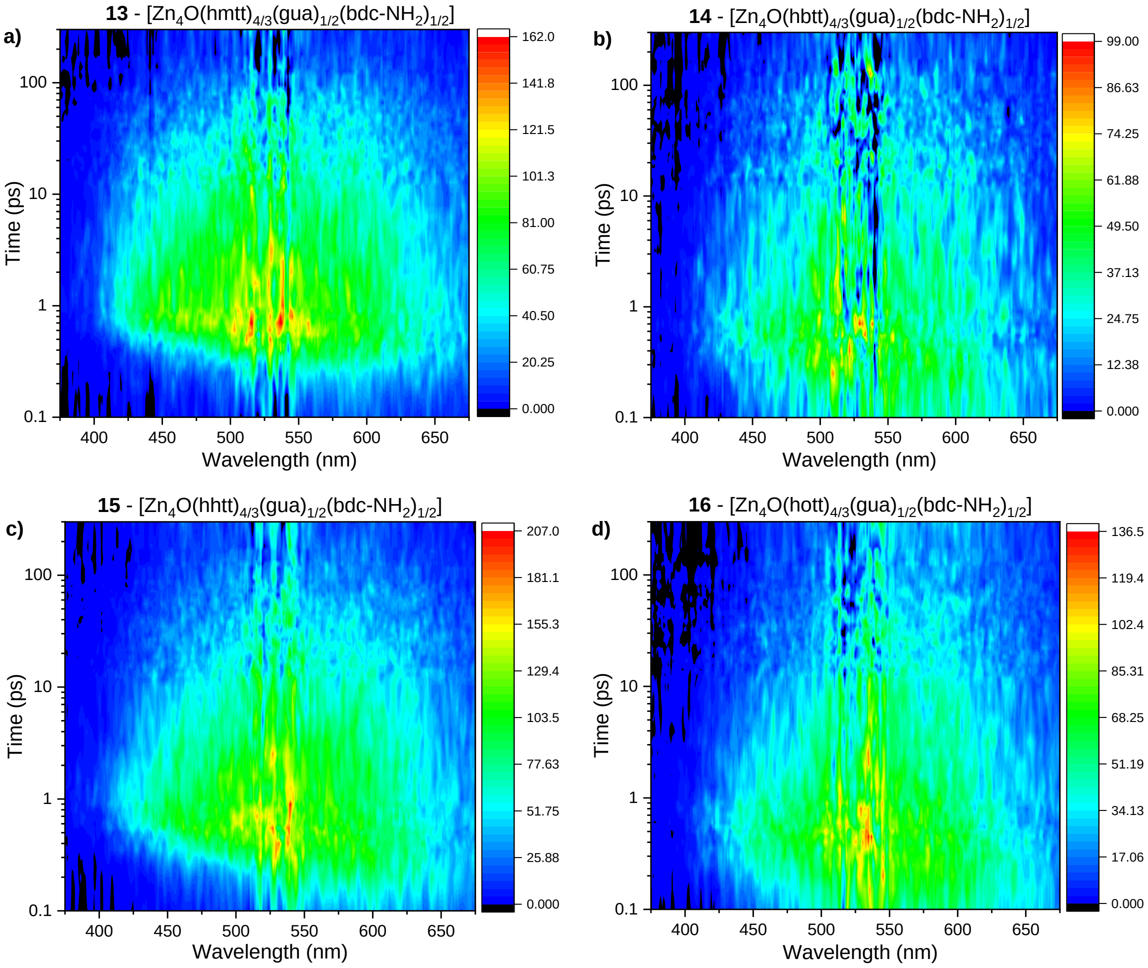

Figure 3.24: TGPLS plots of white-light emitting MUF-77 frameworks excited at 343 nm. **a) 13 b) 14 c) 15** and **d) 16**.

The timescales obtained from the kinetics of **13**, **14**, **15**, and **16** reflect what is observed in the contour plots. Between 400 – 450 nm, the emission decays very quickly with < 20 % of a non-decaying component, which is responsible for the signal seen in the TCSPC of these MOFs. For every MOF in this series, the kinetic profile between 550 – 650 nm show longer decay profiles than those seen between 400 – 450 nm. This is indicative of the gua ligand being an acceptor in these frameworks.

The kinetics averaged between 400 -450 nm could be decomposed into three components (Figure 3.25). At these wavelengths, only the hmtt and bdc-NH_2 are emissive, and all emission must arise from these ligands. The shortest component (< 2 ps) which formed the major portion of the decay could be tentatively assigned to the EEA process between the hxtt ligands. Once again power dependence studies have to be performed to confirm or disprove this process.

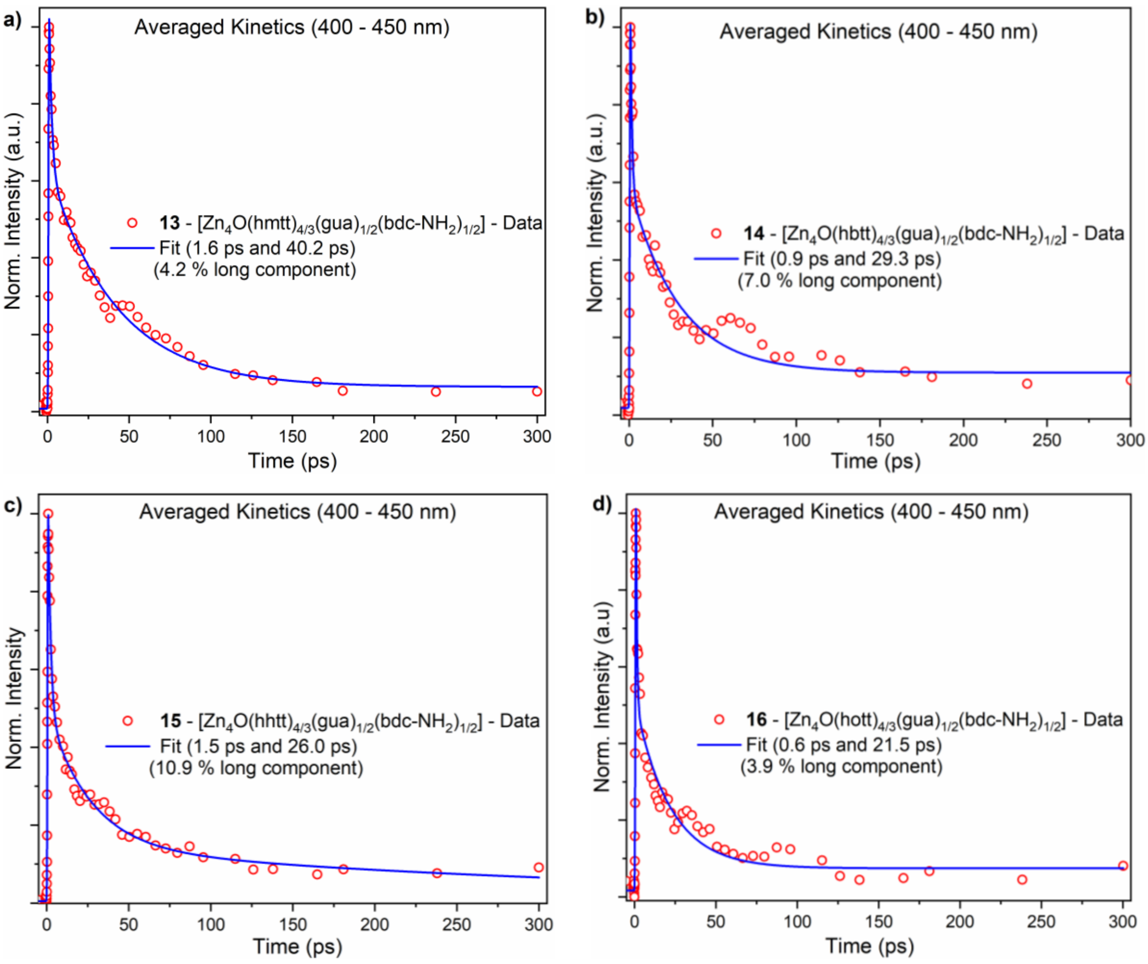

Figure 3.25: Averaged three-component fits for the TGPLS decays averaged between 400 – 450 nm for single crystals of MUF-77 with the ligand combination hxtt/gua/bdc-NH_2. **a) 13 b) 14 c) 15** and **d) 16**.

The second component (~ 20 - 40 ps), is possibly from FRET between hxtt and gua. In **15**, which has the ligand combination hmtt/gua/bdc-NH_2, this component is lasts 40.2 ps which is close to what is for hmtt-gua FRET component seen in **5** (32.9 ps). There is also another event that has a comparable lifetime and that is the FRET between hxtt and bdc-NH_2 (Table 3.4, Entries s -v). Hence, at this point, the assignment of the 20 – 40 ps component for the short wavelength decays of **13**, **14**, **15**, and **16** is pinpointed to combined FRET events where the hxtt ligands are donors with the gua and bdc-NH_2 acting as acceptors.

Finally, the third, non-decaying emission may arise from multiple processes including FRET between bdc-NH_2 to gua, which is calculated to occur in nanoseconds, out of the detection range of TGPLS. Another possibility is the direct emission from the highly emissive bdc-NH_2 ligand, which has a lifetime of 12.5 ns, which is non-decaying in TGPLS. These are the emissions detected in TCSPC at 460 nm, which last for nanoseconds (Table 3.10).

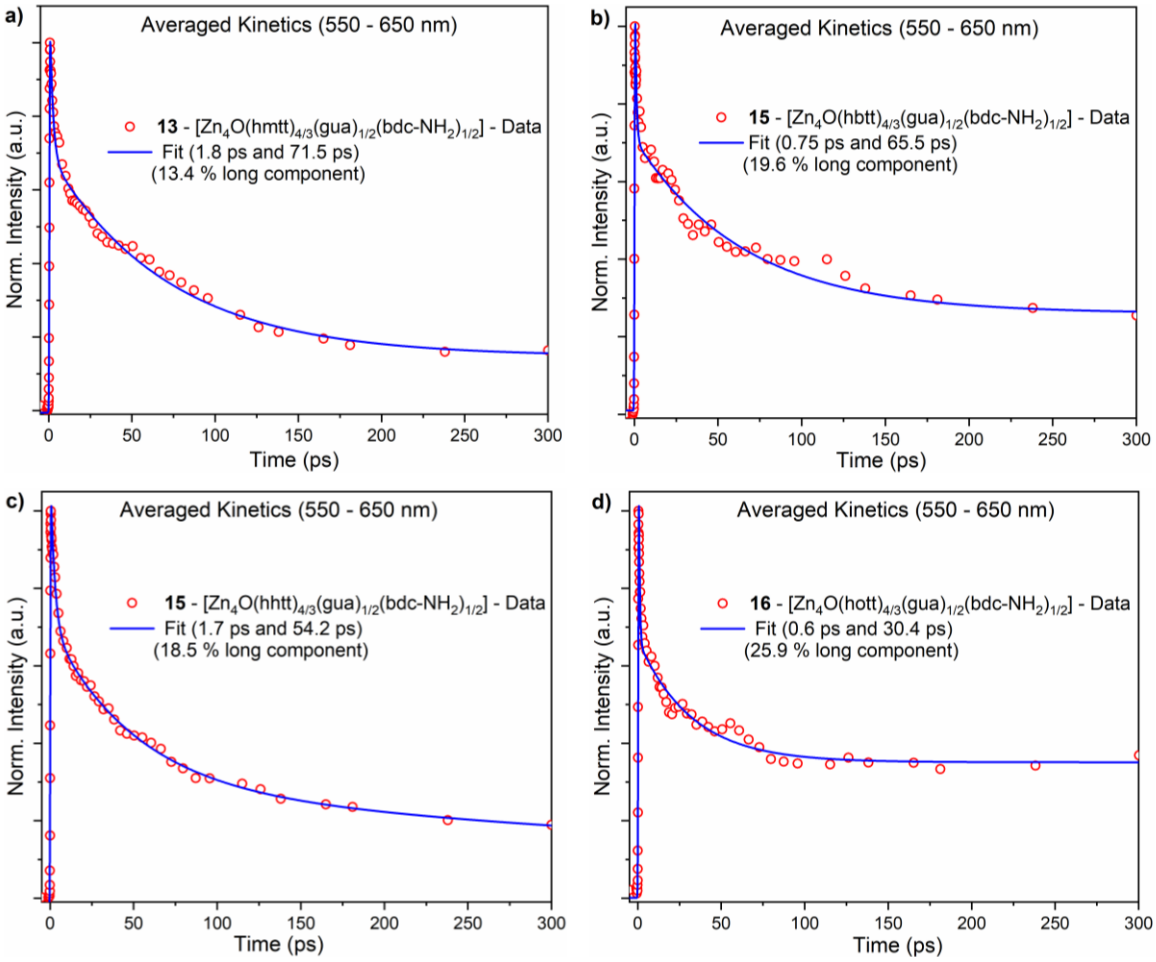

Figure 3.26: Averaged three-component fits for the TGPLS decays averaged between 550 – 650 nm for single crystals of MUF-77 with the ligand combination hxtt/gua/bdc-NH_2. **a) 13 b) 14 c) 15** and **d) 16.**

The 550 – 650 nm region accounts for emission from the gua ligand, which acts as the acceptor in **13**, **14**, **15**, and **16**. Once again, decays could be resolved into three components (Figure 3.26 and Table 3.11). The emissions last much longer than the 400 – 450 nm region. The shortest among these components (0.6 - 2.5 ps) is once again from the suspected ESPT process between the gua ligand and DMF.

The second component (33 – 70 ps) is from FRET between hxtt and gua. This is once again confirmed by matching the lifetime in **13** with that seen in **5**. These components are very close (71.5 ps in **13** and 70.7 ps in **5**), which means they represent the same process. As we proceed from **13** to **16**, the lifetime of this component decreases. This means that hxtt-gua FRET decreases on increasing the alkyl chain length, indicating lower FRET efficiency.

Table 3.11: Lifetimes obtained from the TGPLS of **13**, **14**, **15**, and **16**

MOF Code	Ligand Combination	Wavelength range	τ_1 ps	τ_2 ps	% long component
13	hmtt/gua/bdc-NH_2	400 - 450 nm	1.6 ± 0.1 (47.9 %)	40.2 ± 2.9 (47.9 %)	4.2
14	hbtt/gua/bdc-NH_2	400 - 450 nm	0.9 ± 0.1 (56.5 %)	29.3 ± 2.7 (36.5 %)	7.0
15	hhtt/gua/bdc-NH_2	400 - 450 nm	1.5 ± 0.2 (59.6 %)	26.0 ± 5.7 (29.4 %)	10.9
16	hott/gua/bdc-NH_2	400 - 450 nm	0.6 (fixed) (68.4 %)	21.5 ± 2.7 (37.6 %)	3.9
13	hmtt/gua/bdc-NH_2	550 - 650 nm	1.8 ± 0.3 (38.3 %)	71.5 ± 8.3 (48.3 %)	13.4
14	hbtt/gua/bdc-NH_2	550 - 650 nm	0.75 (fixed) (44.6 %)	65.5 ± 9.6 (23.9 %)	19.6
15	hhtt/gua/bdc-NH_2	550 - 650 nm	1.7 ± 0.4 (35.4 %)	54.2 ± 10.6 (45.1 %)	18.5
16	hott/gua/bdc-NH_2	550 - 650 nm	0.6 (fixed) (50.3 %)	30.4 ± 5.7 (23.7 %)	26.0

This analysis has implications on the steady state emission spectrum wherein the relative intensities of the yellow emission peaks (550 – 700 nm) decrease when compared to the blue emission peak (400 – 470 nm). This is an effect of the FRET between hxtt and gua becoming less efficient as the alkyl chain length increases. This leaves a part of the hxtt emission unquenched, causing the blue peak intensity to increase and the yellow peak intensity to decrease, resulting in the pattern seen in the emission spectrum. Additionally, differences in the bdc-NH_2 to gua FRET efficiency further contribute to variation seen in the emission spectrum. This FRET process is visible as a non-decaying component in the TGPLS and has been characterised by TCSPC.

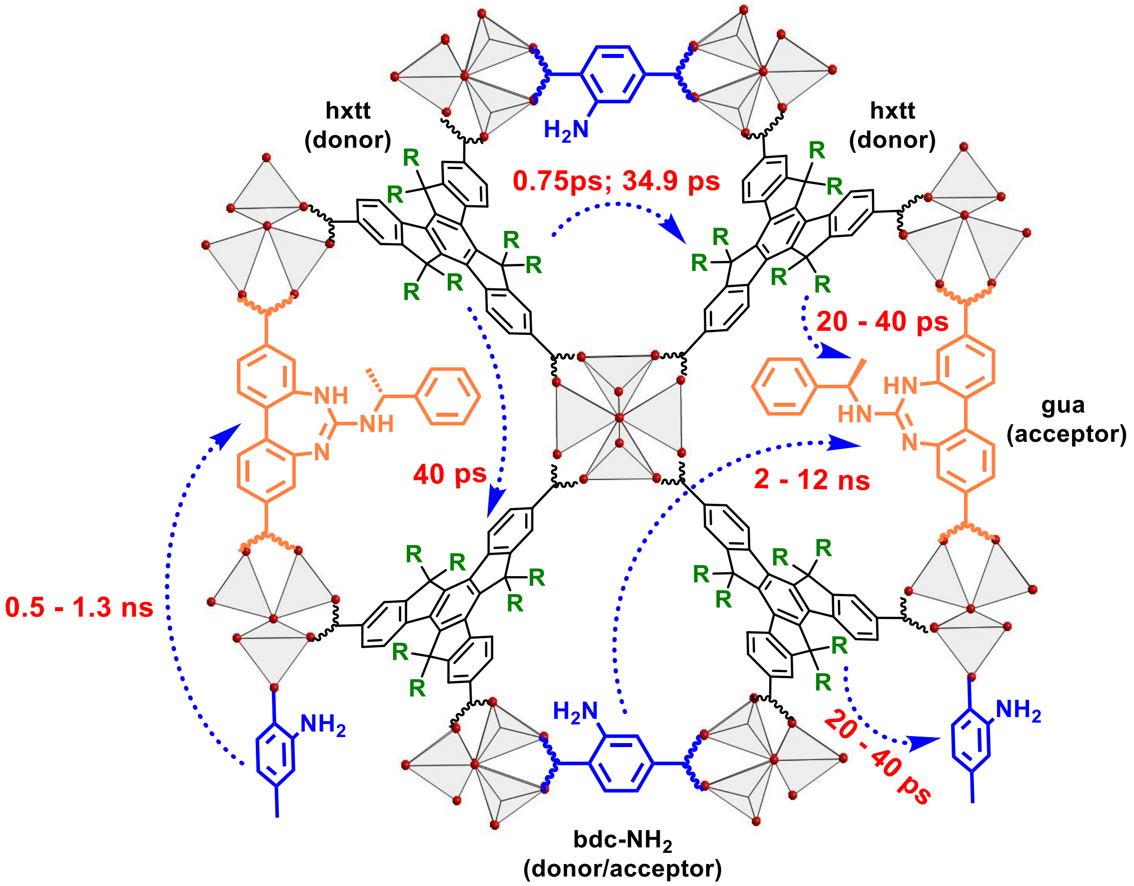

Figure 3.27: Schematic of various FRET pathways and times in MUF-77.

3.3 Conclusions

From these steady-state and ultrafast time-resolved fluorescence measurements, it is evident that MUF-77 is a system with rich photophysical properties. This is brought about by the multicomponent nature of the MOF, which arranges ligands in proximity, enabling multiple excited-state processes, at multiple timescales to be favoured (Figure 3.27). This modulates the luminescence, which is one of many properties that can be controlled in these exciting materials.

This chapter dealt with ultrafast time-resolved fluorescence spectroscopy to understand variations in the emission spectra of MUF-77 systems. The unique structure and ligand arrangements of MUF-77 makes it possible for multiple inter-ligand energy transfer processes to occur. Absorption and emission spectra combined with SCXRD of the ligands was used to calculated FRET efficiencies within these MOFs. From the TCSPC of the parent

MOFs (**1**, **2**, **3**, and **4**) we have calculated the exciton migration to be up to 127 nm which is longer but comparable to reported values. With TGPLS, we were able to resolve many ultrafast energy transfer pathways in the white-light emitting MUF-77 frameworks. A simple change in the alkyl group on one of the linkers can drastically affect the ultrafast decay kinetics as the FRET parameters change ultimately determining their efficiency.

In some cases, the point dipole approximation breaks down causing a mismatch in the calculated versus experimental lifetimes. Additionally, absorption and emission spectra of the ligands in solution have been used as proxy for determining spectral overlap and FRET efficiency i.e. we have assumed that the ligands retain their absorptivity and quantum yield when incorporated into MUF-77. To compensate for these gaps, future work involves performing more accurate calculations to obtain atomic transition densities to better understand exciton migration. These calculations in tandem with experiments such as measuring solid state absorption spectra, dye loading, and power density dependence on the TGPLS kinetics would ultimately enable us to simulate the emission spectra of MUF-77.

Some decay components in the yellow region were in the sub-picosecond range which we suspect may arise from ESPT. TGPLS of gua containing MUF-77 frameworks in protic solvents such as methanol or isopropanol may further promote ESPT, thus affecting the kinetics. Using deuterated protic solvents will also help as the kinetic isotope effect would be evident. During ESPT, new N-H bonds are formed. Femtosecond Stimulated Raman Spectroscopy (FSRS) is another technique that may aid in further studying this process.[243-245] All these experiments are the subject of future work.

3.4 Experimental Section

3.4.1. General Information

Fluorescence spectra were collected with a Horiba Scientific Fluoromax-4 Spectrofluorimeter. Spectra were corrected for detector and grating efficiencies using FluorEssence, the in-house software of the fluorimeter. Absorption spectra were collected using a Shimadzu UV-Vis spectrophotometer.

Time-correlated single photon counting (TCSPC) was carried out using an Edinburgh Photonics FLS-980 spectrophotometer with a picosecond pulsed 375 nm LED LASER EPLED. Data were fit using DecayFit using the equation below:

$$I_t = \left(\sum_{i=1}^{N} \alpha_i e^{-t/\tau_i}\right) + c$$

Here I_t is the intensity at time, α_i is the amplitude of the ith decay component with a lifetime, $\boldsymbol{\tau}_i$ and c is the instrument response function.

Transient grating photoluminescence spectra (TGPLS) were collected using a method described by Chen et al. with a wavelength of 343 nm.[214] The spot size of the excitation beam was 20x20 μm. The pulse energy was 30 nJ at 1300 μW power or 14 nJ at 600 μW power with 44 kHz repetition rate, giving an instrument resolution of 340 fs. Single crystals of MUF-77 were taken in glass sample cells and placed under vacuum. Solutions of ligands in DMF were taken in flat glass cuvettes and stirred to avoid photodamage.

Ultrafast emission spectra were collected between 220 nm to 775 nm, however a longpass filter was used cut off light below 380 nm, that the excitation beam could not be detected. A non-decaying signal was seen between 500 – 540 nm arising from the second harmonic of 1064 nm fundamental laser line. Kinetics were averaged and fit using first-, second- or third-order exponential fit using OriginPro 2018. The fitting equation used is shown below:

$$y = y_0 + \sum_{1}^{n} \left[\left(\frac{A_n}{2} \right) * e^{\left(\frac{x - t_o}{\tau_n} \right)} * e^{\left(\frac{w^2}{4(\tau_n{}^2)} \right)} * \left(\frac{1 + \operatorname{erf}\left(x - t_o - \left(\frac{w^2}{2\tau_n} \right)\right)}{w} \right) \right]$$

Where, y_0 is the y-offset, t_0 is time-zero, w is the width of the irf which is 340 fs, τ_n is the lifetime of the nth component with amplitude, A_n and erf is the error function.

3.4.2. TCSPC of ligands in solution

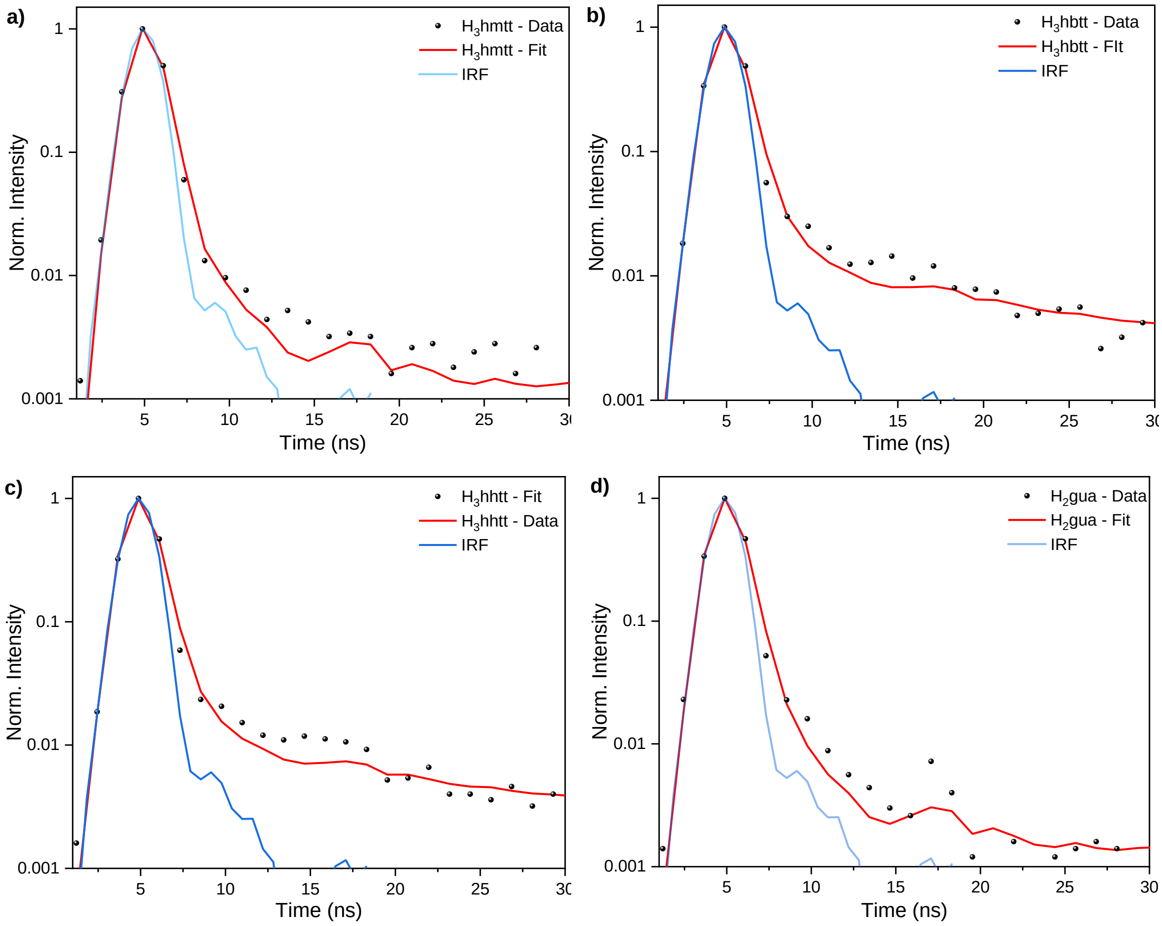

Figure 3.28: TCSPC of solution of ligands in DMF showing fast, unresolvable decays.

Chapter 4 – Stable Radicals in Multicomponent Metal-Organic Frameworks

4.1 Introduction

Exploring new strategies to tune the functional properties of MOFs has been central to research in this area. This has been possible due to the many isoreticular families of MOFs.[3,10] MC-MOFs are a unique class of MOFs with geometrically dissimilar components at distinct positions within the crystal, giving rise to interesting properties.[246] Tunability in their topologies, pore sizes and environments have made MC-MOFs amenable for a variety of applications.[247] These include the classic, yet highly demanding areas of gas storage and separation,[248] catalysis,[175,176,249] luminescence,[86,91,200,202] and chemical sensing.[87,104,177] The exploration of MC-MOFs for more niche applications such as non-linear optics,[250,251] drug delivery,[252,253] and charge conduction[254] is also gaining momentum.

MOFs showing stimuli responsive behaviour i.e. MOFs whose properties change on exposure to physical or chemical stimuli are of special interest.[132,255] These stimuli can include the adsorption or expulsion of guests,[256,257] and fluctuations in temperature,[258] pressure,[259] or light exposure. Photochromism is a phenomenon in which the colour of a material changes on exposure to light i.e. the light acts as the stimulus promoting colour change.[260] This is caused by a reversible interconversion between two forms of a chromophoric component of the MOF, which absorbs two distinct regions of the visible spectrum.[128] This reaction is typically an isomerisation, ring-closure or ring-opening, or radical formation. Although, photochromism is seen in MOFs, it is restricted to a few families of ligands namely spiropyrans, azobenzenes, and diarylethenes.[255,261-263]

Radical generation is a common process underlying photochromism.[264] Radicals in MOFs are primarily based on three types, A, B, and C (Figure 4.1).[265] In Type A, the ligand is a radical with the radical component coordinated directly to a metal or appended to the backbone.[266] Here, the radical bearing ligand is bonded to the metal cluster on only one site. An example for type A is a pyridyl-nitronyl-nitroxide ligand in a cyanide-bridged, Cd^{2+}-based coordination polymer (Figure 4.2).[267]

Type B: where the ligand linking the metal clusters behaves as a radical. The radical bearing ligand is bonded to the metal clusters by multiple bonds. In Type B, the removal of the radical bearing ligand causes a structural change in the MOF.[268] Figure 4.2 shows an example of a Type B radical, tetrathiafulvalene (TTF) ligand which was used to build a Cu^{2+}-based MOF. TTF can exhibit three oxidation states which is useful for exploring charge conduction in MOFs.[269,270]

Type C is where a radical species is encapsulated in the MOF pores as a guest.[265] A variety of commonly known organic ligands have been incorporated as guests in MOFs such as di-*tert*-butyl nitroxide radical (DTBN) trapped in HKUST-1 shown in Figure 4.2.[271] Other examples for type C include nitroxides,[272] thiazyls,[273] nitriles,[17] tetrathiafulvalenes,[274] and napthalenediimides.[129] In most cases for types A, B, and C, the metal ions for the MOF are transition metal or lanthanide ions which contain unpaired electrons. Ligands bound to d^{10} metal-based MOFs featuring radicals are quite uncommon with only a few reports in the literature.[130,275,276]

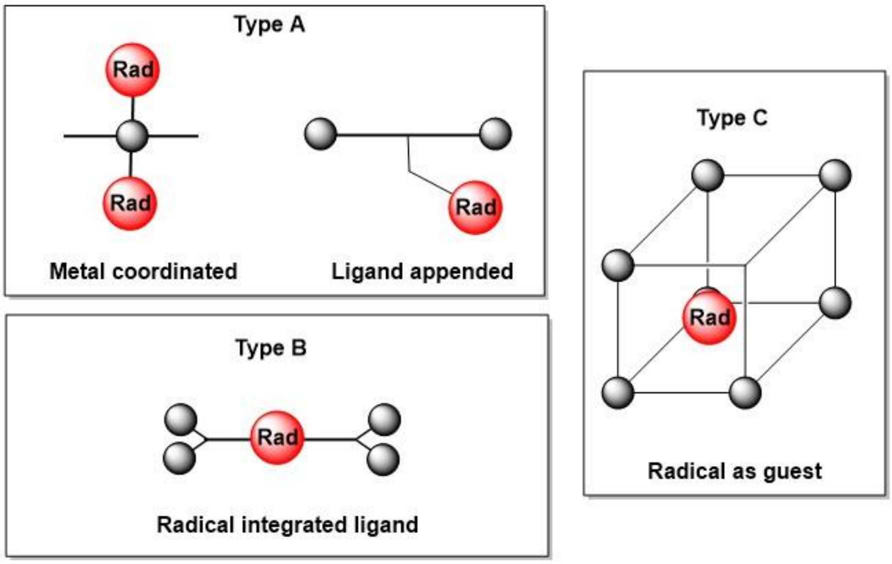

Figure 4.1: Types of radicals incorporated in MOFs. Black spheres represent metal clusters and red spheres represent radicals.

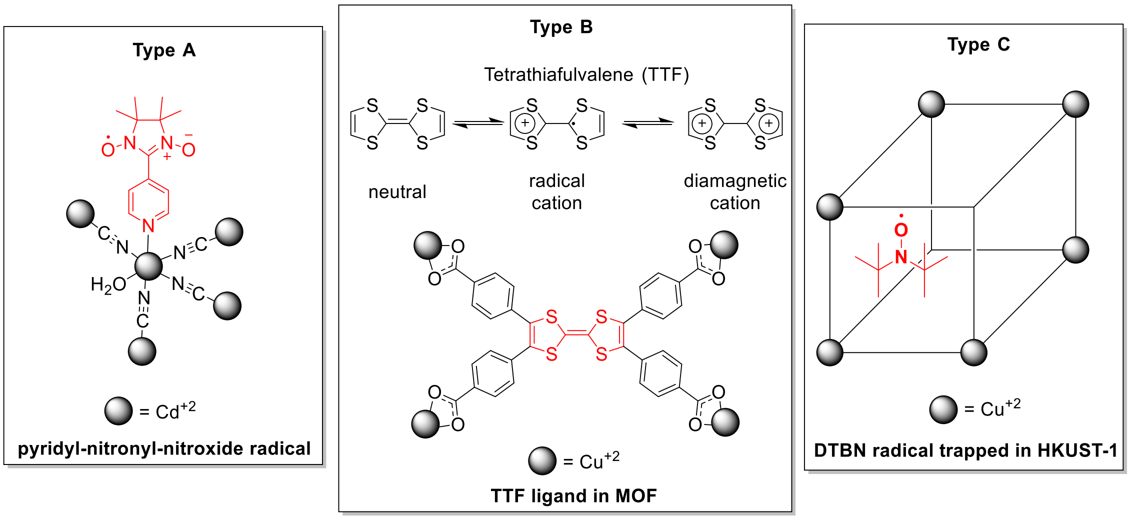

Figure 4.2: Examples for type A, type B, and type C radicals found in the literature. Radical centres are shown in red; metal clusters are shown as black spheres.

This chapter reports a series of zinc-based MUF-7 and MUF-77 frameworks containing a new family of quinoxaline-based ligands. Upon exposure to sunlight or long wavelength UV light (~390 - 410 nm), the crystals undergo colour change from yellow to red. The MOFs stay in their red form if kept in the dark. However, the red colour reverses to yellow on exposure to visible light. We have used a variety of techniques to investigate the reason for this colour change, ultimately pinpointing it to photogenerated pyrazine radicals. To the best of our knowledge, this is the first example of a pyrazine radical in a MOF. We categorise this radical to be of type B since the radical is inherent to the bdc-based ligand of MUF-77.

4.2 Results and Discussion

4.2.1 Initial Discovery and Ligand Synthesis

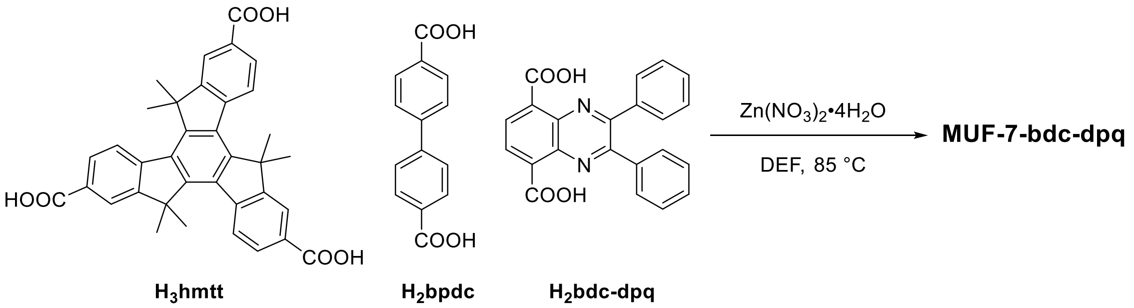

Scheme 4.1: Solvothermal synthesis of photochromic MUF-7 systems.

The story of discovering photochromic MUF-7 begins with quinoxaline-based ligand, H$_2$**bdc-dpq** (Scheme 4.1) which was initially synthesised by Dr. Tian-You Zhou to serve as a modulator for catalysis. Yellow, cubic crystals were obtained using the solvothermal conditions. PXRD proved that these crystals were similar to MUF-7 and hence we called these MOFs, MUF-7-**bdc-dpq**. ^{1}H NMR spectroscopy showed the formula to be $Zn_4O(hmtt)_{4/3}(bpdc)_{1/2}$(**bdc-dpq**)$_{1/2}$, characteristic of MUF-7 systems (ESI; Figure S23).

On exposing these crystals to a 5 mW 405 nm laser pointer for about 5-10 seconds, the colour of the crystals changed from yellow to red i.e. the crystals were photochromic (Figure 4.1a and b). This colour reverted to yellow in a few minutes and the colour change could be repeated many times. PXRD patterns recorded before and after light exposure were identical (Figure 4.3c), meaning that the photochromism was intrinsic to the MUF-7 system. The photochromism was seen only when the **H$_2$dpq-bdc** ligand was incorporated into MUF-7. No colour change was seen upon irradiation of the pure ligand or the ester, both in solid form and in their DMF solutions.

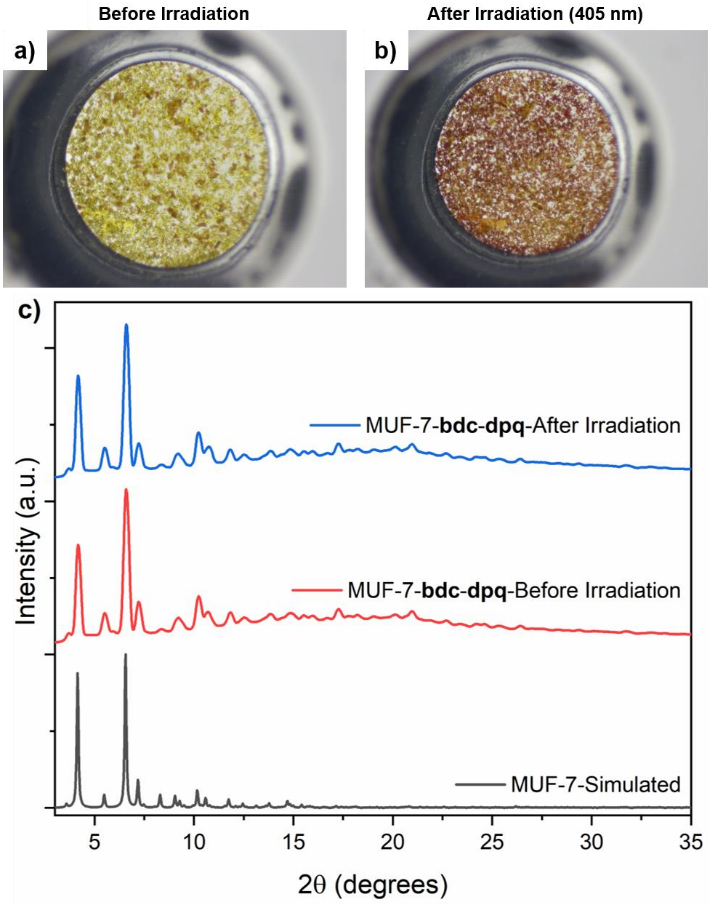

Figure 4.3 : a) Photos of MUF-7-**bdc-dpq** before and **b)** after exposure to a 405 nm laser pointer. **c)** Representative PXRD patterns of the photochromic crystals before and after light exposure compared to a PXRD pattern simulated from the reported SCXRD structure.[76]

I decided to investigate this behaviour further. To do this, I synthesised a series of bdc ligands with quinoxaline moieties using an improved Schiff base coupling procedure (Figure 4.4a and Experimental section 4.4.1).[277] A four-step synthesis starting from commercially available 4,7-dibromo-2,1,3-thiadiazole (**Br_2-BzThAz**) afforded the diester, (**Et_2-bdc-$(NH_2)_2$**). This molecule contains two amino groups making it amenable for a variety of Schiff base coupling reactions. The existing method (dioxane/TFA, 110 °C, 48 hours) for this Schiff base coupling gave less than 35% yield and silica gel column chromatography was necessary to separate the quinoxaline ester.[278] However, based on relevant literature, I developed a newer improved synthesis which gave more than 70% yield and avoided the use of columns.[277] On hydrolysis, the obtained esters gave their corresponding carboxylic acids, which could then be used to make multicomponent MOFs.

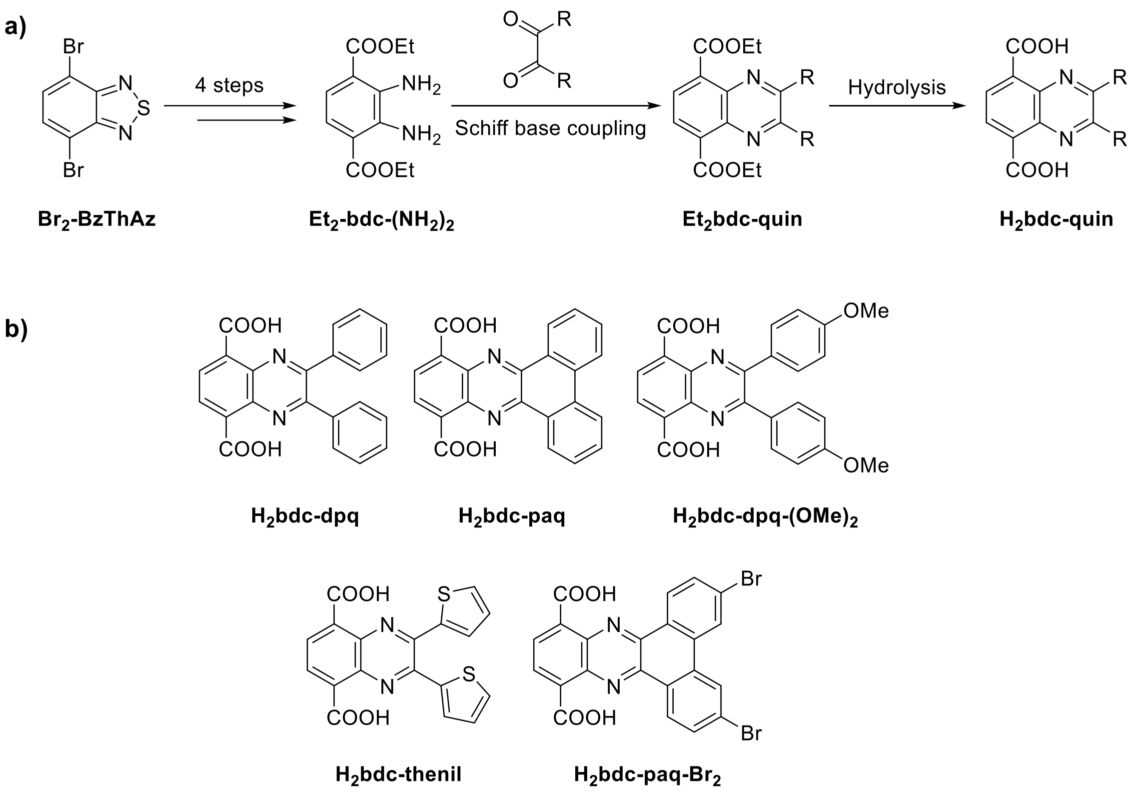

Figure 4.4: **a)** The general scheme for the synthesis of photochromic ligands. **b)** The structure of ligands for photochromic MUF-7 and MUF-77 systems.

To explain the photochromism of MUF-7-**bdc-dpq**, we developed an interim hypothesis based on some existing literature on dimethyldihydropyrenes (Figure 4.5a).[279,280] These are conjugated, organic moieties which interconvert between coloured and colourless forms. In such systems, an intermediate diradical state is formed upon light exposure which causes bond cleavage and converts the molecule to its colourless form. Applying a similar mechanism to MUF-7-**bdc-dpq**, we proposed that the proximity of the two phenyl rings leads to transient diradicals on light exposure. This in turn produces a C-C bond, resulting in a resonance structure with a red colour (Figure 4.5).

However, this theory was soon laid to rest. A molecule like H_2**bdc-paq** (Figure 4.4b), when incorporated into MUF-77, should not show photochromism if this hypothesis were correct. H_2**bdc-paq** already has a C-C bond between the phenyl rings and would be unable to generate a diradical. We synthesised this molecule and grew MOF crystals, by replacing H_2**bdc-dpq** with H_2**bdc-paq** during solvothermal synthesis (Scheme 4.1 and Experimental section 4.4.1). However, this time MUF-77 crystals were obtained, which we named MUF-77-**bdc-paq**. These crystals were also photochromic, turning from yellow to red when exposed to 405 nm light. This meant that the diradical theory shown in Figure 4.5b was not the reason behind the photochromism.

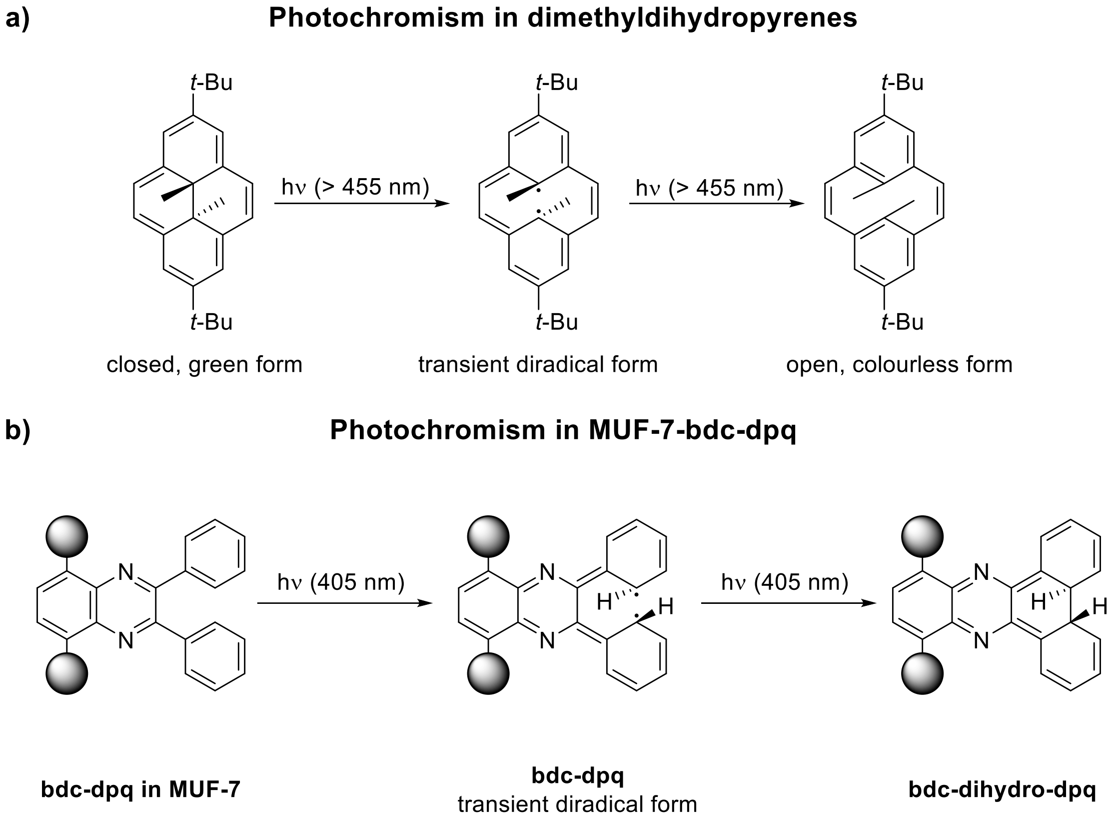

Figure 4.5: a) Mechanism for photochromism in dimethyldihydropyrenes. **b)** Mechanism proposed initially for photochromism in MUF-7-**bdc-dpq**.

The common feature between H$_2$**bdc-paq** and H$_2$**bdc-dpq** was the presence of a quinoxaline system. Could other ligands such as H$_2$**bdc-dpq-(OMe)$_2$**, H$_2$**bdc-thenil** and H$_2$**paq-Br$_2$** (Figure 4.4b), all of which constitute of quinoxaline moieties also be photochromic? We synthesised all these ligands using the method outlined in Scheme 4.2. H$_2$**bdc-dpq-(OMe)$_2$** gave MUF-7 crystals which we named MUF-7-**bdc-dpq-(OMe)$_2$**. The other two ligands gave MUF-77 which we named MUF-77-**bdc-thenil** and MUF-77-**bdc-paq-Br$_2$**. The MOFs were characterised by PXRD and ^{1}H NMR spectroscopy on acid-digested MOFs which showed them to belong to the MUF-7 or MUF-77 type (ESI; Figure S23-S27).

All these MOFs obtained were also photochromic, once again converting from yellow to red upon irradiation (Figure 4.6, Figure 4.7a and b). PXRD patterns were also unchanged before and after photochromism, indicating the retention of the MOF structure. All MOFs retained their red colour when kept in the dark. However, exposure to visible light caused them to revert to their original yellow colour within a few minutes (Figure 4.7c and d). To reiterate, none of the esters or carboxylic acids were photochromic by themselves. Photochromism was exclusively seen when the moieties were incorporated into the MOFs.

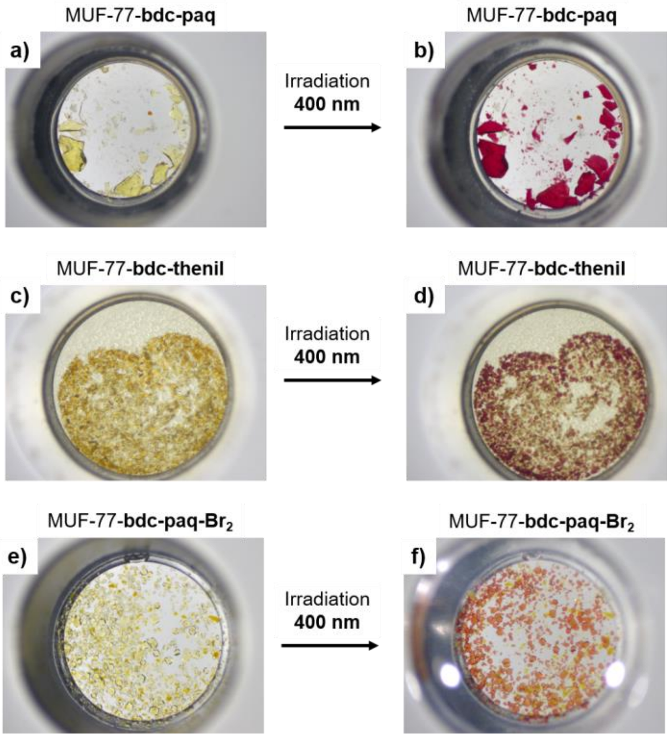

Figure 4.6: Photos of photochromic, single crystals of MUF-77 suspended in DMF, before and after irradiation with 400 nm light.

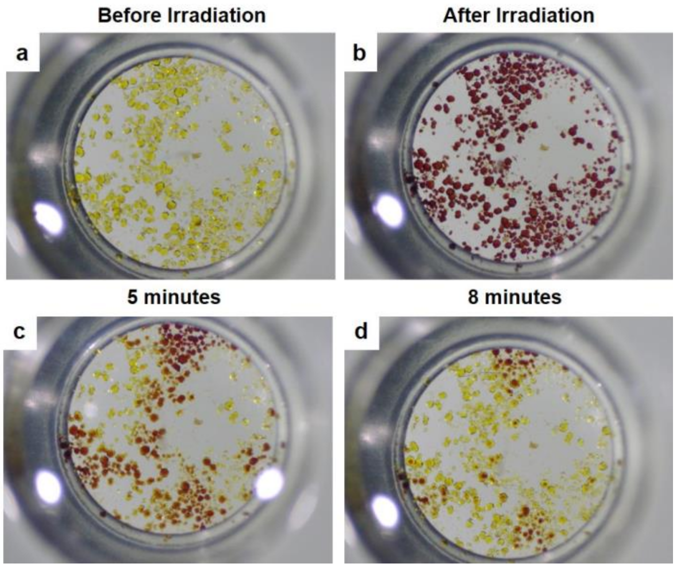

Figure 4.7: Photos of MUF-7-**bdc-dpq-(OMe)**$_2$ **a)** before irradiation with 400 nm light, **b)** after irradiation **c)** 5 minutes and **d)** and 8 minutes after exposure to ambient light showing the crystals returning to their original yellow colour.

This photochromic behaviour was puzzling, and we sought to understand it. One important observation was that there was no photochromism for dried crystals, meaning that the solvent had a role to play. We considered whether the quinoxaline ligands act as excited-state bases (photobases) on light absorption, abstracting protons from the solvent to become protonated at their nitrogen sites.[281-283] However, photochromism was seen when the crystals were suspended in polar, aprotic solvents such as DMF, DBF, and DMSO (Figure 4.7).

This aprotic solvent sensitive behaviour disproved the idea of protonation. Photochromism was not observed in less polar solvents such as dichloromethane, chloroform, and hexane. Radical formation was more likely as polar solvents are known to stabilise radicals and the crystals are photochromic only in such solvents.[284,285] Our next goal was to prove whether or not radical formation was the mechanism for MUF-77 photochromism.

4.2.2 Preliminary experiments to indicate radical formation

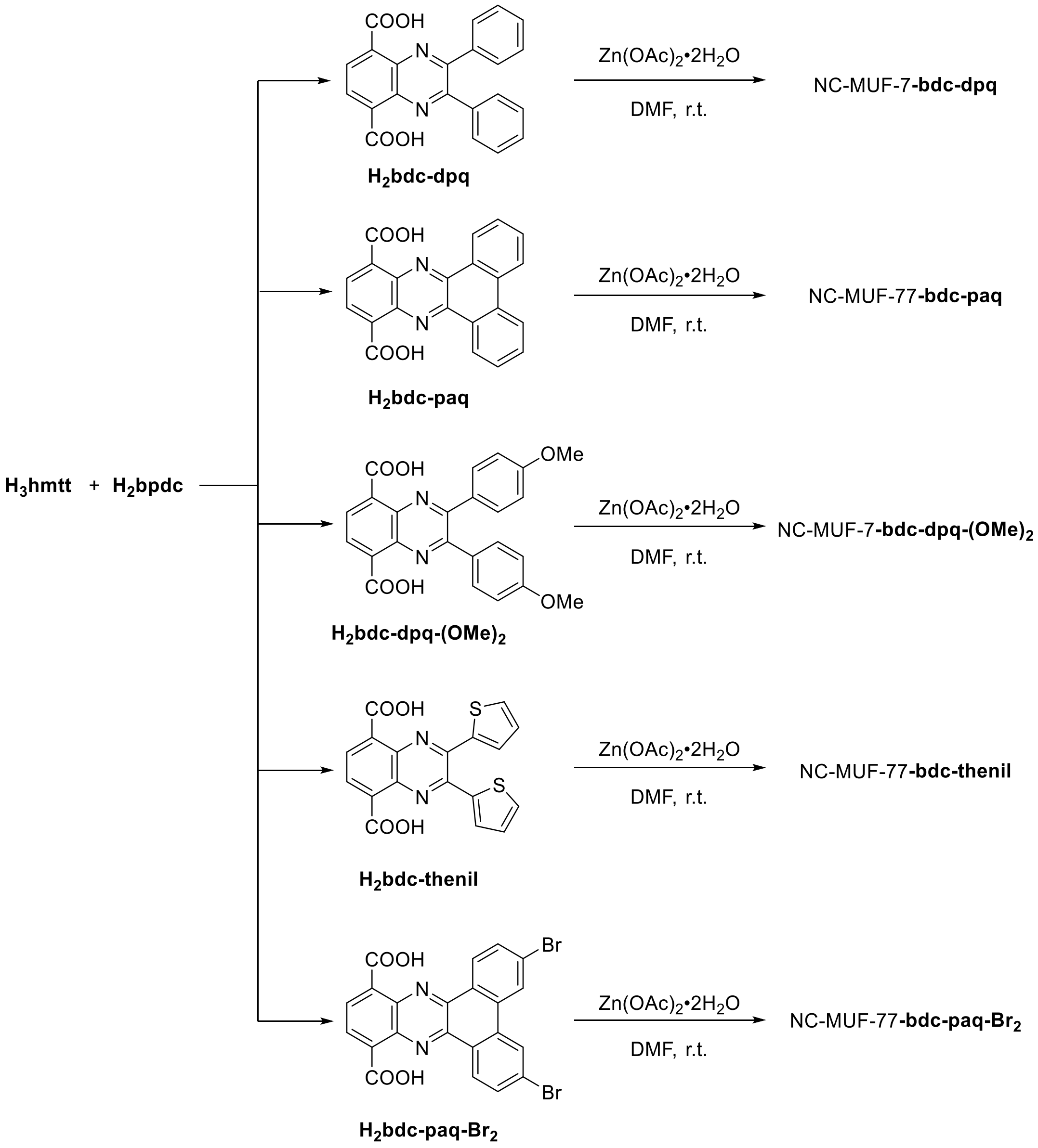

Scheme 4.2: Preparation of photochromic NC-MUF-7 and NC-MUF-77 crystals.

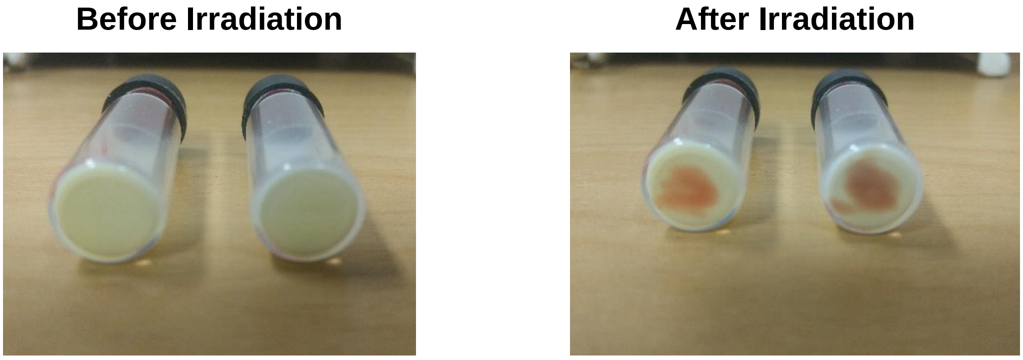

Figure 4.8: Photos of NC-MUF-7-**bdc-dpq** and MUF-77-**bdc-paq** samples before (left) and after exposure (right) to a 405 nm laser pointer. The red colour is seen only at the areas where the sample was irradiated.

The best technique to prove radical formation is EPR spectroscopy. Before we sent the samples to Germany for EPR measurements, we did a few preliminary experiments. To make the crystals more amenable for spectroscopic measurements, we synthesised nanocrystalline versions of the photochromic MOFs (NC-MUF-7 and NC-MUF-77) by using zinc acetate instead of zinc nitrate for the synthesis and keeping it at room temperature (Scheme 4.3 and experimental section 4.4.4). PXRD and NMR confirmed MUF-7 and MUF-77 formation (Experimental section, Figure 4.22 and ESI Figure S28-S32). The obtained nanocrystals also showed similar yellow to red photochromism when suspended in DMF (Figure 4.8) and no photochromism when the dried crystals were exposed to near-UV light. Once again, the PXRD patterns were unchanged upon light exposure (Experimental section, Figure 4.23).

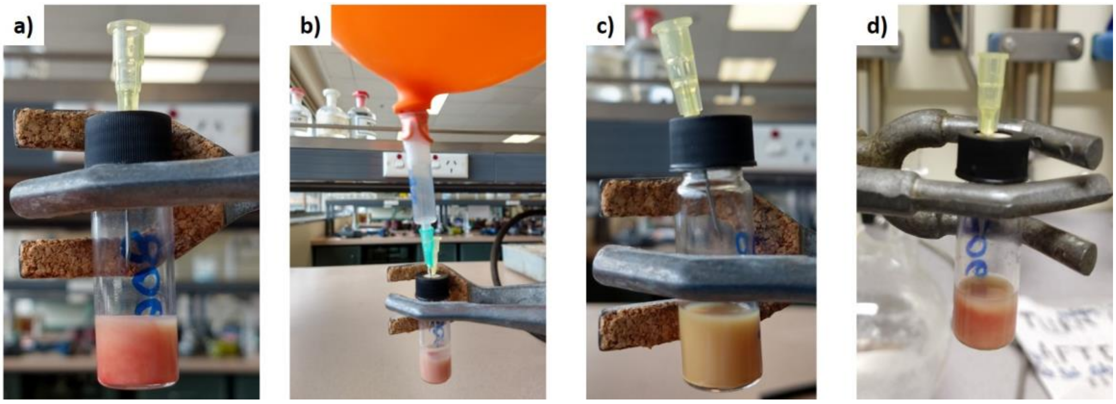

Figure 4.9: Images of NC-MUF-77-**bdc-paq** exposed to oxygen and argon. **a)** Light exposed sample before O_2 bubbling. **b)** During O_2 bubbling. **c)** After 3 minutes of O_2 bubbling showing the non-radical form. **d)** After argon bubbling and 405 nm light exposure with the red, radical form still visible.

One preliminary experiment we performed to prove our radical theory was oxygen bubbling. The two unpaired electrons in the oxygen molecule makes it paramagnetic.[286] If the photochromism was radical based, the unpaired electrons of oxygen would quench the photogenerated radical.[287] Indeed, this was the observation when pure oxygen was bubbled into a DMF suspension of irradiated and red coloured NC-MUF-77-**bdc-paq** (Figure 4.9a and b). The colour returned to its initial state of yellow in less than 3 minutes of O_2 bubbling (Figure 4.9c). The oxygen quenches the photogenerated radical using either of two proposed mechanisms (Figure 4.10a). If a radical cation-anion pair is formed, oxygen gas donates and receives an electron from the radical bearing species. The net charge loss is zero, as all charged species are restored to their neutral form. In the second mechanism, the cationic and anionic centres are located within the same molecule, and once again oxygen gas reacts in the same fashion, quenching the radical (Figure 4.10b).[288]

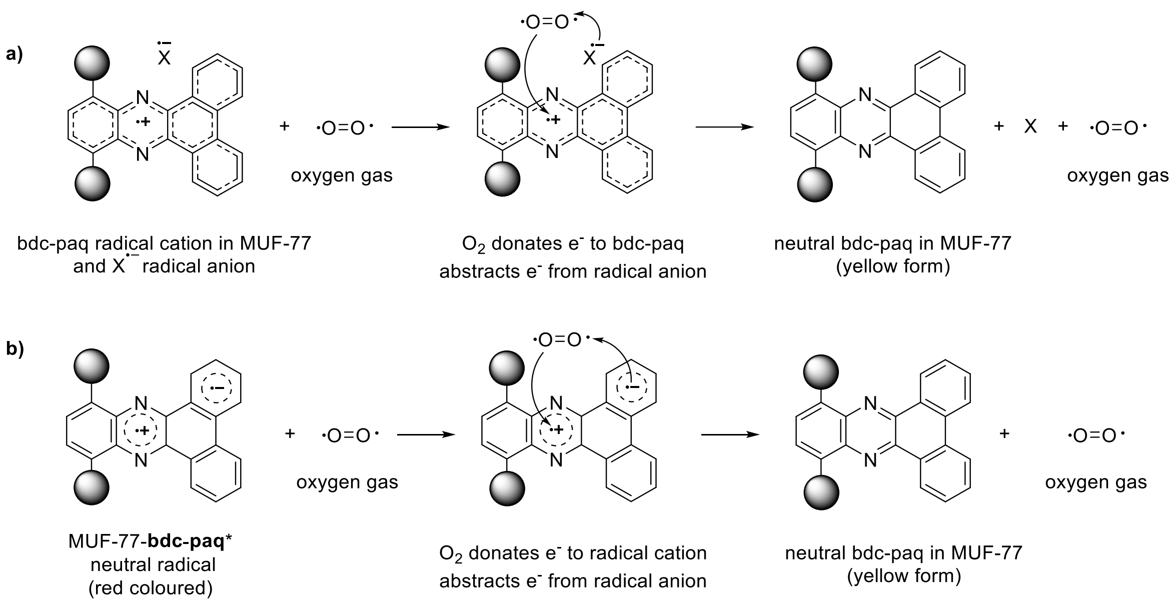

Figure 4.10: Proposed mechanisms for quenching of photogenerated radicals by oxygen gas with MUF-77-**paq-bdc** as an example. **a)** where the anionic and cationic centres are located in different moieties, here X is an unknown species. **b)** mechanism where the anionic and cationic centres are located within the **bdc-paq** ligand. Note that the black spheres represent metal clusters.

Further irradiation of the oxygen bubbled samples did not result in photochromism. This can be due to the dissolved oxygen quenching any new photogenerated radicals. However, when we deoxygenated the samples by bubbling argon for five minutes, the photochromic property reappeared (Figure 4.6d). This provided additional evidence that a radical based mechanism was at play.

We also synthesised nanocrystals of an IRMOF-1 analogue using zinc acetate and H_2**bdc-paq** (called NC-IRMOF-1-**bdc-paq**). Its formula is $[Zn_4O($**bdc-paq**$)_3]$. The similarity in its PXRD pattern confirmed that it is isostructural to IRMOF-1 (Experimental

Section, Figure 4.16). A series of conditions was tried for growing single crystals of IRMOF-1-**bdc-paq**, which were not successful. However, NC-IRMOF-1-**bdc-paq** was not photochromic, even after prolonged irradiation. What would be the reason? MUF-7 and MUF-77 are multicomponent MOFs and have hmtt and bpdc ligands which may be involved in the photochromism. These ligands are not found in IRMOF-1-**bdc-paq**. This experiment showed that the photochromism was unique to MUF-7 and MUF-77 systems.

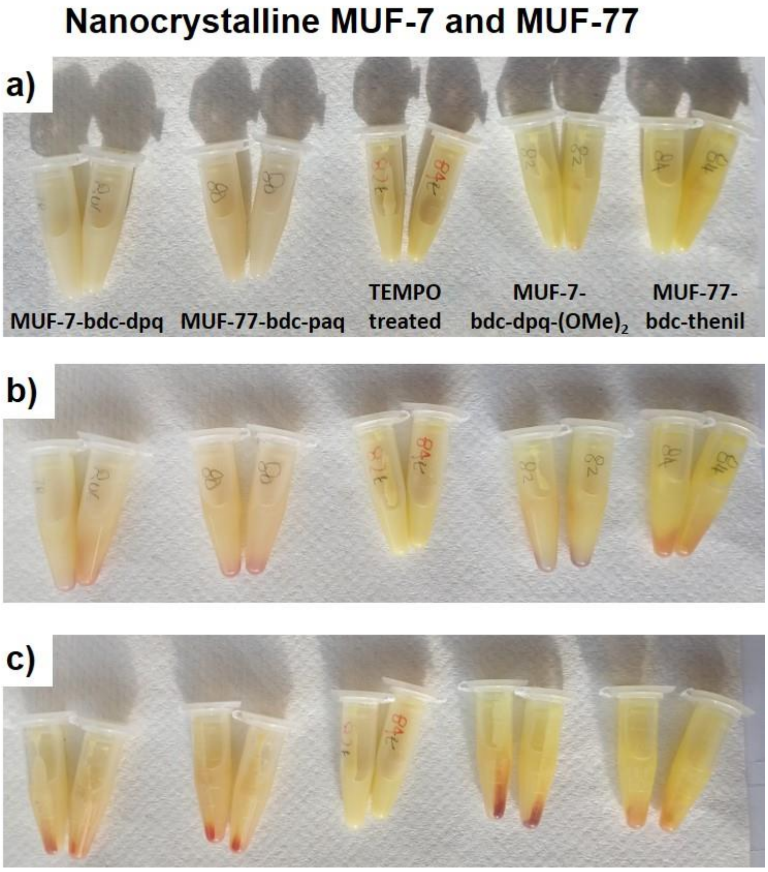

Figure 4.11: Samples of nanocrystalline photochromic MOFs exposed to sunlight. **a)** Before sunlight exposure, **b)** 5 minutes under sunlight, **c)** samples with the area more exposed to sunlight, showing stronger colour change. The pair of samples in the centre (coded **82t** and **84t**) are TEMPO treated samples of NC-MUF-77-**bdc-paq** and NC-MUF-7-**bdc-dpq-(OMe)$_2$.** These samples do not show photochromism.

Next, the nanocrystalline MOFs were exposed to sunlight (Figure 4.11). Colour change was seen for all samples in about five minutes, although to different extents. NC-MUF-77-**bdc-paq** and NC-MUF-7-**bdc-dpq-(OCH$_3$)$_2$** had developed strong red colours. MUF-77-**bdc-thenil** was least photochromic, and the colour change was very faint. NC-MUF-77-**bdc-dpq** and NC-MUF-7-**bdc-dpq-(OCH$_3$)$_2$** were also taken in separate vials and treated with the commercially available radical, (2,2,6,6-Tetramethylpiperidin-1-yl)oxyl (TEMPO). This sample was not photochromic under sunlight or even on exposure to 405 nm laser. The unpaired electron of TEMPO (like oxygen) binds to the photogenerated radical, preventing photochromism.[289-291]

4.2.3 Electron Paramagnetic Resonance (EPR) spectroscopy

With these results in hand; we sent the samples to Leipzig University in Germany for EPR measurements. Frozen suspensions of NC-MUF-77 in DMF at 100 Kelvin were used. Samples were first finely dispersed in DMF by ultrasonication. This was also useful in removing dissolved oxygen which we know would prevent radical formation. The samples were then frozen to 100 K and an EPR spectrum was recorded. The samples were removed from the spectrometer, placed in the dark, warmed to room temperature before illuminating them with a 405 nm laser pointer to convert them to their red form. The illuminated samples were immediately cooled to 100 K and EPR spectra were recorded once again. Finally, samples were warmed again, exposed to visible light until the colour returned to yellow, following which a third spectrum was collected.

Two distinct EPR signals (denoted **A** and **B**) were seen in the spectra after laser light exposure, confirming the radical-based nature of the photochromism. (Figures 4.12a, b, c and Experimental section, Figures 4.27, 4.28, and 4.29). Signal **A** with g = 2.008 originated from a defect commonly found in quartz glass sample cells.[292] EPR signal **B** with g = 2.0037 was seen only for the MUF-7 and MUF-77 samples *after* irradiation. These signals are characteristic of organic radicals, mo{Zhonggao, 2014 #924}re specifically pyrazine radicals, proving that such radicals were formed upon irradiation.[288,293,294] Signal **B** was not observed before irradiation, and neither was it observed after the samples reversed to their yellow form. The irradiation of pure DMF did not give any signal, except signal **A** (Experimental section, Figure 4.30).

However, the intensities for signal **B** for all MOFs were quite weak. This can be attributed to the low weight percentage (10 - 15%) of the radical bearing ligand in MUF-7 and MUF-77. This weak intensity also prevented the use of pulsed EPR techniques such as ESEEM, ENDOR, and HYSCORE which would have further helped in studying the radical behaviour.

From the sunlight exposure experiments, we saw that MUF-7-**bdc-dpq**, MUF-77-**bdc-paq**, and MUF-7-**bdc-dpq-(OMe)$_2$** give the most noticeable colour change. This implies that the degree of radical formation in these samples is relatively high. For these MOFs, EPR spectra were collected before irradiation, and immediately after irradiation. The samples were then placed at room temperature in the dark for 4 hours, and another EPR spectrum was recorded at 100 K.

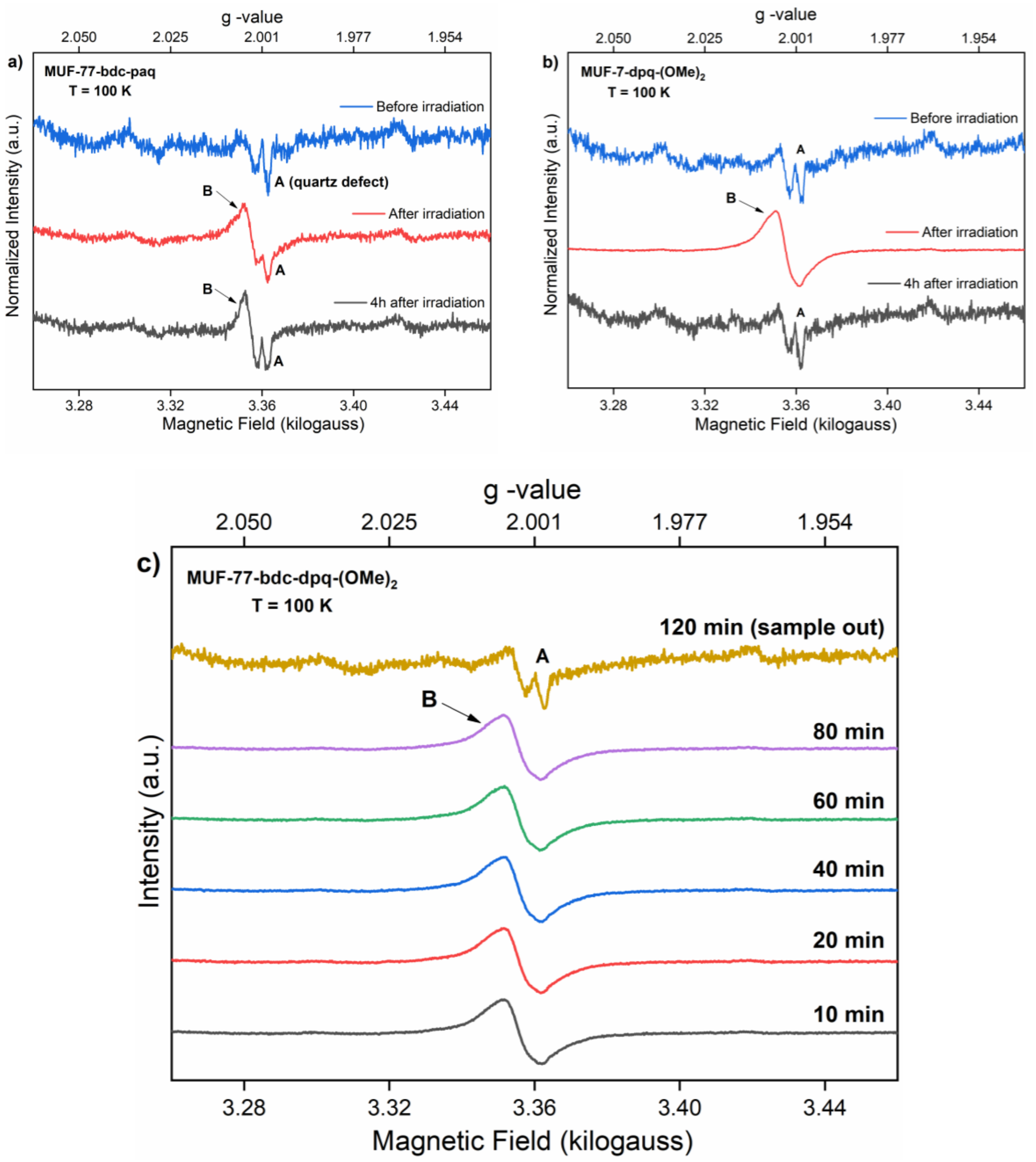

Figure 4.12: EPR spectra of DMF suspensions of **a)** NC-MUF-77-**bdc-paq** and **b)** NC-MUF-77-**bdc-dpq-(OMe)**$_2$. Signal **A** is due to a defect in the quartz sample cell.[292] Signal **B** (g = 2.0037) is from pyrazine radicals. **c)** EPR spectra of NC-MUF-7-**bdc-dpq-(OMe)**$_2$ at different time periods after irradiation showing no loss in the intensity of signal **B**, indicating that the radical is stabile under these conditions. The sample was placed outside the EPR spectrometer prior to the 120-minute spectrum, showing a loss of signal **B**.

NC-MUF-7-**bdc-dpq** showed a strong EPR signal (g = 2.0037) immediately after irradiation, but the signal decays away and was barely visible after four hours (Experimental Section, Figure 4.27). On the other hand, NC-MUF-77-**bdc-paq** retained its signal intensity well beyond 4 hours after irradiation (Figure 4.12a). This difference in stability is possibly due to the higher degree of conjugation in **bdc-paq** compared to **bdc-dpq**. This factor allows the former radical species to have a higher number of resonance stabilised structures when compared to the latter radical, thus increasing its stability.[295] Additionally, the pendant phenyl rings in **bdc-dpq** may undergo rotational motion, favouring radical recombination. Such rotation is not possible in the rigid **bdc-paq** ligand.

NC-MUF-7-**bdc-dpq-(OMe)**$_2$ gave the most intense EPR signal among all the radical generating MOFs (Figure 4.12b). However, this signal also decayed away within four hours. In another experiment, the irradiated NC-MUF-7-**bdc-dpq-(OMe)**$_2$ nanocrystals were kept inside the spectrometer at 100 K. No loss of signal intensity was observed for 80 minutes! (Figure 4.12c). The combined effects of the low temperature with the complete absence of any form of visible light exposure inside the spectrometer is a feasible explanation for this. After about 2 hours, the sample was taken out of the spectrometer and held at room temperature. When the EPR spectrum was recorded once again at 100 K, the pyrazine radical signal could not be seen.

The other two nanocrystalline MOFs i.e. NC-MUF-77-**bdc-thenil** and NC-MUF-77-**bdc-paq-Br**$_2$ also gave signal **B** with g = 2.0037, typical of organic radicals and characteristic of pyrazine radicals. In comparison to the other systems, the EPR peak for NC-MUF-77-**bdc-thenil** was quite weak suggesting a low rate of conversion to its radical form. This is further evidenced when this MOF was exposed to sunlight, where it showed the lowest degree of colour change.

4.2.4 UV-Visible Spectroscopy

We measured UV-Vis spectra of NC-MUF-7 and NC-MUF-77 with a specialised turbid absorption spectrometer. Samples were dispersed in DMF and measured before and after 3-minute exposure to 405 nm light. The spectra before and after irradiation show differences, however these differences were very faint (Figures 4.13 and 4.14). Note that a conventional UV-Vis spectrophotometer cannot be used for measuring spectra of such suspensions as the particles block the light and hence give strong absorbances across the UV-visible range.

All samples gave strong, sharply rising absorption peaks below 450 nm, indicating the absorption in the blue region of the visible spectrum. Once irradiated to their red, radical form, a weak but broad absorption band was seen starting at about 650 nm (Figures 4.7 and 4.8). This absorption peak was more pronounced for NC-MUF-77-**bdc-paq** and NC-MUF-7-**bdc-dpq-(OMe)**$_2$ (Figure 4.13b and c). NC-MUF-77-**bdc-paq-Br**$_2$ (Figure 4.13d) showed less pronounced changes, while NC-MUF-77-**bdc-thenil** only a slight red shift from 394 nm to 403 nm for the irradiated form (Experimental Section, Figure 4.25). The band seen below 650 nm was not observed.

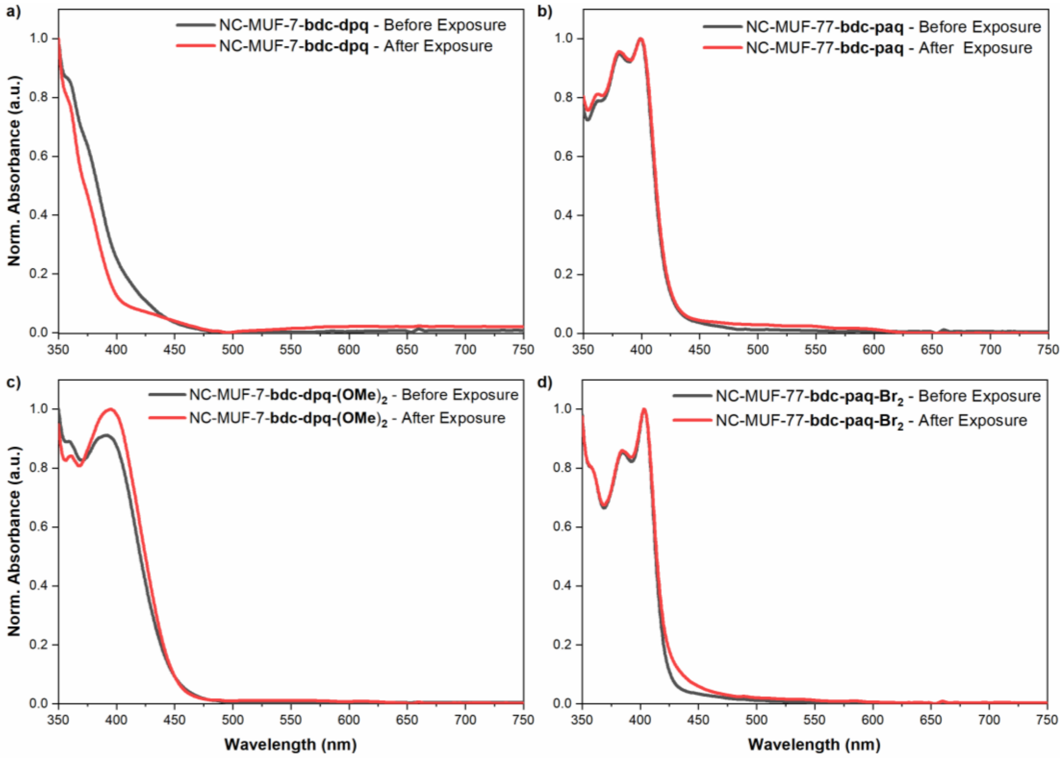

Figure 4.13: UV-Visible spectra of nanocrystalline MOFs before (black) and after light exposure (red).

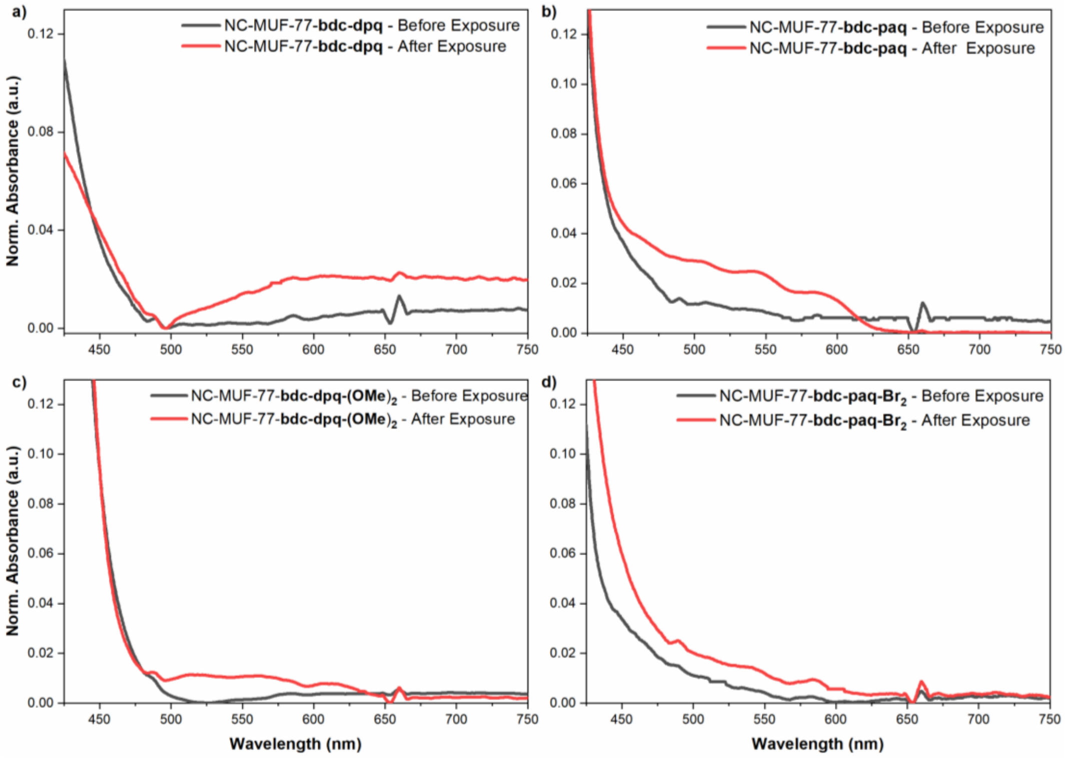

Figure 4.14: UV-Visible spectra of nanocrystalline MOFs before (black) and after light exposure (red), with 425 - 750 nm region zoomed in. The peak at ~ 660 nm is an artefact from the measurement.

The low peak intensities were possibly due to the light source of the spectrometer causing the reversal of the radical form to its non-radical form. Since the samples were finely dispersed in DMF, causing the surface area of the nanocrystals being exposed to light to increase, thus reverting the samples to their non-radical form quite quickly. Based on the EPR signal intensity and extent of colour change to sunlight exposure, NC-MUF-77-**bdc-thenil** is only weakly photochromic and would reverse to its non-radical, yellow form faster than the other MOFs. This causes its UV-Vis spectrum before and after exposure to be somewhat similar.

4.2.5 Single Crystal X-ray Diffraction (SCXRD) measurements:

Now that the existence of long-lived radicals in MUF-7 and MUF-77 was conclusively proven using EPR spectroscopy, we aimed to decipher the structure of the radical. Firstly, PXRD patterns have proven that the overall framework structure does not change upon irradiation. Secondly, the value of $g = 2.0037$ for all samples implies that radicals were generated. Some questions pop up: What is the structure of this radical? Secondly, do the other ligands i.e. hmtt or bpdc receive or donate electrons under irradiation and form radicals? What would be the best way to prove this?

The formation of radicals perturbs the electron density within a radical forming species and thus causes changes in the bond lengths when compared to its non-radical analogue.[296] The same would be true for the pyrazine radical-bearing ligands in MUF-7 and MUF-77. SCXRD is one of the best techniques to probe these bond lengths. An increase in bond length would correspond to a reduction in electron density, and vice-versa. Additionally, bond length changes in other ligands and solvent could also be measured to ascertain their participation in the radical-forming process.

Using SCXRD, we obtained crystal structures of MUF-7-**bdc-dpq**, and MUF-7-**bdc-dpq-(OMe)$_2$**. For each sample, two datasets were collected, one without irradiation and another while being illuminated with a 400 nm UV lamp (Figure 4.15). All diffraction data were collected at room temperature with the single crystal kept under a flow of nitrogen. In total, we obtained four different structures, up to a resolution of 0.91 Å with excellent reliability factors (R_1) of less than 5 % (Figure 4.16 and Experimental section, Table 4.3 and 4.4).

On analysing these structures, some broad conclusions were made: (i) bond length changes between the irradiated and non-irradiated samples were clearly seen within the **bdc-dpq** and **bdc-dpq**-(**OMe**)$_2$ ligands, (ii) the bonds constituting the hmtt ligand also showed variations in length, which meant that they were also involved in the photochromism, (iii) the bpdc ligands do not show any bond length changes and hence do not participate in radical formation. These bond lengths served as controls for these experiments.

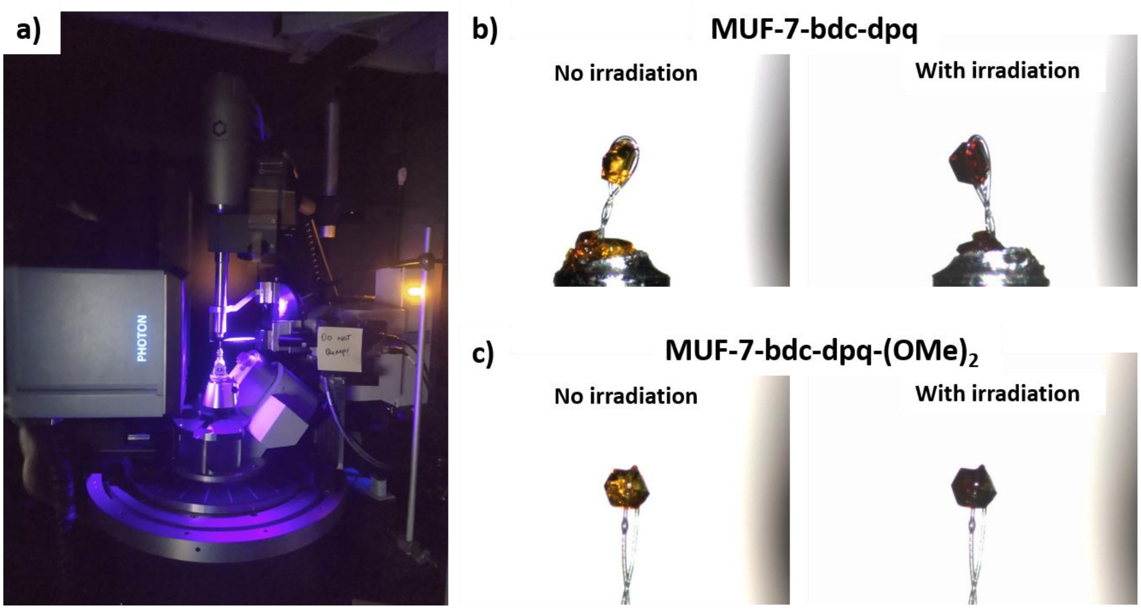

Figure 4.15: a) SCXRD of MUF-7 samples with irradiation from a ~ 400 nm lamp. **b)** Photos of a single crystal of MUF-7-**bdc-dpq** crystal and **c)** MUF-7-**bdc-dpq-(OMe)$_2$** before and after irradiation with the UV lamp, showing photochromism.

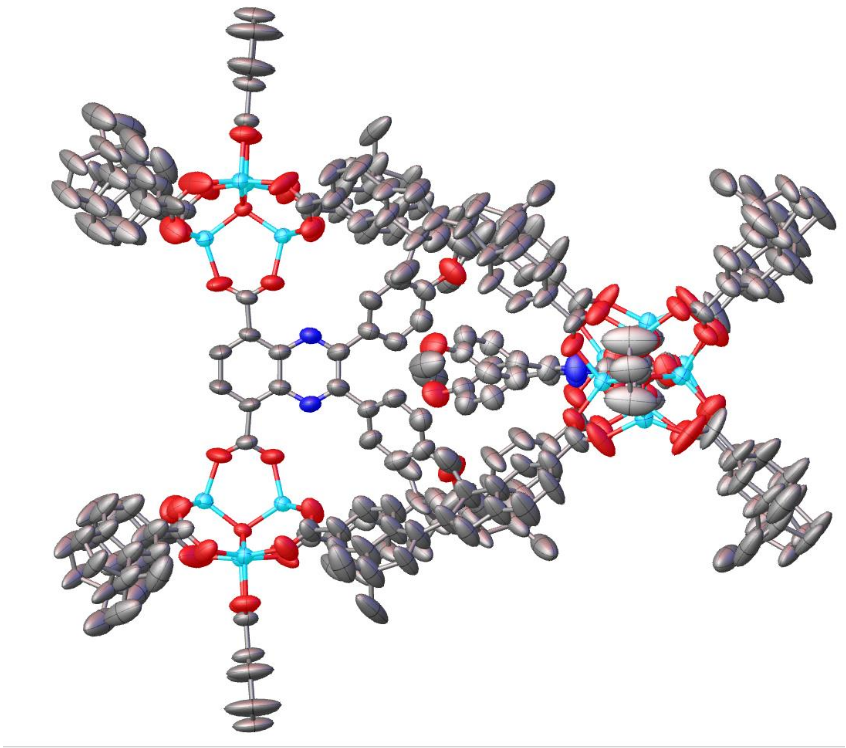

Figure 4.16: Representative SCXRD structure of MUF-7-**bdc-dpq-(OMe)$_2$**. Atoms were refined anisotropically using Olex2 and ellipsoids are shown at 50 % probability. Colour code: zinc: turquoise, nitrogen: deep blue, oxygen: red and carbon: grey. Hydrogen atoms are omitted for clarity.

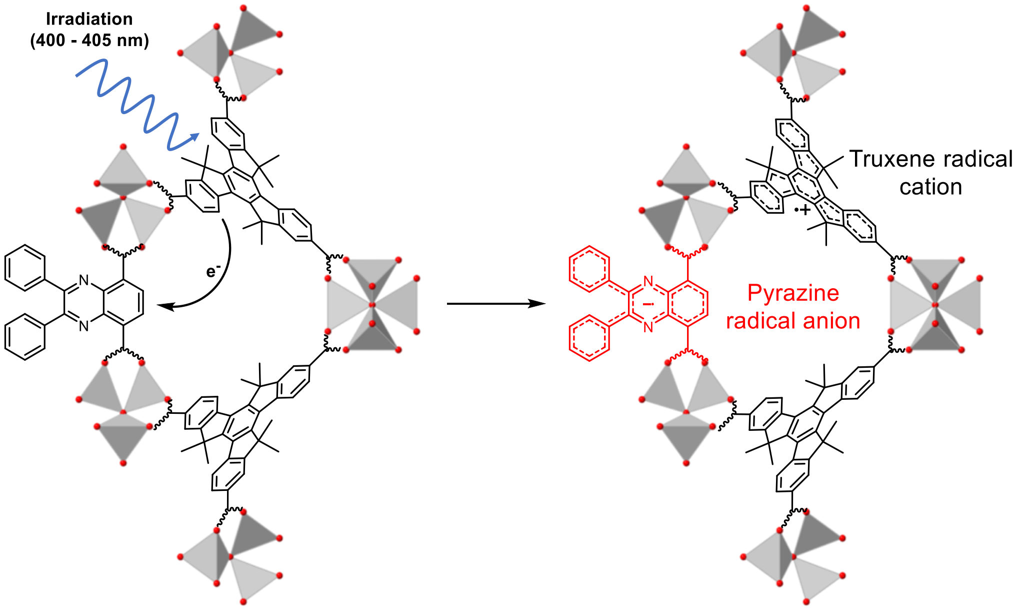

Figure 4.17: A schematic of ligand-ligand charge transfer between truxene-based hmtt ligands and bdc-quin ligands with MUF-7-bdc-dpq as an example. Zn_4O clusters are shown in grey tetrahedra, and oxygen atoms are shown as red spheres.

Based on the above three observations, we developed a working hypothesis that ligand-to-ligand charge transfer (LLCT) between the truxene ligands and the bdc-quin ligands was responsible for generating radicals. Truxene derivatives are known to be electron rich and such derivatives have been used as electron donors in semiconductor devices.[297-302] On the other hand, quinoxalines and pyrazines are electron deficient and hence have a tendency to accept electrons.[303,304] Using this information, we can speculate that irradiation induces an electron to be transferred from the truxene-based hmtt ligands to the bdc-quin ligands. This forms a truxene radical cation and a pyrazine radical anion (Figure 4.16).

To probe actual bond length changes, we first obtained a SCXRD structure of MUF-7-**bdc-dpq** without UV irradiation. Bond lengths of all ligands and the Zn_4O cluster could be determined with an experimental standard deviation (esd), obtained by the refinement process, which reached a maximum of 0.006 Å (~ 0.4 %). Upon irradiation, if the same bonds showed a length difference greater than this uncertainty, we considered a bond length change to have taken place. The bond lengths are mentioned in Table 4.1 and Table 4.2, with the corresponding atom labels shown in Figure 4.18.

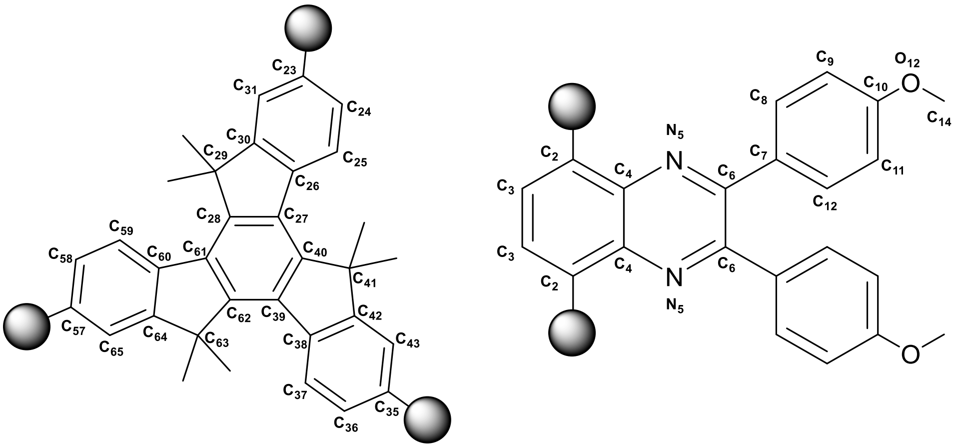

hmtt **bdc-dpq-(OMe)**$_2$

Figure 4.18: Atom labels used for the ligands in the SCXRD structure of and MUF-7-**bdc-dpq-(OMe)**$_2$. Note that for MUF-7-**bdc-dpq**, the atom labels are the same except for the methoxy group, which is absent in the **bdc-dpq** ligand.

For the irradiated sample, we first focused on the **bdc-dpq** ligand in MUF-7-**bdc-dpq**. The $C_6 – C_6$ bond, which is a bond of the pyrazine ring undergoes lengthening from 1.498 Å to 1.544 Å, corresponding to a length increase if 0.046 Å (Figure 4.17). The $N_5 – C_6$ bond closest to the pendant phenyl rings shows a decrease of 0.025 Å. The C – C bonds of the pendant phenyl rings show more significant changes ranging from a minimum shortening of 0.016 Å ($C_8 – C_9$) to a maximum lengthening of 0.052 Å ($C_9 – C_{10}$). The length changes for **bdc-dpq** reported here are consistent with those observed by Chen et al. for pyrene-fused azaacene radical anions.[296]

The hmtt ligand, which may form the radical cation, also shows bond length changes consistent with its involvement (Table 4.1). In hmtt, the maximum bond length change is a shortening of 0.044 Å for the bond between $C_{24} – C_{25}$, and the maximum lengthening seen is 0.025 Å for the bond between $C_{64} – C_{65}$ in one of the outer phenyl rings. The bpdc ligands show little to no change in their bond lengths.

We also monitored the SCXRD structure of MUF-7-**bdc-dpq-(OMe)**$_2$ with and without UV irradiation. In this case, we observed higher bond length differences in **bdc-dpq-(OMe)**$_2$ compared to **bdc-dpq** (Table 4.2). A maximum lengthening of 0.026 Å and 0.022 Å for the $N_5 – C_6$ and $C_6 – C_6$ bonds, respectively. A maximum shortening of 0.052 Å for the $C_2 – C_4$ bond was also observed. The $C_8 – C_9$ bond of the pendant phenyl rings lengthens by 0.022 Å, and the $C_9 – C_{10}$ shortens by 0.04 Å. An important thing to note was that the methoxy groups also played a role. The $C_{10} – O_{12}$ and $O_{12} – C_{14}$ bonds in these groups also underwent shortening by 0.019 Å and 0.043 Å, respectively. The methoxy group being an electron donor group would be able to participate in delocalising the radical and further stabilise it by the captodative effect.[285,305]

Similar lengthening and shortening effects were observed for the bonds in the hmtt ligand, which forms the radical cation. The $C_{28} – C_{27}$ bond of the central phenyl ring was lengthened by 0.035 Å. The bonds bridging the central phenyl ring to the outer phenyl rings i.e. $C_{26} – C_{27}$ showed the maximum shortening upto 0.04 Å, similarly the $C_{60} – C_{61}$ bond also shortened from 1.512 Å to 1.481 Å, corresponding to a shortening of 0.031 Å.

We also collected SCXRD structures of MUF-77-**bdc-paq** and MUF-77-**bdc-thenil**. In both these structures, the bdc ligands were disordered over four positions. Furthermore, unusually long C – N bond lengths were also noted. Typically, these bond lengths range between 1.2 to 1.4 Å. However, in MUF-77-**bdc-paq** and MUF-77-**bdc-paq-Br**$_2$, these bonds lengths were ranged between 1.6 – 1.8 Å. Further investigations to obtain better crystal structures to understand these unusual observations are underway.

Future work on these results for MUF-7-**bdc-dpq** and MUF-7-**bdc-dpq-(OMe)**$_2$ involves some cyclic voltammetry measurements to understand the redox properties of the hmtt and bdc-quin ligands. Additionally, transient absorption spectroscopy measurements would aid in understanding the ultrafast dynamics of the inter-ligand charge transfer process.[306]

Table 4.1: Selected bond lengths of MUF-7-**bdc-dpq** without and with UV irradiation, with esd mentioned within brackets. Atom labels are in mentioned in Figure 4.17.

Ligand	**Bond**	**Length without irradiation (Å)**	**Length with irradiation (Å)**	**Bond length change**	**Ligand**	**Bond**	**Length without irradiation (Å)**	**Length with irradiation (Å)**	**Bond length change**
bdc-dpq	C_2 – C_3	1.297(3)	1.285(3)	-0.012	**hmtt**	C_{23} – C_{24}	1.383(4)	1.373(3)	-0.010
	C_3 – C_3	1.446(4)	1.456(4)	+0.01		C_{25} – C_{26}	1.414(4)	1.420(4)	–
	C_2 – C_4	1.511(3)	1.500(3)	-0.011		C_{26} – C_{27}	1.465(4)	1.447(4)	-0.018
	C_4 – C_4	1.352(5)	1.365(4)	+0.13		C_{24} – C_{25}	1.382(4)	1.338(4)	-0.044
	C_4 – N_5	1.357(3)	1.361(3)	–		C_{27} – C_{28}	1.359(4)	1.371(4)	+0.012
	N_5 – C_6	1.270(3)	1.245(3)	-0.025		C_{40} – C_{41}	1.604(3)	1.606(4)	–
	C_6 – C_6	1.498(5)	1.544(5)	+0.046		C_{36} – C_{37}	1.358(4)	1.373(4)	+0.012
	C_6 – C_7	1.498(3)	1.504(3)	–		C_{39} – C_{62}	1.405(4)	1.421(4)	+0.016
	C_7 – C_8	1.370(3)	1.338(3)	-0.032		C_{64} – C_{65}	1.419(4)	1.444(4)	+0.025
	C_8 – C_9	1.367(3)	1.351(3)	-0.016		C_{58} – C_{59}	1.366(4)	1.362(4)	–
	C_9 – C_{10}	1.314(4)	1.366(4)	+0.052		C_{60} – C_{61}	1.535(4)	1.506(4)	-0.029
	C_{10} – C_{11}	1.484(4)	1.446(4)	-0.038		C_{61} – C_{28}	1.396(4)	1.372(4)	-0.022

	C_{11} – C_{12}	1.394(4)	1.373(3)	-0.021		C_{28} – C_{29}	1.518(4)	1.512(4)	–
	C_{7} – C_{12}	1.347(4)	1.372(3)	-0.025		C_{29} – C_{30}	1.531(5)	1.541(4)	+0.010

Table 4.2: Selected bond lengths of ligands in. MUF-7-**bdc-dpq-(OMe)$_2$** without and with UV irradiation, with esd mentioned within brackets. Atom labels are in mentioned in Figure 4.17.

Ligand	**Bond**	**Length without irradiation (Å)**	**Length with irradiation (Å)**	**Bond length change**	**Ligand**	**Bond**	**Length without irradiation (Å)**	**Length with irradiation (Å)**	**Bond length change**
bdc-dpq-(OMe)$_2$	C_{2} – C_{3}	1.378(5)	1.364(3)	-0.014	**hmtt**	C_{23} – C_{24}	1.369(5)	1.371(3)	–
	C_{3} – C_{3}	1.388(6)	1.387(4)	–		C_{25} – C_{26}	1.411(4)	1.421(4)	+0.010
	C_{2} – C_{4}	1.445(5)	1.393(3)	-0.052		C_{26} – C_{27}	1.544(5)	1.504(4)	-0.018
	C_{4} – C_{4}	1.405(5)	1.402(4)	–		C_{27} – C_{28}	1.364(5)	1.399(4)	+0.035
	C_{4} – N_{5}	1.391(4)	1.397(3)	–		C_{43} – C_{35}	1.359(4)	1.371(4)	+0.012
	N_{5} – C_{6}	1.270(3)	1.296(3)	-0.026		C_{40} – C_{41}	1.517(3)	1.522(4)	–
	C_{6} – C_{6}	1.401(5)	1.423(4)	+0.022		C_{36} – C_{37}	1.410(6)	1.400(4)	–
	C_{6} – C_{7}	1.478(5)	1.490(3)	+0.012		C_{62} – C_{63}	1.523(5)	1.539(4)	+0.016
	C_{7} – C_{8}	1.366(5)	1.361(3)	–		C_{64} – C_{65}	1.419(4)	1.444(4)	+0.025

C_8 – C_9	1.348(5)	1.370(3)	+0.022	C_{58} – C_{59}	1.413(5)	1.400(4)	-0.013
C_9 – C_{10}	1.392(4)	1.352(3)	-0.040	C_{60} – C_{61}	1.512(5)	1.481(4)	-0.031
C_{10} – C_{11}	1.424(4)	1.400(4)	-0.024	C_{61} – C_{28}	1.519(5)	1.520(4)	–
C_{11} – C_{12}	1.367(5)	1.368(3)	–	C_{28} – C_{29}	1.525(4)	1.512(4)	-0.013
C_7 – C_{12}	1.391(4)	1.394(3)	–	C_{29} – C_{30}	1.525(4)	1.512(4)	-0.013
C_{10} – O_{12}	1.390(4)	1.371(3)	-0.019				
O_{12} – C_{14}	1.457(5)	1.414(3)	-0.043				

4.4 Experimental section

4.4.1 General Information:

All starting materials and solvents were used as received from commercial sources without further purification unless otherwise noted. NMR spectra were collected at room temperature using a Bruker Avance 400 MHz or 500 MHz spectrometer, with the use of the solvent proton as an internal standard. All chemical shift (δ) values are in parts per million (ppm).

X-ray diffraction data were collected using either of two methods: (a) Rigaku Spider diffractometer equipped with a Micromax MM007 rotating anode generator with Cu$_\alpha$ radiation (wavelength = 1.54180 Å), high flux Osmic multilayer mirror optics, and a curved image plate detector, and finally processed into 1D diffractograms using 2DP. (b) Bruker D8 Venture diffractometer with Cu$_\alpha$ radiation (wavelength = 1.54180 Å), with a diamond microfocus X-ray source and a Photon III 28 detector. For PXRD, the collected 1D Diffractograms were processed using APEX3. For SCXRD, the crystals were exchanged with ***N*,*N***-dibutylformamide (DBF) and mounted on a nylon loop using paratone oil. The crystal was kept under an atmosphere of nitrogen at 293 K for all measurements.

4.4.2 Ligand Synthesis and Characterisation:

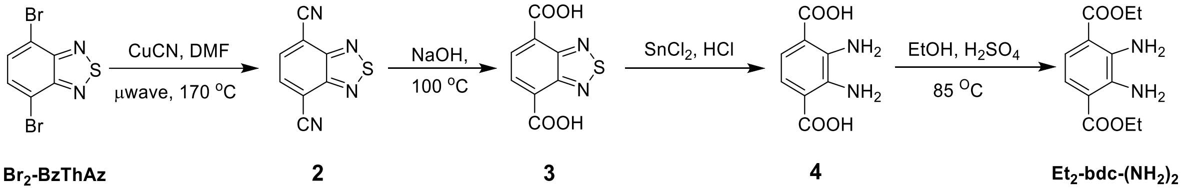

Compound 2:

A total of five 1.25-gram portions of **Br$_2$-BzThAz** (6.25 g, 21.2 mmol, 1 eq.) were mixed with five 1.25-gram portions of CuCN (6.25 g, 70.1 mmol, 3.3 eq.) in five microwave reaction tubes. Dry DMF (5 ml) was added to each tube. The tubes were heated in a microwave reactor at 170 °C for 2 hours each. The portions were combined and acidified $FeCl_3$ solution was added, and the mixture was stirred for 30 minutes. The mixture was extracted with dichloromethane. The organic layers were collected, the solvent dried *in vacuo*, to give the product. (**Yield:** 2.6 g, 13.8 mmol, 65%) ^{1}H NMR (500 MHz, $CDCl_3$) δ 8.16 (s, 2H), consistent with *Chem. Eur. J.* **2019**, *25*, 5246.

Compound 3:

Compound **2** (2.6 g, 13.8 mmol) was dissolved in 80 ml of 20% aq. NaOH solution and heated at 100 °C for 3 hours. The flask was transferred to an ice bath and neutralised with conc. HCl to a pH of 2, a brown solid was obtained. The solid was washed with water, filtered and dried *in vacuo* to give the product. (**Yield:** 1.6 g, 7.1 mmol, 51^{1}H NMR (500 MHz, DMSO-d_6) δ 8.34 (s, 2H), consistent with *Chem. Eur. J.* **2019**, *25*, 5246.

Compound 4:

A mixture of compound **3** (1.5 g, 6.7 mmol), $SnCl_2$ (7.2 g, 38 mmol), and conc. HCl (20 ml) was stirred overnight at room temperature. The solid obtained was filtered and washed with water and dried to give the product. (**Yield:** 0.97 g, 4.94 mmol, 74%) ^{1}H NMR (500 MHz, DMSO-d_6, ppm) δ 7.01 (s, 2H). ^{13}C NMR (125 MHz, DMSO-d_6) 170.41, 140.67, 117.07, 111.78.

Et$_2$-bdc-(NH$_2$)$_2$:

Compound **4** (0.85 g, 4.3 mmol) was suspended in EtOH (70 ml), and conc. H_2SO_4 (7 ml) was added dropwise. The reddish-brown solution was heated at 85 °C for 48 hours. The EtOH was evaporated *in vacuo.* The residual reaction mixture was added dropwise to an ice-cold, saturated, aqueous solution of K_2CO_3 to give a brown solid. The solid obtained was extracted with CH_2Cl_2 and water. The collected organic layers were evaporated to give the product. (**Yield:** 0.65 g, 2.58 mmol, 59%). ^{1}H NMR (500 MHz, $CDCl_3$) δ 7.35 (s, 2H), 4.38 (q, J = 7.0 Hz, 4H), 1.42 (t, J = 7.1 Hz, 6H).^{13}C NMR (100 MHz, $CDCl_3$) δ 168.22, 140.83, 118.29, 114.41, 60.76, 14.28.

General procedure A for the synthesis of quinoxaline esters:

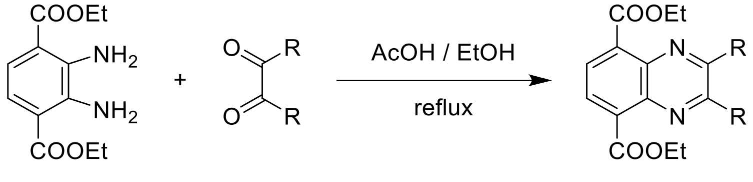

Et$_2$-bdc-(NH$_2$)$_2$ **6, 7, 8, 9, 10**

In a typical synthesis, compound **Et$_2$-bdc-(NH$_2$)$_2$** (1 eq.) was combined with the diketone (1.1 eq.). 9 ml of 1:2 AcOH/EtOH was added and the mixture was heated on reflux for 3 hours. Anhydrous $MgSO_4$ was added and the refluxing was continued for an additional 12 hours. The reaction mixture was added to water, dropwise to precipitate out the crude product. This was washed with 1:1 hexane:CH_2Cl_2 (this fraction was rejected) followed by a wash with pure DCM and MeOH which was collected and dried to give pure compounds **6**, **7**, **8**, **9**, and **10**.

6

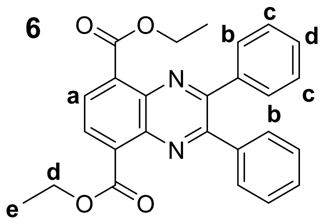

Made by reacting **Et_2-bdc-(NH_2)$_2$** (100 mg, 0.396 mmol, 1 eq.) and benzil (91 mg, 0.436 mmol, 1.1 eq.) acc. to general procedure A. (**Yield:** 135 mg, 0.316 mmol, 79%) ^{1}H NMR (500 MHz, $CDCl_3$, ppm) δ 8.14 (s, 2H, H_a), 7.70 (d, *J* = 7.3 Hz, 2H, H_b), 7.44 – 7.34 (m, 6H, $H_{c,}$ H_d), 4.57 (q, *J* = 7.1 Hz, 2H, H_d), 1.52 (t, *J* = 7.1 Hz, 3H, H_e). ^{13}C NMR (100 MHz, $CDCl_3$) 166.36, 152.99, 138.37, 133.95, 129.77, 129.50, 128.28, 91.90, 14.41. HRMS (ESI) m/z: $[m+H]^+$ calc. for $C_{26}H_{23}N_2O_4$: 427.1613, Found: 427.1646.

7

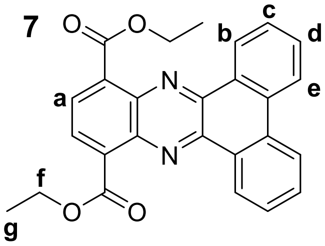

Made by reacting **Et_2-bdc-(NH_2)$_2$** (100 mg, 0.396 mmol, 1 eq.) and 9,10-phenanthrenequinone (90 mg, 0.436 mmol, 1.1 eq.) acc. to general procedure A. (**Yield:** 160 mg, 0.376 mmol, 95%) ^{1}H NMR (500 MHz, $CDCl_3$, ppm) ^{1}H NMR (500 MHz, $CDCl_3$) δ 9.39 (d, *J* = 8.0 Hz, 2H, H_b), 8.60 (d, *J* = 8.0 Hz, 2H, H_e), 8.24 (s, 2H, H_a), 7.85 (t, *J* = 15.2, 7.2 Hz, 2H, H_c), 7.78 (t, *J* = 7.5 Hz, 2H, H_d), 4.69 (q, *J* = 7.1 Hz, 4H, H_f), 1.64 – 1.60 (t, 6H, H_g). ^{13}C NMR (125 MHz, $CDCl_3$) δ 166.68, 142.76, 139.29, 134.47, 132.47, 130.96, 129.86, 129.55, 128.08, 126.78, 123.04, 61.90, 14.48. HRMS (ESI) m/z: $[m+H]^+$ calc. for $C_{26}H_{21}N_2O_4$: 425.1423, Found: 425.1491.

8

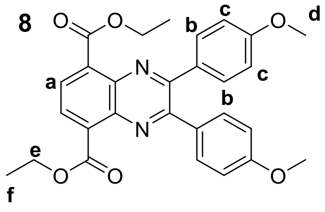

Made by reacting **Et_2-bdc-(NH_2)$_2$** (100 mg, 0.396 mmol, 1 eq.) and 4,4′-dimethoxybenzil (128 mg, 0.436 mmol, 1.1 eq.) acc. to general procedure A. (**Yield:** 158 mg, 0.324 mmol, 82%) %) ^{1}H NMR (500 MHz, $CDCl_3$, ppm) ^{1}H NMR (500 MHz, $CDCl_3$) δ 8.08 (s, 2H, H_a), 7.70 (d, *J* = 8.3 Hz, 2H, H_b), 6.90 (d, *J* = 8.4 Hz, 2H, H_c), 4.57 (q, *J* = 7.2 Hz, 4H, H_e), 3.86 (s, 6H, H_d), 1.53 (t, *J* = 7.1 Hz, 6H, H_f). ^{13}C NMR (100 MHz, $CDCl_3$) δ 166.46, 160.77, 152.32, 138.06, 133.59, 131.60, 130.97, 129.33, 113.77, 61.79, 55.32, 14.43. HRMS (ESI) m/z: $[m+H]^+$ calc. for $C_{28}H_{27}N_2O_6$: 487.1864, Found: 487.1856

9

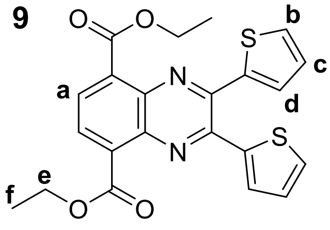

Made by reacting **Et_2-bdc-(NH_2)$_2$** (100 mg, 0.396 mmol, 1 eq.) and 2,2′-thenil (97 mg, 0.436 mmol, 1.1 eq.) acc. to general procedure A. (**Yield:** 127 mg, 0.289 mmol, 73%). ^{1}H NMR (500 MHz, $CDCl_3$, ppm) δ 8.09 (s, 2H, H_a), 7.56 (d, *J* = 5.0 Hz, 2H, H_b), 7.51 (d, *J* = 3.7 Hz, 2H, H_d), 7.06 (t, 2H, H_c), 4.58 (q,

J = 14.2, 7.1 Hz, 4H, H_e), 1.55 (t, J = 7.1 Hz, 6H, H_f). ^{13}C NMR (100 MHz, $CDCl_3$) δ 170.90, 150.90, 145.99, 142.01, 138.47, 135.86, 135.44, 134.39, 132.65, 66.57, 19.30. HRMS (ESI) m/z: $[m+H]^+$ calc. for $C_{22}H_{19}N_2O_4S_2$: 439.0781, Found: 439.0781.

10

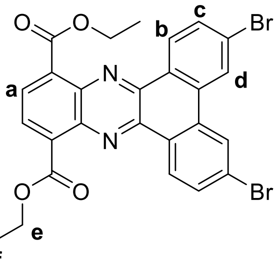

Made by reacting **Et_2-bdc-$(NH_2)_2$** (100 mg, 0.396 mmol, 1 eq.) and 3,6-dibromophenanthronequinone (160 mg, 0.436 mmol, 1.1 eq.) acc. to general procedure A. (Yield**:** 170 mg, 0.291 mmol, 74%) ^{1}H NMR (500 MHz, $CDCl_3$, ppm) ^{1}H NMR (500 MHz, $CDCl_3$) δ 9.17 (d, J = 8.5 Hz, 2H, H_b), 8.59 (s, 2H, H_a), 8.26 (s, 2H, H_d), 7.88 (d, J = 8.5 Hz, 2H, H_c), 4.67 (q, J = 14.2, 7.1 Hz, 4H, H_e), 1.60 (t, J = 7.1 Hz, 6H, H_f).^{13}C NMR (100 MHz, $CDCl_3$) δ 166.31, 141.61, 139.32, 134.35, 132.48, 131.83, 130.21, 128.81, 128.39, 126.23, 126.00, 61.95, 14.59. HRMS (ESI) m/z: $[m+H]^+$ calc. for $C_{26}H_{18}Br_2N_2O_4$: 582.9633, Found: 582.9693.

General procedure B for the synthesis of quinoxaline carboxylic acids:

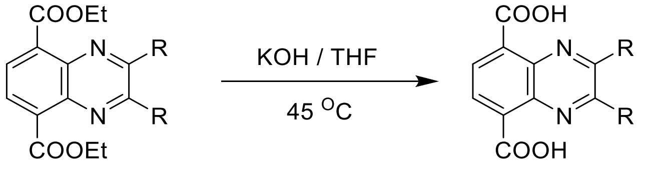

6, 7, 8, 9, 10 **11, 12, 13, 14, 15**

For obtaining quinoxaline carboxylic acid ligands by hydrolysis, the diethylesters (**6**, **7**, **8**, **9**, or **10**) were dissolved in 20 ml of 1:1 THF:2M aq. KOH and heated at 45 °C, overnight. The THF was removed using a separating funnel and the aqueous layer was neutralised using 2M HCl to a pH of 3-4 to precipitate out the carboxylic acids. The solid obtained was filtered and washed with water and dried to give ligands **11**, **12**, **13, 14**, or **15**.

11

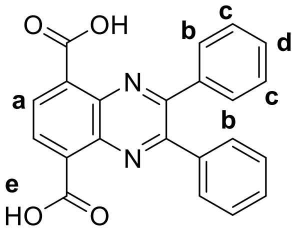

H_2bdc-dpq

Prepared by the hydrolysis of **6** according to general procedure B. (**Yield:** 77 mg, 0.207 mmol, 84%). %) ^{1}H NMR (500 MHz, DMSO-d_6, ppm) δ 14.12 (bs, 1H, H_e), 8.32 (s, 2H, H_a), 7.55 (d, J = 7.0 Hz, 4H, H_b), 7.51 – 7.41 (m, 6H, H_c, H_d). ^{13}C NMR (100 MHz, DMSO-d_6) δ 167.03, 153.71, 138.02, 137.75, 133.45, 131.05, 130.86,

	130.31, 130.12, 128.96, 128.76. HRMS (ESI) m/z: [m-H]$^-$ calc. for $C_{22}H_{13}N_2O_4$: 369.0870, Found: 369.0881.
12 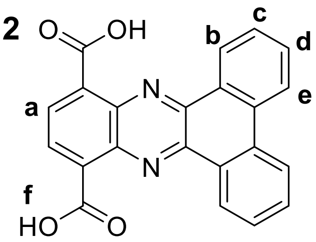 **H_2bdc-paq**	Prepared by the hydrolysis of **7** according to general procedure B. (**Yield:** 95 mg, 0.258 mmol, 84%). ^{1}H NMR (500 MHz, DMSO- d_6, ppm) δ 14.08 (bs, 2H, H_f), δ 9.15 (d, *J* = 7.7 Hz, 2H, H_b), 8.87 (d, *J* = 7.8 Hz, 2H, H_e), 8.39 (s, 2H, H_a), 7.98 (t, 2H, H_d), 7.91 (t, *J* = 7.3 Hz, 2H, H_c). ^{13}C NMR (100 MHz, DMSO-d_6) δ 172.18, 146.71, 143.32, 138.82, 137.25, 137.00, 135.55, 133.81, 133.55, 130.87, 129.11. HRMS (ESI) m/z: [m-H] $^-$ calc. for $C_{22}H_{11}N_2O_4$: 367.0797, Found: 367.0726.
13 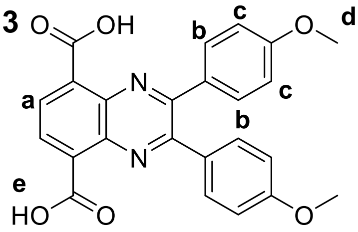 **H_2bdc-dpq-(OMe)$_2$**	Prepared by the hydrolysis of **8** according to general procedure B. (**Yield:** 110 mg, 0.255 mmol, 92%). ^{1}H NMR (500 MHz, DMSO- d_6, ppm) δ 14.26 (bs, 2H, H_e), 8.30 (s, 2H, H_a), 7.53 (d, *J* = 8.8 Hz, 4H, H_b), 7.03 (d, *J* = 8.9 Hz, 4H, H_c), 3.82 (s, 6H, H_d).^{13}C NMR (100 MHz, DMSO-d_6) δ 166.89, 161.09, 153.11, 137.51, 132.55, 131.75, 130.88, 130.15, 114.48, 55.80. HRMS (ESI) m/z: [m-H]$^-$ calc. for $C_{24}H_{17}N_2O_6$: 429.1081, Found : 429.1093.
14 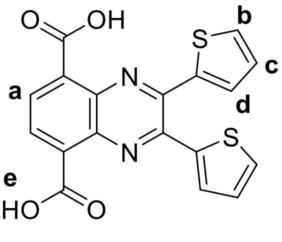	Prepared by the hydrolysis of **9** according to general procedure B. (**Yield:** 75 mg, 0.196 mmol, 86%). ^{1}H NMR (500 MHz, DMSO- d_6, ppm) ^{1}H NMR (500 MHz, DMSO) δ 13.84 (bs, 2H, H_e) 8.21 (s, 2H, H_a), 7.91 (dd, *J* = 5.0, 1.1 Hz, 2H, H_b), 7.41 (dd, *J* = 3.7, 1.1 Hz, 2H, H_c), 7.18 (dd, *J* = 5.0, 3.7 Hz, 2H, H_d). ^{13}C NMR (100 MHz, DMSO- d_6) δ 167.02, 146.69, 140.33, 137.10, 133.25, 131.92, 131.08, 130.79, 128.63. HRMS (ESI) m/z: [m-H]$^-$ calc. for $C_{18}H_9N_2O_4S_2$: 381.0009, Found: 380.9997.
15 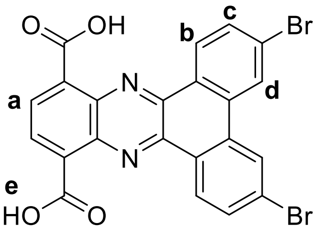 **H_2bdc-paq-Br$_2$**	Prepared by the hydrolysis of **10** according to general procedure B. (**Yield:** 120 mg, 0.273 mmol, 69%). ^{1}H NMR (500 MHz, DMSO- d_6) δ 9.03 (s, 2H, H_d), 8.85 (d, *J* = 8.4 Hz, 2H, H_c), 8.30 (s, 2H, H_a), 8.03 (d, *J* = 8.2 Hz, 2H, H_b). ^{13}C NMR (125 MHz, DMSO- d_6) δ 167.42, 141.00, 138.64, 134.66, 132.86, 132.49, 130.82, 128.20,

	127.81, 127.33, 126.62. HRMS (ESI) m/z: [m-H]$^-$ calc. for $C_{22}H_8Br_2N_2O_4$: 524.8903, Found: 524.8930.

4.4.3 Photochromism of MOFs in different solvents

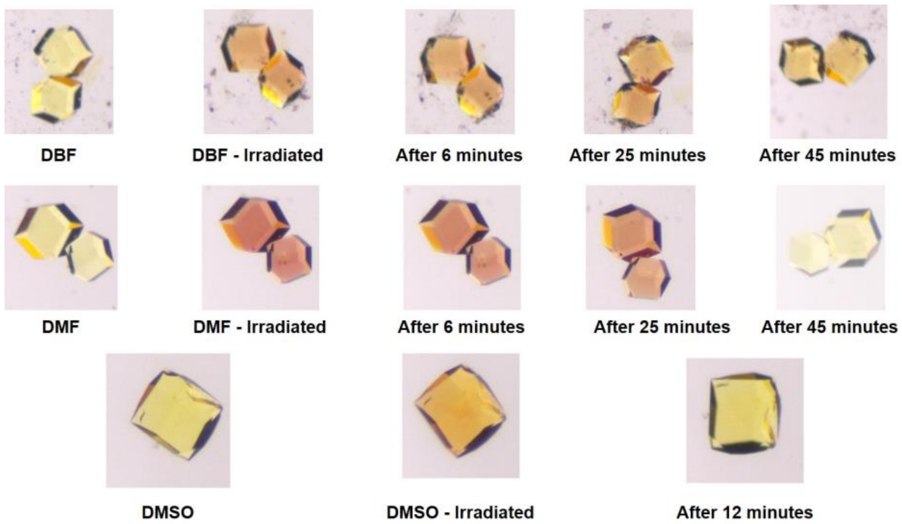

Figure 4.19: Crystals of MUF-77-**bdc-paq** suspended in *N*,*N*-dibutylformamide (DBF), *N*,*N*-dimethylformamide (DMF), and dimethylsulfoxide (DMSO) at different time intervals after irradiation with a 405 nm laser pointer.

4.4.4 Synthesis of photochromic MUF-7 and MUF-77 single crystals

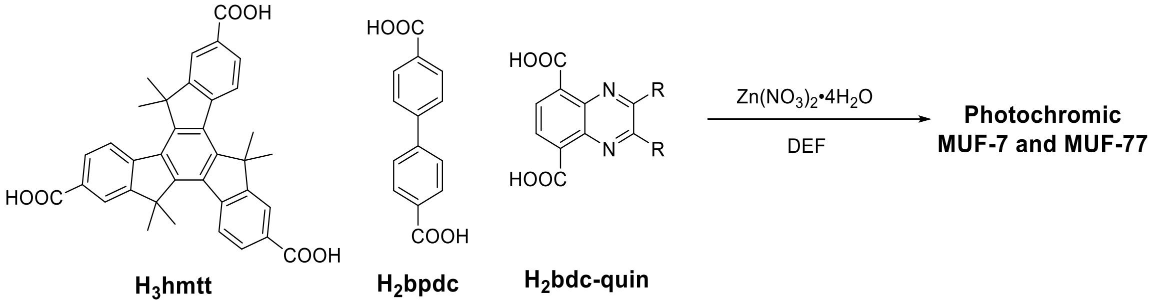

H_3hmtt, H_2bpdc, and H_2bdc-quinoxaline ligand (details in table below) were dissolved in 1 ml of anhy. *N*,*N*-diethylformamide. Zinc nitrate tetrahydrate was added and the sample was sonicated briefly and placed in an isothermal oven kept at 85 °C for 24 hours. The mother liquor was decanted when hot and the crystals were washed with anhy. DMF and stored in DMF at room temperature.

Table 4.3: Quantities of ligands and metal salt required for synthesis of photochromic MUF-7 and MUF-77 frameworks.

MUF system	**H_3hmtt (µmol, eq.)**	**H_2bpdc (µmol, eq.)**	**H_2bdc-quin (µmol, eq.)**	**$Zn(NO_3)_2 \cdot 4(H_2O)$ (µmol, eq.)**
MUF-7-**bdc-dpq**	4.5 mg (8.06, 1)	2.9 mg (12.0, 1.5)	3.4 mg (9.26, 1.15)	15.8 mg (60.4, 7.5)
MUF-77-**bdc-paq**	4.5 mg (8.06, 1)	2.9 mg (12.0, 1.5)	3.4 mg (9.26, 1.15)	15.8 mg (60.4, 7.5)
MUF-7-**dpq-(OMe)$_2$-bdc**	3.5 mg (6.27, 1)	1.9 mg (8.14, 1.3)	5.4 mg (12.5, 2)	12 mg (45.7, 7.3)
MUF-77-**bdc-thenil**	4.5 mg (8.06, 1)	2.9 mg (12.1, 1.5)	3.5 mg (9.26, 1.15)	14.7 mg (56.3, 7.0)
MUF-77-**bdc-paq-Br$_2$**	4.5 mg (8.06, 1)	2.9 mg (12.1, 1.5)	3.5 mg (9.26, 1.15)	14.7 mg (56.3, 7.0)

4.4.5 Synthesis of nanocrystalline photochromic MUF-7 and MUF-77

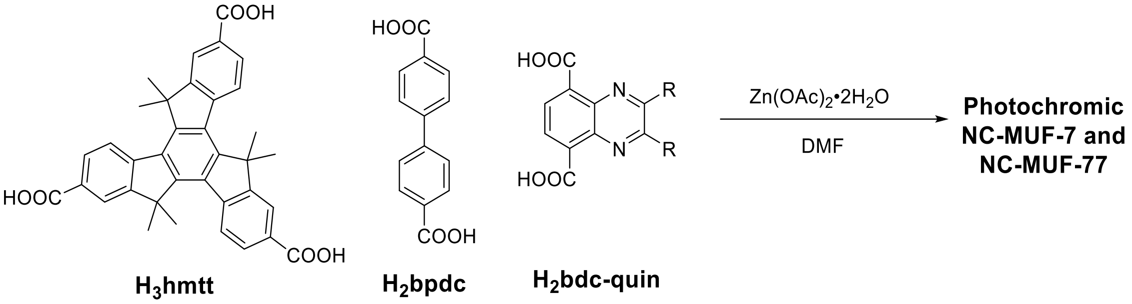

H_3hmtt, H_2bpdc, and H_2bdc-quinoxaline ligands (details in table below) were stirred and dissolved in 1 ml of anhy. *N*,*N*-dimethylformamide. Solid $Zn(OAc)_2{\cdot}2(H_2O)$ was added and the sample and the stirring was continued for another 30 minutes. The resulting suspension was centrifuged thrice with fresh DMF and placed in an isothermal oven at 85 °C, overnight. The crystals were centrifuged again with fresh, dry DMF and stored at room temperature.

Table 4.4: Quantities of ligands and metal salt required for synthesis of nanocrystalline, photochromic MUF-7 and MUF-77 frameworks.

MUF system	**H_3hmtt (μmol, eq.)**	**H_2bpdc (μmol, eq.)**	**H_2quin-bdc (μmol, eq.)**	**$Zn(OAc)_2{\cdot}2(H_2O)$ (μmol, eq.)**
NC-MUF-7-**bdc-dpq**	18 mg (32.2, 2.5)	3.1 mg (12.9, 1)	4.7 mg (12.9, 1)	28.3 mg (128.9, 10)
NC-MUF-77-**bdc-paq**	18 mg (32.2, 2.5)	3.1 mg (12.9, 1)	4.7 mg (12.9, 1)	28.3 mg (128.9, 10)
NC-MUF-7-**bdc-dpq-(OMe)$_2$**	25 mg (44.7, 2.5)	4.3 mg (17.9, 1)	7.7 mg (17.9, 1)	39.2 mg (179.0, 10)
NC-MUF-77-**bdc-thenil**	25 mg (44.7, 2.5)	4.3 mg (17.9, 1)	6.8 mg (17.9, 1)	39.2 mg (179.0, 10)
NC-MUF-77-**bdc-paq-Br$_2$**	20 mg (35.8, 2.5)	3.5 mg (14.3, 1)	7.5 mg (14.3, 1)	37.2 mg (179.0, 12)

4.4.6 PXRD of photochromic MOFs

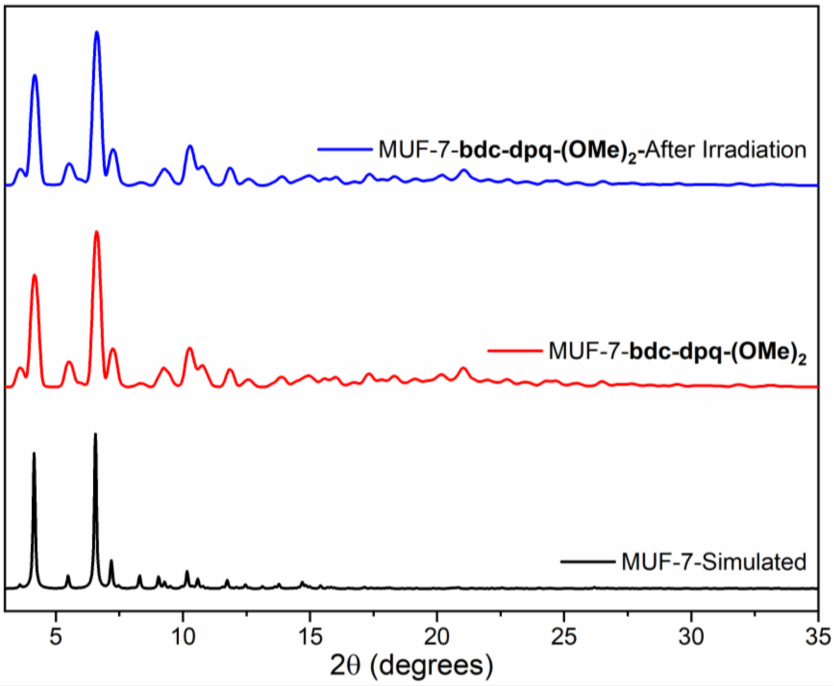

Figure 4.20: PXRD patterns (Cu$_\alpha$ radiation) of photochromic MUF-7-**bdc-dpq-(OMe)$_2$** single crystals compared to the PXRD simulated from the SCXRD structure.

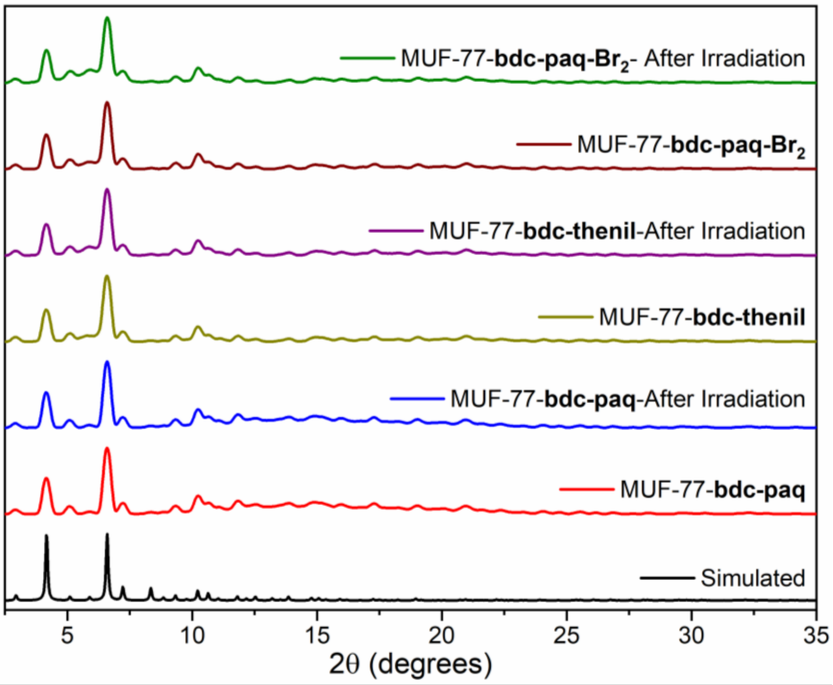

Figure 4.21: PXRD patterns (Cu$_\alpha$ radiation) of photochromic MUF-77 single crystals before and after UV irradiation compared to the PXRD pattern simulated from the SCXRD structure.

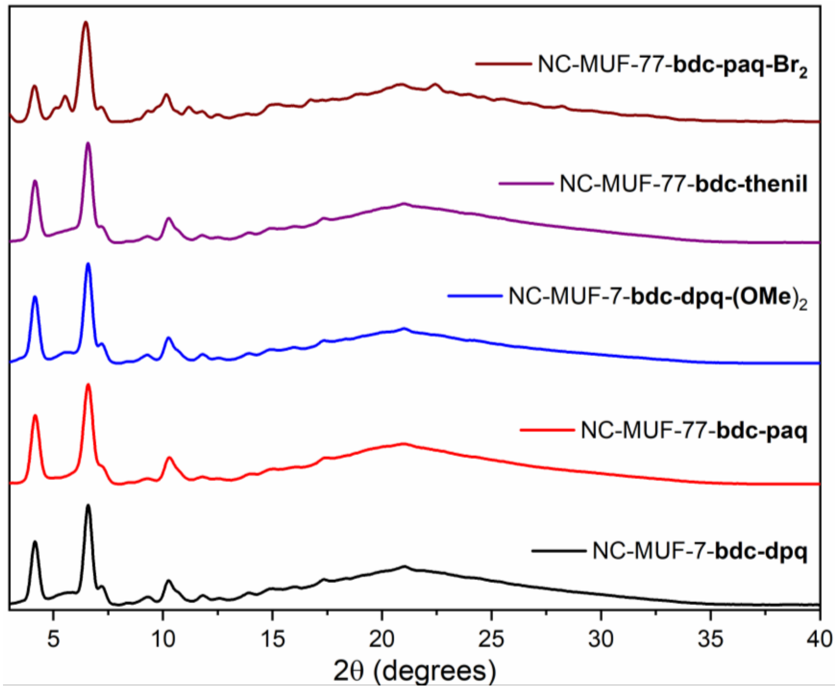

Figure 4.22: PXRD patterns (Cu$_\alpha$ radiation) of photochromic, nanocrystalline MUF-77 crystals.

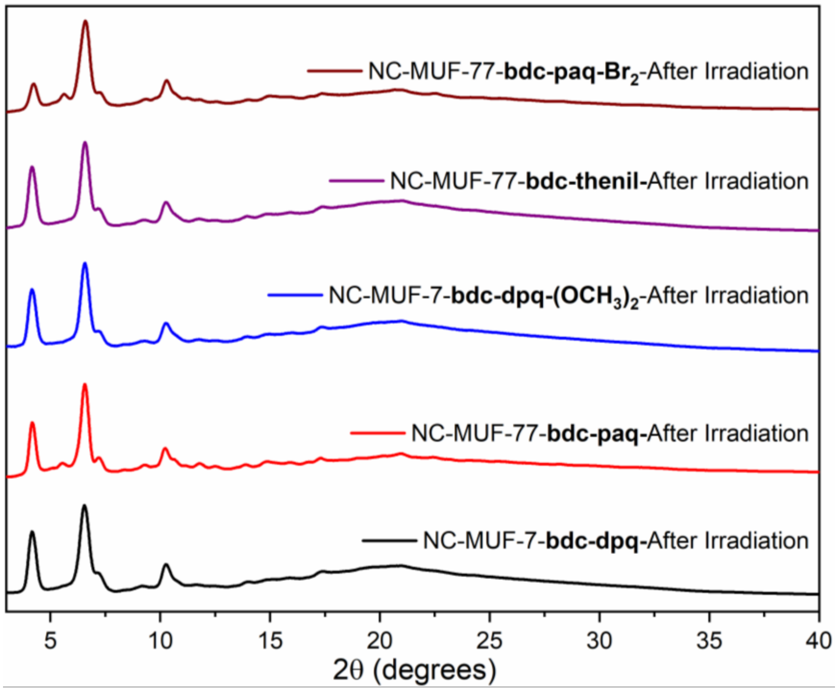

Figure 4.23: PXRD patterns (Cu$_\alpha$ radiation) of photochromic, nanocrystalline MUF-77 crystals after irradiation with a 405 nm laser.

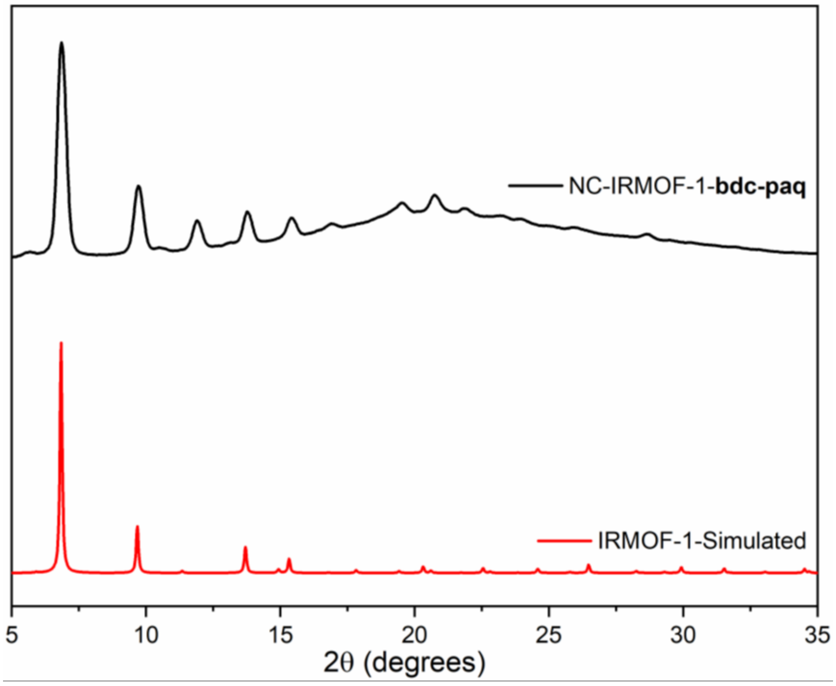

Figure 4.24: PXRD of nanocrystalline, IRMOF-1-**bdc-paq** (black) compared to PXRD pattern simulated from SCXRD structure of IRMOF-1 (red).

4.4.7 UV-Visible Absorption Spectra of NC-MUF-77-bdc-thenil

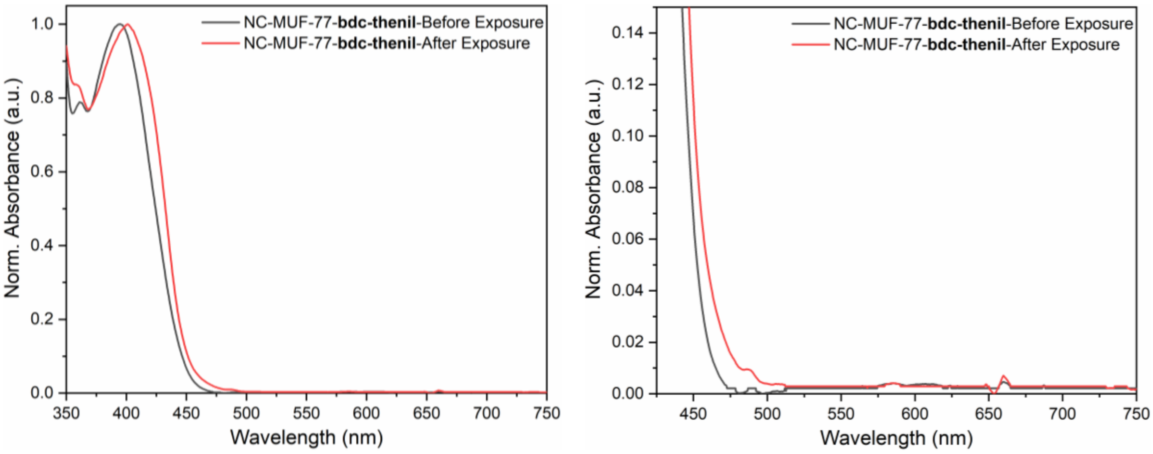

Figure 4.25: UV-Vis spectra of NC-MUF-77-**bdc-thenil** before and after irradiation with 405 nm light. The area between 425-750 nm is shown on the right.

4.4.7 EPR Spectra of photochromic MOFs

EPR spectra were measured using a Bruker EMX Micro X-band spectrometer with a microwave power of 0.2 mW. Samples were homogenised using an ultrasonic bath and inserted into a Helium Oxford Cryostat ESR900 and spectra were recorded at 100 K. Samples were removed and warmed to room temperature before illumination with a 405 nm laser. The illuminated samples were cooled to 100 K and EPR spectra were recorded. Finally, samples were warmed again, exposed to visible light until the colour returned to yellow. The cooled to 100 K and another EPR spectrum was collected.

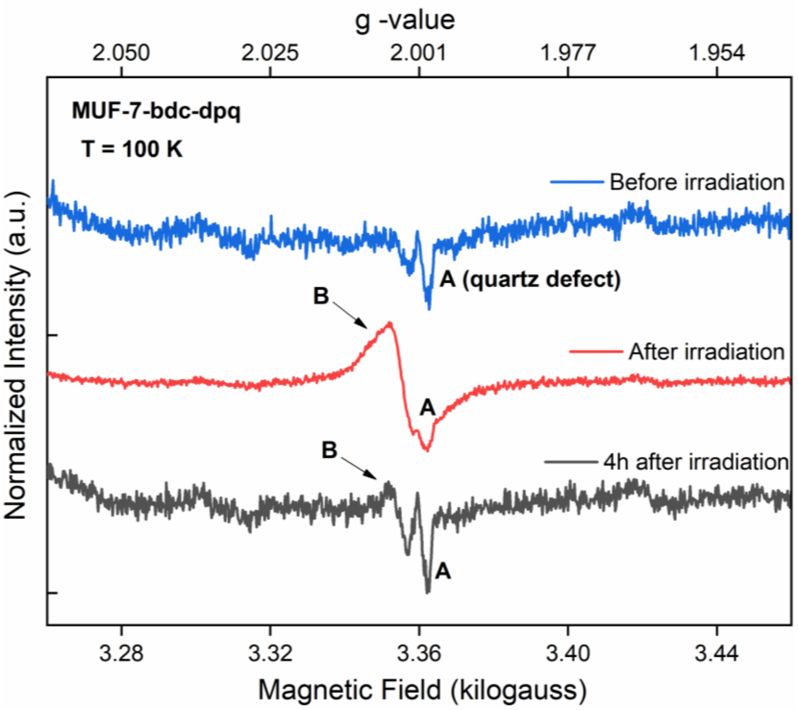

Figure 4.26: EPR spectrum MUF-7-**bdc-dpq** before irradiation, immediately after irradiation and 4 hours after irradiation. Signal **B** is from pyrazine radicals. Signal **A** is from a defect in the quartz sample cell.

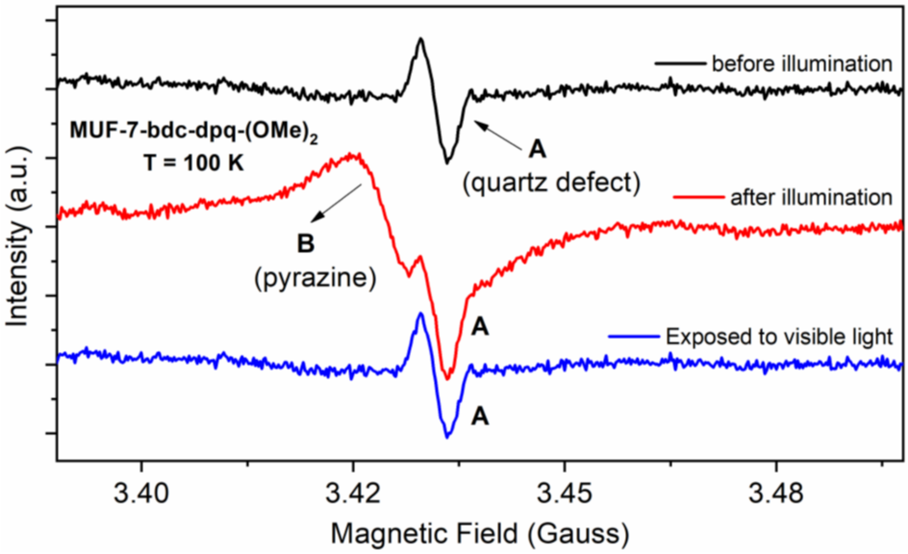

Figure 4.27: EPR spectrum of MUF-7-**bdc-dpq-(OMe)$_2$** before irradiation, after irradiation and after exposure to visible light, showing loss of pyrazine radical signal **B**. Signal **A** is from a defect in the quartz sample cell.

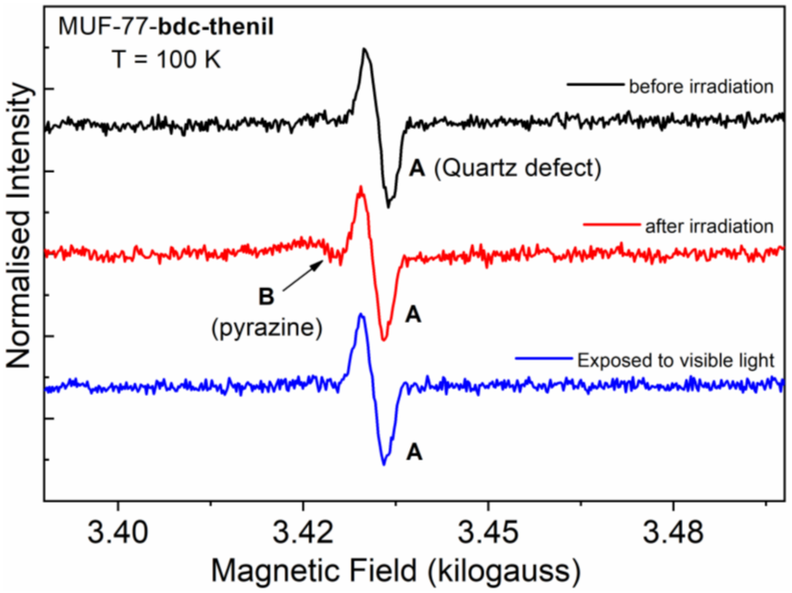

Figure 4.28: EPR spectrum MUF-77-**bdc-thenil** before and after light exposure. Signal **B** is from pyrazine radicals. Signal **A** is from a defect in the quartz sample cell.

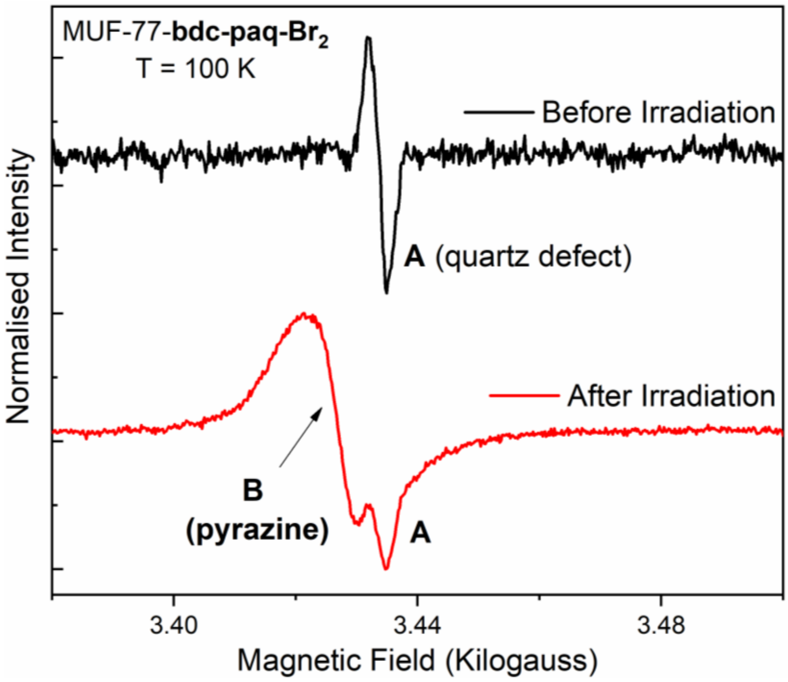

Figure 4.29: EPR spectrum MUF-77-**bdc-paq-Br$_2$** before and after light exposure. Signal **B** (*g* = 2.0037) is from pyrazine radicals. Signal **A** is from a defect in the quartz sample cell. **Note:** This sample was measured with a different resonator.

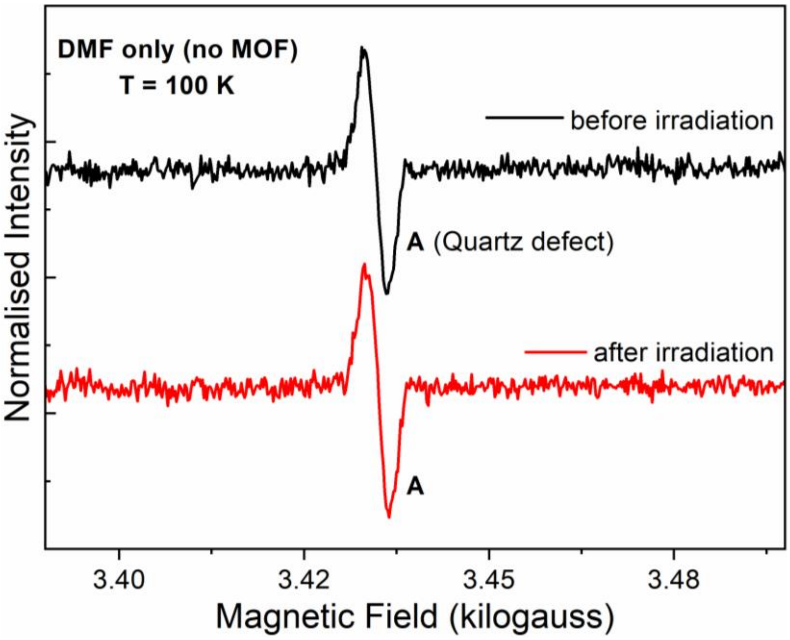

Figure 4.30: EPR spectrum of DMF before and after irradiation with a 405 nm laser pointer. Only signal **A** is visible, which is assigned to a defect in the quartz sample cell.

4.4.7 Crystallographic details for photochromic MUF-7 systems

CIFs for all SCXRD structures can be found at the following link:

https://drive.google.com/drive/folders/1c4unyFa4vUeXKQnRLt7rKzXBN9QWmfJ9?usp=sharing

Table 4.5: Crystallographic details for MUF-7-**bdc-dpq**.

Identification code	MUF-7-**bdc-dpq-** Without Irradiation	MUF-7-**bdc-dpq-** With Irradiation
Empirical formula	$C_{66}H_{46}NO_{13}Zn_4$	$C_{66}H_{46}NO_{13}Zn_4$
Formula weight	1322.52	1322.52
Temperature/K	293.0	293.0
Crystal system	cubic	cubic
Space group	I-43d	I-43d
a/Å	59.5745(16)	59.485(2)
b/Å	59.5745(16)	59.485(2)
c/Å	59.5745(16)	59.485(2)
α/°	90	90
β/°	90	90
γ/°	90	90
Volume/Å^3	211437(17)	210481(21)
Z	48	48
ρ_{calc}g/cm^3	0.499	0.501
μ/mm^{-1}	0.800	0.804
F(000)	32304.0	32304.0
Radiation	CuKα (λ = 1.54178)	CuKα (λ = 1.54178)
2Θ range for data collection/°	3.632 to 116.318	3.638 to 116.34
Index ranges	$-65 \le h \le 62, -61 \le k \le 63, -60 \le l \le 65$	$-63 \le h \le 62, -59 \le k \le 65, -58 \le l \le 63$
Reflections collected	278616	365894
Independent reflections	24575 [R_{int} = 0.0419, R_{sigma} = 0.0250]	24558 [R_{int} = 0.0573, R_{sigma} = 0.0286]
Data/restraints/parameters	24575/18/753	24558/42/753
Goodness-of-fit on F^2	1.047	1.034
Final R indexes [I>=2σ (I)]	R_1 = 0.0242, wR_2 = 0.0561	R_1 = 0.0236, wR_2 = 0.0504
Final R indexes [all data]	R_1 = 0.0298, wR_2 = 0.0577	R_1 = 0.0319, wR_2 = 0.0520
Largest diff. peak/hole / e Å^{-3}	0.18/-0.12	0.15/-0.10
Flack parameter	0.693(5)	0.348(5)

Table 4. 6: Crystallographic details for MUF-7-**bdc-dpq-(OMe)$_2$**.

Identification code	MUF-7-**bdc-dpq-(OMe)$_2$** Without Irradiation	MUF-7-**bdc-dpq-(OMe)$_2$** With Irradiation
Empirical formula	$C_{67}H_{48}NO_{14}Zn_4$	$C_{67}H_{48}NO_{14}Zn_4$
Formula weight	1352.54	1352.54
Temperature/K	293.0	293.0
Crystal system	cubic	cubic
Space group	I-43d	I-43d
a/Å	59.811(2)	59.551(4)
b/Å	59.811(2)	59.551(4)
c/Å	59.811(2)	59.551(4)
α/°	90	90
β/°	90	90
γ/°	90	90
Volume/Å^3	213962(23)	211186(47)
Z	48	48
ρ_{calc}g/cm^3	0.504	0.510
μ/mm^{-1}	0.800	0.810
F(000)	32072.0	32072.0
Radiation	CuKα (λ = 1.54178)	CuKα (λ = 1.54178)
2Θ range for data collection/°	3.618 to 107.004	3.634 to 117.078
Index ranges	$-52 \leq h \leq 59$, $-61 \leq k \leq 48$, $-53 \leq l \leq 62$	$-65 \leq h \leq 54$, $-63 \leq k \leq 61$, $-64 \leq l \leq 64$
Reflections collected	181581	162105
Independent reflections	21069 [R_{int} = 0.0499, R_{sigma} = 0.0348]	24403 [R_{int} = 0.0573, R_{sigma} = 0.0451]
Data/restraints/parameters	21069/6/784	24403/6/784
Goodness-of-fit on F^2	1.049	0.920
Final R indexes [I>=2σ (I)]	R_1 = 0.0276, wR_2 = 0.0640	R_1 = 0.0244, wR_2 = 0.0376
Final R indexes [all data]	R_1 = 0.0350, wR_2 = 0.0663	R_1 = 0.0446, wR_2 = 0.0406
Largest diff. peak/hole / e Å^{-3}	0.08/-0.18	0.08/-0.08
Flack parameter	0.510(7)	0.214(7)

Chapter 5 – Tuning the Outcome of an Intramolecular Aldol Reaction using Multicomponent MOFs

5.1 Introduction

5.1.1 Intramolecular Reactions in MOFs

Intramolecular reactions are chemical transformations in which only one reactant is required. In this chapter the focus is on intramolecular organic transformations. Like many organic reactions, the use of one or more catalysts may be necessary. These reactions typically proceed at faster rates than their intermolecular counterparts. The presence of a lower number of reactants, causes the order of the reaction to reduce, making reactions faster. A higher effective concentration is achieved, as the reactive sites are located within the same molecule.[307,308] In some cases, these reactions result in the formation of a cyclic product from an acyclic reactant (cyclisation)[309] and vice-versa (ring-opening) (Figure 5.1a and b).[310] In other cases, certain moieties within the reactant rearrange to other positions to give an isomerised product (rearrangement) (Figure 5.1c).[311]

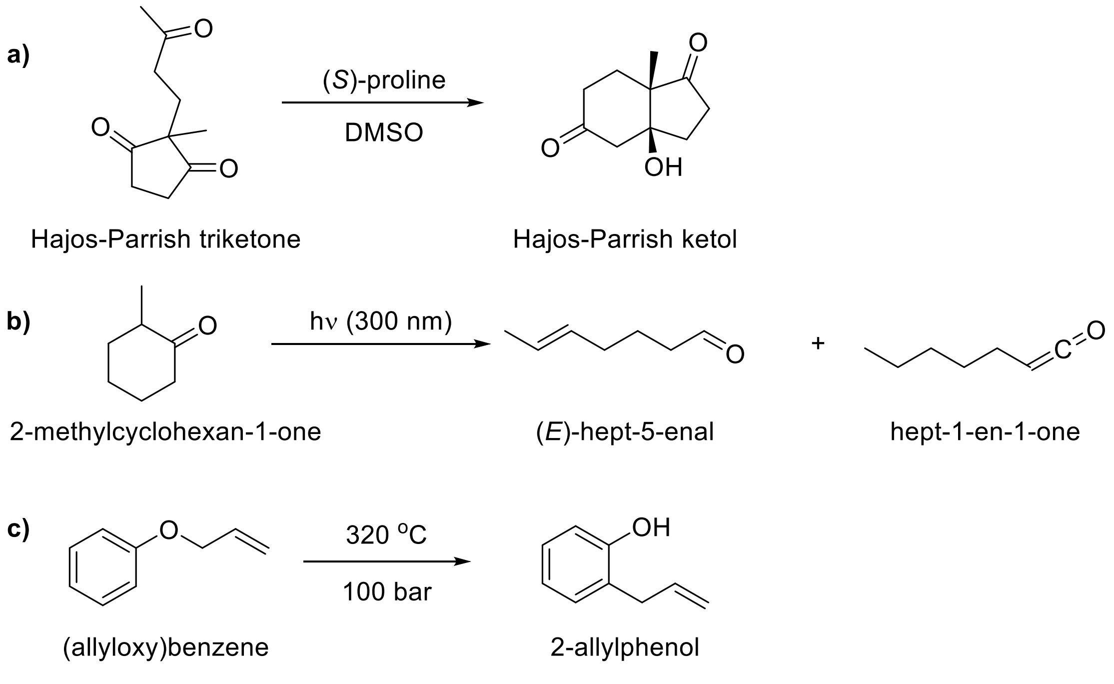

Figure 5.1: Examples of some intramolecular reactions. **a)** Intramolecular aldol reaction of Hajos-Parrish triketone affording a cyclised product.[309] **b)** Photochemical ring opening of 2-methylcyclohexan-1-one.[310] **c)** Claisen rearrangement of allyloxy(benzene).[311]

The use of MOFs for heterogenous catalysis is well-documented with numerous reviews dedicated to the topic.[143-145,312] However, attempts to accelerate intramolecular reactions with MOFs are few. For example: the isomerisation of α-pinene oxide to a mixture of products (campholenic aldehyde, verbenol, and isopinocamphone) was achieved using Lewis acid sites in iron-containing MIL-100, MIL-88B, MIL-88C, and MIL-127 (Figure 5.1a). Due to the lack of chiral centres in the catalysts, no enantiomeric excess was reported.[313] In another study, the use of Lewis acid sites in UiO-66 with substituted linkers containing electron withdrawing groups such as nitro, chloro, and fluoro was observed to strongly influence the cyclisation of (+)-citronellal (Figure 5.1b).[314] A single-site zinc catalyst supported on bipyridine linker containing UiO-66 gave very high yields for the intramolecular hydroamination of o-alkynylanilines (Figure 5.1c).[315] Through this survey, it follows that the use MOFs with organocatalytic ligands for intramolecular transformations is uncommon.

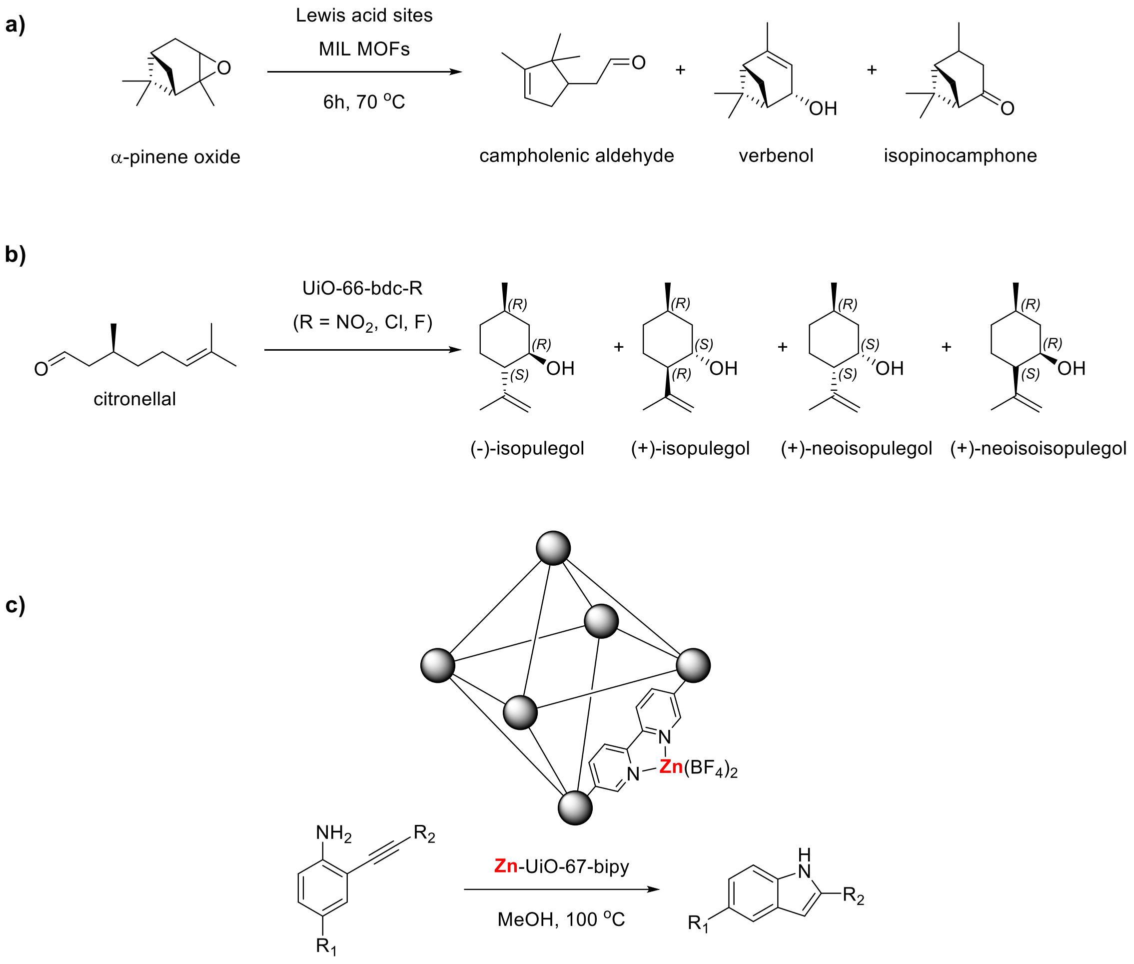

Figure 5.2: Examples of intramolecular reactions catalysed with MOFs **a)** ring-opening of α-pinene oxide **b)** cyclisation of citronellal to isopulegol isomers **c)** intramolecular hydroamination of *o*-alkylnylanilines.

Organocatalysts are vastly functionalisable for optimising catalytic outcomes. Unlike Lewis acid site catalysts, chiral centres can be incorporated into organocatalysts and enantioselectivity can be explored. This is tremendously useful in the synthesis of natural products and drugs, many of which contain chiral centres with only one enantiomer being biologically active.[316]

The incorporation of organocatalysts into the porous and rigid MOFs have advantages in that the pore environment can be programmed to tune the catalytic outcome of organic reactions.[142,249,317] Many papers reporting catalysis in MOFs use multivariate MOFs resulting in a degree of randomness in the distribution of functional groups within the MOF.[58,61] This makes the MOF pore environments dissimilar making it challenging to establish structure-activity relationships.[60]

Unlike multivariate MOFs, multicomponent MOFs have functional groups at predefined positions depending on their location in the ligand. Utilising multicomponent MOFs such as MUF-7, MUF-77, and MUF-777 has added benefits in that catalysts can be appended to specific ligands and precisely positioned in the framework (Figure 5.2).[175,318] Additionally, modulator groups placed remote from the catalytic site can enable non-covalent interactions and impact the outcome of reaction. Such an array of rationally designed catalysts and modulators can form microenvironments within the MOF pores which can also enable selectivity in organic transformations.[176] This feature has been realised in selecting the intermolecular aldol reaction of *m*-nitrobenzaldehyde and acetone over the Henry reaction of *m*-nitrobenzaldehyde and nitromethane. However, for all the applications that have come with these multicomponent MOFs, they have not yet been used for catalysing intramolecular reactions. This chapter aims to utilise MUF-77 for accelerating and tuning this specific class of reactions.

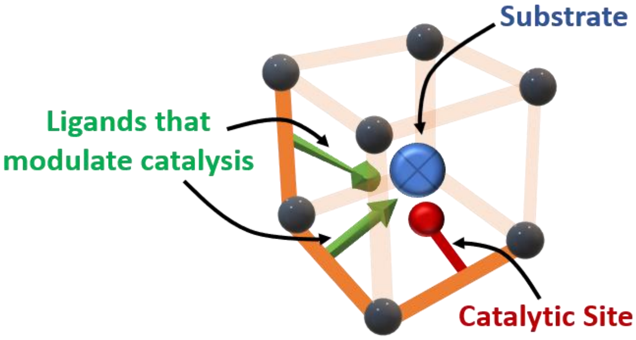

Figure 5.3: Cartoon image showing pore-programming in MOFs which can enable the tuning of reaction outcome. Metal clusters are shown as black spheres and linkers as orange rods.

Intramolecular variants of named organic reactions are well-known.[319,320] The intramolecular version of the aldol reaction is particularly interesting as it can form chiral cyclic products, the relative quantities of which can be controlled by careful choice of catalyst.[321-323] There are two types of intramolecular aldol reactions namely enolexo and enolendo aldol reactions. Both types have been well studied over the years;[324] Baldwin in 1977 formulated a set of rules to predict the size of the rings to be formed.[325] The basis for these rules lies in the ease of formation of the transition state for the reaction. Based on the structure of the reactants, if large bond angle changes or distance distortions are required for achieving a transition state, then it is disfavoured.[326] The difference in these reactions is illustrated in Figure 5.4**.** For the enolendo reaction, the bond broken is inside of the newly formed ring; on the contrary, the enolexo mechanism involves the breaking of the bond outside the newly formed ring.

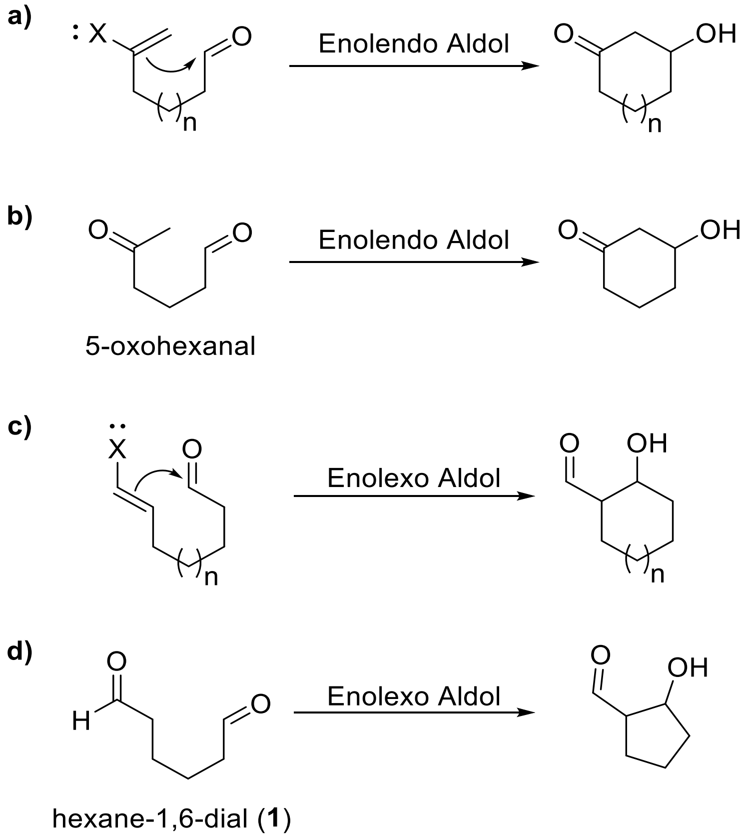

Figure 5.4: a) General scheme of the enolendo aldol reaction with **b)** reaction of 5-oxohexanal as an example. **c)** General scheme of the enolexo aldol reaction with **d)** reaction of hexane-1,6-dial as an example.

5.2 Results and Discussion

5.2.1 Optimising reaction and characterisation conditions

For studying the enolexo aldol reaction of dialdehydes, we chose the conversion of hexane-1,6-dial also called adipaldehyde (**1**) to 2-hydroxycyclopentane-1-carbaldehyde (**2**) catalysed by (*S*)-proline (Scheme 5.1). This reaction reported by List and co-workers was the first catalytic, asymmetric enolexo cyclisation.[327] Though this reaction was first reported in 2003, further work on it was scarce with only two more publications in the literature.[324,328] Based on the classification formulated by Baldwin's rules, the reaction is a 5-*exo*-trig type, meaning that the newly formed ring has five carbon atoms, the bond broken during ring formation is outside (*exo*) the newly formed ring, and the hybridisation at the ring closure point is sp^2 i.e. trigonal.[327]

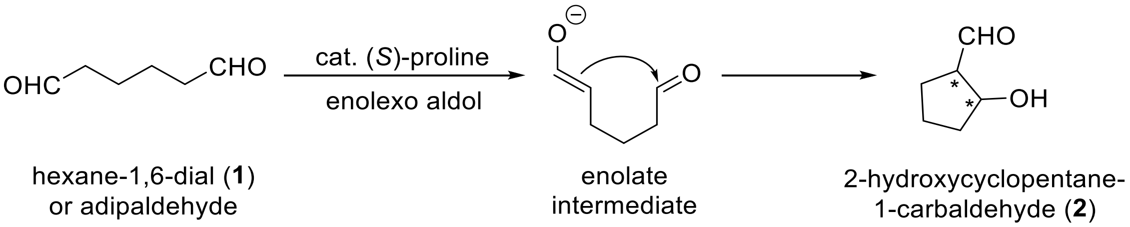

Scheme 5.1: Enolexo aldol reaction of 1,6-hexanedial (**1**) to 2-hydroxycyclopentane-1-carbaldehyde (**2**) catalysed by (*S*)-proline. The two chiral centres are shown with asterisks.

We began studying this reaction by using the literature reported catalyst, (*S*)-proline. We dissolved **1** in $CDCl_3$, added 20 mol% (*S*)-proline and monitored the reaction using ^{1}H NMR spectroscopy. Within the first 30 minutes, changes were immediately noticeable. The new peaks that appeared were not of the expected product, **2**. Instead, the peaks matched those of **3**, a product which is formed as a result of dehydration of **2**. One of the goals of this chapter was to modulate the distribution of chiral products for MOF catalysed reactions. The formation of **3** was unfavourable for realising this goal, as this product has no chiral centres. Dehydration also reduces the amount of product **2**, that could be extracted to perform further useful chemistry. All in all, dehydration is unfavourable, and we sought to prevent this phenomenon.

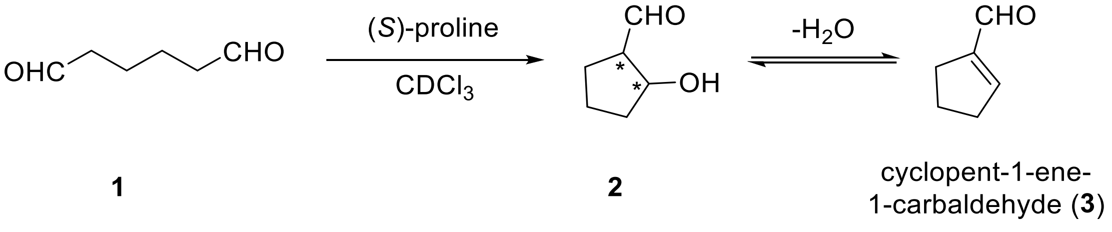

Scheme 5.2: Dehydration of product **2**, giving product **3**. Chiral centres are shown with asterisks. Only **2** has chiral centres and not **3**, making it achiral.

We also screened the catalytic potential of five different esters namely **Me$_2$δ$_2$**, **Meβ**, **Me$_2$q**, **Me$_2$ε** and **Me$_2$ϕ** (Figure 5.5). These esters are precursors to MOF ligands. If they are competent catalysts during screening, they can subsequently be incorporated into MUF-77 and catalysis could be explored. For screening, we used the same conditions as the (*S*)-proline catalysed reaction. However, when the reaction was catalysed by **Me$_2$δ$_2$**, **Meβ**, **Me$_2$q**, and **Me$_2$ε**, we found that these products were also dehydrated. This was frustrating and we suspected that the $CDCl_3$ solvent influenced this dehydration. **Me$_2$ϕ** did not show any catalytic activity.

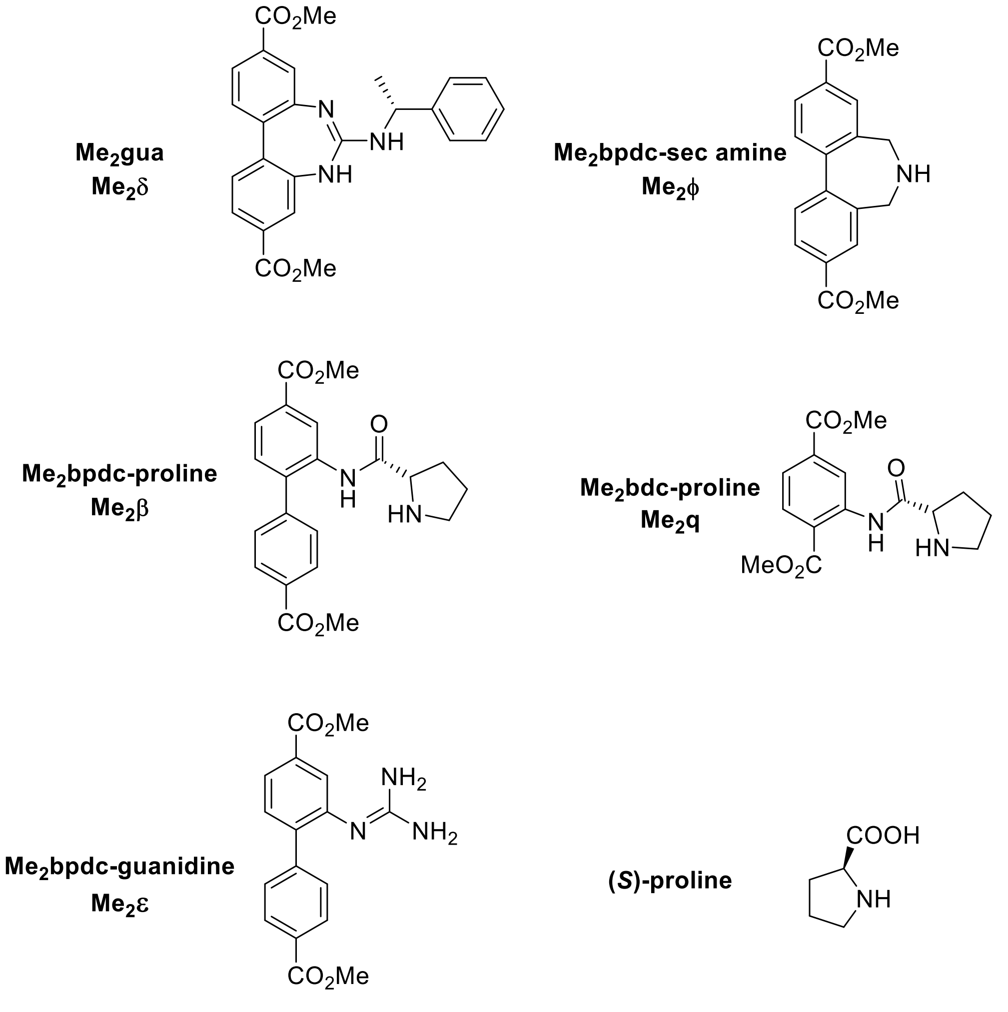

Figure 5.5: The catalysts used for enolexo aldol reaction of **1** in CH_2Cl_2.

Changing the solvent proved helpful as the reaction was also reported to occur in acetonitrile.[324] Using (*S*)-proline as a catalyst, we once again monitored the catalysis with ^{1}H NMR spectroscopy using CD_3CN as a solvent. The formation of *anti* and *syn* diastereomers (**2a** and **2b** in Scheme 5.3) was evident within the first 2 hours and no dehydrated product peaks were seen. After 12 hours, about 90 % of the starting material was consumed, but at this point, the dehydrated product **3** was clearly visible in the ^{1}H NMR spectrum (Figure 5.6). From the NMR integral ratios, an *anti*:*syn* diasteromeric ratio of 1.5:1 could also be determined. We found that about 22 % of the product molecules had undergone dehydration in 12 hours to form **3**. After 48 hours, all products were dehydrated and **3** was the only product. These measurements showed us that the dehydration was much slower in CD_3CN than in $CDCl_3$. This would enable us to quantify the ratios of the four stereoisomers of products **2a** and **2b** using chromatographic techniques.

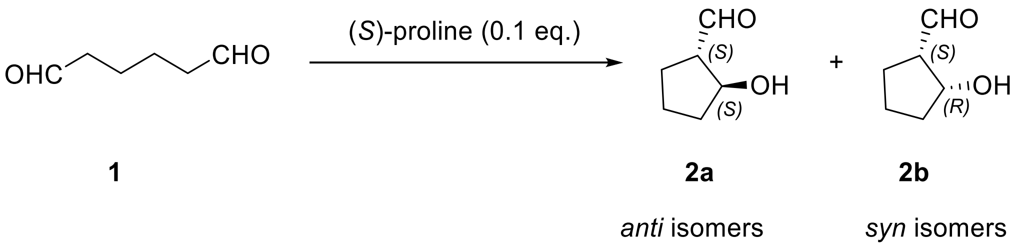

Scheme 5.3: Products **2a** and **2b** were formed for the enolexo reaction of **1**. These were visible in the NMR spectrum when the reaction was performed in CD_3CN, but not visible when performed in $CDCl_3$.

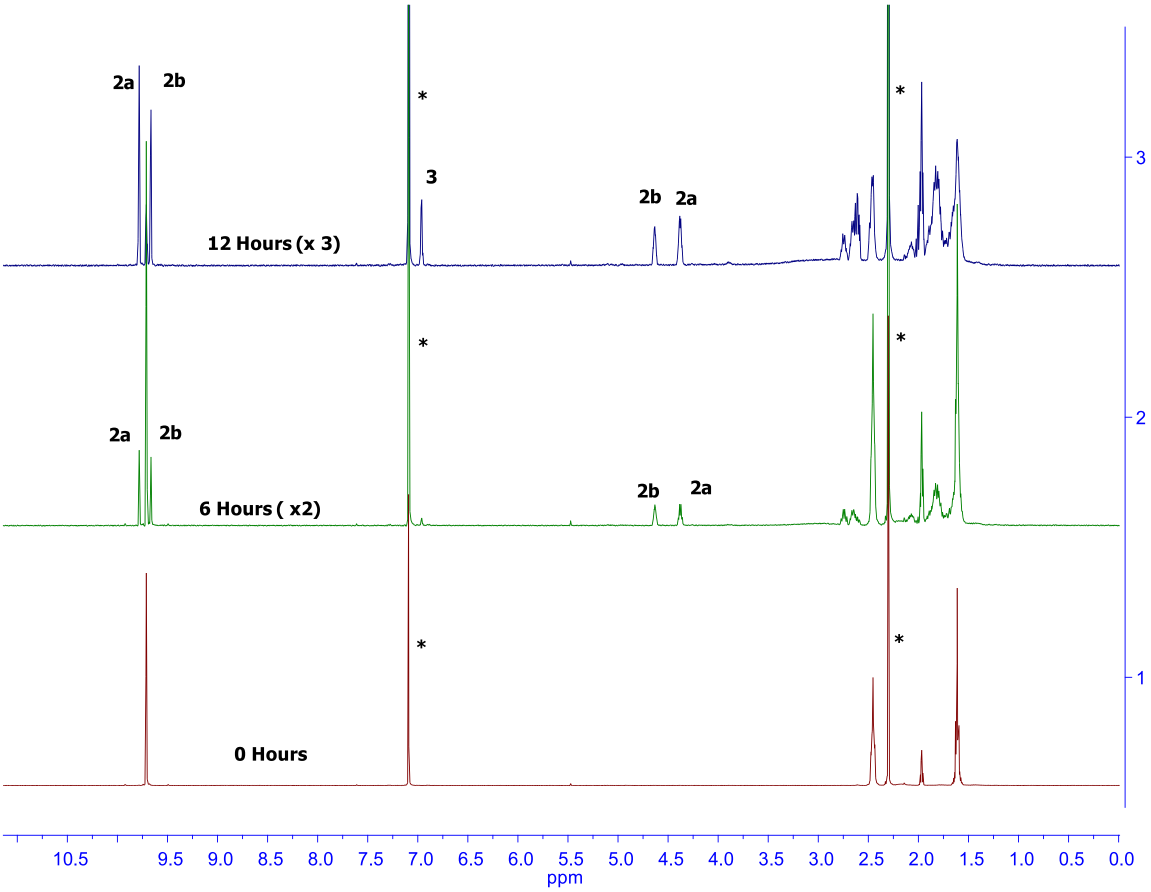

Figure 5.6: ^1H NMR spectra for the (*S*)-proline catalysed enol exocyclisation of **1** in CD_3CN at different time intervals. The peaks for **2a** and **2b** are marked. At 12 hours, the peak from the alkene proton of **3** is visible at 6.9 ppm indicating dehydration. Asterisks indicate peaks of *p*-xylene which was used as an internal standard.

Pidathala et al. used a Horner-Wadsworth-Emmons reaction to derivatise the products and determined the percent enantiomeric excess (% ee) using chiral HPLC.[327] This would be difficult as the derivatisation reaction required inert conditions. Direct analysis by HPLC would be cumbersome, as the products have only weak chromophores. The reaction can also be monitored by 1H NMR spectroscopy, but this technique can differentiate only diastereomers and not enantiomers. As an alternative to both these techniques, chiral gas chromatography (GC) with a flame ionisation detector (FID) was chosen. This method is sensitive, and the absence of chromophores has no effect on signal intensity. The use of a chiral column also makes it possible to quantify other parameters namely, enantiomeric excess (ee) and diastereomeric ratio (d.r.). Here, the enantiomeric excess is the ratio of difference between the amounts of any pair of enantiomers to the sum of their amounts. The diastereomeric ratio is ratio between the total amount of one pair of diastereomers to total amount of the other pair of diastereomers.

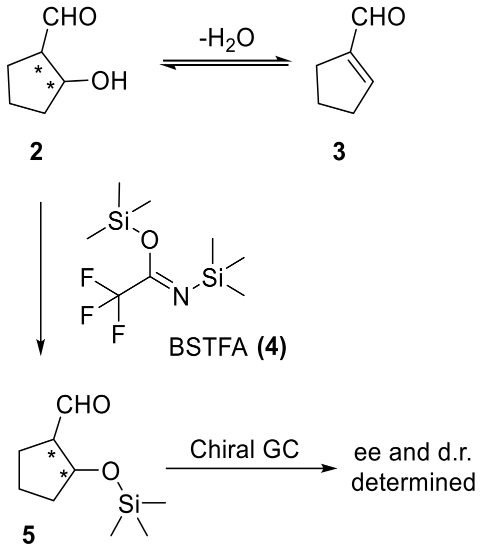

Scheme 5.4: The pathway for analysing the ee and d.r. of the enolexo aldolisation.

GC of the substrate gave a single peak at 14.3 min (Figure 5.7a). This area of this curve is concentration dependent and increases linearly with increase in concentration, enabling us to make a calibration curve (Experimental section, Figure 5.18a). The expected product **2**, has two chiral centres, meaning there are four stereoisomers that could be formed. These include two *anti* enantiomers and two *syn* enantiomers. Unfortunately, chiral GC was not able to separate all these products. Only the *syn* products (**2b**) showed resolved peaks while the *anti* products (**2a**) showed no separation (Figure 5.7b and c). Since, inefficient separation is a fairly common problem in GC analysis, a plethora of derivatising agents are available to overcome this issue.[329] These agents react with a specific functional group of the GC analyte making it more volatile and easily separable. We chose *N*,*O*-bis(trimethylsilyl)trifluoroacetamide (BSTFA, **4**) as the derivatising agent, because it is able to quantitatively react with the hydroxyl group of the products (Scheme 5.4). It is also easy to handle using conventional protocols and does not require inert conditions.

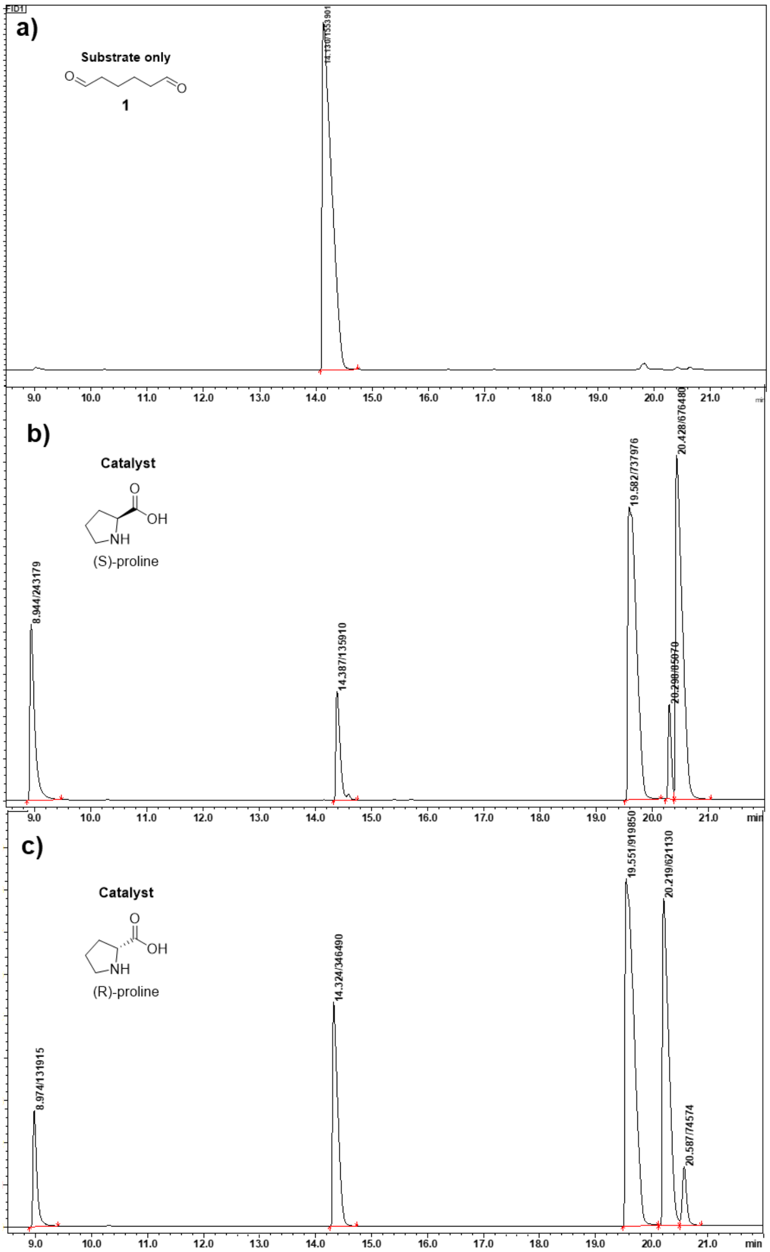

Figure 5.7: a) Gas chromatograms of **1** before reaction. **b)** GC of the enolexo aldolization catalysed by (*S*)-proline with product peaks at 19.7, 20.3 and 20.57 minutes showing sub-optimal separation **c)** GC of the enolexo aldolization catalysed by (*R*)-proline with product peaks at the same retention times. Note that the peaks at 20.3 and 20.6 minutes are of the opposite intensities in comparison to those of **b)** indicating enantiomers. The peak at 8.9 minutes is of the dehydrated product, **3**.

As expected, derivatisation with BSTFA (Experimental section 5.3.3) did help. The four enantiomeric products were separable (Figure 5.8a). To assign the peaks belonging to enantiomers, we used (*R*)-proline instead of (*S*)-proline and performed the same reaction. After derivatisation with BSTFA, the gas chromatogram showed a reversal in the intensities of some peaks, confirming them to be of the enantiomers (Figure 5.8b). For the (*S*)-proline catalysed reaction, the ee and d.r. values were consistent with what was reported in the literature.[324] The use of an achiral catalyst, **Me$_2$ε** gave the peaks of the enantiomers with equal peak areas (Figure 5.8c), as expected for a racemic mixture.

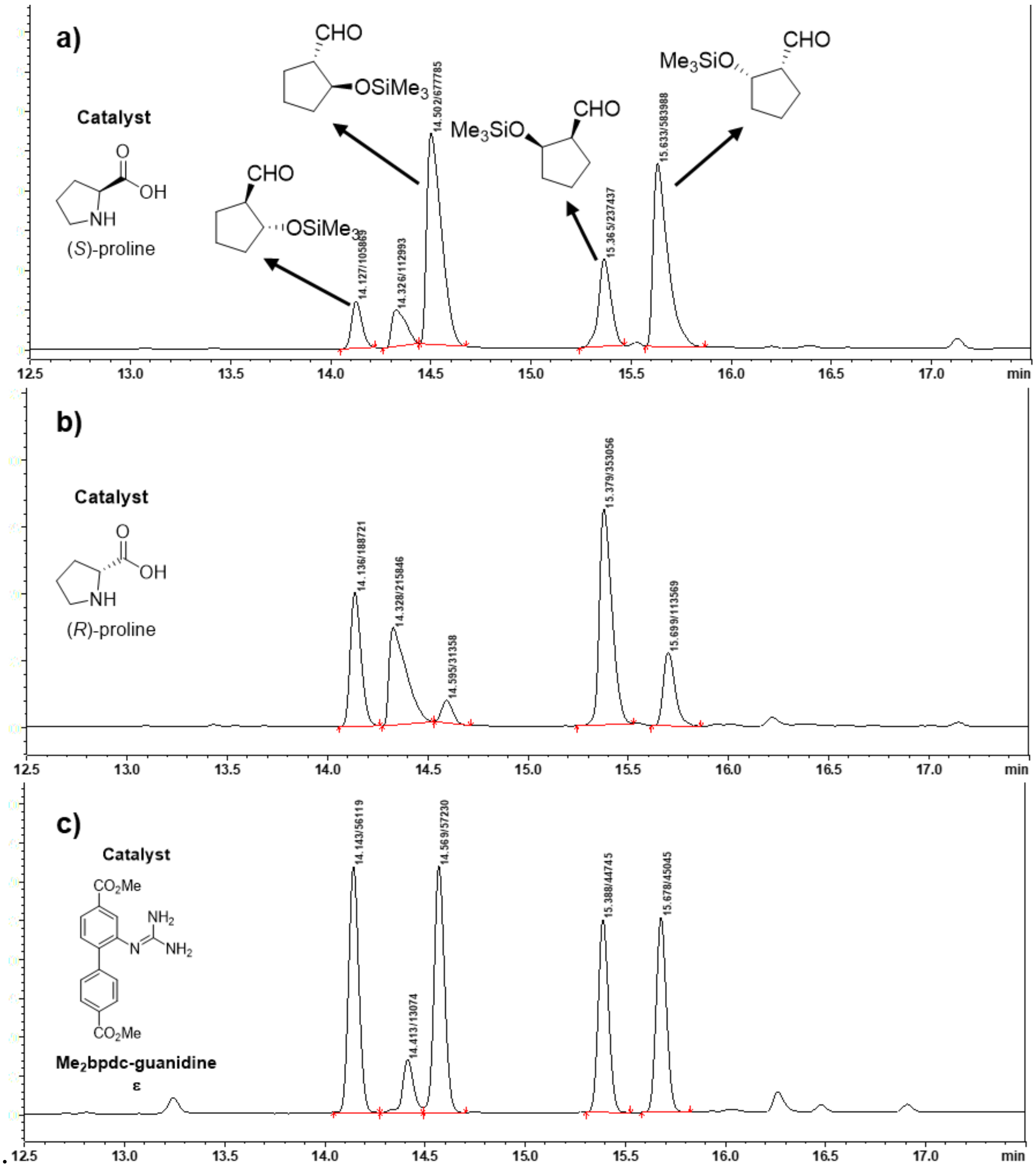

Figure 5.8: Gas chromatograms after 3 hours of enol-exocyclisation of **1** showing peaks of enantiomers after derivatisation with BSTFA (**4**) with unreacted adipaldehyde at 14.3 min **a)** catalysed with (*S*)-proline with the peak assignments mentioned. **b)** catalysed with (*R*)-proline and **c)** catalysed with 20 mol% of achiral catalyst, **Me$_2$ε**.

5.2.2 Quantifying reaction rates and the studying the effect of dehydration

From these GC optimisation experiments, we were able to see peaks for all the products. However, the products lose water to give the achiral product, **3**. The question was, does the dehydration process affect the ee? (Figure 5.9) Among the products (**2a** and **2b**), are some more prone to dehydration than the others or do they all dehydrate similarly? To answer these questions, we collected gas chromatograms for a 10 mol% (*S*)-proline (relative to **1)** catalysed reaction at different time intervals to observe the progress of the reaction. These chromatograms gave us some interesting information.

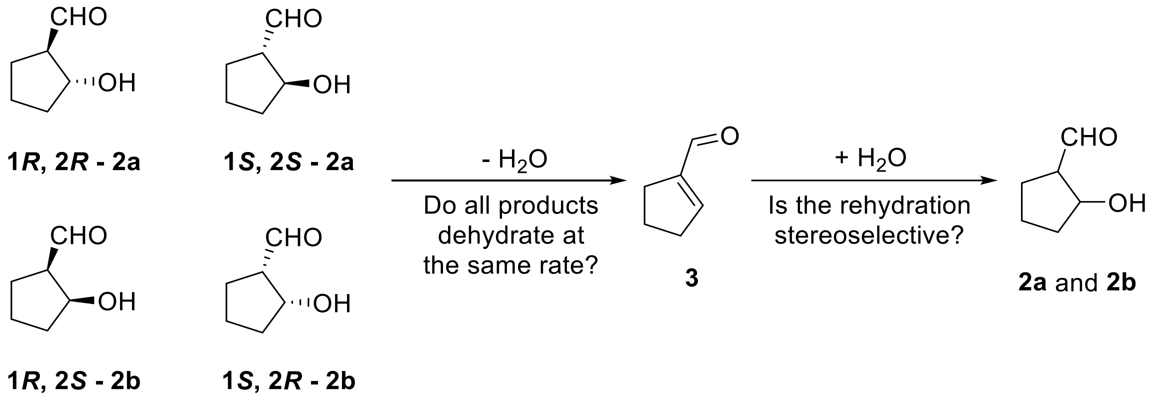

Figure 5.9: Studying the rates of dehydration for products, **2a** and **2b** to identify the effects on the enantiomeric excess.

A straight line was obtained when the reciprocal of adipaldehyde concentration was plotted against time. This means that the consumption of **1**, when catalysed by (*S*)-proline appeared to follow second-order kinetics with respect to **1**. From the slope of this straight line, a rate constant of 5.05 L mol^{-1} min^{-1} was obtained (Figure 5.10a). The second-order kinetics observed are at odds with the known mechanism for intramolecular aldol reactions. Nonetheless, further studies are necessary to understand these kinetics.

On the other hand, a plot of peak area of **3** (Retention Time or RT = 8.9 minutes) over time gave a straight line (Figure 5.10b). This means that the dehydration reaction follows zero-order kinetics in **3**. The *syn* products (**2b**) dehydrate faster than the *anti* products (**2a**) (Figure 5.10c and 5.10d). Among the *syn* products, the product responsible for the peak at 20.6 minutes dehydrates faster than its enantiomer which comes at 20.3 minutes. This indicated that the dehydration may also be (*S*)-proline catalysed (Figure 5.10e).

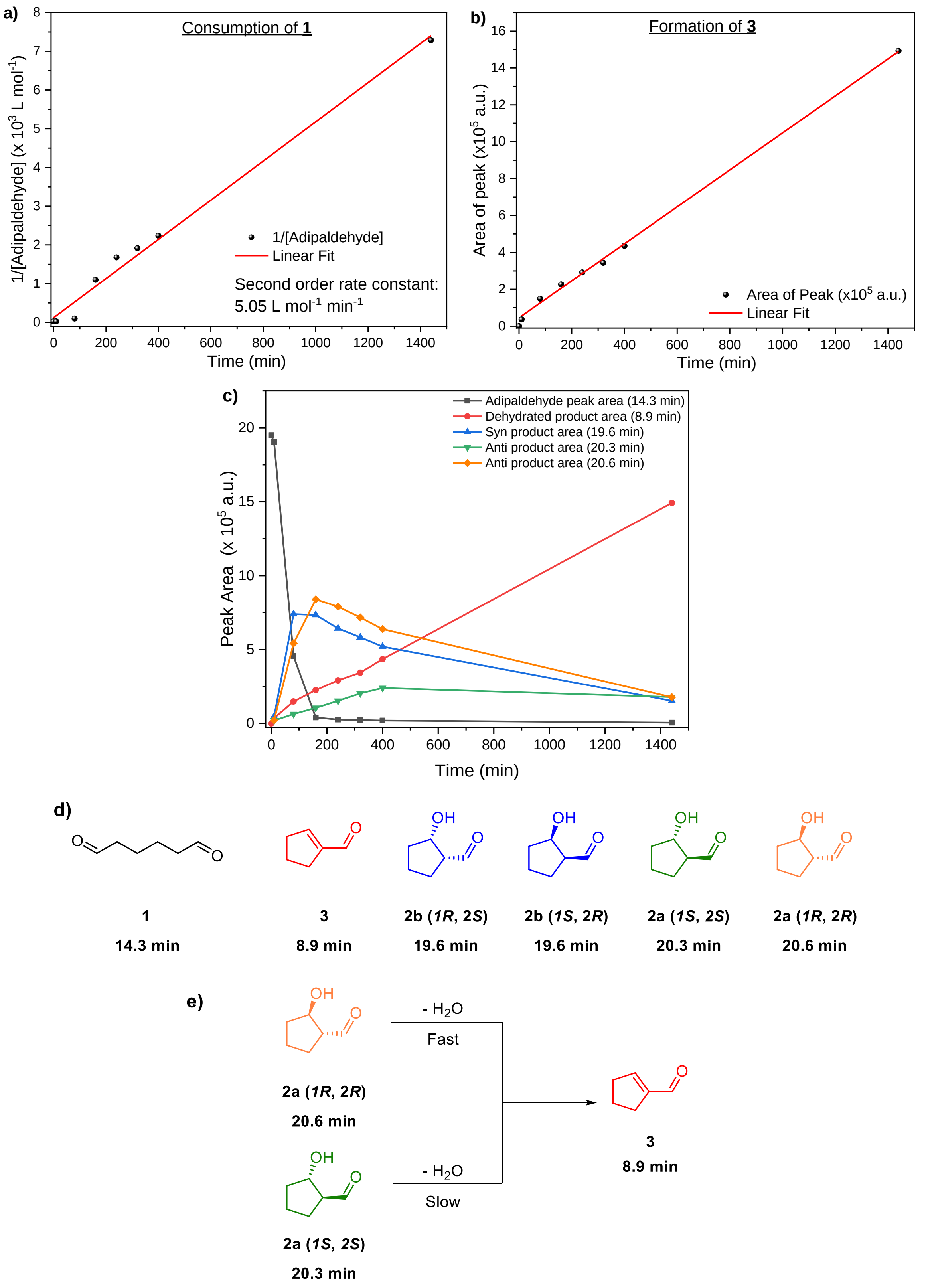

Figure 5.10: a) Graph with reciprocal of adipaldehyde concentration versus time, showing second-order kinetics. **b)** Graph of peak area of dehydrated product (8.9 min) versus time showing zero-order kinetics. **c)** Graph with changes in areas for all peaks seen in gas chromatogram with **d)** showing the structures of the products and their retention times. The colour of the structures matches those in **c)**. **e)** Differences in rates of dehydration brought about by catalysis with (*S*)-proline. Note that the first time point is at 10 minutes for all graphs.

We conducted another experiment, in which we doubled the amount of (*S*)-proline catalyst to 20 mol %. The rate of formation of the dehydrated product doubled in this case. (Experimental section, Figure 5.18b) This was another indicator that (*S*)-proline catalysed the dehydration process.

To further confirm the catalysis of the dehydration, the reaction was repeated with (*R*)-proline as catalyst. Once again, second-order kinetics with respect to **1** were observed, with a comparable rate constant of 1.6 L mol^{-1} min^{-1}, along with zero-order kinetics for the formation of **3** (Experimental section, Figure 5.18b, c). The most important difference was that *syn* products followed dehydration kinetics opposite to that of the (*S*)-proline catalysed reaction (Figure 5.10a). The product appearing at 20.3 minutes dehydrated faster than the product at 20.6 minutes. This was further proof that this reaction was catalysed by proline.

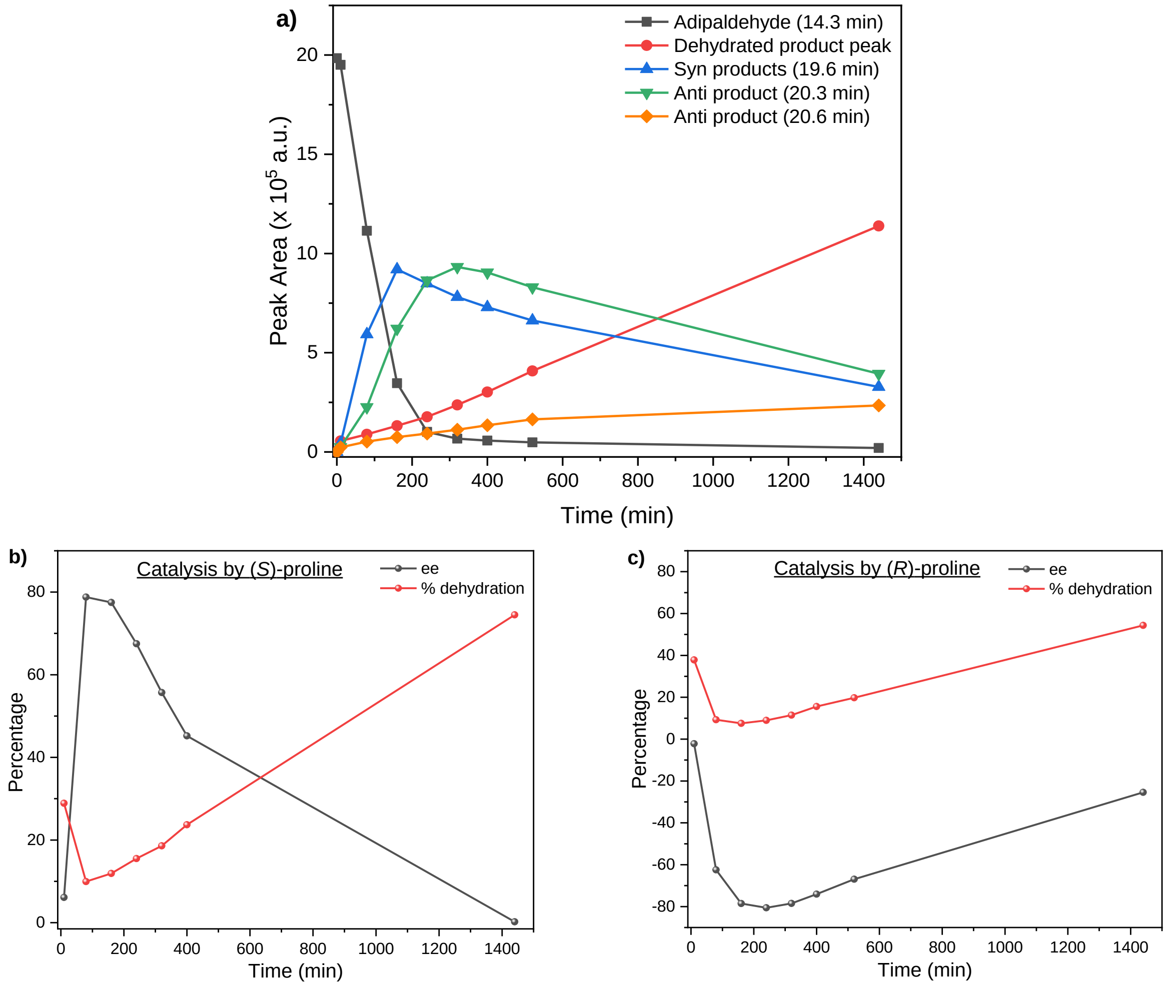

Figure 5.11: a) Plots of GC peak areas versus time for the reaction catalysed by (*R*)-proline. The colours of the lines correspond to the colours of the structures drawn in Figure 5.10**d**. Retention times are shown within brackets. **b)** Comparing changes of % ee of *anti* products and % dehydration versus time for the (*S*)-proline and **c)** (*R*)-proline catalysed reactions, showing a net decrease in % ee with increase in dehydration. Note that the first time point is at 10 minutes for all graphs.

Finally, in both cases an increased amount of dehydration drastically reduces the % ee i.e. dehydration causes racemisation of the products. This is evidenced by plotting the degree of dehydration and % ee of *anti* products versus time (Figure 5.11b and 5.11c). However, if one of the *anti* products dehydrates faster than its enantiomers, shouldn't the ee actually increase? The answer actually lies the fact that dehydration is a reversible process, and the reverse reaction (water addition) is not stereoselective,[330] producing both *anti* enantiomers in equal amounts, thus reducing the ee, resulting the trends seen in Figures 5.11b and c.

5.2.3 Homogenous catalysis

Now that the proper solvent, GC quantification conditions and kinetics of the reaction for (*S*)- and (*R*)-proline were studied, we replicated homogenous catalysis with other available catalysts in CH_3CN. An ideal catalyst for this reaction must consume most of the starting material and dehydrate the products to the least possible degree. High ee values for the *anti* and *syn* products are also desirable. To monitor all these parameters, the percentage consumption and dehydration were both calculated by collecting a gas chromatogram before derivatisation. Once derivatised with BSTFA, GC was performed once again and the *syn* and *anti* ee values were calculated.

Firstly, I tried homogenous catalysis with the prolinamide catalysts bdc-proline (**Me_2q**) and bpdc-proline (**Me_2β**) which showed marked differences in their catalytic performance (Table 5.1). At room temperature, with 10 mol% of catalyst relative to **1**, **Me_2q** showed more than 42% consumption within 6 hours and only about 6.5% of the product molecules formed were dehydrated. Under similar conditions, the consumption of the **Me_2β** catalysed reaction was about 17%, which was less than half the catalytic performance of **Me_2q**. Derivatisation showed roughly similar ee values for the *anti* products for both **Me_2q** and **Me_2β** (39.4 % and 44.0%, respectively).

I then tried catalysis with 10 mol% of the guanidine-based esters **Me_2δ** and **Me_2ε**. The yield for the **Me_2δ** catalysed reaction was very poor. About 2 % of the product was consumed within 24 hours. Increasing the temperature to 45 °C also did not help and the yield was still very low. Due to these factors, I decided not to use **δ** for heterogenous catalysis.

Table 5.1: Homogenous catalysis of the intramolecular aldol reaction of **1**.

Catalyst	**% Consumption (Time)**	**% dehydration**	**% ee(a)**	
			anti	***syn***
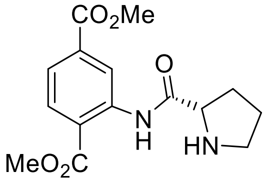 **Me_2q**	42.4 (6 hrs)	6.5	39.5	15.3
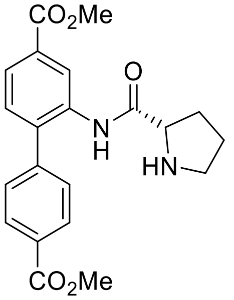 **$Me_2\beta$**	17.2 (6 hrs)	16.9	44.0	8.7
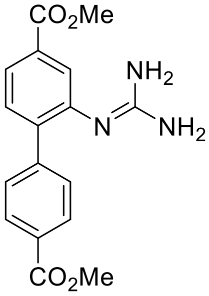 **$Me_2\varepsilon$**	4.0 (24 hrs)	9.4	Achiral catalyst	
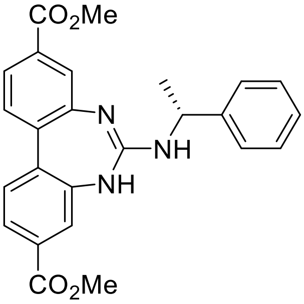 **$Me_2\delta$**	2.0 (24 hrs)	58.1	-(b)	
$Me_2\varepsilon$	39.8 (48 hrs) (c)	7.3	Achiral catalyst	

Notes: Reactions performed at 21 °C with 10 mol% of catalyst with respect to 0.04 M adipaldehyde in acetonitrile. (a) ee was determined in each case as ratio of difference in areas of peaks between the later eluting product and earlier eluting product to their sum of the areas. (b) Derivatisation was not done due to low yield.
(c) Reaction performed at 45 °C.

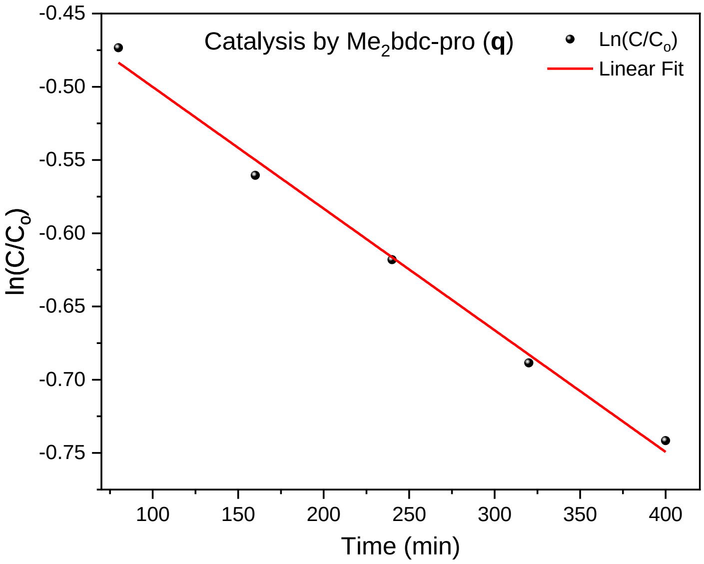

Figure 5.12: First-order kinetics for the consumption of **1** when catalysed by Me$_2$bdc-pro. A rate constant of 8.3 x 10^{-4} L mol^{-1} min^{-1} was obtained. Here C$_o$ and C are concentrations of **1** in the stock solution and measured time, respectively.

Me$_2$ε also proved to be a poor catalyst with only 4 % consumption at room temperature. However, increasing the temperature to 45 °C and doubling the amount of the catalyst to 20 mol% helped a lot. The consumption was boosted to 39.8 %, and only 7.3 % of the product molecules underwent dehydration. We performed kinetics experiments for the catalyst that gave the highest yield in 6 hours i.e. **Me$_2$q**. Gas chromatograms were collected every 80 minutes and parameters similar to the (*S*)-proline kinetics were monitored. The consumption of **1** followed first-order kinetics with respect to **1**, when catalysed by **Me$_2$q**. A plot of ln(C/C$_o$) versus time (C and C$_o$ are concentrations at the measured time and of the stock solution, respectively) gave a straight line (Figure 5.12).

This was very different from the kinetics seen for the (*S*)- and (*R*)-proline catalysed reactions, which followed second-order kinetics. This means that there are major differences in the mechanism for adipaldehyde consumption when promoted by (*S*)- and (*R*)-proline compared to that of the prolinamide ester, **q**. The dehydration reaction followed zero-order kinetics (Experimental section, Figure 5.18e), and was calculated to be 6.5 % which is extremely low compared to (*S*)- and (*R*)-proline. The carboxyl groups of proline may play in promoting dehydration through hydrogen bonding interactions with water. These groups are not present in **Me$_2$q**, thus reducing dehydration to a large extent.

5.2.4 Catalysis with MUF-77 containing bdc-proline ligands

The next step was to replicate catalysis in multicomponent MOFs analogous to MUF-77. The carboxylic acid analogues of the homogenous catalysts (**Me$_2$q**, **Me$_2$β,** and **Me$_2$ε**) were used for MOF synthesis. If the carboxylic acids of **Me$_2$q** and **Me$_2$β** are used directly to make MUF-77, they may coordinate to the zinc ions during MOF formation, giving undesirable phases. Protonation or deprotonation of this site may also occur, rendering the catalyst inactive.[163] Hence, for **q** and **β**, the -NH group on the pyrrolidine moiety was protected by *tert*-butyloxycarbonyl (boc) groups (Scheme 5.5 and 5.6). Four different phase-pure MUF-77-bdc-pro-boc systems were obtained each with an increasing length of alkyl chain on the tritopic linker. Removal of the boc group was achieved by heating dried crystals under a dynamic vacuum at 220 °C for 20 hours.[175] This afforded four different frameworks of MUF-77-bdc-pro, with the prolinyl-NH groups available for catalysis.

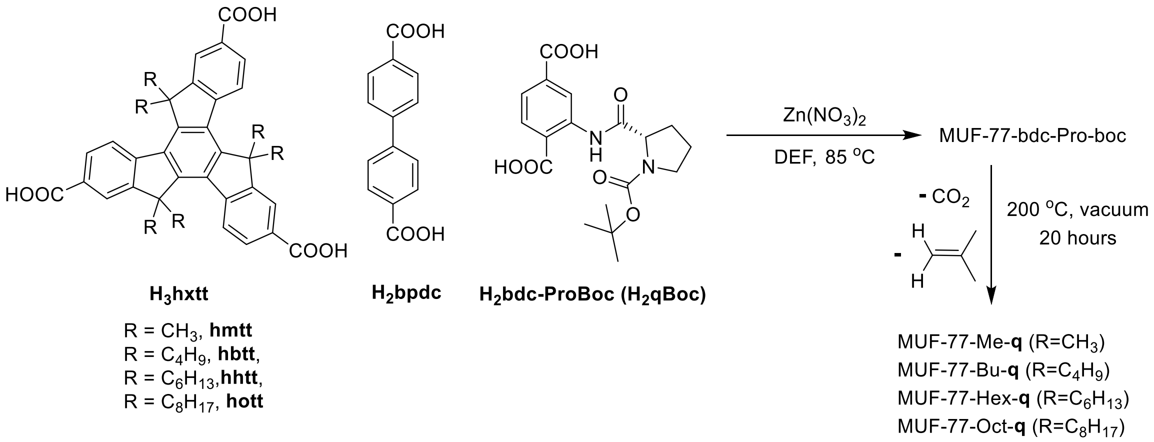

Scheme 5.5: Solvothermal synthesis of MUF-77 with bdc-proline (**q**) catalysts.

Using a weight of MUF-77 crystals corresponding to 10 mol % of proline units with respect to adipaldehyde, catalysis was carried out at room temperature for 6 hours. GC was first performed without BSTFA derivatisation to determine the amount of starting material consumed. The crystals were removed using a syringe filter and the filtrate was treated with BSTFA (**4**) and a second gas chromatogram was obtained to calculate the % ee. PXRD patterns of the MUF-77 crystals were analysed before and after catalysis. The patterns were indistinguishable, indicating that the crystal structure was maintained throughout catalysis (Experimental section, Figure 5.19). Additionally, the crystals did not show any cracks when seen under a microscope (Experimental section, Figure 5.22). For each MUF-77 system, three trials were performed, and the results were consistent with each other.

We first carried out some control experiments: in the first case we did not add any catalyst or MOF. For the second case, we used parent MUF-77-Oct which did not have any catalytic groups as the ligands were unfunctionalized. The third control was using MUF-77-Oct-**q**-Boc. All these three controls showed only a minor change in the peak area of **1** in the GC. The controls proved a few key things a) that a catalyst is required for the aldol transformation, as the stock solution itself shows a minor change, b) the reaction does not occur on the external surface or on any defect sites of the MOF, as MUF-77-Oct did not show any product peaks, and c) the reaction requires free imine groups to proceed, as the framework with boc protected prolinyl-NH sites i.e. MUF-77-Oct-**q**-Boc was also not catalytically active.

All the other frameworks with free prolinyl-NH sites were catalytically active (Table 5.2, Table 5.7, and Figure 5.10). The pore environments in all these MUF-77-**q** systems are unique and are flanked by the same prolinamide catalyst but differing alkyl groups. Reports in the literature have proven that programming the pore can impact the outcome of the catalysis.[175,331] The results of the catalysis for enol-exocyclisation agree with these published observations.

Table 5.2: Comparison of homogenous and heterogenous catalysis of the intramolecular aldol reaction of adipaldehyde with MUF-77 systems containing bdc-proline catalyst.

Framework	**Ligand combination**	**Consumption (%)$^{(a)}$**	**% dehydration**	**% ee$^{(a)(b)}$**	
				anti	***syn***
-	No catalyst	< 2 %$^{(b)}$	-	-	-
-	(*S*)-proline	> 99	32.0	36.4	7.1
-	Me$_2$bdc-pro (**Me$_2$q**)	42.4	6.5	39.5	15.3
MUF-77-Oct	hott/bpdc/bdc	< 2 %$^{(c)}$	-	-	-
MUF-77-Oct-**q**-Boc	hott/bpdc/ bdc-proBoc	< 2%$^{(c)}$	-	-	-
MUF-77-Me-**q**	hmtt/bpdc/bdc-pro	52.2	16.1	50.2	-0.3
MUF-77-Bu-**q**	hbtt/bpdc/bdc-pro	72.9	29.5	35.9	-1.5
MUF-77-Hex-**q**	hhtt/bpdc/bdc-pro	80.2	27.6	36.2	-0.7
MUF-77-Oct-**q**	hott/bpdc/bdc-pro	80.6	55.7	25.3	-2.6

Notes: Reactions performed at 21 °C with 10 mol% of catalyst (a) Refer Table 5.7 for associated errors. (b) ee was determined in each case as ratio of difference in areas of peaks between the later eluting product and earlier eluting product to the sum of their areas. (c) Substrate undergoes oxidation.

Catalysis with the MUF-77-bdc-Pro frameworks showed some interesting trends. The homogenous analogue these MUF-77 systems, Me$_2$**q** consumes 42.4 % of the available adipaldehyde into products within 6 hours. However, on a per proline basis, all the MUF-77 systems are more active than Me$_2$**q**. In some cases, such as MUF-77-Hex-**q** and MUF-77-Oct-**q**, they are about twice as active (Table 5.2). Overall, this means that upon heterogenisation into MUF-77, **q** not only retains its catalytic activity but shows improved performance. The high rate of consumption within 6 hours also means that the substrate can easily diffuse into the pores and interact with the catalytic moiety. This is one of the advantages of using a programmed catalytic microenvironment such as the pores in MUF-77 systems.

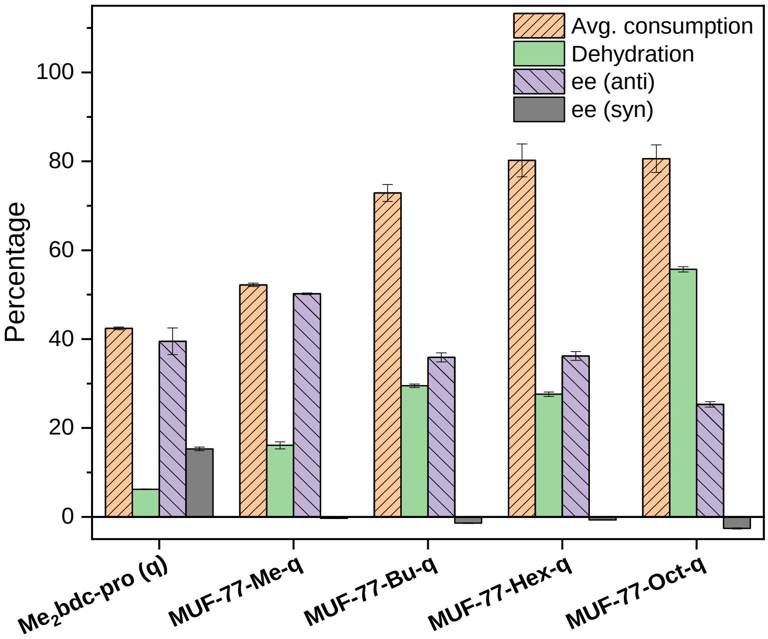

Figure 5.13: Bar diagram comparing heterogenous catalysis with different MUF-77-bdc-pro systems. The ligand combinations are shown along the horizontal axis.

As the length of the alkyl chain increases, differences in all parameters i.e. consumption, the degree of dehydration and % ee are seen (Table 5.2 and Figure 5.13). These alkyl groups are located remote from the catalytic unit and should play little to no role in determining the catalytic outcome. This was, however, not the case. MUF-77-Me-**q** with methyl groups on the truxene linker shows the least consumption (52.2 %) and dehydration, while MUF-77-Oct-**q** with octyl groups shows more than 80 % consumption. It is evident that the consumption of **1** increases as the length of the alkyl chains increases, peaking at MUF-77-Hex-**q** and MUF-77-Oct-**q**. However, the products formed when catalysed by MUF-77-Oct-**q** are more dehydrated when compared to the others (55.7 % vs 25-30%).

The *syn* products, however showed very low % ee (> -5%). Homogenous catalysis with **Me$_2$q** gives a much higher % ee of 15.3 %. We have seen from the kinetic studies with (*S*)-

proline that the *syn* products dehydrate earlier and faster than the *anti* products and this low ee value can be attributed to these kinetic differences. Additionally, these % ee values are low enough to be caused by instrumental errors, as similar values were obtained with the achiral catalyst, **ε**.

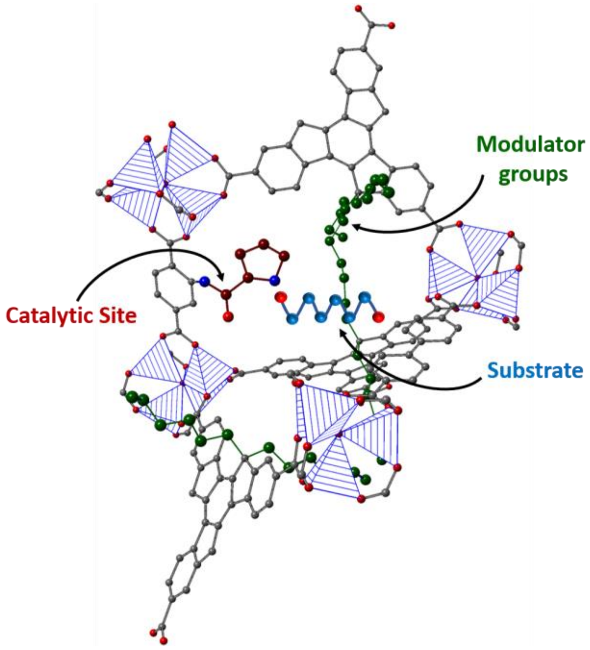

Figure 5.14: A schematic of the catalytic pocket in MUF-77-Hex-**q.** Hexyl chains which serve as modulator groups are shown in green. Zn atoms are shown as striped tetrahedra.

These patterns for intramolecular catalysis could be elucidated by taking considering the pore volumes of these systems. Liu et al. had observed that with increase in the alkyl chain length, a pore size reduction was observed.[78] This is reasonable as the bulkier alkyl groups fill the pore compared to the less bulky ones. This causes the pore volume to reduce from 1.85 cm^3/g for MUF-77-Me to 0.65 cm^3/g for MUF-77-Octyl, respectively. However, these MUF-77 frameworks were made of unfunctionalized bdc and bpdc ligands. Subsequent measurements have shown that these pore volumes are comparable to MUF-77-Me-**q**, where the unfunctionalised bdc ligands are replaced with bdc-pro.[176]

By building on these published results, we tentatively ascribe the trends observed for the MUF-77-catalysed enolexo cyclisation of **1** to the formation of favourable contacts with the modulating alkyl groups on the truxene linkers (Figure 5.14). For MUF-77-Bu-**q**, MUF-77-Hex-**q** and MUF-77-Oct-**q**, the alkyl groups are long enough to work in tandem with the catalytic unit to transform adipaldehyde into products. This is further aided by smaller pore volumes in these MOFs, effectively concentrating the reaction participants in the pore. On the other hand, MUF-77-Me-**q** possesses larger pores with shorter methyl groups reducing the formation of favourable contacts, and hence is less efficient as a catalyst.

An important property of catalysts is their recyclability. Are MUF-77 systems recyclable? PXRD measurements do not show any loss in their crystallinity, but do they lose their efficacy when used for catalysis multiple times? To answer all these questions, we reused the crystals of MUF-77-Bu-**q** and MUF-77-Oct-**q** for catalysis, but this time collected gas chromatograms every 80 minutes, helping us determine kinetic parameters. No loss in catalytic activity was observed. After 400 minutes (6 hours and 40 minutes), similar values were obtained for consumption, degree of dehydration. Additionally, the % ee values for the *anti* products were also similar. This was an excellent indicator that these MUF-77 catalysts were recyclable.

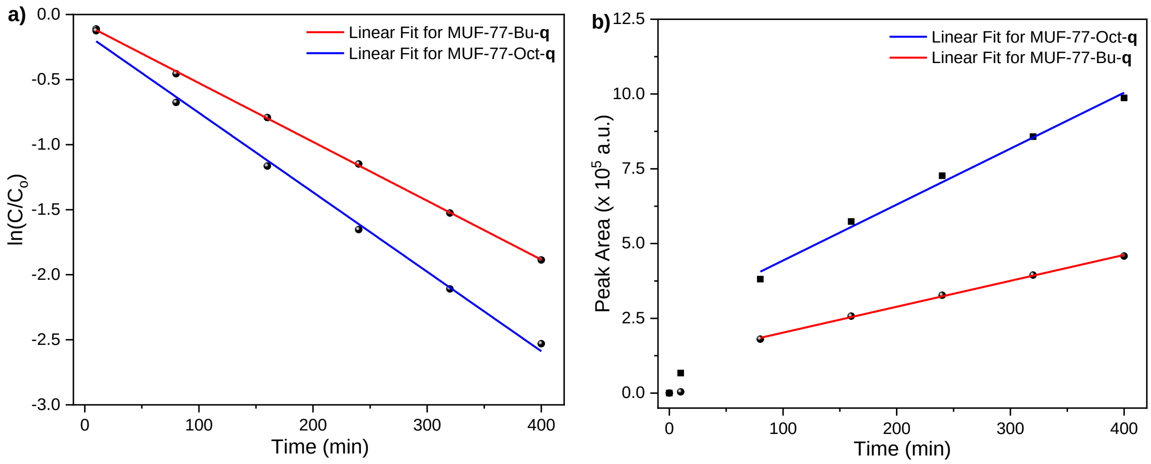

Figure 5.15: a) First-order kinetics for the consumption of **1** catalysed by MUF-77-Bu-**q** and MUF-77-Oct-**q**. Here C and C_o are concentrations of **1** at the measured time and stock solution, respectively. **b)** Zero-order kinetics of the dehydration reaction catalysed by MUF-77-Bu-**q** and MUF-77-Oct-**q**. Note that the first time point is at 10 minutes for all graphs.

Since chromatograms were collected at regular time intervals, kinetics parameters could be calculated. Both MUF-77-Bu-**q** and MUF-77-Oct-**q** gave first-order kinetics for the consumption of **1**, and product dehydration followed zero-order kinetics (Figure 5.15a and b). These patterns are similar to the homogenous catalyst Me_2bdc-pro. This means that the mechanism for catalysis for Me_2bdc-pro and MUF-77-**q** are analogous but are dissimilar to that of (*S*)- or (*R*)-proline.

The rate constants between homogenous and heterogenous catalysts show major differences. From Figure 5.15 and Table 5.3, it is evident that both MUF-77 systems fare better as catalysts for the intramolecular reaction than the homogenous catalyst. In fact, the rate constant for MUF-77-Oct-**q** is about 7.3 times higher than that of **Me₂q**. These rates are roughly similar for the MUF-77 catalysts. However, MUF-77-Oct-**q** dehydrates the product twice as fast as MUF-77-Bu-**q**. This is interesting, as both these catalysts contain the same active moiety, and have the comparable consumption rate constants, but very different dehydration rate constants. The pore environments within these frameworks are different and this is likely to a key factor in causing these differences. In MUF-77-Bu-**q**, the products are stabilised by favourable contacts with the butyl groups of the hbtt linkers and thus dehydrate slowly. Similar favourable contacts are less likely in MUF-77-Oct-**q** and the products are highly prone to dehydration. These kinetics experiments give further proof that programming the pores in a MOF can stabilise the products and affect the ultimate outcome of the reaction.

Table 5.3: Comparing rate constants for homogenous versus MUF-77 catalysed reactions.

Catalyst	Rate constant for consumption of 1 (L mol^{-1} min^{-1})	Rate constant for dehydration (a.u.$^{-1}$ min^{-1})
Me_2bdc-pro (**Me_2q**)	$8.3 \times 10^{-4} \pm 4.0 \times 10^{-5}$	82 ± 6
MUF-77-Bu-**q**	$4.5 \times 10^{-3} \pm 3.7 \times 10^{-5}$	866 ± 17
MUF-77-Oct-**q**	$6.1 \times 10^{-3} \pm 1.8 \times 10^{-4}$	1870 ± 95

Another possible contributor is the dipole moment of the products. The calculated dipole moments (using Avogadro)[332] for the products **2a** and **2b** was 2.9 debye and that of **3** was 2.1 debye. This indicates that **2a** and **2b** were more polar than **3**. In MUF-77-Oct-**q**, the environment inside the pore is likely to be less polar due to the octyl chains and hence the equilibrium shifts towards dehydration i.e. the less polar molecule, **3** is produced. On the other hand, the pores of MUF-77-Bu-**q** stabilise the more polar products **2a** and **2b**, thus reducing dehydration.

5.2.5 Catalysis with MUF-77 containing bpdc-pro ligands

MUF-77-**β** frameworks with bpdc-proline catalysts were synthesised, using solvothermal synthesis and high temperature boc deprotection (Scheme 5.6). Heterogenous catalysis was carried out mimicking the same set of conditions of 10 mol% of catalyst loading to 0.04 M of adipaldehyde. All frameworks showed catalytic activity, to varying levels even though their catalytic moiety was the same. Once again, the frameworks retained their crystallinity after catalysis as evidenced by unchanged PXRD patterns and optical microscopy images (Experimental section, Figure 5.20 and Figure 5.23)

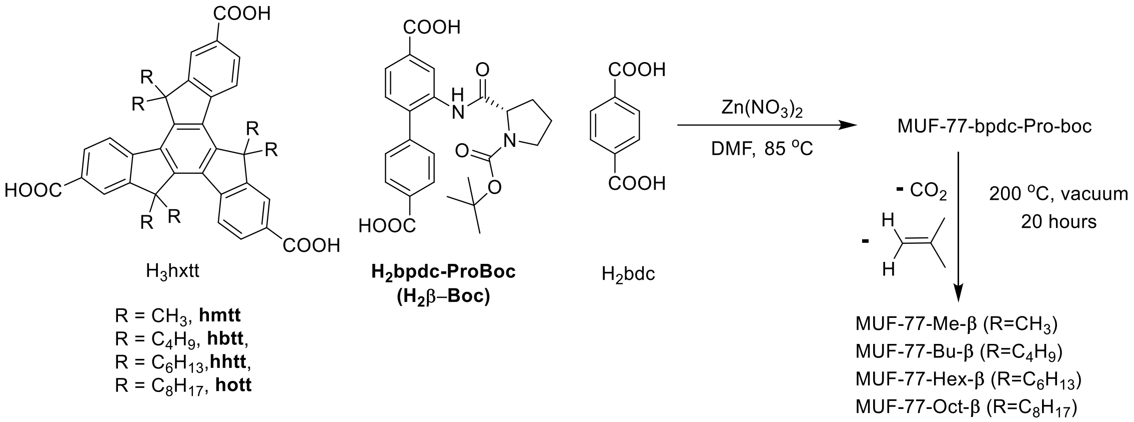

Scheme 5.6: Solvothermal synthesis of MUF-77 with bpdc-proline (**β**) catalysts.

For each MUF-77-**β** system, the consumption is much lower than (*S*)-proline but comparable to that of Me$_2$**β** (Table 5.4, Table 5.7, and Figure 5.16). To reiterate, this means that heterogenisation of Me$_2$**β** into MUF-77 does not affect its catalytic ability but indeed improves it. In fact, in all cases the consumption is higher than Me$_2$bpdc-pro, indicating unhindered diffusion of adipaldehyde into the MOF pores. For MUF-77-Bu-**β** and MUF-77-Oct-**β**, the consumption was 43.6 % and 44.5 %, respectively. These values exceed the consumption of Me$_2$**β** by two times.

Product dehydration is higher than the Me$_2$bpdc-pro catalysed reaction compared to that of MUF-77-Me-**β** and MUF-77-Oct-**β**. The former shows the highest dehydration among the MUF-77-**β** catalysts at 42.1 %. The other frameworks dehydrate the products to a much lower amount. This also means that these frameworks fare better than (*S*)-proline with regard to dehydration. Though MUF-77-Oct-**β** shows the highest consumption, its ee for the *anti* products is the least at 10.3 %. The other frameworks with shorter alkyl chains have this value about three times (MUF-77-Me-**β**) or about four times (MUF-77-Bu-**β** and MUF-77-Hex-**β**) than MUF-77-Oct-**β**. Both these high performing catalysts have a higher ee than (*S*)-proline. The trends seen among MUF-77-**β** catalysts are not as straightforward as MUF-77-**q** catalysts. More complicated non-covalent interactions are at play and is the subject of further investigation.

Table 5.4: Heterogenous catalysis of the intramolecular aldol reaction of adipaldehyde with MUF-77 systems containing bpdc-proline (**β**) catalyst.

Framework	**Ligands or catalyst**	**Consumption (%)$^{(a)}$**	**% dehydration**	**% ee$^{(b)}$**	
				anti	***syn***
-	(*S*)-proline	> 99	32.0	36.4	7.1
-	Me$_2$bpdc-pro (**Me$_2$β**)	17.2	16.9	44.0	8.7
MUF-77-Oct-**β**-Boc	hmtt/bpdc-proBoc/bdc	< 2%$^{(c)}$	-	-	-
MUF-77-Me-**β**	hmtt/bpdc-pro/bdc	19.8	42.1	30.7	3.0
MUF-77-Bu-**β**	hbtt/bpdc-pro/bdc	43.6	11.4	39.2	12.2
MUF-77-Hex-**β**	hhtt/bpdc-pro/bdc	27.7	15.8	39.3	8.0
MUF-77-Oct-**β**	hott/bpdc-pro/bdc	44.5	29.0	10.3	3.6

Notes: Reactions performed at 21 °C with 10 mol% of catalyst (a) Refer Table 5.7 for associated errors. (b) ee was determined in each case as ratio of difference in areas of peaks between the later eluting product and earlier eluting product to the sum of their areas. (c) Substrate undergoes oxidation.

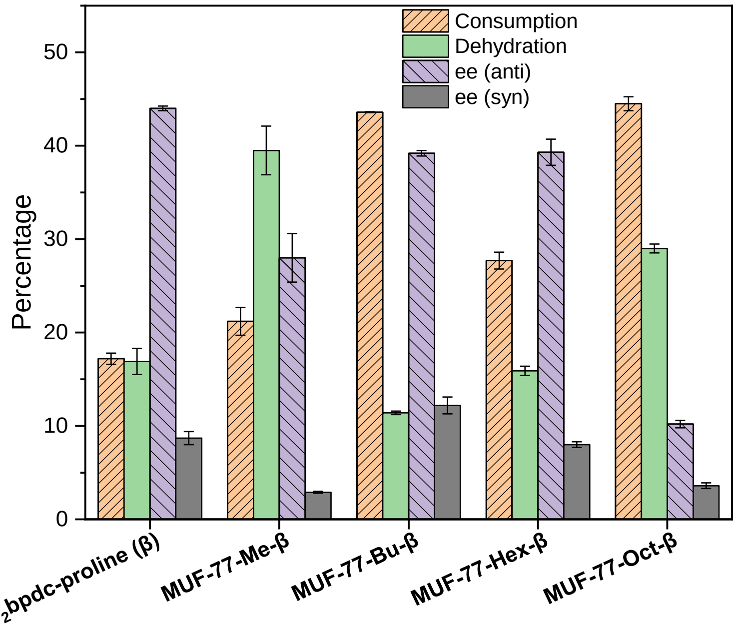

Figure 5.16: A comparison of homogenous and heterogenous catalysis of the intramolecular aldol reaction with MUF-77-**β** frameworks.

An interesting thing to notice for catalysis with MUF-77-**β** is the reversal in the enantioselectivity of *syn* product when compared to MUF-77-**q** catalysts. This is similar to the observations reported for intermolecular aldol reaction of *p*-nitrobenzaldehyde with MUF-77.[175] Experiments to understand this ee reversal behaviour are underway. We suspect that the thermolytic expulsion of the boc groups affects the ultimate chirality of the deprotected framework. Experiments are underway in which nanocrystalline versions of MUF-77-**q** and MUF-77-**β** are to be made. Circular dichroism spectra will be measured for these nanocrystals before thermolysis and at regular intervals of the 20-hour heating period. These spectra would further inform about the suspected racemisation process.

5.2.6 Catalysis with MUF-77 containing bpdc-guanidine ligands

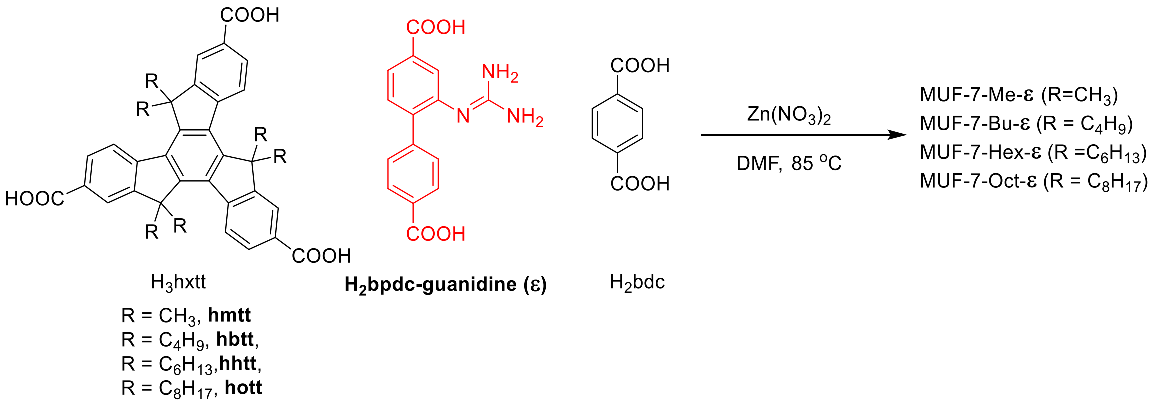

Scheme 5.7: Solvothermal synthesis of MUF-77 with bpdc-**ε** catalysts.

The achiral catalyst, **ε** did not fare particularly well in accelerating the reaction when incorporated into MUF-77. MUF-77-Me-**ε**, MUF-77-Bu-**ε**, MUF-77-Hex-**ε** and MUF-77-Oct-**ε** catalysts were obtained by solvothermal synthesis. These were characterised by PXRD and ^{1}H NMR spectroscopy on acid digested samples (Scheme 5.7 and Experimental section 5.3.4, ESI Figure S33 – S36). No thermal deprotection was necessary as no boc groups were present. Using about 20 mol% of MOF crystals, the aldol reaction was carried out at 45 °C for 48 hours. Once again, we calculated consumption, and the degree of dehydration. As the catalyst is achiral, no ee was expected and hence no derivatisation was necessary. PXRD patterns were unchanged and the crystals did not show any visible cracks on the surface under a microscope (Experimental section Figures 5.21 and 5.24).

A solution of **1** in acetonitrile when heated at 45 °C for 48 hours, slowly reacts with atmospheric oxygen and converts to a mixture of 6-oxohexanoic acid (**6**) and adipic acid (**7**) (Scheme 5.8). Peaks characteristic of **6** and **7** were visible in the mass spectrum (Experimental section, Table 5.7). A gas chromatogram of this sample gave a new peak at a retention time of 27.5 minutes, which is from 6-oxohexanoic acid (Experimental section, Figure 5.17b). Adipic acid has high boiling point of 337 °C and is not visible in the chromatogram as it cannot be volatised at the injector. However, when MUF-77-**ε** catalysts were used, this oxidation process is prevented, and the intramolecular aldol reaction is favoured.

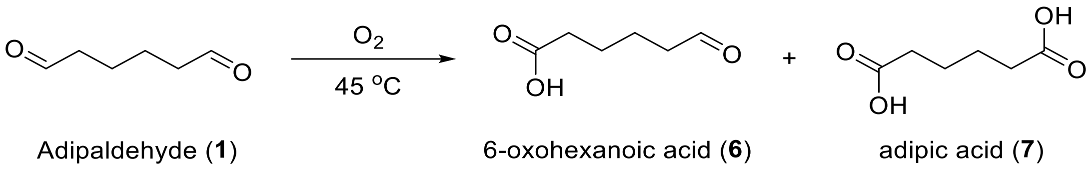

Scheme 5.8: Oxidation of adipaldehyde when heated at 45 °C for 2 days.

The consumption in case of MUF-77-**ε** was lower than MUF-77-**q** catalysts but comparable to MUF-77-**β** catalysts. No ee was observed as the catalyst lacks chiral centres i.e. the peaks at 20.2 and 20.5 minutes were of roughly equal intensities (Experimental section, Figure 5.17c). On the other hand, a *syn*:*anti* diastereomeric ratio could be measured. In almost all cases, the population of the *anti* products was 1.6 - 1.7 times more than the *syn* products (Table 5.4). This can once again be ascribed to differing rates of dehydration of the aldol products, with *syn* diastereomers dehydrating faster than the *anti* diastereomers, thus causing a decrease in the relative amount of *syn* products. A lower d.r. of 1:1.1 was obtained when the reaction was catalysed by MUF-77-Oct-**ε**.

Table 5.5: Heterogenous catalysis of the intramolecular aldol reaction of **1** with MUF-77 systems containing **ε** catalyst.

Framework	**Ligands**	**Consumption (%)**	**% dehydration**	**d.r. (*syn*: *anti*)**
-	Me_2bpdc-guanidine (**Me_2ε**)	39.8	7.3	1:1.7
MUF-7-Me-**ε**	hmtt/bpdc-**ε**/bdc	19.9	19.2	1:1.6
MUF-7-Bu-**ε**	hbtt/bpdc-**ε**/bdc	7.9	17.4	1:1.7
MUF-7-Hex-**ε**	hhtt/bpdc-**ε**/bdc	22.2	18.3	1:1.6
MUF-7-Oct-**ε**	hott/bpdc-**ε**/bdc	67.3	42.2	1:1.1

Notes: Reactions performed with 20 mol% of catalyst at 45 °C for 48 hours. No derivatisation was performed as the catalyst is achiral.

Although its d.r. is the lowest, a high adipaldehyde consumption of 67.3 % was offered by MUF-77-Oct-**ε**. Unfortunately, about 42 % of the product molecules underwent dehydration. Based on the kinetics described in section 5.2.2, the *syn* and *anti* products dehydrate at different rates and this results in these products to be present in roughly equal amounts i.e. the d.r. for MUF-77-Oct-**ε** catalysed reaction is 1:1.1.

MUF-77-Me-**ε**, MUF-77-Bu-**ε**, and MUF-77-Hex-**ε** consumed **1** to a lower extent in comparison to Me$_2$bpdc-guanidine (**Me$_2$ε**), which gave a modest consumption of 39.8 % at 45 °C (Table 5.4). The degrees of dehydration in these samples were more than double the homogenous catalysis value.

5.2.7 Conclusions

In this chapter, variations in the catalytic activity of MUF-77 with prolinamide and guanidine-based catalysts were observed when methyl, butyl, hexyl, and octyl groups were installed on the truxene linkers. These catalytically inactive alkyl groups which are placed away from the catalytic site act as modulators and can ultimately impact the outcome of the reaction. In MUF-77 frameworks, which are multicomponent, the catalyst and modulator are located at predefined sites. This creates pore microenvironments which offer favourable non-covalent contacts with the reaction participants. Being true single-site catalysts, correlations between the modulator groups and the activity can be unambiguously determined to a certain extent.

For the enol-exocyclisation of adipaldehye, the products in many cases are less dehydrated compared to their homogenous controls. MUF-77-Octyl frameworks gave the highest adipaldehyde consumption among each family of catalysts, but with higher levels of dehydration. Additionally, oxidation was prevented as the adipaldehyde substrate selectively proceeds to form the cyclic aldols, whose product distributions can be modulated.

It is important to note that making the ideal catalyst with the highest consumption, least dehydration, and high stereoselectivity was not the goal of this project. These results, however, establish MUF-77 frameworks as a powerful class of catalysts for tuning intramolecular aldol reactions. By taking advantage of the many functionalisable sites on each of the linkers, the applicability of these frameworks could be expanded to more challenging reactions for the synthesis of more complex targets.

5.3 Experimental Section

5.3.1 General information

All starting materials and solvents were used as received from commercial sources without further purification unless otherwise noted. NMR spectra were collected at room temperature using a Bruker Avance 400 MHz or 500 MHz spectrometer, with the use of the solvent proton as an internal standard.

X-ray diffraction data were collected using either of two methods: (a) Rigaku Spider diffractometer equipped with a Micromax MM007 rotating anode generator with Cu_{α} radiation (wavelength = 1.54180 Å), high flux Osmic multilayer mirror optics, and a curved image plate detector, and finally processed into 1D diffractograms using 2DP. (b) Bruker D8 Venture with Cu_{α} radiation (wavelength = 1.54180 Å), generated by a IμS microfocus Diamond sealed tube and detected using a Photon III 28 detector. The collected data were processed into 1D Diffractograms using APEX3 and Diffrac.Eva.

GC conditions: Gas chromatograms was collected using a Shimadzu-2010 instrument with a flame ionisation detector (FID) and Varian Chirasil-Dex CB CP d7502 column (Length: 25 m, Internal diameter: 0.25 mm) for chiral separation. The following conditions were used: Injector temperature: 200 °C; Carrier gas: Nitrogen; Flow rate: 0.83 ml/min; FID temperature: 300 °C. Temperature program: 70 °C for two minutes increased to 180 °C at 4 °C/min and held for three minutes. The conditions are the same for both non-derivatised and derivatised samples.

5.3.2 Synthesis of 1,6-hexanedial

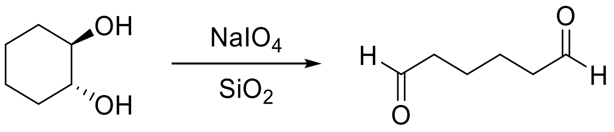

A suspension of silica gel (7.5 g) was stirred in 50 ml of CH_2Cl_2. 10 mL of an aqueous solution of $NaIO_4$ (1.2 g, 5.6 mmol) was added dropwise to yield a flaky suspension. *Trans*-1,2-cyclohexanediol (500 mg, 4.3 mmol) suspended in CH_2Cl_2 was added to the suspension and stirred for 24 hours. The solids were filtered, and the filtrate was dried to yield the product. The product was stored at -20 °C. Yield: 465 mg (95%). ^1H NMR spectrum was found to be consistent with the literature.[333]

5.3.3 Catalysis and derivatisation conditions

Catalysis: A 0.04 M solution of adipaldehyde was made by dissolving adipaldehyde (46 mg, 400 µmol) in 10 mL of dry acetonitrile. 1 ml of this solution was used for catalysis. The catalyst was added, and the reaction was carried out for the set time period. GC was obtained based on the conditions described. **Note:** The adipaldehyde solution was stored at -20 °C.

Derivatisation: After the specified time period for catalysis, a gas chromatogram was obtained. Once the sample was injected into the GC, a 45 µm syringe filter was used to separate MUF-77 from 1 ml of the reaction mixture. The filtrate was treated with 50 µl of BSTFA (**10**) containing 1% TMS and kept on heating at 85 °C for 1 hour. The mixture was reinjected into the GC and the ee and d.r. were determined.

5.3.4 Synthesis of MUF-77

MUF-77-**q** and MUF-77-**β** MOFs were synthesised using published solvothermal methods.[175] In a typical synthesis, the required tritopic ligand, two ditopic ligands and $Zn(NO_3)_2 \cdot 4H_2O$ were dissolved in 5 ml of *N*,*N*-diethylformamide (DEF) in an 18 ml glass vial. The suspension was sonicated briefly before placing the vial in an isothermal oven kept at 85 °C for 18 hours. The hot DEF was decanted and replaced with dry *N*,*N*-dimethylformamide (DMF).

The crystals were taken in a gas sorption tube and washed with acetone five times, and briefly kept under vacuum. This was followed by heating at 200 °C under a dynamic vacuum for 20 hours to remove the boc protecting groups.

Synthesis of MUF-77-ε MOFs

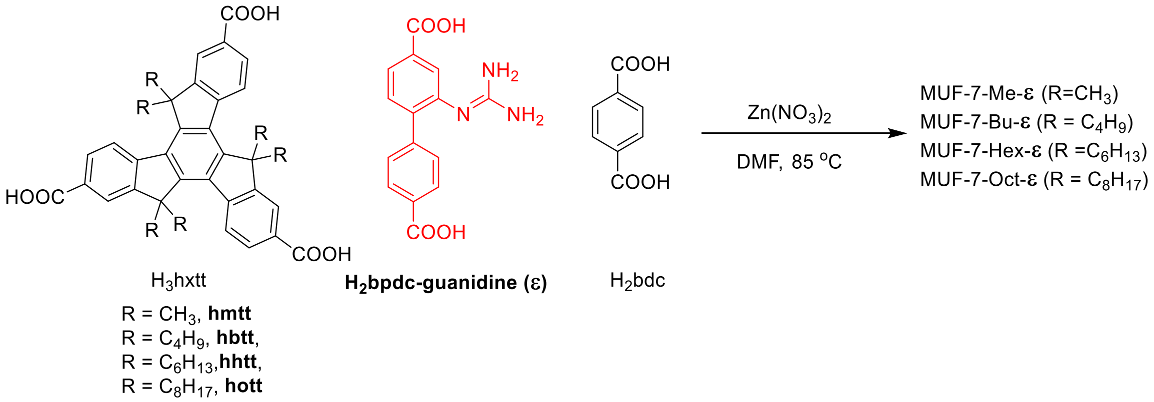

In a typical synthesis, the required tritopic ligand (20 µmol, 1 eq.), H_2bdc (6.6 mg, 40 µmol, 2 eq.), H_2bpdc-guanidine (7.6 mg, 26 µmol, 1.3 eq.), benzoic acid and $Zn(NO_3)_2 \cdot 4H_2O$ (82.5 mg, 315 µmol, 15.7 eq.) were dissolved in 5 mL of *N*,*N*-diethylformamide (DEF) containing 250 µL of water, taken in an 18 mL glass vial. The suspension was sonicated for

30 – 60 seconds before placing the vial in an isothermal oven kept at 85 °C for 18 hours. The hot DEF was decanted and replaced with dry *N*,*N*-dimethylformamide (DMF) and then washed with acetonitrile five times.

The crystals were quickly washed twice with 250 µl of 0.04 M adipaldehyde solution after which 1 ml of the adipaldehyde solution was added. A gas chromatogram was immediately collected, and the reaction was kept at 45 °C for 48 hours, after which another GC was collected. The difference in the peak areas were used to calculate the consumption.

Table 5.6: Peaks seen in the ESI-HRMS for the oxidation of **1**.

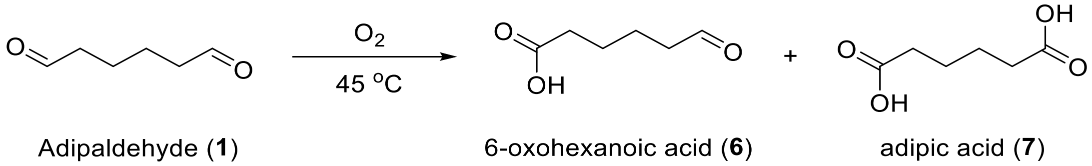

Assignment	Calculated m/z value	Observed m/z value
$[\mathbf{6}+Na]^+$	153.0522	153.0522
$[\mathbf{6}+K]^+$	169.0261	169.0471
$[\mathbf{7}+K]^+$	185.0210	185.0784
$[\mathbf{6}-H]^-$	129.0557	129.0548
$[\mathbf{7}-H]^-$	145.0506	145.0497

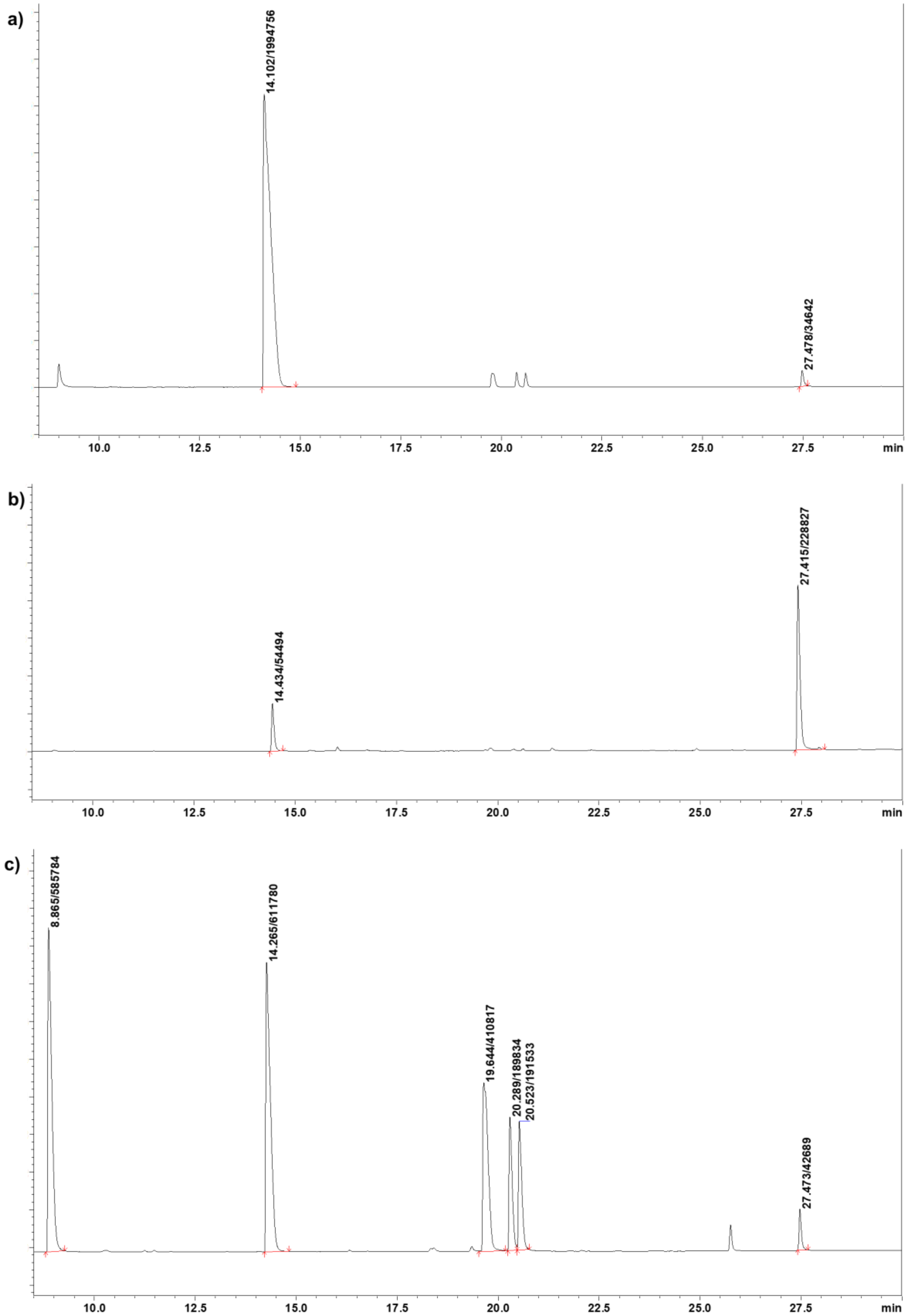

Figure 5.17: Representative gas chromatograms **a)** Stock solution of **1** showing only a small amount of 6-oxohexanoic acid (**6**) at 27.4 min. **b)** Stock solution heated at 45 °C for 48 hours, with a much larger amount of **6**. **c)** After catalysis with MUF-77-Oct-**ε**, showing aldol products; Peak assignment: dehydrated product: 8.8 min, **1**: 14.2 min, *syn* products: 19.6 min, *anti* products: 20.2 and 20.5 min. Note that peaks of the *anti* products are of roughly equal intensities due to the catalyst being achiral.

5.3.5 Kinetics of consumption, dehydration, and detailed table of catalysis results

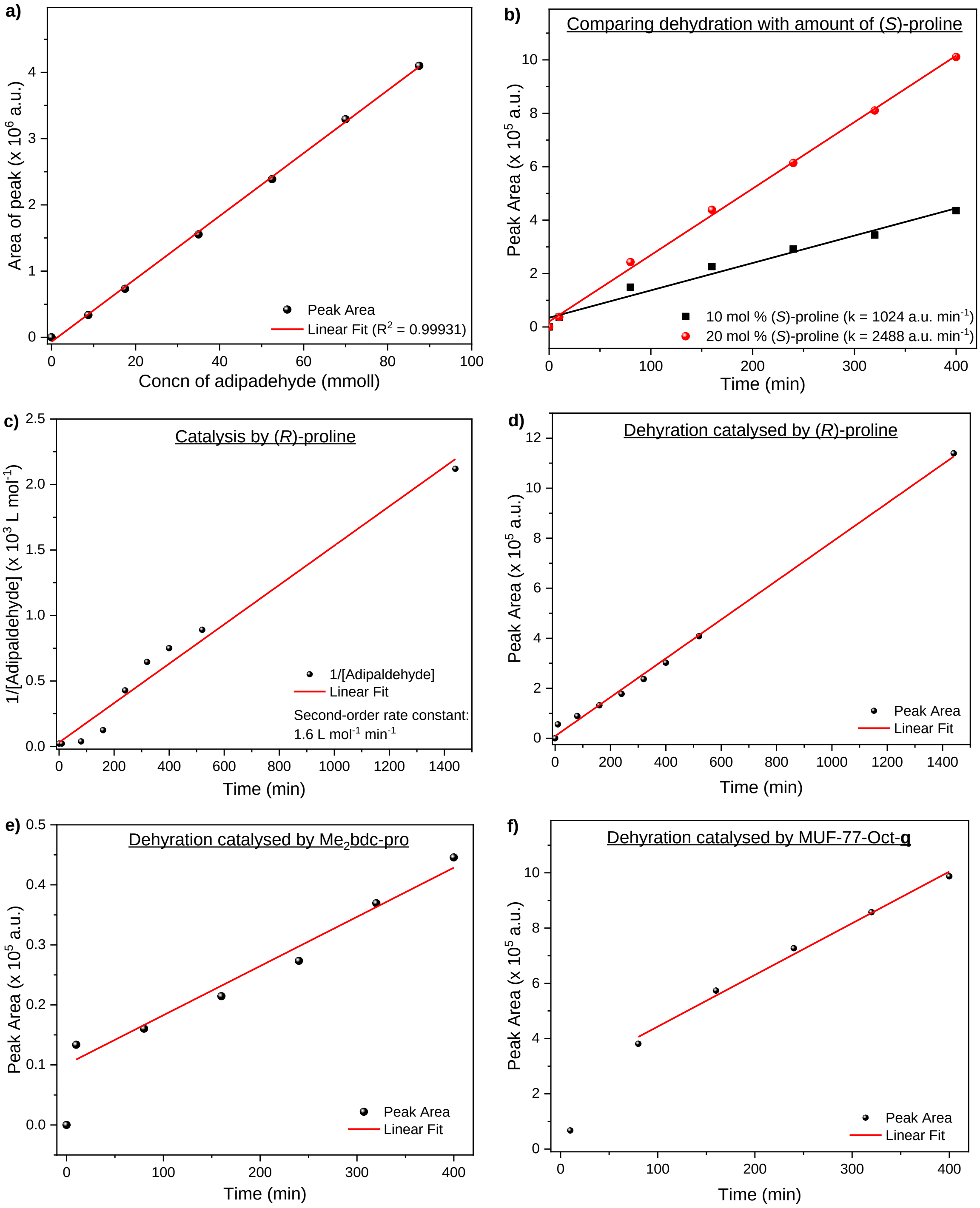

Figure 5.18: **a)** Calibration curve showing linear dependence of area of peak at 14.3 min on the concentration of **1**. **b)** Dependence of amount of (*S*)-proline catalyst on the kinetics of dehydration. **c)** Second-order kinetics for the consumption of **1** when catalysed by (*R*)-proline. **d)** Kinetics for the formation of **3** catalysed by (*R*)-proline, **e)** catalysed by Me_2bdc-pro and **f)** catalysed by MUF-77-Oct-**q**.

Table 5.7: Detailed table of catalysis results with associated errors.

Framework	**Ligand combination /catalyst**	**Consumption (%)**	**% dehydration**	**% ee**(a)	
				anti	***syn***
-	No catalyst	< 2 %(b)	-	-	-
-	(*S*)-proline	> 99	32.0 ± 2.2	36.4	7.1
-	Me$_2$bdc-pro (**Me$_2$q**)	42.4 ± 0.3	6.5 ± 0.1	39.5 ± 3	15.3 ± 0.4
MUF-77-Oct	hott/bpdc/bdc	-	-	-	-
MUF-77-Oct-**q**-Boc	hott/bpdc/bdc-proBoc	-	-	-	-
MUF-77-Me- **q**	hmtt/bpdc/bdc-pro	52.2 ± 0.4	16.1 ± 0.8	50.2 ± 0.2	-0.3 ± 0.1
MUF-77-Bu- **q**	hbtt/bpdc/bdc-pro	72.9 ± 1.9	29.5 ± 0.4	35.9 ± 1.1	-1.5 ± 0.08
MUF-77-Hex- **q**	hhtt/bpdc/bdc-pro	80.2 ± 3.7	27.6 ± 0.5	36.2 ± 1.0	-0.7 ± 0.04
MUF-77-Oct- **q**	hott/bpdc/bdc-pro	80.6 ± 3.1	55.7 ± 0.6	25.3 ± 0.6	-2.6 ± 0.1
-	Me$_2$bpdc-pro (**Me$_2$β**)	17.2 ± 0.6	16.9 ± 1.4	44.0 ± 0.2	8.7 ± 0.7
MUF-77-Oct-**β**-Boc	hmtt/bpdc-proBoc/bdc	-	-	-	-
MUF-77-Me-**β**	hmtt/bpdc-pro/bdc	19.8 ± 1.5	42.1 ± 2.6	30.7 ± 2.6	3.0 ± 0.1
MUF-77-Bu-**β**	hbtt/bpdc-pro/bdc	43.6 ± 0.1	11.4 ± 0.2	39.2 ± 0.3	12.2 ± 0.9

MUF-77-Hex-**β**	hhtt/bpdc-pro/bdc	27.7 ± 0.9	15.8 ± 0.5	39.3 ± 1.4	8.0 ± 0.3
MUF-77-Oct-**β**	hott/bpdc-pro/bdc	44.5 ± 0.7	29.0 ± 0.5	10.2 ± 0.4	3.6 ± 0.3

Notes: Reactions performed at 21 °C with 10 mol% of catalyst relative to **1**. (a) % ee was determined in as the ratio of difference in areas of peaks between the later eluting product and earlier eluting product to the sum of their areas.

5.3.6 PXRD of MOF samples before and after catalysis

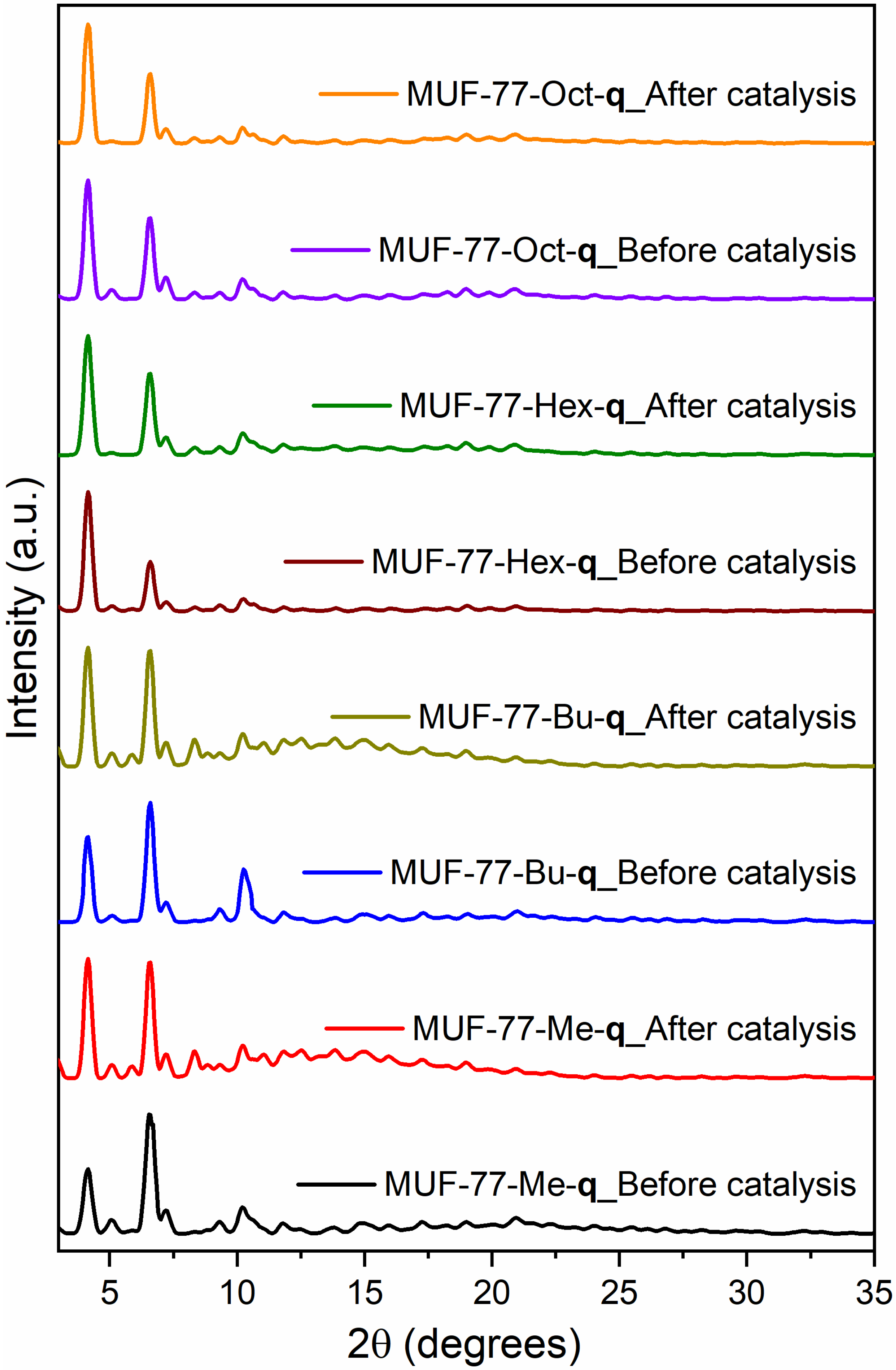

Figure 5.19: PXRD of MUF-77-**q** crystals before and after catalysis.

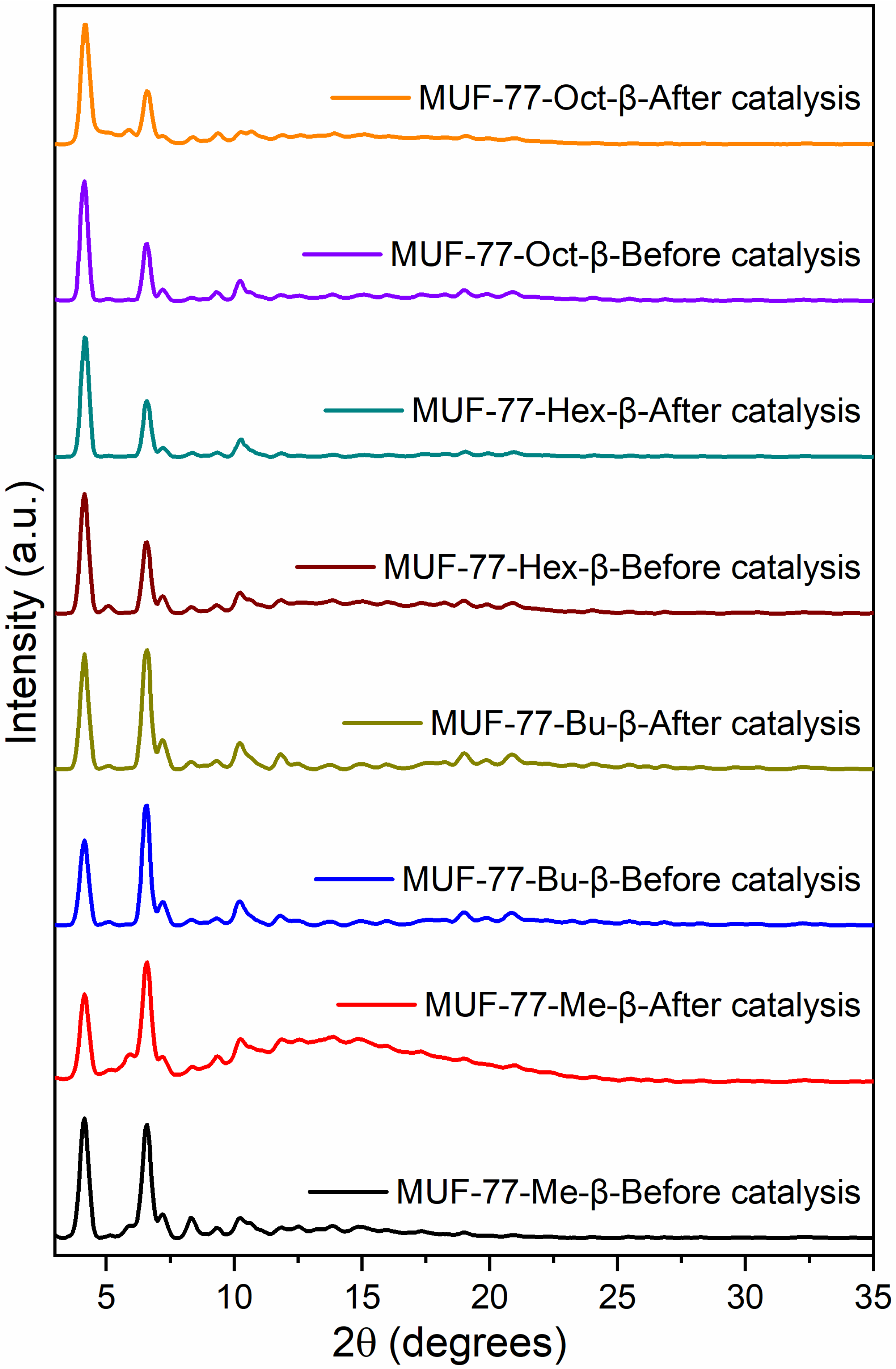

Figure 5.20: PXRD of MUF-77-**β** crystals before and after catalysis.

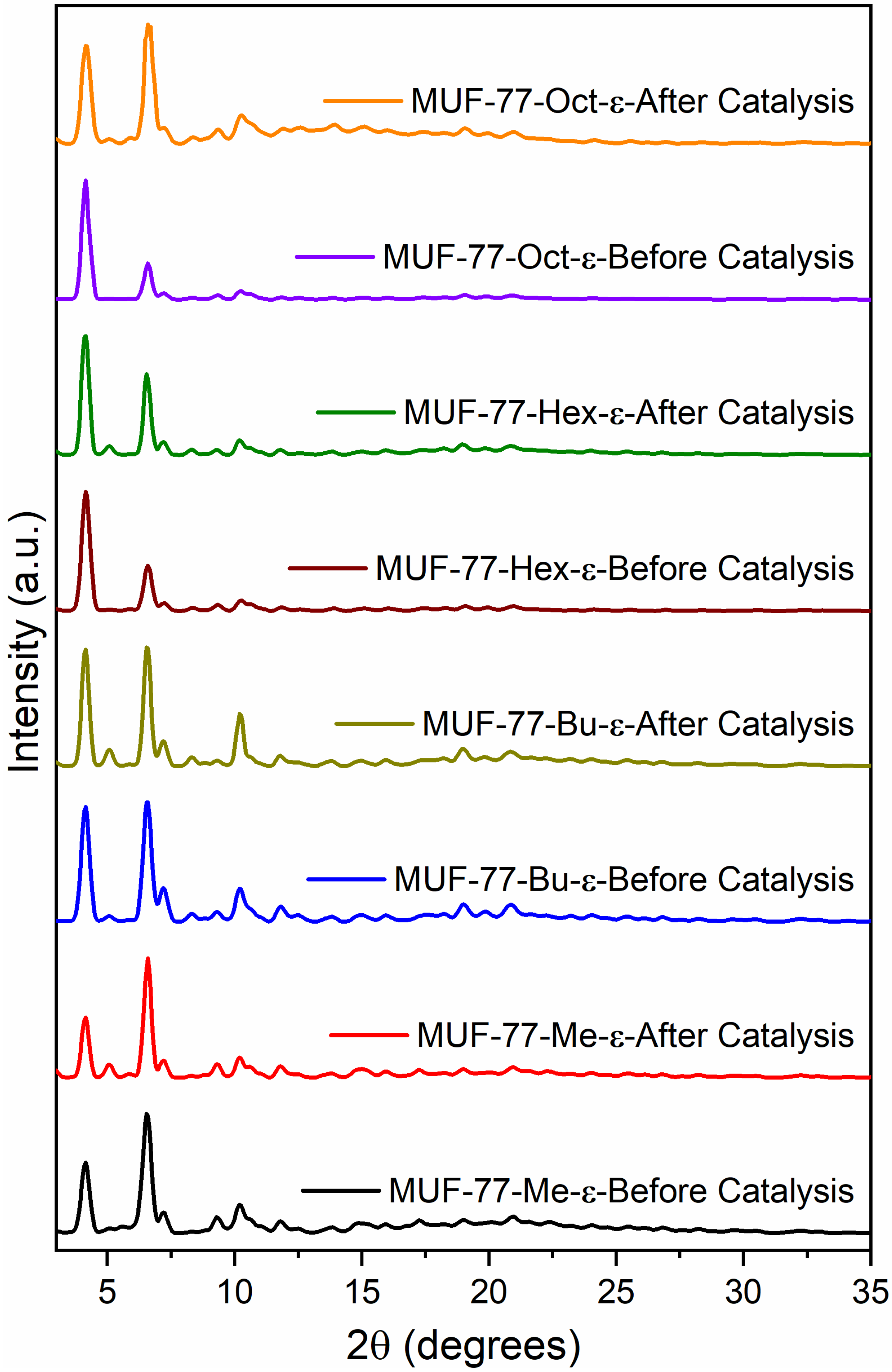

Figure 5.21: PXRD of MUF-77-**ε** crystals before and after catalysis.

5.3.7 Photos of MOF samples before and after catalysis

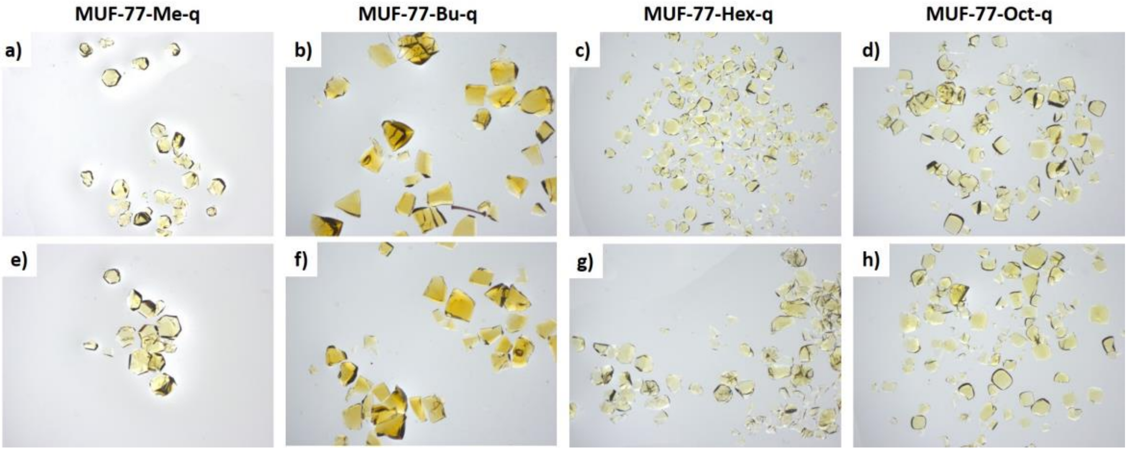

Figure 5.22: Photos of MUF-77-**q** crystals before (**a**, **b**, **c**, and **d**) and after (**e**, **f**, **g**, and **h**) catalysis.

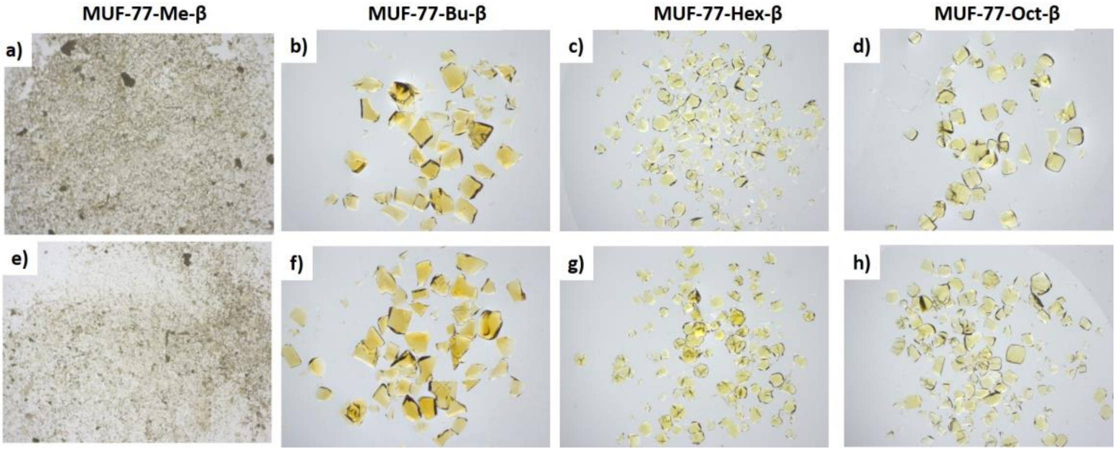

Figure 5.23: Photos of MUF-77-**β** crystals before (**a**, **b**, **c**, and **d**) and after (**e**, **f**, **g**, and **h**) catalysis.

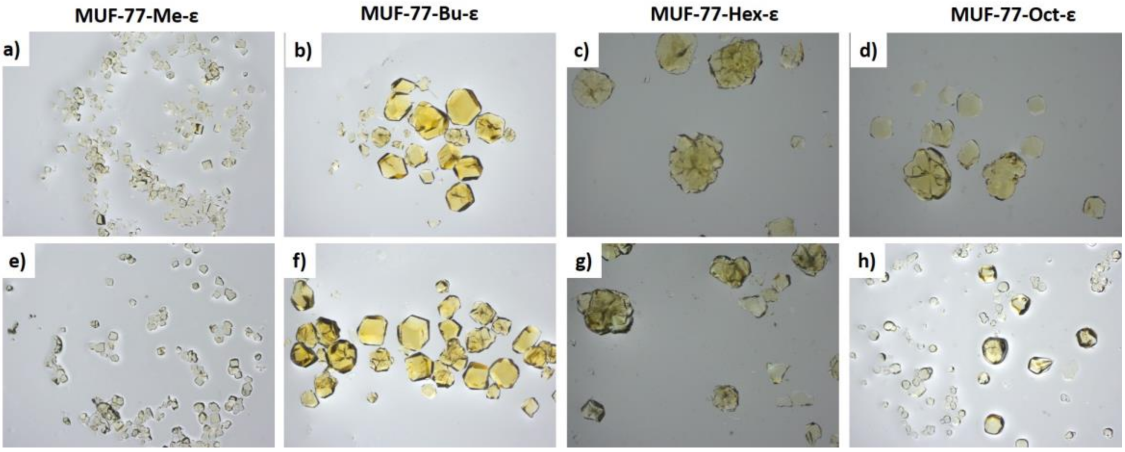

Figure 5.24: Photos of MUF-77-**ε** crystals before (**a**, **b**, **c**, and **d**) and after (**e**, **f**, **g**, and **h**) catalysis.

Chapter 6 - Summary and Perspectives

6.1 Summary

This thesis dealt with the photophysical and catalytic properties of multicomponent MOFs. Chapter 2 described a new method of obtaining white-light emission and Chapter 3 dealt with studying the underlying inter-ligand photophysical interactions. Chapter 4 explained the photochromism of MUF-7 and MUF-77 frameworks based on stabilised pyrazine radicals. Finally, MUF-77 was used to tune the outcome of an intramolecular aldol reaction which is detailed in Chapter 5.

In Chapter 2, we reported the synthesis of nanocrystalline MUF-77, making them amenable for spectroscopic measurements. The multicomponent feature of MUF-77 was used to generate white-light emission upon UV excitation.[200] A combination of luminescence from yellow emissive gua ligand and blue emissive bdc-NH_2 and hxtt ligands gave white light. The spectral output could be modulated by using one of three ways: changing the alkyl group on the tritopic linker, diluting the emissive ligand with its non-luminescent analogue and utilising hydrogen bonding guests.

The variation in the luminescence on changing the alkyl groups was quite intriguing. Further investigations were done using a variety of crystallographic and ultrafast time-resolved spectroscopic techniques, which was described in detail in Chapter 3. Calculation of inter-ligand FRET efficiencies and FRET times was performed by utilising experimentally determined spectral overlaps, quantum yields, inter-ligand distances, and fluorescence lifetimes. By correlating these calculations with experimental luminescence decay times, we were able to pinpoint FRET processes that were responsible for the luminescence variation. Specifically, the efficiency of two FRET processes i.e. between the hxtt and gua coupled with bdc-NH_2 and gua was found to modulate the emission profile.

There were some decay components whose origin is open to investigation. In the blue region, two theories were used to explain the TGPLS kinetic profile of **1**. The first one uses both the step-by-step and jumping beyond nearest neighbour exciton migration to study decay components. This theory is to be tested by studying the effect of guest loading on the decay kinetics. In the second theory, we think that exciton-exciton annihilation (EEA) may cause the sub-picosecond component. The dependence of the timescale and amplitude of this component on the excitation density would inform us further about its origin which will be studied as part of future work. For testing both these theories, parameters such as exciton coupling, and atomic transition densities will be calculated and applied using computational studies.

In the emission region of gua (550 – 650 nm), another fast component with decay times of less than 2 ps was also observed. Guanidine moieties are well known to act as photobases, and hence we tentatively assign this component to excited-state proton transfer (ESPT) between the gua and DMF. Future work to understand this component would involve TGPLS and ultrafast vibrational spectroscopy. For these experiments, the MOF crystals will be suspended in protic solvents which would further promote ESPT. Differences in the ESPT will also be monitored via the kinetic isotope effect using deuterated solvents.

In Chapter 4, we presented a series of MUF-7 and MUF-77 frameworks with bdc-quinoxaline ligands that have photochromic properties. EPR spectroscopy proved that this behaviour was caused by photogenerated pyrazine radicals. The stability of the radicals varied and was dictated by the functional groups on the ligands. Using SCXRD, we studied the bond lengths of the photochromic MUF-7 systems with and without UV irradiation. Based on changes in the bond lengths, we proved that the photochromism is the result of an inter-ligand charge transfer process, forming truxene radical cations and pyrazine radical anions. More experiments are to be performed, which include determining better SCXRD structures of photochromic MUF-77 systems which have disordered bdc ligands. For all MOFs, ultrafast transient absorption spectroscopy will inform us of the time required for radical generation and thus provide a more detailed picture of the charge transfer process, an aspect useful for applications in photovoltaic devices.[334-336] Finally, the photogenerated radicals could potentially be used to initiate radical polymerisation of monomers such as styrene or methyl methacrylate.[283,337,338]

In Chapter 5, we showed the application of MUF-77 for the catalysis of the intramolecular aldol reaction of adipaldehyde. To the best of our knowledge, this is the first example of an enantioselective intramolecular reaction catalysed using MOFs. For our reaction, we used three different catalytic ligands, bdc-proline (**β**), bpdc-proline (**q**), and bpdc-guanidine (**ε**) and explored the effect of changing the alkyl chain on the tritopic linker. This gave us MUF-77 frameworks with different pore microenvironments, which influenced the outcome of the reaction. For the intramolecular reaction of adipaldehyde, significant differences in reactant consumption, enantiomeric excess, and degree of dehydration of the products were observed, even though the catalyst was unchanged.

We reiterate the fact that Chapter 5 focussed on providing proof of concept of intramolecular reaction catalysis in MUF-77. Obtaining catalysts with the highest yield and enantioselectivity was not the goal of the project. Future research would explore structure-activity relationships at a molecular level, and modelling the pore environment with computational methods, so that the reaction outcomes could be predicted and optimised.

6.2 Future work

6.2.1. Tandem reactions in MOFs

As mentioned previously, MUF-77 being a quaternary MOF contains three ligands. This feature would make it an ideal candidate for cascade reactions. Such reactions have the advantage of consuming less energy, time and lower amounts of reagents.[339] For example, in MUF-77 if both bdc and bpdc ligands are functionalised with appropriate catalysts, many tandem reactions can be explored (Figure 6.1). Alkyl groups on the tritopic ligands can be used as modulators to further tune the outcome of the both steps.

Figure 6.1: Schematic of a typical two-step tandem reaction in MUF-77. X and Y represent catalytic groups located on the bdc and bpdc ligands.

Tandem reactions in MOFs are not unheard of, with some reviews dedicated to this area.[339,340] Some tandem schemes involve a binary MOF containing two different catalytic units located at different sites, while many other schemes discuss about one reaction being catalysed by a functionalised ligand followed by a second reaction catalysed by encapsulated metal nanoparticles.[341-343] For example, Figure 6.2 shows the tandem Knoevenagel-hydrogenation reaction of *p*-nitrobenzaldehyde (**1**) and malononitrile (**2**) to yield 2-(4-aminobenzylidene)malononitrile (**4**) as the final product.[344] Amino-functionalised bdc ligands catalyse the Knoevenagel condensation (**A**), and encapsulated palladium nanoparticles catalyse the hydrogenation step (**B**). Selective reduction of only the nitro groups was seen, with other possible products like 2-(4-nitrobenzylidene)malononitrile and 2-(4-aminobenzyl)malononitrile seen in low quantities.

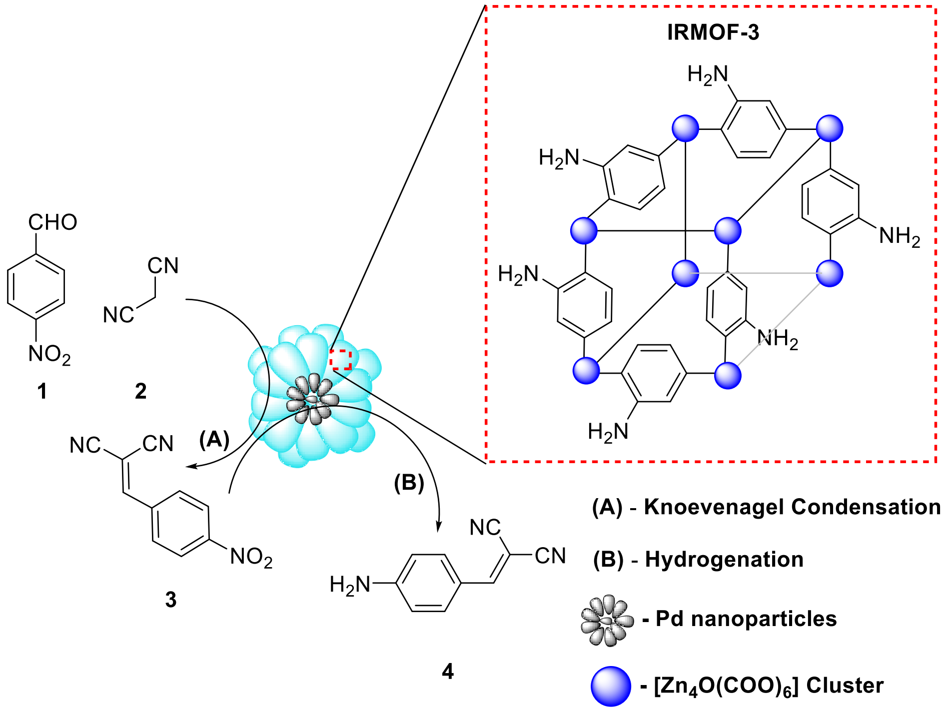

Figure 6.2: Cascade Knoevenagel-hydrogenation reaction with *p*-nitrobenzaldehyde and malononitrile as reactants with Pd nanoparticles encapsulated in IRMOF-3. Some of the bdc-NH$_2$ ligands of IRMOF-3 are shown.

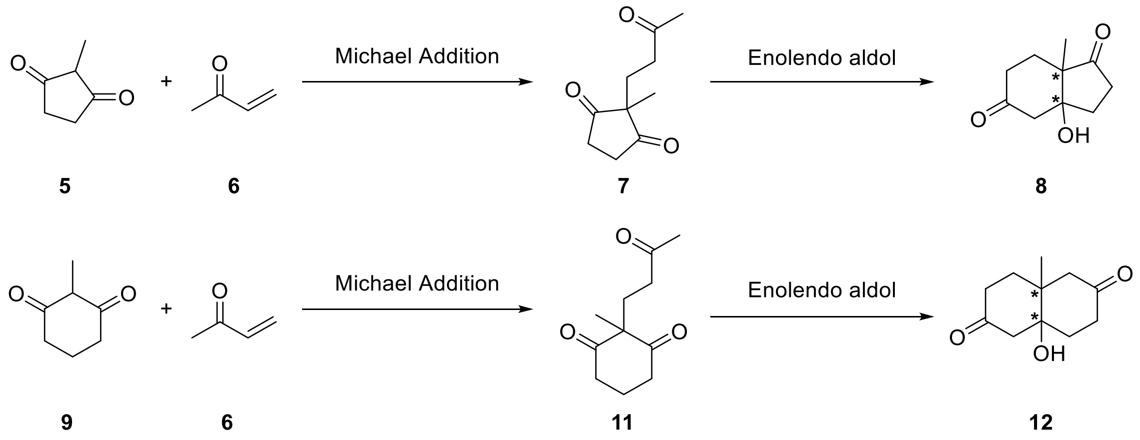

Scheme 6.1: Synthesis of Hajos-Parrish ketones, **8** and **12** using a tandem Michael-enolendo aldol reaction, which can potentially be replicated in MUF-77.

In MUF-77, one tandem reaction that can be explored is the synthesis of Hajos-Parrish ketones (**8** and **12** in Scheme 6.1). This synthesis can be achieved in two steps. The first step is the Michael addition of 2-methyl-1,3-cyclopentanedione (**5**) with methyl vinyl ketone (**6**) to give Hajos-Parrish triketone (**7**). The second step is the proline-catalysed aldol reaction of **7** to give the Hajos-Parrish ketone (**8**). Another substrate is 2-methyl-1,3-cyclopentanedione

(**9**) which upon reaction gives **12**. Both **8** and **12** have two chiral centres and have proven extremely useful as synthons in the synthesis of complex natural products and pharmaceuticals.[345,346]

Catalytic groups such as guanidines and imidazolate can be incorporated into bdc or bpdc scaffolds and then applied for the Michael addition step (Figure 6.3). Prolinamide-based catalysts like bdc-proline, bdc-piperazine, and bpdc-proline can potentially be used to catalyse the aldol reaction step.

Catalysts for Michael Addition

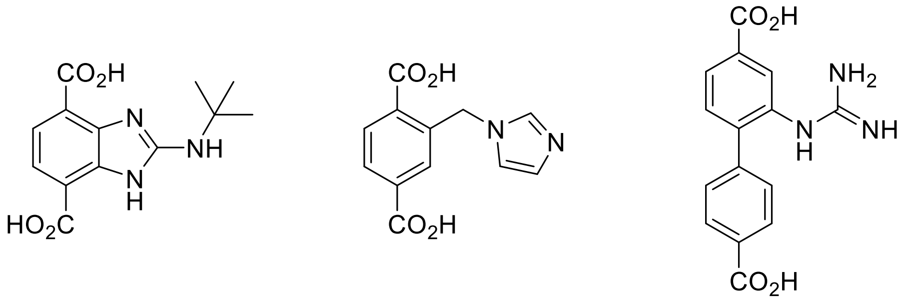

bdc-guanidine bdc-imidazole bpdc-guanidine

Catalysts for enolendo aldol reaction

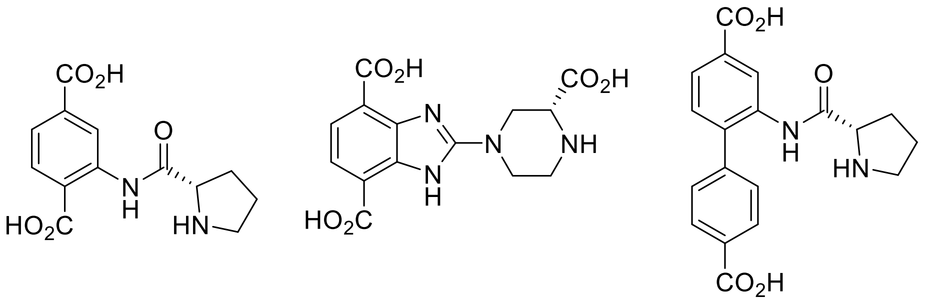

bdc-proline bdc-piperazine bpdc-proline

Figure 6.3: Structures of MUF-77 ligands containing catalytic groups for tandem Michael-enolendo aldol reaction of **5** and **9**.

6.2.2 Red light emission

In Chapter 2, yellow, white and blue emissions were seen on incorporating specialised ligands into MUF-77. A longstanding goal of luminescence is exploring red light emission (RLE) on UV input, which has applications in display devices and sensing. Structures exhibiting RLE typically have donor-acceptor units within its structure to increase Stokes shift.[347-349] Typically, RLE has been obtained using red-emissive dyes trapped in MOF pores or by MOFs made of europium, a red emissive lanthanide.[180,350] Dyes trapped in pores can interact with the MOF linkers, changing the spectrum unpredictably.[179] Most dyes are large conjugated molecules and functionalising them with metal coordinating groups to form MOFs can be quite challenging. On the other hand, lanthanide emissions are sharp and hence have low colour rendering indices (CRI), which is undesirable.[185]

To the best of my knowledge, there are no reports of RLE originating purely from the organic linkers of a MOF. Some bpdc-based ligands can be synthesised which may possibly give RLE and their structures are shown below in Figure 6.4.

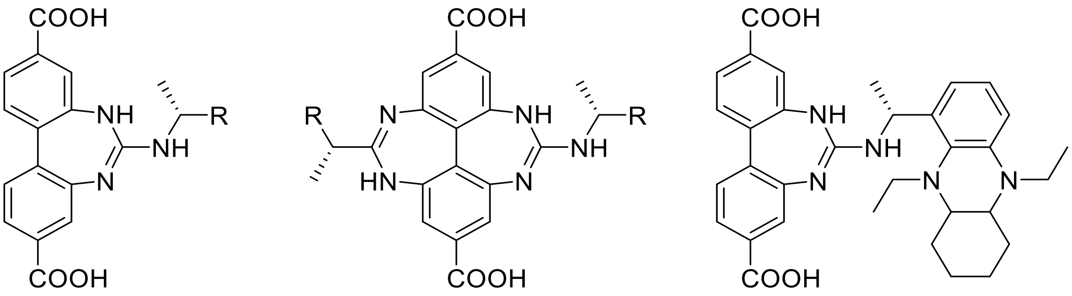

Type 1 Type 2 Type 3

R = phenyl, napthyl, anthracene, pyrene etc.

Figure 6.4: Structures of some ligands which can potentially be used for RLE.

The synthesis of a guanidine functionalised, yellow emissive (λ_{em} = 570 nm) Type 1 ligand with R = phenyl has been published.[200] Changing the R groups may affect the emission. We aim to functionalise this position with more conjugated units such as naphthalene, and anthracene, or use phenyl groups with electron withdrawing groups.[351] Type 2 ligands with bis(guanidine) units exhibit increased conjugation compared to their type 1 analogues and may also possess large Stokes shifts. Their synthesis can possibly be done using a pathway similar to the synthesis of type 1 ligands (Scheme 6.2) by using tetraaminobpdc dimethyl ester instead of diaminobpdc dimethyl ester.

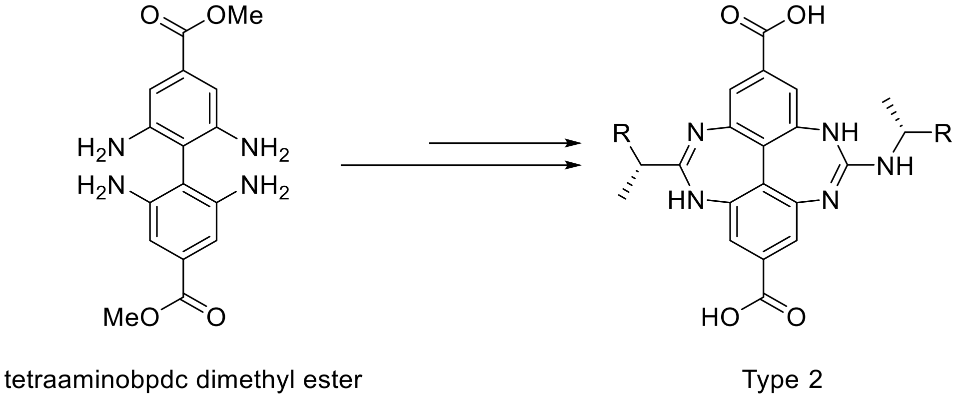

Scheme 6.2: Possible pathway for the synthesis of type 2 RLE ligands.

The structure of type 3 ligands are based on a general strategy first reported by Ren et al.[352] Stokes shifts could be increased by appending 1,4-diethyl-decahydro-quinoxaline (DQ) to an existing fluorophore. The authors used three different dyes with emission maxima at 490 nm, 534 nm and 554 nm. On functionalising them with DQ moieties, the emission maxima shifted to 651 nm, 840 nm, and 780 nm respectively, showing the effectiveness of their strategy. This very idea can be incorporated into bpdc-guanidine ligands to obtain RLE.

6.2.3 Photomodulation of reactions using azobenzene and azopyrazole

The *cis-trans* isomerisation of azobenzene and azopyrazole on light exposure makes them attractive molecular transducers.[139,353] Azobenzene functionalised ligands have been used to tune gas sorption and conduction properties in MOFs.[133,354,355] Our goal is to apply the photoisomerisation of azobenzene to modulate catalytic outcomes in MUF-77. Such a method has been explored by in MOFs.[356,357] However, all these reports have used binary MOFs, which lack multiple handles for controlling catalytic outcomes.

MUF-77 offers multiple modes of modulation owing to its quaternary nature which can offer much better outcomes. The three ligands can be functionalised to make well-defined pores. The azobenzene group can be appended to either of bdc or bpdc and assembled into MUF-7 or MUF-77. Azobenzene photoisomerisation in MOFs can be well studied by using Raman spectroscopy with an excitation wavelength of 785 nm. (Note that 532 nm excitation gives a strong fluorescence background masking the Raman signals).

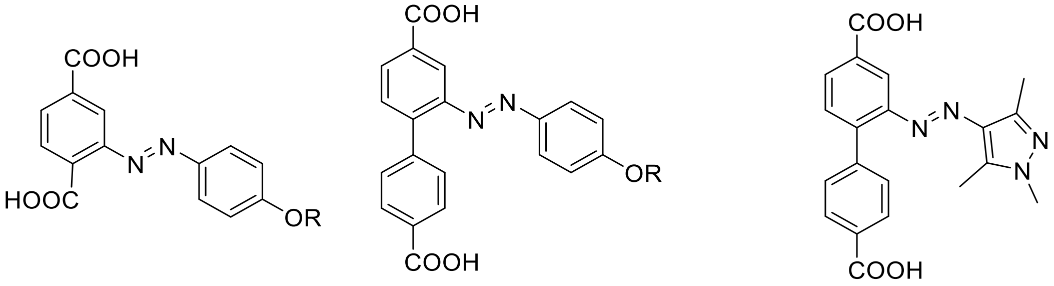

bdc-azobenzene bpdc-azobenzene bpdc-azopyrazole

Figure 6.5: Structures of azobenzene and azopyrazole ligands to be used for photomodulation of catalysis.

The rates of photoisomerisation in azobenzene and azopyrazole ligands are dependent on their absorptivity at the wavelength of incident light. R groups such as H, phenyl or napthyl can further change the absorptivity. These parameters serve as handles for modulation. The wavelength and intensity of light used also provide additional avenues for modulation. However, the stability of MUF-77 under UV light for extended periods will also be a part of the study.

6.2.4 Active modulation of catalysis

The Telfer group has explored catalysis in MUF-77 and studied the impact of using modulators such as alkyl groups on the reaction outcome.[175,176] In Chapter 5 of this thesis, I have proven that such groups can influence the yield, enantioselectivity, and degree of dehydration for intramolecular reactions. The modulators work using non-covalent interactions with the reaction intermediates. The next generation of modulators would be groups that have a more pronounced effect on the reaction outcome. To this end, we plan to develop 'active modulators', groups that bind to intermediates using strong, covalent interactions.

Hong et al. in 2005, reported the first enantioselective intramolecular Baylis-Hillman (B-H) reaction when they reacted hept-2-enedial with (*S*)-proline to obtain 6-hydroxycyclohex-1-ene-1-carbaldehyde. Using chiral GC, they determined that the reaction gave the (*S*) enantiomer as the major product when only (*S*)-proline was used. However, on addition of imidazole, the (*R*) enantiomer was predominant, meaning the enantioselectivity was reversed (Scheme 6.3).[358]

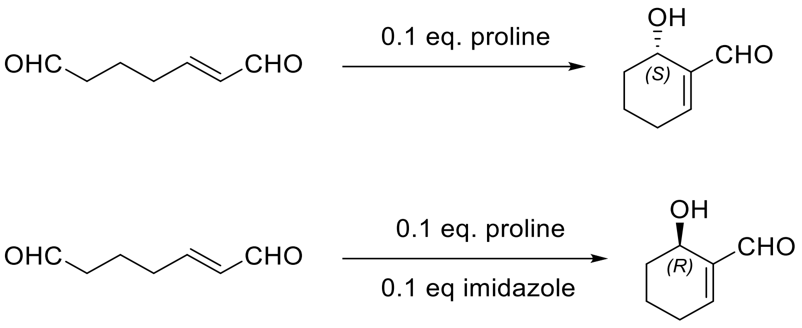

Scheme 6.3: The inversion of enantioselectivity as observed by Hong and co-workers when using imidazole as a co-catalyst.

An examination of the mechanism for this phenomenon was carried out using DFT calculations (Figure 6.6a and 6.6b).[359] As shown in **TS2**, the presence of water was found to be important to catalyse the proton transfer between the imidazole and proline carboxy group. The reversal of enantioselectivity is the result of the H-bonding between the C_2 hydrogen of imidazole, and the proline carboxylate.

a) **Proline only**

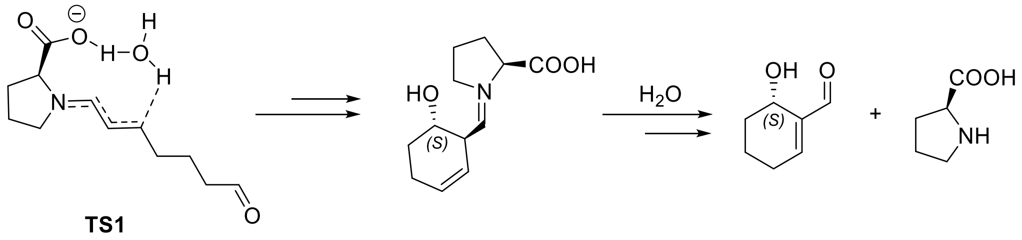

b) **Proline + Imidazole**

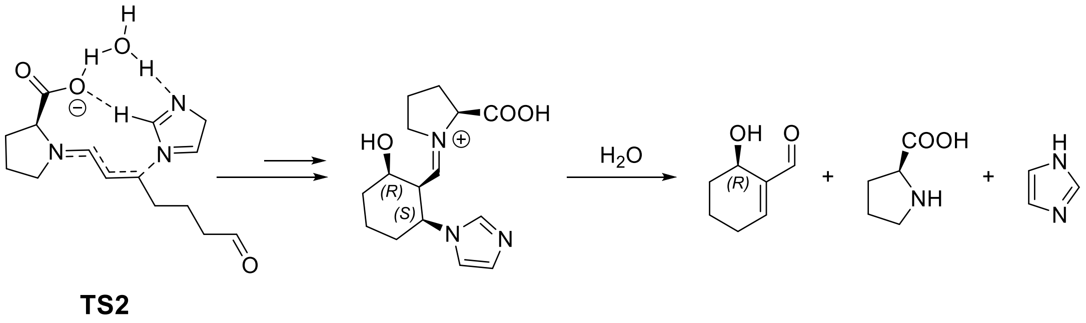

Figure 6.6: a) Mechanism of the proline catalysed Baylis-Hillman reaction and **b)** imidazole co-catalysed reaction verified using DFT calculations. In TS2, the imidazole C_2 hydrogen can H bond to the proline carboxylate due to its acidic character reversing the enantioselectivity.

Attaching one ditopic ligand with proline and the other ditopic with imidazole would enable us in reproducing the same effect in MUF-77 (Scheme 6.4). Based on **TS2,** both proline and imidazole interact simultaneously with the substrate and hence there is a need to bring them together in the MUF-77 framework. This would involve the following steps:

i. Determining the ideal chain length by molecular modelling so that proline and imidazole are in proximity
ii. Synthesis of proline and imidazole functionalised bdc and bpdc ligands with the extended chains
iii. Incorporating the extended chain ditopic linkers in to MUF-77
iv. Catalysing the intramolecular B-H reaction using MUF-77 and determining the enantioselectivity via chiral GC or chiral HPLC. The results will be compared with a control framework that does not feature an imidazole substituent.

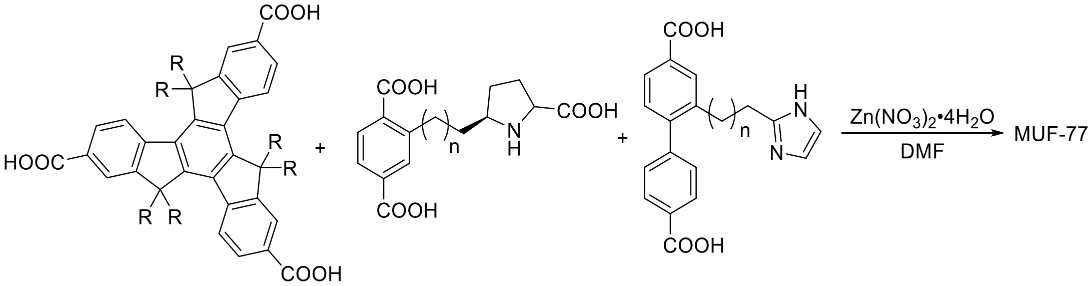

Scheme 6.4: Proposed scheme for making MUF-77 for active catalyst modulation. The chain length (n) is to be determined by molecular modelling so that the imidazole and proline work together during catalysis.

6.2.5 Ligands for Metallocatalysis

Catalysing a reaction using a metal ion or complex is called metallocatalysis. Transition metals with their variable oxidation states and readily available vacant orbitals easily form complexes with organic substrates. This complexation ability has been used extensively for catalysis of reactions involving the formation C-C bonds[360] and C-N bonds[361] and for functionalising C-H bonds.[362]

Metallocatalysis in MOFs has been used for the ring opening[363] and kinetic resolution of epoxides.[364] This was achieved using MOFs with 3d transition metals complexed to salen ligands. Furthermore, many reports of MOFs with metals installed on porphyrin ligands have been known to perform catalysis of challenging organic transformations.[365] To the best of our knowledge, all these studies have been limited to only binary MOFs and not to MC-MOFs.

Our exploration in this regard is discovering new MMOFs systems containing these ligands with other co-ligands. These ligands can be introduced for MOF synthesis with 3d transition metal ions already complexed, or complexation can be done after MOF synthesis via post-synthetic modification (PSM). Characterisation will be done using PXRD, single crystal XRD and NMR spectroscopy. Atomic absorption spectroscopy can help in identifying the concentration of the metal ions.

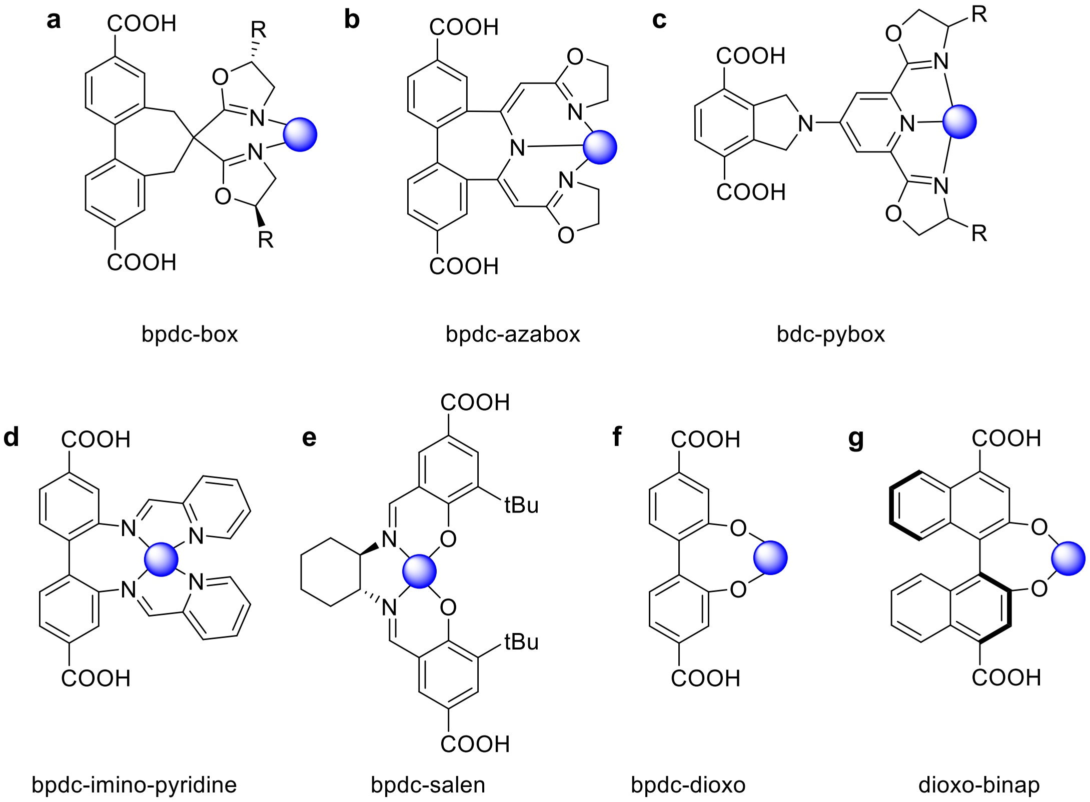

Figure 6.7: Examples of some ligands that can be incorporated into MUF-77 systems to explore metallocatalysis. The blue circles represent complexed metal ions.

Studying various publications, we have found that 3d transition metal complexes of bisoxazoline (box) can catalyse cyclopropanation of olefins, Diels-Alder reactions and many other asymmetric reactions.[366,367] The bpdc-Box ligand (Figure 6.7a) could incorporate such functionality into MUF-77 and catalyse similar reactions. Pyridine-bisoxazolines (pybox) can complex strongly with trivalent lanthanide ions,[368,369] bdc-pybox and bpdc-azabox (Figure 6.8b and c) aim for the same. Relevant catalytic goals will be fundamental organic transformations like aldol, Michael and Diels-Alder reactions.[370] On the other hand, divalent copper and nickel coordinated imino-pyridines (Figure 6.7d) can accelerate Henry reactions.[371] Such functionality can be incorporated most probably by post-synthetic modification, using MUF-77 with the linker set hmtt/bpdc-(NH$_2$)$_2$/bdc and reacting it with pyridine 2-carboxaldehyde, to obtain bpdc-imino-pyridine.

Examples of salen based catalysis in MOFs include the use of 3d transition metals for a diverse variety of reactions, which have been compiled in reviews.[372,373] Metal ions in higher oxidation states such as Mn^{3+}, Ti^{4+}, and V^{5+} have all been used for redox reactions of hydrocarbons. Photocatalytic degradation of organic pollutants in MOFs has been achieved using Fe^{3+} salens. These reactions will be some of our catalysis targets for MUF-77 with bpdc-salen (Figure 6.7e). bpdc-dioxo (Figure 6.7f) is a ligand that can bond with more oxophilic ions such as Al^{+3}, Ti^{+4} and Zr^{+4}. Similarly, dioxo-binap (Figure 6.7g) can result in asymmetric outcomes for many C-C bond forming reactions such as Henry and aldol reactions.

6.2.6 Dual Catalysis and Cooperative Catalysis

This approach uses two different catalysts working at the same time on one substrate. The distinguishing feature of cooperative catalysis is that both catalysts are inactive when used alone. Quaternary MOFs such as MUF-77 would be ideal candidates to replicate cooperative catalysis in heterogenous systems. One model reaction that can be attempted in MUF-77 is the [2+2] cycloaddition of α,β-unsaturated aldehydes to α-hydroxymethyl-substituted nitroalkenes. Cooperative catalysis of this reaction is reported to be done using a secondary amine and thiourea moiety (Scheme 6.5).[374]

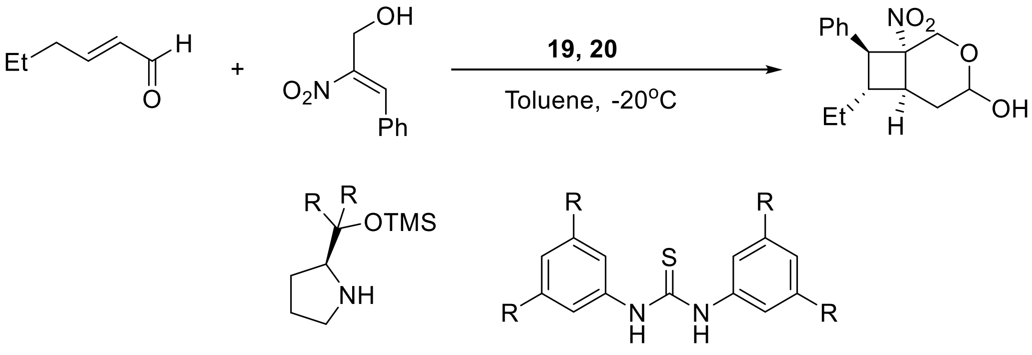

19

20

Scheme 6.5: Cooperative catalysis of [2+2] cycloaddition using a secondary amine and thiourea derivative.[374]

Cooperative catalysis can be replicated in MUF-77 by functionalising two ligands (like bdc or bpdc) with the two different cooperative catalysts. The most viable targets would be those ligands containing secondary amine and thiourea groups.

Our research for realising the goal of cooperative catalysis will involve the following steps:

i. **Identifying the best combination of catalysts**: The catalytic ability of ligands will be tested homogeneously using the esters of the ligands containing catalytic groups.

ii. **Molecular Modelling**: The crystal structure of MUF-77 shows that the bdc and bpdc ligands have a distance of 14.98 Å between them. This is too far away for both catalytic groups to work together in MUF-77. Hence, they must be brought closer together using alkyl chains. Determining the ideal length for the alkyl chains will be done by molecular modelling.[332,375]

iii. **Synthesis of ligands**: Once the chain length is determined, we will proceed with the synthesis of ligands with extended chains terminating with catalytic groups.

iv. **Cooperative catalysis in MUF-77**: The synthesised ligands will be incorporated into MUF-77 (Scheme 6.6). Heterogenous catalysis will be carried out and compared to the homogenous version. The results will be compared to a control framework containing only one of the catalytic groups.

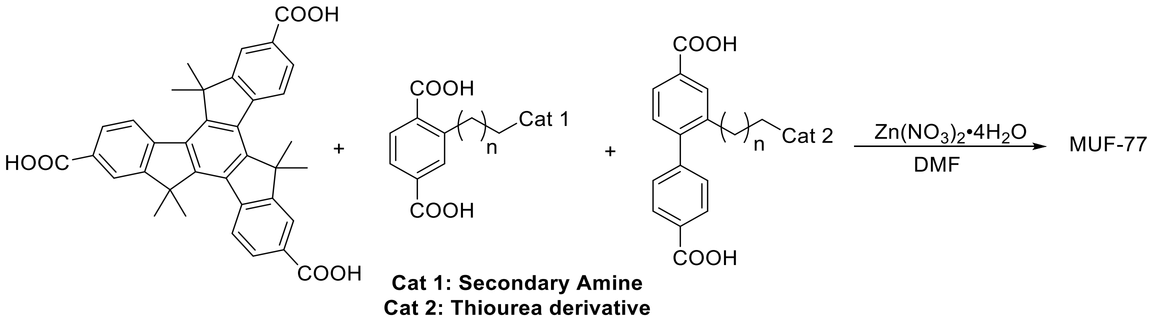

Scheme 6.6: Cooperative catalysis in MUF-77. The position of Cat 1 and Cat 2 can be interchanged between the bpdc or bdc based on the feasibility of synthesis and MUF-77 incorporation.

;

References

(1) Hoskins, B. F.; Robson, R. Design and construction of a new class of scaffolding-like materials comprising infinite polymeric frameworks of 3D-linked molecular rods. *J. Am. Chem. Soc.* **1990,** *112*, 1546.

(2) Batten Stuart, R.; Champness Neil, R.; Chen, X.-M.; Garcia-Martinez, J.; Kitagawa, S.; Öhrström, L.; O'Keeffe, M.; Paik Suh, M.; Reedijk, J. Terminology of metal–organic frameworks and coordination polymers (IUPAC Recommendations 2013). *Pure Appl. Chem.* **2013,** *85*, 1715.

(3) Furukawa, H.; Cordova, K. E.; O'Keeffe, M.; Yaghi, O. M. The chemistry and applications of metal-organic frameworks. *Science* **2013,** *341*, 1230444.

(4) Foo, M. L.; Matsuda, R.; Kitagawa, S. Functional Hybrid Porous Coordination Polymers. *Chem. Mater.* **2014,** *26*, 310.

(5) Kawano, M.; Kawamichi, T.; Haneda, T.; Kojima, T.; Fujita, M. The Modular Synthesis of Functional Porous Coordination Networks. *J. Am. Chem. Soc.* **2007,** *129*, 15418.

(6) Zhang, M.; Chen, Y.-P.; Zhou, H.-C. Structural design of porous coordination networks from tetrahedral building units. *CrystEngComm* **2013,** *15*, 9544.

(7) Cychosz, K. A.; Ahmad, R.; Matzger, A. J. Liquid phase separations by crystalline microporous coordination polymers. *Chem. Sci.* **2010,** *1*, 293.

(8) Kondo, M.; Yoshitomi, T.; Matsuzaka, H.; Kitagawa, S.; Seki, K. Three-Dimensional Framework with Channeling Cavities for Small Molecules: $\{[M_2(4,4'\text{-bpy})_3(NO_3)_4]\cdot xH_2O\}_n$ (M = Co, Ni, Zn). *Angew. Chem. Int. Ed. Engl.* **1997,** *36*, 1725.

(9) Li, H.; Eddaoudi, M.; O'Keeffe, M.; Yaghi, O. M. Design and synthesis of an exceptionally stable and highly porous metal-organic framework. *Nature* **1999,** *402*, 276.

(10) Eddaoudi, M.; Kim, J.; Rosi, N.; Vodak, D.; Wachter, J.; Keeffe, M.; Yaghi, O. M. Systematic Design of Pore Size and Functionality in Isoreticular MOFs and Their Application in Methane Storage. *Science* **2002,** *295*, 469.

(11) Moghadam, P. Z.; Li, A.; Wiggin, S. B.; Tao, A.; Maloney, A. G. P.; Wood, P. A.; Ward, S. C.; Fairen-Jimenez, D. Development of a Cambridge Structural Database Subset: A Collection of Metal–Organic Frameworks for Past, Present, and Future. *Chem. Mater.* **2017,** *29*, 2618.

(12) Sontz, P. A.; Bailey, J. B.; Ahn, S.; Tezcan, F. A. A Metal Organic Framework with Spherical Protein Nodes: Rational Chemical Design of 3D Protein Crystals. *J. Am. Chem. Soc.* **2015,** *137*, 11598.

(13) Griffin, S. L.; Champness, N. R. A periodic table of metal-organic frameworks. *Coord. Chem. Rev.* **2020,** *414*, 213295.

(14) Koyama, H.; Saito, Y. The Crystal Structure of Zinc Oxyacetate, $Zn_4O(CH_3COO)_6$. *Bull. Chem. Soc. Jpn.* **1954,** *27*, 112.

(15) Chui, S. S.-Y.; Lo, S. M.-F.; Charmant, J. P. H.; Orpen, A. G.; Williams, I. D. A Chemically Functionalizable Nanoporous Material $[Cu_3(TMA)_2(H_2O)_3]_n$. *Science* **1999,** *283*, 1148.

(16) Hulvey, Z.; Vlaisavljevich, B.; Mason, J. A.; Tsivion, E.; Dougherty, T. P.; Bloch, E. D.; Head-Gordon, M.; Smit, B.; Long, J. R.; Brown, C. M. Critical Factors Driving the High Volumetric Uptake of Methane in $Cu_3(btc)_2$. *J. Am. Chem. Soc.* **2015,** *137*, 10816.

(17) Talin, A. A.; Centrone, A.; Ford, A. C.; Foster, M. E.; Stavila, V.; Haney, P.; Kinney, R. A.; Szalai, V.; El Gabaly, F.; Yoon, H. P.et al. Tunable Electrical Conductivity in Metal-Organic Framework Thin-Film Devices. *Science* **2014,** *343*, 66.

(18) Hendon, C. H.; Walsh, A. Chemical principles underpinning the performance of the metal–organic framework HKUST-1. *Chem. Sci.* **2015,** *6*, 3674.

(19) García-García, P.; Müller, M.; Corma, A. MOF catalysis in relation to their homogeneous counterparts and conventional solid catalysts. *Chem. Sci.* **2014,** *5*, 2979.

(20) Chae, H. K.; Siberio-Pérez, D. Y.; Kim, J.; Go, Y.; Eddaoudi, M.; Matzger, A. J.; O'Keeffe, M.; Yaghi, O. M.; Materials, D.; Discovery, G. A route to high surface area, porosity and inclusion of large molecules in crystals. *Nature* **2004,** *427*, 523.

(21) Férey, G.; Mellot-Draznieks, C.; Serre, C.; Millange, F.; Dutour, J.; Surblé, S.; Margiolaki, I. A Chromium Terephthalate-Based Solid with Unusually Large Pore Volumes and Surface Area. *Science* **2005,** *309*, 2040.

(22) Bhattacharjee, S.; Chen, C.; Ahn, W.-S. Chromium terephthalate metal–organic framework MIL-101: synthesis, functionalization, and applications for adsorption and catalysis. *RSC Adv.* **2014,** *4*, 52500.

(23) Llewellyn, P. L.; Bourrelly, S.; Serre, C.; Vimont, A.; Daturi, M.; Hamon, L.; De Weireld, G.; Chang, J.-S.; Hong, D.-Y.; Kyu Hwang, Y.et al. High Uptakes of CO_2 and CH_4 in Mesoporous Metal—Organic Frameworks MIL-100 and MIL-101. *Langmuir* **2008,** *24*, 7245.

(24) Ullman, A. M.; Brown, J. W.; Foster, M. E.; Léonard, F.; Leong, K.; Stavila, V.; Allendorf, M. D. Transforming MOFs for Energy Applications Using the Guest@MOF Concept. *Inorg. Chem.* **2016,** *55*, 7233.

(25) Hong, D.-Y.; Hwang, Y. K.; Serre, C.; Férey, G.; Chang, J.-S. Porous Chromium Terephthalate MIL-101 with Coordinatively Unsaturated Sites: Surface Functionalization, Encapsulation, Sorption and Catalysis. *Adv. Funct. Mater.* **2009,** *19*, 1537.

(26) Ehrenmann, J.; Henninger, S. K.; Janiak, C. Water Adsorption Characteristics of MIL-101 for Heat-Transformation Applications of MOFs. *Eur. J. Inorg. Chem.* **2011,** *2011*, 471.

(27) Huang, X.-C.; Lin, Y.-Y.; Zhang, J.-P.; Chen, X.-M. Ligand-Directed Strategy for Zeolite-Type Metal–Organic Frameworks: Zinc(II) Imidazolates with Unusual Zeolitic Topologies. *Angew. Chem. Int. Ed.* **2006,** *45*, 1557.

(28) Park, K. S.; Ni, Z.; Côté, A. P.; Choi, J. Y.; Huang, R.; Uribe-Romo, F. J.; Chae, H. K.; O'Keeffe, M.; Yaghi, O. M. Exceptional chemical and thermal stability of zeolitic imidazolate frameworks. *Proc. Natl. Acad. Sci. U. S. A.* **2006,** *103*, 10186.

(29) Noh, K.; Lee, J.; Kim, J. Compositions and Structures of Zeolitic Imidazolate Frameworks. *Isr. J. Chem.* **2018,** *58*, 1075.

(30) Pan, Y.; Liu, Y.; Zeng, G.; Zhao, L.; Lai, Z. Rapid synthesis of zeolitic imidazolate framework-8 (ZIF-8) nanocrystals in an aqueous system. *Chem. Commun.* **2011,** *47*, 2071.

(31) Nordin, N. A. H. M.; Ismail, A. F.; Mustafa, A.; Goh, P. S.; Rana, D.; Matsuura, T. Aqueous room temperature synthesis of zeolitic imidazole framework 8 (ZIF-8) with various concentrations of triethylamine. *RSC Adv.* **2014,** *4*, 33292.

(32) Wang, C.; Sudlow, G.; Wang, Z.; Cao, S.; Jiang, Q.; Neiner, A.; Morrissey, J. J.; Kharasch, E. D.; Achilefu, S.; Singamaneni, S. Metal-Organic Framework Encapsulation Preserves the Bioactivity of Protein Therapeutics. *Adv. Healthcare Mater.* **2018,** *7*, 1800950.

(33) Wei, T.-H.; Wu, S.-H.; Huang, Y.-D.; Lo, W.-S.; Williams, B. P.; Chen, S.-Y.; Yang, H.-C.; Hsu, Y.-S.; Lin, Z.-Y.; Chen, X.-H.et al. Rapid mechanochemical encapsulation of biocatalysts into robust metal–organic frameworks. *Nat. Commun.* **2019,** *10*, 5002.

(34) Zheng, H.; Zhang, Y.; Liu, L.; Wan, W.; Guo, P.; Nyström, A. M.; Zou, X. One-pot Synthesis of Metal–Organic Frameworks with Encapsulated Target Molecules and Their Applications for Controlled Drug Delivery. *J. Am. Chem. Soc.* **2016,** *138*, 962.

(35) Cavka, J. H.; Jakobsen, S.; Olsbye, U.; Guillou, N.; Lamberti, C.; Bordiga, S.; Lillerud, K. P. A New Zirconium Inorganic Building Brick Forming Metal Organic Frameworks with Exceptional Stability. *J. Am. Chem. Soc.* **2008,** *130*, 13850.

(36) Piscopo, C. G.; Polyzoidis, A.; Schwarzer, M.; Loebbecke, S. Stability of UiO-66 under acidic treatment: Opportunities and limitations for post-synthetic modifications. *Microporous Mesoporous Mater.* **2015,** *208*, 30.

(37) Chavan, S.; Vitillo, J. G.; Gianolio, D.; Zavorotynska, O.; Civalleri, B.; Jakobsen, S.; Nilsen, M. H.; Valenzano, L.; Lamberti, C.; Lillerud, K. P.et al. H_2 storage in isostructural UiO-67 and UiO-66 MOFs. *Phys. Chem. Chem. Phys.* **2012,** *14*, 1614.

(38) Li, L.; Tang, S.; Wang, C.; Lv, X.; Jiang, M.; Wu, H.; Zhao, X. High gas storage capacities and stepwise adsorption in a UiO type metal–organic framework incorporating Lewis basic bipyridyl sites. *Chem. Commun.* **2014,** *50*, 2304.

(39) Hu, Z.; Zhao, D. De facto methodologies toward the synthesis and scale-up production of UiO-66-type metal–organic frameworks and membrane materials. *Dalton Trans.* **2015,** *44*, 19018.

(40) Kim, Y. E.; Kim, S. H.; Kim, D.; Kim, J.; Lee, S. P. Preparation of Mixed Matrix Membranes Containing ZIF-8 and UiO-66 for Multicomponent Light Gas Separation. *Crystals* **2018,** *9*.

(41) Jena, H. S.; Kaczmarek, A. M.; Krishnaraj, C.; Feng, X.; Vijayvergia, K.; Yildirim, H.; Zhao, S.-N.; Van Deun, R.; Der Voort, P. V. White Light Emission Properties of Defect Engineered Metal–Organic Frameworks by Encapsulation of Eu^{3+} and Tb^{3+}. *Cryst. Growth Des.* **2019,** *19*, 6339.

(42) Feng, J.-f.; Liu, T.-f.; Shi, J.; Gao, S.-y.; Cao, R. Dual-Emitting UiO-66(Zr&Eu) Metal–Organic Framework Films for Ratiometric Temperature Sensing. *ACS Appl. Mater. Interfaces* **2018,** *10*, 20854.

(43) Sun, Z.; Ling, Y.; Liu, S. G.; Yang, Y. Z.; Wang, X. H.; Fan, Y. Z.; Li, N. B.; Luo, H. Q. Metal–Organic Framework as a Chemosensor Based on Luminescence Properties for Monitoring Cetyltrimethylammonium Bromide and Its Application in Smartphones. *Inorg. Chem.* **2019,** *58*, 8388.

(44) Dhakshinamoorthy, A.; Santiago-Portillo, A.; Asiri, A. M.; Garcia, H. Engineering UiO-66 Metal Organic Framework for Heterogeneous Catalysis. *ChemCatChem* **2019,** *11*, 899.

(45) Zhang, Y.; Chen, H.; Pan, Y.; Zeng, X.; Jiang, X.; Long, Z.; Hou, X. Cerium-based UiO-66 metal–organic frameworks explored as efficient redox catalysts: titanium incorporation and generation of abundant oxygen vacancies. *Chem. Commun.* **2019,** *55*, 13959.

(46) Feng, Y.; Chen, Q.; Jiang, M.; Yao, J. Tailoring the Properties of UiO-66 through Defect Engineering: A Review. *Ind. Eng. Chem. Res.* **2019,** *58*, 17646.

(47) Bueken, B.; Van Velthoven, N.; Krajnc, A.; Smolders, S.; Taulelle, F.; Mellot-Draznieks, C.; Mali, G.; Bennett, T. D.; De Vos, D. Tackling the Defect Conundrum in UiO-66: A Mixed-Linker Approach to Engineering Missing Linker Defects. *Chem. Mater.* **2017,** *29*, 10478.

(48) Bai, Y.; Dou, Y.; Xie, L.-H.; Rutledge, W.; Li, J.-R.; Zhou, H.-C. Zr-based metal–organic frameworks: design, synthesis, structure, and applications. *Chem. Soc. Rev.* **2016,** *45*, 2327.

(49) Mai, Z.; Liu, D. Synthesis and Applications of Isoreticular Metal–Organic Frameworks IRMOFs-n (n = 1, 3, 6, 8). *Cryst. Growth Des.* **2019,** *19*, 7439.

(50) Tu, B.; Diestel, L.; Shi, Z.-L.; Bandara, W. R. L. N.; Chen, Y.; Lin, W.; Zhang, Y.-B.; Telfer, S. G.; Li, Q. Harnessing Bottom-Up Self-Assembly To Position Five Distinct Components in an Ordered Porous Framework. *Angew. Chem. Int. Ed.* **2019,** *58*, 5348.

(51) Bunck, D. N.; Dichtel, W. R. Mixed Linker Strategies for Organic Framework Functionalization. *Chem. Eur. J.* **2013,** *19*, 818.

(52) Nelson, D. L.; Cox, M. M.; Lehninger, A. L. *Lehninger Principles of Biochemistry*; Seventh ed.; W.H. Freeman/Macmillan Learning, 2017.

(53) Berg, J. M.; Tymoczko, J. L.; Gatto, G. J., Jr.; Stryer, L. *Biochemistry*; Ninth ed.; Macmillan International Higher Education, 2019.

(54) Deng, H.; Doonan, C. J.; Furukawa, H.; Ferreira, R. B.; Towne, J.; Knobler, C. B.; Wang, B.; Yaghi, O. M. Multiple Functional Groups of Varying Ratios in Metal-Organic Frameworks. *Science* **2010,** *327,* 846.

(55) Taddei, M.; Tiana, D.; Casati, N.; van Bokhoven, J. A.; Smit, B.; Ranocchiari, M. Mixed-linker UiO-66: structure–property relationships revealed by a combination of high-resolution powder X-ray diffraction and density functional theory calculations. *Phys. Chem. Chem. Phys.* **2017,** *19,* 1551.

(56) Taylor-Pashow, K. M. L.; Della Rocca, J.; Xie, Z.; Tran, S.; Lin, W. Postsynthetic Modifications of Iron-Carboxylate Nanoscale Metal−Organic Frameworks for Imaging and Drug Delivery. *J. Am. Chem. Soc.* **2009,** *131*, 14261.

(57) Marx, S.; Kleist, W.; Huang, J.; Maciejewski, M.; Baiker, A. Tuning functional sites and thermal stability of mixed-linker MOFs based on MIL-53(Al). *Dalton Trans.* **2010,** *39*, 3795.

(58) Kong, X.; Deng, H.; Yan, F.; Kim, J.; Swisher, J. A.; Smit, B.; Yaghi, O. M.; Reimer, J. A. Mapping of Functional Groups in Metal-Organic Frameworks. *Science* **2013,** *341*, 882.

(59) Krajnc, A.; Bueken, B.; De Vos, D.; Mali, G. Improved resolution and simplification of the spin-diffusion-based NMR method for the structural analysis of mixed-linker MOFs. *J. Magn. Reson.* **2017,** *279*, 22.

(60) Osborn Popp, T. M.; Yaghi, O. M. Sequence-Dependent Materials. *Acc. Chem. Res.* **2017,** *50*, 532.

(61) Osborn Popp, T. M.; Plantz, A. Z.; Yaghi, O. M.; Reimer, J. A. Precise Control of Molecular Self-Diffusion in Isoreticular and Multivariate Metal-Organic Frameworks. *ChemPhysChem* **2020,** *21*, 32.

(62) Chen, W.; Wang, J.-Y.; Chen, C.; Yue, Q.; Yuan, H.-M.; Chen, J.-S.; Wang, S.-N. Photoluminescent Metal−Organic Polymer Constructed from Trimetallic Clusters and Mixed Carboxylates. *Inorg. Chem.* **2003,** *42*, 944.

(63) Koh, K.; Wong-Foy, A. G.; Matzger, A. J. A Crystalline Mesoporous Coordination Copolymer with High Microporosity. *Angew. Chem. Int. Ed.* **2008,** *47*, 677.

(64) Koh, K.; Wong-Foy, A. G.; Matzger, A. J. A Porous Coordination Copolymer with over 5000 m^2/g BET Surface Area. *J. Am. Chem. Soc.* **2009,** *131*, 4184.

(65) Babarao, R.; Jiang, J. Molecular Screening of Metal−Organic Frameworks for CO_2 Storage. *Langmuir* **2008,** *24*, 6270.

(66) Peng, X.; Cheng, X.; Cao, D. Computer simulations for the adsorption and separation of $CO_2/CH_4/H_2/N_2$ gases by UMCM-1 and UMCM-2 metal organic frameworks. *J. Mater. Chem.* **2011,** *21*, 11259.

(67) Bauer, G.; Ongari, D.; Xu, X.; Tiana, D.; Smit, B.; Ranocchiari, M. Metal–Organic Frameworks Invert Molecular Reactivity: Lewis Acidic Phosphonium Zwitterions Catalyze the Aldol-Tishchenko Reaction. *J. Am. Chem. Soc.* **2017,** *139*, 18166.

(68) Tanabe, K. K.; Cohen, S. M. Modular, Active, and Robust Lewis Acid Catalysts Supported on a Metal−Organic Framework. *Inorg. Chem.* **2010,** *49*, 6766.

(69) Wang, Z.; Tanabe, K. K.; Cohen, S. M. Accessing Postsynthetic Modification in a Series of Metal-Organic Frameworks and the Influence of Framework Topology on Reactivity. *Inorg. Chem.* **2009,** *48*, 296.

(70) Müller, M.; Devaux, A.; Yang, C.-H.; De Cola, L.; Fischer, R. A. Highly emissive metal–organic framework composites by host–guest chemistry. *Photochem. Photobiol. Sci.* **2010,** *9*, 846.

(71) Babarao, R.; Jiang, J. Unraveling the Energetics and Dynamics of Ibuprofen in Mesoporous Metal−Organic Frameworks. *J. Phys. Chem. C* **2009,** *113*, 18287.

(72) Padmanaban, M.; Müller, P.; Lieder, C.; Gedrich, K.; Grünker, R.; Bon, V.; Senkovska, I.; Baumgärtner, S.; Opelt, S.; Paasch, S.et al. Application of a chiral metal–organic framework in enantioselective separation. *Chem. Commun.* **2011,** *47*, 12089.

(73) Yao, Q.; Su, J.; Cheung, O.; Liu, Q.; Hedin, N.; Zou, X. Interpenetrated metal–organic frameworks and their uptake of CO_2 at relatively low pressures. *J. Mater. Chem.* **2012,** *22*, 10345.

(74) Schoedel, A.; Boyette, W.; Wojtas, L.; Eddaoudi, M.; Zaworotko, M. J. A Family of Porous Lonsdaleite-e Networks Obtained through Pillaring of Decorated Kagomé Lattice Sheets. *J. Am. Chem. Soc.* **2013,** *135*, 14016.

(75) Schoedel, A.; Cairns, A. J.; Belmabkhout, Y.; Wojtas, L.; Mohamed, M.; Zhang, Z.; Proserpio, D. M.; Eddaoudi, M.; Zaworotko, M. J. The asc Trinodal Platform: Two-Step Assembly of Triangular, Tetrahedral, and Trigonal-Prismatic Molecular Building Blocks. *Angew. Chem. Int. Ed.* **2013,** *52*, 2902.

(76) Liu, L.; Konstas, K.; Hill, M. R.; Telfer, S. G. Programmed Pore Architectures in Modular Quaternary Metal–Organic Frameworks. *J. Am. Chem. Soc.* **2013,** *135*, 17731.

(77) Koh, K.; Wong-Foy, A. G.; Matzger, A. J. Coordination Copolymerization Mediated by $Zn_4O(CO_2R)_6$ Metal Clusters: a Balancing Act between Statistics and Geometry. *J. Am. Chem. Soc.* **2010,** *132*, 15005.

(78) Liu, L.; Telfer, S. G. Systematic Ligand Modulation Enhances the Moisture Stability and Gas Sorption Characteristics of Quaternary Metal–Organic Frameworks. *J. Am. Chem. Soc.* **2015,** *137*, 3901.

(79) Vacher, M.; Fdez. Galván, I.; Ding, B.-W.; Schramm, S.; Berraud-Pache, R.; Naumov, P.; Ferré, N.; Liu, Y.-J.; Navizet, I.; Roca-Sanjuán, D.et al. Chemi- and Bioluminescence of Cyclic Peroxides. *Chem. Rev.* **2018,** *118*, 6927.

(80) Clegg, W.; Bourhill, G.; Sage, I. Hexakis(antipyrine-O)terbium(III) triiodide at 160 K: confirmation of a centrosymmetric structure for a brilliantly triboluminescent complex. *Acta Cryst. E* **2002,** *58*, m159.

(81) Lakowicz, J. R. *Principles of Fluorescence Spectroscopy*; New York ; Berlin : Springer, 2006, 3rd ed, 2006.

(82) Valeur, B.; Berberan-Santos, M. N. *Molecular Fluorescence: Principles and Applications*; Weinheim : Wiley-VCH, 2013, 2nd ed, 2013.

(83) Chou, P.-T.; Chi, Y. Phosphorescent Dyes for Organic Light-Emitting Diodes. *Chem. Eur. J.* **2007,** *13*, 380.

(84) Zhang, X.-F.; Yang, X.; Niu, K.; Geng, H. Phosphorescence of BODIPY dyes. *J. Photochem. Photobiol., A* **2014,** *285*, 16.

(85) Fletcher, K. A.; Fakayode, S. O.; Lowry, M.; Tucker, S. A.; Neal, S. L.; Kimaru, I. W.; McCarroll, M. E.; Patonay, G.; Oldham, P. B.; Rusin, O.et al. Molecular Fluorescence, Phosphorescence, and Chemiluminescence Spectrometry. *Anal. Chem.* **2006,** *78*, 4047.

(86) Dolgopolova, E. A.; Rice, A. M.; Martin, C. R.; Shustova, N. B. Photochemistry and photophysics of MOFs: steps towards MOF-based sensing enhancements. *Chem. Soc. Rev.* **2018,** *47*, 4710.

(87) Kreno, L. E.; Leong, K.; Farha, O. K.; Allendorf, M.; Van Duyne, R. P.; Hupp, J. T. Metal–Organic Framework Materials as Chemical Sensors. *Chem. Rev.* **2012,** *112*, 1105.

(88) Cornelio, J. Luminescence in metal-organic frameworks: origin and applications. *Chem. N.Z.* **2019,** *83*, 30.

(89) Cepeda, J.; Rodríguez-Diéguez, A. Tuning the luminescence performance of metal–organic frameworks based on d^{10} metal ions: from an inherent versatile behaviour to their response to external stimuli. *CrystEngComm* **2016,** *18*, 8556.

(90) Kent, C. A.; Mehl, B. P.; Ma, L.; Papanikolas, J. M.; Meyer, T. J.; Lin, W. Energy Transfer Dynamics in Metal−Organic Frameworks. *J. Am. Chem. Soc.* **2010,** *132*, 12767.

(91) Allendorf, M. D.; Bauer, C. A.; Bhakta, R. K.; Houk, R. J. T. Luminescent metal-organic frameworks. *Chem. Soc. Rev.* **2009,** *38*, 1330.

(92) Wen, Y.; Sheng, T.; Zhu, X.; Zhuo, C.; Su, S.; Li, H.; Hu, S.; Zhu, Q.-L.; Wu, X. Introduction of Red-Green-Blue Fluorescent Dyes into a Metal–Organic Framework for Tunable White Light Emission. *Adv. Mater.* **2017,** *29*, 1700778.

(93) Rocha, J.; Brites, C. D. S.; Carlos, L. D. Lanthanide Organic Framework Luminescent Thermometers. *Chem. Eur. J.* **2016,** *22*, 14782.

(94) An, J.; Shade, C. M.; Chengelis-Czegan, D. A.; Petoud, S.; Rosi, N. L. Zinc-Adeninate Metal−Organic Framework for Aqueous Encapsulation and Sensitization of Near-infrared and Visible Emitting Lanthanide Cations. *J. Am. Chem. Soc.* **2011,** *133*, 1220.

(95) de Bettencourt-Dias, A. *Introduction to Lanthanide Ion Luminescence*, 2014.

(96) Zhao, S.-N.; Wang, G.; Poelman, D.; Voort, P. V. D. Luminescent Lanthanide MOFs: A Unique Platform for Chemical Sensing. *Materials* **2018,** *11*, 572.

(97) Cotton, S. A. *Lanthanide and Actinide Chemistry*; Hoboken, NJ : Wiley, 2006.

(98) Yin, H.-Q.; Wang, X.-Y.; Yin, X.-B. Rotation Restricted Emission and Antenna Effect in Single Metal–Organic Frameworks. *J. Am. Chem. Soc.* **2019,** *141*, 15166.

(99) Cheng, H.; Sun, Q.; Wang, S.; Zhang, Y.; Fan, D.; Huang, J. J.; Jin, S. Elucidating Energy-Transfer Dynamics Within and Beyond Lanthanide Metal–Organic Frameworks. *J. Phys. Chem. C* **2019,** *123*, 30165.

(100) Liu, Z.; He, W.; Guo, Z. Metal coordination in photoluminescent sensing. *Chem. Soc. Rev.* **2013,** *42*, 1568.

(101) Cui, Y.; Yue, Y.; Qian, G.; Chen, B. Luminescent Functional Metal–Organic Frameworks. *Chem. Rev.* **2012,** *112*, 1126.

(102) Bordiga, S.; Lamberti, C.; Ricchiardi, G.; Regli, L.; Bonino, F.; Damin, A.; Lillerud, K. P.; Bjorgen, M.; Zecchina, A. Electronic and vibrational properties of a MOF-5 metal–organic framework: ZnO quantum dot behaviour. *Chem. Commun.* **2004,** *20*, 2300.

(103) Civalleri, B.; Napoli, F.; Noël, Y.; Roetti, C.; Dovesi, R. Ab-initio prediction of materials properties with CRYSTAL: MOF-5 as a case study. *CrystEngComm* **2006,** *8*, 364.

(104) Zhang, Y.; Yuan, S.; Day, G.; Wang, X.; Yang, X.; Zhou, H.-C. Luminescent sensors based on metal-organic frameworks. *Coord. Chem. Rev.* **2018,** *354*, 28.

(105) Tang, Y.-Y.; Ding, C.-X.; Ng, S.-W.; Xie, Y.-S. Syntheses, structures and photoluminescence of Zn(II), Ag(I), Cu(I) and Co(II) coordination polymers of a tetrapyridyl ligand. *RSC Adv.* **2013,** *3*, 18134.

(106) Sahoo, H. Förster resonance energy transfer – A spectroscopic nanoruler: Principle and applications. *J. Photochem. Photobiol. C* **2011,** *12*, 20.

(107) Dexter, D. L. A Theory of Sensitized Luminescence in Solids. *J. Chem. Phys.* **1953,** *21*, 836.

(108) Förster, T. Zwischenmolekulare Energiewanderung und Fluoreszenz. *Ann. Phys.* **1948,** *437*, 55.

(109) Birks, J. B. Excimers and Exciplexes. *Nature* **1967,** *214*, 1187.

(110) Pensack, R. D.; Ashmore, R. J.; Paoletta, A. L.; Scholes, G. D. The Nature of Excimer Formation in Crystalline Pyrene Nanoparticles. *J. Phys. Chem. C* **2018,** *122*, 21004.

(111) Deria, P.; Yu, J.; Smith, T.; Balaraman, R. P. Ground-State versus Excited-State Interchromophoric Interaction: Topology Dependent Excimer Contribution in Metal–Organic Framework Photophysics. *J. Am. Chem. Soc.* **2017,** *139*, 5973.

(112) Jameson, D. M. *Introduction to fluorescence*; Taylor & Francis, 2014.

(113) Di Bartolo, B.; Collins, J. *Biophotonics: Spectroscopy, Imaging, Sensing, and Manipulation*, 2011.

(114) Wilbraham, L.; Coudert, F.-X.; Ciofini, I. Modelling photophysical properties of metal-organic frameworks: a density functional theory based approach. *Phys. Chem. Chem. Phys.* **2016,** *18*, 25176.

(115) Wagie, H. E.; Woehl, J. C.; Geissinger, P. A systematic, quantum-mechanical, finite-order approach for the quantitative determination of molecular internal electric fields in guest–host systems from Stark spectroscopy. *Theor. Chem. Acc.* **2016,** *135*, 114.

(116) Medishetty, R.; Nalla, V.; Nemec, L.; Henke, S.; Mayer, D.; Sun, H.; Reuter, K.; Fischer, R. A. A New Class of Lasing Materials: Intrinsic Stimulated Emission from Nonlinear Optically Active Metal–Organic Frameworks. *Adv. Mater.* **2017,** *29*, 1605637.

(117) Webb, J. E. A.; Chen, K.; Prasad, S. K. K.; Wojciechowski, J. P.; Falber, A.; Thordarson, P.; Hodgkiss, J. M. Quantifying highly efficient incoherent energy transfer in perylene-based multichromophore arrays. *Phys. Chem. Chem. Phys.* **2016,** *18*, 1712.

(118) Park, H. J.; So, M. C.; Gosztola, D.; Wiederrecht, G. P.; Emery, J. D.; Martinson, A. B. F.; Er, S.; Wilmer, C. E.; Vermeulen, N. A.; Aspuru-Guzik, A.et al. Layer-by-Layer Assembled Films of Perylene Diimide- and Squaraine-Containing Metal–Organic Framework-like Materials: Solar Energy Capture and Directional Energy Transfer. *ACS Appl. Mater. Interfaces* **2016,** *8*, 24983.

(119) Oldenburg, M.; Turshatov, A.; Busko, D.; Wollgarten, S.; Adams, M.; Baroni, N.; Welle, A.; Redel, E.; Wöll, C.; Richards, B. S.et al. Photon Upconversion at Crystalline Organic–Organic Heterojunctions. *Adv. Mater.* **2016,** *28*, 8477.

(120) So, M. C.; Wiederrecht, G. P.; Mondloch, J. E.; Hupp, J. T.; Farha, O. K. Metal-organic framework materials for light-harvesting and energy transfer. *Chem. Commun.* **2015,** *51*, 3501.

(121) Adams, M.; Kozlowska, M.; Baroni, N.; Oldenburg, M.; Ma, R.; Busko, D.; Turshatov, A.; Emandi, G.; Senge, M. O.; Haldar, R.et al. Highly Efficient One-Dimensional Triplet Exciton Transport in a Palladium–Porphyrin-Based Surface-Anchored Metal–Organic Framework. *ACS Appl. Mater. Interfaces* **2019,** *11*, 15688.

(122) Lee, C. Y.; Farha, O. K.; Hong, B. J.; Sarjeant, A. A.; Nguyen, S. T.; Hupp, J. T. Light-Harvesting Metal–Organic Frameworks (MOFs): Efficient Strut-to-Strut Energy Transfer in Bodipy and Porphyrin-Based MOFs. *J. Am. Chem. Soc.* **2011,** *133*, 15858.

(123) Khatun, A.; Panda, D. K.; Sayresmith, N.; Walter, M. G.; Saha, S. Thiazolothiazole-Based Luminescent Metal–Organic Frameworks with Ligand-to-Ligand Energy Transfer and Hg^{2+}-Sensing Capabilities. *Inorg. Chem.* **2019,** *58*, 12707.

(124) Dolgopolova, E. A.; Williams, D. E.; Greytak, A. B.; Rice, A. M.; Smith, M. D.; Krause, J. A.; Shustova, N. B. A Bio-inspired Approach for Chromophore Communication: Ligand-to-Ligand and Host-to-Guest Energy Transfer in Hybrid Crystalline Scaffolds. *Angew. Chem. Int. Ed.* **2015,** *54*, 13639.

(125) Mikhnenko, O. V.; Blom, P. W. M.; Nguyen, T.-Q. Exciton diffusion in organic semiconductors. *Energy Environ. Sci.* **2015,** *8*, 1867.

(126) Son, H.-J.; Jin, S.; Patwardhan, S.; Wezenberg, S. J.; Jeong, N. C.; So, M.; Wilmer, C. E.; Sarjeant, A. A.; Schatz, G. C.; Snurr, R. Q.et al. Light-Harvesting and Ultrafast Energy Migration in Porphyrin-Based Metal–Organic Frameworks. *J. Am. Chem. Soc.* **2013,** *135*, 862.

(127) Zhang, Q.; Zhang, C.; Cao, L.; Wang, Z.; An, B.; Lin, Z.; Huang, R.; Zhang, Z.; Wang, C.; Lin, W. Förster Energy Transport in Metal–Organic Frameworks Is Beyond Step-by-Step Hopping. *J. Am. Chem. Soc.* **2016,** *138*, 5308.

(128) Mukhopadhyay, A.; Maka, V. K.; Savitha, G.; Moorthy, J. N. Photochromic 2D Metal-Organic Framework Nanosheets (MONs): Design, Synthesis, and Functional MON-Ormosil Composite. *Chem* **2018,** *4*, 1059.

(129) Pan, M.; Lin, X.-M.; Li, G.-B.; Su, C.-Y. Progress in the study of metal–organic materials applying naphthalene diimide (NDI) ligands. *Coord. Chem. Rev.* **2011,** *255*, 1921.

(130) Garai, B.; Mallick, A.; Banerjee, R. Photochromic metal–organic frameworks for inkless and erasable printing. *Chem. Sci.* **2016,** *7*, 2195.

(131) Fu, Z.; Zhang, J.; Zeng, Y.; Tan, Y.; Liao, S.; Chen, H.; Dai, J. Synthesis and structure of a mixed crystal containing tris(4-pyridiniumyl)-1,3,5-triazine and benzenetetracarboxylate ions: constructing a new photochromic molecular system viaself-assembly. *CrystEngComm* **2012,** *14*, 786.

(132) Coudert, F.-X. Responsive Metal–Organic Frameworks and Framework Materials: Under Pressure, Taking the Heat, in the Spotlight, with Friends. *Chem. Mater.* **2015,** *27*, 1905.

(133) Park, J.; Yuan, D.; Pham, K. T.; Li, J.-R.; Yakovenko, A.; Zhou, H.-C. Reversible Alteration of CO2 Adsorption upon Photochemical or Thermal Treatment in a Metal–Organic Framework. *J. Am. Chem. Soc.* **2012,** *134*, 99.

(134) Healey, K.; Liang, W.; Southon, P. D.; Church, T. L.; D'Alessandro, D. M. Photoresponsive spiropyran-functionalised MOF-808: postsynthetic incorporation and light dependent gas adsorption properties. *J. Mater. Chem. A* **2016,** *4*, 10816.

(135) Calbo, J.; Golomb, M. J.; Walsh, A. Redox-active metal–organic frameworks for energy conversion and storage. *J. Mater. Chem. A* **2019,** *7*, 16571.

(136) D'Alessandro, D. M. Exploiting redox activity in metal–organic frameworks: concepts, trends and perspectives. *Chem. Commun.* **2016,** *52*, 8957.

(137) Dong, R.; Han, P.; Arora, H.; Ballabio, M.; Karakus, M.; Zhang, Z.; Shekhar, C.; Adler, P.; Petkov, P. S.; Erbe, A.et al. High-mobility band-like charge transport in a semiconducting two-dimensional metal–organic framework. *Nat. Mater.* **2018,** *17*, 1027.

(138) Pattengale, B.; Neu, J.; Ostresh, S.; Hu, G.; Spies, J. A.; Okabe, R.; Brudvig, G. W.; Schmuttenmaer, C. A. Metal–Organic Framework Photoconductivity via Time-Resolved Terahertz Spectroscopy. *J. Am. Chem. Soc.* **2019,** *141*, 9793.

(139) Stuart, C. M.; Frontiera, R. R.; Mathies, R. A. Excited-State Structure and Dynamics of cis- and trans-Azobenzene from Resonance Raman Intensity Analysis. *J. Phys. Chem. A* **2007,** *111*, 12072.

(140) Walton, I. M.; Cox, J. M.; Coppin, J. A.; Linderman, C. M.; Patel, D. G.; Benedict, J. B. Photo-responsive MOFs: light-induced switching of porous single crystals containing a photochromic diarylethene. *Chem. Commun.* **2013,** *49*, 8012.

(141) Ma, L.; Abney, C.; Lin, W. Enantioselective catalysis with homochiral metal–organic frameworks. *Chem. Soc. Rev.* **2009,** *38*, 1248.

(142) Gascon, J.; Corma, A.; Kapteijn, F.; Llabrés i Xamena, F. X. Metal Organic Framework Catalysis: Quo vadis? *ACS Catal.* **2013,** *4*, 361.

(143) Lee, J.; Farha, O. K.; Roberts, J.; Scheidt, K. A.; Nguyen, S. T.; Hupp, J. T. Metal–organic framework materials as catalysts. *Chem. Soc. Rev.* **2009,** *38*, 1450.

(144) Dhakshinamoorthy, A.; Li, Z.; Garcia, H. Catalysis and photocatalysis by metal organic frameworks. *Chem. Soc. Rev.* **2018,** *47*, 8134.

(145) Yang, D.; Gates, B. C. Catalysis by Metal Organic Frameworks: Perspective and Suggestions for Future Research. *ACS Catal.* **2019,** *9*, 1779.

(146) Chughtai, A. H.; Ahmad, N.; Younus, H. A.; Laypkov, A.; Verpoort, F. Metal-organic frameworks: versatile heterogeneous catalysts for efficient catalytic organic transformations. *Chem. Soc. Rev.* **2015,** *44*, 6804.

(147) Maina, J. W.; Schütz, J. A.; Grundy, L.; Des Ligneris, E.; Yi, Z.; Kong, L.; Pozo-Gonzalo, C.; Ionescu, M.; Dumée, L. F. Inorganic Nanoparticles/Metal Organic Framework Hybrid Membrane Reactors for Efficient Photocatalytic Conversion of CO_2. *ACS Appl. Mater. Interfaces* **2017,** *9*, 35010.

(148) Wee, L. H.; Bajpe, S. R.; Janssens, N.; Hermans, I.; Houthoofd, K.; Kirschhock, C. E. A.; Martens, J. A. Convenient synthesis of $Cu_3(BTC)_2$ encapsulated Keggin heteropolyacid nanomaterial for application in catalysis. *Chem. Commun.* **2010,** *46*, 8186.

(149) Genna, D. T.; Wong-Foy, A. G.; Matzger, A. J.; Sanford, M. S. Heterogenization of Homogeneous Catalysts in Metal–Organic Frameworks via Cation Exchange. *J. Am. Chem. Soc.* **2013,** *135*, 10586.

(150) Zeng, L.; Guo, X.; He, C.; Duan, C. Metal–Organic Frameworks: Versatile Materials for Heterogeneous Photocatalysis. *ACS Catal.* **2016,** *6*, 7935.

(151) Mo, Q.; Chen, N.; Deng, M.; Yang, L.; Gao, Q. Metallic Cobalt@Nitrogen-Doped Carbon Nanocomposites: Carbon-Shell Regulation toward Efficient Bi-Functional Electrocatalysis. *ACS Appl. Mater. Interfaces* **2017,** *9*, 37721.

(152) Hwang, Y. K.; Hong, D.-Y.; Chang, J.-S.; Jhung, S. H.; Seo, Y.-K.; Kim, J.; Vimont, A.; Daturi, M.; Serre, C.; Férey, G. Amine Grafting on Coordinatively Unsaturated Metal Centers of MOFs: Consequences for Catalysis and Metal Encapsulation. *Angew. Chem. Int. Ed.* **2008,** *47*, 4144.

(153) Horcajada, P.; Surble, S.; Serre, C.; Hong, D.-Y.; Seo, Y.-K.; Chang, J.-S.; Greneche, J.-M.; Margiolaki, I.; Ferey, G. Synthesis and catalytic properties of MIL-100(Fe), an iron(III) carboxylate with large pores. *Chem. Commun.* **2007**, 2820.

(154) Liu, M.; Wu, J.; Hou, H. Metal–Organic Framework (MOF)-Based Materials as Heterogeneous Catalysts for C−H Bond Activation. *Chem. Eur. J.* **2019,** *25*, 2935.

(155) Dhakshinamoorthy, A.; Asiri, A. M.; Garcia, H. Formation of C–C and C–Heteroatom Bonds by C–H Activation by Metal Organic Frameworks as Catalysts or Supports. *ACS Catal.* **2019,** *9*, 1081.

(156) Yuan, L.; Tian, M.; Lan, J.; Cao, X.; Wang, X.; Chai, Z.; Gibson, J. K.; Shi, W. Defect engineering in metal–organic frameworks: a new strategy to develop applicable actinide sorbents. *Chem. Commun.* **2018,** *54*, 370.

(157) Chong, S.; Thiele, G.; Kim, J. Excavating hidden adsorption sites in metal-organic frameworks using rational defect engineering. *Nat. Commun.* **2017,** *8*, 1539.

(158) Sholl, D. S.; Lively, R. P. Defects in Metal–Organic Frameworks: Challenge or Opportunity? *J. Phys. Chem. Lett* **2015,** *6*, 3437.

(159) Firth, F. C. N.; Cliffe, M. J.; Vulpe, D.; Aragones-Anglada, M.; Moghadam, P. Z.; Fairen-Jimenez, D.; Slater, B.; Grey, C. P. Engineering new defective phases of UiO family metal–organic frameworks with water. *J. Mater. Chem. A* **2019,** *7*, 7459.

(160) Gatto, G.; Macchioni, A.; Bondi, R.; Marmottini, F.; Costantino, F. Post Synthetic Defect Engineering of UiO-66 Metal–Organic Framework with An Iridium(III)-HEDTA Complex and Application in Water Oxidation Catalysis. *Inorganics* **2019,** *7*.

(161) Dissegna, S.; Epp, K.; Heinz, W. R.; Kieslich, G.; Fischer, R. A. Defective Metal-Organic Frameworks. *Adv. Mater.* **2018,** *30*, 1704501.

(162) Mautschke, H. H.; Drache, F.; Senkovska, I.; Kaskel, S.; Llabrés i Xamena, F. X. Catalytic properties of pristine and defect-engineered Zr-MOF-808 metal organic frameworks. *Catal. Sci. Technol.* **2018,** *8*, 3610.

(163) Lun, D. J.; Waterhouse, G. I. N.; Telfer, S. G. A General Thermolabile Protecting Group Strategy for Organocatalytic Metal−Organic Frameworks. *J. Am. Chem. Soc.* **2011,** *133*, 5806.

(164) Roberts, J. M.; Fini, B. M.; Sarjeant, A. A.; Farha, O. K.; Hupp, J. T.; Scheidt, K. A. Urea Metal–Organic Frameworks as Effective and Size-Selective Hydrogen-Bond Catalysts. *J. Am. Chem. Soc.* **2012,** *134*, 3334.

(165) Tehrani, A. A.; Abedi, S.; Morsali, A.; Wang, J.; Junk, P. C. Urea-containing metal-organic frameworks as heterogeneous organocatalysts. *J. Mater. Chem. A* **2015,** *3*, 20408.

(166) Zhang, X.; Zhang, Z.; Boissonnault, J.; Cohen, S. M. Design and synthesis of squaramide-based MOFs as efficient MOF-supported hydrogen-bonding organocatalysts. *Chem. Commun.* **2016,** *52*, 8585.

(167) Kutzscher, C.; Nickerl, G.; Senkovska, I.; Bon, V.; Kaskel, S. Proline Functionalized UiO-67 and UiO-68 Type Metal–Organic Frameworks Showing Reversed Diastereoselectivity in Aldol Addition Reactions. *Chem. Mater.* **2016,** *28*, 2573.

(168) Beheshti, S.; Morsali, A. Post-modified anionic nano-porous metal-organic framework as a novel catalyst for solvent-free Michael addition reactions. *RSC Adv.* **2014,** *4*, 37036.

(169) Shi, L.-X.; Wu, C.-D. A nanoporous metal-organic framework with accessible Cu2+ sites for the catalytic Henry reaction. *Chem. Commun.* **2011,** *47*, 2928.

(170) Phan, N. T. S.; Le, K. K. A.; Phan, T. D. MOF-5 as an efficient heterogeneous catalyst for Friedel–Crafts alkylation reactions. *Appl. Catal. A: Gen* **2010,** *382*, 246.

(171) Miao, Z.; Qi, C.; Wensley, A. M.; Luan, Y. Development of a novel Bronsted acid UiO-66 metal-organic framework catalyst by postsynthetic modification and its application in catalysis. *RSC Adv.* **2016,** *6*, 67226.

(172) Gao, W.-Y.; Wu, H.; Leng, K.; Sun, Y.; Ma, S. Inserting CO_2 into Aryl C−H Bonds of Metal–Organic Frameworks: CO_2 Utilization for Direct Heterogeneous C−H Activation. *Angew. Chem. Int. Ed.* **2016,** *128*, 5562.

(173) Tu, B.; Pang, Q.; Xu, H.; Li, X.; Wang, Y.; Ma, Z.; Weng, L.; Li, Q. Reversible Redox Activity in Multicomponent Metal–Organic Frameworks Constructed from Trinuclear Copper Pyrazolate Building Blocks. *J. Am. Chem. Soc.* **2017,** *139*, 7998.

(174) Yuan, S.; Chen, Y.-P.; Qin, J.-S.; Lu, W.; Zou, L.; Zhang, Q.; Wang, X.; Sun, X.; Zhou, H.-C. Linker Installation: Engineering Pore Environment with Precisely Placed Functionalities in Zirconium MOFs. *J. Am. Chem. Soc.* **2016,** *138*, 8912.

(175) Liu, L.; Zhou, T.-Y.; Telfer, S. G. Modulating the Performance of an Asymmetric Organocatalyst by Tuning Its Spatial Environment in a Metal–Organic Framework. *J. Am. Chem. Soc.* **2017,** *139*, 13936.

(176) Zhou, T.-Y.; Auer, B.; Lee, S. J.; Telfer, S. G. Catalysts Confined in Programmed Framework Pores Enable New Transformations and Tune Reaction Efficiency and Selectivity. *J. Am. Chem. Soc.* **2019,** *141*, 1577.

(177) Hu, Z.; Deibert, B. J.; Li, J. Luminescent metal-organic frameworks for chemical sensing and explosive detection. *Chem. Soc. Rev.* **2014,** *43*, 5815.

(178) Liu, M.; Quah, H. S.; Wen, S.; Yu, Z.; Vittal, J. J.; Ji, W. Efficient Third Harmonic Generation in a Metal–Organic Framework. *Chem. Mater.* **2016,** *28*, 3385.

(179) Yue, D.; Jian-Jun, Z.; Shu-Qin, L.; Huajun, Z.; Ying-Ji, S.; Yu-Zhen, P.; Jun, N.; Jing-Si, Y. A Trichromatic and White-Light-Emitting MOF Composite for Multi-Dimensional and Multi-Response Ratiometric Luminescent Sensing. *Chem. Eur. J.* **2018,** *24*, 9555.

(180) Gai, Y.; Guo, Q.; Xiong, K.; Jiang, F.; Li, C.; Li, X.; Chen, Y.; Zhu, C.; Huang, Q.; Yao, R.et al. Mixed-Lanthanide Metal–Organic Frameworks with Tunable Color and White Light Emission. *Cryst. Growth Des.* **2017,** *17*, 940.

(181) Li, Z.-J.; Li, X.-Y.; Yan, Y.-T.; Hou, L.; Zhang, W.-Y.; Wang, Y.-Y. Tunable Emission and Selective Luminescence Sensing in a Series of Lanthanide Metal–Organic Frameworks with Uncoordinated Lewis Basic Triazolyl Sites. *Cryst. Growth Des.* **2018,** *18*, 2031.

(182) Su, Y.; Yu, J.; Li, Y.; Phua, S. F. Z.; Liu, G.; Lim, W. Q.; Yang, X.; Ganguly, R.; Dang, C.; Yang, C.et al. Versatile bimetallic lanthanide metal-organic frameworks for tunable emission and efficient fluorescence sensing. *Commun. Chem.* **2018,** *1*, 12.

(183) Seth, S.; Savitha, G.; Moorthy, J. N. Diverse isostructural MOFs by postsynthetic metal node metathesis: anionic-to-cationic framework conversion, luminescence and separation of dyes. *J. Mater. Chem. A* **2015,** *3*, 22915.

(184) Li, Y.-F.; Wang, D.; Liao, Z.; Kang, Y.; Ding, W.-H.; Zheng, X.-J.; Jin, L.-P. Luminescence tuning of the Dy-Zn metal-organic framework and its application in the detection of Fe(III) ions. *J. Mater. Chem. C* **2016,** *4*, 4211.

(185) Gong, Q.; Hu, Z.; Deibert, B. J.; Emge, T. J.; Teat, S. J.; Banerjee, D.; Mussman, B.; Rudd, N. D.; Li, J. Solution Processable MOF Yellow Phosphor with Exceptionally High Quantum Efficiency. *J. Am. Chem. Soc.* **2014,** *136*, 16724.

(186) Lustig, W. P.; Mukherjee, S.; Rudd, N. D.; Desai, A. V.; Li, J.; Ghosh, S. K. Metal-organic frameworks: functional luminescent and photonic materials for sensing applications. *Chem. Soc. Rev.* **2017,** *46*, 3242.

(187) Huang, W.; Pan, F.; Liu, Y.; Huang, S.; Li, Y.; Yong, J.; Li, Y.; Kirillov, A. M.; Wu, D. An Efficient Blue-Emissive Metal–Organic Framework (MOF) for Lanthanide-

Encapsulated Multicolor and Stimuli-Responsive Luminescence. *Inorg. Chem.* **2017,** *56*, 6362.

(188) Yue, Y.; Binder, A. J.; Song, R.; Cui, Y.; Chen, J.; Hensley, D. K.; Dai, S. Encapsulation of large dye molecules in hierarchically superstructured metal-organic frameworks. *Dalton Trans.* **2014,** *43,* 17893.

(189) Ogi, T.; Iwasaki, H.; Nandiyanto, A. B. D.; Iskandar, F.; Wang, W. N.; Okuyama, K. Direct white light emission from a rare-earth-free aluminium-boron-carbon-oxynitride phosphor. *J. Mater. Chem. C* **2014,** *2*, 4297.

(190) Mech, A.; Monguzzi, A.; Cucinotta, F.; Meinardi, F.; Mezyk, J.; Cola, L. D.; Tubino, R. White light excitation of the near infrared Er^{3+} emission in exchanged zeolite sensitised by oxygen vacancies. *Phys. Chem. Chem. Phys.* **2011,** *13,* 5605.

(191) Khan, A.; Zeb, A.; Li, L.; Zhang, W.; Sun, Z.; Wang, Y.; Luo, J. A Lead-free Semiconducting Hybrid with Ultra-high Color Rendering Index White Light-emission. *J. Mater. Chem. C* **2018,** *6*, 2801.

(192) He, Z.; Zhao, W.; Lam, J. W. Y.; Peng, Q.; Ma, H.; Liang, G.; Shuai, Z.; Tang, B. Z. White light emission from a single organic molecule with dual phosphorescence at room temperature. *Nat. Commun.* **2017,** *8*, 416.

(193) Kamtekar, K. T.; Monkman, A. P.; Bryce, M. R. Recent Advances in White Organic Light-Emitting Materials and Devices (WOLEDs). *Adv. Mater.* **2010,** *22*, 572.

(194) Smith, M. D.; Karunadasa, H. I. White-Light Emission from Layered Halide Perovskites. *Acc. Chem. Res.* **2018,** *51*, 619.

(195) Wang, M.-S.; Guo, S.-P.; Li, Y.; Cai, L.-Z.; Zou, J.-P.; Xu, G.; Zhou, W.-W.; Zheng, F.-K.; Guo, G.-C. A Direct White-Light-Emitting Metal−Organic Framework with Tunable Yellow-to-White Photoluminescence by Variation of Excitation Light. *J. Am. Chem. Soc.* **2009,** *131*, 13572.

(196) Sava, D. F.; Rohwer, L. E. S.; Rodriguez, M. A.; Nenoff, T. M. Intrinsic Broad-Band White-Light Emission by a Tuned, Corrugated Metal–Organic Framework. *J. Am. Chem. Soc.* **2012,** *134,* 3983.

(197) Wu, J.; Zhang, H.; Du, S. Tunable luminescence and white light emission of mixed lanthanide-organic frameworks based on polycarboxylate ligands. *J. Mater. Chem. C* **2016,** *4*, 3364.

(198) Mondal, T.; Mondal, S.; Bose, S.; Sengupta, D.; Ghorai, U. K.; Saha, S. K. Pure white light emission from a rare earth-free intrinsic metal-organic framework and its application in a WLED. *J. Mater. Chem. C* **2018,** *6*, 614.

(199) Lustig, W. P.; Li, J. Luminescent metal–organic frameworks and coordination polymers as alternative phosphors for energy efficient lighting devices. *Coord. Chem. Rev.* **2018,** *373*, 116.

(200) Cornelio, J.; Zhou, T.-Y.; Alkaş, A.; Telfer, S. G. Systematic Tuning of the Luminescence Output of Multicomponent Metal–Organic Frameworks. *J. Am. Chem. Soc.* **2018,** *140*, 15470.

(201) Tranchemontagne, D. J.; Hunt, J. R.; Yaghi, O. M. Room temperature synthesis of metal-organic frameworks: MOF-5, MOF-74, MOF-177, MOF-199, and IRMOF-0. *Tetrahedron* **2008,** *64*, 8553.

(202) Alkaş, A.; Cornelio, J.; Telfer, S. G. Tritopic Triazatruxene Ligands for Multicomponent Metal-Organic Frameworks. *Chem. Asian J.* **2019,** *14*, 1167.

(203) Wyszecki, G.; Stiles, W. S. *Color science : concepts and methods, quantitative data and formulae*; New York : John Wiley & Sons, 2000, 2nd. ed, 2000.

(204) Liang, H.; Wang, X.; Zhang, X.; Liu, Z.; Ge, Z.; Ouyang, X.; Wang, S. Saturated deep-blue emitter based on a spiro[benzoanthracene–fluorene]-linked phenanthrene derivative for non-doped organic light-emitting diodes. *New J. Chem.* **2014,** *38*, 4696.

(205) Doyle, A. G.; Jacobsen, E. N. Small-Molecule H-Bond Donors in Asymmetric Catalysis. *Chem. Rev.* **2007,** *107*, 5713.

(206) Dasheng, L.; Choon‐Hong, T. Chiral Guanidine Catalyzed Enantioselective Reactions. *Chem. Asian J.* **2009,** *4*, 488.

(207) Fu, X.; Tan, C.-H. Mechanistic considerations of guanidine-catalyzed reactions. *Chem. Commun.* **2011,** *47*, 8210.

(208) Woodward, R. B. Structure and the Absorption Spectra of α,β-Unsaturated Ketones. *J. Am. Chem. Soc.* **1941,** *63*, 1123.

(209) Fleming, I.; Williams, D. H. *Spectroscopic Methods in Organic Chemistry*; Seventh edition ed.; Springer, 2019.

(210) Arzhantsev, S.; Maroncelli, M. Design and Characterization of a Femtosecond Fluorescence Spectrometer Based on Optical Kerr Gating. *Appl. Spectrosc.* **2005,** *59*, 206.

(211) Nakamura, R.; Kanematsu, Y. Femtosecond spectral snapshots based on electronic optical Kerr effect. *Rev. Sci. Instrum.* **2004,** *75*, 636.

(212) Mokhtari, A.; Chesnoy, J.; Laubereau, A. Femtosecond time- and frequency-resolved fluorescence spectroscopy of a dye molecule. *Chem. Phys. Lett.* **1989,** *155*, 593.

(213) Peon, J.; Zewail, A. H. DNA/RNA nucleotides and nucleosides: direct measurement of excited-state lifetimes by femtosecond fluorescence up-conversion. *Chem. Phys. Lett.* **2001,** *348*, 255.

(214) Chen, K.; Gallaher, J. K.; Barker, A. J.; Hodgkiss, J. M. Transient Grating Photoluminescence Spectroscopy: An Ultrafast Method of Gating Broadband Spectra. *J. Phys. Chem. Lett* **2014,** *5*, 1732.

(215) Chen, K.; Barker, A. J.; Morgan, F. L. C.; Halpert, J. E.; Hodgkiss, J. M. Effect of Carrier Thermalization Dynamics on Light Emission and Amplification in Organometal Halide Perovskites. *J. Phys. Chem. Lett* **2015,** *6*, 153.

(216) Milam, D. Review and assessment of measured values of the nonlinear refractive-index coefficient of fused silica. *Appl. Opt.* **1998,** *37*, 546.

(217) Pamei, M.; Puzari, A. Luminescent transition metal–organic frameworks: An emerging sensor for detecting biologically essential metal ions. *Nano-Struct. Nano-Objects* **2019,** *19*, 100364.

(218) Porrès, L.; Holland, A.; Pålsson, L.-O.; Monkman, A. P.; Kemp, C.; Beeby, A. Absolute Measurements of Photoluminescence Quantum Yields of Solutions Using an Integrating Sphere. *J. Fluoresc.* **2006,** *16*, 267.

(219) van der Meer, B. W.; van der Meer, D. M.; Vogel, S. S. *Optimizing the Orientation Factor Kappa-Squared for More Accurate FRET Measurements* In *FRET – Förster Resonance Energy Transfer*; Medintz, I.;Hildebrandt, N., Eds. Weinheim, Germany, 2013

(220) Dale, R. E.; Eisinger, J.; Blumberg, W. E. The orientational freedom of molecular probes. The orientation factor in intramolecular energy transfer. *Biophys. J.* **1979,** *26*, 161.

(221) Guan, H.; Li, J.; Zhou, T.; Pang, Z.; Fu, Y.; Cornelio, J.; Wang, Q.; Telfer, S. G.; Kong, X. Probing Nonuniform Adsorption in Multicomponent Metal–Organic Frameworks via Segmental Dynamics by Solid-State Nuclear Magnetic Resonance. *J. Phys. Chem. Lett* **2020,** *11*, 7167.

(222) Steinberg, I. Z.; Haas, E.; Katchalski-Katzir, E. *Long-Range Nonradiative Transfer of Electronic Excitation Energy* In *Time-Resolved Fluorescence Spectroscopy in Biochemistry and Biology*; Cundall, R. B.;Dale, R. E., Eds.; Springer US: Boston, MA, 1983

(223) Rohatgi, A.; *Web Digitiser - Web Based Plot Digitiser*; https://apps.automeris.io/wpd/; Last Accessed 2020-10-21.

(224) Flanders, N. C.; Kirschner, M. S.; Kim, P.; Fauvell, T. J.; Evans, A. M.; Helweh, W.; Spencer, A. P.; Schaller, R. D.; Dichtel, W. R.; Chen, L. X. Large Exciton Diffusion Coefficients in Two-Dimensional Covalent Organic Frameworks with Different Domain Sizes Revealed by Ultrafast Exciton Dynamics. *J. Am. Chem. Soc.* **2020,** *142*, 14957.

(225) Delport, G.; Chehade, G.; Lédée, F.; Diab, H.; Milesi-Brault, C.; Trippé-Allard, G.; Even, J.; Lauret, J.-S.; Deleporte, E.; Garrot, D. Exciton–Exciton Annihilation in Two-Dimensional Halide Perovskites at Room Temperature. *J. Phys. Chem. Lett* **2019,** *10*, 5153.

(226) Lunt, R. R.; Giebink, N. C.; Belak, A. A.; Benziger, J. B.; Forrest, S. R. Exciton diffusion lengths of organic semiconductor thin films measured by spectrally resolved photoluminescence quenching. *J. Appl. Phys.* **2009,** *105*, 053711.

(227) Stranks, S. D.; Eperon, G. E.; Grancini, G.; Menelaou, C.; Alcocer, M. J. P.; Leijtens, T.; Herz, L. M.; Petrozza, A.; Snaith, H. J. Electron-Hole Diffusion Lengths Exceeding 1 Micrometer in an Organometal Trihalide Perovskite Absorber. *Science* **2013,** *342*, 341.

(228) Xing, G.; Mathews, N.; Sun, S.; Lim, S. S.; Lam, Y. M.; Grätzel, M.; Mhaisalkar, S.; Sum, T. C. Long-Range Balanced Electron- and Hole-Transport Lengths in Organic-Inorganic $CH_3NH_3PbI_3$. *Science* **2013,** *342*, 344.

(229) Hume, P. A.; Hodgkiss, J. M. A Projective Method for the Calculation of Excited-State Electronic Coupling: Isolating Charge Transfer/Recombination Processes in Organic Photovoltaics. *J. Phys. Chem. A* **2020,** *124*, 591.

(230) Chandrabose, S.; Chen, K.; Barker, A. J.; Sutton, J. J.; Prasad, S. K. K.; Zhu, J.; Zhou, J.; Gordon, K. C.; Xie, Z.; Zhan, X.et al. High Exciton Diffusion Coefficients in Fused Ring Electron Acceptor Films. *J. Am. Chem. Soc.* **2019,** *141*, 6922.

(231) Shaw, P. E.; Ruseckas, A.; Samuel, I. D. W. Exciton Diffusion Measurements in Poly(3-hexylthiophene). *Adv. Mater.* **2008,** *20*, 3516.

(232) Shaikh, Shaunak M.; Chakraborty, A.; Alatis, J.; Cai, M.; Danilov, E.; Morris, A. J. Light harvesting and energy transfer in a porphyrin-based metal organic framework. *Faraday Discuss.* **2019,** *216*, 174.

(233) Guo, J.; Ohkita, H.; Benten, H.; Ito, S. Charge Generation and Recombination Dynamics in Poly(3-hexylthiophene)/Fullerene Blend Films with Different Regioregularities and Morphologies. *J. Am. Chem. Soc.* **2010,** *132*, 6154.

(234) Tachikawa, T.; Choi, J. R.; Fujitsuka, M.; Majima, T. Photoinduced Charge-Transfer Processes on MOF-5 Nanoparticles: Elucidating Differences between Metal-Organic Frameworks and Semiconductor Metal Oxides. *J. Phys. Chem. C* **2008,** *112*, 14090.

(235) Wiesenhofer, H.; Beljonne, D.; Scholes, G. D.; Hennebicq, E.; Brédas, J. L.; Zojer, E. Limitations of the Förster Description of Singlet Exciton Migration: The Illustrative Example of Energy Transfer to Ketonic Defects in Ladder-type Poly(para-phenylenes). *Adv. Funct. Mater.* **2005,** *15*, 155.

(236) Khan, Y. R.; Dykstra, T. E.; Scholes, G. D. Exploring the Förster limit in a small FRET pair. *Chem. Phys. Lett.* **2008,** *461*, 305.

(237) Cao, L.; Lin, Z.; Shi, W.; Wang, Z.; Zhang, C.; Hu, X.; Wang, C.; Lin, W. Exciton Migration and Amplified Quenching on Two-Dimensional Metal–Organic Layers. *J. Am. Chem. Soc.* **2017,** *139*, 7020.

(238) Lee, E. M. Y.; Tisdale, W. A. Determination of Exciton Diffusion Length by Transient Photoluminescence Quenching and Its Application to Quantum Dot Films. *J. Phys. Chem. C* **2015,** *119*, 9005.

(239) Sun, Q.; Yin, Z.; Wang, S.; Zhao, C.; Leng, J.; Tian, W.; Jin, S. Long-Range Exciton Transport in Perovskite–Metal Organic Framework Solid Composites. *J. Phys. Chem. Lett* **2020**, 9045.

(240) Pacheco-Liñán, P. J.; Fernández-Sainz, J.; Bravo, I.; Garzón-Ruiz, A.; Alonso-Moreno, C.; Carrillo-Hermosilla, F.; Antiñolo, A.; Albaladejo, J. Guanidine Substitutions in Naphthyl Systems to Allow a Controlled Excited-State Intermolecular Proton Transfer: Tuning Photophysical Properties in Aqueous Solution. *J. Phys. Chem. C* **2018,** *122*, 9363.

(241) Li, C.; Hu, B.; Liu, Y. Unraveling the effect of two different polar solvents on the excited-state intramolecular proton transfer of 4′-methoxy-3-hydroxyflavone fluorescent dye. *Spectrochim. Acta A* **2020,** *225*, 117487.

(242) Zhou, P.; Han, K. Unraveling the Detailed Mechanism of Excited-State Proton Transfer. *Acc. Chem. Res.* **2018,** *51*, 1681.

(243) Dasgupta, J.; Frontiera, R. R.; Fang, C.; Mathies, R. A. *Femtosecond Stimulated Raman Spectroscopy* In *Encyclopedia of Biophysics*; Roberts, G. C. K., Ed.; Springer Berlin Heidelberg: Berlin, Heidelberg, 2013

(244) Oscar, B. G.; Liu, W.; Zhao, Y.; Tang, L.; Wang, Y.; Campbell, R. E.; Fang, C. Excited-state structural dynamics of a dual-emission calmodulin-green fluorescent protein sensor for calcium ion imaging. *Proc. Natl. Acad. Sci. U. S. A.* **2014,** *111*, 10191.

(245) Oscar, B. G.; Liu, W.; Rozanov, N. D.; Fang, C. Ultrafast intermolecular proton transfer to a proton scavenger in an organic solvent. *Phys. Chem. Chem. Phys.* **2016,** *18*, 26151.

(246) Pang, Q.; Tu, B.; Li, Q. Metal–organic frameworks with multicomponents in order. *Coord. Chem. Rev.* **2019,** *388*, 107.

(247) Guillerm, V.; Maspoch, D. Geometry Mismatch and Reticular Chemistry: Strategies To Assemble Metal–Organic Frameworks with Non-default Topologies. *J. Am. Chem. Soc.* **2019,** *141*, 16517.

(248) Sumida, K.; Rogow, D. L.; Mason, J. A.; McDonald, T. M.; Bloch, E. D.; Herm, Z. R.; Bae, T.-H.; Long, J. R. Carbon Dioxide Capture in Metal–Organic Frameworks. *Chem. Rev.* **2012,** *112*, 724.

(249) Pascanu, V.; González Miera, G.; Inge, A. K.; Martín-Matute, B. Metal–Organic Frameworks as Catalysts for Organic Synthesis: A Critical Perspective. *J. Am. Chem. Soc.* **2019,** *141*, 7223.

(250) Medishetty, R.; Zaręba, J. K.; Mayer, D.; Samoć, M.; Fischer, R. A. Nonlinear optical properties, upconversion and lasing in metal–organic frameworks. *Chem. Soc. Rev.* **2017,** *46*, 4976.

(251) Mingabudinova, L. R.; Vinogradov, V. V.; Milichko, V. A.; Hey-Hawkins, E.; Vinogradov, A. V. Metal-organic frameworks as competitive materials for non-linear optics. *Chem. Soc. Rev.* **2016,** *45*, 5408.

(252) Cai, W.; Wang, J.; Chu, C.; Chen, W.; Wu, C.; Liu, G. Metal–Organic Framework-Based Stimuli-Responsive Systems for Drug Delivery. *Adv. Sci.* **2019,** *6*, 1801526.

(253) Wang, L.; Zheng, M.; Xie, Z. Nanoscale metal–organic frameworks for drug delivery: a conventional platform with new promise. *J. Mater. Chem. B* **2018,** *6*, 707.

(254) Dey, C.; Kundu, T.; Banerjee, R. Reversible phase transformation in proton conducting Strandberg-type POM based metal organic material. *Chem. Commun.* **2012,** *48*, 266.

(255) Pardo, R.; Zayat, M.; Levy, D. Photochromic organic–inorganic hybrid materials. *Chem. Soc. Rev.* **2011,** *40*, 672.

(256) Lyndon, R.; Konstas, K.; Ladewig, B. P.; Southon, P. D.; Kepert, P. C. J.; Hill, M. R. Dynamic Photo-Switching in Metal–Organic Frameworks as a Route to Low-Energy Carbon Dioxide Capture and Release. *Angew. Chem. Int. Ed.* **2013,** *52*, 3695.

(257) Yanai, N.; Uemura, T.; Inoue, M.; Matsuda, R.; Fukushima, T.; Tsujimoto, M.; Isoda, S.; Kitagawa, S. Guest-to-Host Transmission of Structural Changes for Stimuli-Responsive Adsorption Property. *J. Am. Chem. Soc.* **2012,** *134*, 4501.

(258) Zhao, D.; Rao, X.; Yu, J.; Cui, Y.; Yang, Y.; Qian, G. Design and Synthesis of an MOF Thermometer with High Sensitivity in the Physiological Temperature Range. *Inorg. Chem.* **2015,** *54*, 11193.

(259) Collings, I. E.; Goodwin, A. L. Metal–organic frameworks under pressure. *J. Appl. Phys.* **2019,** *126*, 181101.

(260) Henri, B.-L.; Heinz, D. Organic photochromism (IUPAC Technical Report). *Pure Appl. Chem.* **2001,** *73*, 639.

(261) Irie, M.; Fukaminato, T.; Matsuda, K.; Kobatake, S. Photochromism of Diarylethene Molecules and Crystals: Memories, Switches, and Actuators. *Chem. Rev.* **2014,** *114*, 12174.

(262) Williams, D. E.; Martin, C. R.; Dolgopolova, E. A.; Swifton, A.; Godfrey, D. C.; Ejegbavwo, O. A.; Pellechia, P. J.; Smith, M. D.; Shustova, N. B. Flipping the Switch: Fast Photoisomerization in a Confined Environment. *J. Am. Chem. Soc.* **2018,** *140*, 7611.

(263) Furlong, B. J.; Katz, M. J. Bistable Dithienylethene-Based Metal–Organic Framework Illustrating Optically Induced Changes in Chemical Separations. *J. Am. Chem. Soc.* **2017,** *139*, 13280.

(264) Kumar, S.; Kumar, Y.; Keshri, S. K.; Mukhopadhyay, P. Recent Advances in Organic Radicals and Their Magnetism. *Magnetochemistry* **2016,** *2*.

(265) Faust, T. B.; D'Alessandro, D. M. Radicals in metal–organic frameworks. *RSC Adv.* **2014,** *4*, 17498.

(266) Lin, H.-H.; Mohanta, S.; Lee, C.-J.; Wei, H.-H. Syntheses, Crystal Engineering, and Magnetic Property of a Dicyanamide Bridged Three-Dimensional Manganese(II)−Nitronyl Nitroxide Coordination Polymer Derived from a New Radical. *Inorg. Chem.* **2003,** *42*, 1584.

(267) Kitazawa, T.; Sato, H.; Kachi-Terajima, C.; Yoshida, K.; Takagaki, H.; Kanadani, C.; Saito, T. Aqua cadmium cyanide coordination polymer with nitronyl nitroxide radical. *Polyhedron* **2011,** *30*, 3054.

(268) Zhou, Y.; Han, L. Recent advances in naphthalenediimide-based metal-organic frameworks: Structures and applications. *Coord. Chem. Rev.* **2020**, 213665.

(269) Narayan, T. C.; Miyakai, T.; Seki, S.; Dincă, M. High Charge Mobility in a Tetrathiafulvalene-Based Microporous Metal–Organic Framework. *J. Am. Chem. Soc.* **2012,** *134*, 12932.

(270) Xie, L. S.; Skorupskii, G.; Dincă, M. Electrically Conductive Metal–Organic Frameworks. *Chem. Rev.* **2020,** *120*, 8536.

(271) Jee, B.; Koch, K.; Moschkowitz, L.; Himsl, D.; Hartman, M.; Pöppl, A. Electron Spin Resonance Study of Nitroxide Radical Adsorption at Cupric Ions in the Metal−Organic Framework Compound $Cu_3(btc)_2$. *J. Phys. Chem. Lett* **2011,** *2*, 357.

(272) Sheveleva, A. M.; Kolokolov, D. I.; Gabrienko, A. A.; Stepanov, A. G.; Gromilov, S. A.; Shundrina, I. K.; Sagdeev, R. Z.; Fedin, M. V.; Bagryanskaya, E. G. Structural Dynamics in a “Breathing” Metal–Organic Framework Studied by Electron Paramagnetic Resonance of Nitroxide Spin Probes. *J. Phys. Chem. Lett* **2014,** *5*, 20.

(273) Potts, S. V.; Barbour, L. J.; Haynes, D. A.; Rawson, J. M.; Lloyd, G. O. Inclusion of Thiazyl Radicals in Porous Crystalline Materials. *J. Am. Chem. Soc.* **2011,** *133*, 12948.

(274) Inokuma, Y.; Arai, T.; Fujita, M. Networked molecular cages as crystalline sponges for fullerenes and other guests. *Nat. Chem.* **2010,** *2*, 780.

(275) Tan, Y.; Fu, Z.; Zeng, Y.; Chen, H.; Liao, S.; Zhang, J.; Dai, J. Highly stable photochromic crystalline material based on a close-packed layered metal–viologen coordination polymer. *J. Mater. Chem.* **2012,** *22*, 17452.

(276) Yong, G.-P.; Li, Y.-Z.; Zhang, Y.-M.; She, W.-L. Magnetic and luminescent properties of Cd(II)- and Fe(II)-anion radical frameworks: various networks or structures influenced by metal ion sizes or in situ forming mechanisms of anion radical ligand. *CrystEngComm* **2012,** *14*, 1439.

(277) Estrada, L. A.; Neckers, D. C. Synthesis and Photophysics of Dibenz[a,c]phenazine Derivatives. *Org. Lett.* **2011,** *13*, 3304.

(278) Ferguson, A.; Liu, L.; Tapperwijn, S. J.; Perl, D.; Coudert, F.-X.; Van Cleuvenbergen, S.; Verbiest, T.; van der Veen, M. A.; Telfer, S. G. Controlled partial interpenetration in metal–organic frameworks. *Nat. Chem.* **2016,** *8*, 250.

(279) Sawada, T.; Kihara, T.; Fujikawa, Y.; Narazaki, Y. Synthesis and photochromic properties of quinoxalino[e]-annelated dimethyldihydropyrene with planar chirality. *Tetrahedron Lett.* **2013,** *54,* 5963.

(280) Sawada, T.; Akazawa, Y.; Narazaki, Y.; Kubo, S.; Nanamura, K. Synthesis and photochromic circular dichroism of 2,7-di-tert-butyl-10b,10c-dimethyl-pyrazino[2,3-e]dihydropyrene. *Can. J. Chem.* **2015,** *93*, 1321.

(281) Cummings, S. D.; Eisenberg, R. Acid-Base Behavior of the Ground and Excited States of Platinum(II) Complexes of Quinoxaline-2,3-dithiolate. *Inorg. Chem.* **1995,** *34*, 3396.

(282) Zivic, N.; Kuroishi, P. K.; Dumur, F.; Gigmes, D.; Dove, A. P.; Sardon, H. Recent Advances and Challenges in the Design of Organic Photoacid and Photobase Generators for Polymerizations. *Angew. Chem. Int. Ed.* **2019,** *58*, 10410.

(283) Arsu, N.; Aydın, M. Photoinduced free radical polymerization initiated with quinoxalines. *Die Angewandte Makromolekulare Chemie* **1999,** *270*, 1.

(284) Litwinienko, G.; Beckwith, A. L. J.; Ingold, K. U. The frequently overlooked importance of solvent in free radical syntheses. *Chem. Soc. Rev.* **2011,** *40*, 2157.

(285) Peterson, J. P.; Winter, A. H. Solvent Effects on the Stability and Delocalization of Aryl Dicyanomethyl Radicals: The Captodative Effect Revisited. *J. Am. Chem. Soc.* **2019,** *141*, 12901.

(286) Housecroft, C. E.; Sharpe, A. G. *Inorganic Chemistry*; Fifth edition ed.; Pearson, 2018.

(287) Winterbourn, C. C.; Kettle, A. J. Radical–radical reactions of superoxide: a potential route to toxicity. *Biochem. Biophys. Res. Commun.* **2003,** *305*, 729.

(288) Brisar, R.; Hollmann, D.; Mejia, E. Pyrazine Radical Cations as a Catalyst for the Aerobic Oxidation of Amines. *Eur. J. Org. Chem.* **2017,** *2017*, 5391.

(289) Zhonggao, Z.; Liangxian, L. TEMPO and its Derivatives: Synthesis and Applications. *Curr. Org. Chem.* **2014,** *18*, 459.

(290) Siu, J. C.; Sauer, G. S.; Saha, A.; Macey, R. L.; Fu, N.; Chauviré, T.; Lancaster, K. M.; Lin, S. Electrochemical Azidooxygenation of Alkenes Mediated by a TEMPO–N_3 Charge-Transfer Complex. *J. Am. Chem. Soc.* **2018,** *140*, 12511.

(291) Haidasz, E. A.; Meng, D.; Amorati, R.; Baschieri, A.; Ingold, K. U.; Valgimigli, L.; Pratt, D. A. Acid Is Key to the Radical-Trapping Antioxidant Activity of Nitroxides. *J. Am. Chem. Soc.* **2016,** *138*, 5290.

(292) Weeks, R. A. Paramagnetic Spectra of E_2' Centers in Crystalline Quartz. *Physical Review* **1963,** *130*, 570.

(293) Fessenden, R. W.; Neta, P. ESR Spectra of radicals produced by reduction of pyridine and pyrazine. *Chem. Phys. Lett.* **1973,** *18*, 14.

(294) Eiermann, U.; Neugebauer, F. A.; Chandra, H.; Symons, M. C. R.; Wyatt, J. L. Radical cations and anions of pyrazines: an electron paramagnetic resonance study. *J. Chem. Soc., Perkin Trans.* **1992,** *2*, 85.

(295) Van Hoomissen, D. J.; Vyas, S. Impact of Conjugation and Hyperconjugation on the Radical Stability of Allylic and Benzylic Systems: A Theoretical Study. *J. Org. Chem.* **2017,** *82*, 5731.

(296) Chen, C.; Ruan, H.; Feng, Z.; Fang, Y.; Tang, S.; Zhao, Y.; Tan, G.; Su, Y.; Wang, X. Crystalline Diradical Dianions of Pyrene-Fused Azaacenes. *Angew. Chem. Int. Ed.* **2020,** *59*, 11794.

(297) Goubard, F.; Dumur, F. Truxene: a promising scaffold for future materials. *RSC Adv.* **2015,** *5*, 3521.

(298) Zhao, K.-Q.; Chen, C.; Monobe, H.; Hu, P.; Wang, B.-Q.; Shimizu, Y. Three-chain truxene discotic liquid crystal showing high charged carrier mobility. *Chem. Commun.* **2011,** *47*, 6290.

(299) Li, C.; Wang, Y.; Zou, Y.; Zhang, X.; Dong, H.; Hu, W. Two-Dimensional Conjugated Polymer Synthesized by Interfacial Suzuki Reaction: Towards Electronic Device Applications. *Angew. Chem. Int. Ed.* **2020,** *59*, 9403.

(300) Echeverri, M.; Gámez-Valenzuela, S.; González-Cano, R. C.; Guadalupe, J.; Cortijo-Campos, S.; López Navarrete, J. T.; Iglesias, M.; Ruiz Delgado, M. C.; Gómez-Lor, B. Effect of the Linkage Position on the Conjugation Length of Truxene-Based Porous Polymers: Implications for Their Sensing Performance of Nitroaromatics. *Chem. Mater.* **2019,** *31*, 6971.

(301) Battula, V. R.; Singh, H.; Kumar, S.; Bala, I.; Pal, S. K.; Kailasam, K. Natural Sunlight Driven Oxidative Homocoupling of Amines by a Truxene-Based Conjugated Microporous Polymer. *ACS Catal.* **2018,** *8*, 6751.

(302) Gámez-Valenzuela, S.; Echeverri, M.; Gómez-Lor, B.; Martínez, J. I.; Ruiz Delgado, M. C. In silico design of 2D polymers containing truxene-based platforms: insights into their structural and electronic properties. *J. Mater. Chem. C* **2020**.

(303) Singh, P. P.; Aithagani, S. K.; Yadav, M.; Singh, V. P.; Vishwakarma, R. A. Iron-catalyzed Cross-Coupling of Electron-Deficient Heterocycles and Quinone with Organoboron Species via Innate C–H Functionalization: Application in Total Synthesis of Pyrazine Alkaloid Botryllazine A. *J. Org. Chem.* **2013,** *78*, 2639.

(304) Song, X.; Kong, L.; Du, H.; Li, X.; Feng, H.; Zhao, J.; Xie, Y. Effects of Pyrazine Derivatives and Substituted Positions on the Photoelectric Properties and Electromemory Performance of D–A–D Series Compounds. *Materials* **2018,** *11*.

(305) Hioe, J.; Šakić, D.; Vrček, V.; Zipse, H. The stability of nitrogen-centered radicals. *Org. Biomol. Chem.* **2015,** *13*, 157.

(306) Köhler, J.; Quast, T.; Buback, J.; Fischer, I.; Brixner, T.; Nuernberger, P.; Geiß, B.; Mager, J.; Lambert, C. Ultrafast charge-transfer dynamics of donor-substituted truxenones. *Phys. Chem. Chem. Phys.* **2012,** *14*, 11081.

(307) Mui, P. W.; Konishi, Y.; Scheraga, H. A. Comparison of intramolecular and intermolecular reactions in protein folding. *J. Protein Chem.* **1986,** *5*, 29.

(308) Bender, M. L.; Neveu, M. C. Intramolecular Catalysis of Hydrolytic Reactions. IV. A Comparison of Intramolecular and Intermolecular Catalysis1,2. *J. Am. Chem. Soc.* **1958,** *80*, 5388.

(309) Hajos, Z. G.; Parrish, D. R. Asymmetric synthesis of bicyclic intermediates of natural product chemistry. *J. Org. Chem.* **1974,** *39*, 1615.

(310) Semisch, C.; Margaretha, P. Photochemistry of 2-(Trifluoromethyl)cyclohexanone. *Helv. Chim. Acta* **1984,** *67*, 664.

(311) Ouchi, T.; Mutton, R. J.; Rojas, V.; Fitzpatrick, D. E.; Cork, D. G.; Battilocchio, C.; Ley, S. V. Solvent-Free Continuous Operations Using Small Footprint Reactors: A Key Approach for Process Intensification. *ACS Sustain. Chem. Eng.* **2016,** *4*, 1912.

(312) Jiao, J.; Gong, W.; Wu, X.; Yang, S.; Cui, Y. Multivariate crystalline porous materials: Synthesis, property and potential application. *Coord. Chem. Rev.* **2019,** *385*, 174.

(313) Dhakshinamoorthy, A.; Alvaro, M.; Chevreau, H.; Horcajada, P.; Devic, T.; Serre, C.; Garcia, H. Iron(III) metal–organic frameworks as solid Lewis acids for the isomerization of α-pinene oxide. *Catal. Sci. Technol.* **2012,** *2*, 324.

(314) Vermoortele, F.; Vandichel, M.; Van de Voorde, B.; Ameloot, R.; Waroquier, M.; Van Speybroeck, V.; De Vos, D. E. Electronic Effects of Linker Substitution on Lewis Acid Catalysis with Metal–Organic Frameworks. *Angew. Chem. Int. Ed.* **2012,** *51*, 4887.

(315) Li, B.; Ju, Z.; Zhou, M.; Su, K.; Yuan, D. A Reusable MOF-Supported Single-Site Zinc(II) Catalyst for Efficient Intramolecular Hydroamination of o-Alkynylanilines. *Angew. Chem. Int. Ed.* **2019,** *58*, 7687.

(316) Singh, J.; Hagen, T. J. Chirality and Biological Activity. *Burger's Medicinal Chemistry and Drug Discovery* **2010**, 127.

(317) Liu, J.; Chen, L.; Cui, H.; Zhang, J.; Zhang, L.; Su, C.-Y. Applications of metal-organic frameworks in heterogeneous supramolecular catalysis. *Chem. Soc. Rev.* **2014,** *43*, 6011.

(318) Alkaş, A. *Synthesis of multicomponent metal-organic frameworks and investigations of their physical properties : a thesis presented in partial fulfilment of the requirements of the degree of Doctor of Philosophy in Chemistry at Massey University, Manawatu, New Zealand*, Massey University, 2019.

(319) Smith, M.; March, J. *March's Advanced Organic Chemistry : Reactions, Mechanisms, and Structure*; 6th ed. / Michael B. Smith, Jerry March ed.; Wiley-Interscience, 2007.

(320) Clayden, J.; Greeves, N.; Warren, S. G. *Organic Chemistry*; 2nd ed.; Oxford University Press, 2012.

(321) Meyer, C. C.; Ortiz, E.; Krische, M. J. Catalytic Reductive Aldol and Mannich Reactions of Enone, Acrylate, and Vinyl Heteroaromatic Pronucleophiles. *Chem. Rev.* **2020,** *120*, 3721.

(322) Kotani, S.; Nakajima, M. Recent advances in asymmetric phosphine oxide catalysis. *Tetrahedron Lett.* **2020,** *61*, 151421.

(323) Lam, Y.-h.; Houk, K. N. Origins of Stereoselectivity in Intramolecular Aldol Reactions Catalyzed by Cinchona Amines. *J. Am. Chem. Soc.* **2015,** *137*, 2116.

(324) List, B. *Amine-catalyzed Aldol Reactions* In *Modern Aldol Reactions*; Mahrwald, R., Ed.; Wiley-VCH Verlag GmbH: Weinheim, 2008

(325) Baldwin, J. E.; Thomas, R. C.; Kruse, L. I.; Silberman, L. Rules for ring closure: ring formation by conjugate addition of oxygen nucleophiles. *J. Org. Chem.* **1977,** *42*, 3846.

(326) Gilmore, K.; Mohamed, R. K.; Alabugin, I. V. The Baldwin rules: revised and extended. *Wiley Interdisciplinary Reviews: Computational Molecular Science* **2016,** *6*, 487.

(327) Pidathala, C.; Hoang, L.; Vignola, N.; List, B. Direct Catalytic Asymmetric Enolexo Aldolizations. *Angew. Chem. Int. Ed.* **2003,** *42*, 2785.

(328) Rahimi, M.; Geertsema, E. M.; Miao, Y.; van der Meer, J.-Y.; van den Bosch, T.; de Haan, P.; Zandvoort, E.; Poelarends, G. J. Inter- and intramolecular aldol reactions promiscuously catalyzed by a proline-based tautomerase. *Org. Biomol. Chem.* **2017,** *15*, 2809.

(329) Orata, F. *Derivatization Reactions and Reagents for Gas Chromatography Analysis* In *Advanced Gas Chromatography - Progress in Agricultural, Biomedical and Industrial Applications*; Mohd, M. A., Ed.; InTech, 2012

(330) Hartmann, E.; Vyas, D. J.; Oestreich, M. Enantioselective formal hydration of α,β-unsaturated acceptors: asymmetric conjugate addition of silicon and boron nucleophiles. *Chem. Commun.* **2011,** *47*, 7917.

(331) Xiao, D. J.; Oktawiec, J.; Milner, P. J.; Long, J. R. Pore Environment Effects on Catalytic Cyclohexane Oxidation in Expanded Fe_2(dobdc) Analogues. *J. Am. Chem. Soc.* **2016,** *138*, 14371.

(332) Hanwell, M. D.; Curtis, D. E.; Lonie, D. C.; Vandermeersch, T.; Zurek, E.; Hutchison, G. R. Avogadro: an advanced semantic chemical editor, visualization, and analysis platform. *J. Cheminformatics* **2012,** *4*, 17.

(333) Wang, Y.-Z.; Deng, X.-X.; Li, L.; Li, Z.-L.; Du, F.-S.; Li, Z.-C. One-pot synthesis of polyamides with various functional side groups via Passerini reaction. *Polymer Chemistry* **2013,** *4*, 444.

(334) Sakamoto, M.; Cai, X.; Hara, M.; Tojo, S.; Fujitsuka, M.; Majima, T. Transient Absorption Spectra and Lifetimes of Benzophenone Ketyl Radicals in the Excited State. *J. Phys. Chem. A* **2004,** *108*, 8147.

(335) Buntinx, G.; Naskrecki, R.; Poizat, O. Subpicosecond Transient Absorption Analysis of the Photophysics of 2,2‘-Bipyridine and 4,4‘-Bipyridine in Solution. *The Journal of Physical Chemistry* **1996,** *100*, 19380.

(336) Skotnicki, K.; De la Fuente, J. R.; Cañete, A.; Bobrowski, K. Spectral and Kinetic Properties of Radicals Derived from Oxidation of Quinoxalin-2-One and Its Methyl Derivative. *Molecules* **2014,** *19*.

(337) Baldovi, H. G.; Krüger, M.; Reinsch, H.; Alvaro, M.; Stock, N.; Garcia, H. Transient absorption spectroscopy and photochemical reactivity of CAU-8. *J. Mater. Chem. C* **2015,** *3*, 3607.

(338) Sun, L.; Jiang, X.; Yin, J. Study of methoxyphenylquinoxalines (MOPQs) as photoinitiators in the negative photo-resist. *Prog. Org. Coat.* **2010,** *67*, 225.

(339) Huang, Y.-B.; Liang, J.; Wang, X.-S.; Cao, R. Multifunctional metal-organic framework catalysts: synergistic catalysis and tandem reactions. *Chem. Soc. Rev.* **2017,** *46*, 126.

(340) Dhakshinamoorthy, A.; Garcia, H. Cascade Reactions Catalyzed by Metal Organic Frameworks. *ChemSusChem* **2014,** *7*, 2392.

(341) Dau, P. V.; Cohen, S. M. A Bifunctional, Site-Isolated Metal–Organic Framework-Based Tandem Catalyst. *Inorg. Chem.* **2015,** *54*, 3134.

(342) Rösler, C.; Esken, D.; Wiktor, C.; Kobayashi, H.; Yamamoto, T.; Matsumura, S.; Kitagawa, H.; Fischer, R. A. Encapsulation of Bimetallic Nanoparticles into a Metal–Organic Framework: Preparation and Microstructure Characterization of Pd/Au@ZIF-8. *Eur. J. Inorg. Chem.* **2014,** *2014*, 5514.

(343) Lu, G.; Li, S.; Guo, Z.; Farha, O. K.; Hauser, B. G.; Qi, X.; Wang, Y.; Wang, X.; Han, S.; Liu, X.et al. Imparting functionality to a metal–organic framework material by controlled nanoparticle encapsulation. *Nat. Chem.* **2012,** *4*, 310.

(344) Zhao, M.; Deng, K.; He, L.; Liu, Y.; Li, G.; Zhao, H.; Tang, Z. Core–Shell Palladium Nanoparticle@Metal–Organic Frameworks as Multifunctional Catalysts for Cascade Reactions. *J. Am. Chem. Soc.* **2014,** *136*, 1738.

(345) Danishefsky, S. J.; Masters, J. J.; Young, W. B.; Link, J. T.; Snyder, L. B.; Magee, T. V.; Jung, D. K.; Isaacs, R. C. A.; Bornmann, W. G.; Alaimo, C. A.et al. Total Synthesis of Baccatin III and Taxol. *J. Am. Chem. Soc.* **1996,** *118*, 2843.

(346) Lee, H. M.; Nieto-Oberhuber, C.; Shair, M. D. Enantioselective Synthesis of (+)-Cortistatin A, a Potent and Selective Inhibitor of Endothelial Cell Proliferation. *J. Am. Chem. Soc.* **2008,** *130*, 16864.

(347) Lin, W.; Yuan, L.; Cao, Z.; Feng, Y.; Song, J. Through-Bond Energy Transfer Cassettes with Minimal Spectral Overlap between the Donor Emission and Acceptor Absorption: Coumarin–Rhodamine Dyads with Large Pseudo-Stokes Shifts and Emission Shifts. *Angew. Chem. Int. Ed.* **2010,** *49*, 375.

(348) Ueno, Y.; Jose, J.; Loudet, A.; Pérez-Bolívar, C.; Anzenbacher, P.; Burgess, K. Encapsulated Energy-Transfer Cassettes with Extremely Well Resolved Fluorescent Outputs. *J. Am. Chem. Soc.* **2011,** *133*, 51.

(349) Zhang, Y.; Chen, Z.; Song, J.; He, J.; Wang, X.; Wu, J.; Chen, S.; Qu, J.; Wong, W.-Y. Rational design of high efficiency green to deep red/near-infrared emitting materials based on isomeric donor–acceptor chromophores. *J. Mater. Chem. C* **2019,** *7,* 1880.

(350) Liu, W.; Huang, X.; Xu, C.; Chen, C.; Yang, L.; Dou, W.; Chen, W.; Yang, H.; Liu, W. A Multi-responsive Regenerable Europium–Organic Framework Luminescent Sensor for Fe3+, CrVI Anions, and Picric Acid. *Chem. Eur. J.* **2016,** *22*, 18769.

(351) Matikonda, S. S.; Ivanic, J.; Gomez, M.; Hammersley, G.; Schnermann, M. J. Core remodeling leads to long wavelength fluoro-coumarins. *Chem. Sci.* **2020,** *11*, 7302.

(352) Ren, T.-B.; Xu, W.; Zhang, W.; Zhang, X.-X.; Wang, Z.-Y.; Xiang, Z.; Yuan, L.; Zhang, X.-B. A General Method To Increase Stokes Shift by Introducing Alternating Vibronic Structures. *J. Am. Chem. Soc.* **2018,** *140*, 7716.

(353) Weston, C. E.; Richardson, R. D.; Haycock, P. R.; White, A. J. P.; Fuchter, M. J. Arylazopyrazoles: Azoheteroarene Photoswitches Offering Quantitative Isomerization and Long Thermal Half-Lives. *J. Am. Chem. Soc.* **2014,** *136*, 11878.

(354) Wang, Z.; Müller, K.; Valášek, M.; Grosjean, S.; Bräse, S.; Wöll, C.; Mayor, M.; Heinke, L. Series of Photoswitchable Azobenzene-Containing Metal–Organic Frameworks with Variable Adsorption Switching Effect. *J. Phys. Chem. C* **2018,** *122*, 19044.

(355) Brown, J. W.; Henderson, B. L.; Kiesz, M. D.; Whalley, A. C.; Morris, W.; Grunder, S.; Deng, H.; Furukawa, H.; Zink, J. I.; Stoddart, J. F.et al. Photophysical pore control in an azobenzene-containing metal–organic framework. *Chem. Sci.* **2013,** *4*, 2858.

(356) Hoang, L. T. M.; Ngo, L. H.; Nguyen, H. L.; Nguyen, H. T. H.; Nguyen, C. K.; Nguyen, B. T.; Ton, Q. T.; Nguyen, H. K. D.; Cordova, K. E.; Truong, T. An azobenzene-containing metal–organic framework as an efficient heterogeneous catalyst for direct amidation of benzoic acids: synthesis of bioactive compounds. *Chem. Commun.* **2015,** *51*, 17132.

(357) Gong, L. L.; Yao, W. T.; Liu, Z. Q.; Zheng, A. M.; Li, J. Q.; Feng, X. F.; Ma, L. F.; Yan, C. S.; Luo, M. B.; Luo, F. Photoswitching storage of guest molecules in metal–organic framework for photoswitchable catalysis: exceptional product, ultrahigh photocontrol, and photomodulated size selectivity. *J. Mater. Chem. A* **2017,** *5*, 7961.

(358) Chen, S.-H.; Hong, B.-C.; Su, C.-F.; Sarshar, S. An unexpected inversion of enantioselectivity in the proline catalyzed intramolecular Baylis–Hillman reaction. *Tetrahedron Lett.* **2005,** *46*, 8899.

(359) Duarte, F. J. S.; Cabrita, E. J.; Frenking, G.; Santos, A. G. Density Functional Study of Proline-Catalyzed Intramolecular Baylis–Hillman Reactions. *Chem. Eur. J.* **2009,** *15*, 1734.

(360) Mc Cartney, D.; Guiry, P. J. The asymmetric Heck and related reactions. *Chem. Soc. Rev.* **2011,** *40*, 5122.

(361) Guram, A. S.; Buchwald, S. L. Palladium-Catalyzed Aromatic Aminations with in situ Generated Aminostannanes. *J. Am. Chem. Soc.* **1994,** *116*, 7901.

(362) Lyons, T. W.; Sanford, M. S. Palladium-Catalyzed Ligand-Directed C−H Functionalization Reactions. *Chem. Rev.* **2010,** *110*, 1147.

(363) Xia, Q.; Li, Z.; Tan, C.; Liu, Y.; Gong, W.; Cui, Y. Multivariate Metal–Organic Frameworks as Multifunctional Heterogeneous Asymmetric Catalysts for Sequential Reactions. *J. Am. Chem. Soc.* **2017,** *139*, 8259.

(364) Zhu, C.; Yuan, G.; Chen, X.; Yang, Z.; Cui, Y. Chiral Nanoporous Metal–Metallosalen Frameworks for Hydrolytic Kinetic Resolution of Epoxides. *J. Am. Chem. Soc.* **2012,** *134*, 8058.

(365) Lin, Z.; Zhang, Z.-M.; Chen, Y.-S.; Lin, W. Highly Efficient Cooperative Catalysis by CoIII(Porphyrin) Pairs in Interpenetrating Metal–Organic Frameworks. *Angew. Chem. Int. Ed.* **2016,** *55*, 13739.

(366) Ollevier, T. Iron bis(oxazoline) complexes in asymmetric catalysis. *Catal. Sci. Technol.* **2016,** *6*, 41.

(367) Deng, C.; Liu, H.-K.; Zheng, Z.-B.; Wang, L.; Yu, X.; Zhang, W.; Tang, Y. Copper-Catalyzed Enantioselective Cyclopropanation of Internal Olefins with Diazomalonates. *Org. Lett.* **2017,** *19*, 5717.

(368) Schaus, S. E.; Jacobsen, E. N. Asymmetric Ring Opening of Meso Epoxides with TMSCN Catalyzed by (pybox)lanthanide Complexes. *Org. Lett.* **2000,** *2*, 1001.

(369) Keith, J. M.; Jacobsen, E. N. Asymmetric Hydrocyanation of Hydrazones Catalyzed by Lanthanide−PYBOX Complexes. *Org. Lett.* **2004,** *6*, 153.

(370) Mikami, K.; Terada, M.; Matsuzawa, H. “Asymmetric” Catalysis by Lanthanide Complexes. *Angew. Chem. Int. Ed.* **2002,** *41*, 3554.

(371) Chinnaraja, E.; Arunachalam, R.; Subramanian, P. S. Enantio- and Diastereoselective Synthesis of β-Nitroalcohol via Henry Reaction Catalyzed by Cu(II), Ni(II), Zn(II) Complexes of Chiral BINIM Ligands. *ChemistrySelect* **2016,** *1*, 5331.

(372) Yuan, G.; Jiang, H.; Zhang, L.; Liu, Y.; Cui, Y. Metallosalen-based crystalline porous materials: Synthesis and property. *Coord. Chem. Rev.* **2019,** *378*, 483.

(373) Abd El Sater, M.; Jaber, N.; Schulz, E. Chiral Salen Complexes for Asymmetric Heterogeneous Catalysis: Recent Examples for Recycling and Cooperativity. *ChemCatChem* **2019,** *11*, 3662.

(374) Talavera, G.; Reyes, E.; Vicario, J. L.; Carrillo, L. Cooperative Dienamine/Hydrogen-Bonding Catalysis: Enantioselective Formal [2+2] Cycloaddition of Enals with Nitroalkenes. *Angew. Chem. Int. Ed.* **2012,** *51*, 4104.

(375) BIOVIA, Dassault Systemes, *Biovia Discovery Studio*, San Diego, USA, 2020.

DRC 16 Forms

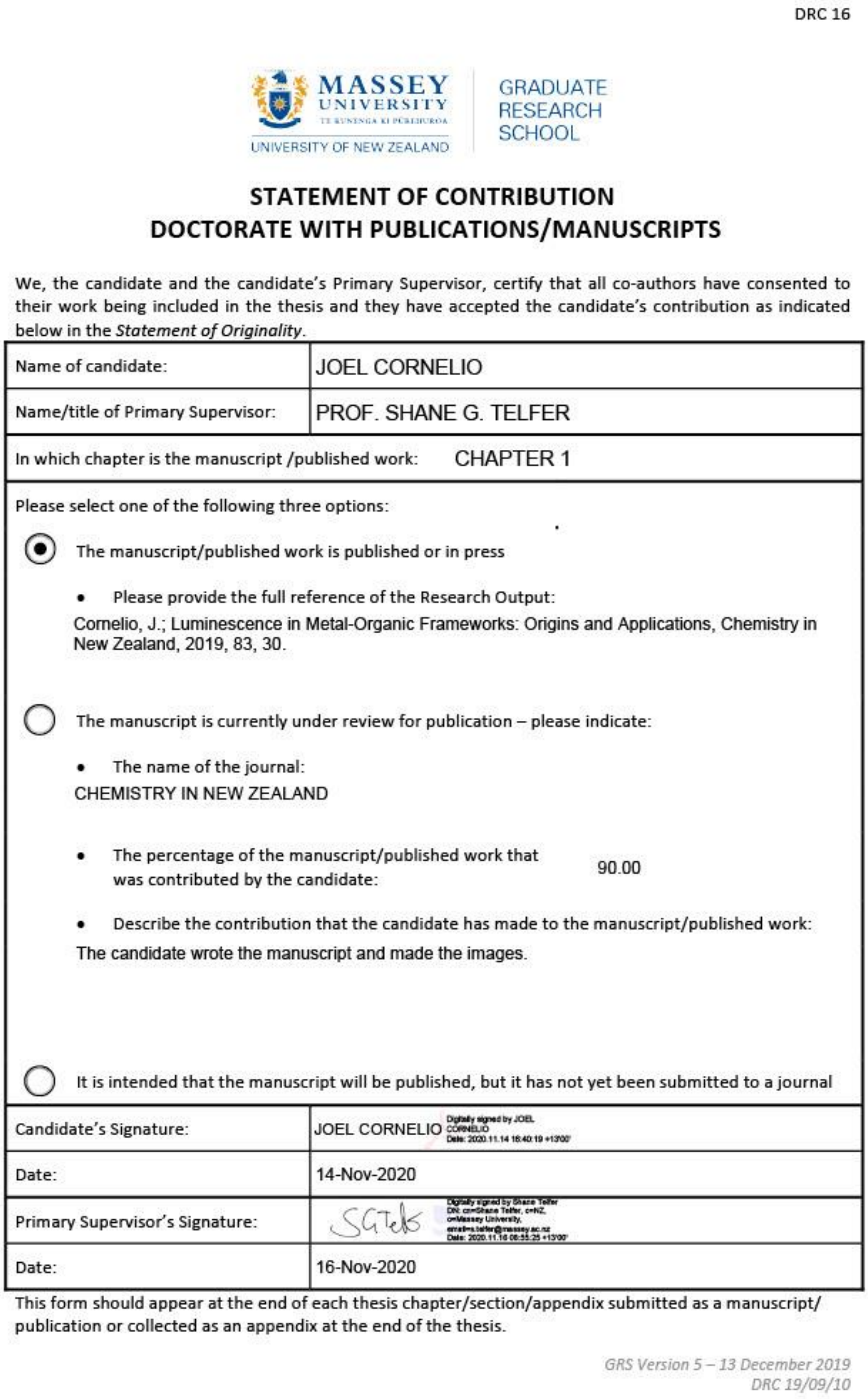

DRC 16

MASSEY UNIVERSITY
TE KUNENGA KI PŪREHUROA
UNIVERSITY OF NEW ZEALAND
GRADUATE RESEARCH SCHOOL

STATEMENT OF CONTRIBUTION
DOCTORATE WITH PUBLICATIONS/MANUSCRIPTS

We, the candidate and the candidate's Primary Supervisor, certify that all co-authors have consented to their work being included in the thesis and they have accepted the candidate's contribution as indicated below in the *Statement of Originality*.

Name of candidate:	JOEL CORNELIO
Name/title of Primary Supervisor:	PROF. SHANE G. TELFER

In which chapter is the manuscript /published work: CHAPTER 1

Please select one of the following three options:

● The manuscript/published work is published or in press

- Please provide the full reference of the Research Output:

Cornelio, J.; Luminescence in Metal-Organic Frameworks: Origins and Applications, Chemistry in New Zealand, 2019, 83, 30.

○ The manuscript is currently under review for publication – please indicate:

- The name of the journal:

CHEMISTRY IN NEW ZEALAND

- The percentage of the manuscript/published work that was contributed by the candidate: 90.00

- Describe the contribution that the candidate has made to the manuscript/published work:

The candidate wrote the manuscript and made the images.

○ It is intended that the manuscript will be published, but it has not yet been submitted to a journal

Candidate's Signature:	JOEL CORNELIO Digitally signed by JOEL CORNELIO Date: 2020.11.14 16:40:19 +13'00'
Date:	14-Nov-2020
Primary Supervisor's Signature:	Digitally signed by Shane Telfer DN: cn=Shane Telfer, c=NZ, o=Massey University, email=s.telfer@massey.ac.nz Date: 2020.11.16 08:55:25 +13'00'
Date:	16-Nov-2020

This form should appear at the end of each thesis chapter/section/appendix submitted as a manuscript/ publication or collected as an appendix at the end of the thesis.

GRS Version 5 – 13 December 2019
DRC 19/09/10

DRC 16

MASSEY UNIVERSITY
TE KUNENGA KI PŪREHUROA
UNIVERSITY OF NEW ZEALAND
GRADUATE RESEARCH SCHOOL

STATEMENT OF CONTRIBUTION
DOCTORATE WITH PUBLICATIONS/MANUSCRIPTS

We, the candidate and the candidate's Primary Supervisor, certify that all co-authors have consented to their work being included in the thesis and they have accepted the candidate's contribution as indicated below in the *Statement of Originality*.

Name of candidate:	JOEL CORNELIO
Name/title of Primary Supervisor:	PROF. SHANE G. TELFER

In which chapter is the manuscript /published work: CHAPTER 2

Please select one of the following three options:

● The manuscript/published work is published or in press

- Please provide the full reference of the Research Output:

Cornelio,J.; Zhou, T.Y.; Alkas, A.; Telfer S.G.; Systematic Tuning of the Luminescence Output of Multicomponent Metal–Organic Frameworks, Journal of the American Chemical Society, 2018, 140, 15470-15476.

○ The manuscript is currently under review for publication – please indicate:

- The name of the journal:

JOURNAL OF THE AMERICAN CHEMICAL SOCIETY

- The percentage of the manuscript/published work that was contributed by the candidate: 60.00

- Describe the contribution that the candidate has made to the manuscript/published work:

The candidate synthesised and characterised the MOFs, measured their fluorescence, and wrote the first draft of the manuscript and supporting information.

○ It is intended that the manuscript will be published, but it has not yet been submitted to a journal

Candidate's Signature:	JOEL CORNELIO Digitally signed by JOEL CORNELIO Date: 2020.11.14 18:34:12 +13'00'
Date:	14-Nov-2020
Primary Supervisor's Signature:	Digitally signed by Shane Telfer DN: cn=Shane Telfer, c=NZ, o=Massey University, email=s.telfer@massey.ac.nz Date: 2020.11.16 08:58:20 +13'00'
Date:	16-Nov-2020

This form should appear at the end of each thesis chapter/section/appendix submitted as a manuscript/ publication or collected as an appendix at the end of the thesis.

GRS Version 5 – 13 December 2019
DRC 19/09/10

Electronic Supplementary Information

^{1}H NMR spectra of digested MOFs

The following protocol was used for digestion of the MOFs for ^{1}H NMR spectroscopy: The sample was washed or centrifuged five times with dry CH_2Cl_2 or acetone, then desolvated *in vacuo*. 0.60 mL of DCl/DMSO-*d6* (10 µL/600 µL) solution was used to digest around 3 mg of MOF. A ^{1}H NMR spectrum was acquired of the resulting clear solution of the dissolved framework.

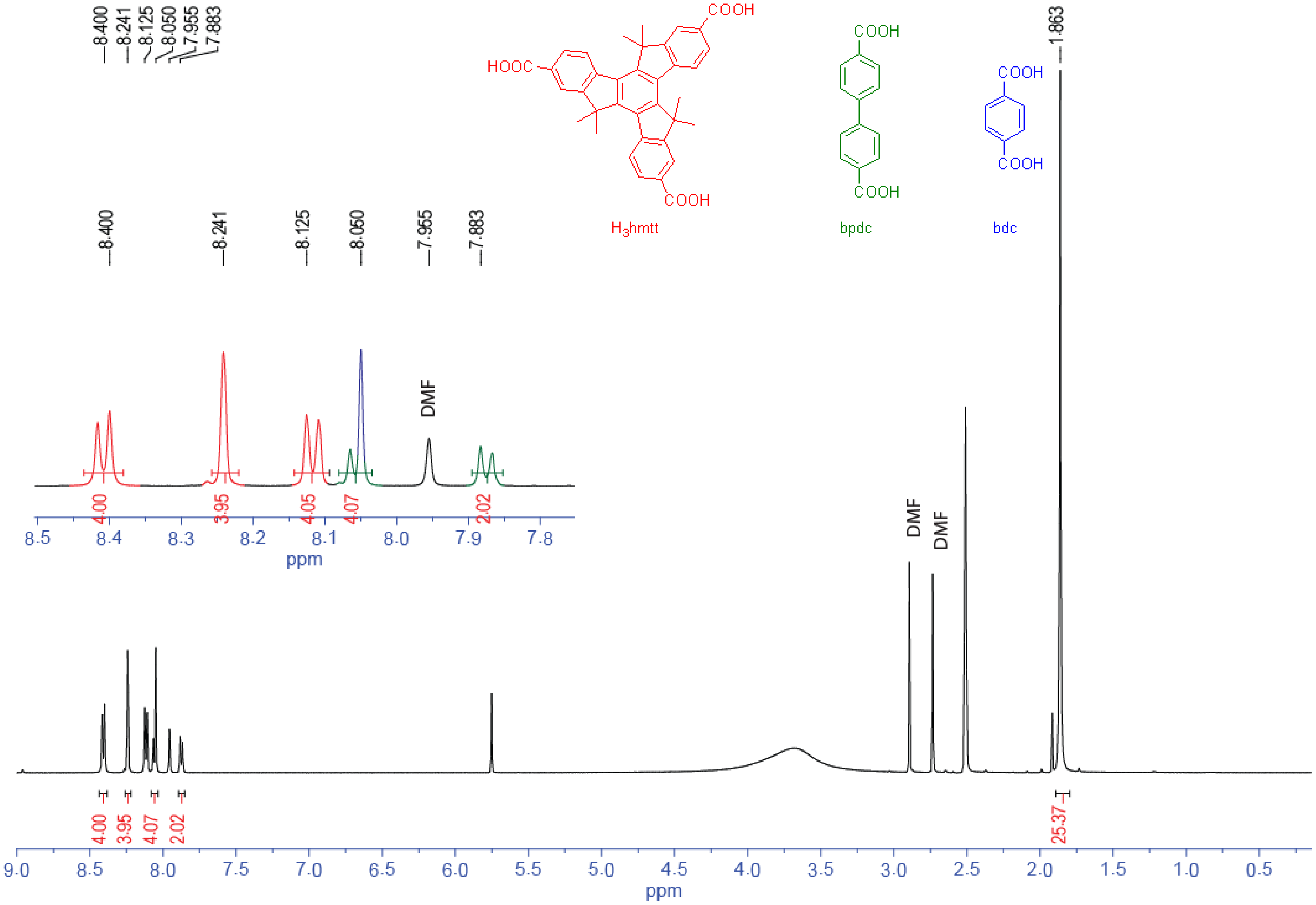

Figure S1: ^{1}H NMR spectrum of digested **1** - [Zn$_4$O(hmtt)$_{4/3}$(bpdc)$_{1/2}$(bdc)$_{1/2}$] showing integrals that match with the formula.

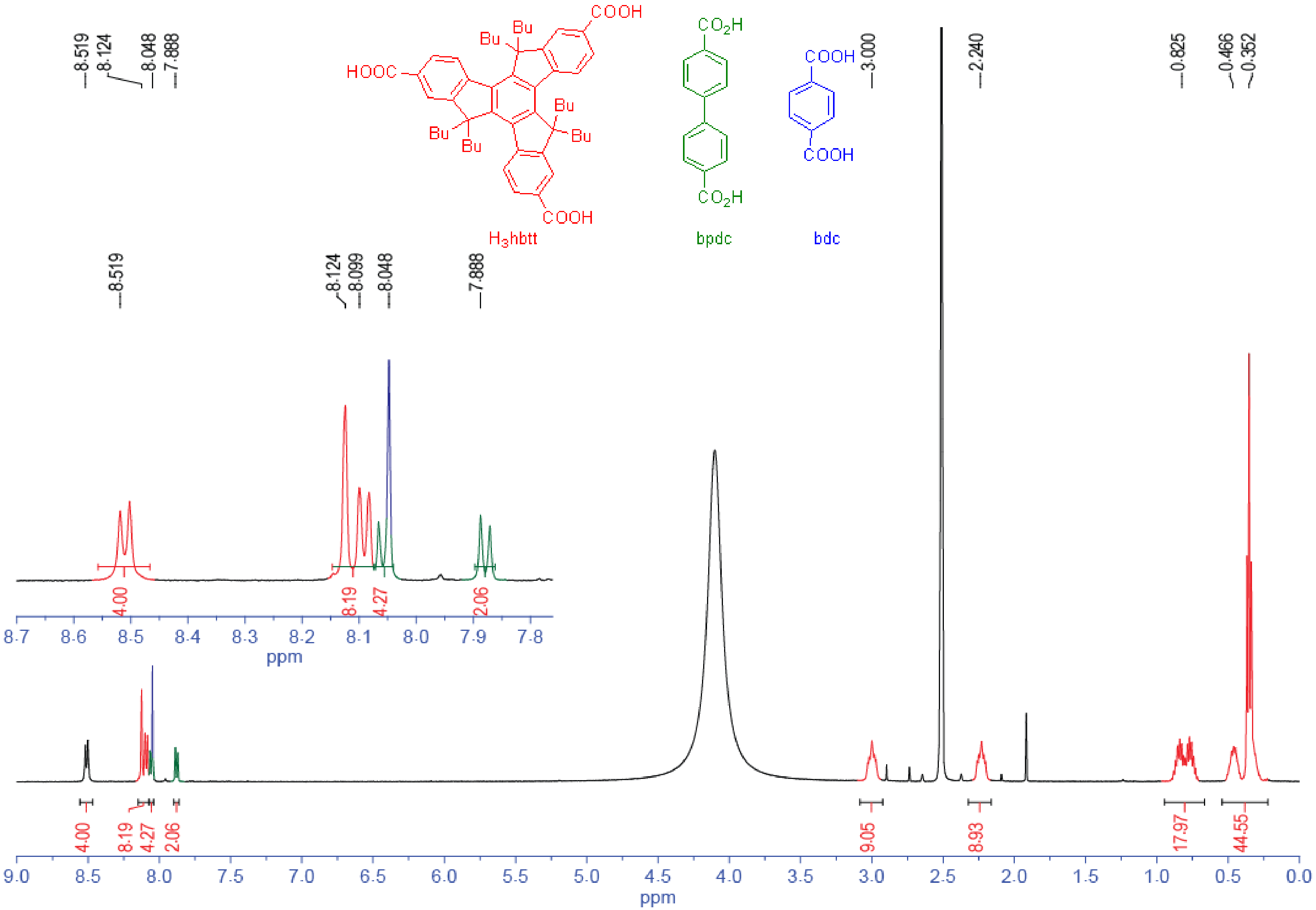

Figure S2: ^{1}H NMR spectrum of digested **2** - [$Zn_4O(hbtt)_{4/3}(bpdc)_{1/2}(bdc)_{1/2}$] showing integrals that match with the formula.

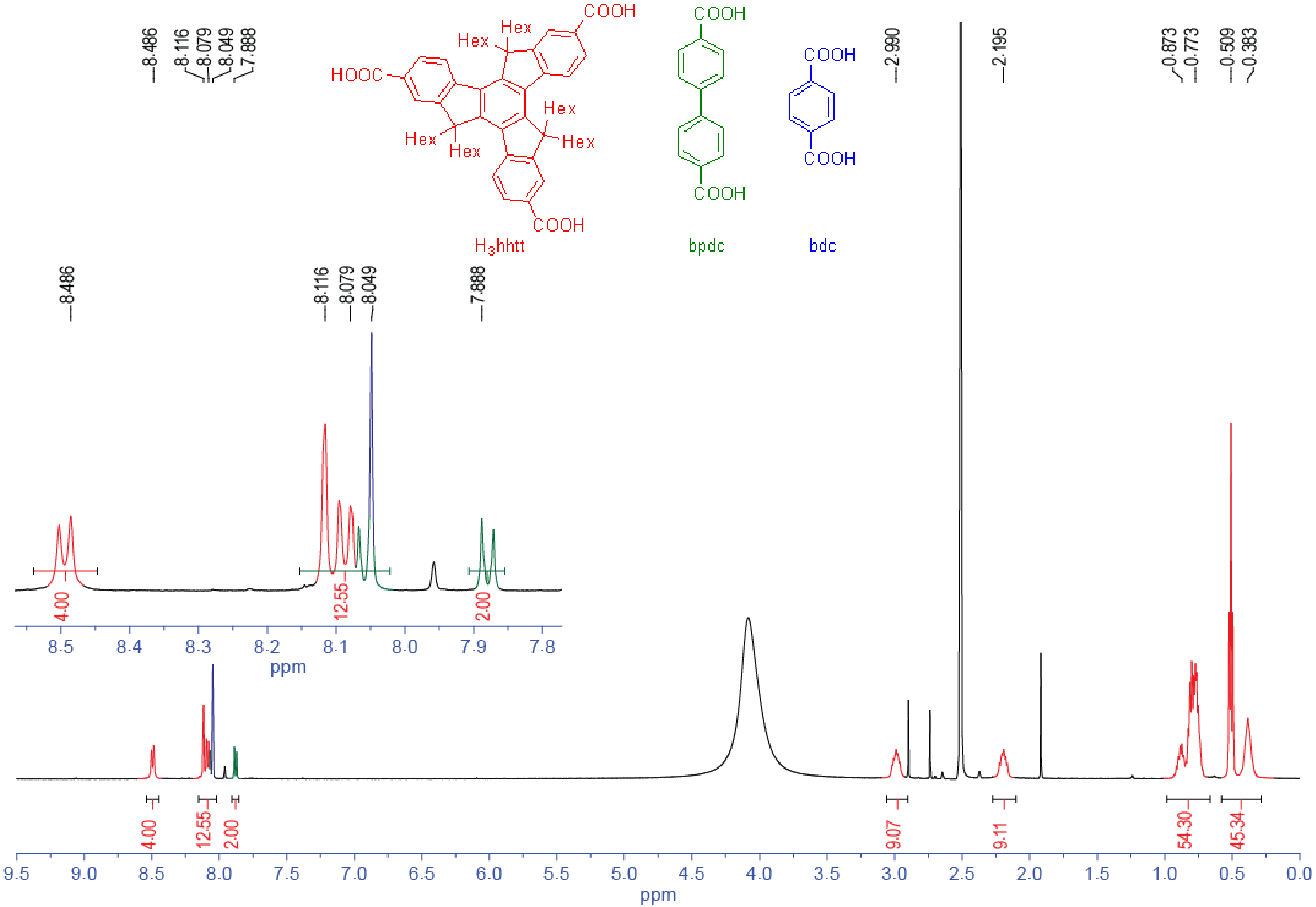

Figure S3: ^{1}H NMR spectrum of digested **3** - [$Zn_4O(hhtt)_{4/3}(bpdc)_{1/2}(bdc)_{1/2}$] showing integrals that match with the formula.

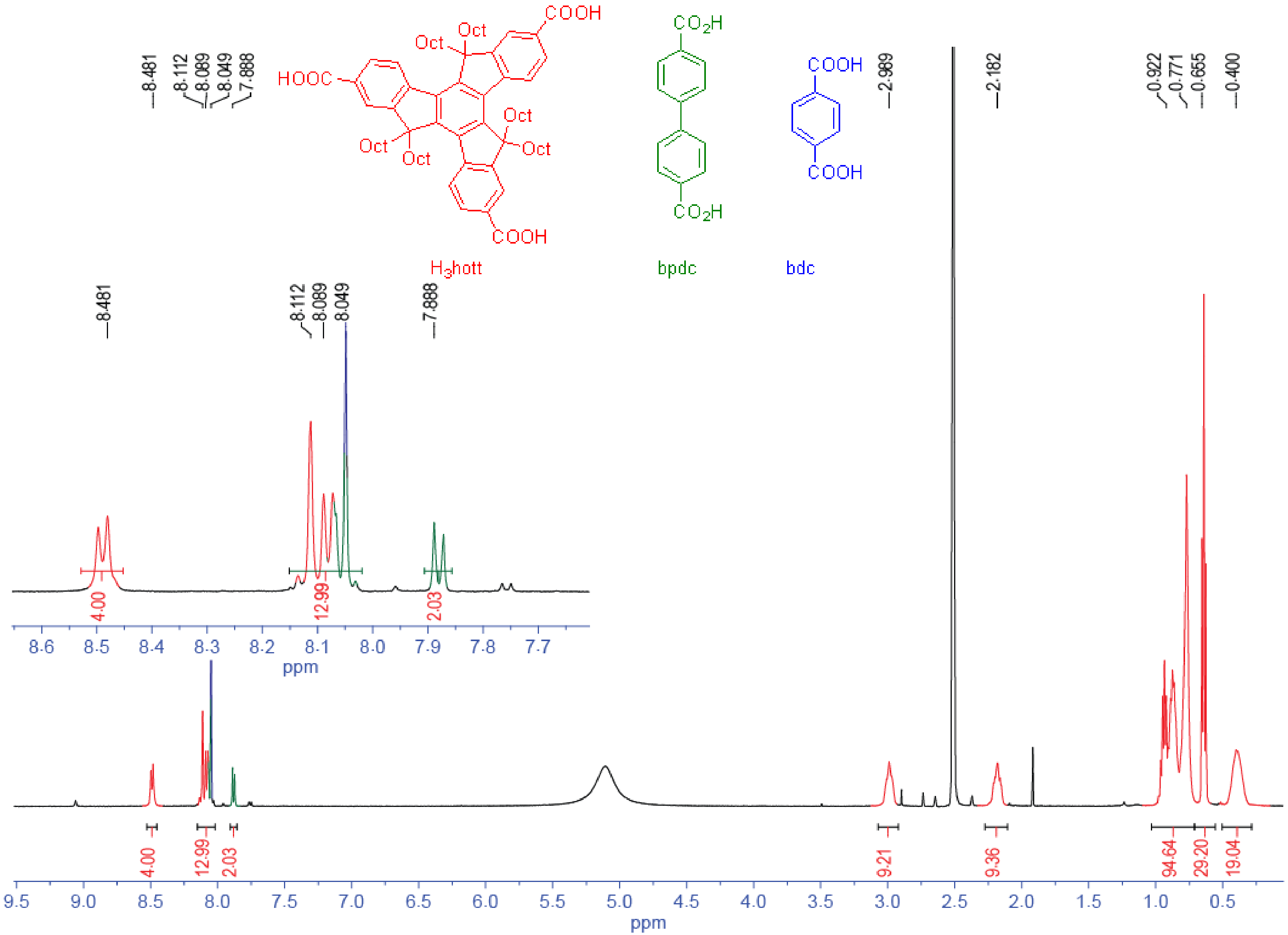

Figure S4: ^{1}H NMR spectrum of digested **4 -** [$Zn_4O(hott)_{4/3}(bpdc)_{1/2}(bdc)_{1/2}$] showing integrals that match with the formula.

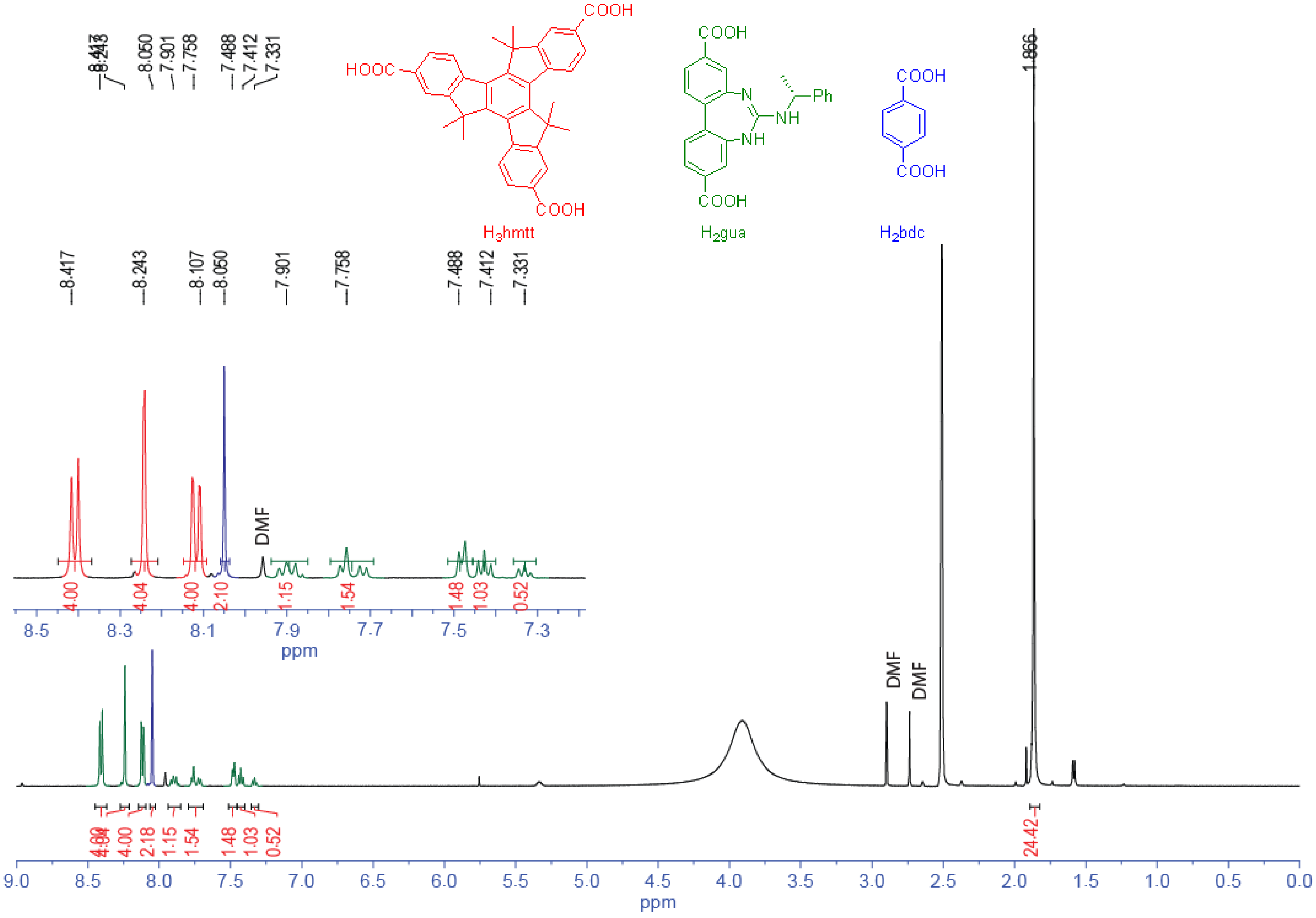

Figure S5: ^{1}H NMR spectrum of digested **5** - [Zn$_4$O(hmtt)$_{4/3}$(gua)$_{1/2}$(bdc)$_{1/2}$] showing integrals that match with the formula.

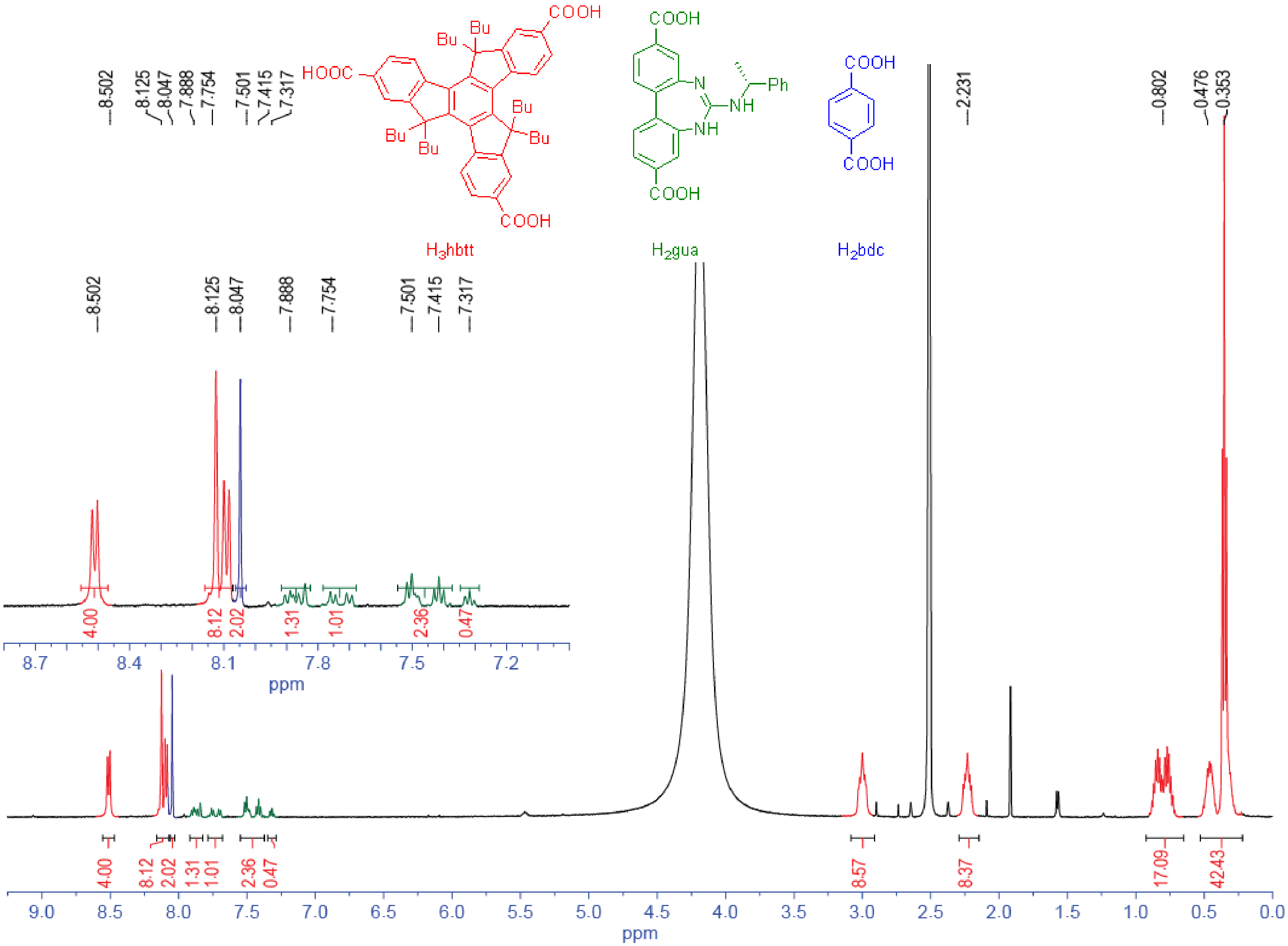

Figure S6: ^{1}H NMR spectrum of digested **6 -** [Zn$_4$O(hbtt)$_{4/3}$(gua)$_{1/2}$(bdc)$_{1/2}$] showing integrals that match with the formula.

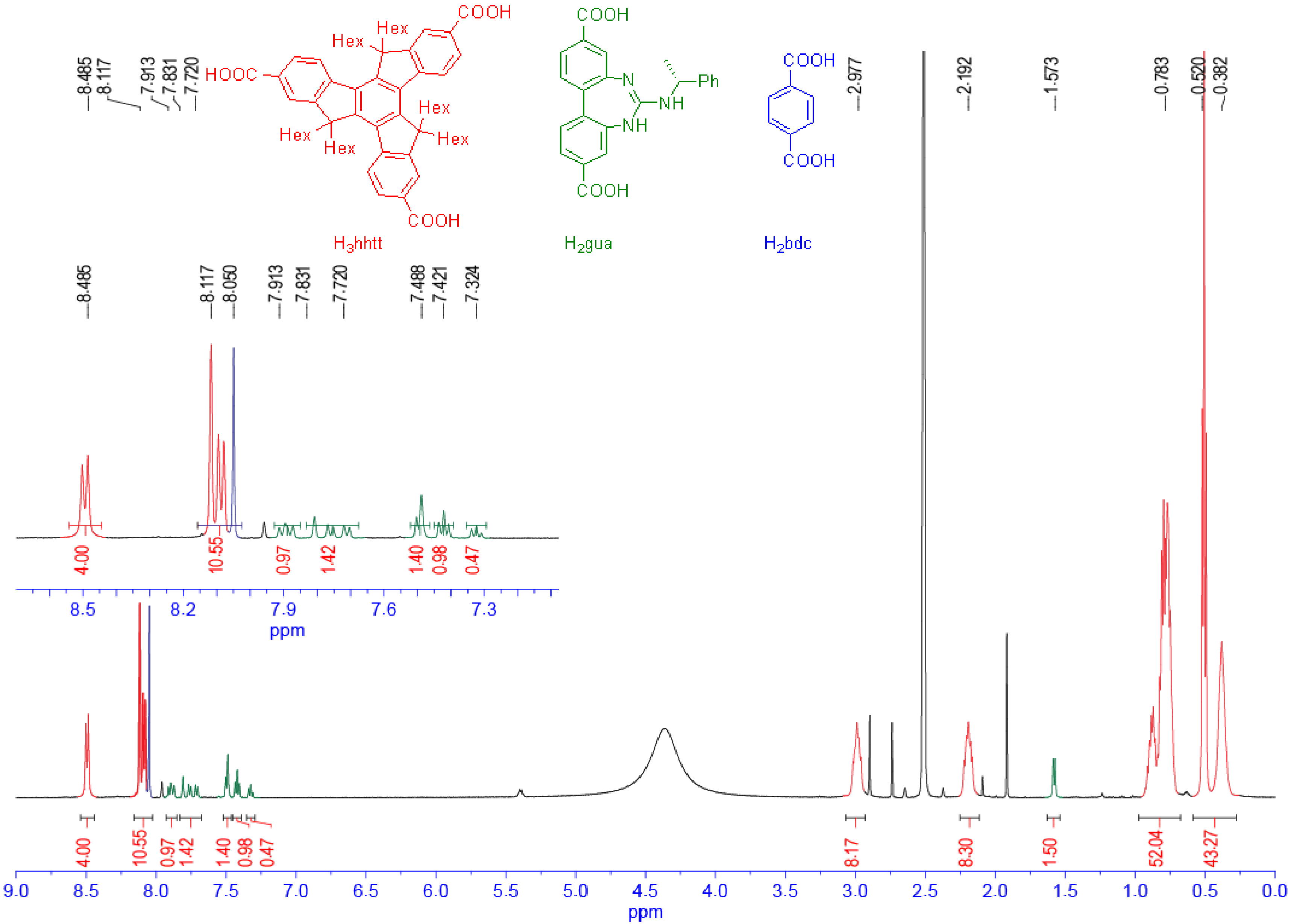

Figure S7: ^{1}H NMR spectrum of digested **7 -** [$Zn_4O(hhtt)_{4/3}(gua)_{1/2}(bdc)_{1/2}$] showing integrals that match with the formula.

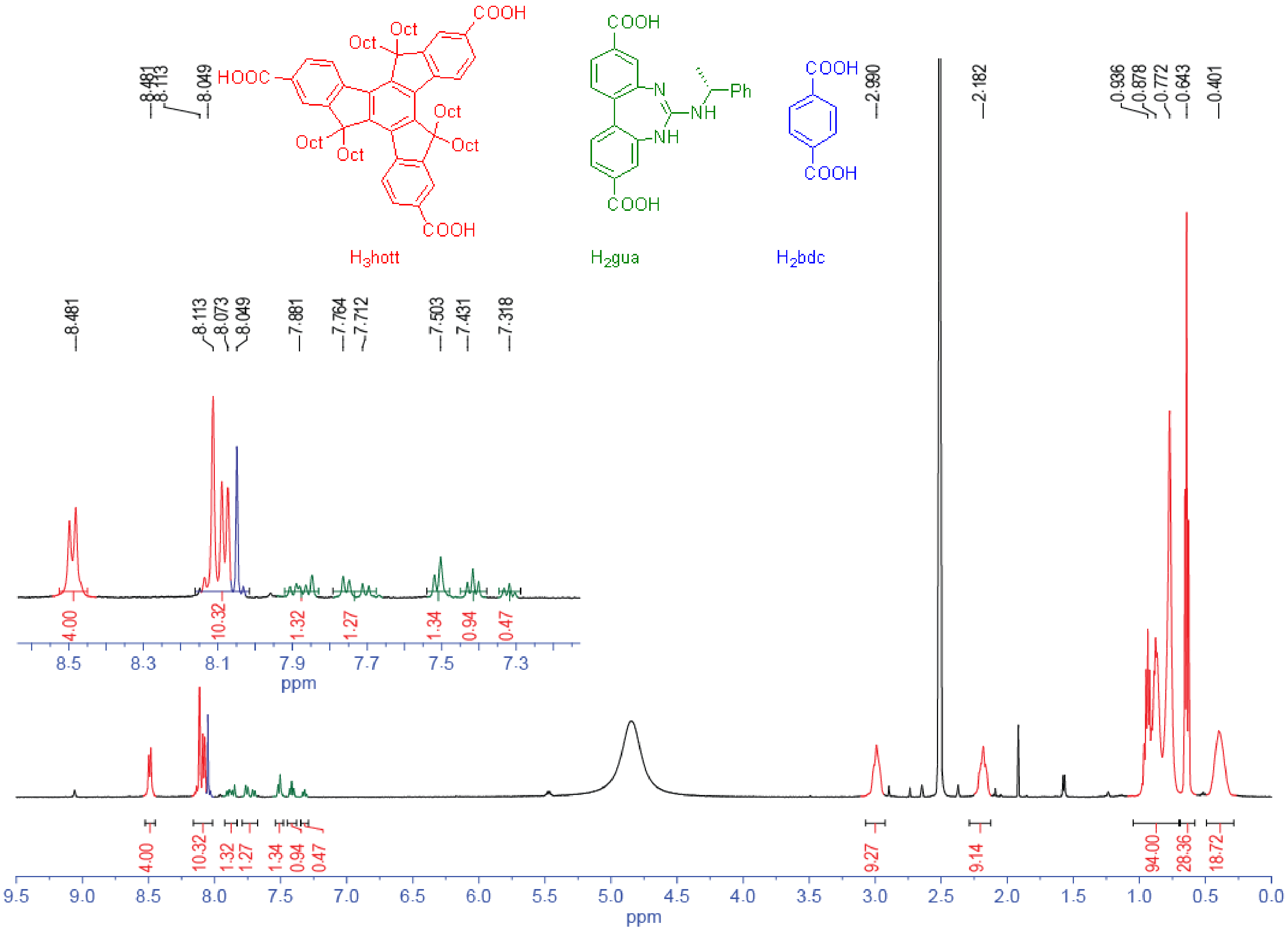

Figure S8: ^{1}H NMR spectrum of digested **8 -** [$Zn_4O(hott)_{4/3}(gua)_{1/2}(bdc)_{1/2}$] showing integrals that match with the formula.

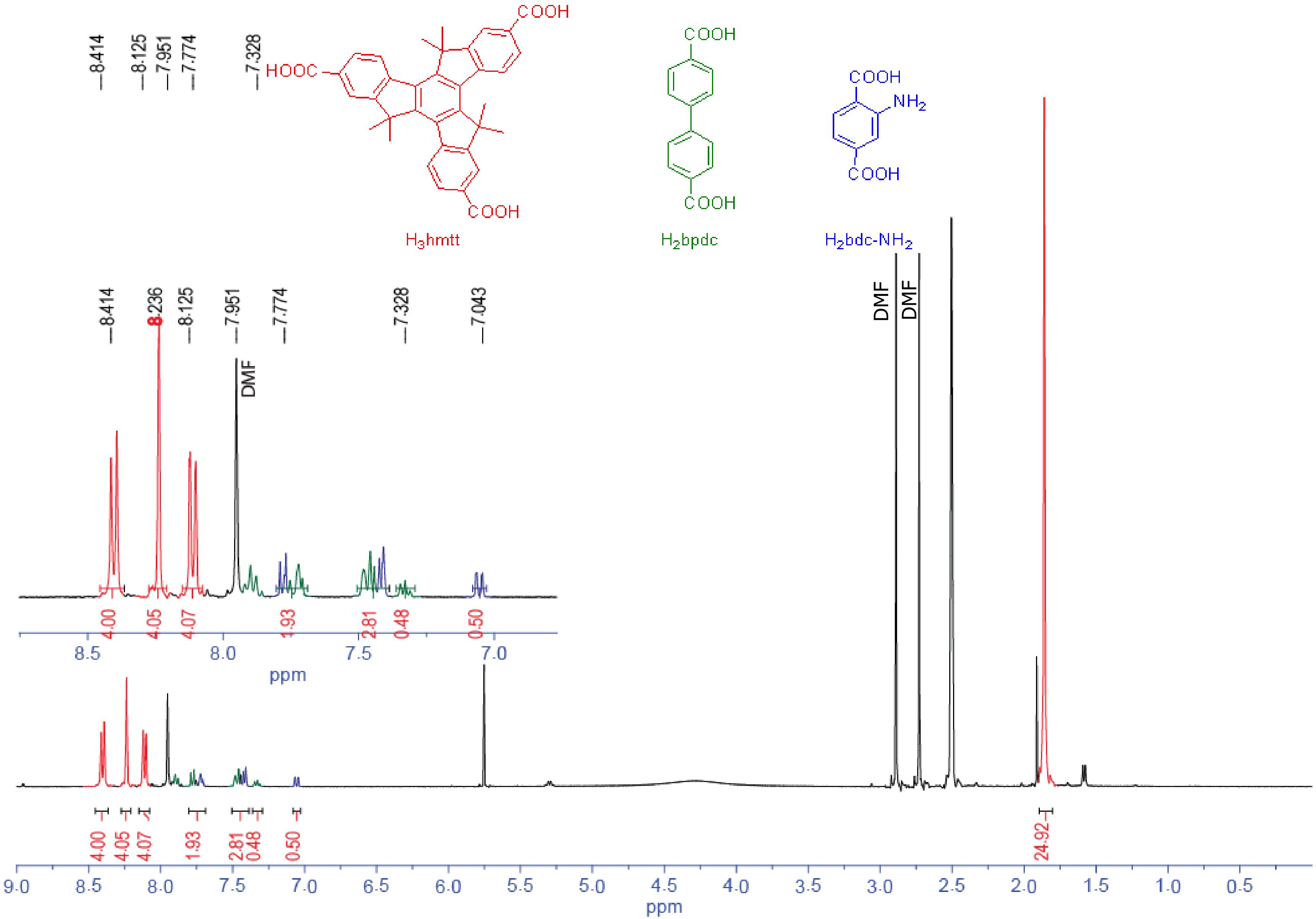

Figure S9: ^{1}H NMR spectrum of digested **9** - [Zn$_4$O(hmtt)$_{4/3}$(bpdc)$_{1/2}$(bdc-NH$_2$)$_{1/2}$] showing integrals that match with the formula.

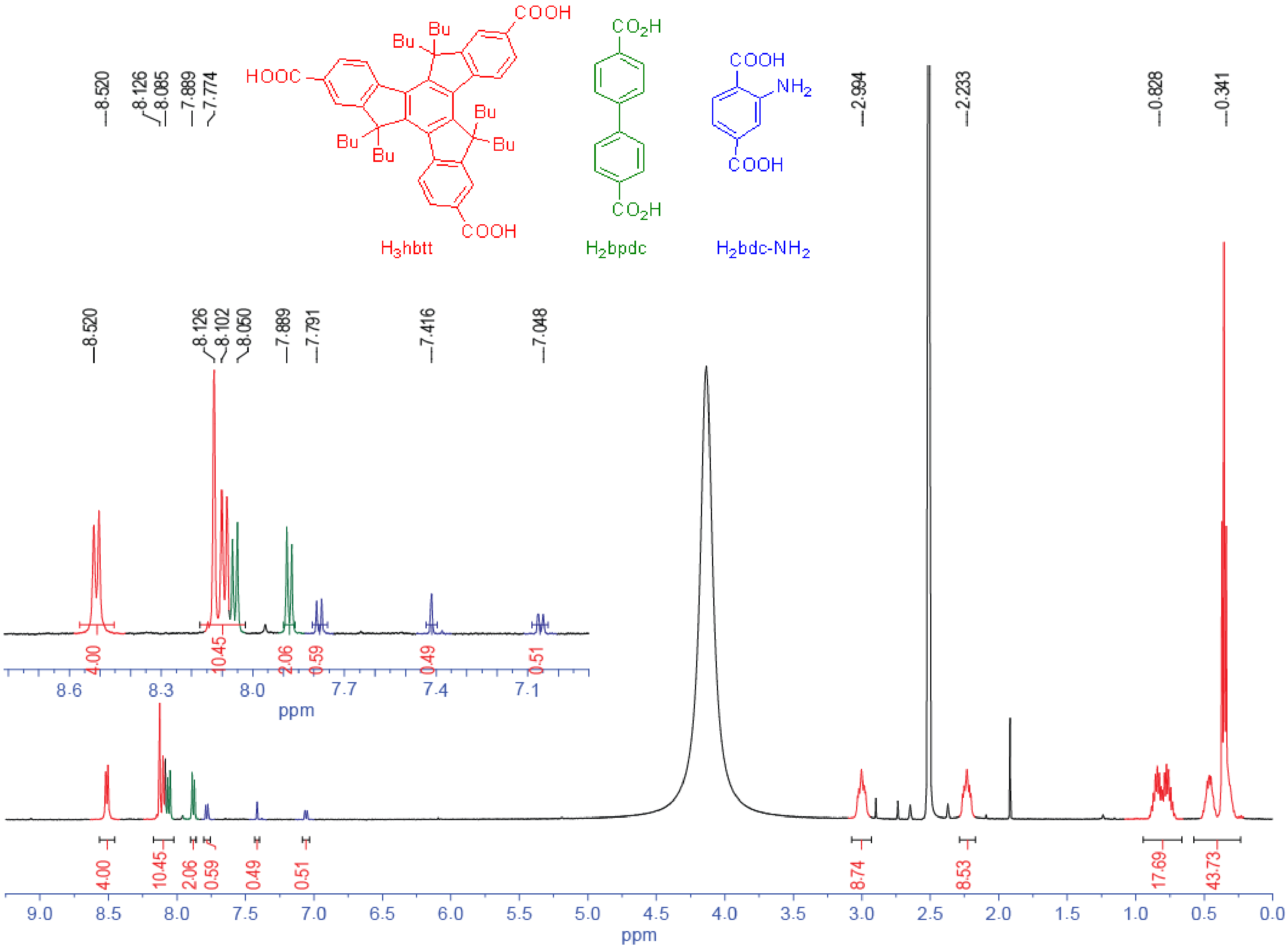

Figure S10: ^{1}H NMR spectrum of digested **10 -** [$Zn_4O(hbtt)_{4/3}(bpdc)_{1/2}(bdc\text{-}NH_2)_{1/2}$] showing integrals that match with the formula.

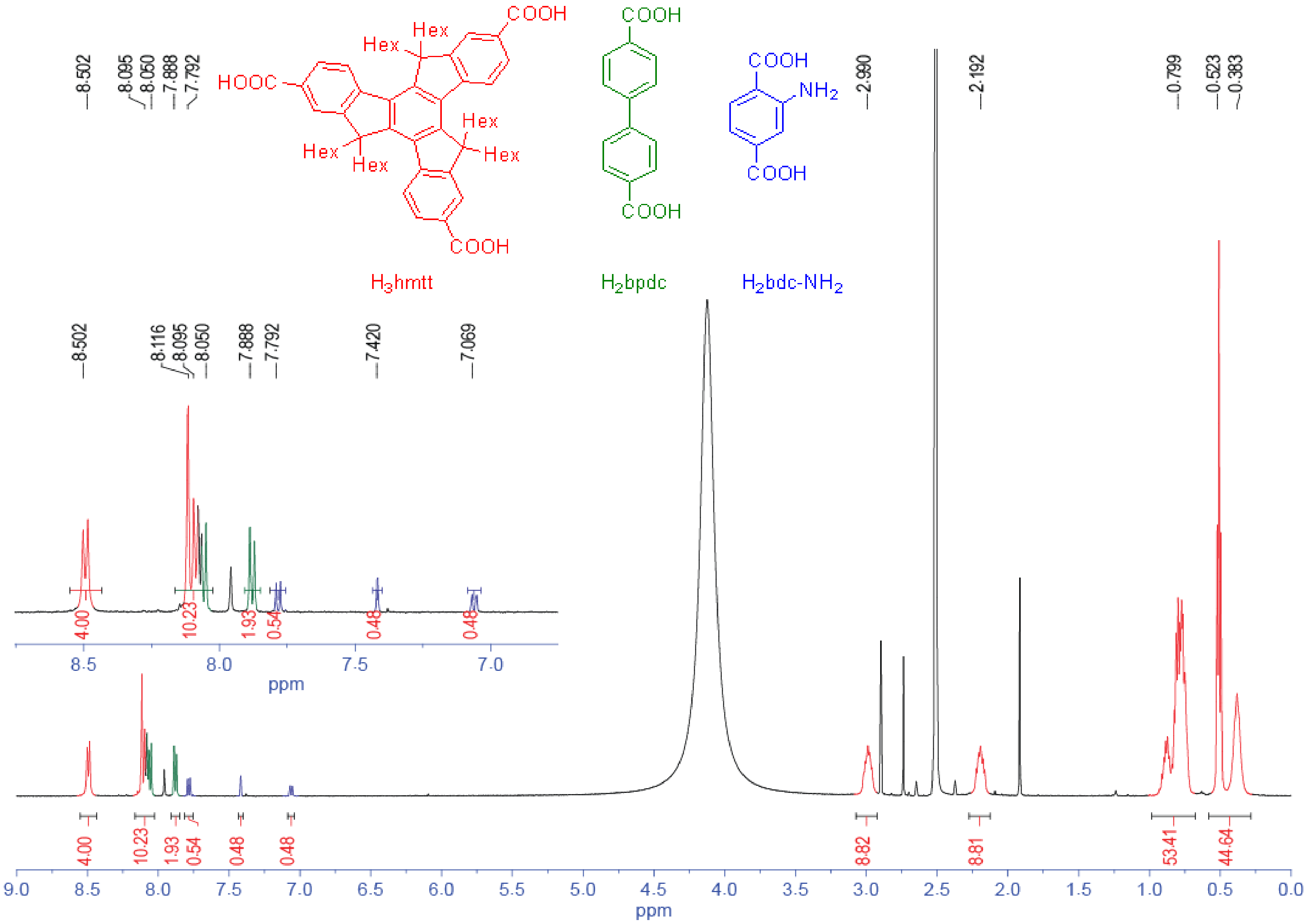

Figure S11: ^{1}H NMR spectrum of digested **11 -** [$Zn_4O(hhtt)_{4/3}(bpdc)_{1/2}(bdc\text{-}NH_2)_{1/2}$] showing integrals that match with the formula.

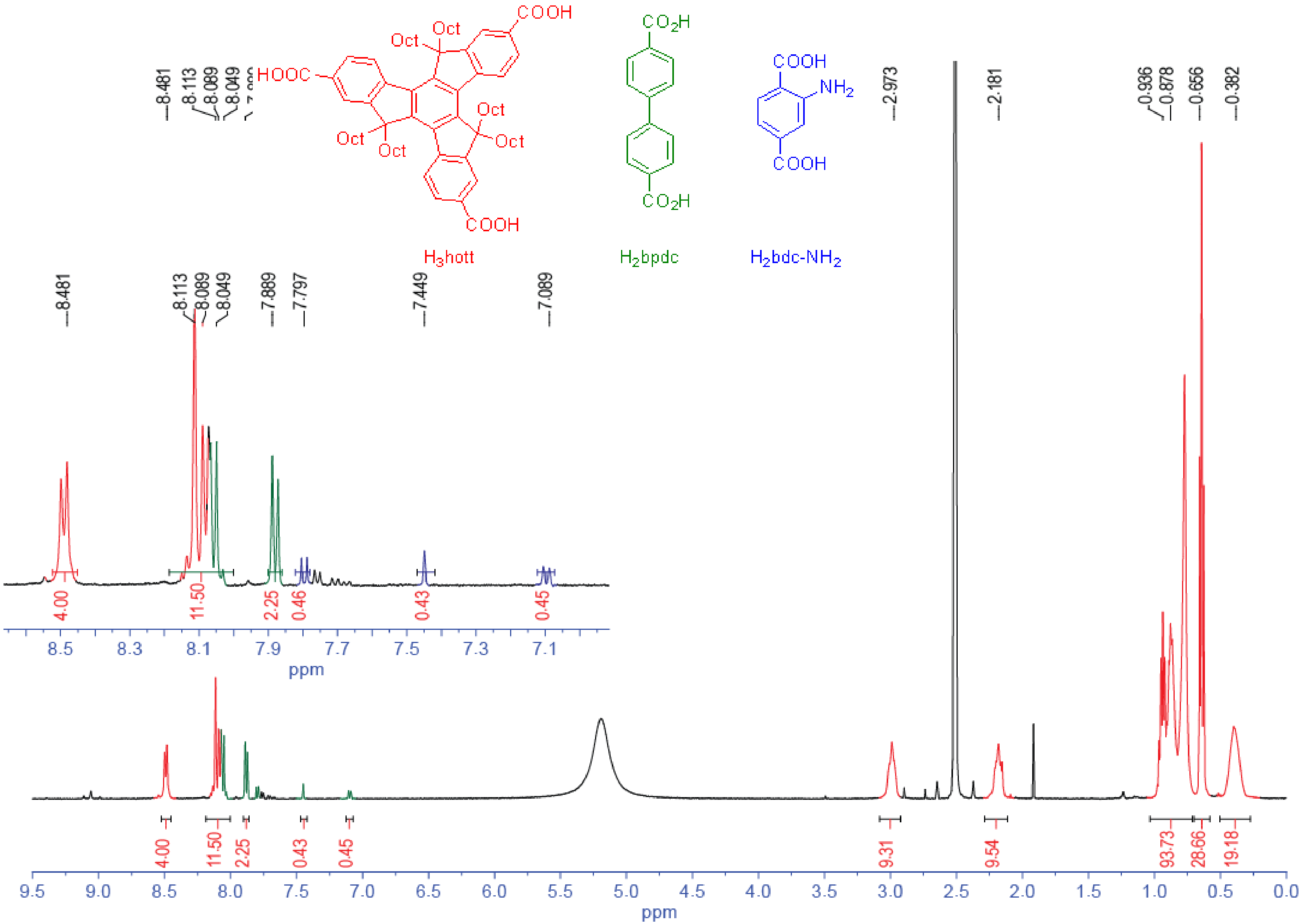

Figure S12: ^{1}H NMR spectrum of digested **12 -** [$Zn_4O(hott)_{4/3}(bpdc)_{1/2}(bdc\text{-}NH_2)_{1/2}$] showing integrals that match with the formula.

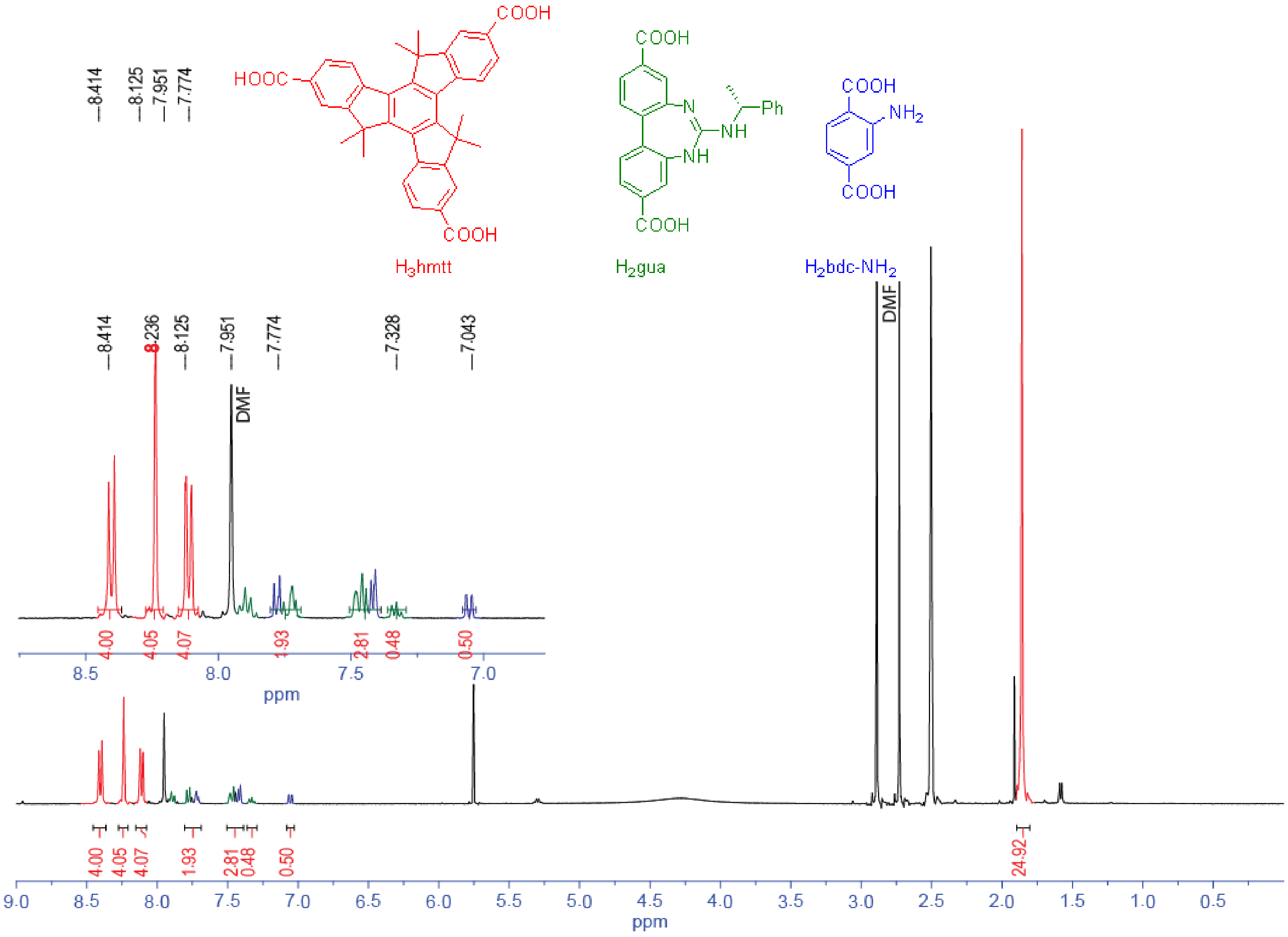

Figure S13: ^{1}H NMR spectrum of digested **13 -** $[\mathrm{Zn_4O(hmtt)_{4/3}(gua)_{1/2}(bdc\text{-}NH_2)_{1/2}}]$ showing integrals that match with the formula.

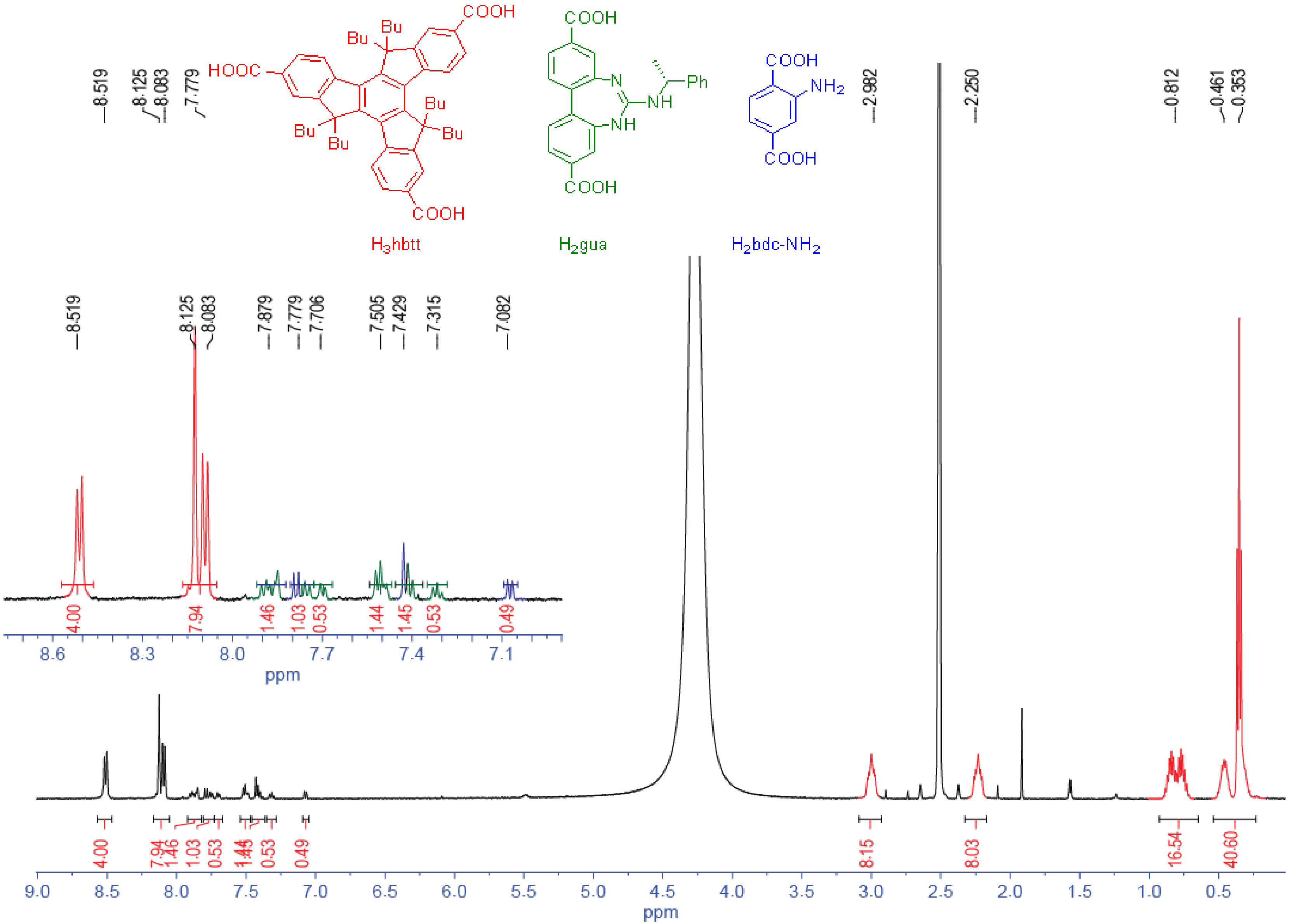

Figure S14: ^{1}H NMR spectrum of digested **14 -** [$Zn_4O(hbtt)_{4/3}(gua)_{1/2}(bdc\text{-}NH_2)_{1/2}$] showing integrals that match with the formula

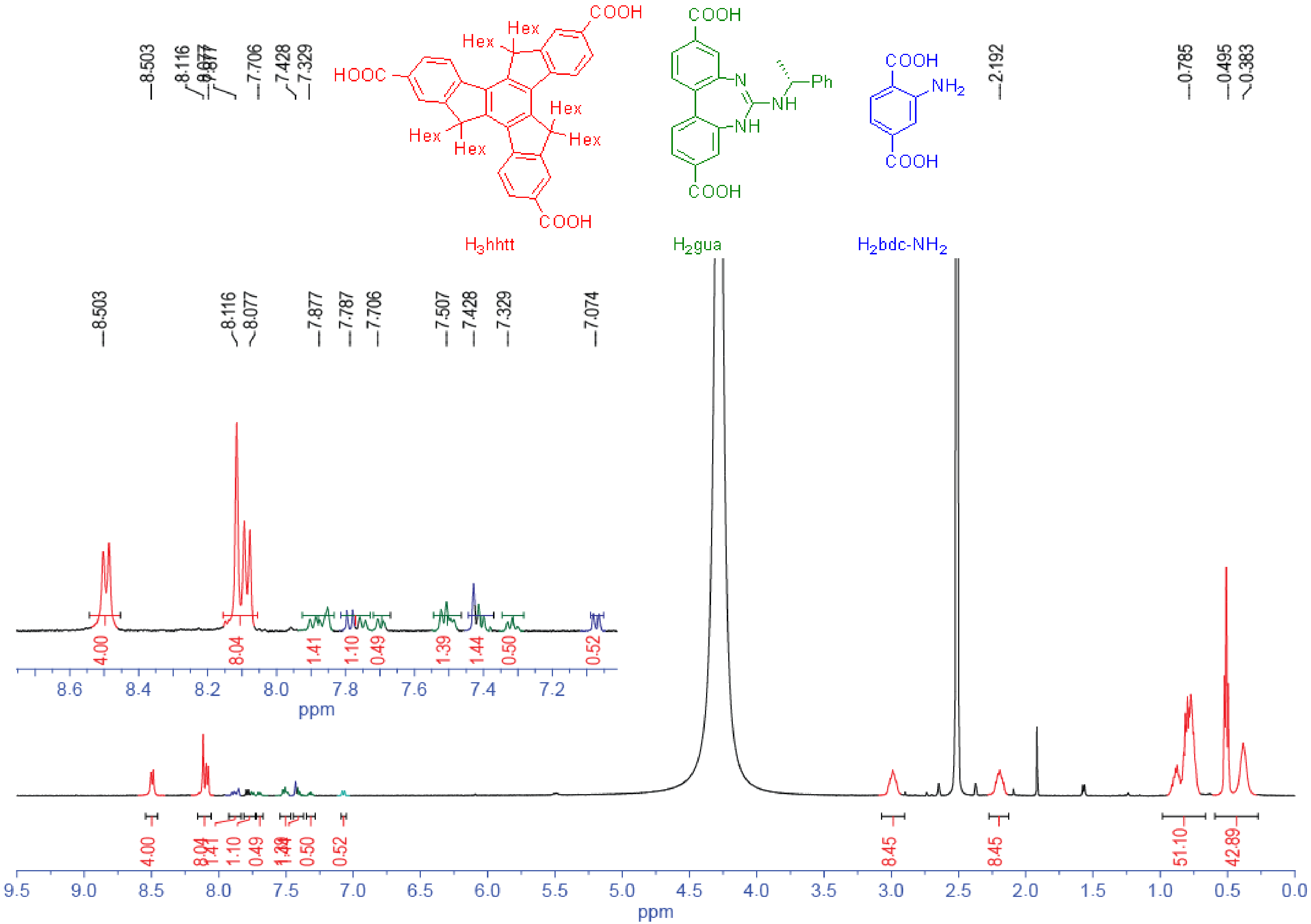

Figure S15: ^{1}H NMR spectrum of digested **15 -** [$Zn_4O(hhtt)_{4/3}(gua)_{1/2}(bdc\text{-}NH_2)_{1/2}$] showing integrals that match with the formula

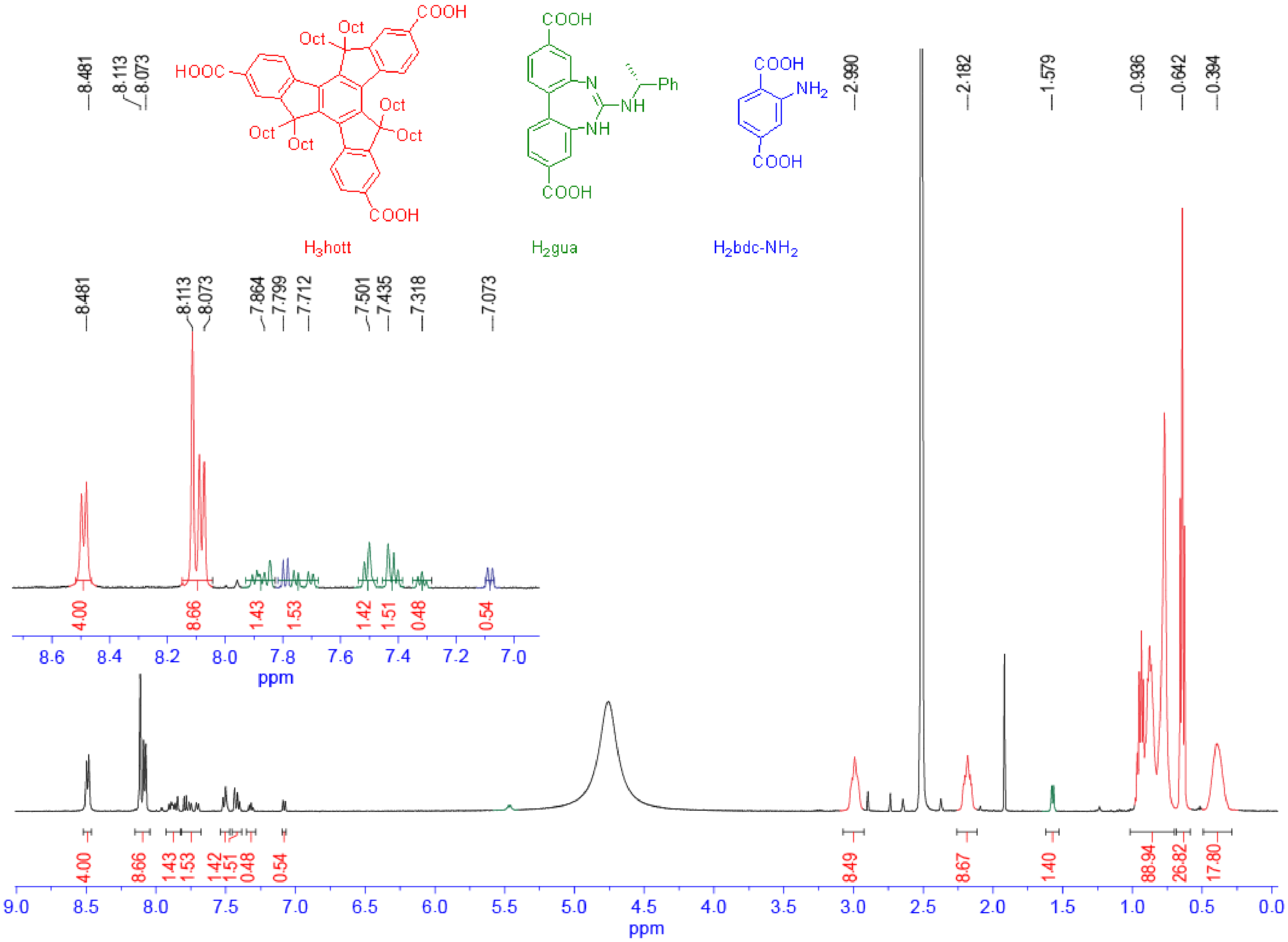

Figure S16: ^{1}H NMR spectrum of digested **16 -** [$Zn_4O(hott)_{4/3}(gua)_{1/2}(bdc\text{-}NH_2)_{1/2}$] showing integrals that match with the formula.

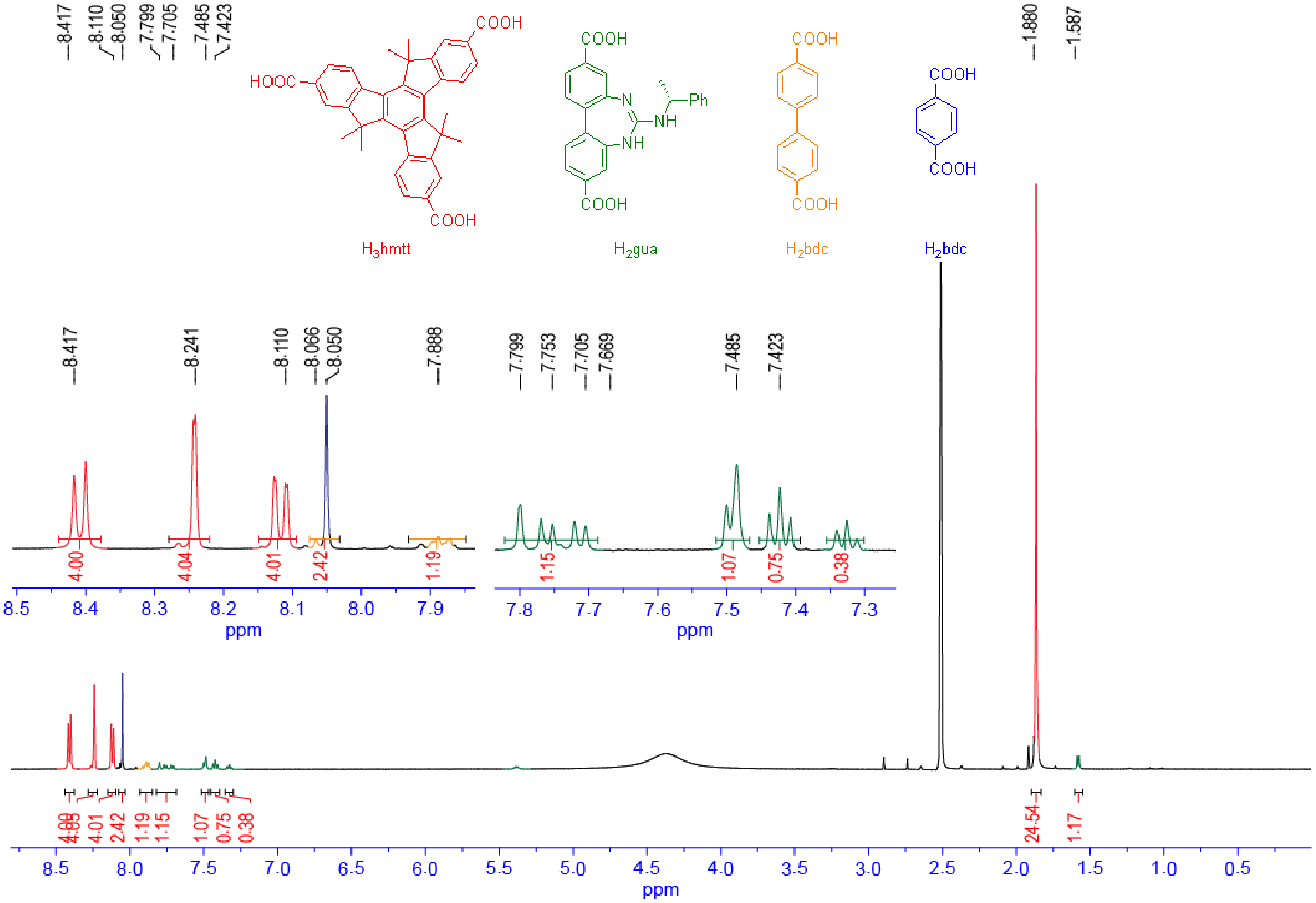

Figure S17: ^{1}H NMR spectrum of digested **17** – [Zn$_4$O(hmtt)$_{4/3}$(gua)$_x$(bpdc)$_y$(bdc)$_{1/2}$] with gua : bpdc = 4:1 showing integrals that match with the formula.

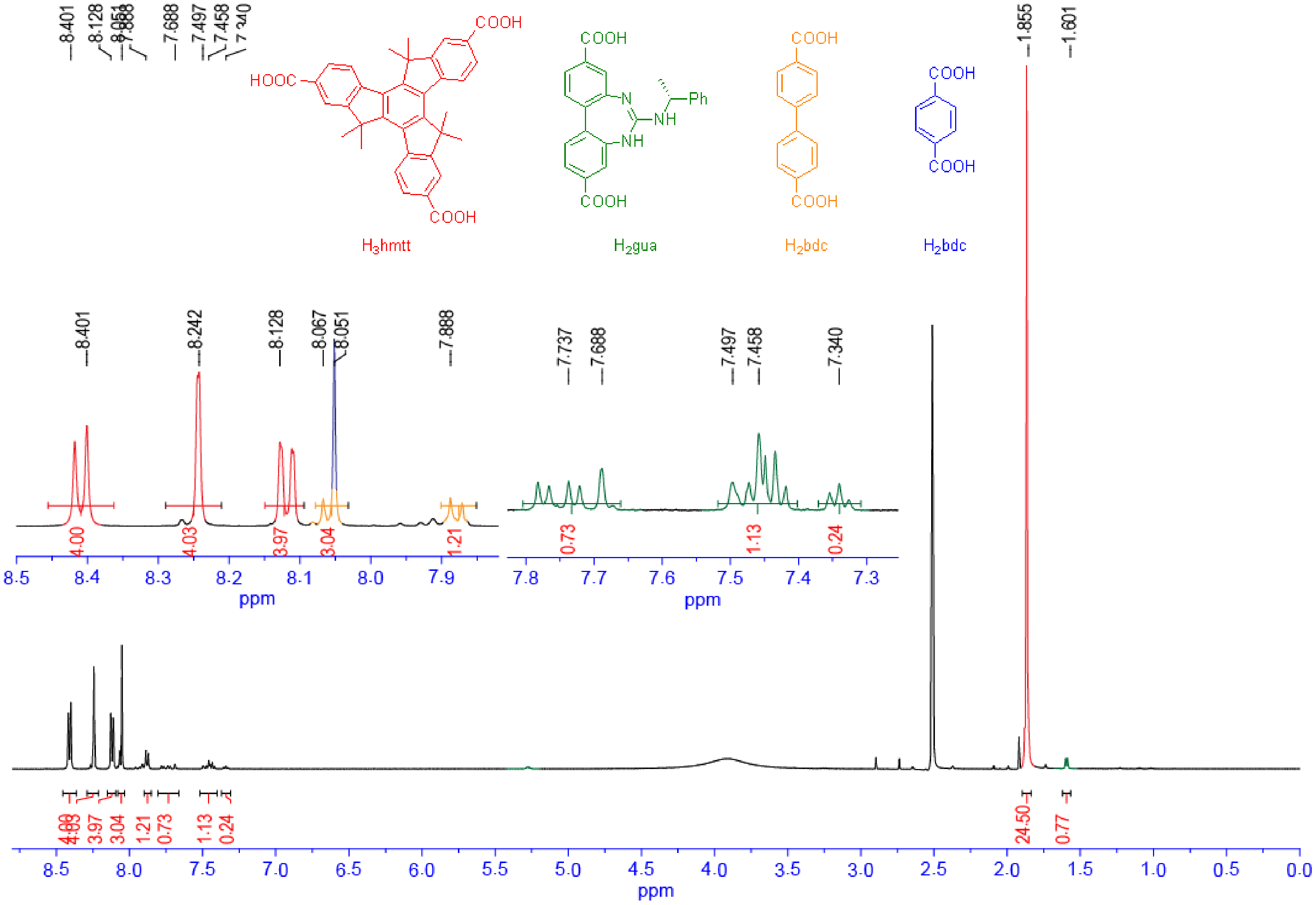

Figure S18: ^{1}H NMR spectrum of digested **18** – [$Zn_4O(hmtt)_{4/3}(gua)_x(bpdc)_y(bdc)_{1/2}$] with gua : bpdc = 1: 1 showing integrals that match with the formula.

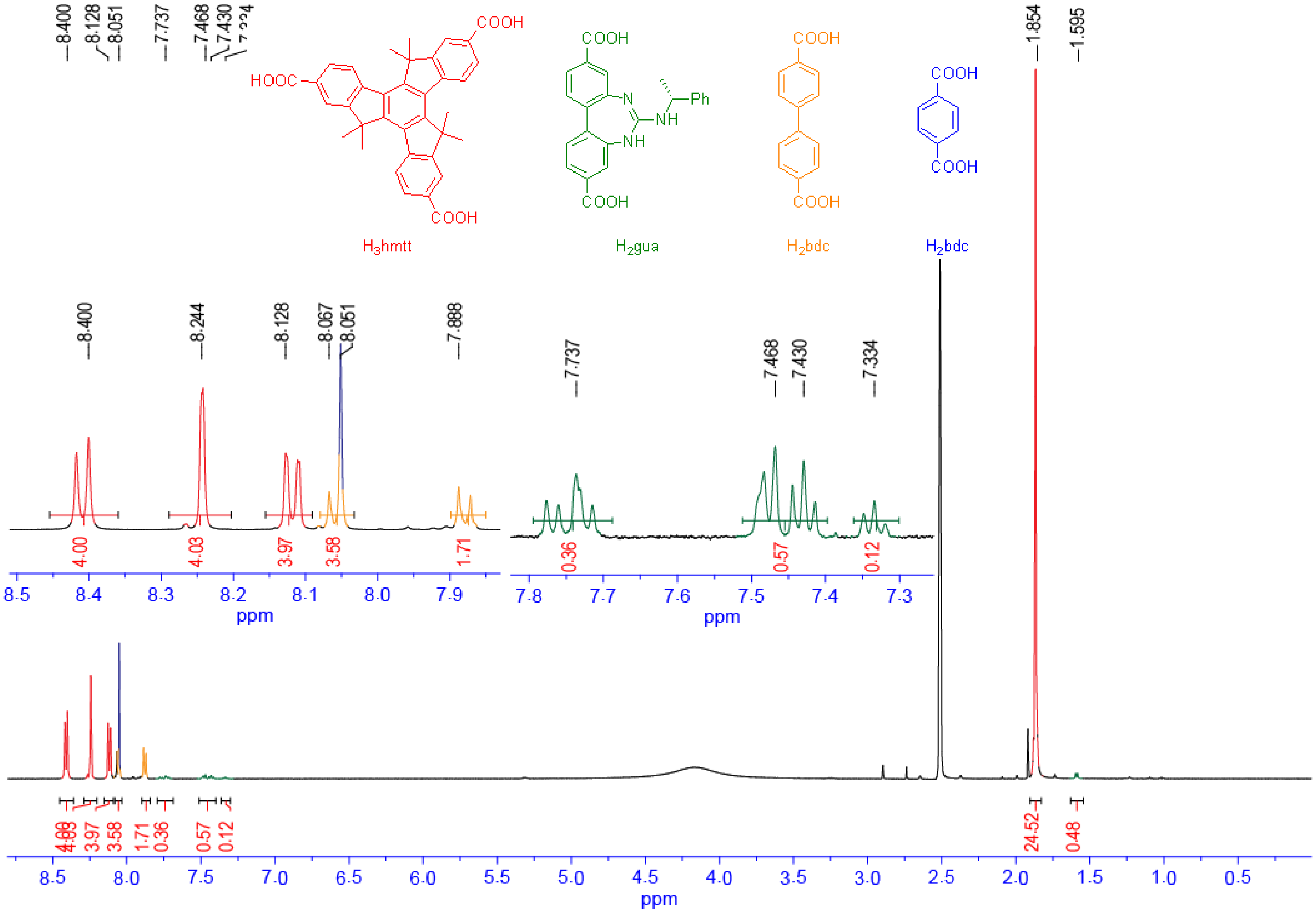

Figure S19: ^{1}H NMR spectrum of digested **19** – [Zn$_4$O(hmtt)$_{4/3}$(gua)$_x$(bpdc)$_y$(bdc)$_{1/2}$] with gua : bpdc = 1 : 3 showing integrals that match with the formula.

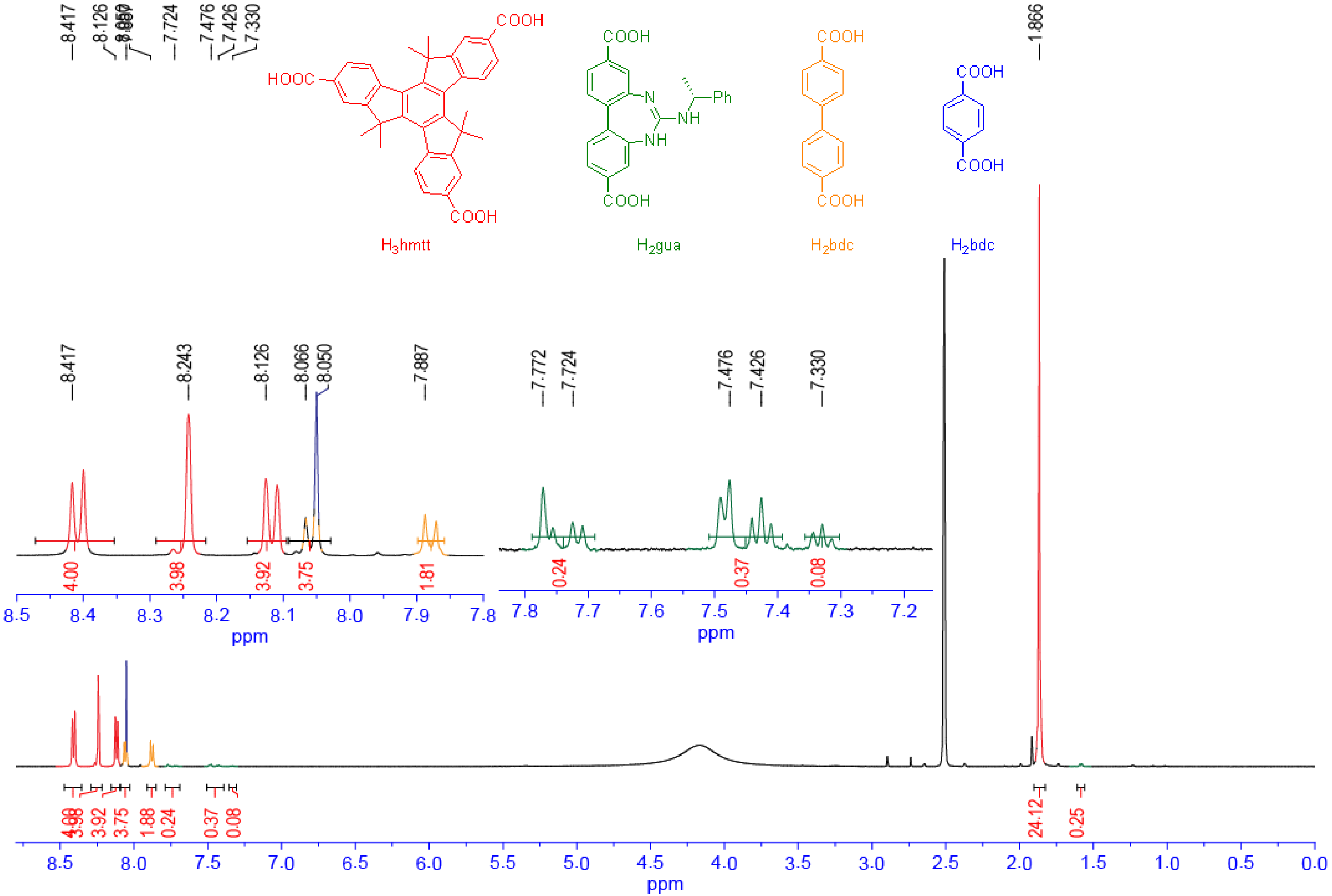

Figure S20: ^{1}H NMR spectrum of digested **20** – [Zn$_4$O(hmtt)$_{4/3}$(gua)$_x$(bpdc)$_y$(bdc)$_{1/2}$] with gua : bpdc = 1 : 5.6 showing integrals that match with the formula.

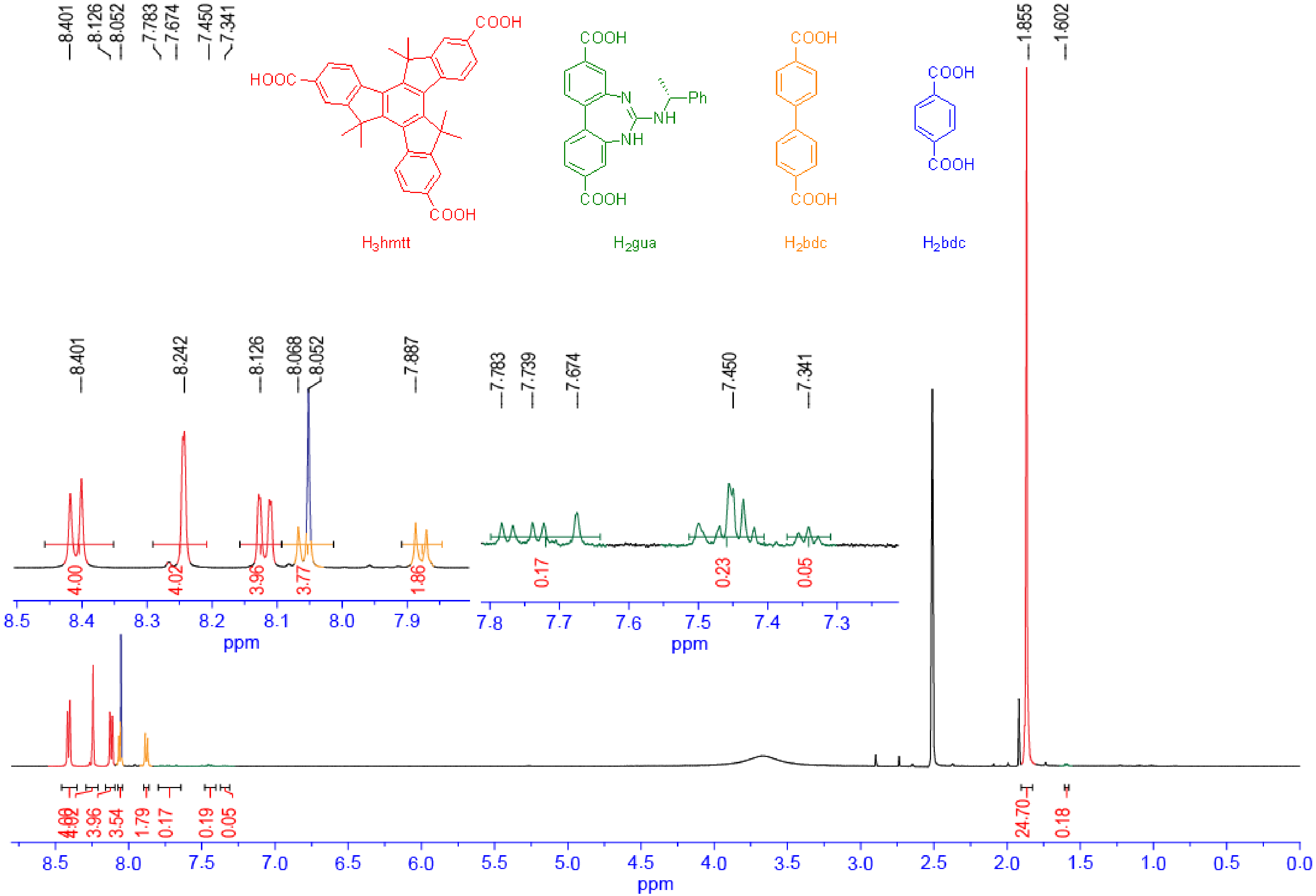

Figure S21: ^{1}H NMR spectrum of digested **21** – [Zn$_4$O(hmtt)$_{4/3}$(gua)$_x$(bpdc)$_y$(bdc)$_{1/2}$] with gua : bpdc = 1 : 9 showing integrals that match with the formula.

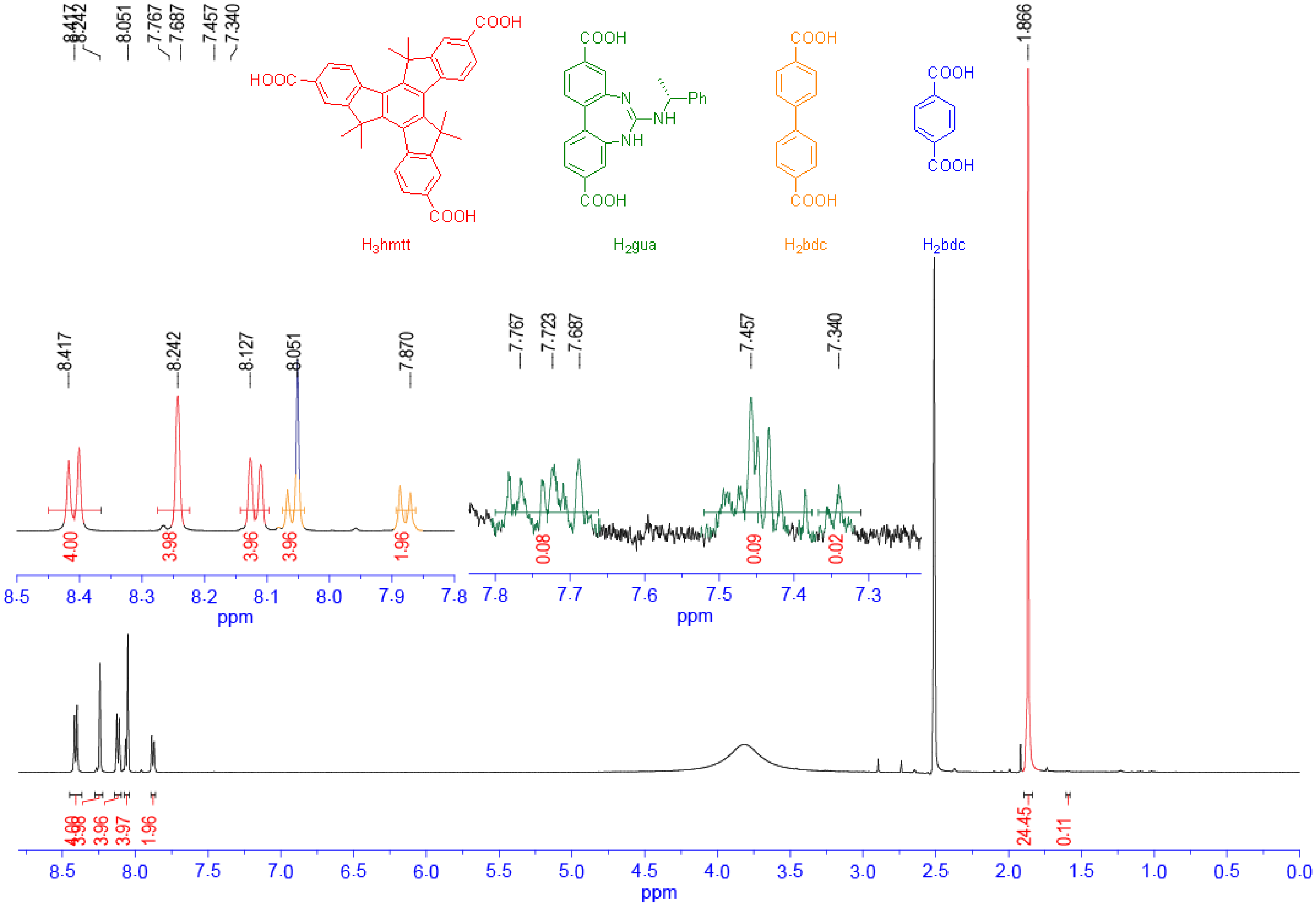

Figure S22: ^{1}H NMR spectrum of digested **22** – [Zn$_4$O(hmtt)$_{4/3}$(gua)$_x$(bpdc)$_y$(bdc)$_{1/2}$] with gua : bpdc = 1 : 19 showing integrals that match with the formula.

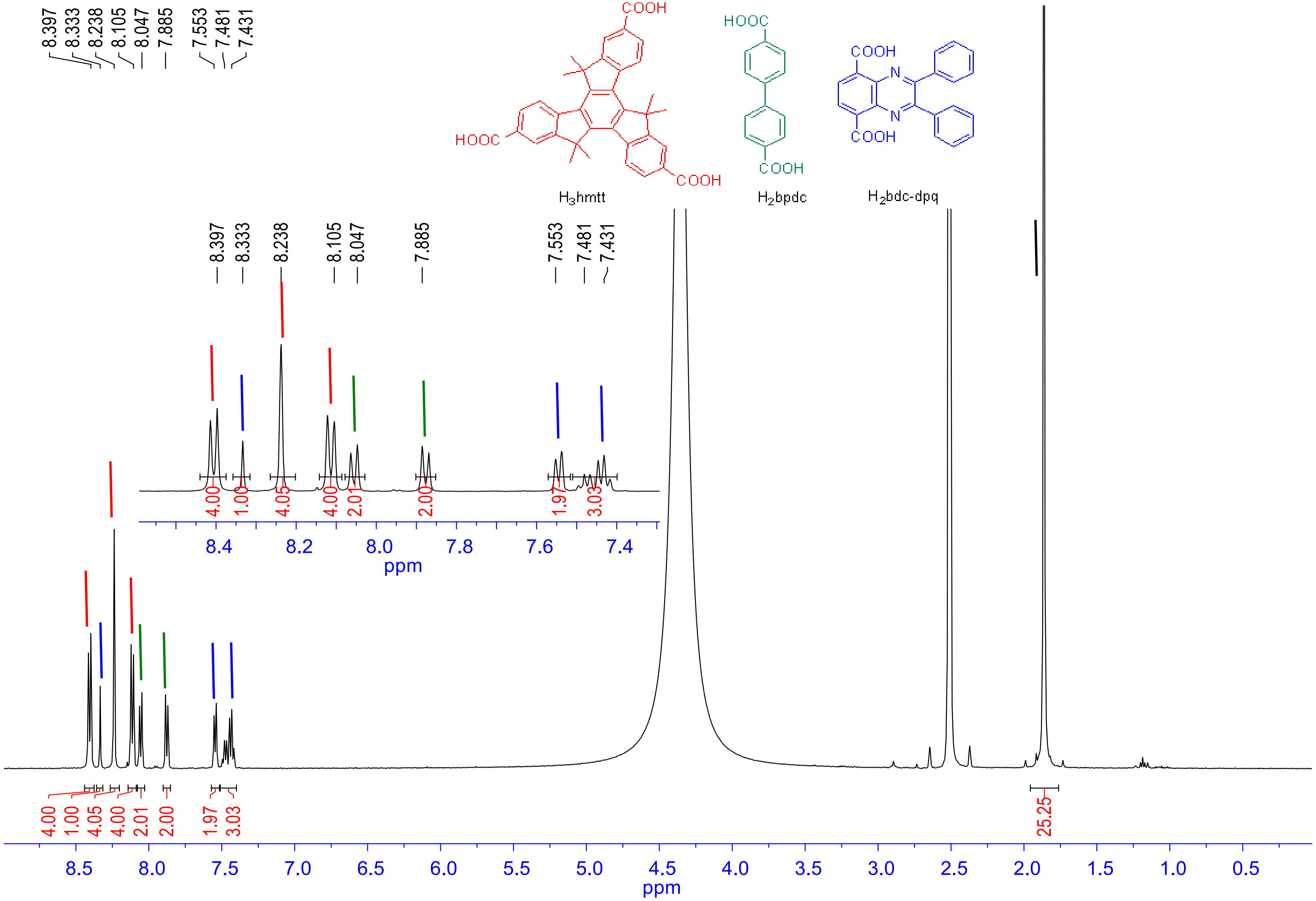

Figure S23: ^{1}H NMR spectrum of digested MUF-7-**bdc-dpq** - [Zn$_4$O(hmtt)$_{4/3}$(bpdc)$_{1/2}$(**bdc-dpq**)$_{1/2}$] showing integrals that match with the formula.

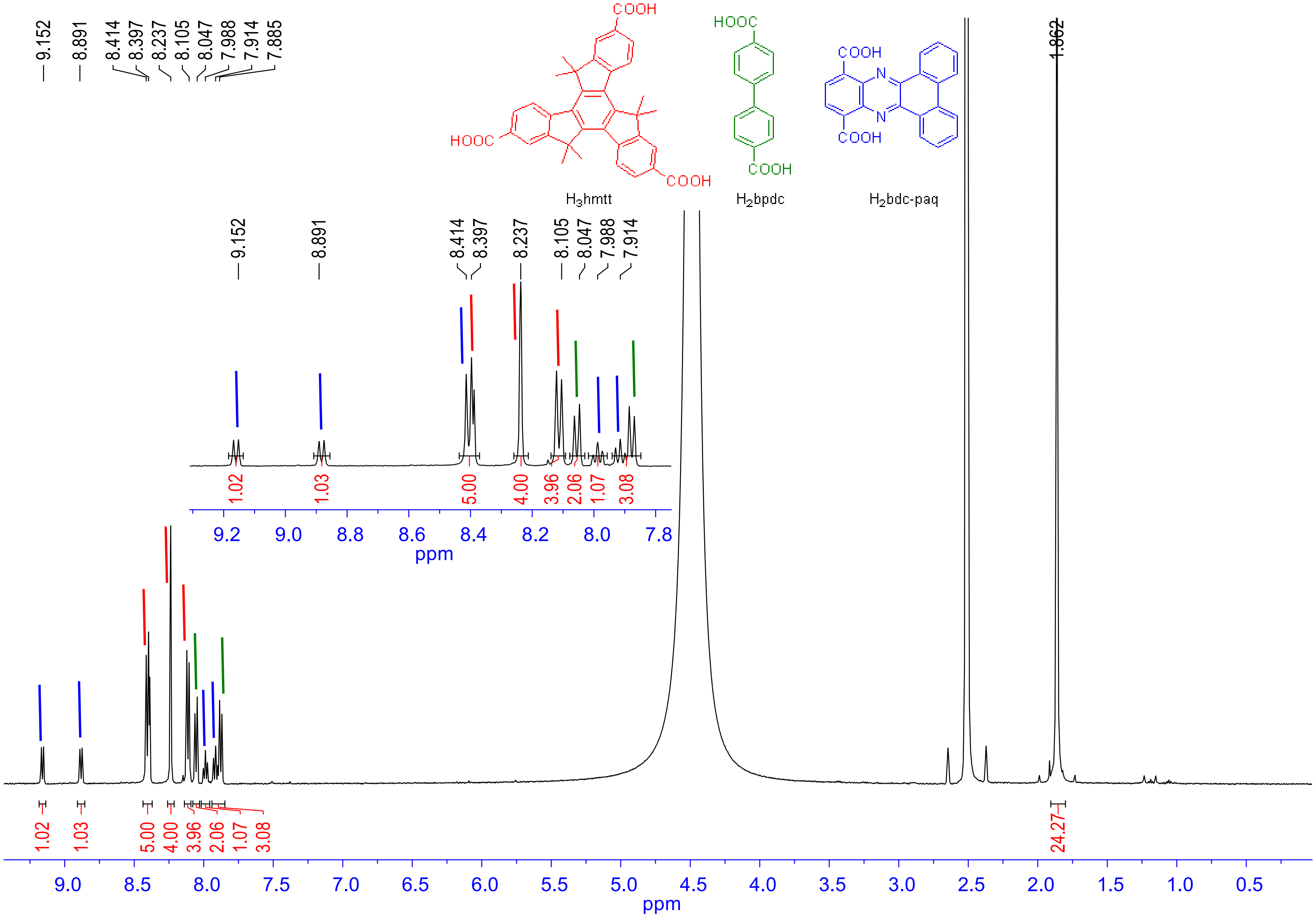

Figure S24: ^{1}H NMR spectrum of digested MUF-77-**bdc-paq-** [Zn$_4$O(hmtt)$_{4/3}$(bpdc)$_{1/2}$(**bdc-paq**)$_{1/2}$] showing integrals that match with the formula.

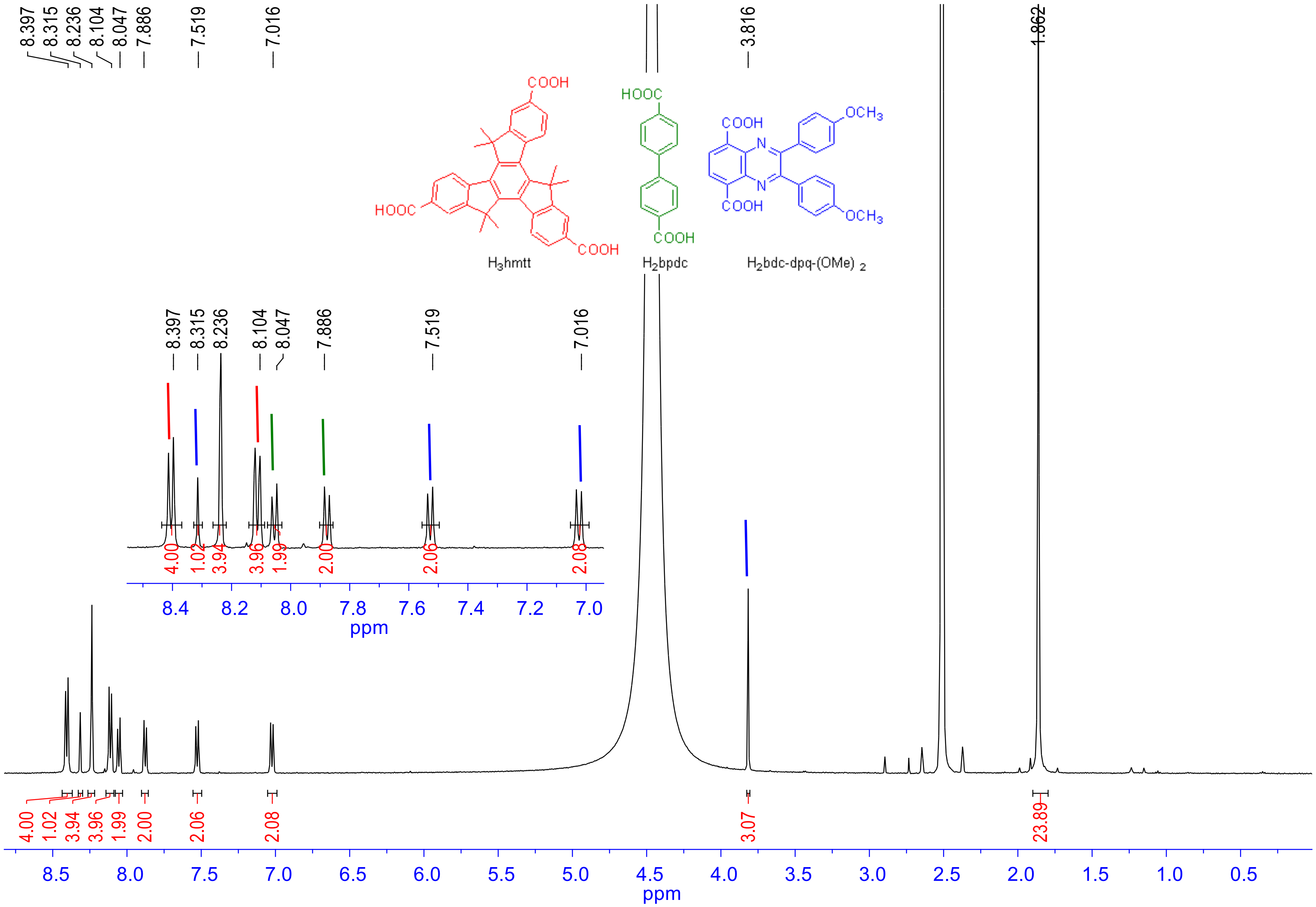

Figure S25: ^{1}H NMR spectrum of digested MUF-7-**bdc-dpq-(OMe)$_2$** - [$Zn_4O(hmtt)_{4/3}(bpdc)_{1/2}$**(bdc-dpq-(OMe)$_2$)**$_{1/2}$] showing integrals that match with the formula.

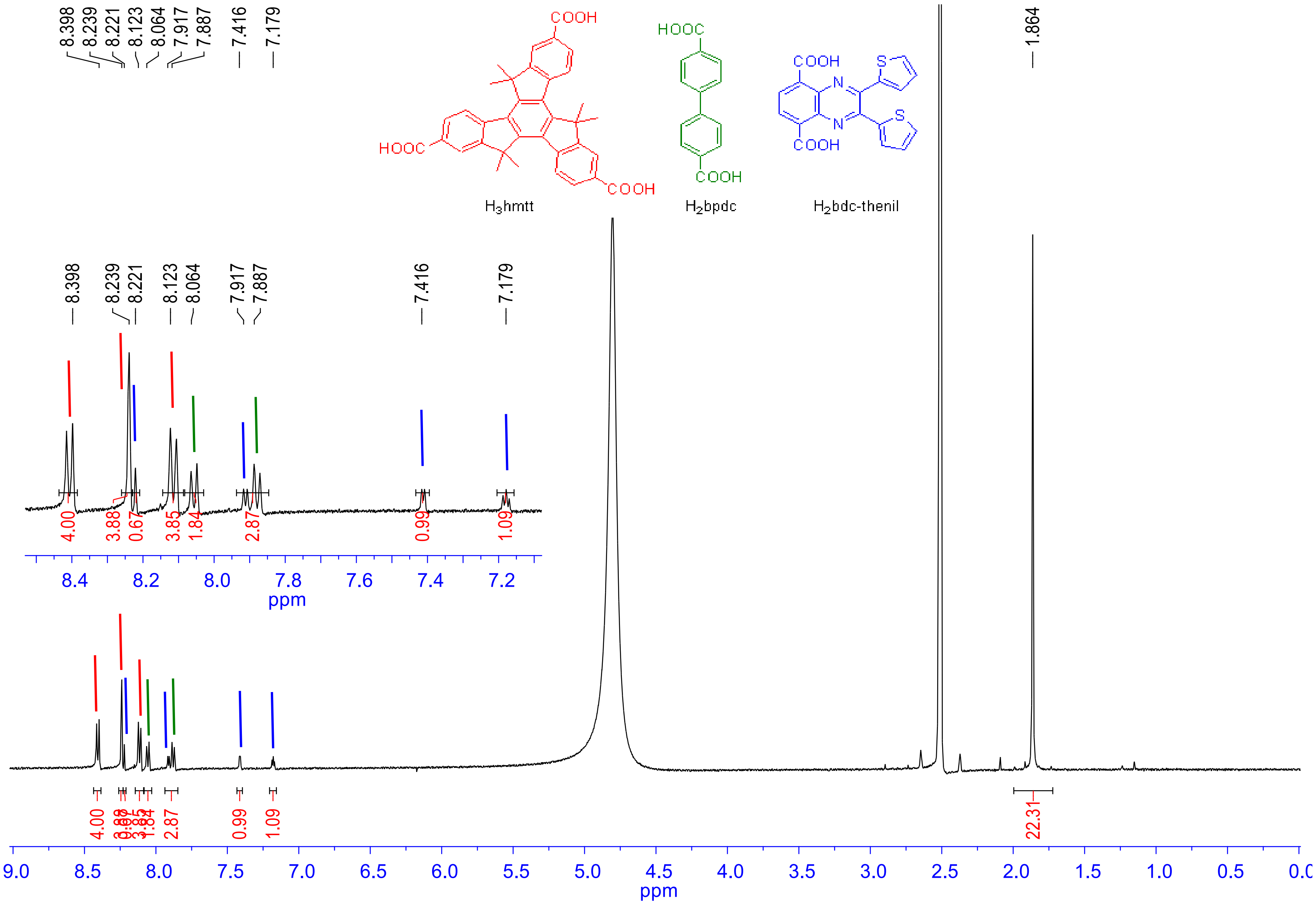

Figure S26: ^{1}H NMR spectrum of digested MUF-77-**bdc-thenil** - [$Zn_4O(hmtt)_{4/3}(bpdc)_{1/2}$(**bdc-thenil**)$_{1/2}$] showing integrals that match with the formula.

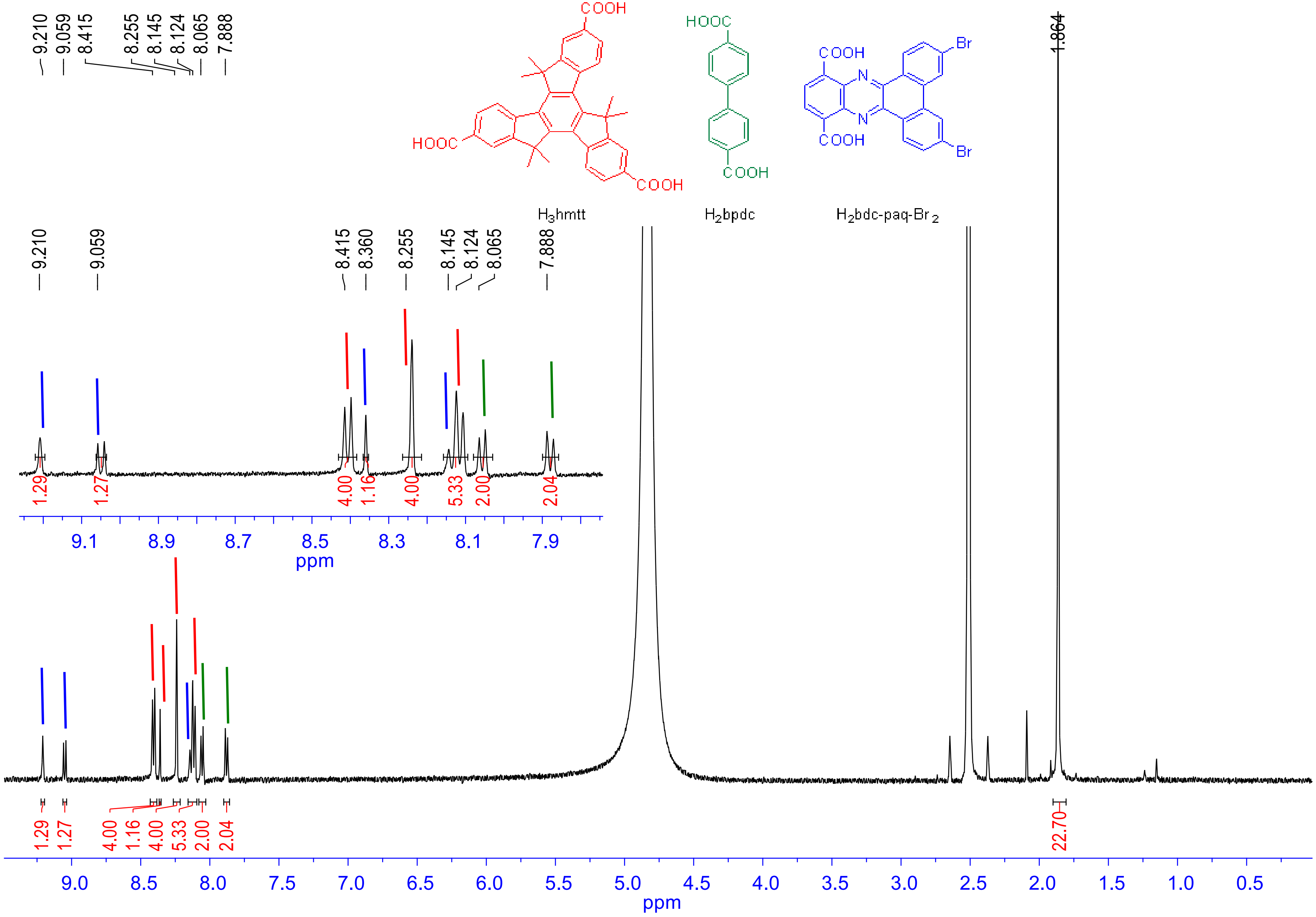

Figure S27: ^{1}H NMR spectrum of digested MUF-77-**bdc-paq-Br$_2$** - [Zn_4O(hmtt)$_{4/3}$(bpdc)$_{1/2}$(**bdc-paq-Br$_2$**)$_{1/2}$] showing integrals that match with the formula.

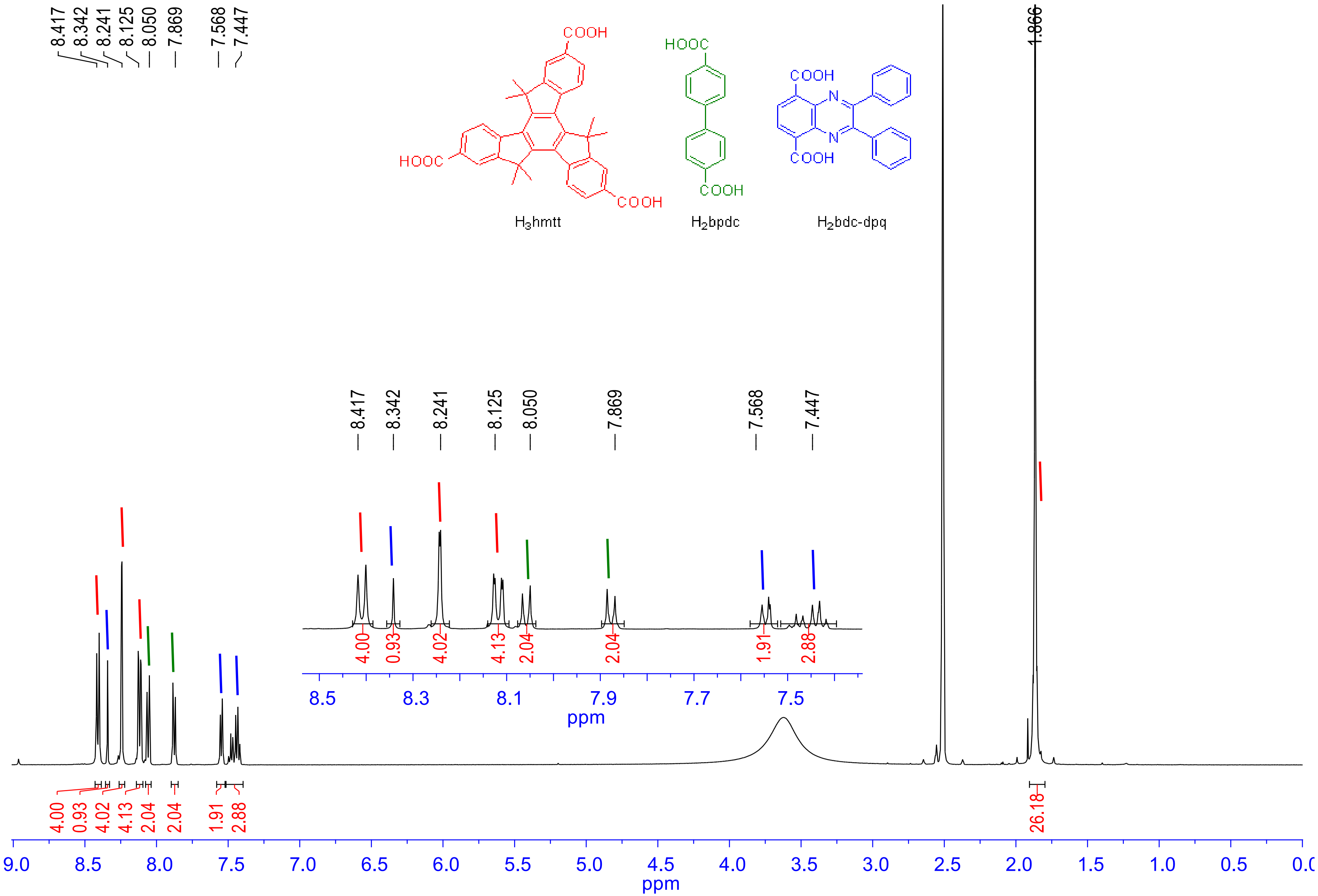

Figure S28: ^{1}H NMR spectrum of digested NC-MUF-7-**bdc-dpq** - [Zn$_4$O(hmtt)$_{4/3}$(bpdc)$_{1/2}$(**bdc-dpq**)$_{1/2}$] showing integrals that match with the formula.

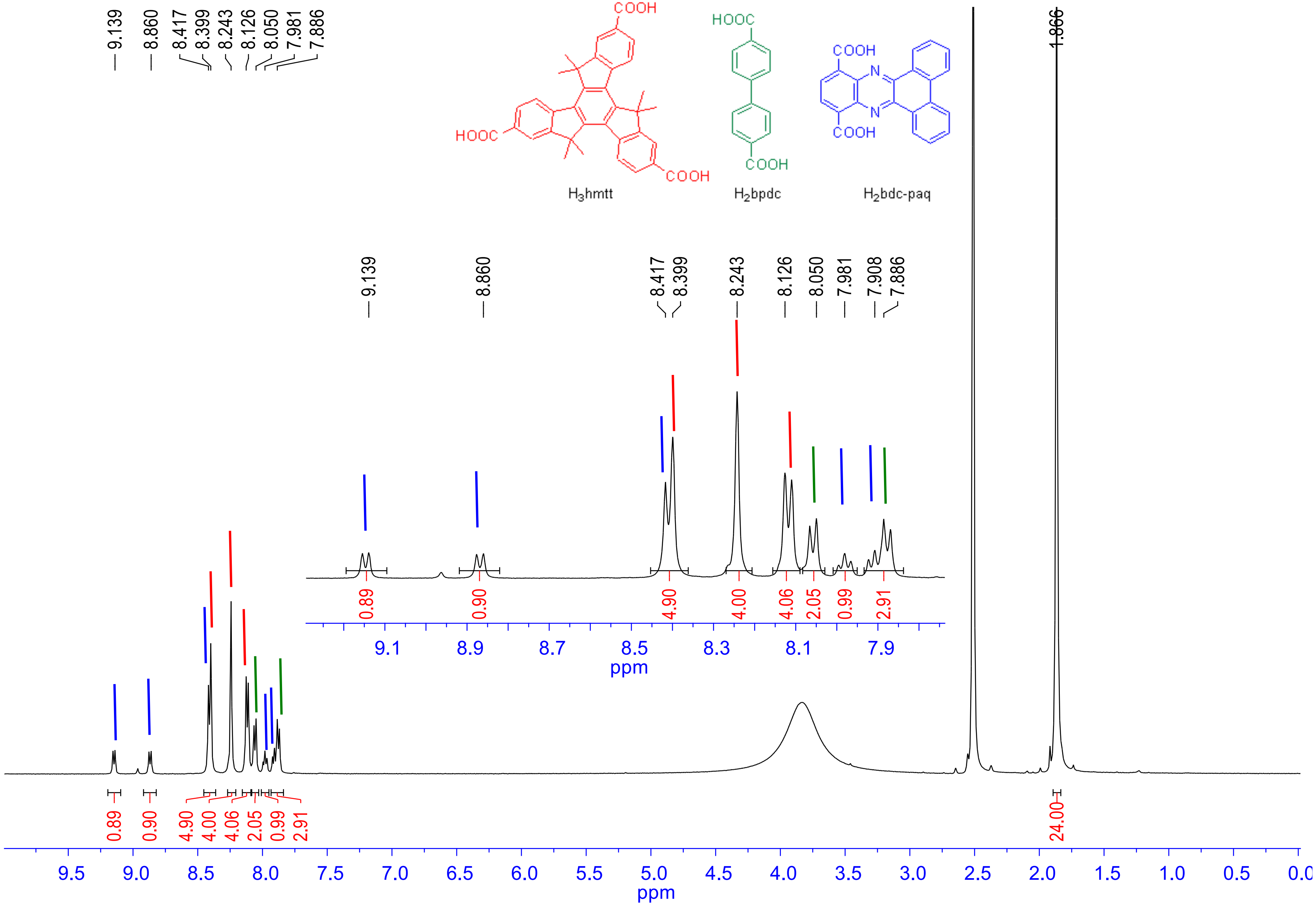

Figure S29: ^{1}H NMR spectrum of digested, NC-MUF-77-**bdc-paq** - [Zn$_4$O(hmtt)$_{4/3}$(bpdc)$_{1/2}$(**bdc-paq**)$_{1/2}$] showing integrals that match with the formula.

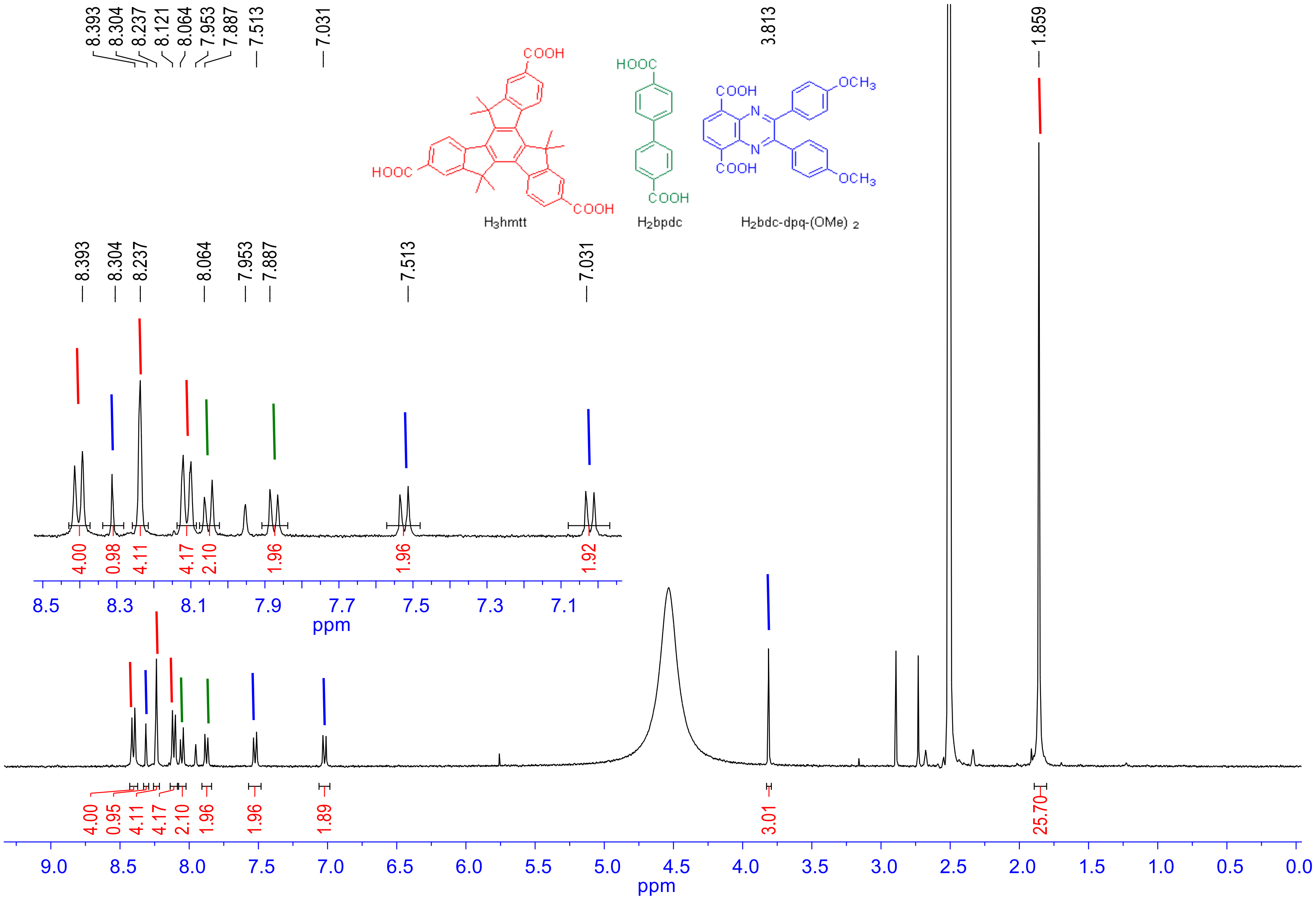

Figure S30: ^{1}H NMR spectrum of digested NC-MUF-77-**bdc-dpq-(OMe)$_2$** - [Zn$_4$O(hmtt)$_{4/3}$(bpdc)$_{1/2}$**(bdc-dpq-(OMe)$_2$)**$_{1/2}$] showing integrals that match with the formula.

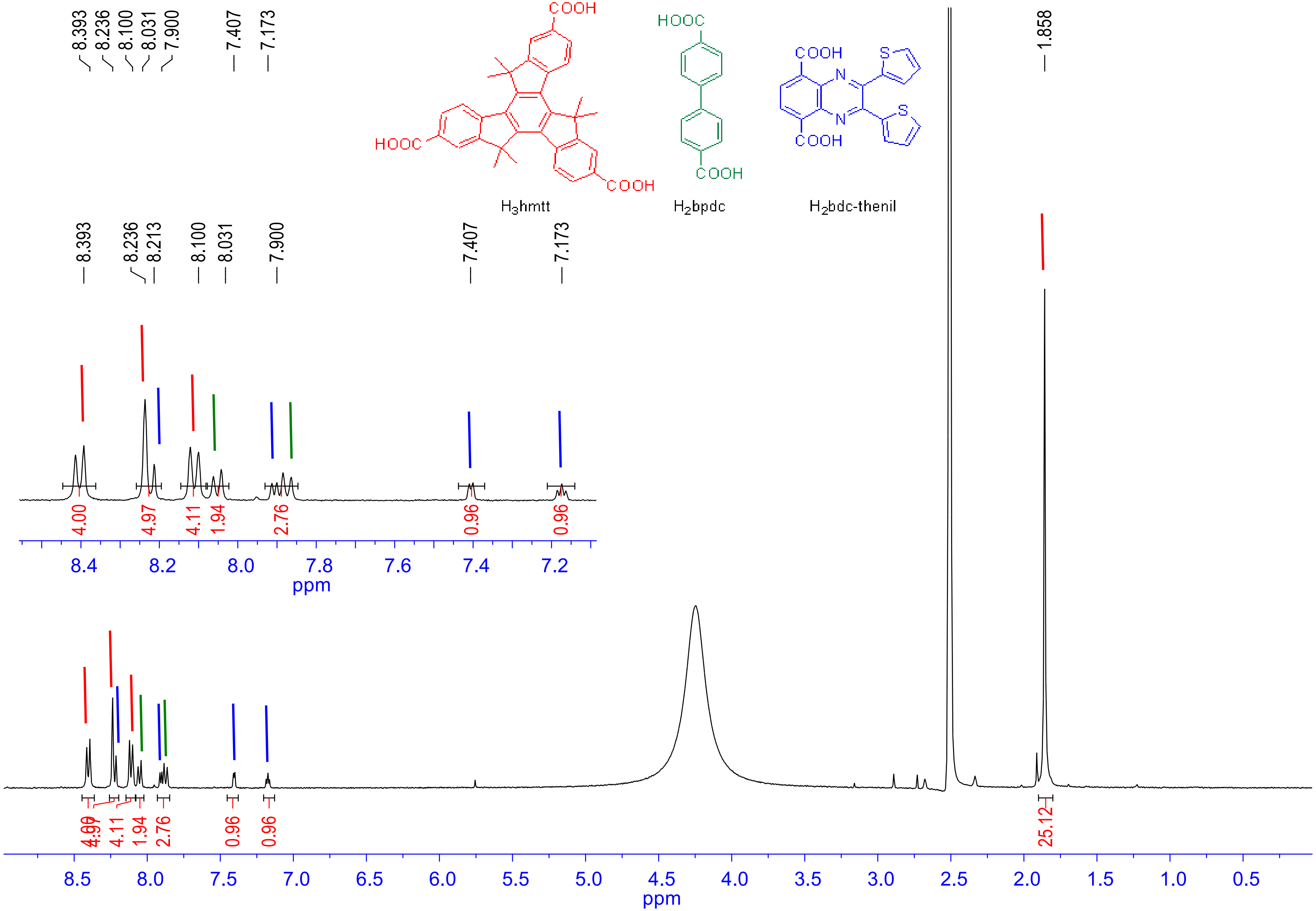

Figure S31: ^{1}H NMR spectrum of digested NC-MUF-77-**bdc-thenil** - [$Zn_4O(hmtt)_{4/3}(bpdc)_{1/2}$(**bdc-thenil**)$_{1/2}$] showing integrals that match with the formula.

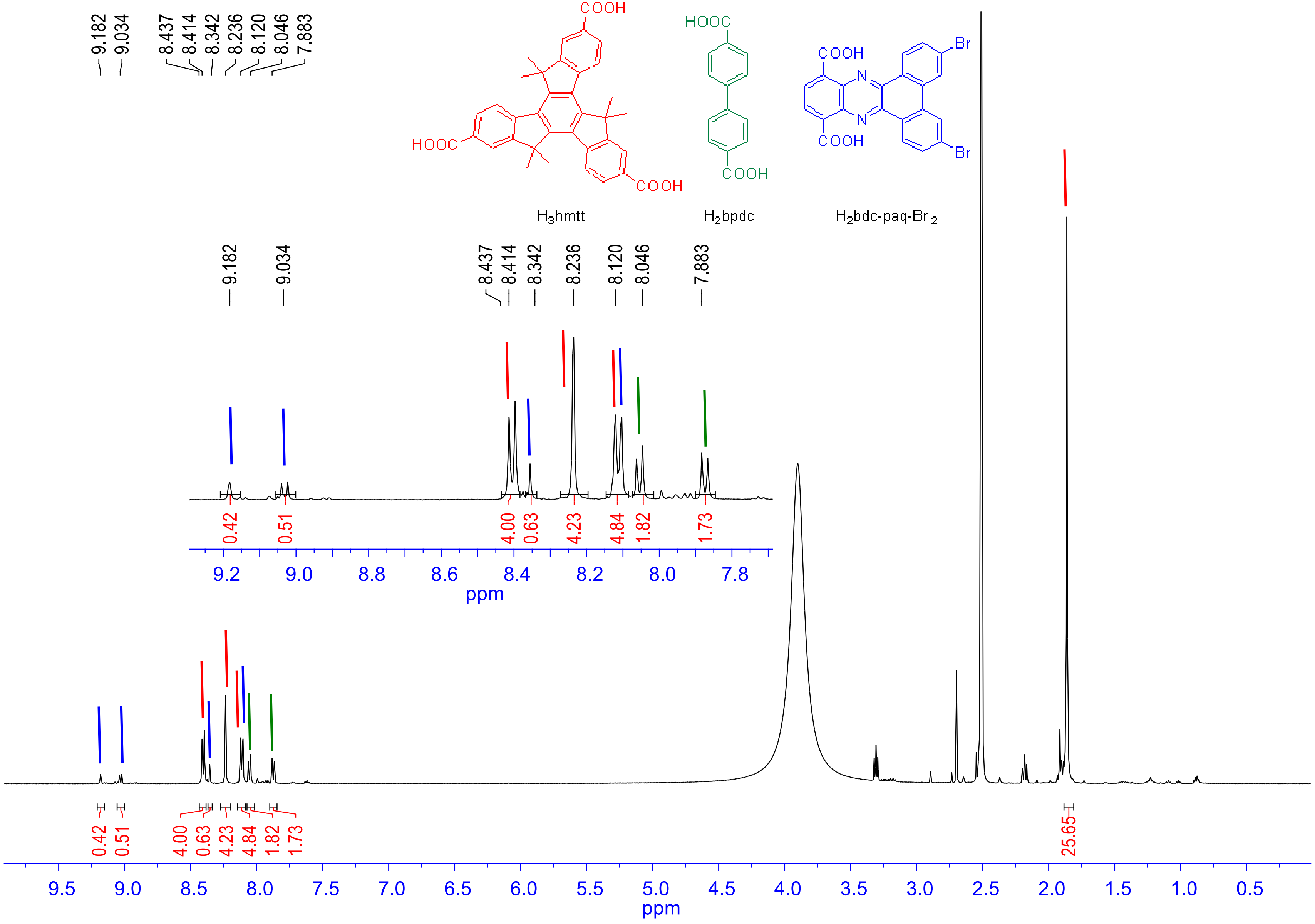

Figure S32: ^{1}H NMR spectrum of digested NC-MUF-77-bdc-**paq-Br$_2$ -** [Zn$_4$O(hmtt)$_{4/3}$(bpdc)$_{1/2}$(**bdc-paq-Br$_2$**)$_{1/2}$].

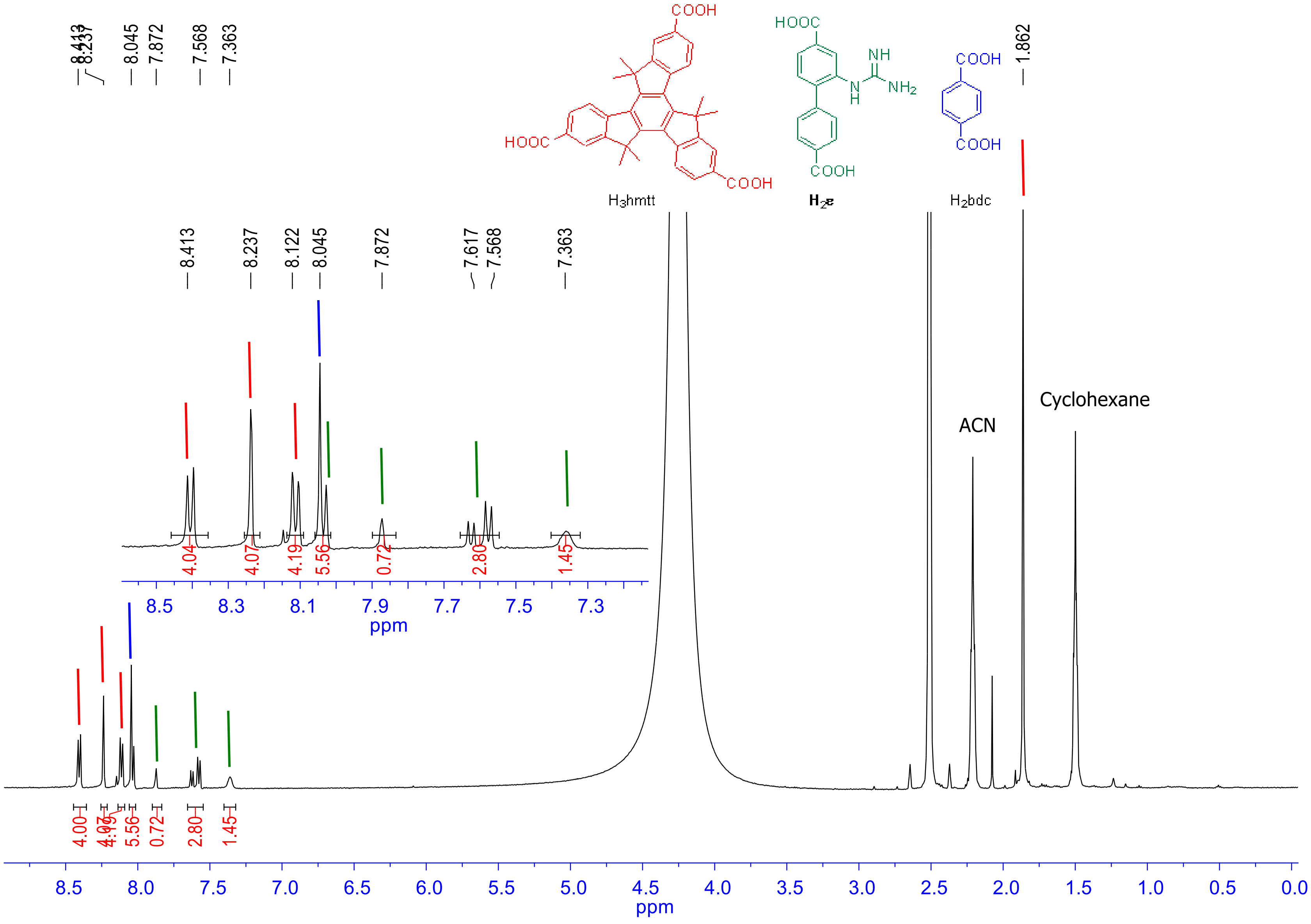

Figure S33: ^{1}H NMR spectrum of digested MUF-77-Me-**ε** - [$Zn_4O(hmtt)_{4/3}(bpdc\text{-}\varepsilon)_{1/2}(bdc)_{1/2}$] showing integrals that match with the formula.

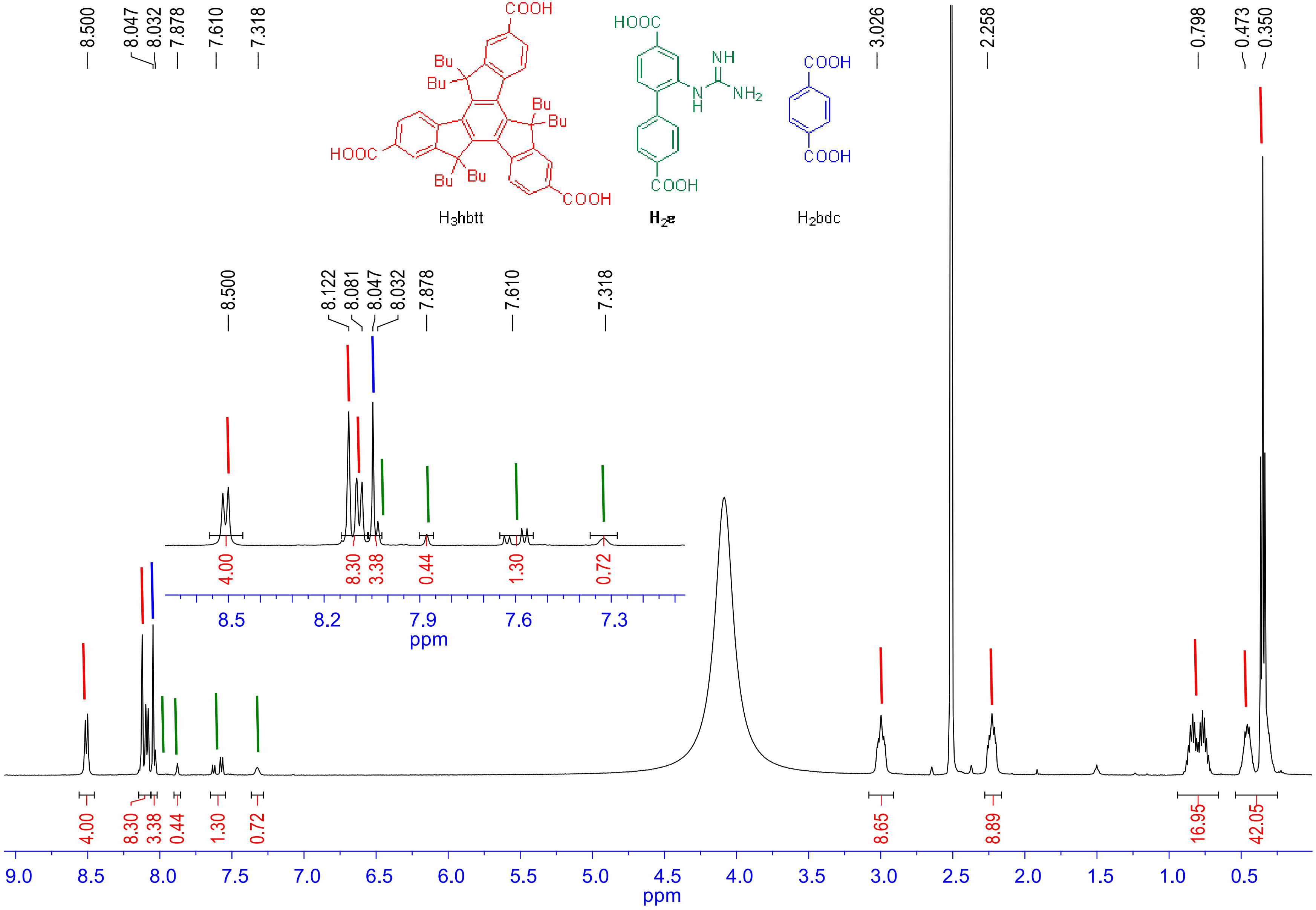

Figure S34: ^{1}H NMR spectrum of digested MUF-77-Bu-**ε** - [$Zn_4O(hbtt)_{4/3}$(bpdc-**ε**)$_{1/2}$(bdc)$_{1/2}$] showing integrals that match with the formula.

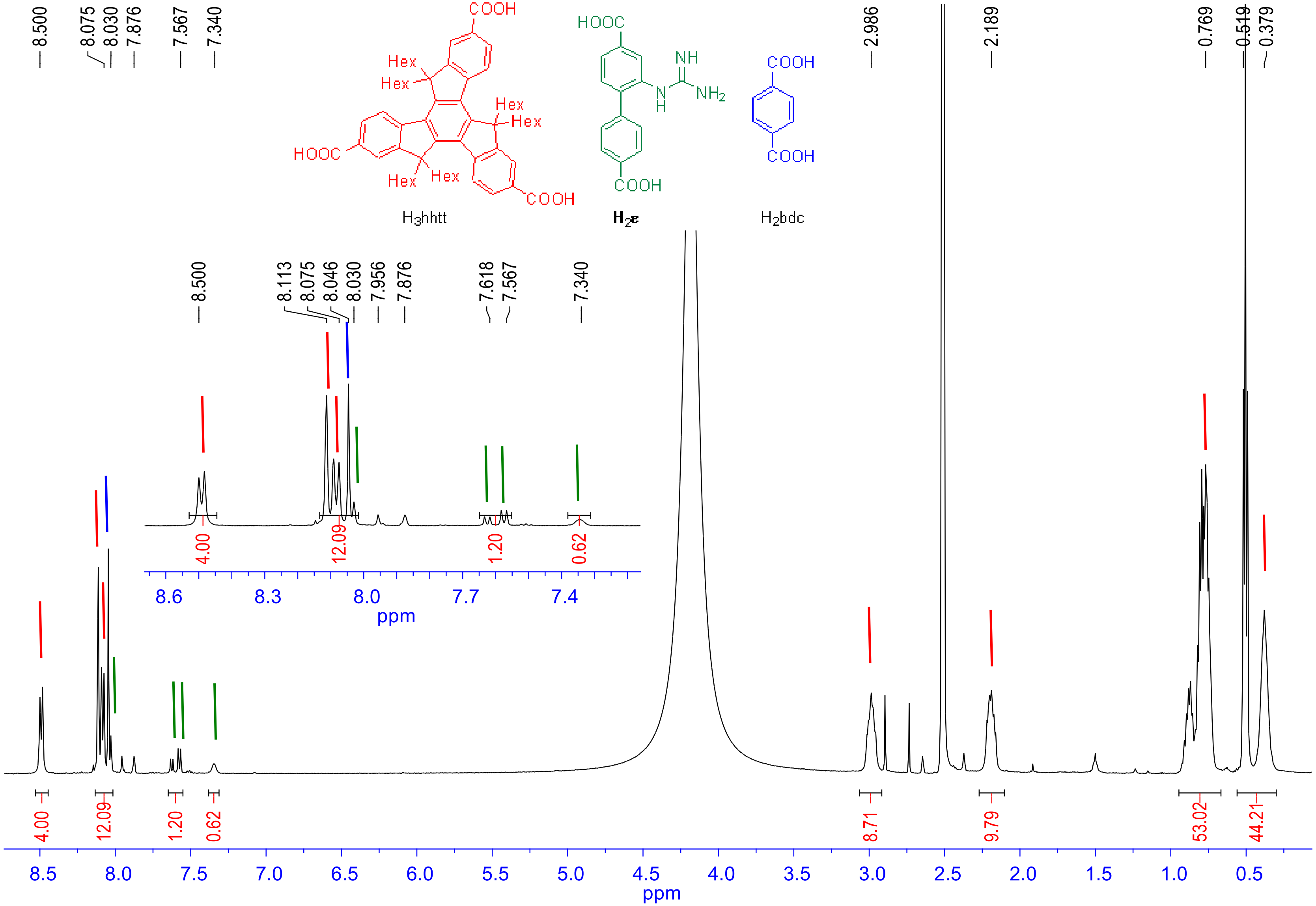

Figure S35: ^{1}H NMR spectrum of digested MUF-77-Hex-**ε** - [$Zn_4O(hhtt)_{4/3}(bpdc\text{-}\boldsymbol{\varepsilon})_{1/2}(bdc)_{1/2}$] showing integrals that match with the formula.

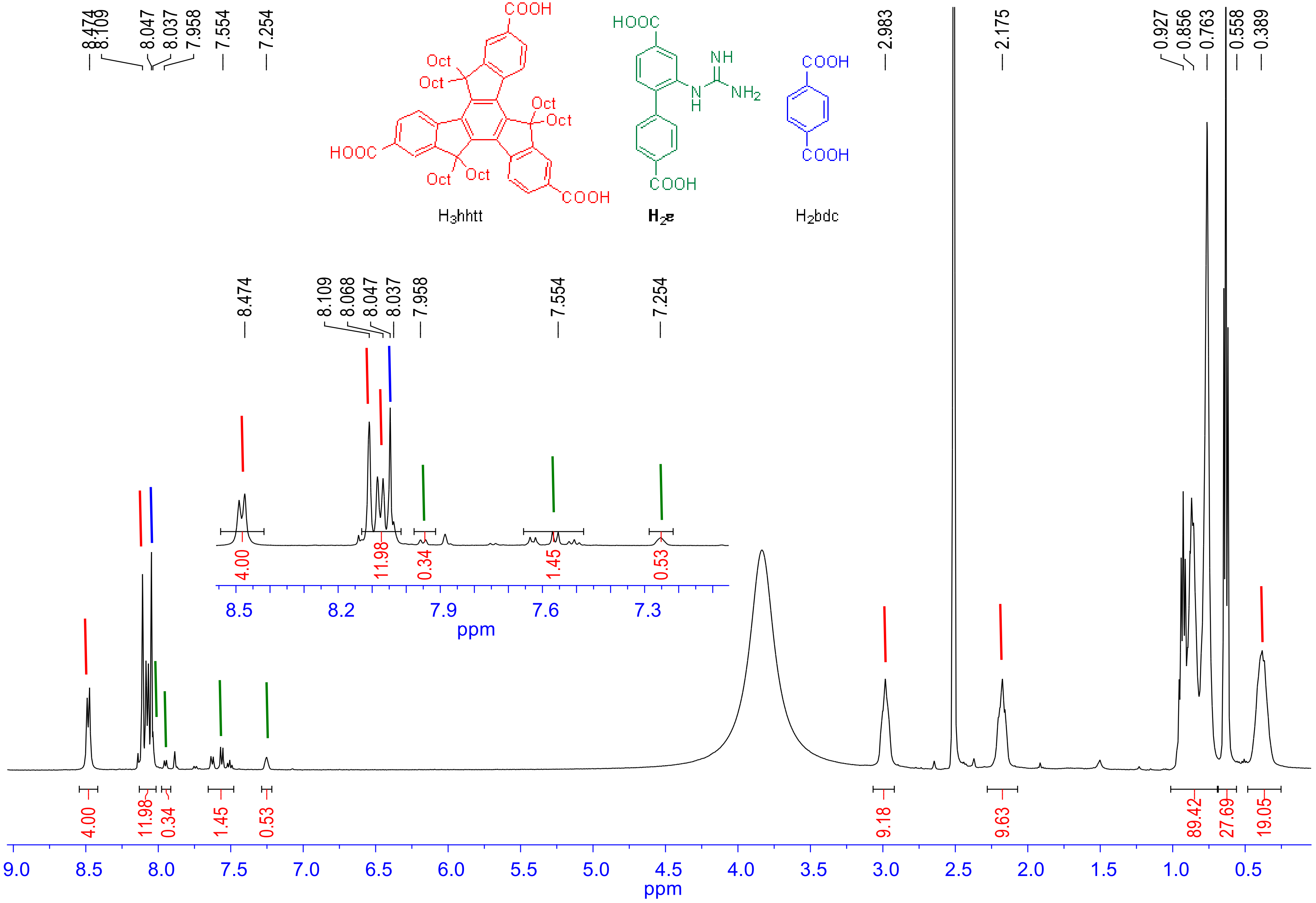

Figure S36: ^{1}H NMR spectrum of digested MUF-77-Oct-**ε** - [$Zn_4O(hott)_{4/3}(bpdc\text{-}\boldsymbol{\varepsilon})_{1/2}(bdc)_{1/2}$] showing integrals that match with the formula.